John von Neumann Institute for Computing

The NIC Research Groups

Thomas Lippert

published in

NIC Symposium 2006 ,
G. Münster, D. Wolf, M. Kremer (Editors),
John von Neumann Institute for Computing, Jülich,
NIC Series, Vol. **32**, ISBN 3-00-017351-X, pp. 1-2, 2006.

http://www.fz-juelich.de/nic-series/volume32

The NIC Research Groups

Thomas Lippert

Central Institute for Applied Mathematics, John von Neumann Institute for Computing (NIC)
Research Center Jülich, 52425 Jülich, Germany
Department C, Bergische Universität Wuppertal, 42097 Wuppertal, Germany
E-mail: th.lippert@fz-juelich.de

With the foundation of the John von Neumann Institute for Computing (NIC) in 1987, the former "Höchstleistungsrechenzentrum HLRZ" and first National German Supercomputing Centre, the NIC contractors—at that time the Forschungszentrum Jülich (FZJ), the German Electron Synchrotron (DESY) and the once National Research Centre for Information Technology (GMD)—decided to fund topical research groups working in selected fields of computational science.

Currently, FZJ operates the research group "Computational Biology and Biophysics". The group succeeds the former research group "Complex Systems", which acted at the interface between biology and physics, and was led by Prof. Peter Graßberger. After Graßberger's retirement, the Computational Biology and Biophysics group started in July 2005 under Prof. Ulrich Hansmann. At Zeuthen, DESY supports the research group "Elementary Particle Physics" which is led by Dr. Karl Jansen. In 2006, the "Gesellschaft für Schwerionenforschung, GSI" in Darmstadt will join the NIC with the intention to establish a new research group in the field of "Computational Hadron Physics".

The staff positions for the Computational Biology and Biophysics group at FZJ comprise the group head, six researchers and two Ph.D. students. At NIC-DESY/Zeuthen in addition to the head again six researchers and two Ph.D. students are assigned to the group. Both groups complement their teams by several third party funded positions. It is a distinctive feature of the NIC research groups that their leading persons are recruited for three years with the option for prolongation to six years. The candidate must be a professor with a permanent position at a University or research institute. This policy guarantees a high flexibility for re-orientation of research towards new developments.

The mission of the NIC groups is to carry out excellent, internationally recognized research in topical fields of the computational sciences, including life sciences, by means of supercomputers of highest performance, state-of-the-art data processing capabilities and fastest connections to Grids and the Web. The objective of the groups is to act both as cores and as hubs for the establishment of novel fields in computational science, and to foster novel developments in these fields, thus generating highest visibility of the computational science activities of the NIC.

Furthermore, the NIC research groups concentrate on the development of new methods and algorithms. The Complex Systems group, for example, has introduced a highly cited approach for sequential sampling, the "Pruned Enriched Rosenbluth Method" (PERM), a depth first algorithm including importance sampling and re-sampling. To mention an important application, PERM is most efficient for the simulation of low energy configurations of lattice heteropolymers. The Elementary Particle Physics group has substantially boosted the simulation efficiency of light dynamical fermions by exploiting several techniques as

twisted mass fermions and combinations of algorithmic improvements including Hasenbusch preconditioning. One should remark that the group in the past has paved the way for the polynomial HMC scheme, now a standard technique which has led to the Rational Hybrid Monte Carlo method. RHMC is used for instance by the QCDSF group, which is led by Prof. Schierholz, a member of the NIC research group, to simulate very small quark masses. The Computational Biology and Biophysics group has contributed with the SMMP algorithm, now a freely available simulation package for protein folding which is widely used. The group is continuing the development of the "generalized ensemble approach" with the goal to predict the structure of stable domains in proteins with finally up to 200 residues.

A third major activity of the NIC research groups is to act as pilot users and driving forces in the development of novel computing technologies. In the past, DESYs Elementary Particle Physics group was a forerunner in the usage of the Italian APE100 system and was involved in the joint construction of APEmille and apeNEXT. Today, the NIC scientists are among the first to utilize and to develop algorithms for the 45 Teraflop/s Blue Gene /L leadership-class system installed at NIC-Jülich in January 2006.

In the future, the NIC research groups will play a major role in the realization of the integrated Helmholtz supercomputing concept. The research groups are foreseen to act as the scientific focal points in simulation laboratories, created for the respective fields. Following an open model, the simulation labs will be jointly operated by the NIC support teams at the Central Institute for Applied Mathematics (ZAM) at FZJ and by members of the scientific communities, maintaining a web portal for dissemination of best practice and providing Grid based access to algorithms, optimized code elements, simulation data and other data bases.

The NIC research groups are an essential element of NIC's strategy towards a European supercomputing centre. Their deep integration in existing pan-European research communities became evident at the workshops for the preparation of the European scientific case for supercomputer infrastructures in Barcelona (11/2005) and Cadarache (2/2006).

In the coming years, the NIC will continue this successful research model and intends to establish further groups. The NIC as a virtual computational science institute will be expanded in order to meet the continuously growing importance of supercomputing, computational methods and algorithms for computational science and engineering.

The next three contributions will give an overview of the activities of the NIC research groups, starting with the Complex Systems groups, led until June 2005 by Prof. Peter Graßberger, followed by the new Computational Biology and Biophysics group, led by Prof. Ulrich Hansmann since July 2005, and finally presenting the Elementary Particle Physics group of Dr. Karl Jansen.

John von Neumann Institute for Computing

The NIC Complex Systems Research Group

Peter Grassberger

published in

NIC Symposium 2006 ,
G. Münster, D. Wolf, M. Kremer (Editors),
John von Neumann Institute for Computing, Jülich,
NIC Series, Vol. **32**, ISBN 3-00-017351-X, pp. 3-11, 2006.

http://www.fz-juelich.de/nic-series/volume32

The NIC Complex Systems Research Group

Peter Grassberger

John von Neumann Institute for Computing
Research Centre Jülich, 52425 Jülich, Germany
E-mail: p.grassberger@fz-juelich.de

We give an overview over the main research activities in our group during the last two years. It is mostly concentrated on two subjects: Efficient sequential Monte Carlo methods and pattern analysis. As regards sequential Monte Carlo algorithms, we mainly developed a fast algorithm for the simulation of lattice animals and lattice trees. This follows in spirit our PERM ("pruned-enriched Rosenbluth method") algorithm which was highly successful for polymers and other problems, but it involves a number of non-trivial departures from plain PERM. In the following, we will discuss results on various aspects of the animal problem obtained with this algorithm. As regards pattern analysis, our main long-term commitment is to EEG analysis for understanding epilepsy. One very important technique in this is independent component analysis (ICA), which allows quite generally to decompose a signal into weakly interdependent sources. One essential ingredient in ICA is an algorithm to estimate this interdependency with least bias. In our group we first developed a new estimator of mutual information (the main information-based measure of interdependency), and we then used this in two new classes of ICA algorithms. The first is a conventional algorithm called MILCA ("mutual information based least-dependent component analysis"), the other is a simulated annealing method using Markov chain Monte Carlo and is today the most efficient algorithm for problems with non-negative sources arising in spectral analysis.

1 Introduction

The John von Neumann Institute has two research groups. One is for high energy physics, the other for various problems of statistical physics and complex systems at the interface between physics and biology. In the present paper I want to give a brief review of the activities during the last two years when I was head of the group for complex systems.

As also during the previous years, our group was active in two main fields: Efficient Monte Carlo sampling by means of recursive sequential algorithms, and signal analysis. Although members of the group have also worked on other important problems, I will in the following concentrate on these two, and will present one achievement in each.

2 PERM Simulations for Lattice Animals

As regards Monte Carlo methods, one distinguishes Markov chain (Metropolis-Hastings) methods and sequential methods. It is fair to say that simulations in statistical physics use overwhelmingly the Metropolis strategy, and sequential algorithms have traditionally occupied niches like neutron transport theory[1], diffusion type quantum Monte Carlo methods[2], and some algorithms (called "static" in this field) for sampling polymer configurations[3–6]. But the last years have seen a resurgence of sophisticated sequential methods, mostly among statisticians[8], while physicists have still been more busy with more sophisticated algorithms of the Metropolis type.

Our group has made a major contribution with the PERM algorithm (for a review, see[7]), which is a recursively implemented ("depth first") version of sequential sampling with importance sampling and re-sampling[8]. Although this is a general purpose strategy and was applied to as different problems as reaction-diffusion systems[9], percolation[7], and sequence analysis[10], its main application was to polymer statistics. It allowed e.g. the first detailed test of the logarithmic corrections predicted for so-called Θ-polymers by the renormalization group[11], and provides today the most efficient algorithm for determining low energy configurations of lattice heteropolymers which provide toy models for protein folding[12].

During the last two years, we have applied the basic strategy of PERM to the simulation of lattice animals and lattice trees. Lattice animals (or "polyominoes", as they are also called by mathematicians[13]) are just connected clusters of sites on some regular lattice, similar to percolation clusters. But while the latter come with non-trivial statistical weights which are due to the fact that percolation clusters are created by randomly removing bonds or sites from a fully occupied lattice, the animal ensemble is defined so that all clusters with the same number of sites have the same weight. Thus understanding the animal problem essentially corresponds to counting the numbers of different cluster shapes. The interest for statistical physics derives on the one hand from the fact that lattice animals form the simplest model in the universality class of randomly branched polymers[14]. On the other hand, they are closely related to a number of other problems. A famous theorem, conjectured by Parisi and Sourlas[15] and proven much later[16], connects lattice animals in d dimensions to the Lee-Yang problem in $d-2$ dimensions. As a consequence, some critical exponents are known exactly in 3 and 4 dimensions, while other exponents are not known exactly even in 2 dimensions, because animals are not conformally invariant[17].

Efficient simulations of lattice animals have always posed a problem. For lattice trees (which are just animals with tree topology) a version of the pivot algorithm[18] is fairly efficient, but even that is much more cumbersome and slow than algorithms for percolation clusters or for unbranched polymers. For percolation clusters, in particular, one has very simple growth algorithms first given by Leath[19], which can be implemented either as breadth or as depth first[20].

Our PERM algorithm starts by growing slightly subcritical percolation clusters and re-weighs them as appropriate for the animal ensemble. It is crucial that this can be done while the cluster is still growing. So one can check whether the weight is just right, too small, or too large (as measured against the average over previous clusters; at the start, when there are not yet any previous clusters, every cluster is 'just right'). If it is too large, the cluster is "cloned", each clone receives half of the weight, and continues to grow independently of the other. If the weight is too small, the cluster is killed with probability 1/2 and the weight of the survivors is doubled. All this could be done with an explicit population of clusters as in an evolutionary (genetic) algorithm, but we found it more convenient to use a depth-first (stack oriented, recursive) implementation. Notice that here "depth-first" refers not to the way how an individual cluster grows, but to the way how the state space tree of different growth paths is sampled. Indeed, we found that for an efficient algorithm it is crucial to use a breadth-first growth algorithm.

The algorithm involves a number of other parameters and choices, all of which are crucial for efficiency, although very precise choices of the parameters are often not needed. For instance, we have to choose the control parameter of the percolation process with which

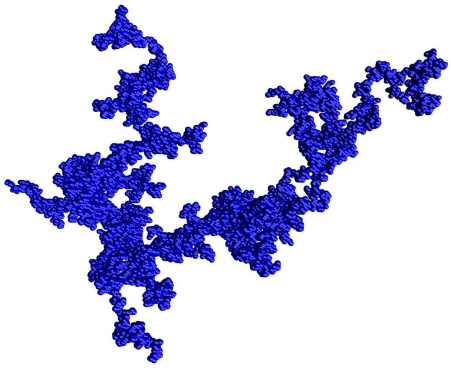

Figure 1. A typical 3-d lattice animal with 16000 sites on the bcc lattice. According to our simulations, there are about $10^{16776.0\pm0.4}$ different cluster shapes of this size.

we start, and we have to choose a "fitness function" which tells us when to clone and kill. All these details are described in[21]. A large typical animal (16,000 sites) is shown in Fig.1, animals of somewhat smaller sizes were simulated with high statistics in all dimensions between 2 and 9.

Among the results obtained with this algorithm is, first of all, the verification that the critical exponents are in agreement with the Parisi-Sourlas conjecture, with exponents as obtained by field theoretic methods for the Lee-Yang problem. For the exponent ν in 2 dimensions ($\langle R^2\rangle \sim N^{2\nu}$ where R is the radius of gyration and N is the number of sites) we obtain excellent agreement with exact enumeration results.

For clusters grafted to an attractive surface we find the expected phase transition between desorbed and adsorbed phases, and we verify partially a striking prediction by Janssen and Lyssy[22]: The cross-over exponent is exactly 1/2 in 3 and 4 dimensions. In $d = 2$, Janssen and Lyssy also conjectured a value 1/2, but with less theoretical justification. Indeed we find small deviations for $d = 2$ which seem to be significant.

In order to understand whether conformal invariance is replaced for lattice animals by some other simple property, we simulated clusters grafted to the apex of $2 - d$ cones and wedges (a cone is a wedge whose two sides are glued together)[23]. While the exponent ν is independent of the opening angle α of the wedge/cone, the entropic exponent θ does depend on α. For conformally invariant theories, this dependence is $\theta \propto 1/\alpha$. While we found this to be true in the limit $\alpha \to 0$, the dependence for large angles is linear, $\theta \propto \alpha$. In spite of the suggestive simplicity of this result, we have not found an easy explanation.

Finally, we have simulated collapse transitions due to attractive forces between the 'monomers' making up to clusters. There are two natural parameters for this attraction[24]. Correspondingly, one obtains a 1-dimensional collapse line in a 2-dimensional phase plot. Critical (bond) percolation is obtained with special choices of these two parameters and sits exactly on the phase transition line. Away from it, the exact location of the transition

line is not known, as are also the critical exponents associated with it. Even worse, also the topology of the phase diagram is still debated[24, 25]. Our simulations[26] gave very precise results in part of the phase diagram, but not in all. In particular, we still cannot clearly resolve the dispute about its topology.

3 Independent Component Analysis and Other Applications of Mutual Information

As said above, we have a long-standing commitment to understand the EEG of epilepsy patients. The main goals there are to predict seizures in advance (typically a few minutes), and to locate the epileptic focus precisely for later resection. The latter should be done preferentially only from data obtained during from seizure-free intervals. A recent review of the successes and difficulties encountered by our collaboration on this project is in[27].

One of the main features of epilepsy is the very strong EEC signal during seizures, which can only be generated by strong synchronization effects. One expects interdependencies between the EEC signals obtained from different regions in the brain to show some traces of this also when there is no seizure. Thus we started already rather early to study interdependence measures[28]. We did not use at that time mutual information (MI), theoretically the ideal measure because of its strong information theoretic background[29], because of the well-known problems to obtain unbiased MI estimates (for a recent discussion, see e.g. Ref. 30).

This changed when we found that a class of estimators, based on the k-th nearest neighbour method of Kozachenko and Leonenko[31] for estimating differential Shannon entropies for real-valued variables, has surprisingly good properties[32]. It has small statistical errors, is reasonably fast when implemented carefully, and seems to have zero bias when applied to random variables which actually are independent. The latter purely numerical observation (we have no proof for it) is very astonishing, and is particular useful for applications to independent component analysis (ICA)[33].

It was therefore mainly to the latter that we applied it up to now. ICA is based on the assumption that a set of simultaneously measured signals $x_i(t_k)$ are actually composed of more or less independent sources. In the simplest case, there is no additional noise (or, otherwise said, some of the sources are just noise), these sources are strictly independent, and the signals are obtained from them by linear superposition with a constant (i.e. time independent) and instantaneous *mixing matrix* $\mathbf{A}$. In "blind source separation", both $\mathbf{A}$ and the sources are assumed to be unknown, and the goal is to recover them from the statistics of the signals alone. Obviously, when the number of possible sources is not larger than the number of measured components, this is done by applying an instantaneous time-constant "demixing" matrix $\mathbf{W} = \mathbf{A}^{-1}$ such that the reconstructed sources $s_i(t) = (\mathbf{W}\mathbf{x}(t))_i$ are as independent as possible.

A crucial ingredient for any version of ICA is obviously a good measure of statistical dependencies. If one takes the simple linear correlation coefficients, then the problem can be solved by linear analysis, the result being just a principle component decomposition. Usually this is used as a first step in the analysis ("pre-whitening"), and ICA proper is obtained by using a more sophisticated (in general non-linear) measure of dependence. Very popular are various approximations to MI or higher order cumulants like skewness

Figure 2. Estimated independent components of the heart beat of a pregnant woman, using the public domain JADE algorithm. Traces nr. 5 and 6 are dominated by the heart beat of the fetus, but the signals are still quite noisy.

or kurtosis (e.g. in the JADE[34] and FastICA[33] algorithms), but also time-delayed linear correlations are used, as e.g. in the TDSEP algorithm[35].

In real world applications, the mixing might be not strictly linear or might involve some time delays, or the true sources might be not strictly independent. Thus we have to expect the reconstructed sources not to be strictly independent either. Our strategy is then to lump together sources whose MIs are above a given threshold into one multi-dimensional source. This is done by using a hierarchical clustering algorithm where MI is used as proximity measure[36]. Possible time delays can be incorporated easily by working with delay embeddings[37] familiar from nonlinear analysis of univariate signals. In order to see the contribution of any particular reconstructed (multi-dimensional) source to the measured signals, one turns off all other sources and applies the inverse of the reconstructed demixing matrix.

When implemented in a rather standard way, i.e. with pre-whitening and with an iterated deterministic gradient descent method for the minimization of MI, we called our algorithm MILCA ("MI based least dependent component analysis"). By applying it to various test cases, we invariably found it to be better than all competitors, with the exception of a recent method also based on k-th nearest neighbour entropy estimators[38]. The latter uses a rather time consuming trick which the authors called 'data augmentation'. When we included augmentation in our bag of tricks, our algorithm did even beat that method.

In Figs. 2 to 4 we show the more realistic case of the heart beat (ECG) of a pregnant woman. The original data[39] have 8 channels recorded for 5 seconds. In Fig. 2 we show the results obtained with a standard public domain algorithm, JADE[34]. We see that the heartbeat of the fetus is reasonably well separated from that of the mother and from sources which mainly consist of noise. When applying MILCA, we compare two versions: one without delay embedding, and one with three delay times, which blows the number of

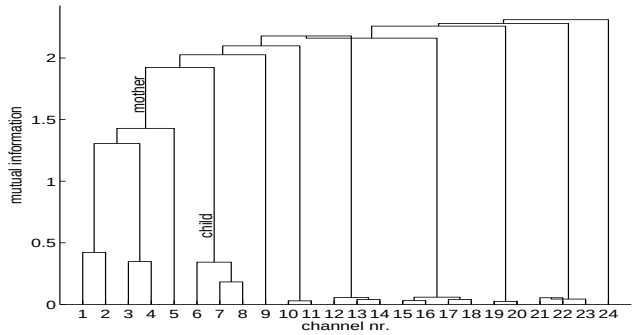

Figure 3. Dendrogram obtained from the dependencies between the 24 sources reconstructed with MILCA. Heights of each cluster correspond to the MI between its elements.

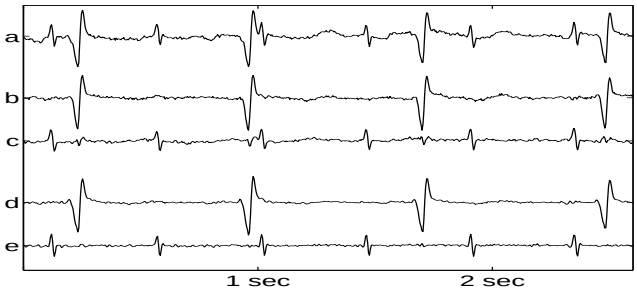

Figure 4. Short segment (a) of the original EC; (b) of the mother and (c) of the fetus contributions estimated with MILCA, but without delay embedding; and (d), (e) mother and fetus contributions obtained with delay embedding.

channels from 8 up to 24. In Fig. 3 we show the dendrogram obtained from the cluster analysis for the latter. We see two main clusters, obviously the heartbeat of the mother and the heartbeat of the fetus, while the other sources seem to be just noise. Suppressing everything except one of these two main clusters and applying the inverse demixing, we obtain the contributions of the two hearts to the full ECG. For better visibility we only show blow-ups of part of one single channel. This original recording of this channel is seen in Fig. 4a. In Figs. 4b and 4c we see the mother and fetus contributions, as estimates with MILCA without delay embedding. Finally, in Figs. 4d and 4e we see the results obtained with delay embedding. Even the heart beat of the fetus, which seems sometimes to be completely masked by the mother heart beat in the original data, is now recovered with extremely small noise.

Another large field of applications for blind source separation is spectroscopy. There one has typically a spatially (or temporally) inhomogeneous mixture of different substances, so that spectra obtained from different locations (at different times) correspond to different superpositions of the pure spectra. Here frequency plays the rôle that time had played before. Most ICA algorithms are based on the assumption that the signals are iid

(independent and identically distributed), i.e. that time correlations are absent. This is certainly a rather poor assumption for spectra. Also, spectra of different chemical substances often have large overlaps. Finally, many spectra not only are non-negative, they also have spectral regions where the intensity is close to zero. In such cases, looking just for decompositions with minimal MI might give rather poor results. In particular, this might lead to unphysical solutions with negative intensities. Indeed, negativities are in many cases introduced already in the prewhitening pre-processing step, and are then maintained during the main part of the ICA algorithm. There are methods to eliminate these negativities in a post-processing step, but then there is no control what happens to the independencies during this post-processing[40]. MILCA as described above performs thus for several test cases from the literature as good as typical state of the art codes, but not spectacularly good[40].

A more elegant way is to abandon prewhitening completely, and to perform an iterative demixing where non-negativity is preserved during each individual step. It turns out that a constraint greedy deterministic algorithm would then be very inefficient. Instead, we propose in[42] a Metropolis-type simulated annealing[41] algorithm with MI as cost function and with non-negativity as hard constraint. Results obtained with this SNICA ("stochastic non-negative independent component analysis") algorithm show that it gives better performance than any other algorithm proposed so far[42].

4 Discussion and Outlook

Obviously, there remains much to do. We started our work on ICA with the intention to apply it to the EEC, mainly of epilepsy patients. So far we have not done it, and since I now retired, I can only hope that others will continue with this work. There are of course many more applications of MI, in practically all fields of science. Whether our new MI estimators will become useful there, is a yet open question.

On the other side, there are also many more potential applications of sequential sampling algorithms. I mentioned already sequence analysis, where the generation of large samples of sequence pairs (or tuples, more generally) with prescribed statistics is needed for testing the significance of a found alignment. Another possible application is the generation of large random networks with given global properties (e.g. degree sequences)[43], which is also needed for null hypothesis testing.

Finally, there is a growing interest in the statistical community to apply Monte Carlo methods to Bayesian inference problems. This has obvious connections to nonlinear time series analysis, and would therefore tie together the two lines of research discussed in this review. Of course it was our long-time hope to bridge this gap sooner or later, but it seems now that this has to be done by other researchers.

Acknowledgments

It is a pleasure to thank my collaborators over all these years, in particular Walter Nadler, Hsiao-Ping Hsu, Ralph Andrzejak, Jochen Arnhold, Sergej Astakhov, Erwin Gerstner, Alexander Kraskov, Thomas Kreuz, Klaus Lehnertz, Vishal Mehra, Harald Stögbauer, and Lei Yang. I also want to thank the Forschungszentrum Jülich for the excellent support we had during this time.

References

1. H. Kahn, 'Use of Different Monte Carlo Sampling Techniques', in ed. H.A. Meyer, *Symposion on the Monte Carlo Method* (Wiley, New York 1956).
2. W. von der Linden, Phys. Rep. **220**, 53 (1992).
3. M.N. Rosenbluth *et al.*, J. Chem. Phys. **23**, 356 (1955).
4. F.T. Wall *et al.*, J. Chem. Phys. **30**, 634, 637 (1959).
5. S. Redner *et al.*, J. Phys. **A 14**, 2679 (1981).
6. T. Garel and H. Orland, J. Phys. **A 23**, L621 (1990).
7. P. Grassberger, Computer Physics Commun. **147**, 64 (2002).
8. J.S. Liu, *Monte Carlo Strategies in Scientific Computing*, Springer Series in Statistics (Springer, New York 2001).
9. V. Mehra and P. Grassberger, Phys. Rev. E **65**, 050101 (2002); Physica D **168**, 244 (2002).
10. R. Bundschuh and P. Grassberger, work in progress.
11. P. Grassberger, Phys. Rev. E **56**, 3682 (1997).
12. H.-P. Hsu, V. Mehra, W. Nadler and P. Grassberger, Phys. Rev. E **68**, 021113 (2003).
13. S. Golomb, *Polyominoes: Puzzles, Patterns, Problems and Packings* (Princeton Univ. Press, Princeton, N.J. 1994).
14. T. C. Lubensky and J. Isaacson, Phys. Rev. A **20**, 2130 (1979).
15. G. Parisi and N. Sourlas, Phys. Rev. Lett. **46**, 871 (1981).
16. J.Z. Imbrie, J. Phys. A: Math. Gen. **37**, L137 (2004).
17. J.D. Miller and K. De'Bell, J. Physique I 3, 1717 (1993).
18. E J Janse van Rensburg and N Madras, J. Phys. A: Math. Gen. **25** 303 (1992).
19. P. Leath, Phys. Rev. B **14**, 5046 (1976).
20. R. Tarjan, SIAM J. Comput. **1**, 146 (1972).
21. H.-P. Hsu, W. Nadler, and P. Grassberger, J. Phys. A: Math. Gen. **38**, 775 (2005).
22. H. K. Jassen and A. Lyssy, J. Phys. A: Math. Gen. **25** L679 (1992); Europhys. Lett. **29**, 25 (1995).
23. H.-P. Hsu, W. Nadler, and P. Grassberger, Phys. Rev. E **71**, 065104 (2005).
24. S. Flesia, D.S. Gaunt, C.E. Soteros, and S.G. Whittington, J. Phys. A: Math. Gen. **27**, 5831 (1994).
25. M. Henkel and F. Seno, Phys. Rev. E **53**, 3662 (1996).
26. H.-P. Hsu and P. Grassberger, J. Stat. Mech. P06003 (2005).
27. F. Mormann *et al.*, Clinical Neurophys. **116**, 569 (2005).
28. J. Arnhold, P. Grassberger, K. Lehnertz, und C.E. Elger, Physica D 134, 419 (1999).
29. T.M. Cover and J.A. Thomas, *Elements of Information Theory* (Wiley, New York 1991).
30. C.J. Cellucci, A.M. Albano, and P.E. Rapp, Phys. Rev. E **71**, 066208 (2005).
31. L.F. Kozachenko and N.N. Leonenko, Probl. Inf. Transm. **23**, 95 (1987).
32. A. Kraskov, H. Stögbauer, and P. Grassberger, Phys. Rev. E **69**, 066138 (2004).
33. A. Hyvärinen, J. Karhunen, and E. Oja, *Independent Component Analysis* (Wiley, New York 2001).
34. J.-F. Cardoso, Neural Computation **11**, 157 (1999).
35. F. Meinecke, A. Ziehe, M. Kawanabe, and K.-R. Müller, IEEE Trans. Biomed. Eng. **49**, 1514 (2002).

36. A. Kraskov, H. Stögbauer, R.G. Andrzejak, and P. Grassberger, e-print q-bio.QM/0311039 (2003).
37. E. Ott, *Chaos in Dynamical Systems* (Cambridge Univ. Press, Cambrige 1993).
38. E.G. Learned-Miller and J.W. Fisher III, J. Machine Learning Res. **4**, 1271 (2003).
39. B.L.R. De Moor (ed), "Daisy: Database for the identification of systems", www.esat.kuleuven.ac.be/sista/daisy (1997).
40. S.A. Astakhov, H. Stögbauer, A. Kraskov, and P. Grassberger, e-print physics/0412029 (2004).
41. S. Kirkpatrick, C.D. Gelatt, and M.P. Vecchi, Science **220**, 671 (1983).
42. S.A. Astakhov, H. Stögbauer, A. Kraskov, and P. Grassberger, preprint (2005), accepted for Angewandte Chemie.
43. Y. Chen, P. Diaconis, S.P. Holmes, and J.S. Liu, J. Amer. Statist. Assoc. **100**, 109 (2005).

John von Neumann Institute for Computing

Computational Biology and Biophysics at NIC

Ulrich H.E. Hansmann

published in

NIC Symposium 2006 ,
G. Münster, D. Wolf, M. Kremer (Editors),
John von Neumann Institute for Computing, Jülich,
NIC Series, Vol. **32**, ISBN 3-00-017351-X, pp. 13-20, 2006.

http://www.fz-juelich.de/nic-series/volume32

Computational Biology and Biophysics at NIC

Ulrich H. E. Hansmann

John von Neumann Institute for Computing (NIC)
Research Centre Jülich, 52425 Jülich, Germany
E-mail: u.hansmann@fz-juelich.de
Dept.of Physics, Michigan Technological University
Houghton, MI 49931,USA

We summarize shortly the research program of the newly installed research group "Computational Biology and Biophysics" at NIC. This group exists since July 2005 and investigates the Biophysics and Biochemistry of biological macromolecules by means of high performance computing.

1 Introduction

As of July 1st 2005 the "Complex Systems" group at NIC has been replaced by the new research group "Computational Biology and Biophysics" anticipating that this area of research will in the next years have more and more a need for high performance computing. This is because a new challenge has emerged after the successful deciphering of whole genomes: for most sequences we do not know the function of the corresponding proteins, the workhorses in a cell that are responsible for transporting molecules, catalyzing biochemical reactions, or fighting infections.

Proteins are only functional if they assume specific shapes. Despite decades of research it is still an open question how these structures emerge from a protein's chemical composition (the sequence of amino acids as specified in the genome). An answer to this question could lead to a deeper understanding of various diseases that are caused by the miss-folding of proteins, and enable the design of novel drugs with customized properties.

Computer experiments offer one way to gain such knowledge but are extremely difficult for realistic protein models[1]: all-atom models of proteins lead to a rough energy landscape with a huge number of local minima separated by high energy barriers. Consequently, sampling of low-energy conformations becomes a hard computational task, and physical quantities cannot be calculated accurately from simple low-temperature molecular dynamics or Monte Carlo simulations. The difficulties become even more pronounced if the structure of a protein depends on its interaction with other bio-molecules. Overcoming these obstacles may be one of the defining challenges in high performance computing for the next few years and will require the use of massive parallel computers such as JUMP and the new BlueGene computer JUBL in Jülich.

Research in the new group is concerned with the development and test of algorithms for these machines that allow atomistic simulations of stable domains in proteins (usually of order 50-200 residues), i.e. for overcoming the protein-folding problem[2]. Protein-protein interactions are the topic of another line of research. Especially interesting are the conditions under which proteins mis-fold and aggregate. As abnormally folded and aggregated proteins are related to the outbreak of various diseases, such simulations may

provide insight into the mechanism of their pathogenesis. Protein-ligand binding and protein interaction networks belong to the same research direction and provide an interface for collaborations with bioinformatics groups.

Related to the above described research is the development and publication of new software for simulations of protein. These programs will be included in future updates of SMMP[3], the freely available program package that was developed by my group.

2 Algorithms for Protein Simulations

The key-idea behind the novel techniques employed by us is to replace the canonical weights, that suppress the crossing of an energy barrier of height ΔE by a factor $\propto \exp(-\Delta E/k_B T)$ (k_B is the Boltzmann constant and T the temperature of the system), with such weights that allow the system to escape out of local minima. Often the weights are chosen in such a way that a Monte Carlo or molecular dynamics simulation will lead to a uniform distribution of a pre-chosen physical quantity. For instance, in multicanonical sampling[4] the weight $w(E)$ leads to a distribution

$$P(E) \propto n(E) w(E) = \text{const}, \tag{1}$$

with $n(E)$ the density of states. A free random walk in the energy space is performed that allows the simulation to escape from any local minimum. From this simulation one can calculate the thermodynamic average of any physical quantity A by re-weighting[5]:

$$< \mathcal{A} >_T \;=\; \frac{\int dx\; \mathcal{A}(x)\; w^{-1}(E(x))\; e^{-E(x)/k_B T}}{\int dx\; w^{-1}(E(x))\; e^{-E(x)/k_B T}}\;. \tag{2}$$

Here, x labels the configurations. The weights $w(E)$ are not *a priori* known and estimators have to be determined by an iterative procedure described in Refs. 4,6. The first application of this technique to protein studies can be found in Ref. 7.

The computational effort increases in multicanonical simulations with the number of residues as $\approx N^4$. While this is a much better numerical performance than in canonical simulations where one would expect a supercritical slowing down (i.e. the computer time would grow as $\propto e^{aN}$ with a an unknown constant), this scaling limits the size of systems that can be studied. In general, the computational effort in generalized-ensemble algorithms scales as $\propto X^2$ where X is the variable in which one wants a flat distribution. This is because these algorithms generate an unbiased $1D$ random walk in the ensemble coordinate. In the multicanonical algorithm the coordinate is the potential energy $X = E$. Since $E \propto N^2$ the scaling relation for multicanonical simulations is recovered. Hence, a better scaling of the computer time can be obtained by choosing a more appropriate ensemble coordinate than the energy. We have demonstrated this recently for the 36 residue villin headpiece sub-domain HP-36[8] using the helicity as system coordinate. We are now extending this approach to proteins that have not only helices as secondary structure elements. This requires to explore possible parameters for generalized-ensembles other than the energy or the helicity. Examples are the simple scoring function of Chang et al.[9] or the so-called hydrophobic ratio of Silverman[10].

All generalized-ensemble techniques are designed to explore low energy configurations but avoiding at the same time entrapment in local minima. In *energy landscape paving* (ELP), a new optimization method that proved to be very promising in protein studies[11],

this is achieved by performing low-temperature Monte Carlo simulations with a modified energy expression that steers the search away from regions already explored:

$$w(\tilde{E}) = e^{-\tilde{E}/k_B T} \quad \text{with} \quad \tilde{E} = E + f(H(q,t)) \; . \tag{3}$$

Here, T is a (low) temperature, $\tilde{E}$ serves as a replacement of the energy E, and $f(H(q,t))$ is a function of the histogram $H(q,t)$ in a pre-chosen "order parameter" q. Within ELP the weight of a local minimum state decreases with the time the system stays in that minimum till it is no longer favored. The system will then explore higher energies till it falls into a new local minimum. Obviously, for $f(H(q,t)) = f(H(q))$ the method reduces to the various generalized-ensemble methods[2] (for instance for $f(H(q,t)) = \ln H(E)$ to multicanonical sampling).

Another way of enhancing the sampling of low-energy protein configurations that is especially interesting for parallel computing is parallel tempering (also known as replica exchange)[12], a technique that was first introduced to protein folding in Ref. 13. In its most common form, one considers an artificial system built up of *N non–interacting* copies of the molecule, each at a different temperature T_i. In addition to standard Monte Carlo or molecular dynamics moves that affect only one copy, parallel tempering introduces a new *global* update[12]: the exchange of conformations between two copies i and $j = i + 1$ with probability

$$w(\mathbf{C}^{old} \rightarrow \mathbf{C}^{new}) = \min(1, \exp(-\beta_i E(C_j) - \beta_j E(C_i) + \beta_i E(C_i) + \beta_j E(C_j))) \; . \tag{4}$$

This exchange of conformations leads to a faster convergence of the Markov chain than is observed in regular canonical simulations. Note that parallel tempering does not require Boltzmann weights. The method can be combined easily with other generalized-ensemble techniques as was demonstrated first in Ref. 13.

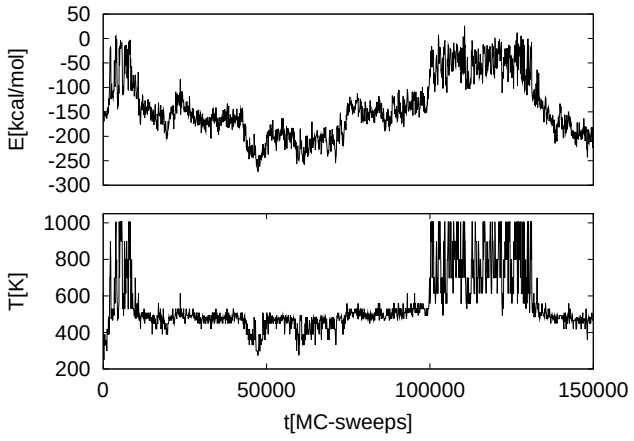

Figure 1. Time series of energy and temperature for a Parallel Tempering simulation of the protein HP-36

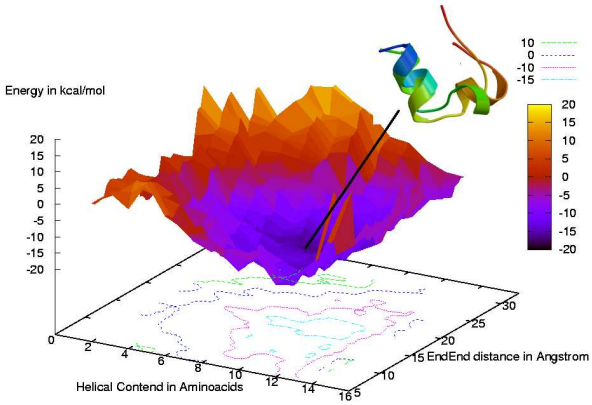

Figure 2. Energy landscape of the 20-residue trp-cage protein

I show as an example in Fig. 1 the time series of temperature and energy of one arbitrary chosen replica as obtained in a parallel tempering simulation of the 36-residue protein HP-36 (the figure is taken from Ref. 14). Note how the resulting random walk in temperature leads to one in energy that enables escapes out of local minima. In this way sampling of low-energy structures will be enhanced. A simple implementation of this and other modern protein simulation techniques can be found in the free program package SMMP (Simple Molecular Mechanics for Proteins)[3] which is available from www.phy.mtu.edu/biophys/smmp.htm. The present version allows only simulation of isolated molecules but we are now re-writing the program to allow simulation of more than one (interacting) macromolecules. The package is written in FORTRAN but we are currently working on a C++ version. Test, modification and/or optimization of SMMP for Grid-computing are also planned.

3 Physics of Folding

Current applications focus on probing the mechanism of folding in small proteins and the conditions under which proteins mis-fold and aggregate. It is now widely believed that the energy landscape of proteins (in contrast to random heteropolymers) resembles a partially rough funnel with a free energy gradient toward the native structure (for a review, see, for instance, Ref. 15). Folding occurs by a multi-pathway kinetics and the particulars of the funnel landscape determine the transitions between the different thermodynamic states[16,17]. Fig. 2 shows as an example a two-dimensional projection of the folding funnel of the 20-residue trp-cage protein as determined in a computer simulation. Configurations found at the bottom of the funnel resemble closely the experimentally determined structure (the figure is taken from Ref. 18).

In the above described case we have used that the protein is built up out of only α-helices. This allows in a simple way the definition of an "order parameter" for the fold-

ing process. The situation is different for $\alpha\beta$-proteins such as Fsd-Ey, the LysM-domain and Chymotrypsin Inhibitor 2. These molecules have both α-helices and β-sheets as secondary structure elements and are therefore of higher complexity. While they allow a more general study of small proteins, the problem is that there is no obvious reaction coordinate describing folding. However, such coordinate can be extracted *a posteriori* from generalized-ensemble simulations using the fact that these techniques allow one to sample whole ensembles of low-energy structures and to construct the corresponding energy landscape.

Analyzing the data from simulations of the 28-residue protein Fsd-Ey and the 48-residue LysM domain with clustering techniques, our group attempts to sample the ensemble of local minima of both proteins. For each pair is probed whether there is a path between them that does not require crossing a free energy barrier of pre-set height. In this way, one obtains a connectivity network for the protein energy landscape. While it is interesting in itself to study the topology of these networks, the main emphasis is on identifying the "optimal" path(s) that lead from high energy configurations down to the native state. Using dimension reduction techniques we try to identify the true degrees of freedom in the protein motion along the optimal path in the connectivity network. While protein motion is in general non-linear, we start the investigation with principal component analysis (PCA) albeit this is a globally linear method and leads to a higher dimensional than necessary sub-space. We hope that the combination of our sophisticated sampling techniques with PCA will help identifying the true degrees of freedom and reaction coordinates for describing the folding process. We use these techniques to test whether the energy landscape of Fsd-Ey, the LysM-domain, Chymotrypsin Inhibitor 2, and apo calbindin D9K can be described with the funnel concept, how the tertiary structure formation is related to collapse and secondary structure formation, whether there are nucleation sites, and whether entropic or energetic factors guide the path(s) toward the native structure. The relative stability of secondary structure elements is another question that we want to probe.

The above mentioned tools is also used by us to research the effect of various solvent representations on protein simulations. We use the data from simulations of Fsd-Ey and later the LysM-domain to study the energy landscape of these proteins as a function of the solvent representation. Especially interesting is how the distribution of low-energy states depends on the solvent model and how it differs from the gas phase model. In this way, we will study systematically the accuracy of the model, and explore potential avenues for their betterment. Separating the effects of intramolecular and hydration interactions, such research allows one also to study to which extent folding is determined by intrinsic properties of the protein.

4 Mis-folding and Aggregation

Particularly interesting and important are situations where proteins fold incorrectly as abnormal protein folding and aggregation appears to be involved as a general mechanism in a number of diseases such as Alzheimer's, Huntington's or spongiform encephalopathies (prion-mediated)[19]. The most common of these diseases is Alzheimer's. Associated with its neuropathology are amyloid deposits, composed mainly of the β-amyloid peptide (βA). It is found in body fluids in a soluble form that has partial α-helical structure. In Alzheimer's disease, βA undergoes a conformational change toward a β-sheet structure

Figure 3. Low-energy configurations of the peptide EKYLRT

in which it is insoluble and assembles in fibrils 60-90 Å in diameter. Fibrillar amyloids form lesions 10-200 μm in diameter known as senile plaques. These plaques are surrounded by degenerating and swollen nerve terminals, and found in extra-cellular space of the brain. The neurotoxity of the βA-peptide is related to the degree of β-aggregation. A similar situation is observed in a family of inherited neurodegenerative diseases that includes Huntington disease[20]. These polyglutamine (polyQ) disorders are characterized by long (> 35) glutamine repeats in the affected proteins forming protein aggregates that show a fibrillar morphology similar to that observed in Alzheimer[21]. Hence, the analysis of the structural changes in polyQ molecules or the βA-peptide, and their subsequent aggregation, could contribute to developing understanding of the biogenesis of the corresponding neurological disorders[19]. A possible mechanism for the growth of the toxic fibrils may be that the incorrectly folded protein induces mis-folding in close-by molecules. For instance, the peptide EKAYLRT likes to form a β-strand when in the vicinity of an other β-strand (Fig3b) , while further away (or isolated) it tends to form an α-helix (Fig. 3a). The figure is taken from Ref. 22.

We start our research with investigating the mechanism of β-sheet versus α-helix formation in polyQ peptides. Chains of increasing length are simulated in order to compare our results with the observed pathogenic threshold of $\sim 35 - 40$ glutamines. We expect to find as local minima the soluble α-helix form and the insoluble β-sheet structure, but other structures may also exist at room temperature as local minima in the free energy landscape. The relative weight of the different structures as a function of chain length are determined and the separating free energy barriers measured. This will allow us estimating the life times of these conformers and to identify possible pathways between these local free-energy minima. Principal component analysis will be used to identify the true degrees of freedom describing the motion along these pathways.

The autocatalytic properties of βA or polyQ fibrils let us expect that surface effects play an important role in the formation of β-sheets and the aggregation of the β-sheet

form. Hence, we simulate the molecule in the presence of hydrophobic (which will model previously aggregated molecules) or hydrophilic surfaces. We are especially interested in observing how the free-energy landscape of the peptide is modified through the presence of the surface, and how this change in the energy landscape depends on the characteristics (especially its hydrophobicity) of the surface. We expect that such a detailed investigation of the free energy landscape of βA and its change with environment will lead to a better understanding of the mechanism of β-formation in this peptide. Simulations and analysis will then be repeated for the 42-residue β-A peptide, and the mechanism of mis-folding and aggregation compared for both molecules.

5 Closing Remarks

I have outlined a group of research projects in the newly found research group "Computational Biology and Biophysics" that uses high performance computing to study proteins and their interactions. Their center piece is the continuing development of novel algorithms (the "generalized-ensemble" approach) toward the final goal of structure prediction of stable domains in proteins (usually of order 50-200 residues). One challenge in the next years will be to extend these lines of research to larger and medically relevant proteins. Other research will focus on the interaction of proteins with different biological molecules (flexible docking) in order to understand how biomolecules interact and regulate each other in a cell. Application of the current research may also include the use of proteins for assembling nanostructures.

Acknowledgments

The presented work is in part also supported through research grants of the National Science Foundation (CHE-0313618) and the National Institutes of Health (GM62838), both USA.

References

1. U.H.E. Hansmann, *Comp. Sci. Eng.* **5** (2003) 64.
2. *Protein folding* in silico - *The Quest for Better Algorithms*, in: A. Hartmann and H. Rieger (eds), *New Optimization Algorithms in Physics*, VCH-Wiley (2004).
3. F. Eisenmenger, U.H.E. Hansmann, Sh. Hayryan, C.-K. Hu, *Comp. Phys. Comm.* **138** (2001) 192.
4. B. Berg and T. Neuhaus, *Phys. Lett.* **B267** (1991) 249; B. Berg and T. Neuhaus, *Phys. Rev. Lett.* **68** (1992) 9.
5. A.M. Ferrenberg and R.H. Swendsen, *Phys. Rev. Lett.* **61** 2635 (1988); **63** (1989) 1658(E), and references given in the erratum.
6. U.H.E. Hansmann and Y. Okamoto, *Physica A* **212** (1994) 415.
7. U.H.E. Hansmann and Y. Okamoto, *J. Comp. Chem* **14** (1993) 1333.
8. C.J. McKnight, D.S. Doehring, P.T. Matsudaria and P.S. Kim, *J. Mol. Biol.* **260** (1996) 126.

9. I. Chang, M. Cieplak, R.I. Dima, A. Maritan and J.R. Banavar, *Proc. Nat. Acad. Sci. USA* **98** (2001) 14350.
10. B.D. Silverman, *Proc. Nat. Acad. Sci. USA* **98** (2001) 4996.
11. U.H.E. Hansmann and L.T. Wille, *Phys. Rev. Let.*, **88** (2002) 068105.
12. K. Hukushima and K. Nemoto, *J. Phys. Soc. (Japan)*, **65** (1996) 1604; G.J. Geyer, *Stat. Sci.* **7** (1992) 437.
13. U.H.E. Hansmann, *Chem. Phys. Lett.* **281** (1997) 140.
14. C.-Y. Lin, C.-K. Hu and U.H.E. Hansmann, *Proteins: Structure, Function and Genetics*, **52** (2003) 436.
15. K.A. Dill and H.S. Chan, *Nature Structural Biology* **4** (1997) 10.
16. J.D. Bryngelson and P.G. Wolynes, *Proc. Natl. Acad. Sci. (USA)* **84** (1987) 7524.
17. J.N. Onuchic, Z. Luhey-Schulten and P.G. Wolynes, *Annu. Rev. Phys. Chem.* **48** (1997) 545.
18. A. Schug, W. Wenzel and U.H.E. Hansmann, *J. Chem. Phys.*, **122** (2005) 194711.
19. J-C. Rochet and P.T. Lansbury, *Curr Op Struc Biol* **10** (2000) 60.
20. L. Masino and A. Pastore, *Brain Res. Bull.* **56** (2001) 183.
21. P.A. Temussi, L. Masino, and A. Pastore, *EMBO J.* **22** (2003) 355.
22. Y. Peng and U.H.E. Hansmann, *Phys. Rev. E*, **68** (2003) 041911.

John von Neumann Institute for Computing

The Quest for Solving QCD by Numerical Simulations: The NIC Research Group Elementary Particle Physics

Karl Jansen

published in

NIC Symposium 2006 ,
G. Münster, D. Wolf, M. Kremer (Editors),
John von Neumann Institute for Computing, Jülich,
NIC Series, Vol. **32**, ISBN 3-00-017351-X, pp. 21-27, 2006.

http://www.fz-juelich.de/nic-series/volume32

The Quest for Solving QCD by Numerical Simulations: The NIC Research Group Elementary Particle Physics

Karl Jansen

NIC, DESY Zeuthen
Platanenallee 6, 15738 Zeuthen, Germany
E-mail: Karl.Jansen@desy.de

We discuss the activities of the NIC research group Elementary Particle Physics and show that the group could achieve important results over the last two years in the field of lattice gauge theory.

1 Introduction

Results from lattice QCD simulations enter more and more the particle data booklet (pdg)[1] which can be considered to be the "bible" for high energy physicists. In fig. 1 we show the relative difference between lattice QCD predictions and the experimental findings of only those physical observables for which lattice results have been taken by the particle data group itself[1]. The figure demonstrates that some of the observables are known from lattice QCD simulations already rather precisely. Moreover, no deviation from the predictions of QCD are detected presently, confirming thus QCD as our theory of the strong interaction at least to the accuracy obtained so far in experiment and from lattice simulations.

Although it is certainly very much encouraging that lattice results are taken seriously as a theoretical input to interprete and to compare experimental data, it has to be admitted

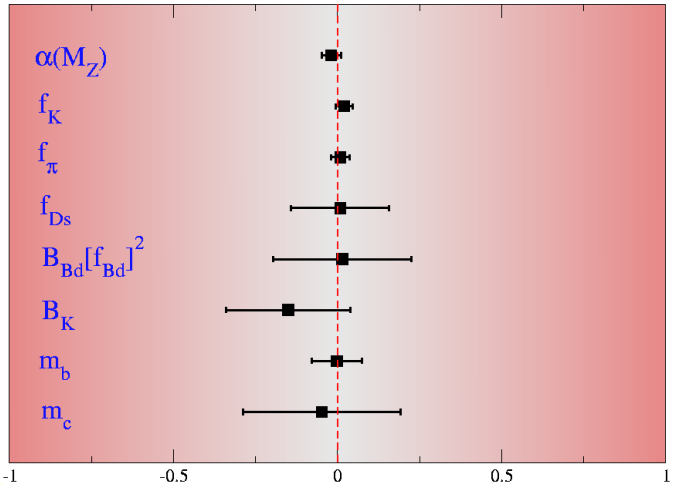

Figure 1. Comparison of lattice and experimental results for a number of physical quantities taken from the particle data booklet. Shown is the relative difference between the lattice prediction from QCD and the experimental finding.

that lattice calculations still have a number of systematic errors and that full dynamical simulations still present a challenge. The NIC research group Elementary Particle Physics focuses in its work in understanding and controlling these systematic errors and facing and overcoming the problem of dynamical quarks. This report about the work of the group will summarize the results of these attempts and presents some very important achievements that could be obtained over the last two years.

Before entering the main research area of lattice QCD, I would like to mention that the research group is also concerned with aspects of non-perturbative aspects of quantum field theories different from QCD:

- In the 2-dimensional Schwinger model, a prototype model to study aspects of much harder to tackle 4-dimensional QCD, a detailed scaling test of various fermion actions could be achieved with a precision that showed in part deviations from analytical, approximative predictions[2]. In addition, new ways of simulating chiral invariant overlap fermions dynamically were addressed[3].

- In another 2-dimensional model, the Gross-Neveu model, the phase structure in the large-N approximation could be computed analytically, revealing interesting insights that can also be relevant for QCD[4].

- A special class of gauge actions were investigated that are constructed such that the topology of the gauge fields is fixed in the numerical simulations. It could be demonstrated that the topology is indeed stabilized using these actions, although a complete fixation could not be achieved[5].

2 Results for Lattice QCD

2.1 Phase Diagram of Lattice QCD

The NIC research group achieved for the first time a comprehensive picture of the phase diagram of lattice QCD[6–11]. The knowledge about the existence and the structure of the Wilson lattice QCD phase diagram can certainly be considered as a breakthrough in lattice field theory and the work by the group received a lot of attention and has been represented at numerous conferences and workshops.

The reason is that, somewhat surprisingly, the phase structure turns out to be rather complicated. Instead of a single phase transition line at which the pseudo scalar mass vanishes as suggested by the continuum picture, various phase transitions were found. The most relevant for a continuum limit is a first order phase transition with the peculiar property that unlike in the continuum the pseudo scalar mass does not vanish, but assumes a non-zero, minimal value. Our present understanding of the lattice QCD phase diagram is sketched in fig. 2.

The phase structure and many properties of the corresponding phase transitions can be computed both, numerically and analytically using tools from chiral perturbation theory[12–17]. Both of these approaches provide a consistent picture that leads to the phase diagram of fig. 2. For a more detailed discussion of the properties and consequences of the existence of the first order phase transition, we refer to our project discussion in this proceedings volume.

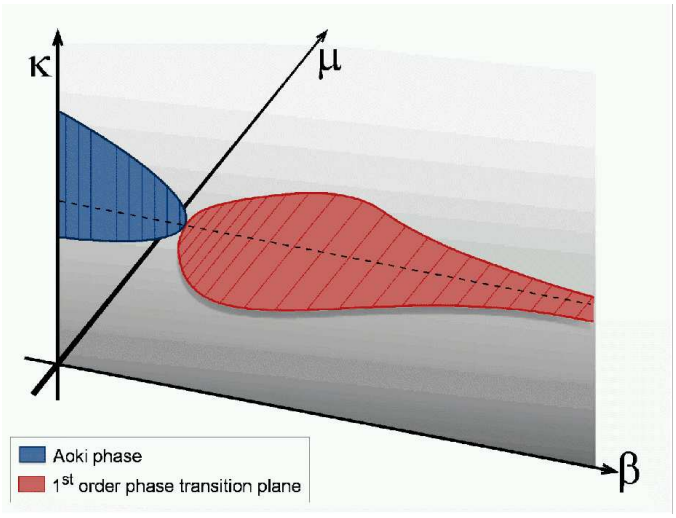

Figure 2. Current knowledge of the lattice QCD zero-temperature phase diagram with Wilson fermions as a function of the inverse gauge coupling $\beta \propto 1/g^2$, the hopping parameter κ (which is inversely proportional to the quark mass) and the twisted mass parameter μ.

Another major part of the work of the NIC research groups was a detailed scaling test of a new formulation of lattice fermions, so-called twisted mass fermions[18,19]. This test came out very positive[20–23]. Again we refer to the report about this project in these proceedings.

2.2 The Strange Quark Mass

One important and essential strength of lattice QCD simulations is that even the fundamental parameters of QCD, the strong coupling α_s and the values of the quark masses can be directly and ab-initio computed from the QCD Lagrangian alone. Lattice QCD is presently the only method that allows for such an ambitious goal. The recent years have seen even progress in calculating these fundamental parameters in the very demanding situation of dynamical quarks, see the discussion below. The NIC research group has very actively pursued such simulations and were one of the first to give a number for a value of the strange quark mass[24–26]. We show a compilation of world-wide results for the strange quark mass m_s in fig.3. Here the lattice results are converted to the more commonly used $\overline{\rm MS}$ renormalization scheme and a scale of 2GeV was taken.

2.3 Algorithmic Improvements – Shifting of the Berlin Wall

The biggest obstacle today in "solving" QCD at least numerically is the shear cost of the numerical simulations for which even nowadays state of the art supercomputers are not sufficient. The dilemma has been most drastically discussed a the 2001 Berlin lattice symposium. A number of research groups world-wide has been asked to present their status of dynamical simulations and estimate the cost. The example of the CP-PACS collaboration, represented by A. Ukawa at the conference provided the rightmost curve in fig. 4.

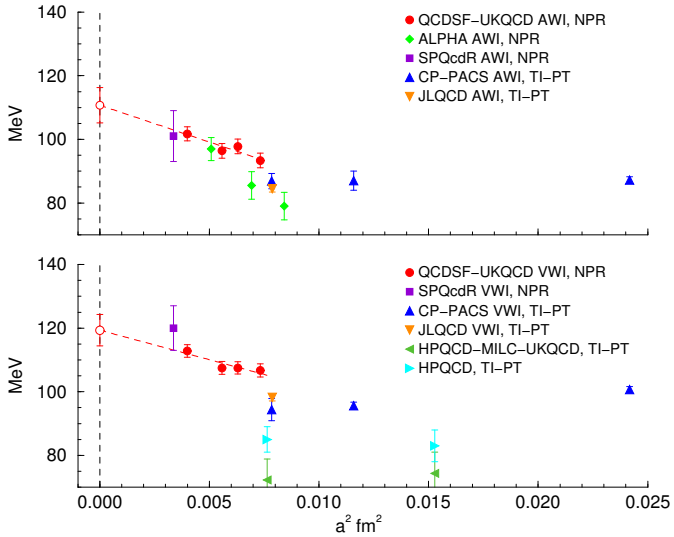

Figure 3. Results for $m_s^{\overline{\rm MS}}(2GeV)$ versus $a^2\mathrm{fm}^2$ using the axial Ward identity (AWI, upper plot) and vector Ward identity (VWI, lower plot). The results are presented with the collaborations preferred units and scales. NPR denotes non-perturbative renormalisation, while TI-PT denotes tadpole improved perturbation theory. The results from the HPQCD collaboration are for $N_f = 2+1$ flavours, the other results are all for $N_f = 2$ flavours.

This result showed that the simulation cost increases dramatically when the ratio of the pseudo scalar to the vector meson mass are driven to its value as observed in experiment and which is represented by the arrow in the plot. The vertical axis shows the teraflop years needed to generate 1000 configurations. The sharp, wall-like increase of the simulation cost triggered the name "Berlin wall" and plots showing this behavior are titled nowadays as Berlin wall plots.

By combining several algorithmic techniques to simulate dynamical quarks, the NIC research group[27,28] has been able to substantially shift this Berlin wall, see fig. 4. Indeed the shift is so dramatic that simulations with realistic values of of the pseudo scalar and vector meson masses seems perfectly feasible, at least for a value of the lattice spacing of $a \approx 0.09$fm and a box length of about 2.4fm. Although lowering the value of the lattice spacing and increasing the box length to 3fm (or even larger) would increase the computation cost again, such simulations seem not to be completely out of range as the old location of the Berlin wall had suggested.

2.4 apeNEXT

We close this section with a remark about the status of the massively parallel apeNEXT system, the latest development in the APE-line[29–31]. These machines are constructed for a peak performance of 10 teraflops. The hardware of the apeNEXT systems is now ready, tested and working in prototype installations. The APE group is starting to install large systems Europe-wide in Italy (12Teraflops), France (2Teraflops) and Germany (3Teraflops DESY, 5Teraflops Bielefeld). It is to be expected that these installations will provide a major and most important computer resource for lattice physicists in Germany.

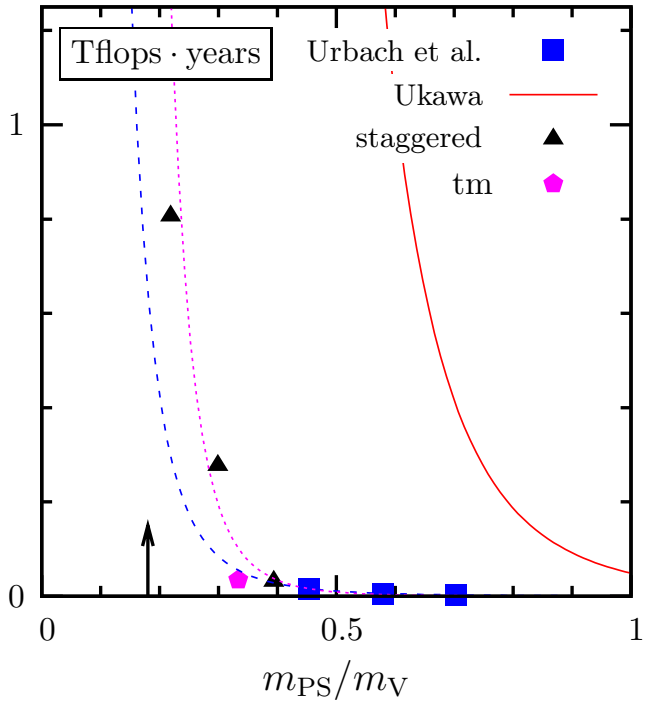

Figure 4. Shift of the Berlin wall through recent algorithmic improvements.

3 Conclusion

The NIC research group has worked very successfully in the last years. It has tested the Wilson twisted mass formulation of lattice QCD and found it to be a most promising tool for future QCD simulations. The group has explored the phase diagram of lattice QCD and obtained for the first time a comprehensive picture of the phase structure which is, moreover, in accordance with analytical results from chiral perturbation theory. As an example of a physics result we presented the computation of the mass of the strange quark in the case of dynamical quarks which is one of the most important quantities to come from lattice simulations.

The group found a new version of an algorithm to simulate dynamical quarks which shifted the Berlin wall considerably such that even simulations at the physical point where the pion mass assumes its experimentally measured value become possible. In parallel, machines of the apeNEXT type are now ready to be installed, providing computer power in the 10 teraflops regime.

All these results of the NIC research group are substantial improvements, if not breakthroughs in lattice gauge theory and the next years will certainly see the fruits of this work resulting in the computation of many physically relevant quantities.

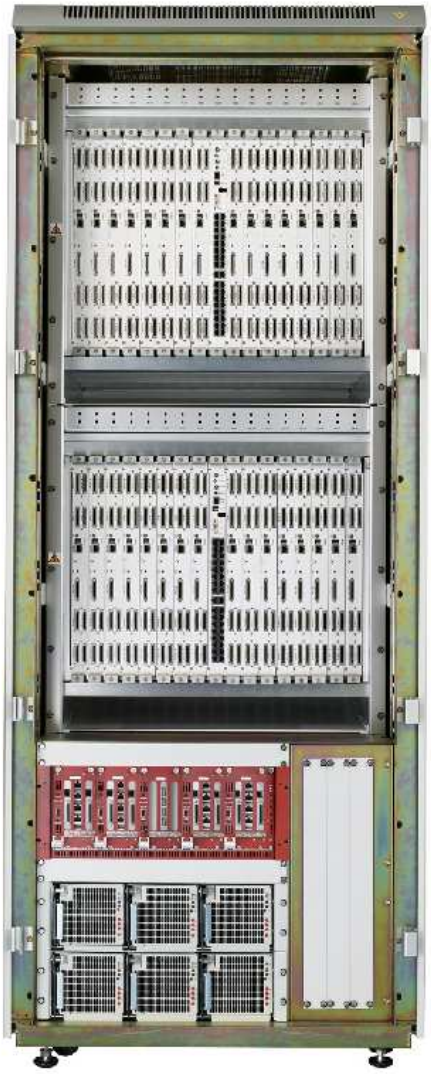

Figure 5. One rack of the apeNEXT installation in Zeuthen. A rack as shown here, has 512 nodes and can deliver 640 gigaflops

Acknowledgment

In the work presented here all members of the NIC research group Elementary Particle Physics have been involved: Stefano Capitani, Thomas Chiarappa, Nils Christian, Martin Gürtler, Kei-ichi Nagai, Mauro Papinutto, Dirk Pleiter, Beatrix Pollakowski, Gerrit Schierholz, Andrea Shindler, Thomas Streuer, Carsten Urbach, Volker Weinberg, Urs Wenger, Ines Wetzorke and James Zanotti. I thank all the members of the group for their excitement, strong motivation and hard work for producing physics results and their help in preparing this proceedings contribution.

References

1. Particle Data Group, S. Eidelman *et al.*, Phys. Lett. **B592**, 1 (2004).
2. N. Christian, K. Jansen, K.-i. Nagai and B. Pollakowski, PoS **LAT2005**, 239 (2005), [hep-lat/0509174].
3. N. Christian, K. Jansen, K. Nagai and B. Pollakowski, hep-lat/0510047.
4. K.-i. Nagai and K. Jansen, hep-lat/0510076.
5. W. Bietenholz *et al.*, hep-lat/0511016.
6. F. Farchioni *et al.*, Eur. Phys. J. **C39**, 421 (2005), [hep-lat/0406039].
7. F. Farchioni *et al.*, Nucl. Phys. Proc. Suppl. **140**, 240 (2005), [hep-lat/0409098].
8. F. Farchioni *et al.*, hep-lat/0410031.
9. F. Farchioni *et al.*, Phys. Lett. **B624**, 324 (2005), [hep-lat/0506025].
10. F. Farchioni *et al.*, PoS **LAT2005**, 033 (2005), [hep-lat/0509036].
11. F. Farchioni *et al.*, hep-lat/0509131.
12. S. R. Sharpe and J. M. S. Wu, Phys. Rev. **D71**, 074501 (2005), [hep-lat/0411021].
13. S. R. Sharpe and J. M. S. Wu, Phys. Rev. **D70**, 094029 (2004), [hep-lat/0407025].
14. S. Aoki and O. Bär, Phys. Rev. **D70**, 116011 (2004), [hep-lat/0409006].
15. G. Münster, JHEP **09**, 035 (2004), [hep-lat/0407006].
16. G. Munster, C. Schmidt and E. E. Scholz, Nucl. Phys. Proc. Suppl. **140**, 320 (2005), [hep-lat/0409066].
17. L. Scorzato, Eur. Phys. J. **C37**, 445 (2004), [hep-lat/0407023].
18. ALPHA, R. Frezzotti, P. A. Grassi, S. Sint and P. Weisz, JHEP **08**, 058 (2001), [hep-lat/0101001].
19. R. Frezzotti and G. C. Rossi, JHEP **08**, 007 (2004), [hep-lat/0306014].
20. K. Jansen, A. Shindler, C. Urbach and I. Wetzorke, Phys. Lett. **B586**, 432 (2004), [hep-lat/0312013].
21. K. Jansen, Nucl. Phys. Proc. Suppl. **129**, 3 (2004), [hep-lat/0311039].
22. K. Jansen, M. Papinutto, A. Shindler, C. Urbach and I. Wetzorke, Accepted for publication in Phys. Lett. **B** (2005), [hep-lat/0503031].
23. XLF, K. Jansen, M. Papinutto, A. Shindler, C. Urbach and I. Wetzorke, JHEP **09**, 071 (2005), [hep-lat/0507010].
24. QCDSF, M. Gockeler *et al.*, PoS **LAT2005**, 078 (2005), [hep-lat/0509159].
25. M. Gockeler *et al.*, hep-ph/0502212.
26. QCDSF, M. Gockeler *et al.*, hep-ph/0409312.
27. C. Urbach, K. Jansen, A. Shindler and U. Wenger, hep-lat/0506011.
28. K. Jansen, A. Shindler, C. Urbach and U. Wenger, PoS **LAT2005**, 118 (2005), hep-lat/0510064 .
29. ApeNEXT, F. Bodin *et al.*, Nucl. Phys. Proc. Suppl. **140**, 176 (2005).
30. ApeNEXT, F. Bodin *et al.*, ECONF **C030626**, FRAP15 (2003), [hep-lat/0309007].
31. F. Bodin *et al.*, ECONF **C0303241**, THIT005 (2003), [hep-lat/0306018].

John von Neumann Institute for Computing

Astrophysics

Peter L. Biermann

published in

NIC Symposium 2006 ,
G. Münster, D. Wolf, M. Kremer (Editors),
John von Neumann Institute for Computing, Jülich,
NIC Series, Vol. **32**, ISBN 3-00-017351-X, pp. 29-30, 2006.

http://www.fz-juelich.de/nic-series/volume32

Astrophysics

Peter L. Biermann

Max-Planck-Institute for Radioastronomy, 53010 Bonn, Germany
Department of Physics and Astronomy, University of Bonn, Germany
E-mail: plbiermann@mpifr-bonn.mpg.de

Today we know that the universe is full of dark energy, dark matter, a few percent in mass of ordinary matter, and a very small mass fraction in super-massive black holes. As the universe evolves, large scale structure is evolving, with ever larger scales, and ever more massive black holes at the centers of big galaxies. Although we do not even have any clue what dark energy is, and even wonder, whether the term itself might mislead us, we are beginning to try some ideas as to what dark matter is. Using the assumption, that dark matter interacts only gravitationally, and can be described as some unknown particle, with the help of supercomputers we can simulate the structure formation of the universe, and we can also try to understand how the black holes interact and grow. The interaction of black holes with stars may correspond to observable features at both the stellar mass scale, possibly related to Gamma Ray Bursts, as well as the super-massive mass scale, typically found in galactic nuclei. Nowadays we observe both Gamma Ray Bursts as well as Active Galactic Nuclei at redshifts beyond 6, so at a time, when the age of the universe was less than 1 billion years, while today our age is 13.7 billion years. Only with the large scale simulations can we hope to describe the universe, from the very large scale structure, all the way down to the early growth of black holes.

Large scale simulations of the universe

The radiation residuals of the Big Bang are still observable in the angular structure and the spectrum of the microwave background, predicted in the late 1940ies, and now observed. The WMAP project has finally given us in 2003 a good set of numbers that describe the universe in terms of dark energy (0.73 of critical density), dark matter (0.23), and baryonic matter (0.04). We do not understand dark energy, we surmise that dark matter is some unknown particle, and observationally we find only ten percent of the baryonic matter, certain to be there. And yet, the mathematical description is remarkably accurate, with residual errors in the range of typically 1 - 2 percent. Therefore, only large scale extensive simulations help us even ask all the right questions, of what we observe out there, like the missing dwarf galaxies. The work of Gottlöber et al. is an example of what can be done, and has to be done, going for the proper microphysics of the formation and evolution of dwarf galaxies to understand their scarcity in the real world.

Black holes

One aspect which is important here is the formation of the massive black holes at the centers of the biggest galaxies. They clearly form early in the universe, as observed, and

their early growth is a puzzle for some. How can one grow a black hole from a stellar size to 3 billion solar masses in much less than 1 billion years? Or do black holes of stellar size and super-massive scale form differently, say, from exploding super-massive stars? Or does dark matter enter here, by feeding the early black holes so very efficiently?

There are many indications that the physics of black holes at the various masses scales scale with mass, all the way from stellar mass to the super-massive scale, and if that is true, it is of very general merit to try to understand also the stellar explosions, which may lead to black holes, as Gamma Ray Bursts are generally believed to represent.

Also, as most super-massive black holes are rather quiescent most of the time, the occasional encounter with a star yields a great way to understand its physics. This may have been observed already, and so simulations such as done by Rosswog and Spurzem et al. allow us to study black hole physics in extreme situations.

Outlook

The next stage will certainly be on the one hand to test various models for what dark matter particles are - if particles are the correct starting point - and to include spin of the black holes in all such simulations. There is evidence that the spin of many black holes is near maximum, and that leads to many new effects, which may be observable; one such effect is the flip of the spin direction upon the merger of a super-massive black holes with another smaller black hole, whose orbital spin points in a very different direction. There are observations which strongly suggest such an interpretation. On the other hand, from particle physics we have a few clues now, that suggest that the growth of black holes, and the nature of dark matter may be related questions.

Only simulations on the structure formation in the universe, and including the effect of the birth, growth and influence of black holes, allow us to study these questions further.

John von Neumann Institute for Computing

The Large and Small Scale Structure of the Universe

Stefan Gottlöber, Gustavo Yepes, and Matthias Hoeft

published in

NIC Symposium 2006 ,
G. Münster, D. Wolf, M. Kremer (Editors),
John von Neumann Institute for Computing, Jülich,
NIC Series, Vol. **32**, ISBN 3-00-017351-X, pp. 31-38, 2006.

http://www.fz-juelich.de/nic-series/volume32

The Large and Small Scale Structure of the Universe

Stefan Gottlöber[1], **Gustavo Yepes**[2], **and Matthias Hoeft**[3]

[1] Astrophysical Institute Potsdam
An der Sternwarte, 14482 Potsdam, Germany
E-mail: sgottloeber@aip.de

[2] Grupo de Astrofísica, Universidad Autónoma de Madrid, Madrid 28049, Spain
E-mail: gustavo.yepes@uam.es

[3] International University Bremen, Campus Ring 1, 28759 Bremen, Germany
E-mail: m.hoeft@iu-bremen.de

We use high resolution cosmological simulations to study the formation and evolution of small and large scale cosmological structures.

1 Introduction

The exciting observational developments of the past couple of decades have been followed closely by comparable progress in our theoretical understanding of the main processes that govern the evolution of structure in the Universe. A substantial part of this progress is due to the increasing possibilities to simulate the formation and evolution of structure on different scales using the new generation of massively parallel supercomputers. The standard model of cosmological structure formation is based on surprisingly few parameters which can be measured at present with high accuracy: the current rate of universal expansion, H_0, the mass density parameter, $\Omega_{\rm mat}$, the value of the cosmological constant, Ω_Λ, the primordial baryon abundance, Ω_b, and the overall normalization of the power spectrum of initial density fluctuations, typically characterized by σ_8, the present-day rms mass fluctuations on spheres of radius $8h^{-1}$ Mpc.

Within the last decade new satellite and earth based observations have been used to determine the cosmological parameters. Most of the cosmologists agree in the "concordance" cosmological model according to which at present the evolution of the Universe is dominated by a cosmological constant ($\Omega_\Lambda = 0.7$). The Universe is spatially flat ($\Omega_\Lambda + \Omega_{\rm mat} = 1$) and the matter consists mainly of dark matter particles (85 %) the nature of which is not yet known. Baryons contribute only by 15 % to the matter density in the Universe. The present expansion rate of the Universe, the Hubble parameter is $H_0 = 70$ km/s/Mpc and the amplitude of the power spectrum is given by $\sigma_8 = 0.9$.

Based on those few numbers numerical simulations allow us to compute the abundance and distribution of galaxies in the Universe. Whereas for the largest objects, clusters of galaxies, simulations and observational surveys do agree very well, there is a discrepancy on the scale of small objects, dwarf galaxies. In fact simulations over-predict substantially the abundance for both, isolated dwarf galaxies in cosmological low density regions and galactic satellites. Numerous solutions have already been proposed, ranging from modifying the dark matter properties to attributing it to the effect of stellar feedback. However, the nature of the discrepancy is still controversial. The abundance of observable dwarf

galaxies depends one the large scale environment as well as on local processes. Therefore, a convincing solution can only be found in numerical simulations which take into account both effects.

Our simulations on the NIC supercomputers were in particular designed to derive realistic abundances of small objects in the Universe, like dwarf galaxies. This entails that a cosmological representative volume has to be simulated. The formation of a galaxy is still affected by tidal fields of massive objects at distances of millions of light years. The simulation has to cover such a volume. A dwarf galaxy is in contrast stretched over a few thousand light years at most. The numerical challenge is to cope with more than seven orders of magnitude in spatial and mass resolution. During the past two years we have carried out several simulations which gave considerable new insight into the interplay between large-scale environment and the small scale galaxy formation.

2 Numerical Simulations

During the early inflationary phase of the evolution of the Universe quantum fluctuations became classical perturbations in the density field. These perturbations are predicted to be scale free. At present we cannot measure the fluctuations directly, but we observe their imprint on the cosmic microwave background radiation at recombination, about 400,000 years after the Big Bang. Those temperature fluctuations of the radiation field and the associated density fluctuations are of the order of 10^{-5}. They can be well described by linear perturbation theory. After recombination baryonic density fluctuations are decoupled from the radiation field and start to grow in the potential wells of the dark matter fluctuation. The density fluctuations become soon nonlinear, so that the further evolution can be studied only numerically. In the early eighties first codes have been developed to handle the nonlinear evolution of density perturbations. These codes could follow only 32^3 particles, present codes can handle billions of particles.

Since 85 % of (dark) matter is mainly responsible for the gravitational dynamics, first codes have taken into account only the gravitational interaction of dark matter particles. Nevertheless, these dark matter codes gave and still give many new insights into the formation of large and small scale structures. State-of-the-art hydrodynamical simulations follow also the baryonic gas physics (including radiative cooling) and the formation of stars and their back reaction onto the baryonic gas. Consequently, they are numerically much more expensive and they do not yet reach the same high resolution as pure dark matter codes do.

2.1 The Initial Conditions

The initial Gaussian density fluctuations predicted by inflationary models can be described completely by a power spectrum with a spectral index $n = 1$. This has been confirmed by observations within the present accuracy of measurements. Since fluctuations grow differently during the radiation and the matter dominated phases of the cosmic expansion, the moment when matter density equals radiation density is imprinted on the original power spectrum. The characteristic scale (the horizon at this time) corresponds to the maximum of the present day power spectrum at about 500 Mpc. Moreover, baryonic and dark matter fluctuations grow differently. The resulting changes are described by the transfer functions,

which can be calculated by solving numerically the Boltzmann equation. The transfer function depends on the cosmological model, in particular on the measured mean density of dark matter and baryons, the geometry (i.e. the total density) and the expansion rate. The transfer function of the concordance model is well known and the power spectrum of the initial density perturbations can be calculated. The amplitude of the power spectrum is chosen in accordance with the observed temperature fluctuations of the cosmic microwave background and the present day large scale (quasi linear) density fluctuations.

To start a numerical simulation one has first to decide about the size of the box the evolution of which should be simulated. For a given number of particles (which is limited by the power of the computer) this is always a compromise between higher mass resolution (smaller boxes) and a representative volume of the Universe (larger box). Due to the periodical boundary conditions the Universe is assumed to be homogeneous on scales larger than the box size. For a given box size and number of particles one creates a statistical realization of the power spectrum. The displacement of the particles is determined by the entire set of waves that can be represented numerically in the simulation box of size L, i.e. the initial displacements and velocities of N particles are calculated using all waves ranging from the fundamental mode $k = 2\pi/L$ to the Nyquist frequency $k_{\rm Ny} = 2\pi/L \times N^{1/3}/2$.

If we are interested in the evolution of certain objects in a cosmological environment we use a mass refinement technique. To construct suitable initial conditions, we first create an unconstrained random realization at very high resolution which is limited by the available memory (At the SP4 of NIC we can calculate the initial displacement of up to 2048^3 (~ 8.6 billion) particles.) Then we reduce the resolution by merging particles and assigning to them a velocity and a displacement equal to the average values of the original small-mass particles. We run at small computational costs a simulation which evolves 128^3 or 256^3 particles until the present epoch and selected from this simulation regions or objects in which we are interested.

Now we can construct for this region the initial density field with very high accuracy whereas the surrounding field is given by much larger masses. To this end we go back to the original sample of small-mass particles in the regions of interest. We construct a series of shells around this region where we progressively merge more and more of the particles until the low resolution is reached again far away from the objects of interest. This procedure ensures that the selected objects evolve in the proper cosmological environment and with the right gravitational tidal fields.

2.2 The Code

For most of our simulations we use the publicly available code GADGET-2. It allows to include both the dominant dark matter component and the baryonic matter, i.e. gas and stars. This code was developed by Volker Springel. It is a full MPI N-body code based on the *TREE-PM* algorithm. The gravitational forces acting on each particle are splitted in two parts, a long range force due to distant particles and the short range gravitational forces due to the neighboring particles. The long range force is evaluated by means of the classical *Particle-Mesh* algorithm, which consists of solving the Poisson equation on a regular mesh by Fast Fourier Transforms. The short range forces are computed by means of a Tree algorithm which categorize the particles according to the distance to any other one.

The baryonic component is also discretized in particles carrying the fluid information with them. The hydrodynamical quantities at any position in space can be found using interpolation from the fluid particles. The equations of gas dynamics are solved by means of the *Smoothed Particle Hydrodynamics* method.

In addition to the modeling of gravity and gas dynamics, the code also implements additional physics for the baryons, like Compton cooling due to interactions with photons of cosmic background radiation, radiative cooling due to atomic recombination and photoionization by ultraviolet photons due to the presence of a homogeneous background coming from quasar and galactic sources. When gas cools, its density increases and eventually it will form dense molecular clouds in which stars will be born. Although the physics of this process is not well known, the code implements a model of the star-gas interactions that attempts to mimic the multiphase nature of the interstellar medium. The final outcome of the model is to transform gas particles into collisionless star particles representing star-burst.

Switching on and off the different models implemented in the code, one can use it to simulate the pure dark matter gravitational evolution (using the N-body algorithm only), or the dark matter and gas dynamics (using N-body and SPH), or everything together (N-body + SPH + star formation).

All the different parts of the code are done in parallel using MPI routines. The parallelization is done by domain decomposition of the simulation volume to distribute the particles among the different processors. If only N-body and SPH algorithms are used, the code scales pretty well with the number of processors. When the non-adiabatic physics module (cooling, heating, star formation) is switched on, the enormous differences in density and timing between star forming regions and the rest of the simulation makes the scaling not very efficient beyond several dozens of processors.

2.3 The Data Analysis

With 1 billion of particles a numerical code produces per time step at least 28 Gb of data (3 positions, 3 velocities and one id for each particle), in case of multi mass simulations also masses must be stored. It is a challenge to find structures and substructures in the distribution of those particles. To find structures at virial over-density one can use a friends-of-friends algorithm with a certain linking length (0.17 of the mean interparticle distance for the concordance model at redshift zero). The resulting particle clusters are in general three-axial objects. Substructures can be identified as particle clusters at smaller linking lengths (higher over-densities). The more different linking lengths are used the better substructures will be resolved. Thus a whole hierarchy of friends-of-friends clusters have to be calculated. To this end we have developed a hierarchical friends-of-friends algorithm which is based on the calculation of the minimum spanning tree of the given particle distribution.

The minimum spanning tree of any point distribution is a unique, well defined quantity which describes the clustering properties of the point process completely. The minimum spanning tree of n points contains $N-1$ connections. Based on the minimum spanning tree we sort the particles in such a way that we get a cluster-ordered sequence $P=\{p_1,p_2,...,p_n\}$. Any cluster is a segment of the sequence P, i.e. it consist of points $p_i,p_{i+1},...,p_j$ for some indexes i and j. Neighboring clusters, i.e. clusters which merged immediately after increasing r, are neighboring segments on P. Let us denote the length at which clusters $p_i,p_{i+1},...,p_j$ and $p_{j+1},p_{j+2},...,p_k$ merge, by $r_{j+1/2}$. The sequences

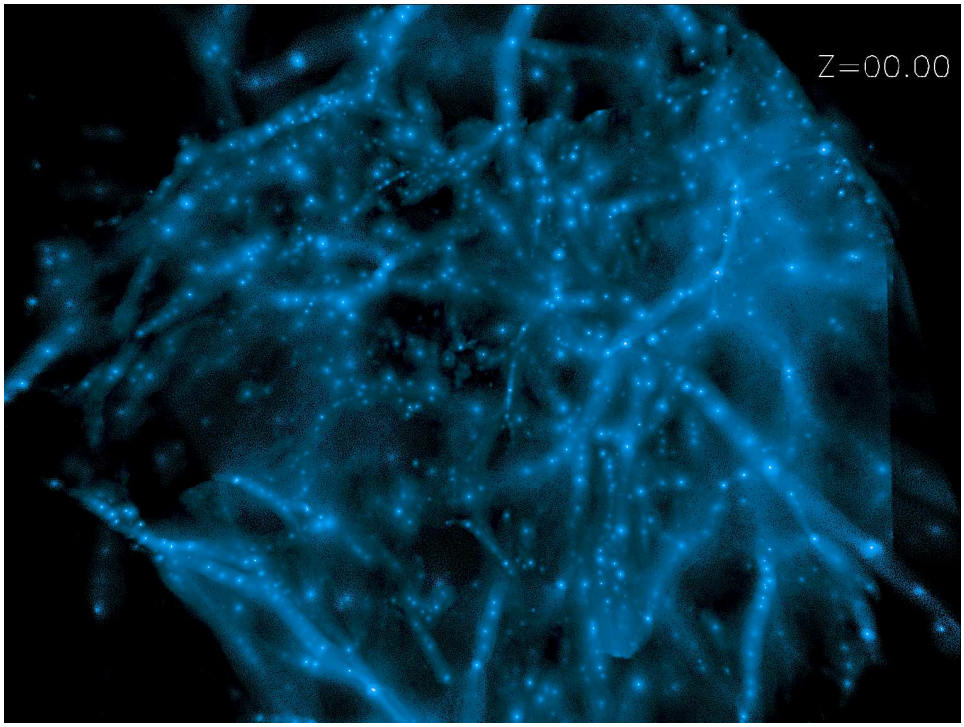

Figure 1. Gas distribution in a void region of $10h^{-1}$ Mpc in diameter. The color represent the gas density. The bright spots are the areas of high density gas that has cooled down to form stars in dwarf galaxies.The 3d positions of 2 million gas particles of mass $10^5 M_\odot$ are shown.

P and R are sufficient for deriving the complete list of clusters at any linking length r. In fact, the segment $p_i, p_{i+1}, ..., p_j$ of the sequence P is an r-cluster if and only if $r_{i-1/2} > r$, $r_{j+1/2} > r$ and $r_{k+1/2} \leq r, \quad k = i, i+1, ..., j-1$. In other words, if all points would be located on a line with distances $r_{j+1/2}, j = 1, 2, ..., n-1$ between neighboring points, the line would break into the sequence of all r-clusters after cutting of all segments larger than r. Obviously, the sequences P and R (each of length $n_p \times 4$ byte) is the most compact form to store the information about the whole hierarchy of friends-of-friends clusters.

The minimum spanning tree and the cluster analysis are done within MPI programs. The basic idea of parallelization is the calculation of separate trees in different regions of the box and merging the subtrees later on. The algorithm is very fast. We need on 8 CPUs of the SP4 at NIC about 30 minutes for the MST and another 10 minutes for the FOF analysis on 11 density (resp. linking length) levels for a simulation with 512^3 particles.

3 Problems at Short Scales: The Overproduction of Dwarf Galaxies

The major problem of the standard Cold Dark Matter (CDM) scenario of structure formation is the overproduction of small structures. All CDM simulations predict that there should be many dwarf galaxies orbiting around the big ones, like our Milky Way, and that

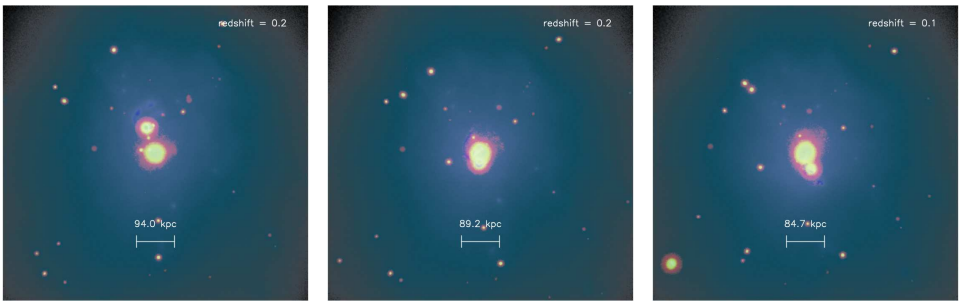

Figure 2. Interaction between two galaxies. Blue gives the gas distribution and yellow/red the distribution of stars. This galaxy is a small part from a $50h^{-1}$Mpc simulation box. One can also clearly see the distribution of satellite galaxies and gas clouds.

there should be a large population of such objects in void regions, in which no bright galaxy has been formed. In the Universe, neither we see so many satellites around disk galaxies nor we detect a population of dwarfs in voids. One way out of this discontenting situation is the claim that baryonic physics is responsible for the absence of luminous matter within the small dark halos. After all, the predictions from N-body simulations correspond to the dark matter distribution only. The baryons could have a different distribution than the dark component and stars could be formed only under special conditions.

In order to get a deeper insight into this question we have carried out a series of hydrodynamical simulations with increasing resolution of a void region of 10 Mpc in diameter, extracted from a larger box. We have included all the relevant physical processes of the baryonic matter: i.e cooling, UV photoionization, star formation and stellar feedback.

In Figure 1 we show the gas density within the void. The little white dots indicate where the gas has collapse due to cooling and have formed a dwarf galaxy. This plot shows that a void region is far from being empty. Moreover, it mimics the filamentary structure that is seen at much larger scales. But how many of these little gas spots have been able to produce a reasonable amount of stars that can allow us to see them today with powerful enough telescopes? Thanks to the kind of simulations we have done in the JUMP supercomputer at NIC we can compute the luminosity of these objects as a function of the physics we put in. The main conclusion of our study is that, although there is a considerable effect of suppressing star formation in these little objects due to the cosmic ultraviolet photoionization background, it is not enough to actually suppress all dwarf galaxies to form stars. If results from these simulations were correct, we should see a substantial amount of faint objects in voids. Therefore, another mechanism apart from photoionization should be responsible for suppressing the luminosity of dwarf dark halos in voids.

We are currently investigating this problem of excess of short scale structure in regions of higher density. To this end, we are now simulating, with the same resolution as in the void regions, other parts of the original box in which denser structures form, ranging from isolated galaxies, small groups and even clusters of galaxies. These simulations are of course much more demanding in terms of computational resources and will take longer to finish. In Figure 2 we show one example of the interaction of two galaxies and their satellites.

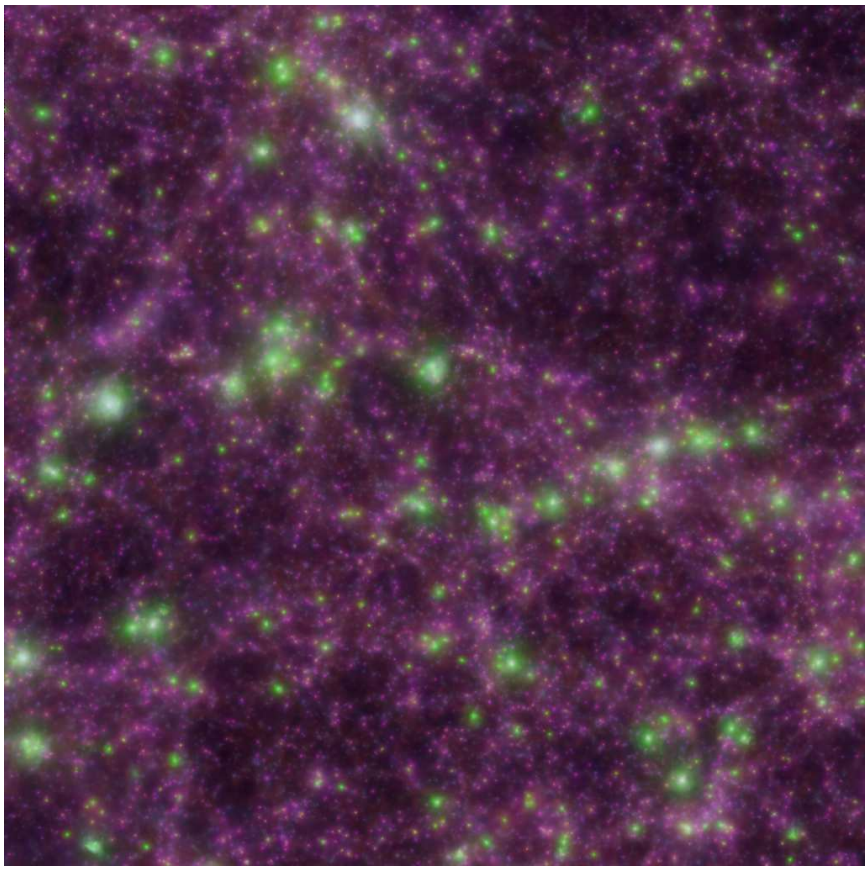

Figure 3. Gas distribution, color coded according to temperature, for a small part ($75h^{-1}$ Mpc) of a hydrodynamical simulation with 2 billion particles.

4 Large Scale Structure of the Universe

The problem of the formation of Large Scale Structures in the Universe is another interesting research topic that can only be investigated with very big simulations. If only collisionless dark matter is used in a simulation, the number of particles that can currently be treated is of the order of 10^{10}, using computational resources equivalent to 16 nodes of JUMP. Although these simulations provide a very detailed description of the structure formed by dark matter, they lack the baryonic physics, so a direct comparison with observational results is not possible. If one wants to include gas dynamics in the simulation, then one has to reduce the number of particles. We have investigated the structures formed both in gas and dark matter by means of these kind of large simulations. In particular we studied the correlation of orientations of clusters of galaxies and of super-clusters using a simulation with 2×512^3 particles done in JUMP.

Using 16 nodes of 32 CPUs each on JUMP we can run a 2 billion simulation with dark matter and gas together. Recently, we have investigated the structures formed both in gas

and dark matter using such an extreme simulation. Due to the large volume ($500h^{-1}$ Mpc cubic box) most of the structures in the simulation evolve independently to some extent. Thus we could resort to the slower communication of a PC cluster system and run the simulation in the new massively parallel IBM supercomputer *MareNostrum* (BSC, Spain) during about 500 wall clock hours using 512 PowerPC processors (256000 CPU hours, 1 Tbyte of memory). All the post-processing of the data has been done again in JUMP, where we can use our memory-intensive MPI + OpenMP programs for analysis. In Figure 3 the gas distribution in a small part of the simulation is shown.

5 Outlook

Simulations with a very large number of particles running in parallel supercomputers are the main tool for studying cosmological structure formation. But running a big simulation is just the starting point of the research work. All the data processing takes usually as much computing time as the simulation itself.

Over the next years our groups are planning to simulate as accurate as never before the formation and evolution of our local neighborhood in the Universe. These constrained simulations will be done within one of the DEISA Extreme Computing projects in which NIC participates.

Acknowledgments

Simulations described here would be impossible without the excellent user support and help by NIC and other supercomputer centers.

References

1. S. Basilakos, M. Plionis, G. Yepes, S. Gottlöber, V. Turchaninov, *The Shape-Alignment relation in ΛCDM Cosmic Structures*, MNRAS, accepted (astro-ph/0505620).
2. S. Gottlöber, V. Turchaninov, *Halo Shape and its Relation to Environment* EDP Sciences (Paris), in print, astro-ph/0511675.
3. M. Hoeft, G. Yepes, S. Gottlöber, V. Springel, *Dwarf galaxies in voids: Suppressing star formation with photo-heating*, MNRAS, submitted, astro-ph/0501304.
4. V. Springel, *The cosmological simulation code* GADGET-2, MNRAS 364 (2005), 1105.

John von Neumann Institute for Computing

Stellar Encounters with Black Holes

Stephan Rosswog

published in

NIC Symposium 2006 ,
G. Münster, D. Wolf, M. Kremer (Editors),
John von Neumann Institute for Computing, Jülich,
NIC Series, Vol. **32**, ISBN 3-00-017351-X, pp. 39-46, 2006.

http://www.fz-juelich.de/nic-series/volume32

Stellar Encounters with Black Holes

Stephan Rosswog

School of Engineering and Science
International University Bremen, 28759 Bremen, Germany
E-mail: s.rosswog@iu-bremen.de

I describe the results that have been obtained within the project *Stellar encounters with Black Holes* on the JUMP supercomputer of the John von Neumann Institute for Computing in Jülich. The main results from three types of encounters are summarized: the coalescence of a Neutron Star Black Hole binary system that merges due to the emission of gravitational waves, the disruption of a solar type star by a stellar-mass Black Hole and finally the tidal compression and possible thermonuclear explosion of a White Dwarf by a Black Hole of a few hundred solar masses.

1 Introduction

Like human beings stars undergo evolutionary stages from birth to death. Depending on their initial mass they will finally end up as either as a White Dwarf, a Neutron Star or a Black Hole.

The most common stars with masses comparable to that of our Sun, but below 8 $M_\odot$, will become White Dwarfs (1 $M_\odot$ = one solar mass= $1.99 \cdot 10^{33}$ g; in the following I will refer to such stars as Main Sequence stars). Such a White Dwarf is a burnt out stellar corpse, with a size similar to our planet earth, but a mass comparable to that of our Sun. Often White Dwarfs are surrounded by beautifully colored, so-called planetary nebulae. Rarer, more massive stars ($M > 8\ M_\odot$) will end their lives in one of the most spectacular fireworks that our Universe has to offer: a (core-collapse) Supernova explosion. Once such a massive star has used up the nuclear fuel in its center, its balance between the outward directed pressure forces and the inward-pulling gravity is lost and the star starts to collapse under its own gravitational attraction. If the star is not too massive, say below 25 $M_\odot$, this collapse can be halted once the matter in the stellar center has been compressed to densities similar to the those inside an atomic nucleus ($\rho_{\rm nuc} \approx 3 \cdot 10^{14}$ g cm^{-3}). Above this density matter becomes extremely incompressible and this brings the collapse to a halt, reverses it and launches an outward moving shock wave that initiates the Supernova explosion. Such an explosion will leave behind an extremely dense stellar remnant: a Neutron Star. With a mass of 1.4 $M_\odot$, but a radius of about 15 km, this ultra-compact star itself has densities around nuclear density and can therefore be regarded as a "giant atomic nucleus". For even heavier stars ($M > 25\ M_\odot$) not even the matter pressure at nuclear densities can stop the collapse, the ultimate fate of such stars is the formation of a Black Hole.

As every star will finally form such a compact remnant, the Universe contains myriards of them. The problem is their detection as, under normal circumstances, they do not reveal much about themselves. In some regions of the Universe, for example close to the centers of galaxies or in dense gravitationally bound stellar systems, so-called Globular Clusters, the stellar densities are large enough to frequently allow for collisions. In a given place, say a specific globular cluster, such encounters may be rare by standards of a human lifetime,

but as some of the encounters release huge amounts of energy, they may be visible way beyond their own host galaxy. Therefore, despite being a rare event *per galaxy* they may still possess a large *observable* rate.

I will discuss here several types of such collisions that have -in part or completely- been calculated using the JUMP supercomputer facilities: the coalescence of a stellar-mass Black Hole Neutron Star binary system (see Sect. 3), the disruption of a solar-type star by a Black Hole (see Sect. 4) and finally the close encounter of a White Dwarf with a Black Hole of several hundred solar masses (see Sect. 5).

2 Model Ingredients and Numerical Methods

The different types of encounters require very different input physics. Encounters between *Black Holes and a Main Sequence star* are well described by just following the gas dynamics around the hole. The equation of state is well approximated by using a simple polytropic law. As all interesting length scales of the cases we investigated are much larger than the Schwarzschild radius of the Black Hole, the gravity from the hole can be treated to a very good approximation in a Newtonian way.

In the *Neutron Star Black Hole* case a crucial model ingredient is the equation of state (EOS). It must be able to handle the hadronic physics from several times nuclear density (several times 10^{14} g cm^{-3}) down to densities of a few g cm^{-3}. The expected temperatures are in a range of up to a few times 10^{11} Kelvin, so about 10 000 times larger than in the center of the Sun. Therefore, despite the very high densities (where often temperature effects can be neglected) the EOS has to take effects from a non-zero temperature into account. To include neutrino emission also quantities like chemical potentials etc. have to be provided by the EOS. A detailed treatment of the different neutrino flavors is also implemented in our models. In terrestrial material the mean free path of a neutrino of a few MeV is of the order of astronomical units (= distance from earth to the Sun), i.e. such material is completely transparent to neutrinos. In the center of a Neutron Star, however, the neutrino mean free path can be as short as 10 cm, but parts of the debris of a disrupted Neutron Star can again be completely neutrino-transparent. Therefore the neutrino treatment has to account for such opacity effects. In the Neutron Star Black Hole case, relativistic effects are important and they are incorporated into the simulation via a Paczynski-Wiita potential[7]. For details of the physics and the implementation the interested reader is referred to Rosswog et al.[9–17].

For our *Black Hole White Dwarf* cases we are interested in the question whether/under which conditions the White Dwarf can explode by thermonuclear fusion. This means in particular that the energy release due to nuclear reactions has to be fed back into the hydrodynamics. This is computationally extremely challenging as each fluid element (in our case an SPH-particle, see below) has to know its nuclear composition and has to evolve this composition in time. Once nuclear burning becomes important, the nuclear reaction time scales can be shorter than the hydrodynamic time scales by many orders of magnitude. Therefore it is indispensable to apply operator splitting methods. Our approach to this computational challenge is described in detail in Rosswog and Ramirez-Ruiz (2006) and Ramirez-Ruiz and Rosswog (2006)[18,19].

In all of the described cases the Smoothed Particle Hydrodynamics (SPH) method is used to solve the equations of hydrodynamics. It is a Lagrangian particle scheme, i.e. all

the information about the flow is carried by particles that are evolved in time. The corresponding equations can be derived form a Lagrangian, therefore the exact conservation of mass, energy, linear and angular momentum are guaranteed even for the discretized fluid equations. As in many of the problems angular momentum and its transport via gravitational torques determines the dynamical evolution, its conservation is an indispensable asset. The computationally most expensive part, common to all of these simulations, is the treatment of self-gravity of the fluid. It is calculated via a parallelized binary tree (see e.g. Benz 1990[3]) that scales like $N \log N$ (N being the SPH particle number) rather than the N^2-dependence of the brute force, pairwise evaluation of gravity.

3 Coalescence of Neutron Stars with Black Holes

Binary systems consisting of two compact objects, either two Neutron Stars or a Neutron Star and a stellar-mass Black Hole, are among the most promising sources for gravitational waves that could be detected in the near future by ground-based detector facilities. The gravitational waves carry away energy and angular momentum from the binary system, therefore the two components of the system will slowly drift towards coalescence.

This final coalescence releases a tremendous amount of energy: more than 10^{53} ergs, more than the energy our Sun could emit during the whole age of the Universe, are released in fractions of a second. Such coalescences seem to be responsible[4, 8, 5, 6, 1, 14] for a good fraction of the most violent explosions in the Universe since the Big Bang: Gamma-ray bursts, tremendoulsy violent explosions that emit copious amounts of gamma-rays.

We have simulated the last milliseconds in the life of a Neutron Star Black Hole binary system. For technical reasons we have started this investigation focusing on the high-mass end of the expected Black Hole mass distribution, i.e. we focused on Black Holes with masses larger than 14 $M_\odot$. Black Holes possess a so-called *innermost stable circular orbit* at a radius $R_{\rm ISCO}$, inside of which no particle can revolve around the hole in a stable, circular fashion. Our recent simulations[17] show that the Neutron Star, once it has come close enough to the Black Hole, transfers a large portion of its mass directly into the hole. Only after that stage an accretion disk can form. Such disks are observed everywhere in the Universe where gas with enough angular momentum is pulled towards an accreting object: they occur around new-born stars, in freshly formed planetary systems, around the supermassive Black Holes in the centers of Galaxies and they are believed to be a vital ingredient for the central engine of a Gamma-ray burst. However, none of our investigated cases formed the hot (several 10^{10} Kelvin) and massive ($\approx$ 0.1 $M_\odot$) accretion disk that is needed to launch a Gamma-ray burst. Instead, the disk that finally forms has only a relatively small mass. Most of it resides inside the innermost stable circular orbit and is therefore falling rapidly towards the hole without having enough time to heat up. A small amount of the initial Neutron Star mass takes up a lot of the orbital angular momentum and transports it outward in rapidly expanding tidal tail. A snapshot of such a disruption process is displayed in Figure 1, movies can be found at `http://www.faculty.iu-bremen.de/srosswog/movies.html`.

This does not necessarily mean that Neutron Star Black Hole mergers generally have to be ruled out as Gamma-ray burst central engines. However, the high mass end of the distribution that we began our study with does not seem to be promising. So if these systems do not produce a Gamma-ray burst how else would they make themselves known? They

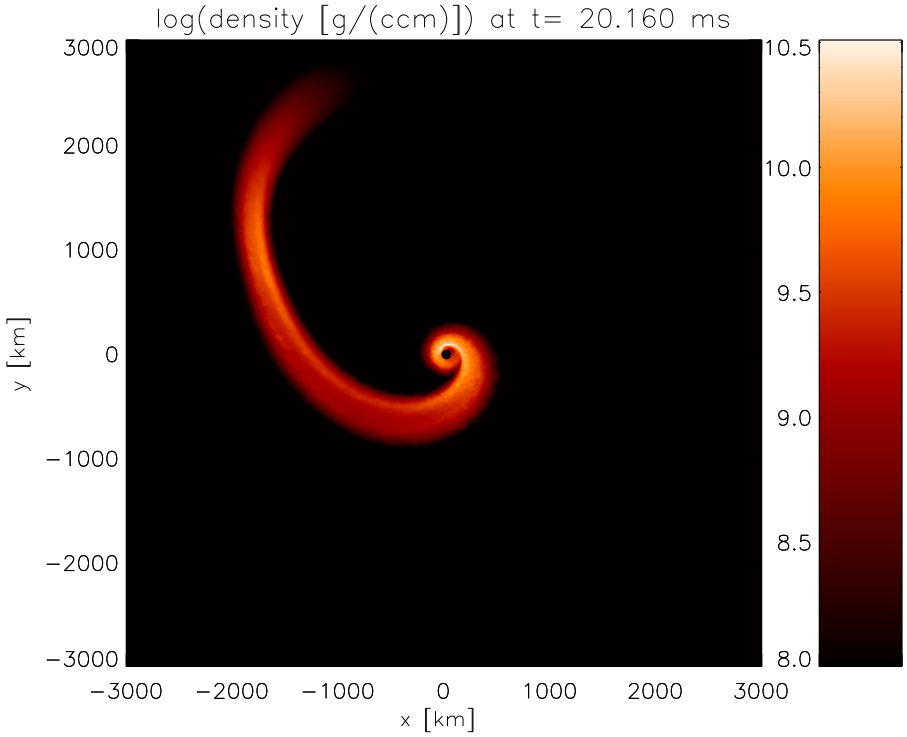

Figure 1. Snapshot of the tidal disruption process of a 1.4 solar mass Neutron Star by a Black Hole of 14 solar masses. Color-coded is the column density through the Neutron Star debris.

will definitely be a strong source of gravitational waves. The tidal tails also hold some promise for observation. Depending (quite sensitively) on the mass of the Black Hole, up to 0.2 $M_\odot$ of the Neutron Star get thrown out into space with velocities of about half the speed of light. This material initially has very high densities where nature favors very large nuclei containing hundreds of neutrons and protons. As this material expands very rapidly, the physical conditions and therefore the preferred nuclei change continuously. This leads to a constant transmutation/decay of the present nuclei and goes along with constant electromagnetic emission. This could (like a type Ia Supernova) lead to an electromagnetic emission that is powered by radioactive decays. It will produce a flash with a maximum intensity in the optical/near infrared band[17].

4 Disruption of Main Sequence Stars by Black Holes

In dense stellar systems like globular clusters stellar-mass Black Holes, with, say, 10 $M_\odot$, will also collide with the most common type of stars: Main Sequence stars like our Sun. This will in most cases be a fatal event for the star. Such a disruption of solar-type star would occur on substantially longer time scales than the previously described encounter with a Neutron Star, here the disruption process will take many hours.

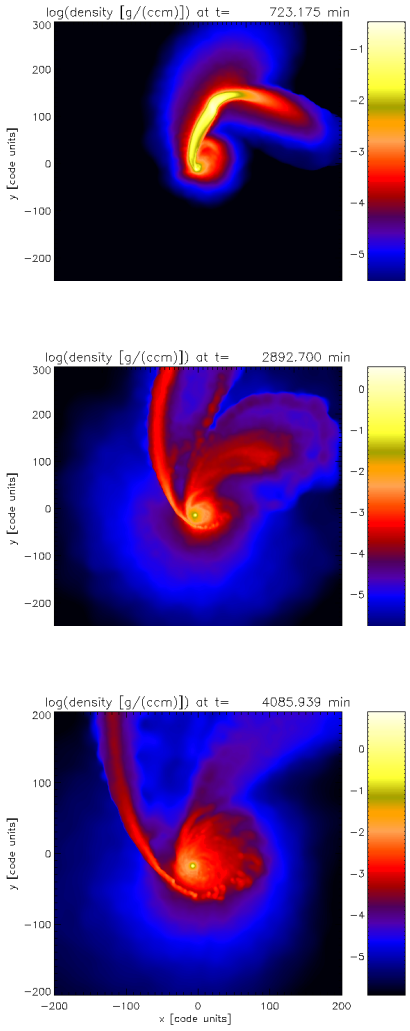

Figure 2. A solar-type star becomes tidally disrupted by a 10 $M_\odot$ Black Hole. After a first close fly by the hole grabs some of the stellar material in the form of an accretion disk while most of the stellar debris gets flung out again (panel one). The self-gravity of the latter material is strong enough to lead to the formation of a stellar core-like object (high density region in panel one) that falls -in a second approach- back towards the Black Hole. This approach completely disrupts the star (panel two) whose remains continue to rain down on the accretion disk around the Black Hole (panel three; 1 code unit= 10^{10} cm).

A movie of such a simulation can be found under `http://www.faculty.iu-bremen.de/srosswog/pop_science.html`. Some snapshots of such a disruption process of a solar-type star by a 10 $M_\odot$ Black Hole are displayed in Figure 2. After the first close encounter the Black Hole grabs some material that gathers in an accretion disk

around the hole while most of the debris is flung away from the Black Hole (first panel). The self-gravity of this latter material is strong enough to form a stellar core of about 0.3 $M_\odot$ which then falls back towards the Black Hole. In a nearly central collision with the hole this core is completely disrupted and its remains rain down onto the previously formed accretion disk (second and third panel of Fig. 2).

Depending on the closeness of the impact, the accretion process may have to compete against nuclear burning processes that are triggered by the disruption. In some cases the hydrogen of the star will ignite explosively (i.e. on a time scale shorter than the one on which the star can react) as a particular, hydrogen-explosion Supernova.

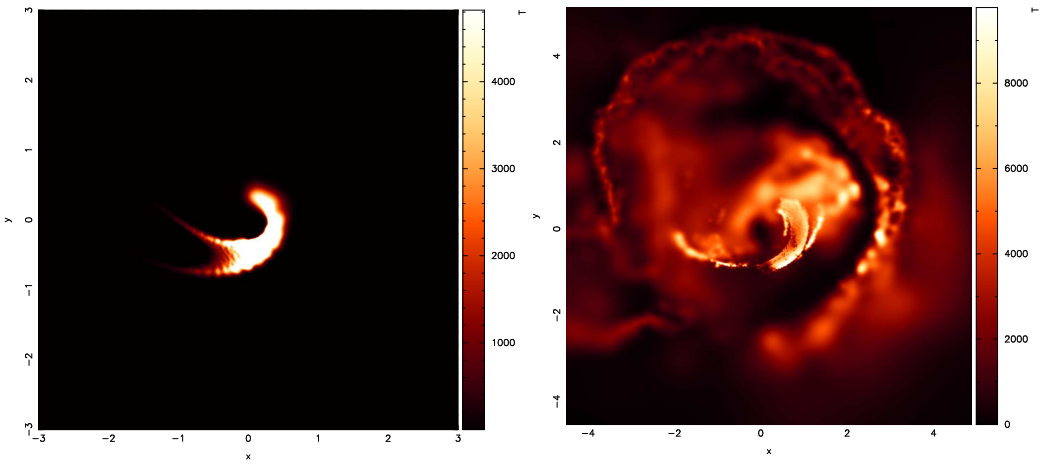

Figure 3. Tidal ignition and detonation of a White Dwarf. As the Carbon-Oxygen White Dwarfs passes the point of maximum compression it heats up to about $5 \cdot 10^9$ K and ignites its nuclear fuel (left panel; temperatures are in units of 10^6 K). During the passage more than its entire gravitational binding energy is released via nuclear burning processes, therefore the White Dwarf blows up in a violent explosion.

5 White Dwarf Explosions Induced by Black Hole Fly Bys

As most stars in the Universe have masses comparable to that of our Sun, the most common remains after a stellar lifetime will be White Dwarfs. In a Globular cluster about 10 % of the disrupted stars will be White Dwarfs[2]. A star passing a Black Hole will be disrupted if the tidal forces (similar to the forces that produce the tides on earth) overwhelm the self-gravity of the star. As we want to know whether a White Dwarf can be compressed enough to trigger a thermonuclear explosion, we are interested in the strongest possible encounters with the distance of closest approach being much smaller than the tidal radius where the star becomes disrupted. Such requirements cannot be met by all types of Black Holes as for the most massive ones, such as the one in the center of our Galaxy, the White Dwarf would be swallowed by the Black Hole before it can be disrupted. Therefore for this study only Black Holes with masses smaller than 10^4 $M_\odot$ are interesting.

In a good fraction of the investigated cases the White Dwarfs become strongly enough compressed so that the temperatures rise beyond 10^9 K, i.e. to more than a hundred times the temperatures in the center of the Sun. At the end of their normal stellar lifetimes White Dwarfs had stopped nuclear burning as there was no means to reach high enough temperatures to ignite the ashes form previous burning stages (mostly Helium, Carbon or Oxygen). In such a fly by, however, a White Dwarf can reach much higher temperatures than ever before in its life. They are large enough to ignite the ashes the White Dwarf is made of and the nuclear reactions that now set in can become extremely fast: more than 10^{51} ergs, more than the energy our Sun would radiate in a billion years, will be released within fractions of a second. A White Dwarf cannot react on this short time scale by expanding and thus slowing down the nuclear reactions, it has to take up all this thermonuclear energy and then blow up in a violent detonation.

An example of a thermonuclear explosion induced by tidal compression is shown in Fig. 3. A 1.2 $M_\odot$ White Dwarf composed of Carbon and Oxygen passes close to a 500 solar mass Black Hole. At the point of maximum compression more than $5 \cdot 10^9$ K are reached which ignites the White Dwarf. The deposition of more than 10^{51} ergs results in a violent thermonuclear explosion.

6 Concluding Remarks

I have summarized the current status of our project *Stellar encounters with Black Holes* (S.R., International University Bremen, Germany and E. Ramirez-Ruiz, Institute for Advanced Study, Princeton, USA). This project contains several sub-projects that are very different in terms of the involved physics and astrophysical questions that we hope to answer. The implications of these sub-projects range from gravitational waves over the production of heavy elements to stellar explosion mechanisms and Gamma-ray bursts.

We achieved substantial progress over the time span of this project. Several questions have found satisfactory answers, but also many more interesting ideas and exciting new questions have turned up in the course of this work. They will certainly keep us -and JUMP- busy for the next few years.

Acknowledgments

It is a pleasure to thank Dr. Daniel Price for making his data analysis and visualization software SUPERSPHPLOT freely available. It has been used to produce Figure 3.

References

1. Barthelmy, S. et al., accepted for Nature (2005).
2. Baumgardt, H. et al., ApJ 613, 1143 (2004).
3. Benz,W. et al., ApJ 348, 647 (1990).
4. Berger, E. et al., accepted to Nature (2005).
5. Bloom, J. et al., ApJ in press (2005).
6. Hjorth, J. et al., ApJL, Nature 437, 859 (2005).
7. Paczynski, B. and Wiita, P.J., A&A 88, 23 (1980).

8. Prochaska, J.X. et al., submitted to ApJ Letters, astro-ph/0510022 (2005).
9. Rosswog, S. et al., A&A 341, 499 (1999).
10. Rosswog, S. et al., A&A 360, 171 (2000).
11. Rosswog, S. and Davies, M.B., MNRAS 334, 481 (2002).
12. Rosswog, S. and Ramirez-Ruiz, MNRAS 336, L7 (2002).
13. Rosswog, S. and Liebendörfer, M.B. MNRAS 342, 673 (2003).
14. Rosswog, S. et al., MNRAS 345, 1077 (2003).
15. Rosswog, S. and Ramirez-Ruiz, MNRAS 343, L36 (2002).
16. Rosswog, S. et al., MNRAS 351, 1121 (2004).
17. Rosswog, S., ApJ, 634, 1202 (2005).
18. Rosswog, S. and Ramirez-Ruiz, E., to be submitted.
19. Ramirez-Ruiz, E. and Rosswog, S., to be submitted.

John von Neumann Institute for Computing

Black Holes in Galactic Nuclei

Christoph Eichhorn, Patrick Glaschke,
and Rainer Spurzem

published in

NIC Symposium 2006 ,
G. Münster, D. Wolf, M. Kremer (Editors),
John von Neumann Institute for Computing, Jülich,
NIC Series, Vol. **32**, ISBN 3-00-017351-X, pp. 47-54, 2006.

http://www.fz-juelich.de/nic-series/volume32

Black Holes in Galactic Nuclei

Christoph Eichhorn[1,2]**, Patrick Glaschke**[1]**, and Rainer Spurzem**[1]

[1] Astronomisches Rechen-Institut, Zentrum Astronomie Univ. Heidelberg
Mönchhofstr. 12-14, 69120 Heidelberg, Germany

[2] Institut für Raumfahrtsysteme, Univ. Stuttgart
Pfaffenwaldring 31, 70550 Stuttgart, Germany

This project studies the formation, growth, and co-evolution of single and multiple massive black holes (MBHs) and compact objects like neutron stars, white dwarfs, and stellar mass black holes in galactic nuclei and star clusters, focusing on the role of stellar dynamics. In this paper we focus on one exemplary topic out of a wider range of work done, the study of orbital parameters of binary black holes in galactic nuclei (mass, spin, eccentricity, orbit orientation) as a function of initial parameters. In some cases the classical evolution of black hole binaries in dense stellar systems drives them to surprisingly high eccentricities, which is very exciting for the emission of gravitational waves and relativistic orbit shrinkage. Such results are interesting to the emerging field of gravitational wave astronomy, in relation to a number of ground and space based instruments designed to measure gravitational waves from astrophysical sources (VIRGO, Geo600, LIGO, LISA).

1 Introduction

MBH formation and their interactions with their host galactic nuclei is an important ingredient for our understanding of galaxy formation and evolution in a cosmological context, e.g. for predictions of cosmic star formation histories or of MBH demographics (to predict events which emit gravitational waves). If galaxies merge in the course of their evolution, there should be either many binary or even multiple black holes, or we have to find out what happens to black hole multiples in galactic nuclei, e.g. whether they come close enough together to merge under emission of gravitational waves, or whether they eject each other in gravitational slingshot. For numerical simulations of the problem all models depend on an unknown scaling behaviour, because the simulated particle number is not yet realistic due to limited computing power (Milosavljevic & Merritt 2001, 2003, Makino & Funato 2004, Berczik, Merritt & Spurzem 2005). Dynamical modelling of non-spherical dense stellar systems (with and without central BH) is even less developed than in the spherical case. Here we present a set of numerical models of the formation and evolution of binary black holes in rotating galactic nuclei. Since we are interested in the dynamical evolution of MBH binaries in their final phases of evolution (the last parsec problem) we somehow abstract from the foregoing complex dynamics of galactic mergers. We assume that after some violent dynamic relaxation a typical initial situation consists of a spherical or axisymmetric coherent stellar system (galactic nucleus), where fluctuations in density and potential due to the galaxy merger have decayed, which is reasonable on an (astrophysically) short time scale of a few ten million years. The MBHs, which were situated in the centre of each of the previously merged galaxies, are located at the boundary of the dense stellar core, some few hundred parsec apart. This situation is well observable
(e.g. Komossa et al. 2003).

According to the standard theory, the subsequent evolution of the black holes is divided in three intergradient stages (Begelman, Blandford & Rees 1980): 1. Dynamical friction causes an transfer of the black holes' kinetic energy to the surrounding field stars, the black holes spiral to the center where they form a binary. 2. While hardening, the effect of dynamical friction reduces and the evolution is dominated by superelastic scattering processes, that is the interaction with field stars closely encountering or intersecting the binaries' orbit, thereby increasing the binding energy. 3. Finally the black holes coalesce through the emission of gravitational radiation.

In this paper, the behavior of the orbital elements of a black hole binary in a dense stellar system is investigated. The evolution of the eccentricity has been discussed for some time (Makino et al. 1993, Hemsendorf, Sigurdsson & Spurzem 2002, Milosavljevic & Merritt 2001, Berczik, Merritt & Spurzem 2005, Makino & Funato 2005). According to Peters & Mathews (1963) and Peters (1964) the timescale of coalescence due to the emission of gravitational radiation is given by

$$t_{gr} = \frac{5}{64} \frac{c^5 a_{gr}^4}{G^3 M_1 M_2 (M_1 + M_2) F(e)} \tag{1}$$

wherein M_1, M_2 denote the black hole masses, a_{gr} the characteristic separation for gravitational wave emission, G the gravitational constant, c the speed of light and

$$F(e) = (1 - e^2)^{-7/2} \left(1 + \frac{73}{24} e^2 + \frac{37}{96} e^4 \right) \tag{2}$$

a function with strong dependence on the eccentricity e. Thus the coalescence time can shrink by several orders of magnitude if the eccentricity is high enough, resulting in a strengthened burst of gravitational radiation. Highly eccentric black hole binaries would represent appropriate candidates for forthcoming verification of gravitational radiation through the planned mission of the Laser Interferometer Space Antenna mission LISA.

The evolution of the semi-major axis can be consulted to characterize the hardening process of the binary. The behavior of the inclination is potentially interesting to predict processes related to angular momentum exchange between the black holes and the field stars, and in particular to strengthen the hypothesis of of the connection between the appearance of so-called X-shaped galaxies and supermassive black hole mergers in galactic nuclei (Merritt 2002, Zier & Biermann 2002).

2 Numerical Method, Initial Models

The simulations have been performed using NBODY6++, a parallelized version of Aarseth's NBODY6 (Aarseth 1999, Spurzem 1999, Aarseth 2003). The code includes a Hermite integration scheme, KS-regularization (Kustaanheimo & Stiefel 1965) and the Ahmad-Cohen neighbour scheme (Ahmad & Cohen 1973). No softening of the interaction potential of any two bodies is introduced; this allows an accurate treatment of the effects due to superelastic scattering events, which play a crucial part in black hole binary evolution and require a precise calculation of the trajectories throughout the interaction. The code and its parallel performance has been described in detail in this series and elsewhere (Spurzem 1999, Khalisi et al. 2003). The survey has been carried out for a total particle number $N = 64\,000$ including two massive black holes with $M_1 = M_2 = 0.01$ embedded

in a dense stellar system of 63998 equal-mass particles $m_* = 1.5625 \cdot 10^{-5}$. The total mass of the system is normalized to unity.

The initial stellar distribution was taken from generalized King models with rotation (Lagoute & Longaretti 1996, Longaretti & Lagoute 1996, Einsel & Spurzem 1999). Main parameters are the dimensionless central potential W_0, describing the degree of central concentration, and the dimensionless rotation parameter ω_0. We have performed a series of models for $W_0 = 0, 3, 6$, $\omega_0 = 0.0, 0.3, 0.6$ (the last value means that there is a 20% fraction of rotational kinetic energy in the system, which is still a mild flattening); furthermore we have varied the initial velocity of the MBHs to be v_c, $\sqrt{2}v_c$, and $0.136v_c$, where v_c is the tangential velocity of a circular orbit at the initial MBH position. Other parameters of the problem, which we have not yet varied extensively, are the mass ratio of the black holes to the stars and the mass ratio of the black holes to each other.

3 Simulations

3.1 Evolution of the Binding Energy

We measure the relative two-body energy, angular momentum and other orbital elements of the MBH binary from the beginning of our simulations. In the first evolutionary stage, each black hole individually suffers from dynamical friction with the surrounding low mass stars, which is the main process of losing energy. Note that for simplicity we also use the above defined energy (and also the eccentricity definition e of a bound two-body orbit) even if the MBH binary is not yet bound. In such a case E and e are just numerical values which give informations about the relative state of motion of the two MBHs, but do not imply that they are already bound.

The role of dynamical friction decreases when a permanently bound state occurs, as the dynamical friction force acts preferentially on the motion of the now formed binary rather than on the individual black holes. Superelastic scattering events of field stars at the binary shall be more and more important for the reduction of its energy. These events cause a stochastic variation of E and e in our models. Nevertheless energy and angular momentum (which determined e) undergo a diffusive process with a net change of orbital parameters on top of the stochastic variations. In the stage when superelastic scattering dominates the picture, the energy loss rate is commonly written in terms of the dimensionless hardening constant H

$$\frac{d}{dt}\left(\frac{1}{a}\right) = HG\frac{\rho}{\sigma} \tag{3}$$

where a is the separation of the black holes, ρ the mass density and σ the velocity dispersion in the environment of the binary (see e.g. Merritt 2001). In other words, the process leads to a continous hardening of the MBH binary, provided there are always enough interaction partners available (the "loss cone is full", see discussions in Milosavljevic & Merritt 2003, Berczik, Merritt & Spurzem 2005).

Our measured hardening constants are in majority slightly below the $H = 8.4$ published elsewhere (Hemsendorf, Sigurdsson & Spurzem 2002), where a Plummer model was used, however. The lower values can be possibly explained by the fact that dynamical friction might still have a noticeable influence. Regarding our calculated a_h as criteria for

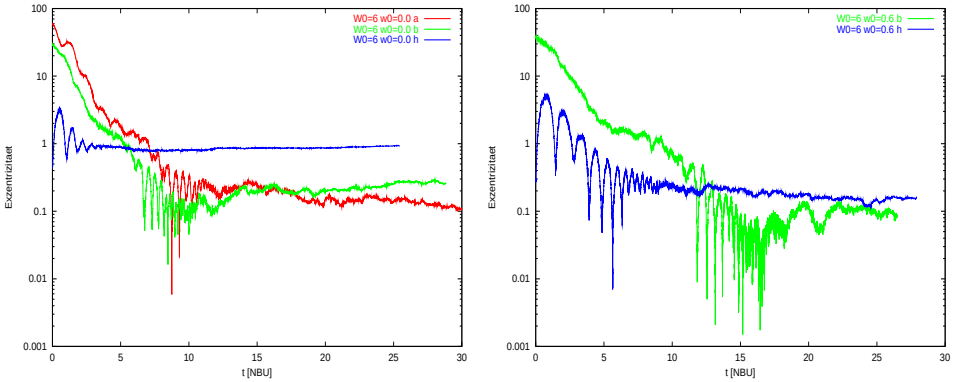

Figure 1. Time evolution of the MBH eccentricity. King parameter $W_0 = 6$; $\omega_0 = 0.0$ *left*, no rotation, $\omega_0 = 0.6$ *right*, rotation. Different initial velocities are indicated with different colours, $v_0 = 0.136 v_c$ *blue*, $v_0 = v_c$ *green*, and $v_0 = \sqrt{2} v_c$ *red*.

the domination of superelastic scattering events, the hardening separation could be significantly smaller if σ increases during the simulation as $a_h \propto \sigma^{-2}$. An enhanced σ can be expected for ρ/σ =const. if it is assumed that the black hole would capture stars during the simulation and raise the central density.

3.2 Eccentricity

The eccentricity is given by

$$e = \sqrt{1 + \frac{2El^2}{\mu (G M_1 M_2)^2}} \tag{4}$$

where M_i ($i = 1, 2$) are the masses of the two black holes, $\mu = M_1 M_2/(M_1 + M_2)$ is the reduced mass, G the gravitational constant, E the energy, and l the specific angular momentum of the two black holes relative to each other. Fig.1 shows some results for the calculated eccentricity evolution. Each plot assorts simulations of a fixed pair of King parameters under variation of the initial velocity.

Obviously, simulations with an initial velocity comparable to the circular velocity tend to end up in low-eccentricity motions of the black hole components, while $v_0 = 0.136 v_c$ runs reach generally higher final eccentricities. This behavior was already indicated by Makino et al. (1993), who simulated two black holes of the masses $M = 0.01$ im a Plummer sphere of 16348 particles. They found very high final eccentricities $e \sim 0.99$ applying very low initial velocities, while their largest value, $v_0 = 0.5 v_c$, reached a noticeably smaller final $e \sim 0.665$.

The dependency of the final eccentricity on initial velocities can be understood by considering the black hole trajectories. In Fig. 2, for $v_0 = v_c$, the black holes spiral at first independently of each other to the center. The influence of dynamical friction causes a steady loss of kinetic energy. Within the time interval $t = [10.11; 20.14]$, the total energy becomes negative and the binary reaches a bound state; in the following the binary hardens, the separation decreases due to superelastic scattering events and the circular motion center

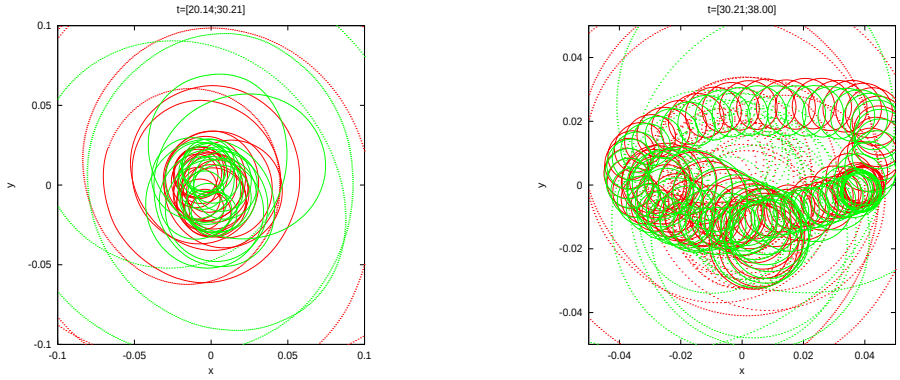

Figure 2. Trajectories for the model $W_0 = 3$, $\omega_0 = 0.3$, $v_0 = v_c$ in the projection on the xy-plane. Red and green mark the orbit of a black hole respectively. Solid lines indicate the trajectories passed through in the time interval mentioned above each figure, the dotted lines hint the orbit before. Note the scaling of the axes in different figures.

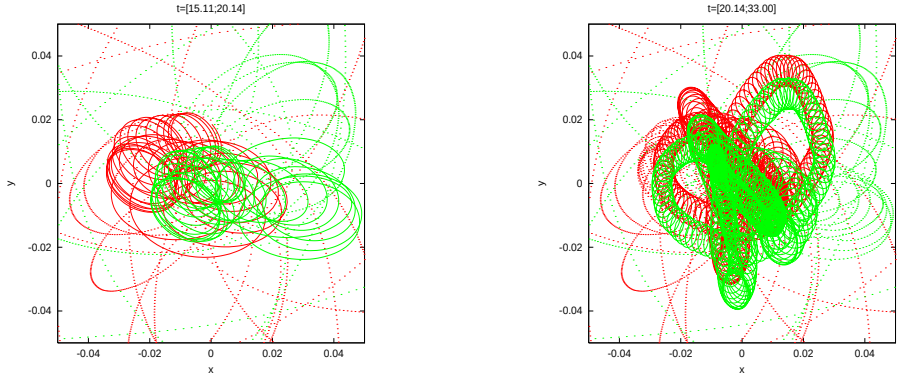

Figure 3. the same as in Fig.2, but with $v_0 = 0.136 v_c$

of mass of the binary itself becomes visible. At the time the attractive force between the black holes becomes comparable to the gravitational force of the stellar distribution, the individual trajectories of the black holes are still circular around the systems center of mass. This means that the circular orbits generated by the initial velocity is ”conserved” until the binary reaches a bound state and beyond as dynamical friction is not strong enough to change the trajectories dramatically.

A different situation arises for $v_0 = 0.136$. As a consequence of the low velocity, the black holes must plunge near to the center, but dynamical friction is at the time of the closest encounter (the pericenter of the relative motion) not sufficiently effective to prevent the re-swing to the outer regions and to circularize the orbits in this way. Therefore, the initial form of the orbits is kept until the end of the simulation. We have studied a much wider parameter range than described here and also looked at other orbital elements of the

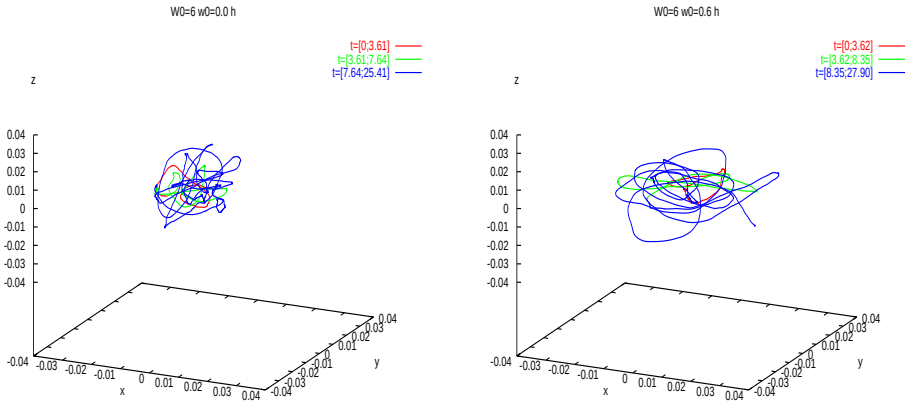

Figure 4. Three-dimensional diagram of the centre-of-mass trajectories of our MBH, $W_0 = 6$ and $v_0 = 0.136 v_c$. The rotation parameters are $\omega_0 = 0.0$ *left* and $\omega_0 = 0.6$ *right*. The different colours indicate the orbits in the denoted time intervals respectively.

MBH (e.g. its inclination relative to the galactic plane, which could be an observable due to the large scale radio jets emitted from the central MBH engines in galactic nuclei), and we have also studied the effect of co- and counterrotation (different angular momentum axis of the stellar system and the initial MBH motion). The interested reader will find a complete review of our results in Eichhorn & Spurzem (2006, MNRAS, in preparation).

3.3 Brownian Motion

The center of mass (CM) of a hardened binary is expected to to perform an irregular motion in the central region of the stellar system. This motion is often described by the concept of Brownian motion, as it is characterized by a friction force (dynamical friction) and a fluctuating force (as the result of scattering events and encounters of field stars). We have measured and analysed the Brownian motion of an MBH due to superelastic scatterings in detail, but show here only one exemplary picture as a typical result.

We conclude from this section: (1) The final eccentricity is strongly dependent on the initial black hole velocities. (2) The eccentricity is dependent on the rotation parameter of the model. (3) Determined hardening rates agree within the expected systematic and statistical error with previously published work. (4) Only weak changes in the inclination and in the orientation of the angular momentum vector direction have been observed, consistent with simulations by Milosavljevic & Merritt (2001). (5) Counter rotation simulations yield noticeably different results in eccentricity, in one case actually an extreme large value $\bar{e} = 0.997$. (6) Brownian motion of the center of mass of the binary is influenced by the rotation of the stellar system (points (4) to (6) are just given here but not discussed in further detail).

4 Computational and Algorithmic Issues

We use a timing model for our parallel code which is flexible and usable for many different kinds of hardware. It is

$$T = \alpha\Big(\frac{N^2}{n_p} + \frac{NN_n}{n_p} + A\ln_2 n_p + BN\Big) \tag{5}$$

where T is the total wall clock time, the four summands (from left to right) are the regular and irregular (neighbour) force computation time, latency and bandwidth dominated communication time (note that a new communication scheme is assumed here, which reduces the latency, which is not yet included in all our simulations. In the old case the latency scaled linearly with n_p). N, N_n, n_p are the total particle number, the neighbour number in the Ahmad-Cohen neighbour scheme, and n_p the processor number used. α, A, B are a time and two dimensionless constants depending on the hardware. Measurements on the IBM Jump deliver values of $\alpha \approx 0.3\mu$ sec, $A \approx 500$, $B \approx 2$, with fluctuations of a factor of 2 to 3 depending on details of the simulation. With these new data we can derive a new value for the optimal neighbour number, which is $N_{n,\mathrm{opt}} \propto N^{3/5}$ for small N (up to about 10^4) and $N_{n,\mathrm{opt}} \propto N^{1/5}$ for larger N. This is significantly smaller than the previously proposed value of Makino & Hut (1988), $N_{n,\mathrm{opt}} \propto N^{3/4}$. With a smaller neighbour number less communication is required and thus larger processor numbers can be used. Our algorithm always works best if we have a balance between communication and computation (this work and more details will be found in Glaschke, 2006, Ph.D. thesis in preparation, and be published elsewhere, too).

Note also, that despite a very good efficiency of our code the use of special purpose hardware such as GRAPE is more efficient for the largest particle numbers (such as 10^5 or 10^6). Recent supercomputers which combine standard CPUs with application acceleration processors (e.g. CRAY XD1 with FPGA chips) offer a promising path to join both advantages (A. Ernst, ongoing work in progress).

5 Outlook, Other Subprojects

In ongoing studies we are right now transcending the limits of Newtonian dynamics. At the termination of the simulations shown above, in particular the very high e-cases, relativistic corrections cause measurable (in the sense of the accuracy of the numerical model) changes in the orbital elements. We have included these terms as perturbative forces in the KS regularisation up to the so-called Post-Newtonian order 2.5, which includes two orders of perihel shifts and the lowest dissipative term, sufficient to describe gravitational radiation (Kupi, Amaro-Seoane & Spurzem 2005, in preparation). In future work more relativistic effects could be included, such as spin-spin and spin-orbit couplings, and linear momentum recoil at MBH binary coalescence. A collaboration with G. Schäfer and G. Achamveedu (Jena) is being developed to properly formulate these terms. Scaling requires that one cannot simulate such systems without realistic particle number. Such models are proposed in the DEISA scheme.

6 Acknowledgements

Computing time at NIC Jülich on the IBM Jump is acknowledged. Financial support comes partly from Volkswagenstiftung, SFB439 at the University of Heidelberg and the Studienstiftung des Deutschen Volkes (P.G.). It is always a pleasure to acknowledge Sverre Aarseth, without his help and continuous support over many years this work would not be possible.

References

1. Aarseth S.J., 1999a, Publ. Astr. Soc. Pac. 111, 1333.
2. Aarseth, S., 2003, *Gravitational N-body simulations* (Cambridge University Press, Cambridge), p.173.
3. Ahmad A., Cohen L., Journal of Computational Physics 1973, 12, 349.
4. Begelman M.C., Blandford R.D., Rees M.J., 1980, Nature, 287, 307.
5. Berczik, P., Merritt, D., Spurzem, R. 2005, ApJ, in press (astro-ph/0507260).
6. Einsel C., Spurzem R., 1999, 1999, MNRAS, 302, 81.
7. Hemsendorf M., Sigurdsson S., Spurzem R., 2002, ApJ, 581, 1256.
8. Khalisi, E., Omarov, C.T., Spurzem, R., Giersz, M., Lin, D.N.C. 2003, in "High Performance Computing in Science and Engineering", Springer Vlg., pp. 71-89.
9. Komossa S., Burwitz V., Hasinger G., Predehl P., Kaastra J.S., Ikebe, Y., 2003, ApJ, 582, L15.
10. Kustaanheimo P., Stiefel E., Journal für die reine und angewandte Mathematik 1965, 218, 204.
11. Lagoute C., Longaretti P.-Y., 1996, A&A, 308, 441.
12. Longaretti P.-Y., Lagoute C., 1996, A&A, 308, 453.
13. Makino J., Fukushige T., Okumura S.K., Ebisuzaki T., 1993, PASJ 45, 303.
14. Makino J. , Funato Y. 2004, ApJ, 602, 93.
15. Merritt D., 2001, ApJ, 565, 245.
16. Merritt, D., 2002, ApJ 568, 998.
17. Milosavljević M., Merritt D., 2001, ApJ, 563, 34.
18. Milosavljević M. , Merritt D. 2003, ApJ, 596, 860.
19. Peters P.C., 1964, Phys.Rev., 136, B1224.
20. Peters P.C., Mathews J. 1963, Phys. Rev. 131, 435.
21. Spurzem R., 1999, Journal of Computational and Applied Mathematics, 109, 407.
22. Zier C., Biermann P.L., 2002, A&A, 396, 91.

John von Neumann Institute for Computing

Chemistry

Sigrid Peyerimhoff

published in

NIC Symposium 2006 ,
G. Münster, D. Wolf, M. Kremer (Editors),
John von Neumann Institute for Computing, Jülich,
NIC Series, Vol. **32**, ISBN 3-00-017351-X, pp. 55-56, 2006.

http://www.fz-juelich.de/nic-series/volume32

Chemistry

Sigrid Peyerimhoff

Institute for Physical and Theoretical Chemistry
University of Bonn, Wegelerstr. 12, 53115 Bonn, Germany
E-mail: unt000@uni-bonn.de

Computational chemistry has become an important area in all fields of chemistry; its significance in molecular physics and pharmacy is also well-recognized. In the design of new materials quantumchemical calculations to determine structural and stability properties of molecules or molecular aggregates are routinely performed parallel to experiments. Similarly, the calculation of energy surfaces to determine various minima (corresponding to isomers) or to locate reaction barriers is undertaken quite efficiently in cooperation with experimental work. Density functional (DFT) procedures are frequently the "work horse" because of their simplicity and because they account for some of the electron corelation. First principle simulations, i.e. a combination of electron structure calculation with molecular dynamic (MF) treatments are used for an increasing number of problems. In such calculations up to a few hundred particles and their motion may be treated in small time intervals. Such studies require large modern computer facilities such as the Jülich installation and cannot be done efficiently on small workstation clusters.

The examples chosen in this year's book show the impact of modern simulation techniques, a wide area of applications, the intense cooperation between computational and experimental work and the need for further theoretical developments in computational chemistry.

An unusual and novel study is the simulation of mechanically-induced chemical reactions. Such investigation is important for the detailed interpretation of single molecule Atomic Force Microscopy (AFM). At the same time it gives information on rupture processes, identifies mechanisms which lead to permanent deformation or ultimate material failure in elastomers. Tailor-made chemical modifications investigated on the computer can design ways to enhance material performance. The study of cooperative effects of various hydrogen bridges in biological materials and in solution requires also first-principle simulations and cannot be performed by molecular dynamics treatments based only on classical mechanics. One of the contributions shows how physical properties of water and ice depend on size and the geometrical arrangment of small clusters; treated are up to 24 particles.

The study of catalytic properties of transition metal ions and of surfaces are always in the main stream of computational chemistry work. This year's contributions are excellent examples of joint experimental and computational studies. The hydrogenation of an organic substance on a platinum surface (and an alloy of platinum with a second metal Sn) is investigated with high resolution electron energy loss spectroscopy (HREELS) in conjunction with DFT calculations. All of the measured peaks in the HREELS spectra could be assigned from the calculations and lead to a deeper understanding of the absorption complex and the catalytic mechanism. Another contribution related to catalysis treats the question of rearrangement and decomposition pathways of molecular (transition-metal containing)

complexes. This is a typical question in coordination and organometallic chemistry. The novel feature in this study is the characterization of more local properties in terms of the compliance matrix (related to the Hessian matrix) at a stationary point which describes the stiffness of a molecular system, i.e. its resistance against distortion. In this case more qualitative considerations can be extracted for further experiments.

The final contribution demonstrates again the large range of computational chemisty projects. It is basic quantumtheoretical work and deals with relativistic effects of small molecules with heavy atoms. The wavefunction is obtained in the 4-component form based on the Dirac and not the Schrödinger equation. Two compontens can be interpreted as the "usual" spin-dependent electronic wavefunctions while the other two describe anti-matter, i.e. positrons. This procedure is merged with the most accurate quantumchemistry methods (configuration interaction and coupled cluster treatment) which are designed to account for electron correlation. The resulting implementation is the best theoretical method available at present to determine with high accuracy spectroscopic properties of molecules containing heavy elements. So far its applicability is restricted to small molecules, however.

All articles show the impact of computational chemistry in various areas and at the same time underline the essential role of the John von Neumann Institute for such work.

John von Neumann Institute for Computing

Understanding Mechanically Induced Chemical Reactions

Elizabeth M. Lupton, Christoph Bräuchle,
and Irmgard Frank

published in

NIC Symposium 2006 ,
G. Münster, D. Wolf, M. Kremer (Editors),
John von Neumann Institute for Computing, Jülich,
NIC Series, Vol. **32**, ISBN 3-00-017351-X, pp. 57-64, 2006.

http://www.fz-juelich.de/nic-series/volume32

Understanding Mechanically Induced Chemical Reactions

Elizabeth M. Lupton, Christoph Bräuchle, and Irmgard Frank

Department of Chemistry and Biochemistry, and Center for Nanoscience
Ludwig Maximilians University Munich, Butenandtstr. 5-13
81377 Munich, Germany
E-mail: {Elizabeth.Lupton, Christoph.Braeuchle, Irmgard.Frank}@cup.uni-muenchen.de

We have used high level computer simulations to investigate modification of the chemical reactivity of molecules under tensile stress. The application of a mechanical force can affect the electronic structure and steric protection, opening up unexpected reaction pathways. These phenomena have implications for the interpretation of single molecule atomic force microscopy experiments which investigate the forced rupture of polymers, and the chemical basis of material failure under a mechanical load.

1 Introduction: Improving Material Performance

The demand for new advanced materials, which while remaining stable over a range of physical and chemical conditions are also non-toxic and can be produced efficiently, is constantly challenged by the development of new technologies. Understanding how materials respond in different environments to mechanical manipulation on the molecular level is essential for the improvement of performance and adaption for new applications. The advent of single molecule experiments combined with high level computer simulations examine modified chemical processes which can occur in a material subjected to extreme mechanical and environmental conditions.

Siloxanes are inorganic polymers with a flexible backbone made up of alternating silicon and oxygen atoms, with bulky methyl groups attached to the silicon atoms (fig.1). Their high flexibility and durability, and stability at high and low temperatures leads to their application in a wide range of situations as adhesives, coatings, sealants and lubricants. From aerospace down to microelectronics on account of their insulating and optical properties, and medical applications because of their non-toxicity, they are an important class of material for situations where mechanical strength and resistance to chemical degradation play a crucial role. To understand the chemical basis of their strength, a collaboration combining single molecule atomic force microscopy (AFM) with quantum chemistry simulations seeks to characterize stress induced bond rupture processes.

2 Understanding Single Molecule Atomic Force Microscopy

Single Molecule AFM[1,2] has principally been used to investigate weak interactions in biological systems[3,4], but can also be used to investigate stronger covalent binding in synthetic materials. In a single molecule AFM experiment a single polymer is pulled from a substrate by an AFM tip until one of the bonds, either in the polymer backbone, at the attachments, or within the substrate is ruptured yielding a force curve and rupture force, the magnitude of which being dependent on the strength of the disrupted interaction. Grandbois and coworkers[5] found the rupture force corresponding to a covalent silicon - carbon bond at the

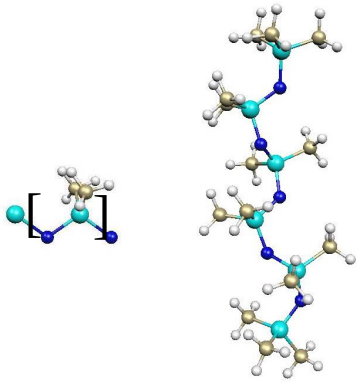

Figure 1. The siloxane monomer (left) and the equilibrium geometry of the siloxane hexamer (right). Turquoise: silicon, blue: oxygen, gold: carbon, white: hydrogen.

attachment of a polysaccharide polymer to an amylose functionalized silica substrate to be 2.0 ± 0.3 nN. In order to identify the breaking bond within the system, static quantum chemistry calculations[6,7] were used to compared the strengths of different possible bonds at the attachment. Scenarios in which the strength of a synthetic single molecule have also been investigated are that of a knot in a polyethylene molecule[8–10] and a study of a thiol molecule pulled from a gold surface[11], both investigated using first principles molecular dynamics simulations. While simulating systems representing AFM experiments, the strength of polymers has been found to be dependent on pulling rate and oligomer length[12] and the solvent surrounding the stretched molecule[13] using Car-Parrinello molecular dynamics simulations. In order to correctly interpret the experimental force curves, theoretical investigations of the systems are necessary to identify the breaking bond, the chemical mechanism of rupture, the influence of solvent and other species in the surrounding environment, and the surface / tip attachment. It is these issues which we address in this study of siloxane rupture taking into account the possible modifications of the chemical reactivity caused by the application of tensile stress. We also seek to determine how the single molecule behavior relates to processes in the bulk siloxane elastomer subjected to a mechanical load.

3 Simulating Molecules under Stress

We use first principles molecular dynamics simulations (Car-Parrinello Molecular Dynamics[14,15]) where a full calculation of the electronic structure using density functional theory[16,17] is performed 'on the fly' for each step of a molecular dynamics trajectory. Using the parallel computing facilities at the John von Neumann Institute for Computing, Jülich, we can follow the evolution of the electronic structure of systems containing up to 300 atoms on a timescale of the order of a few picoseconds at room temperature. In the experiments a siloxane elastomer is covalently attached between a silica substrate and silica tip and pulled in a hexamethyldisiloxane (HMDS - the siloxane dimer) solvent. In the sim-

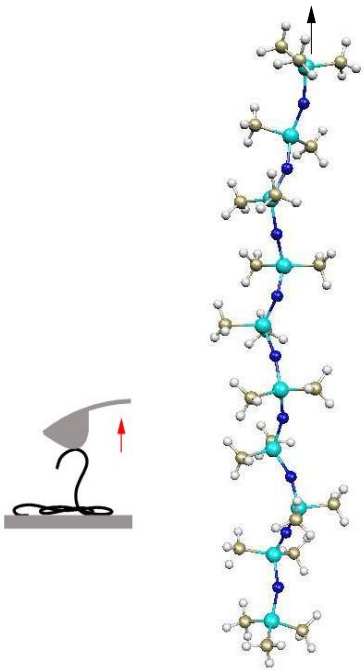

Figure 2. The diagram shows the siloxane decamer (ten silicon atoms in the backbone) in the simulation. The lower terminal silicon atom is fixed and the opposite terminal silicon atom is pulled at a predefined rate in the direction indicated by the arrow so applying a tensile stress to the molecule. The inset shows a schematic representation of the AFM set up with one molecule attached between a substrate and tip.

ulations siloxane oligomers of varying lengths (containing up to ten silicon atoms in the backbone) are pulled at varying rates in different environments to describe the high force regime of the AFM experiment (fig. 2). The mechanically induced rupture process can be characterized and the factors which determine which covalent bond breaks assessed. This information is then used to assign the mechanically measured rupture force.

4 Bond Rupture in the High Force Regime

The ways in which the siloxane elastomer can respond to an applied stress are shown for the siloxane decamer (10 silicon atoms in the backbone) in fig.3. The high flexibility of the molecule stems from the easy deformation of the Si-O-Si bond angle shown in 3 i), which can take values up to 180^O, allowing the polymer to be considered as a chain of spaced silicon atoms. The average values of the stiffer O-Si-O bond angle and Si-O bond length increase simultaneously and it can be seen in 3 ii) and iii) that although extreme values for individual angles and bond lengths can occur, the siloxane does not rupture until a threshold molecular extension has been reached.

The evolution of the electronic structure can be followed as the molecule is stretched and is visualized with localized electron orbitals as shown in fig.4. As the molecule is

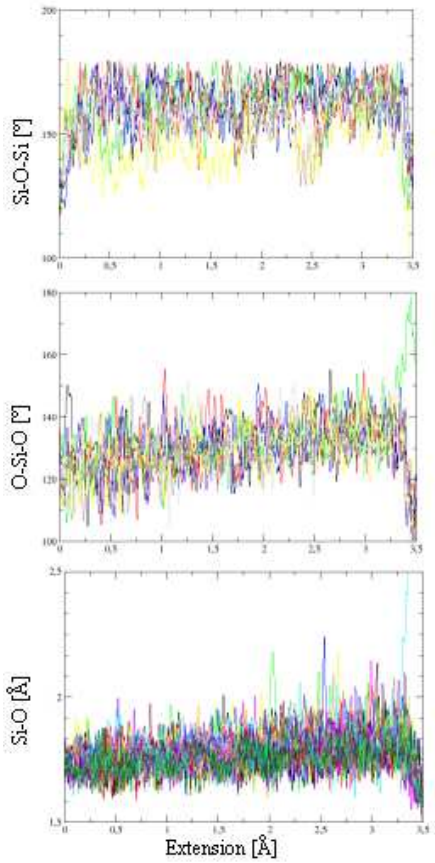

Figure 3. The response of the siloxane decamer to tensile stress, each colour represents a different bond angle or bond length as indicated in the polymer backbone. i) shows the flexibility of the Si-O-Si bond angle which can take values up to 180^o in the simulations. ii) shows how the average value of the stiffer O-Si-O bond increases. iii) shows the increase of the average Si-O bond length. Although individual bonds can reach values of over 2.0Å, the siloxane does not rupture until the total extension has reached a threshold value[18].

stretched the Si-O-Si bonds become polarized, then an Si-O bond breaks via an ionic mechanism, whereby a negative charge is left on the oxygen atom and a positive charge on the silicon, and finally proton transfer occurs from a methyl group to the negatively charged oxygen to neutralize the products. In the case of the longer oligomers (hexamer and decamer), the charged fragments recede rapidly to their coiled equilibrium geometries before proton transfer can occur leaving charged species in the system. The force required to rupture a covalent silicon - oxygen bond can be calculated from the simulations and is shown to be dependent on the pulling rate and oligomer length: slower rates and longer oligomers lead to lower forces. We have calculated a rupture force of 4.4 nN for a siloxane decamer pulled at 55 m/s[18] which is an upper bound for the force as the experimental elastomers are longer and the pulling rates slower.

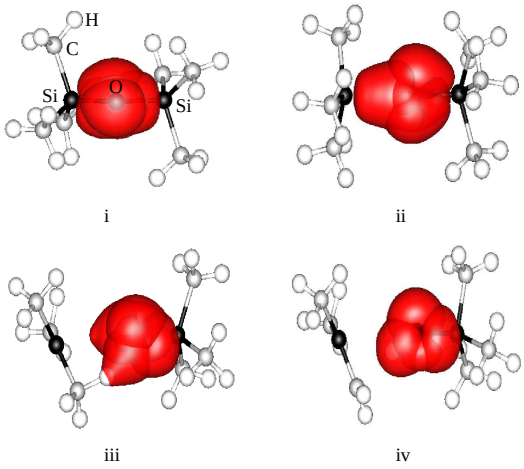

Figure 4. The localized orbitals (Wannier functions) of the electrons in the Si-O-Si backbond of the siloxane dimer. i) shows the equilibrium starting electronic structure. ii) shows the polarization as the molecule is stretched. iii) shows the rupture of an Si-O bond. iv) shows the proton transfer which neutralizes the rupture products[18].

The computer simulations show that the siloxane oligomers are highly flexible and efficient at quickly distributing strain throughout the molecule. Once ruptured, either proton transfer can occur depending on the immediate surroundings to neutralize the products, or charged species are formed which could react further. Both outcomes have implications for understanding the origins of stress induced material failure[18].

5 Mechanically Induced Chemistry: Interaction with the Environment

As the siloxane elastomer is stretched the silicon - oxygen bonds become polarized, leading to local concentrations of charge in the backbone, and the backbone becomes more exposed as the methyl groups surrounding it become more spread out (fig. 2). This could alter the reactivity of the normally inert siloxanes under tensile stress and open up new reaction pathways with species in the surroundings. We are currently investigating possible reactions with solvent molecules as used in the single molecule atomic force microscopy experiments, and with trace amounts of water which could play a role in material failure using computer simulations.

The solvent used in the experiments is hexamethyldisiloxane (HMDS - the siloxane dimer) and we are simulating the stretching of a siloxane oligomer surrounded by HMDS molecules at an appropriate density(fig. 5). Although there is no attraction between the species if no force is applied to the elastomer, in its stretched state the polarized Si-O bond and the exposure of the backbone aid the close approach of a solvent molecule. During our simulations no attraction or interaction between the species was detected, their close approach being hindered by the methyl groups, and so the solvent should not influence the outcome of the experiments.

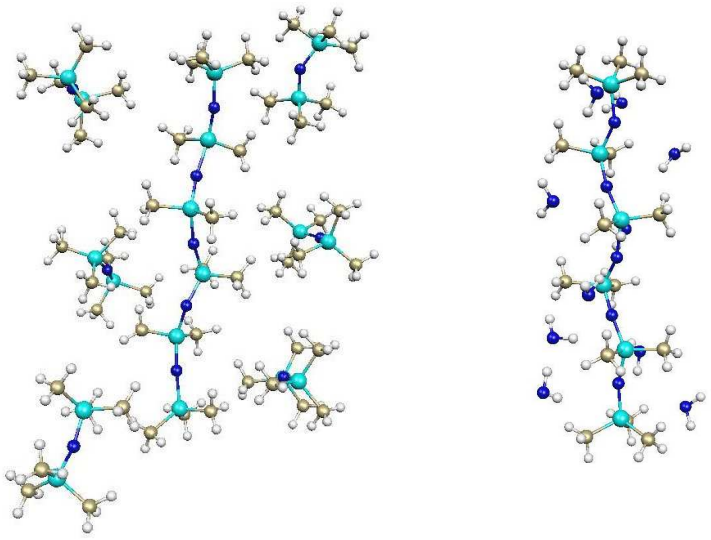

Figure 5. The left hand figure shows the stretched siloxane hexamer surrounded by HMDS solvent molecules during a simulation at an appropriate density. The right hand figure shows the siloxane hexamer surrounded by water molecules, the simulation is to determine whether a water molecule can approach the siloxane and cause its rupture.

We are also studying the influence of water on the rupture reaction mechanism. This protic solvent could attack the polarized Si-O bond before the maximum extension has been reached, resulting in lower measured rupture forces.

6 Pulling Elastomers from Silica

We have started simulating the pulling of a siloxane elastomer from a silica surface (fig. 6). In the sinlge molecule atomic force microscopy experiments a siloxane polymer is covalently bound between a silica substrate and silica AFM tip and our simulations model what is happening at the attachment bonds as the polymer is pulled away from the surface. The substrate, attachment and siloxane molecule are all systems containing covalent silicon - oxygen bonds: but which bond is most likely to break in the experiment and to what extent can the substrate be deformed? Our simulations will show which bond is most likely to break and identify the factors which determine which bond will break, allowing the experiment to be tuned into investigating specific interactions.

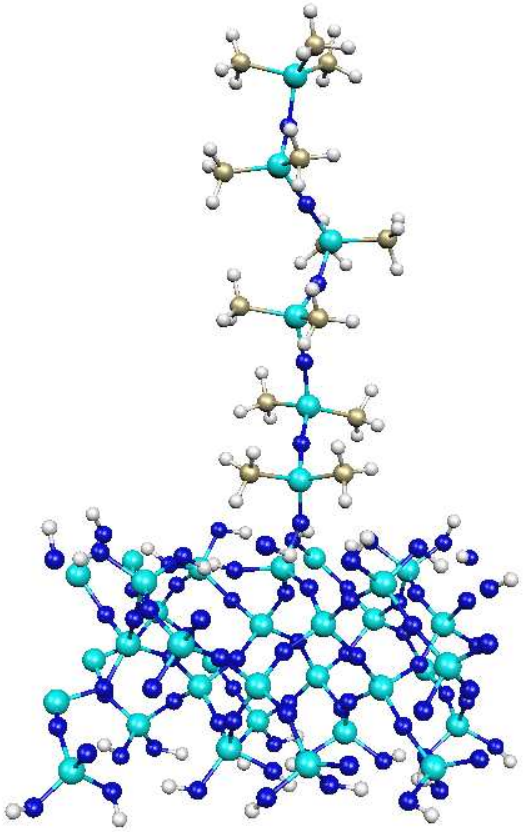

Figure 6. The siloxane hexamer pulled from a silica surface.

7 Conclusions: Implications of Mechanically Induced Chemistry for the Elastomer under Stress

Our simulations have shown how the application of a tensile stress to siloxane elastomers can alter their chemical reactivity by modifying their electronic structure and altering the steric protection of bonds thereby opening up new reaction pathways. We can identify and describe chemical rupture mechanisms as probed in single atomic force microscopy experiments to identify the factors which determine the strength of an individual molecule. We are also performing calculations to understand how reaction fragments can react with one another in the bulk siloxane. Understanding rupture processes is key to identifying the mechanisms which lead to permanent deformation and ultimate material failure in elastomers. The modified chemistry of the stretched polymer therefore plays an important role in the behavior of materials under stress and in developing ways to enhance material performance.

Acknowledgments

This work is carried out as part of a cooperation between the Institute for Physical Chemistry (Chair: Prof. C. Bräuchle) at the Ludwig Maximilians University in Munich, and Wacker Chemie, Burghausen. We are indebted to the John von Neumann Institute for Computing in Jülich for computing time on the Jump cluster. We have also used resources at the Leibniz Rechenzentrum in Munich.

References

1. T. Hugel, M. Seitz, Macromol. Rapid Commun. **22**, 989 (2001).
2. A. Janshoff, M. Neitzert, Y. Oberdörfer, H. Fuchs, Angew. Chem. Int. Ed. **39**, 3212 (2000).
3. H. Clausen-Schaumann, M. Seitz, R. Krautbauer, H. E. Gaub, Curr. Opin. Chem. Biol. **40**, 524 (2000).
4. B. Heymann, H. Grubmüller, Phys. Rev. Lett. **84**, 6126 (2000).
5. M. Grandbois, M.Beyer, M. Rief, H. Clausen-Schaumann, H.E. Gaub, Science **283**, 1727 (1999).
6. M. K. Beyer, J. Chem. Phys. **112**, 7307 (2000).
7. M.K. Beyer, H. Clausen-Schaumann, Chem. Rev. **105**, 2921 (2005).
8. A. M. Saitta, P. D. Soper, E. Wasserman, M. L. Klein, Nature **399**, 46 (1999).
9. A. M. Saitta,M. L. Klein, J. Chem. Phys. **111**, 9434 (1999).
10. A. M. Saitta, M. L. Klein, J. Phys. Chem. B **104**, 2197 (2000).
11. D. Krueger, H. Fuchs, R. Rousseau, D. Marx, M. Parrinello, Phys. Rev. Lett. **89**, 186402 (2002).
12. U.F. Roehrig, I. Frank, J. Chem. Phys. **115**, 8670 (2001).
13. D. Aktah, I. Frank, J. Am. Chem. Soc. **124**, 3402 (2002).
14. R. Car, M. Parrinello, Phys. Rev. Lett. **55**, 2471 (1985).
15. CPMD, J. Hutter et al, *Max-Plank-Institut für Festkörperforschung and IBM Research 1990-96*.
16. P. Hohenberg, W. Kohn, Phys. Rev. B **136**, 864 (1964).
17. W. Kohn, L.J. Sham, Phys. Rev. A **140**, 1133 (1965).
18. E.M. Lupton, C. Nonnenberg, I. Frank, F. Achenbach, J. Weis, C. Bräuchle, Chem. Phys. Lett. **414**, 132 (2005).

John von Neumann Institute for Computing

Cooperativity in Large Water Clusters Liquid Water, Ice and Clathrates

Roger A. Klein

published in

NIC Symposium 2006 ,
G. Münster, D. Wolf, M. Kremer (Editors),
John von Neumann Institute for Computing, Jülich,
NIC Series, Vol. **32**, ISBN 3-00-017351-X, pp. 65-74, 2006.

http://www.fz-juelich.de/nic-series/volume32

Cooperativity in Large Water Clusters Liquid Water, Ice and Clathrates

Roger A. Klein

Institute for Physiological Chemistry
University of Bonn, Nussallee 11, 53115 Bonn, Germany
E-mail: klein@institut.physiochem.uni-bonn.de

Long-range order in the form of water clusters is what gives liquid water, ice and gas clathrates their particular properties. Liquid water, made up of hydrogen-bonded, cross-linked H_2O molecules, should boil nearly 200^{o}C lower at approximately -100^{o}C instead of at +100^{o}C, based on its position as a Group VIA hydride together with H_2S, H_2Se and H_2Te. The presence of cooperative hydrogen bonding between the water monomers gives rise to liquid and solid phases with considerable long-range order which helps to explain many of their physical properties. Liquid water is thought to be composed of 'flickering' clusters of hexagonally coordinated molecules in which the O-H bonds and the two lone-pair electrons of the oxygen atom are arranged in a tetrahedrally symmetric fashion. Thus each water molecule in liquid water, and indeed in Ice Ih, is bound on average by four hydrogen bonds to neighbouring water molecules as a double hydrogen bond donor / double hydrogen bond acceptor. Because the $O\text{-}H_D...O_A\text{-}H$ hydrogen bonds form extended networks of alternating donors and acceptors there is considerable cooperativity which enhances the stability of these networks and is the explanation for the unusual properties of water, such as its specific heat or boiling point.

All the ice polymorphs consist of variations on the theme of tetracoordinated water molecules in the form of hexagons. On the other hand, the gas clathrates are composed of tetracoordinated water molecules hydrogen bonded to give structures formed of edge-sharing pentagons which are stable under moderate pressures and reduced temperatures, such as are found on the ocean floor. Deep-sea methane clathrates, produced naturally, are arguably the largest renewable energy resource available if methods for the recovery of the methane gas without disturbing the equilibtrium of the oceans could be developed.

This project is centred on understanding the electronic and quantum chemical interactions which stabilise these hydrogen-bonded water clusters with hexagonal (water and ice) or pentagonal (clathrates) motifs and which give rise to their particular physicochemical properties. Because it is necessary to study water clusters as large as $(H_2O)_{24}$ at a high level of quantum chemical theory, it is essential to use computational facilities such as those available on the IBMSC-Jump machine at NIC in Jülich.

1 Introduction

Accurate electronic models of the molecular structure of liquid water are necessary not only in order to understand the behaviour of water itself but are also particularly important for the modelling of biologically significant molecules such as proteins or nucleic acids which are hydrated in aqueous solution, being surrounded by a structured solvation shell of water molecules. Modelling of the behaviour of the aqueous solvation shell made up of hydrogen-bonded water molecules is critically dependent on correctly parametrising the force-fields used for molecular mechanics (MM) and molecular dynamics (MD).

The methane clathrates, which are found in the deep oceans[1], represent a large, potentially usable renewable energy resource as the methane is produced by radioactive decay from the earth's core[2]. Clathrates are, however, unstable at ambient temperatures and

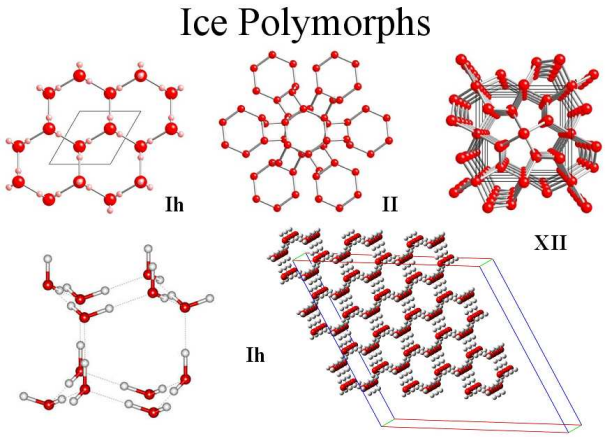

Figure 1. Schematic picture of the various ice polymorphs reported.

pressures so that an understanding of the physical chemistry of these supramolecular aggregates is required in order to able to extract them without disturbing the environmental equilibrium. Explosive de-gassing of a large body of methane clathrates would lead potentially to an environmental disaster as methane CH_4 is a highly effective 'greenhouse' gas. Methane clathrate under high pressure is also thought to be the source of the methane in Titan's atmosphere[3].

Whether one is dealing with liquid water, ice or gas clathrates, cooperative effects between hydrogen-bonded water molecules are highly important in determining physical behaviour as well as the electronic properties of these supramolecular aggregates.

2 Background

Liquid water is thought of in terms of so-called 'flickering clusters' of hexagonal, interlocked ring systems made up of six hydrogen-bonded water molecules[4]. This produces some long-range order even in liquid water at ambient temperatures, extending on average out to at least the second or third hydration shell, as evidenced by radial distribution functions determined from X-ray or neutron scattering experiments[5,6]. The degree of structuring detected by NMR chemical shifts is temperature dependent. The various polymorphs of ice represent an extension of the use of a hexagonal motif in forming a solid structure with very considerable long-range order and, interestingly, a density some 10% less than that of liquid water. Fig. 1 gives a schematic overview over different ice polymorphs as determined by X-ray and neutron diffraction. All of these are based on a hexagonal six-membered ring of water molecules as the structural motif.

On the other hand, gas clathrates are made up of edge-fused pentagonal arrays of water molecules[7,8], hydrogen bonded to one another so that there is a repetitive donor-acceptor pattern. The structure for the sI methane clathrate in shown in Fig. 2 with two views at right angles to one another.

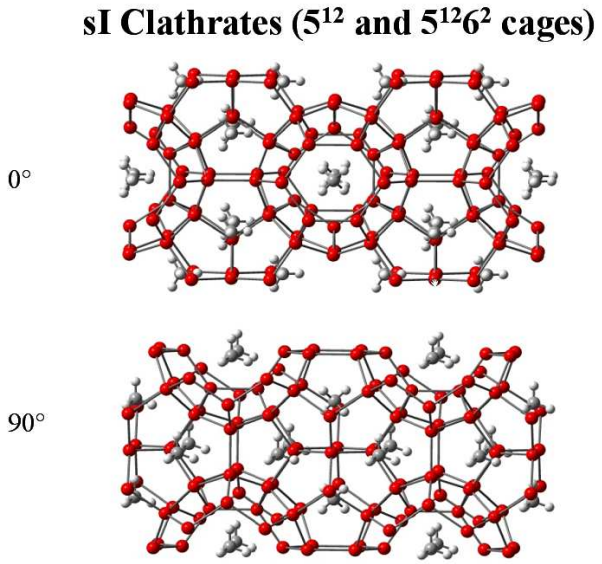

Figure 2. Structure of the methane clathrate taken from X-ray data.

3 Cooperativity

Cooperativity may be defined as occurring when the total effect, for example, stabilisation energy, exceeds the simple, additive sum of the individual, isolated effects, e.g., the interaction energy between two water molecules in the water dimer, making up the total. The term cooperativity may also be applied to hydrogen bonding in water clusters, in which the electron density and its Laplacian at the bond critical point (BCP) for each hydrogen bond are greater than those observed for the water dimer.

Cooperativity may be thought of as synonymous with synergism. This is most clearly seen in the physical synchronisation, or phase-locking, of the O–H vibrational stretching modes in the calculated IR spectrum for water clusters. Cooperativity or synergism are also responsible for the very large OH-stretch IR red-shifts, of the order of 500–600 cm^{-1}, observed for large water clusters both experimentally and theoretically. The physical basis for this cooperativity expressed as synchronisation of the O–H stretching vibrations in liquid water, lies in ultrafast relaxation (approx. 4 pS), a short Förster radius and consequently highly efficient resonant intermolecular transfer of vibrational energy[9, 10].

3.1 Electron Density Topology

An analysis of the electron density topology for a relatively weak interaction such as a hydrogen bond can provide extensive information on the type of bonding present. The electron density distribution is obtained by generating a wave function file in Cartesians, followed by an analysis of the shape of the three-dimensional electron density surface, i.e., its topology. Four types of non-degenerate Morse critical points can be distinguished.

All critical points are charactersised by a rank and signature. A bond critical point (BCP) has a rank of 3 and a signature of -1, abbreviated to (3,-1), meaning that the surface is three-dimensional and that there are two negative curvatures and one positive curvature at critical point. A BCP represents an electron density minimum along the axis joining the nuclear attractors, and a maximum in the plane orthogonal to this line. Other critical points are associated with rings (3,+1), cages (3,+3) and nuclei (3,-3). Bader has proposed an electron density partitioning system involving the zero-flux condition which he has incorporated into his 'Atoms in Molecules' theory - the so-called AIM theory[11]. This partitioning scheme has the advantage that it is mathematically and quantum mechanically more rigorous than other methods for partitioning electron density space. The value of the electron density and its Laplacian (*equation 1*) at the BCP enables a distinction to be made between a 'shared' interaction – typical for a covalent bond – and a 'closed shell' interaction - characteristic of weaker interactions such as hydrogen bonding, electrostatic and van der Waals type interactions. A negative Laplacian indicates a relative excess of charge at the BCP, characteristic of covalent bonding or a *shared* interaction, and a positive value the reverse, typical of a *closed–shell* interaction.

$$\boldsymbol{\nabla^2\rho(r)} = \frac{\partial^2\rho(r)}{\partial x^2} + \frac{\partial^2\rho(r)}{\partial y^2} + \frac{\partial^2\rho(r)}{\partial z^2} \quad \text{..... (1)}$$

Cooperativity is manifest by shortening of the H...O hydrogen bond donor-acceptor distance and by an increase in the electron density at the (3,-1) bond critical point (BCP), as shown in Fig. 3 and Fig. 4, as well as in the Laplacian of rho, $\nabla^2\rho(r)$. Natural bond orbital (NBO) analysis[12] shows increasing orbital overlap for the oxygen lone-pair bonding orbital and the O–H antibonding orbital, $n_O \Longrightarrow$ [O-H]*, with increasing electron occupancy in the [O-H]* antibonding orbital and enhanced second-order perturbation or Fock matrix element deletion stabilisation energies, as well as increasing *%s* character of the lone pair electrons.

At an atomic level, increasingly cooperative hydrogen bonding in large water clusters is associated with an increased negative charge (electrostatic monopole moment) on the oxygen acceptor atom, stabilisation of the oxygen atom, with decreased charge (increased positive charge) on the hydrogen donor atom, *destabilisation* of the hydrogen, and a marked decrease in both atomic dipole polarisation and atomic volume for the hydrogen atom. Increased polarisation of the donor and acceptor in terms of charge, $\delta - ...\delta+$, corresponds with the classical Pauling view of hydrogen bonding. Wave function contraction for the hydrogen atom, i.e., a reduction in atomic volume, is very marked as the strength of hydrogen bonding increases. From a non-bonded value of around 21-22 au for the hydrogen atom (3.11-3.26 Å^3, equivalent to an atomic radius of approx. 0.91-0.92 Å), values of 8-9 au are typical for strongly cooperative environments in tetrahedrally symmetric water clusters. In other highly symmetric, strongly hydrogen bonded structures such as protonated hydrated carbonyl compounds, atomic volume for the hydrogen atom is further reduced to as low as 6 au (0.6 Å^3), with atomic dipole polarisation being close to zero.

Increasing cooperativity is more associated with a greater degree of tetrahedral symmetry in water clusters, together with occupation of both pairs of H-donor and lone-pair acceptor sites, than with cluster size alone, once an optimal ring size of five or six water molecules has been reached. Thus it is no accident that the hexagonal motif in liquid water and ice, or the edge-fused pentagonal motif in the gas clathrates, both represent a structural element for bi-coordinated water molecules in which cooperativity is maximised. Although

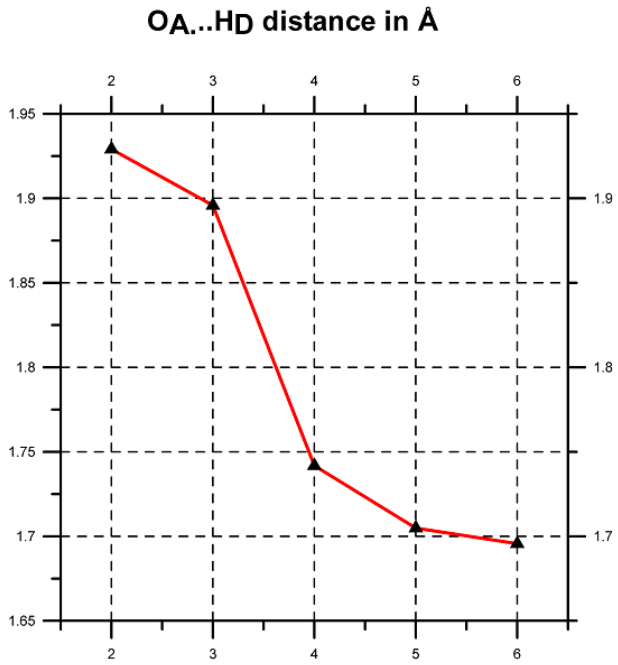

Figure 3. Donor-acceptor (-H...O-) distances for the hydrogen bonds in simple rings.

further coordination of the water molecules ultimately giving almost perfect tetrahedrally symmetrically 4-coordinated waters in the cluster, does not appear to alter the electron density topological parameters of the hydrogen bond bond critical points (BCPs) by more than a few percent over and above the values for five or six-membered rings, the effects on the environment of the oxygen atoms are profound as evidenced by the ^{17}O chemical shielding tensors, and the ^{17}O chemical shift, as described in the next section.

3.2 Chemical Shielding Tensors

Calculations in our laboratory of the absolute shielding tensor for ^{17}O-water monomer in the gas-phase at the MPW1PW91/6-311+G(2d,p) level of theory have yielded a value of 327.3 ppm. This is excellent agreement with the rovibrationally corrected value of 327.7 ± 0.3 ppm arrived at by Vaara et al.[13]. Traditionally, attempts at calculating the ^{17}O-NMR chemical shift for liquid water modelled by water clusters at a quantum mechanical level have not achieved adequate accuracy compared to the experimental value for the ice Ih to gas-phase shift of 48.6 ppm[14]. Indeed, use of self-consistent reaction field (SCRF) methods such as the polarised continuum model (PCM) or COSMO not only fail to predict the correct magnitude for the ^{17}O chemical shift but also give the wrong absolute sign, with *upfield* shifts for small clusters[15–17].

We have recently shown that *ab initio* quantum chemical methods using a combination of a hybrid density functional and a Pople triple split-valence basis set with diffuse and polarisation functions, is able to predict the full range of ^{17}O chemical shift and, inciden-

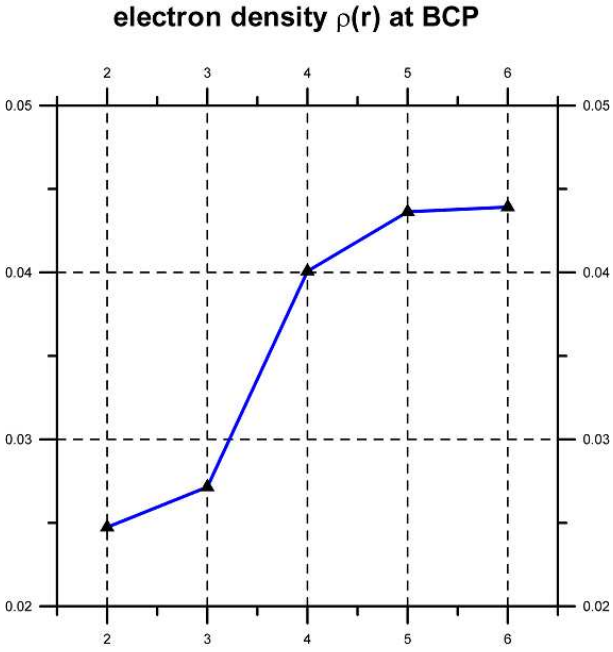

Figure 4. Electron density at the BCP for the hydrogen bonds in simple rings.

tally, also the ^{1}H-proton chemical shift, on going from gas-phase water to ordered ice, so long as account is taken of water coordination geometry, filling all four hydrogen bonding donor-acceptor sites and ring cooperativity[17].

The ^{17}O NMR chemical shielding tensors show a consistent decrease (chemical shift increases) as ring cooperativity and geometry improve and the water molecule is ultimately tetracoordinated with almost ideal tetrahedral sp^3 symmetry. In this case, each water molecule has two O-H donors and two lone-pair acceptors occupied on the oxygen atom.

The asymptotic value for the ^{17}O chemical shielding tensor approaches 272 ppm, giving a chemical shift compared to gas-phase water of 55 ppm. Our results are illustrated[17] graphically in Fig. 5 and Fig. 6.

This calculated shift of 55 ppm is sufficient to account for the experimentally observed values. A deshielding (downfield shift) of 40 ppm is observed experimentally on going from vapour phase water at 100^{o}C to liquid water at room temperature. Approximately a further 8 ppm deshielding takes place on going from liquid water to ice Ih, making in total some 48 ppm compared to the gas-phase value[14]. At an electronic level, increasing cooperativity and enhanced tetrahedral coordination result in the oxygen atom becoming increasingly negatively charged, energetically stabilised, with an increased paramagnetic component to the shielding tensor and decreased shielding anisotropy, as the electric field gradient (EFG) decreases.

Our explicit atomic level electronic model of ordered water molecules in liquid water and ice provides chemical shift values that are totally consistent with values obtained

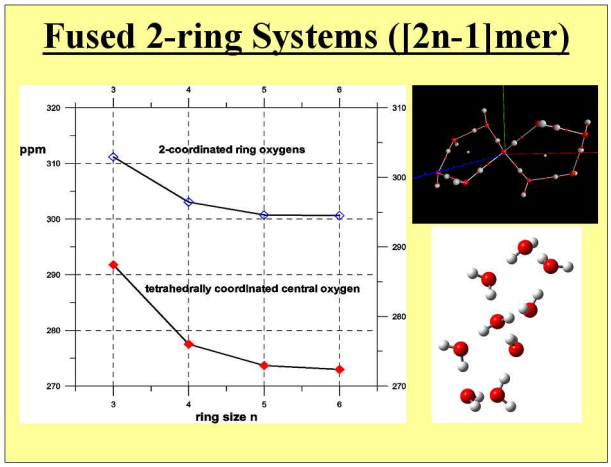

Figure 5. Oxygen-17 NMR chemical shielding tensor in simple rings with a tetra-coordinated water.

experimentally by NMR. In particular, since neither water vapour at 100^{O}C is completely dissociated nor is ice completely ordered at 0^{O}C, our results currently provide probably the most accurate model of the electronic environment of the oxygen atom in water permitting not only an explanation of the change in chemical shift on going from water vapour to liquid, and from liquid to ice, but also a quantitative explanation of the chemical shift temperature sensitivity in the range 0-100^{O}C. The only other realistic chemical shift values for water have been provided by combined quantum mechanics and molecular dynamics, the CPMD approach of Car-Parrinello[18], as reported by Pfrommer et al.[14] and Pennanen et al.[19]. Whereas our *ab initio* cluster method provides an explicit *snapshot* of water order and its electronic environment, the CPMD approach provides a time average for a water molecule embedded in its solvation shell of neighbouring water molecules.

3.3 IR and Raman Spectroscopy

Cooperative effects in water clusters result in substantial red-shifts in both the IR and Raman spectra, often amounting to some hundreds of wave numbers. The example of the heptadecamer (n = 17) cluster is shown in Fig. 7. Increased red-shifting of the O–H stretching vibration is common to all systems in which extensive hydrogen bond cooperativity occurs[20,22,21]. In larger systems such as hydrated glucopyranose[21] or water clusters the O–H vibrations are strongly synchronised or phase-locked. Scaled values of the IR and Raman frequencies for large water clusters are extremely good approximations to the experimental values and spectral shape for liquid water and ice, lying within a few percent of the spectroscopically determined value (*unpublished data*).

4 Conclusions

Tetrahedrally coordinated water clusters containing either the hexagonal or pentagonal ring motif, provide an explicit means of investigating theoretically the physics and physical chemistry of water at an atomic and electronic level, as found in nature as liquid water,

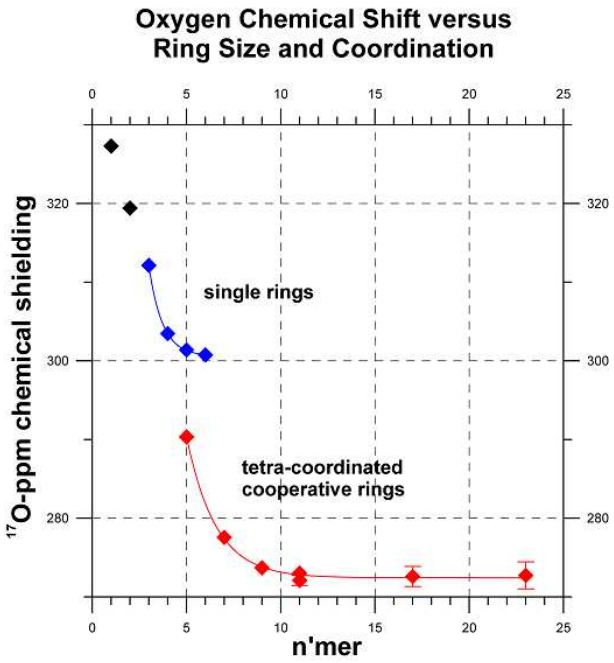

Figure 6. Oxygen-17 NMR chemical shielding tensor in small ring systems and large water clusters. The effects of ring size and coordination, defined in terms of hydrogen bonding, on the chemical shielding tensor in water clusters. Reference values for the water monomer and dimer are shown in black; two-coordinated water molecules in single ring systems are shown in blue; and tetrahedrally four-coordinated waters in cooperative clusters are shown as red diamonds.

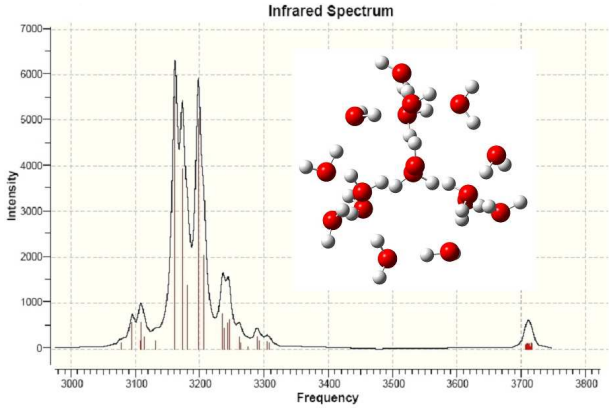

Figure 7. Calculated IR spectrum (scaled) for the heptadecamer water cluster, shown as inset.

ice or in the form of gas hydrates. Water is an extremely polar liquid which shows extensive long-range order even in the fluid phase, and is characterised by a network of highly

cooperative hydrogen bonds giving rise to synchronisation of the O–H vibrational modes. Clarification of the detailed physical properties of water at atomic and sub-atomic level remains a pre-requisite to understanding its unique role as the solvent without which biological life as we know it would not exist.

Acknowledgments

I would like to thank the following colleagues with whom I have collaborated or held useful discussions during the course of the work reported here: Benedetta Mennucci (Pisa); Jacopo Tomasi (Pisa); Mark Zottola (Birmingham Alabama); Jose Sordo (Oviedo); Ernst Bause (Bonn). I should also like to acknowledge computer time on the IBMSC-JUMP machine made available in the form of of a project grant by the John Neumann Institute for Computing (NIC), Research Centre Jülich.

References

1. Davidson,D. W.; Garg,S. K.; Gough,S. R.; Handa,Y. P.; Ratcliffe,C. I.; Ripmeester,J. A.; Tse,J. S.; *Laboratory analysis of a naturally occurring gas hydrate from sediment of the Gulf of Mexico*, Geochim. Cosmochim. Acta **50**, 619–623 (1986).
2. *Gas Hydrates on the Brink*, Nature **420**, 622–623 (2002).
3. Loveday, J. S.; Nelmes, R. J.; Guthrie, M.; Belmonte, S. A.; Allan, D. R.; Klug, D. D.; Tse, J. S.; Handa, Y. P.; *Stable Methane Hydrate Above 2 GPa and the Source of Titan's Atmospheric Methane*, Nature **410**, 661–663 (2001).
4. Stillinger, F. H.; *Water revisited*, Science **209**, 451–457 (1980).
5. Soper, A. K.; Phillips, M. G.; *A new determination of the structure of water at 25^{o}C*, Chem.Phys. **107**, 47–60 (1980).
6. Soper, A. K.; Bruni, F.; Ricci, M. A.; *Site-site Pair Correlation Functions of Water from 25^{o}C to 400^{o}C: Revised Analysis of New and Old Diffraction Data*, J. Chem. Phys. **106**, 247–254 (1997).
7. English, N. J.; Macelroy, J. M. D.; *Structural and Dynamical Properties of Methane Clathrate Hydrates*, J. Comp. Chem. **24**, 1569–1581 (2003).
8. Kirchner, M. T.; Boese, R.; Billups, W. E.; Norman, L. R.; *Gas Hydrate Single-Crystal Structure Analysis*, J. Amer. Chem. Soc. **126**, 9407–9412 (2004).
9. Nitzan, A.; *Ulrafast relaxation in water*, Nature **402**, 472–475 (1999).
10. Woutersen, S.; Bakker, H. J.; *Resonant intermolecular transfer of vibrational energy in liquid water*, Nature **402**, 507–509 (1999).
11. Bader, R. F.W.; *Atoms in Molecules. A Quantum Theory* (Oxford University Press, Oxford, UK, 1990).
12. Weinhold,F.; Landis,C. R.; *Valency and Bonding. A Natural Bond Orbital Donor-Acceptor Perspective* (Cambridge University Press, Cambridge, UK, 2005).
13. Vaara, J.; Lounila, J.; Ruud, K.; Helgaker, T.; *Rovibrational Effects, Temperature Dependence and Isotope Effects on the Nuclear Shielding Tensors of Water. A New Absolute Shielding Scale*, J. Chem. Phys. **109**, 8388–8397 (1998).
14. Pfrommer, B. G.; Mauri, F.; Louie, S. G.; *NMR Chemical Shifts of Ice and Liquid Water. Effects of Condensation*, J. Amer. Chem. Soc. **122**, 123–129 (2000).

15. Chesnut, D B.; *Structures, Energies and NMR Shieldings of Some Small Water Clusters on the Counterpoise Corrected Potential Energy Surface*, J. Phys. Chem. A. **106**, 6876–6879 (2002).
16. Tomasi, J.; Mennucci, B.; Cammi, R.; *Quantum Mechanical Continuum Solvation Models*, Chem. Rev. **105**, 2999–3093 (2005).
17. Klein, R. A.; Mennucci, B.; Tomasi, J.; *Ab Initio Calculations of ^{17}O NMR-Chemical Shifts for Water. The Limits of PCM Theory and the Role of Hydrogen-Bond Geometry and Cooperativity*, J. Phys. Chem. A **108**, 5851–5863 (2004).
18. Car, R.; Parrinello, M.; *Unified Approach to Molecular Dynamics and Density Functional Theory*, Phys. Rev. Lett. **55**, 2471–2474 (1985).
19. Pennanen, T. S.; Vaara, J.; Lantto, P.; Sillanpaa, A. J.; Lassonen, K.; Jokisaari, J.; *Nuclear Magnetic Shielding and Quadrupole Coupling Tensors in Liquid Water. A Combined Molecular Dynamics Simulation and Quantum Chemical Study*, J. Amer. Chem. Soc. **126**, 11093–11102 (2004).
20. Klein, R. A.; *Ab Initio Conformational Studies on Diols and Binary Diol-Water Systems Using DFT Methods. Intramolecular Hydrogen Bonding and 1:1 Complex Formation with Water*, J. Comp. Chem. **23**, 585–599 (2002).
21. Klein, R. A.; *Electron Density Topological Analysis of Hydrogen Bonding in Glucopyranose and Hydrated Glucopyranose*, J. Amer. Chem. Soc. **124**, 13931–13937 (2002).
22. Klein, R. A.; *Hydrogen Bonding in Diols and Binary Diol-Water Systems Investigated Using DFT Methods. II. Calculated Infrared OH-Stretch Frequencies, Force Constants, and NMR Chemical Shifts Correlate with Hydrogen Bond Geometry and Electron Density Topology. A Reevaluation of Geometrical Criteria for Hydrogen Bonding*, J. Comp. Chem. **24**, 1120–1131 (2003).

John von Neumann Institute for Computing

Adsorption of Complex Molecules from Vibrational Spectroscopy: A Joint Theoretical and Experimental Approach

Jan Haubrich, David Lofferda, Francoise Delbecq, Philippe Sautet, Alexander Krupski, Conrad Becker, and Klaus Wandelt

published in

NIC Symposium 2006 ,
G. Münster, D. Wolf, M. Kremer (Editors),
John von Neumann Institute for Computing, Jülich,
NIC Series, Vol. **32**, ISBN 3-00-017351-X, pp. 75-82, 2006.

http://www.fz-juelich.de/nic-series/volume32

Adsorption of Complex Molecules from Vibrational Spectroscopy: A Joint Theoretical and Experimental Approach

Jan Haubrich[1,2], David Lofferda[2], Francoise Delbecq[2], Philippe Sautet[2], Alexander Krupski[1], Conrad Becker[1], and Klaus Wandelt[1]

[1] Institute for Physical and Theoretical Chemistry
University of Bonn, Wegelerstr. 12, 53115 Bonn, Germany
E-mail: janh@thch.uni-bonn.de
[2] Laboratoire de Chimie, UMR CNRS 5182, Ecole Normale Supérieure de Lyon
46 Allée d'Italie, 69364 Lyon Cedex 07, France

Studies on heterogeneous catalysis such as the selective hydrogenation of α,β-unsaturated aldehydes on transition metal surfaces represent a challenge to both experimentalists and theoreticians. Although numerous studies have been dedicated to systems like acrolein or prenal on Pt(111) in recent years, the details of the molecule-surface bonding still remain under debate. Yet the selectivities of such processes depend crucially on the structure of adsorption complexes. Their characterization is even more complicated when alloy surfaces, which are often used to optimize the properties of the catalyst, are considered.

Here we present a joint experimental and theoretical study on molecule-surface bonding of prenal on Pt(111) and two Pt-Sn surface alloys based on the interpretation of HREEL spectra using *ab initio* density-functional theory (DFT). HREELS experiments carried out on the three model-catalysts show highly complex spectra of the adsorbed prenal at low temperatures. By comparing the HREEL spectra with the results of the vibrational analysis obtained from the DFT calculations, we are able to identify stable adsorption geometries, interpret the normal modes corresponding to the measured loss peaks and point to likely reaction paths.

1 Introduction

Investigations of reaction mechanisms, selectivities or activities in catalytic processes require a profound understanding of the interactions of the reactants, intermediates and products with the catalyst itself. Since the surface structures of industrial catalysts are usually highly complex, model systems with defined surface structures have to be used to perform such investigations. Besides using mono- and multimetallic single-crystaline samples, also alloying the surface of a monometallic substrate with a second metal can be used to create well defined model catalyst surfaces.

A considerable number of studies have been performed to understand the hydrogenation process and the adsorption properties of α,β-unsaturated aldehydes on single crystal surfaces and alloys (See Refs. 1–4 and references therein). Most of these studies are dedicated to the close-packed Pt(111) surface and well-ordered Pt-Sn/Pt(111) surface alloys as model catalysts.

The hydrogenation of α,β-unsaturated aldehydes can lead to three different products. Saturated aldehydes (Fig. 1), which represent the thermodynamically favoured hydrogenation products, the saturated alcohols and unsaturated alcohols, which are of particular interest for the chemical and pharmaceutical industry. The selectivity of this reaction depends

strongly on the aldehyde itself as well as the catalyst[1,3]. For instance it is known, that the substitution of methyl-groups on the β-carbon of the C=C bond, leading from acrolein (propenal) to crotonaldehyde (2-butenal) and to prenal (3-Methyl-2-butenal), increases the selectivity towards the unsaturated alcohol. Similarly alloying the catalyst with other metals can increase the selectivity, which is in fact observed, when one alloys a Pt catalyst with Sn[1]. Generally it is expected, that double bonds interacting with the surface are more easily hydrogenated. Therefore, changes in the adsorption modes on the various model catalysts could help to explain the observed selectivities.

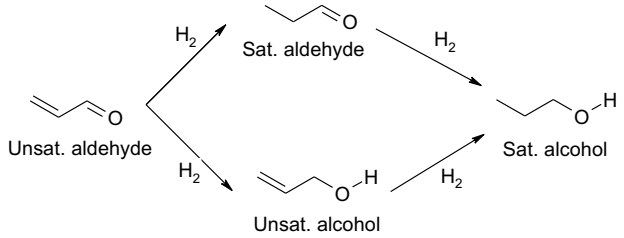

Figure 1. Possible hydrogenation reactions of α,β-unsaturated aldehydes.

We employ high resolution electron energy loss spectroscopy (HREELS) in conjunction with density functional theory (DFT) to gain deeper insights into molecule-surface interactions, surface processes and modifications by alloying effects.

In particular, the Pt(111) surface and two ultra-thin Pt-Sn surface alloys have been chosen as model catalysts. For the experiments and the density functional theory calculations in the present project, emphasis has been placed on the examples of crotonaldehyde and prenal. Extending previous studies[3], in this work all possible adsorption geometries on Pt(111), Pt_2Sn(111) and Pt_3Sn(111) have been investigated. In addition to the total energy calculations we report the computation of the vibrational spectra (HREELS, RAIRS) in comparison with recent experiments performed in Bonn.

Here we focus on the adsorption of prenal. The varity of the conceivable adsorption complexes of prenal on the three model-catalysts is increased by the fact, that prenal exists in two rota-isomers, namely (s)-trans prenal and (s)-cis prenal. Both isomers differ in the relative orientation of the C=C and C=O double bonds. In the gas phase both isomers are energetically very similar, cis prenal being by 3.5 kJ/mol less stable.

Details regarding the theoretical calculations and the experiments are presented in Sec. 2. The follwing discussion in Sec. 3 gives important results of the studies of prenal on three model catalyst surfaces. Finally some conclusions will be drawn in Sec. 4 showing the potential and also limits of this joint theoretical and experimental approach.

2 The Theoretical and Experimental Approaches

2.1 Computational Details

The DFT calculations have been performed using the VASP program[5] at the general gradient approximation (GGA, Perdew-Wang 91[6]) with PAW pseudopotentials[7]. A tight

convergence of the plane-wave expansion is obtained with a cut-off of 400 eV. For both the Pt(111) and Pt_2Sn(111)/Pt(111) surfaces a 3×3 cell of the adsorbate was considered (coverage of 1/9 monolayer, ML), consisting of a 4 layer metallic slab and a 5 layer thick vacuum with adsorption of the molecules on one side of the slab. For the Pt_3Sn(111)/Pt(111) surface a $(2\sqrt{3} \times 2\sqrt{3})R30^\circ$ adsorbate periodicity was used. In the cases of the Pt_2Sn(111)/Pt(111) and Pt_3Sn(111)/Pt(111) surface, a single alloy layer is modeled above a Pt(111) bulk[8,9]. For the geometry optimizations, only the two uppermost metal layers and the molecule are relaxed whereas the two lowest metal planes are kept frozen. 2D Brillouin zone integration is performed on a sufficiently converged $3 \times 3 \times 1$ k-point grid. The vibrational frequencies are calculated by numerical computation of the 2^{nd} derivatives of the potential energy surface, neglecting any coupling between molecular modes and surface phonons lying in the 0-200 cm^{-1} range (see Ref. 4 for more details). Therefore only the harmonic modes with frequencies above 320 cm^{-1} will be given. The HREELS loss intensities are calculated from the 1^{st} derivatives of the z-component of the dynamical dipole moments[4]. Due to the large number of possible adsorption structures of prenal and crotonaldehyde on the three chosen surfaces and the size of the supercells, this project turned out to be computationally highly demanding. Numerous of the calculations have been performed at the computer center (ZAM) of the Forschungszentrum Jülich utilizing the newly established massively-parallel IBM supercomputer JUMP.

2.2 Experimental Details

The experiments were performed in an ultrahigh vacuum chamber (base pressure 10^{-8} Pa) equipped with a high resolution electron energy loss spectrometer (HREELS, VSW IB2000), a back-view LEED optics, an Auger electron spectrometer (AES) and a quadrupole mass spectrometer (QMS)[9]. The HREEL spectra were recorded with a primary electron energy of 4.7 eV in a specular geometry 60° off normal incidence. The Pt(111) sample was cleaned by repeated cycles of Ar^+ sputtering at 900K (2 keV) and annealing to 1150K.

The ordered Pt_nSn(111)/Pt(111) surface alloys have been prepared by depositing Sn films at 300K onto the Pt(111) and subsequent annealing[9]. The amount of Sn deposited was characterized by Auger electron spectroscopy. After annealing the Sn films to 600K, a LEED pattern with a $(\sqrt{3} \times \sqrt{3})R30^\circ$ symmetry indicates the formation of a Pt_2Sn(111) surface alloy (Fig. 2). At higher temperatures of 1000K, the $p(2 \times 2)$ symmetry of a Pt_3Sn(111) surface alloy was found.

To characterize the thermal stability and reactivity of prenal on these surfaces, additionally TPD and LEED experiments of prenal adsorbed at 100K were performed. On Pt(111) the desorption of the prenal multilayer is detected at 160K followed by a desorption state at 199K. Furthermore decomposition reactions are observed giving rise to desorption of H_2 and CO. The HREELS experiments carried out between 100K and 500K on Pt(111) show highly complex spectra of the adsorbed prenal and its fragments, which form above 300K. On Pt_2Sn/Pt(111) and Pt_3Sn/Pt(111) this fragmentation process is suppressed. The HREELS experiments on these surfaces show only intact prenal species on the surface.

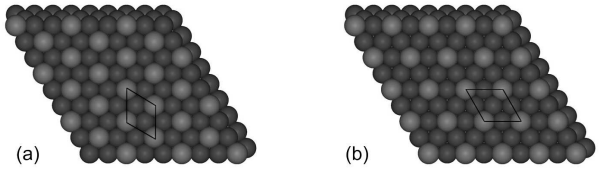

Figure 2. (a) Model of the $Pt_2Sn(111)/Pt(111)$ $(\sqrt{3}\times\sqrt{3})R30°$ surface. This surface shows only platinum top and brigde adsorption sites. (b) Model of the $Pt_3Sn(111)/Pt(111)$ $p(2\times 2)$ surface. On this surface pure platinum threefold hollow sites are present, too.

3 Identification of the Adsorption Modes of Prenal

3.1 Prenal/Pt(111)

The HREEL spectrum of prenal on Pt(111) shown here (Fig. 3) was obtained after adsorption at 100K and subsequent annealing to 205K in order to desorb the multilayer phase as determined by TPD experiments. It is highly complex and the loss signals measured show characteristic intensity changes and shifts compared to the signals of a prenal multilayer. The latter can be well described using the frequencies obtained from the calculation of prenal in the gas phase.

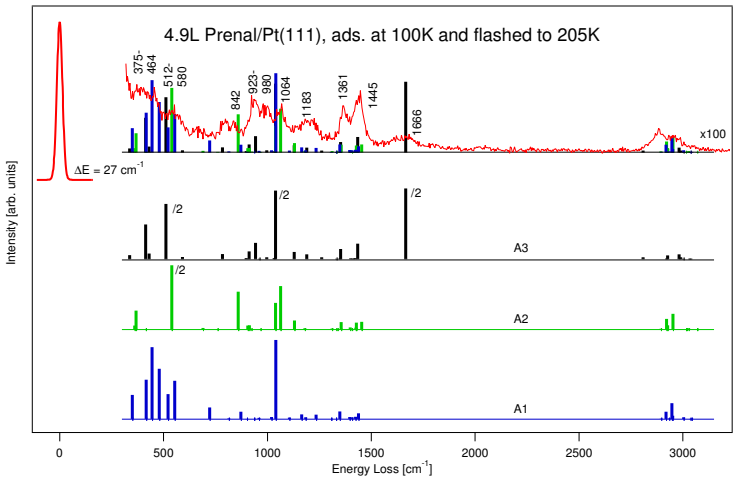

Figure 3. HREELS experiments and DFT calculations of prenal/Pt(111).

The theoretical modelling of the HREEL spectrum of the monolayer of prenal/Pt(111) requires the calculated spectra of η^4-(s)-trans-diσ(CC)+diσ(CO) (59 kJ/mol, A1), η^3-(s)-cis-diσ(CC) (49 kJ/mol, A2) and η^2-(s)-trans-diσ(CC) (54 kJ/mol, A3) binding sites. Two additional adsorption sites, η^4-(s)-cis-π(CC)+diσ(CO) (47 kJ/mol) and η^2-(s)-cis-diσ(CC)

(48 kJ/mol) can also not be excluded, neither from their adsorption energies nor from their vibrational fingerprints.

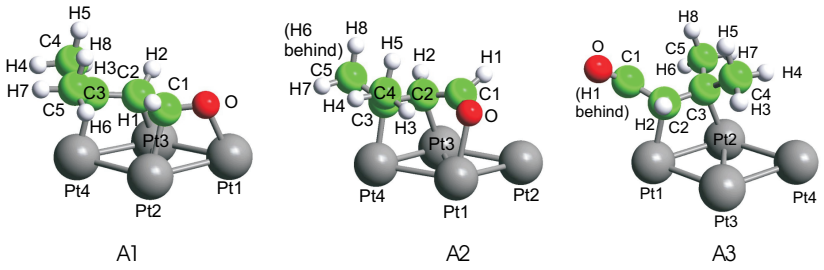

Figure 4. The identified adsorption geometries of prenal on Pt(111): η^4-(s)-trans-diσ(CC)+diσ(CO) (59 kJ/mol, A1), η^3-(s)-cis-diσ(CC) (49 kJ/mol, A2) and η^2-(s)-trans-diσ(CC) (54 kJ/mol, A3).

As seen from the superposition of these computed HREEL spectra with the experimental spectrum, the agreement of the frequencies is excellent in the region between 300 and 2000 cm^{-1} with errors of ca. 1%. Below 300 cm^{-1} the neglect of the surface phonons during the vibrational analysis and the limited thickness of the 4 layer metal slab leads to slightly larger errors (ca. 3%). In the CH-stretching region above 2500 cm^{-1} also sizeable errors are induced in the calculations. These are due to the anharmonicity of the potential and Fermi-couplings, which are ignored in the numerical frequency analysis.

All of the measured loss peaks in the HREEL spectra can be assigned from the DFT calculations. The most important assignments are presented in table 3.1.

Experimental: [cm^{-1}]	Assignment from DFT [cm^{-1}]:
1666	ν(C=O) of η_2-(s)-trans (1686).
	ν(C2=C3) of η_2-(s)-trans (1189), inactive.
1445	sym. and asym. δ'(CH$_3$),
1361	δ"(CH$_3$) and u(CH$_3$) of all ads. sites.
1181	ν(C2=C3) of η_3-(s)-cis (1181).
1183, 1164	ν(C2=C3) and ν(C=O) of η_4-(s)-trans, both weak.
1064	ν(C1-C2) of η_3-(s)-cis (1063),
	ν(C1-C2) of η_2-(s)-trans (1039) and
	γ_s"(C4H$_3$, C5H$_3$) of η_4-(s)-trans (1040).
923-980	mainly γ_{as}(C1H1, C2H2) of η_2-(s)-trans (943).
842	γ_s(C1H1, C2H2) of η_3-(s)-cis (859).
512-580	ν(Pt-C3) of η_2-(s)-trans (511), ν_{as}(Pt-CC) of
	η_3-(s)-cis (539), ν_{as}(Pt-CC) (554) and
	δ(O-C1-C2) (521) of η_4-(s)-trans.
464, 375	δ(C2=C3-C4,C5) (444), ν_s(Pt-CC) (417) of
	η_4-(s)-trans and δ(C3-C4,C5) of η_2-(s)-trans (413).

To highlight the sensitivity of the double bond stretching frequencies to the various adsorption modes, their positions shall be compared at this point. At 1666 cm^{-1} the ν(C=O) vibration of the η^2-(s)-trans-diσ(CC) agrees with the experiment. It is only slightly shifted compared to the gas phase value of 1677 cm^{-1} since it is not directly involved in the interaction to the substrate. The corresponding ν(C=C) vibration of this site is shifted strongly to 1189 cm^{-1} in agreement with its diσ(C=C) bonding configuration. In the case of the η^3-(s)-cis-diσ(CC) geometry both vibrational normal modes are computed with sizeable shifts at 1453 cm^{-1} (ν(C=O), inactive) and 1181 cm^{-1} (ν(C=C)). The frequency of the latter mode again indicates the diσ(C=C) bonding configuration. At 1183 cm^{-1} the ν(C=C) normal mode of the η^4-(s)-trans-diσ(CC)+diσ(CO) site is calculated with weak intensity in agreement with the measured spectrum. Its ν(C=O) vibration is computed at 1164 cm^{-1}.

3.2 Prenal/Pt_3Sn(111)

Also in the case of prenal on the Pt_3Sn/Pt(111) surface alloy a model can be deduced by combining the HREELS experiments with the DFT calculations (Fig. 5). Experimentally it is seen in TPD and HREELS, that prenal adsorption is completely reversible on this surface and that the adsorption strength of the monolayer species is sizeably decreased compared to Pt(111).

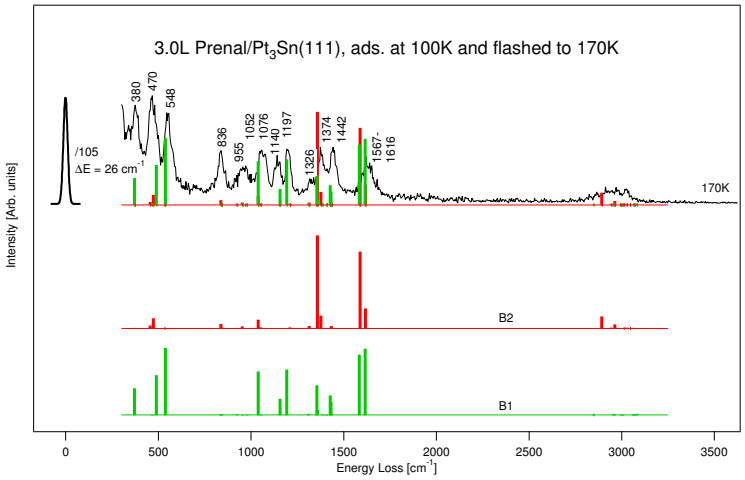

Figure 5. HREELS experiments and DFT calculations of prenal/Pt_3Sn(111).

The analysis of this model system leads to the identification of two η^1-(s)-trans-top-OSn adsorption structures (Fig. 6), in which prenal interacts solely with the oxygen of the aldehydic function with Sn atoms on the surface. Both related sites differ only by the relative orientation of the molecule. Due to the alloying with Sn the adsorption energies decrease strongly: With 39 (B1) and 31 kJ/mol (B2) the adsorption energies are only 66% of those on pure Pt(111).

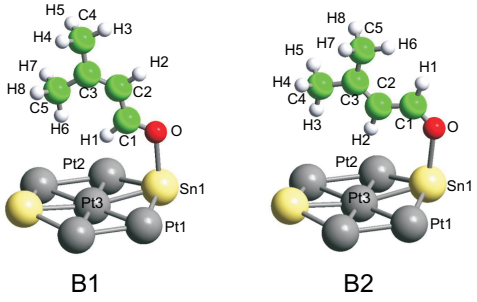

Figure 6. The two identified η^1-(s)-trans-top-OSn adsorption geometries of prenal on $Pt_3Sn(111)$.

Again a full vibrational assignment can be given from the DFT calculations. Importantly, the ν(C=O) and ν(C=C) vibrations of the two η^1-(s)-trans-top-OSn adsorption structures lead to an intensive loss signal between 1567 and 1616 cm^{-1}. The DFT calculations indicate as expected, that the ν(C=O) normal modes (1616/1615 cm^{-1}) of these adsorption complexes show larger shifts compared to the gas phase due to the interaction with the surface than the ν(C=C) vibrations (1588/1583 cm^{-1}). In the gas phase calculations, the ν(C=O) and ν(C=C) vibrations appear at 1677 and 1633 cm^{-1} respectively.

3.3 Prenal/$Pt_2Sn(111)$

For adsorption of prenal on Pt_2Sn/Pt(111), only small shifts and slight changes in relative loss intensities are found in the HREEL spectra for all the considered exposures. This suggests that prenal is weakly bound on this surface alloy, which is being supported by the calculated adsorption energies ($<$ 20.0 kJ/mol). Using only the most stable sites such as η^3-(s)-trans-π(CC)-OSn, we are not only unable to reproduce the HREEL spectra satisfactorily, but even find several signals that are not present experimentally. On the other hand, the best correspondence is achieved by considering the calculated spectra of η^2-(s)-trans-diσ(CC) and η^2-(s)-trans-π(CC) (both ca. 1.5 kJ/mol). These calculated spectra show the smallest difference compared to the gas phase frequencies. By fixing prenal at a distance of 4 Å parallel to the surface in the calculations, it is not only possible to reproduce the gas phase frequencies in agreement with the measured HREEL spectra, but also the computed intensities are well in agreement with the loss intensities detected.

Here both the theory and the experiment have difficulties to reach a convincing explanation when considered on their own. Yet the combination of the results from both approaches allows to reach the conclusion, that prenal is physisorbed in this case.

4 Conclusions

In the present study, the interactions of a multifunctional molecule (prenal) with mono- and bimetallic model catalyst surfaces has been investigated with combined experimental (HREELS) and theoretical (DFT) studies. Besides the adsorption on Pt(111), also the key

role of alloying the Pt surface with a second metal (Sn) on the adsorption of such complex molecules is adressed. Although qualitatively a larger number of possible adsorption complexes can be conceived on the Pt-Sn surface alloys, the presence of Sn simplifies the number of competitive stable adsorption states, hence leading to less complex HREEL spectra.

In terms of the adsorption energy, Sn induces a direct destabilization of the molecule-surface interaction. While on $Pt_3Sn(111)$ prenal is still chemisorbed, it only physisorbs when the surface concentration of Sn is increased like in the case of the $Pt_2Sn(111)$ surface alloy. According to the change of adsorption sites from flat geometries like η^4 and η^3 on Pt(111), in which both double bonds are interacting with the surface, to the vertical η^1-top-OSn sites on $Pt_3Sn(111)$, an increase of selectivity may be expected, since on this alloy surface the interacting C=O bond will probably be preferred for hydrogenation.

This study shows how a joint experimental and theoretical approach not only provides a good understanding of the vibrational spectra of the adsorbed prenal but also leads to a deeper understanding of the adsorption complexes on the pure Pt(111) and the discussed model-catalyst surfaces $P_3Sn/Pt(111)$ and $P_2Sn/Pt(111)$.

Acknowledgments

The authors thank the CNRS-DFG bilateral project for financial support. JH thanks the Ecole Normale Supérieur de Lyon, the Department of Theoretical Chemistry Bonn and the John von Neumann Institute for Computing (NIC) Jülich for CPU time and assistance and the Fonds der Chemischen Industrie for his scholarship grant. AK is grateful to the Alexander von Humboldt and Hertie Foundations for a fellowship.

References

1. (a) T. B. L. W. Marinelli, S. Nabuurs, V. Ponec, J. Catal. **151**, 431 (1995). (b) T. Birchem, C. M. Pradier, Y. Berthier, G. Cordier, J. Catal. **146**, 503 (1994).
2. (a) D. I. Jerdev, A. Olivas, B. E. Koel, J. Catal. **205**, 278 (2002). (b) E. Janin, H. von Schenck, S. Ringler, J. Weissenrieder, T. Akermark, M. Gthelid, J. Catal. **215**, 245 (2003).
3. (a) F. Delbecq, P. Sautet, J. Catal. **211**, 398 (2002). (b) F. Delbecq, P. Sautet, J. Catal. **220**, 115 (2003).
4. D. Loffreda, Y. Jugnet, F. Delbecq, J. C. Bertolini, P. Sautet, J. Phys. Chem. B **108**, 9085 (2004).
5. (a) G. Kresse, J. Hafner, Phys. Rev. B **47**, 558 (1993). (b) G. Kresse, J. Hafner, Phys. Rev. B **48**, 13115 (1993).
6. J. P. Perdew, Y. Wang, Phys. Rev. B **45**, 13244 (1992).
7. G. Kresse, D. Joubert, Phys. Rev. B **59**, 1758 (1999).
8. (a) M. T. Paffett, R. G. Windham, Surf. Sci. **208**, 34 (1989). (b) M. Galeotti, A. Atrei, U. Bardi, G. Rovida, M. Torrini, Surf. Sci. **313**, 349 (1994).
9. J. Breitbach, D. Franke, G. Hamm, C. Becker, K. Wandelt, Surf. Sci. **18**, 507 (2002).

John von Neumann Institute for Computing

Rearrangement of Molecular Complexes

Rainer Streubel and Gerd von Frantzius

published in

NIC Symposium 2006 ,
G. Münster, D. Wolf, M. Kremer (Editors),
John von Neumann Institute for Computing, Jülich,
NIC Series, Vol. **32**, ISBN 3-00-017351-X, pp. 83-90, 2006.

http://www.fz-juelich.de/nic-series/volume32

Rearrangement of Molecular Complexes

Rainer Streubel and Gerd von Frantzius

Institut für Anorganische Chemie
Gerhard-Domagk-Str. 1, Universität Bonn, Germany
E-mail: {r.streubel, gfrantzi}@uni-bonn.de

1 Introduction

Experimental and computational investigations of rearrangement and decomposition pathways of molecular phosphine transition-metal complexes are of fundamental interest in coordination and organometallic chemistry and in catalysis. One of the central topics of our research group is the chemistry of 2*H*-azaphosphirene complexes **1** and the generation, reaction and/or rearrangement of reactive intermediates **2** (i) (so called phosphinidene complexes) and **3** (nitrilium phosphanylide complexes) (ii) from precursor **1**[1–3]. Recently, we had discovered that electrophilic terminal phosphinidene tungsten complexes **2** with bulky substituents at phosphorus (R = C_5Me_5 or $CH(SiMe_3)_2$) do not dimerize in the absence of trapping reagents[4]. Therefore we became interested in their fate. The computational studies comprise a density functional method-based study of the hypersurfaces of phosphinidene complexes **2** and nitrilium phosphanylide complexes **1** as well as a characterization of bonding situations by the method of the compliance matrix; probing and establishing this rarely used method - especially in the field of transition metal complexes - makes it a goal in itself and will be discussed below.

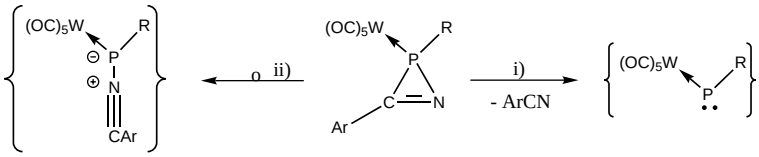

3 **1** **2**

Scheme 1. Rearrangement and decomposition of 2*H*-azaphosphirene complexes **1**.

2 Computational Methods

All optimizations and frequency calculations were performed using GAUSSIAN 03 RevB.03[5] on the IBM Regatta p690 cluster (JUMP) of the John von Neumann Institute for Computing (NIC) at the Forschungszentrum Jülich. The standard method throughout this work is B3LYP/6-311G(d,p) combined with an effective core potential description of tungsten using the Los Alamos LanL2DZ (for short: B3LYP/6-311**/LanL2DZ)[6]. Stationary points have been characterized by analytical second derivatives (the Hessian) with respect to redundant cartesian coordinates. Transition states (one imaginary frequency)

were identified by a reaction path following (IRC). The Hessian provided by the GAUSSIAN 03 calculation was transformed to non-redundant internal coordinates using Pulays INTC/FCTINT set of algorithms[7]. The inversion of the transformed Hessian to the compliance matrix was accomplished by standard methods.[8]. A typical production job, e.g. $C_{19}H_{24}NO_5PSi_2W$ **1** (Scheme 1) with 242 electrons, uses more than 1000 Gaussian-basis functions and thus needs parallelized computations on fast processors, *which can only be provided by a computing centre like the John von Neumann Institute for Computing (NIC).*

3 Usage and Interpretation of the Compliance Matrix

The physical model behind force constants and thus compliance constants is a spring model: if the molecule at equilibrium geometry is distorted by a vibrational movement the various internal coordinates (modeled by springs) interact according to the molecular force field. In the harmonic approximation to vibrational theory the molecular hypersurface describing a vibrational movement is locally approximated by a quadratic form (H_{ik}) in the displacements of the internal coordinates (bonds, angles, dihedrals and linear combinations thereoff) from their equilibrium values

$$2V = \Delta x^t (H_{ik}) \Delta x, \tag{1}$$

where (H_{ik}) is the matrix of second derivatives (Hessian) at a stationary point, the diagonal elements H_{kk} are the force constants[9]. Equivalently the change in potential energy during a vibration is described by a quadratic form in the forces (force displacements Δf to be precise) instilled in the coordinates upon distortion from equilibrium geometry

$$2V = \Delta f^t (C_{ik}) \Delta f, \tag{2}$$

where (C_{ik}) = $(H_{ik})^{-1}$ is the compliance matrix (inverse Hessian) at a stationary point, the diagonal elements C_{kk} of which are the compliance constants (in [Å/mdyn] for bond stretchings and in [rad/mdyn] for angle bendings); the off-diagonal elements are associated with the couplings of the coordinates. While in the spring model force constants H_{kk} describe the stiffness (resistance against distortion) the compliance constants C_{kk} are associated with the compliance of coordinate k[10].

4 Experimental and Theoretical Results

4.1 Formation of a Nitrilium Phosphanylide Complex

From experimental investigations of the thermolysis of 2*H*-azaphosphirene complex **1a**[11] the existence of nitrilium phosphanylide complex **3a** (Scheme 1, path ii), R = $CH(SiMe_3)_2$, Ar = Ph) as a reactive intermediate has been concluded, although, due to its assumed short lifetime, there was no spectroscopic evidence for the intermediacy of **3a**, so far. The DFT-calculations on the hypersurface of **1a** unambiguously showed that nitrilium phosphanylide complex **3a** is an isomer; the formation of which via a still unknown transition state proceeds endergonically by 19 kJ/mol. A comparison of selected experimental (X-ray crystal structure) and calculated bond lengths of **1a** as well as calculated bond lengths of **3a** can be taken from table 1. There is satisfying agreement between experiment and theory concerning the geometry of **1a**. It is noteworthy, that in **3a** the almost linear benzonitrile unit

(angle NCC in **1a**: 135 degree) is attached to a strongly pyramidal phosphorus (sum of bond angles at P: 326 degree); the compliance constant of the P-N contact (0.552 Å/mdyn) provides a likely description of **3a** as a N-P donor adduct of benzonitrile to phosphinidene complex **2b** (see Scheme 2, Figure 2 below).

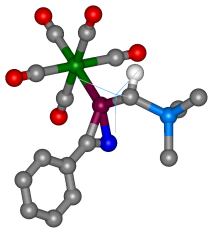

1a

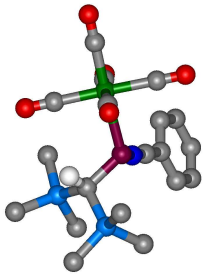

3a

	1a **Exp.** [Å], [°]	**1a** **Calc.** [Å], [°]	**3a** **Calc.** [Å], [°]
W-P	2.470(2)	2.551	2.628
P-C(N)	1.759(5)	1.781	-
P-C(H)	1.808(5)	1.849	1.892
P-N	1.795(4)	1.821	1.752
C-N	1.272(7)	1.271	1.165
Σ ∠ (P)			326

Figure 1. (hydrogens except PCH are omitted) Table 1

4.2 Formation of a *P*-SiMe$_3$-Substituted η^1-*E*-Phosphaalkene Complex[12]

As experimentally shown heating diluted ortho-xylene solutions of 2*H*-azaphosphirene complex **1a** afforded almost quantitatively and stereoselectively the *P*-SiMe$_3$-substituted η^1-*E*-phosphaalkene complex **4a** (Scheme 2). The rearrangement of the thermally generated short-lived phosphinidene complex [(OC)$_5W${PCH(SiMe$_3$)$_2$}] **2** to complex **4** was completely unexpected; we assume that a 1,2-(C-P)-trimethylsilyl shift takes place in this case. Although the chemistry of short-lived electrophilic terminal phosphinidene tungsten complexes[13] has received increased attention during the last years, partially because of the versatility of 2*H*-azaphosphirene complexes,[14] only a single example of a rearrangement yielding a *P*-Cl-substituted η^1-phosphaalkene complex - via a 1,2-chlorine shift - has been reported, so far[15].

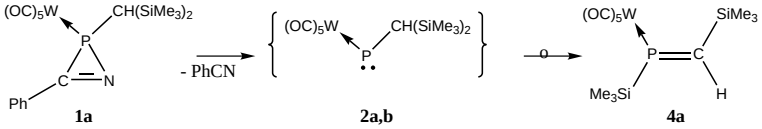

1a **2a,b** **4a**

Scheme 2. Rearrangement of transient phosphinidene complexes **2a,b** into **4a,b**.

DFT calculations in order to study the rearrangement of pentacarbonyl-tungsten phosphinidene complexes **2a** (*anti*-periplanar) and **2b** (*syn*-periplanar) to the corresponding phosphaalkene complexes **4a** and **4b** revealed that the formation of the C-P double bonds proceeds via transition state complexes **TSa** and **TSb** (Figure 2; hydrogens except P=CH are omitted).

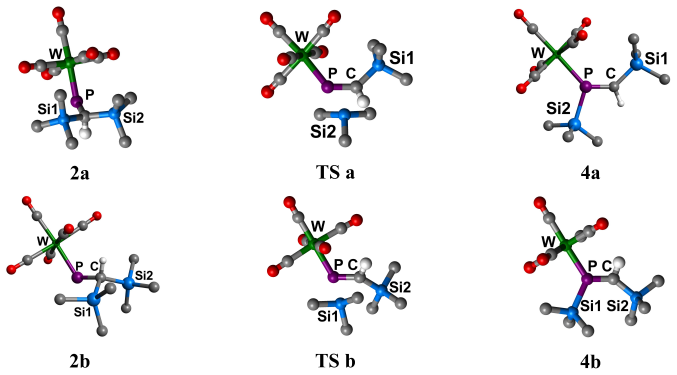

Figure 2. Phosphinidene complexes **2a,b**, transition states **TSa,b** and phosphaalkene complexes **4a,b**.

In consequence, this rearrangement represents an interesting and unique example of an intramolecular 1,2-silyl shift in phosphinidene complex chemistry. Relative energies of the 1,2-silyl migration of **2a,b** to corresponding **4a,b** can be taken from figure 3. *Anti*-periplanar phosphinidene complex **2a** rearranges via transition state **TSa** to the *E*-

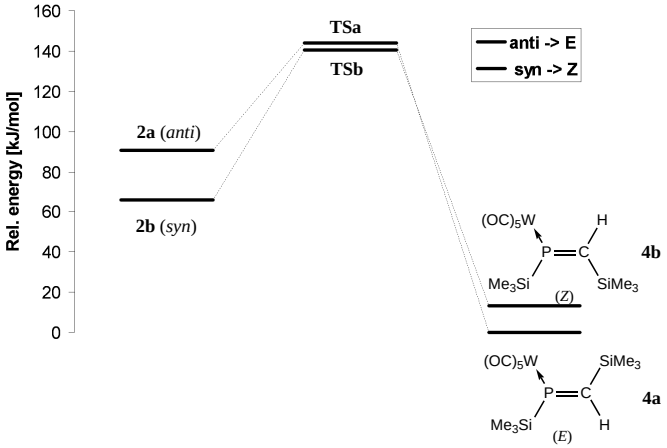

Figure 3. Energy profile of the 1,2-(C to P)-silyl migrations in **2a** and **2b**.

phosphaalkene complex **4a**. C_1 symmetric phosphinidenes **2a,b** exhibit a long and a short C-Si bond; the former is the one involved in forming the three-membered ring of the transition state which contains a five-coordinated silicon center. From an estimated singlet-triplet gap of about 40 kJ/mol under thermal reaction conditions phosphinidene complex **2a** can choose from two concurrent pathways: either undergo a fast reaction from the triplet excited state or - in the absence of suitable reaction partners - rearrange to *E*-phosphaalkene complex **4a**; the reverse 1,2-silyl shift is hindered by a substantial barrier of about 144 kJ/mol. These findings agree well with experimental results where reaction conditions

could be optimized to synthesize pentacarbonyltungsten phosphaalkene complex **4a** from the 2*H*-azaphosphirene complex **1a**. Apart from a smaller barrier (54 kJ/mol **2a** to **4a** vs. 74 kJ/mol for **2b** to **4b**) the major difference between **TSa** and **TSb** can be seen by comparison of the P-Si and C-Si bond lengths involved in the transition state. While **TSa** is early (according to the C-Si bond lengths) in **TSb** the position of the silicon center is almost in between the originating carbon and the phosphorus.

4.3 Further Local Minima on the Hypersurface of $[(OC)_5W\{PCH(SiMe_3)_2\}]$

So far at least six further local minima and a transition state have been located; four of them are shown in scheme 3 and figure 4.

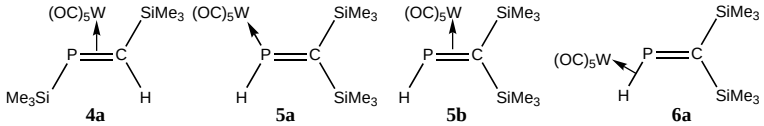

Scheme 3.

Due to the $CH(SiMe_3)_2$ substituent at phosphorus phosphinidene complexes **2a,b** can also undergo a 1,2-*H*-shift to yield phosphaalkene complexes **5a,b** and, by a still unknown transition state, highly unusual complex **6a**. The nature of the related transition-state complex **6b** (figure 4) remains to be clarified since reaction path following calculations were not conclusive yet. There is no automated way to find isomers of a given sum formular. From the literature[16] the ability of phosphinidene complexes to undergo intramolecular C-H insertions is known. Thus we could locate corresponding isomers **7a,b** (Scheme 4, Figure 4; only selected hydrogens are shown for clarity), which are thermodynamically more stable than phosphinidene complexes **2a,b** by 100 kJ/mol and even more stable than the phosphaalkene complexes **4** by 30 kJ/mol (**7b**) and by 20 kJ/mol (**7a**) respectively.

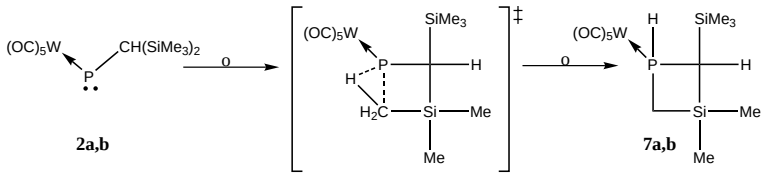

Scheme 4. Intramolecular C-H insertion reaction of phosphinidene complexes **2a,b** to yield **7a,b**.

5 Use of Compliance Constants for the Description of Bonding Situations

A compliance constant is the displacement of a bond due to the application of a unit force on that bond including reorganization. That means, a higher numerical value is connected

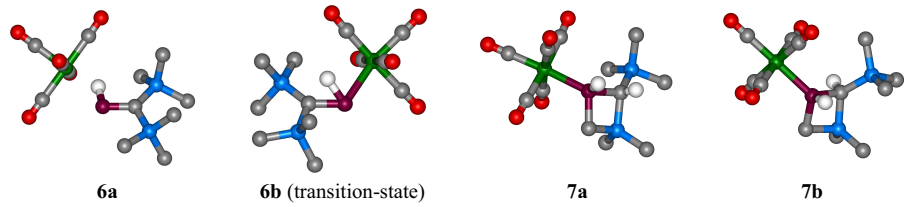

Figure 4.

with a weaker bond. Introduced to vibrational theory by Decius[17] and others[18] experimental compliance fields obtained by Jones and Swanson from vibrational data clarified the bonding forces in metal cyanides and carbonyls[19], while Williams used compliance matrices for the description of chemical reactivity[20]. Calculations of full compliance fields have been used to investigate Ga-Ga[21] and Si-C[22] multiple bonds, the metal-metal bond character in homoleptic transition metal carbonyls[23], hydrogen bonds in Watson-Crick base pairs[24] and polyphosphorus compounds[25]. Recently, Andreoni and coworkers used compliance constants plus Car-Parinello molecular dynamic simulations in order to analyze a proposed Si-Si triple bond[26]. We could show recently the usefulness of compliance constants in the description of agostic interactions[27]. In order to use compliance constants (diagonal elements of the compliance matrix) to assess the strength of a particular bond type (e.g. a tungsten-phosphorus bond) a set of reference compounds has to be calculated (Figure 5). From the statistic three different strengths of bonding interactions can be inferred: tungsten-phosphorus triple bonds range from 0.2-0.3 Å/mdyn while phosphinidene complexes of the type $[(OC)_5WR]$ seem to have a $W(CO)_5$ unit doubly bonded to phosphorus; ordinary W-P single bonds have compliance constants greater than 0.7 Å/mdyn.

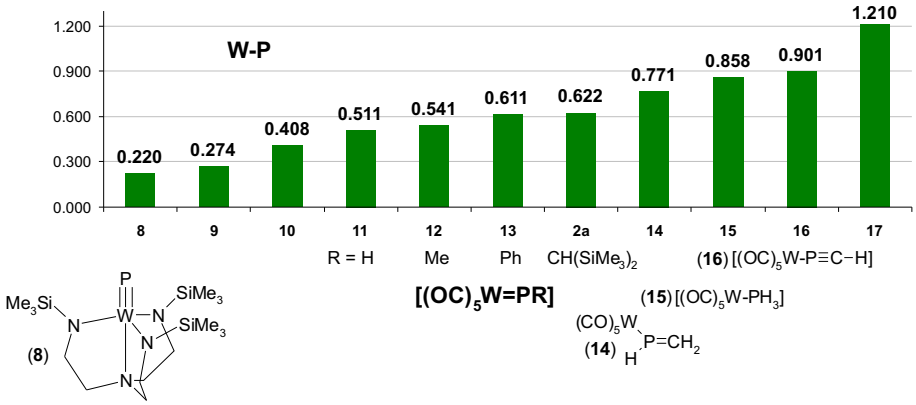

Figure 5. Compliance constants of P-C bonded compounds[28].

By a similar procedure phosphorus-carbon triple (0.1 Å/mdyn), double (0.15-0.2 Å/mdyn) and single bonds (0.3-0.4 Å/mdyn) can be identified (Figure 6). For example the P-C compliance constant of phosphaalkene complex $[(OC)_5W\{HP{=}C(SiMe_3)_2\}]$ (Scheme 3) falls

well within the range of a double bond (0.192 Å/mdyn).

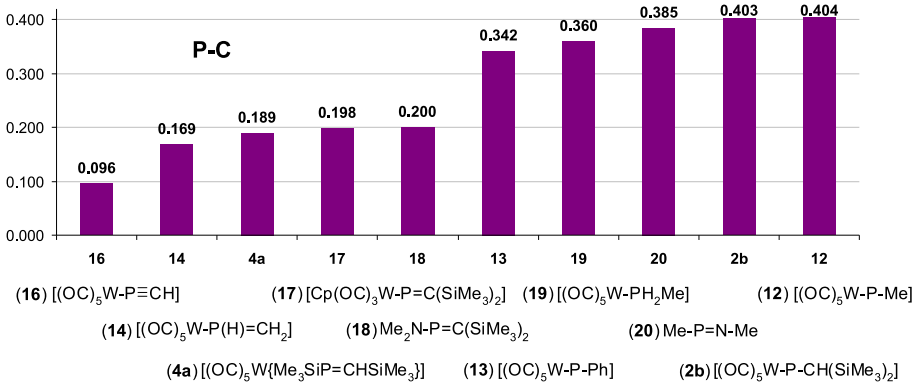

Figure 6. Compliance constants of P-C bonded compounds[29].

Acknowledgments

We are grateful to the *Deutsche Forschungsgemeinschaft* and the *Fonds der Chemischen Industrie* for financial support; we thank the John von Neumann Institute for Computing (NIC) at the Forschungszentrum Jülich for providing computational resources.

References

1. Review on the chemistry of λ^3-2*H*-azaphosphirene metal complexes: R. Streubel, *Coord. Chem. Rev.* **2002**, *227*, 175.
2. Review on phospha-organic chemistry: F. Mathey, *Angew. Chem. Int. Ed.* **2003**, *42*, 1578.
3. Reviews on phosphinidene complexes: K. Lammertsma, *Top. curr. Chem.* **2002**, *229*, 35; F. Mathey, *Angew. Chem. Int. Ed.* **2003**, *42*, 1586.
4. a) H. Wilkens, A. Ostrowski, J. Jeske, F. Ruthe, P. G. Jones, R. Streubel, *Organometallics* **1999**, *18*, 5627; b) R. Streubel, U. Schiemann, N. Hoffmann, Y. Schiemann, P. G. Jones, D. Gudat, *Organometallics* **2000**, *19*, 475.
5. Gaussian 03, Revision B.02/B.03, Gaussian, Inc., Wallingford CT, **2004**.
6. a) A. D. Becke, *J. Chem. Phys* **1993**, *98*, 5648. b) R. Krishnan, J. S. Blinkley, R. Seeger, J. A. Pople, *J. Chem. Phys.* **1980**, *72*, 650. c) A. D. McLean, G. S. Chandler, *J. Chem. Phys.* **1988**, *53*, 1995. d) P. J. Hay, W. R. Wadt, *J. Chem. Phys.* **1988**, *82*, 270.
7. G. Fogarasi, X. Zhou, P. W. Taylor, P. Pulay, *J. Am. Chem. Soc* **1992**, *114*, 8191.
8. W. H. Press, S. A. Teukolsky, W. T. Vetterling, B. P. Flannery, Numerical Recipes in Fortran: The Art of Scientific Computing, Cambridge University Press, Cambridge, **1994**.

9. E. B. Wilson, *J. Chem. Phys.* **1939**, *7*, 1047.
10. L. H. Jones, B. I. Swanson, *Acc. Chem. Res.* **1976**, *9*, 128.
11. R. Streubel, A. Ostrowski, S. Priemer, U. Rohde, J. Jeske, P. G. Jones, *Eur. J. Inorg. Chem.* **1998**, 257.
12. E. Ionescu, Gerd v. Frantzius, R. Streubel, *Manuscript in Preparation*.
13. Recent reviews: F. Mathey, N. G. Tran Huy, M. Marinetti, *Helv. Chim. Acta* **2001**, *84*, 2938; K. Lammertsma, M. J. M. Vlaar, *Eur. J. Org. Chem.* **2002**, 1127.
14. a) R. Streubel, *Coord. Chem. Rev.* **2002**, *227*, 172; ; b) R. Streubel, *Top. Curr. Chem.* **2002**, *223*, 91.
15. B. Deschamps, F. Mathey, *J. Organomet. Chem.* **1988**, *354*, 83 (Cu(I) catalyzed shift).
16. A. H. Cowley, A. R. Barron, *Acc. Chem. Res.* **1988**, *21*, 81.
17. J. C. Decius, *J. Chem. Phys.* **1963**, *38*, 241.
18. See: D. Papousek, J. Pliva, *Spectrochimica Acta* **1965**, *21*, 1147.
19. L. H. Jones, B. I. Swanson, *Acc. Chem. Res.* **1976**, *9*, 128.
20. I. H. Williams, *Chem. Phys. Lett.* **1982**, *88*, 462.
21. J. Grunenberg, *J. Chem. Phys.* **2001**, *115*, 6360.
22. a) J. Grunenberg, *Angew. Chem.* **2001**, *113*, 4150. b) J. Grunenberg, R. Streubel, G. von Frantzius, W. Marten, *J. Chem. Phys.* **2003**, *119*, 165.
23. Y. Cie, H. F. Schaefer III, *Z. Phys. Chem.* **2003**, *217*, 189.
24. J. Grunenberg, *J. Am. Chem. Soc.* **2004**, *126*, 1631.
25. S. Katsyuba, R. Schmutzler, J. Grunenberg, *J. Chem. Soc., Dalton Trans.* **2005**, *9*, 1700.
26. C. A. Pignedoli, A. Curioni, W. Andreoni, *Chem. Phys. Chem.* **2005**, *6*, 1795.
27. G. von Frantzius, R. Streubel, K. Brandhorst, J. Grunenberg, *Organometallics*, Web Release Date: 08-Dec- **2005**.
28. The complexes used for this calculation were first published by the following authors: **8**: R. Schrock, N.C. Zanetti, *Angew. Chem. Int. Ed. Engl.* **1995**, *34*, 2044. **9**: $[(OC)_5WP]^+$ (this work). **10**: $[(OC)_2CpW{=}P^tBu_2]$ J. Klaus, W. Malisch, W. Reich, A. Meyer, U. Schubert, *Angew. Chem.* **1986**, *98*, 103. **11-13**: K. Lammertsma, *Top. Curr. Chem.* **2003**, *229*, 95. **2a**: $[(OC)_5W\{PCH(SiMe_3)_2\}]$ (this work). **15**: G. Frenking, K. Wichmann, N. Frhlich, J. Grobe, W. Golla, D. Le Van, B. Krebs, M. Läge, *Organometallics* **2002**, *21*, 2921. **17**: $[(OC)_3CpW\text{-}P{=}C(SiMe_3)_2]$ D. Gudat, E. Niecke, W. Malisch, U. Hofmockel, S. Quashie, A. H. Cowley, A.M. Arif, B. Krebs, M. Dartmann, *J. Chem. Soc., Chem. Commun.* **1985**, 1687.
29. The complexes used for this calculation were first published by the following authors: **16**: This work. **14**: W. W. Schoeller, A. B. Rozhenko, S. Grigoleit, *Eur. J. Inorg. Chem.* **2001**, 2891. **4a**: $[(OC)_5W\{Me_3SiP{=}C(H)SiMe_3\}]$ (this work). **17**: $[(OC)_3CpW\text{-}P{=}C(SiMe_3)_2]$ D. Gudat, E. Niecke, W. Malisch, U. Hofmockel, S. Quashie, A. H. Cowley, A.M. Arif, B. Krebs, M. Dartmann, *J. Chem. Soc., Chem. Commun.* **1985**, 1687. **18**: M. I. Povolotskii, V. V. Negrebetskii, *J. Gen. Chem. USSR* **1988**, *58*, 206. **12,13**: K. Lammertsma, *Top. Curr. Chem.* **2003**, *229*, 95. **19**: H. Vahrenkamp, et al, *Z. Naturf. B.* **1985**, *40*, 1250; F. Nief, F. Mercier, F. Mathey, *J. Organomet. Chem.* **1987**, *328*, 349. **20**: K. Miqueu, J.-M. Sotiropoulos, G. Pfister-Guillouzo, V. Romanenko, *Eur. J. Inorg. Chem.* **2000**, *3*, 477. **2b**: $[(OC)_5W\{PCH(SiMe_3)_2\}]$ (this work).

John von Neumann Institute for Computing

A Relativistic 4-Component Multi-Reference Coupled Cluster Method. Application to the CsLi Molecule

Timo Fleig and Lasse K. Sørensen

published in

NIC Symposium 2006 ,
G. Münster, D. Wolf, M. Kremer (Editors),
John von Neumann Institute for Computing, Jülich,
NIC Series, Vol. **32**, ISBN 3-00-017351-X, pp. 91-98, 2006.

http://www.fz-juelich.de/nic-series/volume32

A Relativistic 4-Component Multi-Reference Coupled Cluster Method. Application to the CsLi Molecule

Timo Fleig and Lasse K. Sørensen

Institute of Theoretical and Computational Chemistry
Heinrich Heine University Düsseldorf
Universitätsstraße 1, 40591 Düsseldorf, Germany
E-mail: {timo, lasse}@theochem.uni-duesseldorf.de

Spectroscopic accuracy in electronic-structure calculations on heavy-element molecules requires a simultaneous and high-level treatment of electron correlation and contributions owing to special relativity. We present a general-order multi-reference coupled-cluster approach in the 4-component relativistic framework and its large-scale application to the spectroscopic properties of the CsLi molecular ground state. Using different relativistic Hamiltonians and varying levels of electron correlation, we find that electron correlation leads to a larger bond contraction than inclusion of "scalar" relativistic effects. By considering full iterative Triple excitations in the coupled cluster treatment, we attain benchmark precision for the bond length and the harmonic vibrational frequency in the $^1\Sigma$ ground state.

1 Introduction

The smallest building blocks of matter of interest in chemistry and physics are comprised — at the level above elementary particles — by atoms and small molecules. A detailed understanding of these systems is highly desirable, both for the sake of knowledge about the small systems themselves as well as the implications of this knowledge for larger molecules. A "small" molecule will be understood as consisting of not more than six or seven atoms.

The first and foremost piece of information about atoms and small molecules relevant to chemistry and molecular physics is delivered by the investigation of the electron "cloud" surrounding the nuclei, the electronic structure. The theoretical framework for such investigations is provided by quantum mechanics, and the quantum mechanical methodology for carrying out the relevant calculations is at the heart of quantum chemistry.

The accurate quantum chemical treatment of molecules containing heavy atoms from the 5th period of the periodic table and beyond puts high requirements on the applied methods. In particular, the precise determination of molecular spectra and properties, the understanding of reactions etc. crucially depends on the description of electron correlation which for heavy elements necessarily includes an adequate consideration of special relativity. The focus of our applied work lies on the precise determination of spectroscopic properties of small molecules containing heavy elements. This includes, e.g., high-precision calculations of molecular equilibrium bond lengths, harmonic vibrational frequencies, and dissociation energies within or even better than chemical accuracy (1 kcal/mole for energy differences).

To obtain high precision in properties, the quantum chemical treatment must go beyond Hartree-Fock theory, i.e. a mean-field approach to the electron-electron interaction.

Electron correlation must be described as precisely as possible. Alongside with improving computer technology and increasing system size of standard molecular applications, the coupled-cluster (CC) method has established itself as the most efficient *ab initio* method for the assessment of a large fraction of the correlation energy[1,2]. The exponential (or product) parameterization of the wave function leads to size-extensive model theories — i.e. the correlation energy scales correctly with the number of interacting particles — already at the level of truncated cluster expansions. Furthermore, the exponential *Ansatz* accounts for a compact representation of the wave function thus outperforming e.g. configuration interaction (CI) theory at a given excitation level.

Non-relativistic implementations of the CC method with the cluster excitation operator acting on a single-determinant reference (SRCC) have become widely used and are available in many quantum chemistry program packages (e.g.[3–5]). The SRCC method is a valid and good approach in situations where the wave function of the system is dominated by the single reference, e.g. the Hartree-Fock state, which is the case in many molecules of chemical interest. It lacks applicability or becomes less efficient, though, when a given state of interest is described by several electronic configurations of similar weights. This occurs in typical open-shell systems, like compounds of the transition metal, lanthanide, and actinide atoms[6,7], in bond-breaking regions of molecules with multiple bonds[8], or in the calculation of excited states[9].

The most elegant way to overcome these difficulties is to re-define the reference space in terms of a model space containing multiple determinants. These multi-reference coupled-cluster (MRCC) methods are generally demanding both on the implementational as well as the computational side and have therefore not become standard tools of quantum chemistry, yet. A type of these are the state-selective or state-specific (SS) methods, where a single reference comprised by a multideterminantal expansion with fixed weights is employed[10,11].

Relativistic generalizations of the CC method have also been explored in the last decade. The problematic objective here consists in the inclusion of internal magnetic couplings, in particular the spin-orbit interaction. As spin and orbital angular momenta are coupled, the concomitant quantum numbers lose relevance, and the methods require severe structural modifications. The earlier SR implementations of closed- and open-shell type[12–15] using the no-pair Dirac-Coulomb Hamiltonian have recently been succeeded by Fock-Space CC implementations[16,17] capable of simultaneously determining potential surfaces for different oxidation states and electronic levels of molecules[9]. The treatment of general open-shell systems is still impossible with this method, as the same set of molecular orbitals is used for all ionization levels of the treated system, which hampers convergence when Fock space sectors higher than 2/-2 need to be included.

2 Method

The goal of our project is to obtain a *universally applicable* coupled cluster method which suffers no limitations due to the number of open shells of a system state or the importance of relativistic contributions and possible non-additivity of relativistic contributions and electron correlation. The most rigorous theoretical framework to account for all these relativistic effects is Dirac's relativistic quantum mechanics. Here, the Hamiltonian and the wave function obtain 4-component form, the additional components owing to the descrip-

tion of anti-matter, e.g. positrons. In 4-component relativistic theory, scalar relativistic and magnetic effects are intertwined and consistently included. Our approach is based on 4-component theory and approximative ansatzes within the 4-component framework, both with respect to method development and application, and solutions are obtained to the Dirac (-Coulomb), not the Schrödinger equation.

The precursor implementation we set out from is the general CI and CC program LUCIA[18,19]. This very general approach to the CC method belongs to the category of state-selective multi-reference CC techniques and allows for including cluster operators of arbitrary excitation level. Its generality further rests upon the concept of generalized active spaces (GAS), where the occupied and virtual orbital spaces are subdivided into a number of subspaces with defined occupation constraints, thus representing a multi-reference expansion of the wave function. The reference model space is therefore comprised by a (CAS) expansion onto which the cluster operators act. In contrast to single-reference CC, the excitation manifold is extended to include excitations also from the additional reference functions up to the specified level of cluster expansion.

The following hierarchical tree shall help provide a complete overview of the methodology we have recently implemented in a local version of the quantum chemistry program package DIRAC[20] and its interrelations:

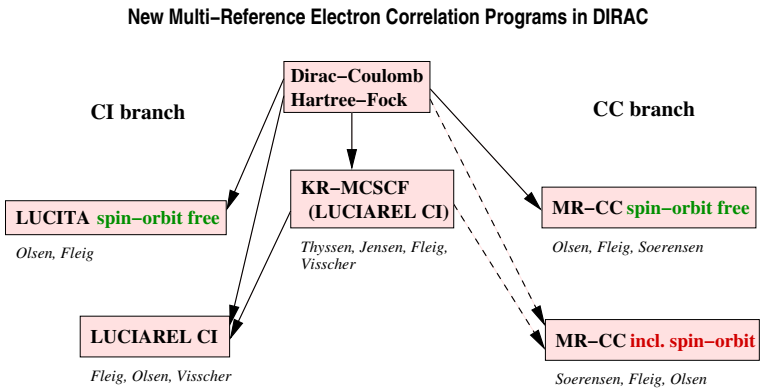

Figure 1. An overview of the new relativistic 4-component electron correlation programs in DIRAC and the main authors of the modules.

We have completed the spin-orbit free implementation of the multi-reference CC method within this framework, and report applications in the following section. This allows for electronic structure calculations on systems where spin-orbit interaction does not affect properties severely, but where the so-called “scalar relativistic” effects need to be accounted for. The latter lead to orbital contractions and self-consistent decontractions and thus modify the electron density of the system, strongly affecting properties in heavy-element systems. In the 4-component framework, scalar relativistic effects are conveniently treated through the spin-free Dirac operator[21]. Our implementation generally treats relativistic contributions and electron correlation simultaneously and on the same footing.

The full spin-orbit MR-CC code is currently being implemented by modification of the fully relativistic CI program LUCIAREL[22,23] which is invoked from the new 4-component multi-configuration self-consistent-field (MCSCF) program (KR-MCSCF)[23,24].

3 Application

3.1 Motivation

A number of small molecules containing heavy atoms have electronic ground states with very small contributions from spin-orbit coupling. This is the case in diatomic molecules with Σ states, examples of which are the ground states of the group 1 and group 2 diatomic compounds ($\mathrm{KCs}, \mathrm{NaCs}, \mathrm{Rb_2}, \mathrm{Cs_2}, \mathrm{BaLi}$ and the like) and some molecules formed from group 1 and lanthanide atoms (e.g. RbYb). The ultracold formation of these molecules[25] and their capture into optical and magnetic traps[26] is of particular interest in the study of Bose-Einstein condensation[27]. In the ground states of these molecules the relativistic effects are typically dominated by so-called scalar contributions such as mass-velocity and the Darwin term in the molecular Hamiltonian. These effects cannot be neglected in any heavy-element calculation since they are decisive for the determination of the shape and spatial extent of the orbitals and therfore also the bonding situation in molecules. The relatively weak bonding in such molecules also calls for an extensive treatment of dynamic electron correlation as insufficiencies in the correlation treatment are likely to lead to large errors in spectroscopic properties.

3.2 Problem and Approach

The chemical bond in the CsLi molecule can be reasonably described by considering only the σ bond formed from the 6s orbital on Cs and the 2s on Li, resulting in a $^1\Sigma^+$ ground state. Correlation of the close-lying 5p and 5s orbitals (10 electrons in total) of Cs will give a significant improvement on the desription of the bond. Further improvement is expected when correlating the outer core 4d electrons of Cs and the 1s electrons of Li (22 electrons in total) and going to higher excitation levels.

A series of calculations using our new implementation within the DIRAC program package[20] has been performed[28]. Our goal is to determine with highest precision the contributions of scalar relativity, spin-orbit coupling, and electron correlation to spectroscopic properties of the CsLi molecule. For this, we use a Levy-Leblond (non-relativistic), spin-orbit free and the Dirac-Coulomb Hamiltonian which includes all leading relativistic terms. The calculations are carried out with large uncontracted basis sets ($\{24\mathrm{s}18\mathrm{p}13\mathrm{d}3\mathrm{f}\}$ functions on Cs and $\{11\mathrm{s}5\mathrm{p}2\mathrm{d}1\mathrm{f}\}$ functions on Li).

3.3 Results

Results for different levels of electron correlation ((0) Hartree-Fock, 10-electron coupled cluster, 22-electron coupled cluster) are compiled in table 1.

The most striking overall trend is the large bond contraction upon correlating the electrons. Our finding shows that the decrease in bondlength stems from moving density from the predominantly delocalized bonding orbital to the more diffuse and localized low-lying

Method	corr. el.	R_e[Å]	ω_e [cm^{-1}]	D_e [eV]
DCHF-SF	0	3.9092	173.868	-
DCHF	0	3.9094	173.833	-
CCSD-LL	10	3.7313	184.561	0.8480
CCSD-SF	10	3.6700	187.102	0.8257
CCSD	10	3.6688	187.277	0.8382
MRCCSD(2in2)-SF	10	3.6699	186.333	0.7916
CCSD(T)-SF	10	3.6419	186.508	-
CCSD(T)	10	3.6405	186.605	-
CCSDT-LL	10	3.7025	183.862	0.7665
CCSDT-SF[a]	10	3.6416	186.205	0.7432
CCSDT-SF	10	3.6423	186.358	
CCSD-LL	22	3.7196	185.196	0.9001
CCSD-SF	22	3.6562	187.935	0.8798
CCSD	22	3.6560	188.372	0.8806
CCSD(T)-SF	22	3.6242	187.294	-
CCSD(T)	22	3.6232	187.385	-
CCSDT-SF[a]	22	3.6225	186.522	0.7522
CIPSI[b]		3.615	187.1	
MELD[c]		3.65	183	0.72
CIPSI[d]		3.604		0.717

Table 1. Spectroscopic properties of CsLi in its $^1\Sigma$ ground state at various correlation levels and using different Hamiltonians. LL denotes the Levy-Leblond, SF the spin-orbit free Hamiltonian. MR characterizes a multi-reference CC expansion.
[a] Cutoff for virtuals at 6.2 a.u., [b] Reference[29], [c] Reference[30], [d] Reference[31]

$3p_x$ and $3p_y$ orbitals on Li but not the $3p_z$ thereby making the molecule more ionic and leading to bond contraction. This is found by specifying various active orbital spaces (GAS). As expected, the bond also becomes considerably shorter when including scalar relativistic effects since the predominantly bonding 6s orbital on the Cs atom is contracted. The inclusion of spin-orbit coupling, on the other hand, has virtually no effect on any of the properties here. This is clearly visible by comparing the CCSD-SF and CCSD calculations which refer to the fully relativistic Dirac-Coulomb Hamiltonian. The effect of outer core correlation in general is small compared to the correlation effect as such (less than 10% of the latter) though not neglible and about one third of scalar relativistic contributions. It is just slightly smaller than increasing the excitation level from CCSD-SF (Singles and Doubles) to CCSDT-SF (Singles, Doubles, and full iterative Triples). A multi-reference expansion improves results especially on dissociation, as the separated atoms and the bonded molecule are described at better balance than in single-reference treatments.

Conclusively, an extensive correlation treatment in this weakly bound molecule is very important to approach spectroscopic accuracy. The reported reference calculations have

been carried out using effective core potentials and configuration interaction for describing electron correlation. No experimental results are available for direct comparison, but we draw confidence for the accuracy of our calculations from the systematic study of all relevant contributions and the stepwise improvement of the computational approach. We are currently investigating the convergence of the dissociation energy with extensive MR calculations correlating 22 electrons.

4 Concluding Remarks

The coupled cluster implementation we are pursuing here opens the possibility of the high-precision calculation of molecular spectroscopic (and electric) properties due to the arbitrary cluster excitation level and the possibility of using multi-reference expansions. The largest calculation reported here (CCSDT-SF 22) includes roughly 100 million cluster amplitudes and requires significant amounts of machine core memory. JUMP provides both fast processors for running large-scale calculations of this quality as well as ample memory for storing the required intermediate quantities such as amplitude vectors, molecular integrals, etc.

These requirements will become even more important when we have completed our initial implementation including spin-orbit terms. We plan to apply the new program in electronic-structure calculations of actinide-containing molecules, in particular small uranium and plutonium compounds with several unpaired electrons. Currently, there is no quantum-chemical methodology available for the treatment of such molecules which may guarantee chemical accuracy for the properties we are interested in.

Acknowledgments

We gratefully acknowledge financial support by the Deutsche Forschungsgemeinschaft through the priority program SPP 1145, grants no. FL 356/2-1, FL 356/2-2 and thank the John von Neumann Institute for Computing at the Forschungszentrum Jülich for providing computer time. We also thank Markus Pernpointner and Peter Schmelcher for valuable discussions on the application side.

References

1. R. J. Bartlett. Recent advances in coupled cluster methods. In *Recent Advances in Computational Chemistry*, volume 3. World Scientific, Singapore, 1997.
2. J. Paldus and X. Li. A critical assessment of coupled cluster method in quantum chemistry. In I Prigogine and S A Rice, editors, *Advances in Chemical Physics*, volume 110, pages 1–175. John Wiley & Sons, Inc., 1997.
3. ACES II, a CC and an MBPT suite of codes by J. F. Stanton, J. Gauss, J. D. Watts, W. J. Lauderdale, and R. J. Bartlett, *Intern. J. Quantum Chem. Symp.***26**, 879 (1992), with contributions by J. Almløf and P. R. Taylor (MOLECULE), T. Helgaker, H. J. Jensen, P. Jørgensen, J. Olsen, P. R. Taylor (ABACUS), and D. Bernholdt.

4. 2000. Molcas Version 5. K. Andersson, M. Barysz, A. Bernhardsson, M. R. A. Blomberg, D. L. Cooper, T. Fleig, M. P. Fülscher, C. de Graaf, B. A. Hess, G. Karlström, R. Lindh, P-Å Malmqvist, P. Neogrády, J. Olsen, B. O. Roos, A. J. Sadlej, M. Schütz, B. Schimmelpfennig, L. Seijo, L. Serrano-Andrés, P. E. M. Siegbahn, J. Stålring, T. Thorsteinsson, V. Veryazov and P-O. Widmark, Lund University, Sweden.
5. MOLPRO, a package of *ab initio* programs designed by H. J. Werner and P. J. Knowles, version 2002.1. See `http://www.molpro.net` for authors.
6. C. M. Marian. *Theoretische Spektroskopie zweiatomiger Übergangsmetallverbindungen*. Habilitationsschrift, University of Bonn, 1991.
7. Paul von Ragué Schleyer, editor. *Encyclopedia of Computational Chemistry (ECC)*, pages 1 – 11. John Wiley & Sons, 1997. M. Dolg, Lanthanides and Actinides.
8. J. W. Krogh and J. Olsen. A general coupled cluster study of the N_2 molecule. *Chem. Phys. Lett.*, 344:578, 2001.
9. L. Visscher, E. Eliav, and U. Kaldor. Formulation and implementation of the relativistic Fock-space coupled-cluster method for molecules. *J. Chem. Phys.*, 115:9720, 2001.
10. N. Oliphant and L. Adamowicz. Multireference coupled-cluster method using a single-reference formalism. *J. Chem. Phys.*, 94:1229, 1991.
11. N. Oliphant and L. Adamowicz. The implementation of the multireference coupled-cluster method based on the single-reference formalism. *J. Chem. Phys.*, 96:3739, 1991.
12. E. Ilyabaev and U. Kaldor. Relativistic coupled cluster calculations for closed-shell atoms. *Chem. Phys. Lett.*, 194:95, 1992.
13. E. Ilyabaev and U. Kaldor. The relativistic open-shell coupled cluster method: Direct calculation of excitation energies in the Ne atom. *J. Chem. Phys.*, 97:8455, 1992.
14. L. Visscher, K. G. Dyall, and T. J. Lee. Kramers-restricted closed-shell CCSD theory. *Int. J. Quantum Chem.: Quantum Chem. Symp.*, 29:411, 1995.
15. L. Visscher, T. J. Lee, and K. G. Dyall. Formulation and implementation of a relativistic unrestricted coupled-cluster method including noniterative connected triples. *J. Chem. Phys.*, 105:8769, 1996.
16. A. Landau, E. Eliav, and U. Kaldor. Intermediate Hamiltonian Fock-space coupled-cluster method. *Chem. Phys. Lett.*, 313:399, 1999.
17. A. Landau, E. Eliav, Y. Ishikawa, and U. Kaldor. Mixed-sector intermediate Hamiltonian Fock-space coupled-cluster approach. *J. Chem. Phys.*, 121:6634, 2004.
18. J. Olsen. The initial implementation and applications of a general active space coupled cluster method. *J. Chem. Phys.*, 113:7140, 2000.
19. Program LUCIA, a general CI code written by J. Olsen, University of Aarhus, with contributions from H. Larsen and M. Fülscher.
20. Written by H. J. Aa. Jensen, T. Saue, L. Visscher with contributions from V. Bakken, E. Eliav, T. Enevoldsen, T. Fleig, O. Fossgaard, T. Helgaker, J. Laerdahl, C. V. Larsen, P. Norman, J. Olsen, M. Pernpointner, J. K. Pedersen, K. Ruud, P. Salek, J. N. P. van Stralen, J. Thyssen, O. Visser, and T. Winther. "DIRAC04, a relativistic *ab initio* electronic structure program, release dirac04.0 (2004)", 2004.
21. K. G. Dyall. An exact separation of the spin-free and spin-dependent terms of the Dirac-Coulomb-Breit Hamiltonian. *J. Chem. Phys.*, 100:2118, 1994.
22. T. Fleig, J. Olsen, and L. Visscher. The generalized active space concept for the

relativistic treatment of electron correlation. II: Large-scale configuration interaction implementation based on relativistic 2- and 4-spinors and its application. *J. Chem. Phys.*, 119:2963, 2003.

23. T. Fleig, H. J. Å. Jensen, J. Olsen, and L. Visscher. The generalized active space concept for the relativistic treatment of electron correlation. III: Large-scale configuration interaction and multi-configuration self-consistent-field four-component methods with application to UO_2. J Chem Phys, accepted for publication, 2005.
24. J. Thyssen, H. J. Å. Jensen, and T. Fleig. A four-component relativistic multi-configuration self-consistent-field method for molecules, 2005. J Chem Phys, submitted.
25. M. W. Mancini, G. D. Telles, A. R. L. Caires, V. S. Bagnato, and L. G. Marcassa. Observation of Ultracold Ground-State Heteronuclear Molecules. *Phys. Rev. Lett.*, 92:133203–1, 2004.
26. T. Takekoshi, B. M. Patterson, and R. J. Knize. Observation of Optically Trapped Cold Cesium Molecules. *Phys. Rev. Lett.*, 81:5105, 1998.
27. A. E. Leanhardt, T. A. Pasquini, M. Saba, A. Schirotzek, Y. Shin, D. Kielpinski, D. E. Pritchard, and W. Ketterle. Cooling Bose-Einstein Condensates Below 500 Picokelvin. *Science*, 301:1513, 2003.
28. L. K. Sørensen, T. Fleig, and J. Olsen. Implementation of a higher-order multi-reference Coupled Cluster program in the 4-component spin-free dirac formalism. Chem Phys Lett, to be published, 2005.
29. M. Korek, A. R. Allouche, K. Fakhreddine, and A. Chaalan. Theoretical study of the electronic structure of LiCs, NaCs, and KCs molecules. *Can. J. Phys.*, 78:977, 2000.
30. G. Igel-Mann, U. Wedig, P. Fuentealba, and H. Stoll. Ground-state properties of alkali dimers XY (X,Y = Li to Cs). *J. Chem. Phys.*, 84:5007, 1986.
31. M. Aymar and O. Dulieu. Calculation of accurate permanent dipole moments of the lowest $^{1,3}\Sigma^+$ states of heteronuclear alkali dimers using extended basis sets. *J. Chem. Phys.*, 122:204302, 2005.

John von Neumann Institute for Computing

Elementary Particle Physics

Gernot Münster

published in

NIC Symposium 2006 ,
G. Münster, D. Wolf, M. Kremer (Editors),
John von Neumann Institute for Computing, Jülich,
NIC Series, Vol. **32**, ISBN 3-00-017351-X, pp. 99-100, 2006.

http://www.fz-juelich.de/nic-series/volume32

Elementary Particle Physics

Gernot Münster

Institut für Theoretische Physik, Universität Münster
Wilhelm-Klemm-Str. 9, 48149 Münster, Germany
E-mail: munsteg@uni-muenster.de

In the physics of elementary particles a peculiar and fascinating situation has emerged. On the one hand, a theoretical model for the description of the fundamental building blocks of matter and their interactions exists, which has been confirmed in all those cases where experimental tests can be performed. This theory is called the Standard Model of elementary particle physics. On the other hand, the Standard Model offers many open problems, which are difficult to tackle experimentally or theoretically, but whose solutions are important for the foundation of the Standard Model as well as for its phenomenological predictions. How does this come about?

The Standard Model is formulated in the framework of relativistic quantum field theory. The fundamental constituents of matter are fermions, which obey the Pauli principle. These are the quarks, out of which the strongly interacting hadrons are built, and the leptons, which comprise the electrons and their heavier sisters muon and tau, as well as the neutrinos. Apart from gravity, which is negligible in the subnuclear world, three types of fundamental interactions are known. These are the familiar electromagnetic forces, the weak interactions and the so-called strong interactions. The latter are responsible for the binding of quarks into hadrons, like protons, neutrons or mesons. In the Standard Model the interactions are described in a mathematically very elegant way in terms of force mediating fields, which are associated with an infinite-dimensional symmetry, the local gauge symmetry.

The greatest challenges in the theory of elementary particles are provided by the strong interactions. The corresponding sector of the Standard Model is Quantum Chromodynamics (QCD). A characteristic feature of the strong interactions is their "asymptotic freedom". This property implies that for processes at high energies or small distances the coupling strength is small, so that perturbation theory can be applied to derive theoretical predictions. The Nobel price for physics was awarded in 2004 to Gross, Politzer and Wilczek for the discovery of asymptotic freedom in QCD. The flip side of the coin is that the coupling increases at low energies such that the region of applicability of perturbation theory ends there. Low-energy properties of hadrons, including their mass spectrum, are of a genuine non-perturbative nature. In particular, the confinement of quarks, namely the fact that they only exist bound inside hadrons, cannot be understood perturbatively.

The numerical simulation of QCD on high-performance computers is one of the most powerful methods to investigate the non-perturbative regime. For this purpose the theory is discretized on a space-time lattice with lattice spacing a and finite extent L. Monte Carlo simulations of QCD and other physically interesting field theories have become a field of very active international research. They also constitute a driving force for the development of algorithms and machines.

The first aim of Monte Carlo simulations of QCD is to test its claim to correctly describe the physics of strongly interacting particles. This means that non-perturbative quantities are computed, which can be compared to experimentally known values. Notably the spectrum of masses belongs to this class. Secondly, a large amount of present activities is devoted to the calculation of fundamental parameters of the Standard Model, like quark masses, coupling constants and mixing angles. These parameters are not directly accessible and difficult or even impossible to determine experimentally. Thirdly, one of the most interesting aims is of course to arrive at predictions for new quantities or phenomena.

Systematic errors in Monte Carlo calculations of QCD are due to the finite lattice spacing a and the finite lattice size L. Much effort is devoted to reach the regime of sufficiently small lattice spacings, where properties of physics in the continuum can be extracted reliably.

In recent years QCD simulations have reached a stage, where dynamical quarks can be incorporated in physically relevant situations. Due to the Fermi statistics of quarks it is not possible to incorporate them directly in terms of number valued variables. Their contribution to the dynamics has to be included through the so-called fermion determinant. Its calculation requires a huge amount of computing resources, so that in the past it often has been neglected in the quenched approximation, where it is replaced by a constant. Present supercomputer resources allow to implement situations where the fermion determinant is taken into account on sufficiently fine and sufficiently large lattices.

In simulations with dynamical quarks another source of systematic errors occurs. The masses of the lightest quarks in nature are rather small. The necessary computer time increases drastically with decreasing quark masses. This has so far prevented calculations with realistic values for the lightest quark masses. The article by Jansen describes attempts to solve this problem by using new types of actions for lattice QCD.

Another aspect of the physics of quarks in lattice QCD is their chiral symmetry. This symmetry of massless QCD in the continuum is broken by straightforward lattice discretizations. In order to minimize the effects of this artificial symmetry breaking one can employ lattice actions which represent chiral symmetry as good as possible. Overlap fermions are an example. They are used in the calculations described in the article of Schierholz. In this work the spectrum of hadron masses is calculated, as well as nucleon matrix elements, which give valuable information about the internal structure of nucleons.

Overlap fermions are also being used by Wittig and collaborators in their research about the decays of kaons. They address non-perturbative problems in connection with these mesons, which are important for the understanding of the symmetries of the Standard Model and their violations.

New types of particles are the subject of the article of Schäfer et al. Pentaquarks, hadrons made out of five quarks, have been searched experimentally in recent years, but not been identified convincingly. In the calculations described here the question whether pentaquarks exist is addressed in the framework of lattice QCD.

John von Neumann Institute for Computing

Exact and Improved Lattice Chiral Symmetry

Karl Jansen

published in

NIC Symposium 2006 ,
G. Münster, D. Wolf, M. Kremer (Editors),
John von Neumann Institute for Computing, Jülich,
NIC Series, Vol. **32**, ISBN 3-00-017351-X, pp. 101-108, 2006.

http://www.fz-juelich.de/nic-series/volume32

Exact and Improved Lattice Chiral Symmetry

Karl Jansen

NIC, DESY, Zeuthen
Platanenallee 6, 15738 Zeuthen, Germany
E-mail: Karl.Jansen@desy.de

We present an overview of our quenched and dynamical tests of Wilson twisted mass fermions at full twist as a promising candidate for large scale numerical simulations to "solve" Quantum Chromodynamics.

1 Introduction

This project performed at the John von Neumann Institute for Computing aims at realistic simulations of our theory of strong interactions, Quantum Chromodynamics (QCD), on a 4-dimensional Euclidean lattice, where with "realistic" we mean the following: the three lightest –up, down, and strange– quarks should be taken as dynamical degrees of freedom in the simulation; the masses of these quarks should be tuned such that the experimentally observed values of the masses of the pion and the kaon are reproduced; the linear box length should be about $L = 3$fm, since, e.g. the diameter of the proton is about 1fm and it should fit comfortably; finally, the simulations have to be performed at a number of fine enough values of the lattice spacing a, i.e. $0.05\mathrm{fm} \leq a \leq 0.1$fm in order to obtain a well controlled continuum extrapolation.

Unfortunately, the original formulation of lattice QCD by Wilson[1] has been found to possess some shortcomings which drive the above sketched realistic scenario very difficult, if not impossible with present and near future computer technology. The original Wilson lattice QCD formulation exhibits lattice spacing effects that are linear in the lattice spacing a and hence even a value of $a = 0.05$fm might not be sufficient to perform a controlled continuum extrapolation. Even more severely, although connected, this formulation breaks chiral symmetry[a] explicitly.

The *spontaneous* breaking of this chiral symmetry can explain the observed spectrum of light mesons and has important consequences for the understanding and interpretation of QCD. In particular, it is possible to write down an effective, low-energy theory of QCD, the so-called chiral perturbation theory Lagrangian, which relies on chiral symmetry and the mechanism of spontaneous chiral symmetry breaking and which has become a most important and powerful tool to analyze QCD phenomena at low energies[2,3].

2 New Lattice QCD Actions

The last years have seen a number of attempts to overcome the above mentioned difficulties of the original Wilson fermion action. In this project we have studied two of such formulations, the chiral invariant overlap fermions[4–7] and Wilson twisted mass fermions[8]. The

[a] Chiral symmetry is a symmetry of *continuum* QCD and means the invariance of the theory under the interchange of massless left- and right-handed fermions.

approach of chiral invariant formulations of lattice QCD has been discussed in a previous NIC proceedings contribution[9].

Unfortunately, the beauty of an exact lattice chiral symmetry comes with a rather high price of simulation cost which drives *dynamical* simulations with these kind of lattice fermions unrealistic presently. An alternative promising candidate are ***maximally twisted Wilson fermions***[10,8]. This recent development adds a so-called twisted mass term $i\mu\gamma_5\tau_3$ to the usual Wilson Dirac operator. The action of twisted mass fermions then takes the form

$$S[U,\psi,\bar{\psi}] = a^4 \sum_x \bar{\psi}(x)(D_W + m_0 + i\mu\gamma_5\tau^3)\psi(x) \equiv \bar{\Psi} D_{\rm tm} \Psi \ . \qquad (1)$$

Here, D_W is the standard, massless Wilson Dirac operator, m_0 is the bare quark mass parameter and μ the twisted mass parameter. Note that the Pauli-matrix τ_3 acts in flavour space. A first intriguing property of Wilson twisted mass fermions is that $\det[D_{\rm tm}] = \det[D_W(m_0)^2 + \mu^2]$. This determinant is regulated by the twisted mass parameter and cannot exhibit dangerously small or even negative eigenvalues as in the case of the standard Wilson Dirac operator. Note that the appearance of such very low-lying eigenvalues render dynamical simulations very costly, if not impossible.

A second, very remarkable property of Wilson twisted mass fermions is that they can be O(a) improved[b] without the need of additional improvement terms as they are needed for pure Wilson fermions[11,12]. The O(a)-improvement can be obtained by choosing the bare quark mass m_0 to assume a critical value $m_{\rm crit}$ which can be realized by searching for that value of m_0 where, e.g., the quark mass is zero[c].

The twisted mass fermion action of eq. (1) can be derived from the standard Wilson fermion action by performing an axial transformation on the fermion fields, i.e. $\psi \rightarrow e^{i\omega\gamma_5\tau^3/2}\psi$. This "twisting" of the fermion fields is maximal when $\omega = \pi/2$. Since the angle ω is related to the parameters m_0 and μ of eq. (1) by $\tan\omega = \mu/m$ with $m = m_0 - m_{\rm crit}$, maximal twist is obtained when $m_0 = m_{\rm crit}$ which was the condition for automatic O(a)-improvement. Another important aspect of Wilson twisted mass fermions in practice is that it reduces the unphysical mixing of operators[13,14]. Finally also non-degenerate quark masses can be realized, keeping the positivity of the fermionic determinant intact[14].

Given all these advertised advantages, our collaboration set out to investigate the potential of Wilson twisted mass fermions and test this new approach to lattice QCD. Our first aim was to see, whether Wilson twisted mass fermions are able to allow for simulations at considerably smaller pseudo scalar masses than with standard Wilson fermions[d]. Even more challenging is the question whether the values of pseudo scalar masses that are reachable with Wilson twisted mass fermions are comparable with those of chiral invariant overlap fermions.

The results of this first test of Wilson twisted mass fermions[15] is shown in fig. 1. This figure is a striking demonstration of the potential of Wilson twisted mass fermions. The smallest value of the pseudo scalar mass is basically identical with the one of overlap fermions and much smaller than the one from standard Wilson fermions.

A most intriguing question is, of course, whether one or the other formulation of lattice fermions does have an advantage in the computational cost. We have therefore explored

[b] In an O(a)-improved theory, the lattice spacing effects that appear linear in the lattice spacing are reduced and sometimes, as in the case of non-perturbative O(a)-improvement, even eliminated.
[c] Usually the so-called PCAC quark mass is taken for this purpose.
[d] We do not differentiate here whether original or non-perturbatively O(a)-improved Wilson fermions are used.

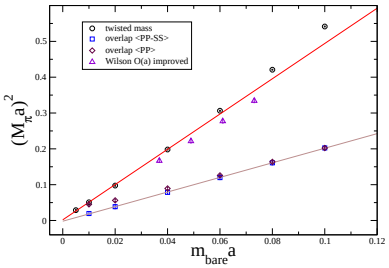

Figure 1. Comparison of quenched results for the pseudo scalar mass squared as a function of the bare quark mass for three lattice fermions: standard $\mathcal{O}(a)$ improved Wilson fermions, twisted mass fermions and overlap fermions.

V, m_π	Overlap	Wilson TM	rel. factor
$12^4, 720$Mev	48.8(6)	2.6(1)	18.8
$12^4, 390$Mev	142(2)	4.0(1)	35.4
$16^4, 720$Mev	225(2)	9.0(2)	25.0
$16^4, 390$Mev	653(6)	17.5(6)	37.3
$16^4, 230$Mev	1949(22)	22.1(8)	88.6

Table 1. The time in seconds on the NIC IBM JUMP machine to compute one propagator component using overlap or Wilson twisted mass fermions.

a large variety of algorithmic tricks to find the best and fastest way of computing one component of a fermion propagator with Wilson twisted mass and with overlap fermions[16]. The timing of these tests are listed in table 1 for a number of pseudo scalar mass values. Clearly, these results show that Wilson twisted mass fermions are at least one order of magnitude cheaper to simulate than overlap fermions while reaching similar small values of the pseudo scalar mass.

The next question is, whether Wilson twisted mass fermions indeed show the anticipated O(a)-improvement when m_0 is tuned to some $m_{\rm crit}$. That this is indeed the case can be seen in fig. 2[17–19]. Here we show the pion decay constant as a function of a^2 at a fixed, small pseudo scalar mass of $m_{\rm PS} \approx 280$MeV for two definitions of the critical quark mass m_0. For both definitions, the pion decay constant follows a linear behaviour in a^2, thus confirming that the lattice spacing effects that appear in O(a) are indeed canceled. The figure also illustrates that different definitions of $m_{\rm crit}$, although leading to O(a)-improvement, can have rather different strengths of the O(a^2) effects. Hence, the lesson from this is that care has to be taken to use an optimal definition of $m_{\rm crit}$. We remark that such an optimal definition is given by choosing the vanishing of the so-called PCAC quark as the value of $m_{\rm crit}$[19]. The effect of different choices of $m_{\rm crit}$ and the consequences on the $O(a^2)$ artefacts has been theoretically studied in chiral perturbation theory in refs.[20–22] and put on a more general ground in ref.[23].

In fig. 3 we show the *continuum* behaviour of the pion decay constant (left figure)[19] and the average momentum of a parton in a pion (right figure)[24]. Both graphs show that with Wilson twisted mass QCD the behaviour of physical observables can be studied as a

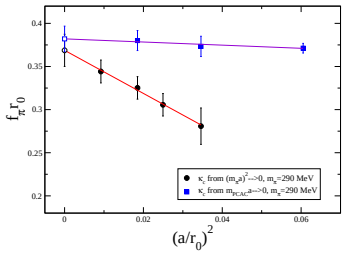

Figure 2. Scaling of the pseudo scalar decay constant f_π using two definitions of $m_{\rm crit}$ corresponding to two choices of κ_c.

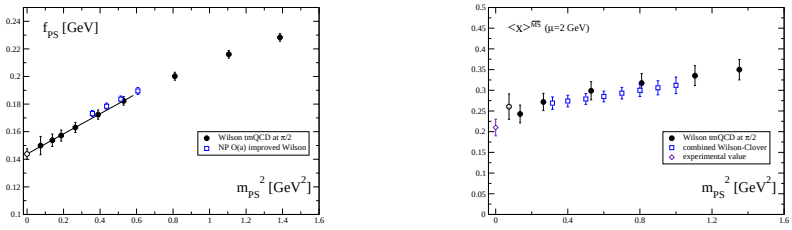

Figure 3. Continuum values of the pion decay constant (left) and the average momentum of a parton in a pion (right) as a function of the pseudo scalar mass in physical units.

function of the pseudo scalar mass down to small values below 300MeV *in the continuum*. It should be stressed that in principle even smaller values of the pseudo scalar mass could be reached and that it is only a question of computer resources to perform such simulations. Of course, in the here discussed quenched approximation it is presumably not worth spending too much computer time since this approximation has an unknown systematic error which does not allow for any reliable comparison with experiment in the end.

3 Dynamical Wilson Twisted Mass Simulations

The results discussed in the previous section are extremely encouraging if one thinks of simulations with dynamical quarks. Since the twisted mass parameter μ regulates the determinant, the simulations are expected to run very smoothly and light pseudo scalar masses of $m_{\rm PS} < 300$MeV ought to be reachable. Our collaboration decided therefore to start a scaling test for dynamical Wilson twisted mass fermions also for the case of two flavours of *dynamical fermions*. As in the quenched approximation, we had the expectation that the pion mass in its role as a Goldstone particle can be made as small as required from the experimental data and that the only obstacle in doing so ought to be the lack of computer resources given the algorithms that exist presently.

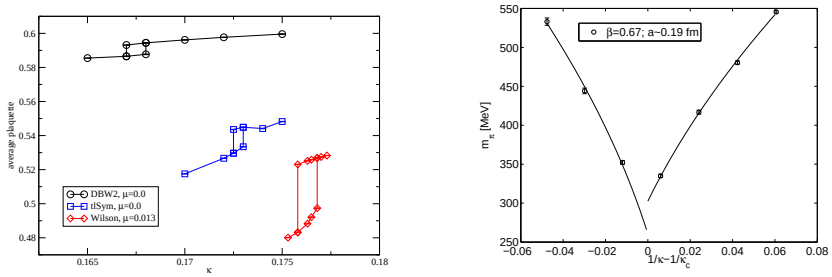

Figure 4. Left: Hysteresis curves for different gauge actions. Right: Non-vanishing minimal pseudo scalar mass in comparison to the predicted behaviour of chiral perturbation theory.

This expectation is guided by the continuum picture, where we have a jump of the scalar condensate at zero quark mass with the associated zero pseudo scalar mass as a result of the Goldstone theorem applied to the spontaneous breaking of chiral symmetry in QCD. This picture implies that the point of zero pseudo scalar mass is approached in a completely smooth way when the quark mass is lowered. To our surprise, we found that this picture fails completely! We refer to refs.[25–28] for a detailed account of this work. Instead of such a smooth behaviour, we found signs of rather strong first order phase transitions manifesting themselves in hysteresis effects, as known e.g. in magnetic systems, and long-living metastabilities with co-existing states. In fig. 4 we show such hysteresis effects employing different gauge actions demonstrating that the strength of the hysteresis and hence the strength of the first order phase transition depends strongly on the choice of the gauge action. Although such hysteresis effects are only first and somewhat naive indicators of the existence of a first order phase transition, in a number of works we studied the phenomenon in more detail and could indeed establish the existence of the first order phase transition.

Maybe, it is true that lattice QCD is already a rather old and mature field and almost nothing really new can be discovered. So it holds also for the case at hand: in a paper by Sharpe and Singleton[29] already in 1998, using the tool of lattice chiral perturbation theory the possibility of such a first order phase transition has been discussed and several properties of the phase transition were computed. The most remarkable and important of these properties is *that the pseudo scalar mass cannot reach zero, but only a certain minimal value*. In fig. 4 (right) we demonstrate this effect which shows up most clearly by the fact that the pseudo scalar masses from the positive and negative quark mass side intersect before reaching zero. We show also the anticipated behaviour from chiral perturbation theory[21, 30, 20, 31–33] as the solid lines.

4 Conclusion

In this project, our collaboration has performed a detailed investigation of Wilson twisted mass fermions at full twist. The work has been presented at several international symposia and workshops and summaries of our work can be found in refs.[34, 28, 35]. In the quenched approximation, we have verified that maximally twisted Wilson fermions indeed lead to an

O(a)-improvement of physical observables leaving even $O(a^2)$ effects small when the right definition of the critical quark mass is chosen.

For dynamical fermions, we could establish that for values of the lattice spacing relevant for a continuum extrapolation, we hit the phenomenon of a first order phase transition with a non-zero and moreover large value of a minimal pseudo scalar mass. Although this phenomenon is in accordance with results from chiral perturbation theory, it came somewhat a surprise. Anyhow, the phenomenon of this first order phase transition needed to be clarified before a large scale dynamical simulation could be started. Our collaboration has performed a detailed study of this question using numerical simulations and analytical techniques from chiral perturbation theory. As a result, we now have for the first time a comprehensive understanding of the lattice QCD phase diagram and the properties of the first order phase transition, see the report of the NIC research group elementary particle physics in these proceedings for a generic picture of the Wilson lattice QCD phase diagram.

As a main consequence of this work, we now know the action and the parameters where dynamical simulations can be performed without being affected by the first order phase transition. This is then the starting point for a detailed scaling study of Wilson twisted mass QCD also in the dynamical case. First simulations in this direction have already been started. Given the considerable algorithmic improvements obtained recently by our collaboration[36] and also by others[37], such simulations are realistic with present computer technology.

Acknowledgment

The work presented here has been achieved by a most exciting collaboration where many surprising and new, unexpected phenomena were detected and investigated. I am indebted to W. Bietenholz, S. Capitani, T. Chiarappa, N. Christian, F. Farchioni, R. Frezzotti, M. Hasenbusch, P. Hofmann, G. McNeille, C. Michael, I. Montvay, G. Münster, K. Nagai, M. Papinutto, J. Pickavance, G. Rossi, E. Scholz, L. Scorzato, S. Shcheredin, A. Shindler, N. Ukita, C. Urbach, U. Wenger and I. Wetzorke. for their excitement, strong motivation and hard work to produce all the physics results in the present project.

References

1. K. G. Wilson, Phys. Rev. **D10**, 2445 (1974).
2. J. Gasser and H. Leutwyler, Phys. Rept. **87**, 77 (1982).
3. J. Gasser and H. Leutwyler, Ann. Phys. **158**, 142 (1984).
4. P. H. Ginsparg and K. G. Wilson, Phys. Rev. **D25**, 2649 (1982).
5. P. Hasenfratz, V. Laliena and F. Niedermayer, Phys. Lett. **B427**, 125 (1998), [hep-lat/9801021].
6. M. Lüscher, Phys. Lett. **B428**, 342 (1998), [hep-lat/9802011].
7. P. Hernandez, K. Jansen and M. Luscher, Nucl. Phys. **B552**, 363 (1999), [hep-lat/9808010].
8. R. Frezzotti and G. C. Rossi, JHEP **08**, 007 (2004), [hep-lat/0306014].
9. W. Bietenholz *et al.*, physics/0309072.

10. ALPHA, R. Frezzotti, P. A. Grassi, S. Sint and P. Weisz, JHEP **08**, 058 (2001), [hep-lat/0101001].
11. K. Jansen *et al.*, Phys. Lett. **B372**, 275 (1996), [hep-lat/9512009].
12. M. Luscher, S. Sint, R. Sommer, P. Weisz and U. Wolff, Nucl. Phys. **B491**, 323 (1997), [hep-lat/9609035].
13. R. Frezzotti and G. C. Rossi, Nucl. Phys. Proc. Suppl. **128**, 193 (2004), [hep-lat/0311008].
14. R. Frezzotti and G. C. Rossi, JHEP **10**, 070 (2004), [hep-lat/0407002].
15. W. Bietenholz *et al.*, JHEP **12**, 044 (2004), [hep-lat/0411001].
16. T. Chiarappa *et al.*, hep-lat/0409107.
17. K. Jansen, A. Shindler, C. Urbach and I. Wetzorke, Phys. Lett. **B586**, 432 (2004), [hep-lat/0312013].
18. K. Jansen, M. Papinutto, A. Shindler, C. Urbach and I. Wetzorke, Accepted for publication in Phys. Lett. **B** (2005), [hep-lat/0503031].
19. XLF, K. Jansen, M. Papinutto, A. Shindler, C. Urbach and I. Wetzorke, JHEP **09**, 071 (2005), [hep-lat/0507010].
20. S. Aoki and O. Bär, Phys. Rev. **D70**, 116011 (2004), [hep-lat/0409006].
21. S. R. Sharpe and J. M. S. Wu, Phys. Rev. **D71**, 074501 (2005), [hep-lat/0411021].
22. S. R. Sharpe, Phys. Rev. **D72**, 074510 (2005), [hep-lat/0509009].
23. R. Frezzotti, G. Martinelli, M. Papinutto and G. C. Rossi, hep-lat/0503034.
24. S. Capitani *et al.*, hep-lat/0511013.
25. F. Farchioni *et al.*, Eur. Phys. J. **C39**, 421 (2005), [hep-lat/0406039].
26. F. Farchioni *et al.*, Nucl. Phys. Proc. Suppl. **140**, 240 (2005), [hep-lat/0409098].
27. F. Farchioni *et al.*, hep-lat/0410031.
28. F. Farchioni *et al.*, hep-lat/0509131.
29. S. R. Sharpe and J. Singleton, Robert, Phys. Rev. **D58**, 074501 (1998), [hep-lat/9804028].
30. S. R. Sharpe and J. M. S. Wu, Phys. Rev. **D70**, 094029 (2004), [hep-lat/0407025].
31. G. Münster, JHEP **09**, 035 (2004), [hep-lat/0407006].
32. G. Munster, C. Schmidt and E. E. Scholz, Nucl. Phys. Proc. Suppl. **140**, 320 (2005), [hep-lat/0409066].
33. L. Scorzato, Eur. Phys. J. **C37**, 445 (2004), [hep-lat/0407023].
34. R. Frezzotti, Nucl. Phys. Proc. Suppl. **140**, 134 (2005), [hep-lat/0409138].
35. A. Shindler, hep-lat/0511002.
36. C. Urbach, K. Jansen, A. Shindler and U. Wenger, hep-lat/0506011.
37. M. Luscher, Comput. Phys. Commun. **165**, 199 (2005), [hep-lat/0409106].

John von Neumann Institute for Computing

Hadron Masses and Nucleon Matrix Elements

Gerrit Schierholz

published in

NIC Symposium 2006 ,
G. Münster, D. Wolf, M. Kremer (Editors),
John von Neumann Institute for Computing, Jülich,
NIC Series, Vol. **32**, ISBN 3-00-017351-X, pp. 109-116, 2006.

http://www.fz-juelich.de/nic-series/volume32

Hadron Masses and Nucleon Matrix Elements

Gerrit Schierholz

NIC, DESY Zeuthen
Platanenallee 6, 15738 Zeuthen, Germany
E-mail: gsch@mail.desy.de

We[1] present first results from a simulation of quenched overlap fermions with improved gauge field action. Among the quantities we study are the hadron masses and selected nucleon matrix elements. To make contact with continuum physics, we compute the renormalization constants of quark bilinear operators nonperturbatively.

1 Introduction

Lattice calculations at small quark masses, i.e. in the chiral regime, require actions with good chiral properties. Overlap fermions[2] have an exact chiral symmetry on the lattice[3] and thus are predestinated for this task. A further advantage of overlap fermions is that they are automatically $O(a)$ improved[4].

Previous calculations of hadron observables from quenched overlap fermions have been limited to larger quark masses and/or coarser lattices due to the high cost of the simulations[5–8]. To ensure that the correlation functions involved are not overshadowed by the exponential decay of the overlap operator[9], the lattice spacing a should be small enough. Ideally $m_H a \ll 1$, where m_H is the mass of the hadron. In addition, the spatial extent of the lattice L should satisfy $L \gg 1/(2f_\pi)$ in order to be able to make contact with chiral perturbation theory[10].

Over the past years we have done extensive simulations of quenched overlap fermions[7,11,12]. In this contribution we shall report a few of our results on hadron masses and nucleon structure functions.

The massive overlap operator is defined by

$$D = \left(1 - \frac{am_q}{2\rho}\right) D_N + m_q \tag{1}$$

with the Neuberger-Dirac operator D_N given by

$$D_N = \frac{\rho}{a}\left(1 + \frac{D_W(\rho)}{\sqrt{D_W^\dagger(\rho) D_W(\rho)}}\right), \quad D_W(\rho) = D_W - \frac{\rho}{a}, \tag{2}$$

where D_W is the massless Wilson-Dirac operator with $r = 1$, and $\rho \in [0, 2]$ is a (negative) mass parameter. The operator D_N has $n_- + n_+$ exact zero modes, $D_N \psi_n^0 = 0$ with $n = 1, \cdots, n_- + n_+$, where n_- (n_+) denotes the number of modes with negative (positive) chirality, $\gamma_5 \psi_n^0 = -\psi_n^0$ ($\gamma_5 \psi_n^0 = +\psi_n^0$). The index of D_N is thus given by $\nu = n_- - n_+$. The 'continuous' modes λ_i, $D_N \psi_i = \lambda_i \psi_i$, satisfy $(\psi_i^\dagger, \gamma_5 \psi_i) = 0$ and come in complex conjugate pairs λ_i, λ_i^*.

To evaluate D_N it is appropriate to introduce the hermitean Wilson-Dirac operator $H_W(\rho) = \gamma_5 D_W(\rho)$, such that

$$D_N = \frac{\rho}{a}\left(1 + \gamma_5 \,\mathrm{sgn}\{H_W(\rho)\}\right), \tag{3}$$

where $\mathrm{sgn}\{H\} = H/\sqrt{H^2}$. The sign function can be defined by means of the spectral decomposition

$$\mathrm{sgn}\{H_W(\rho)\} = \sum_i \mathrm{sgn}\{\mu_i\}\, \chi_i \chi_i^\dagger \,, \tag{4}$$

where χ_i are the normalized eigenvectors of $H_W(\rho)$ with eigenvalue μ_i. Equation (4) is, however, not suitable for numerical evaluation. We write

$$\mathrm{sgn}\{H_W(\rho)\} = \sum_{i=1}^{N} \mathrm{sgn}\{\mu_i\}\, \chi_i \chi_i^\dagger + P_\perp^N H_W(\rho) \,, \tag{5}$$

where

$$P_\perp^N = 1 - \sum_{i=1}^{N} \chi_i \chi_i^\dagger \tag{6}$$

projects onto the subspace orthogonal to the eigenvectors of the N lowest eigenvalues of $|H_W(\rho)|$, and approximate $P_\perp^N H_W(\rho)$ by a minmax polynomial[13]. More precisely, we construct a polynomial $P(x)$, such that

$$\left| P(x) - \frac{1}{\sqrt{x}} \right| < \epsilon \,, \quad x \in [\mu_{N+1}^2, \mu_{\max}^2] \,, \tag{7}$$

where μ_{N+1} ($\mu_{\max}$) is the lowest (largest) eigenvalue of $|P_\perp^N H_W(\rho)|$. We then have

$$\mathrm{sgn}\{H_W(\rho)\} = \sum_{i=1}^{N} \mathrm{sgn}\{\mu_i\}\, \chi_i \chi_i^\dagger + P_\perp^N H_W(\rho)\, P(H_W^2(\rho)) \,. \tag{8}$$

The degree of the polynomial will depend on ϵ and on the condition number of $H_W^2(\rho)$, $\kappa = \mu_{\max}^2/\mu_{N+1}^2$, on the subspace $\{\chi_i \,|\, (1 - P_\perp^N)\chi_i = 0\}$.

We use the Lüscher-Weisz gauge action[14]

$$S[U] = \frac{6}{g^2} \left[c_0 \sum_{\text{plaquette}} \frac{1}{3} \,\mathrm{Re\,Tr}\,(1 - U_{\text{plaquette}}) + c_1 \sum_{\text{rectangle}} \frac{1}{3} \,\mathrm{Re\,Tr}\,(1 - U_{\text{rectangle}}) \right.$$
$$\left. + c_2 \sum_{\text{parallelogram}} \frac{1}{3} \,\mathrm{Re\,Tr}\,(1 - U_{\text{parallelogram}}) \right] \,, \tag{9}$$

where $U_{\text{plaquette}}$ is the standard plaquette, $U_{\text{rectangle}}$ denotes the closed loop along the links of the 1×2 rectangle, and $U_{\text{parallelogram}}$ denotes the closed loop along the diagonally opposite links of the cubes. The coefficients c_1, c_2 are taken from tadpole improved perturbation theory[15]:

$$\frac{c_1}{c_0} = -\frac{(1 + 0.4805\alpha)}{20 u_0^2} \,, \quad \frac{c_2}{c_0} = -\frac{0.03325\alpha}{u_0^2} \tag{10}$$

with $c_0 + 8c_1 + 8c_2 = 1$, where

$$u_0 = \left(\frac{1}{3} \mathrm{Tr}\, \langle U_{\text{plaquette}} \rangle \right)^{\frac{1}{4}} \,, \quad \alpha = -\frac{\log(u_0^4)}{3.06839} \,. \tag{11}$$

β	V	am_q						
8.00	$16^3\,32$	0.0168	0.0280	0.0420	0.0560	0.0840	0.1400	0.1960
8.45	$16^3\,32$				0.0280	0.0560	0.0980	0.1400
8.45	$24^3\,48$		0.0112	0.0196	0.0280	0.0560	0.0980	0.1400

Table 1. Couplings, lattice volumes and mass parameters of the simulation.

We write

$$\beta = \frac{6}{g^2}\, c_0\,. \tag{12}$$

After having fixed β, the parameters c_1, c_2 are determined. In the classical continuum limit $u_0 \to 1$ the coefficients c_1, c_2 assume the tree-level Symanzik values[16] $c_1 = -1/12$, $c_2 = 0$.

The simulations are done on the lattices and at the quark masses listed in Table 1. We set the scale by the scale parameter r_0. In the literature we find[15] $r_0/a = 3.69(4)$ at $\beta = 8.0$ and $r_0/a = 5.29(7)$ at $\beta = 8.45$, respectively. Taking $r_0 = 0.5$ fm, this results in the lattice spacings 0.135 fm at $\beta = 8.0$ and 0.09 fm at $\beta = 8.45$, respectively. The couplings have been chosen such that the $16^3\,32$ lattice at $\beta = 8.0$ and the $24^3\,48$ lattice at $\beta = 8.45$ have approximately the same physical volume. This allows us to study both scaling violations and finite size effects.

We have projected out $N = 40$ lowest lying eigenvectors at $\beta = 8.0$ and $N = 50$ ($N = 10$) at $\beta = 8.45$ on the $24^3\,48$ ($16^3\,32$) lattice. These numbers scale roughly with the physical volume of the lattice. The degree of the polynomial P has been adjusted such that $1/\sqrt{H_W^2(\rho)}$ is determined with a relative accuracy of better than 10^{-7}.

The mass parameter ρ influences the simulation in two ways. First, it affects the locality properties[9] of the Neuberger-Dirac operator. Secondly, the condition number of $P_\perp^N H_W^2(\rho)$, $\kappa = \mu_{\max}^2/\mu_{N+1}^2$, depends on ρ as well. We have chosen $\rho = 1.4$, which is a trade-off between a small condition number κ and good locality properties. Our simulations cover the range of pseudoscalar masses $250 \lesssim m_{PS} \lesssim 900\,\mathrm{MeV}$ as we shall see. The lowest quark mass was chosen such that $m_{PS} L \gtrsim 3$. On all our lattices we have $L \gg 1/(2f_\pi)$.

$O(a)$ improvement, both for masses and on- and off-shell operator matrix elements, is achieved by simply replacing D_N by[4]

$$D_N^{\mathrm{imp}} \equiv \left(1 - \frac{aD_N}{2\rho}\right)^{-1} D_N \tag{13}$$

in the calculation of the quark propagator. In the following we shall always use the improved propagator, without mentioning this explicitly. While the eigenvalues of D_N lie on a circle of radius ρ around $(\rho, 0)$ in the complex plane, the eigenvalues of D_N^{imp} fall onto the imaginary axis.

The inversion of the overlap operator D is done by solving the system of equations

$$Ax = y\,, \tag{14}$$

where $A = D^\dagger D$ and y is a suitable vector. We use the conjugate gradient algorithm for that. The speed of convergence depends on the condition number of the operator A,

$\kappa(A) = \nu_{\max}/\nu_{\min}$, where $\nu_{\max}$ ($\nu_{\min}$) is the largest (lowest) eigenvalue of A. For reasonable values of the quark mass we have $\kappa(A) \propto 1/m_q^2$. Thus, the number of iterations, n_D, needed to achieve a certain accuracy will grow like $n_D \propto 1/m_q$ as the quark mass is decreased.

The convergence of the algorithm can be accelerated by a preconditioning method. Instead of (14) we solve the equivalent system of equations

$$ACx = Cy \equiv \tilde{A}x\,, \tag{15}$$

where C is a nonsingular matrix, which we choose such that $\kappa(\tilde{A}) \ll \kappa(A)$. Our choice is

$$C = 1 + \sum_{i=1}^{n} \left(\frac{1}{\nu_i} - 1 \right) v_i\, v_i^\dagger\,, \tag{16}$$

where v_i (ν_i) are the normalized eigenvectors (eigenvalues) of A. The condition number of the operator $\tilde{A}$ is by a factor ν_{n+1}/ν_1 smaller than the condition number of the operator A, and the number of iterations in the conjugate gradient algorithm reduces to $n_D \propto 1/\sqrt{\nu_{n+1} + m_q^2}$, which depends only weakly on the quark mass m_q. We have chosen $n = 80$, and the inversion was stopped when a relative accuracy of 10^{-7} was reached.

In the calculation of meson and baryon correlation functions we use smeared sources to improve the overlap with the ground state, while the sinks are taken to be either smeared or local. We use Jacobi smearing for source and sink[17]. To set the size of the source, we have chosen $\kappa_s = 0.21$ for the smearing hopping parameter and employed $N_s = 50$ smearing steps.

To further improve the signal of the correlation functions, we have deployed low mode averaging by breaking the quark propagator into two pieces,

$$\sum_{i=1}^{n_\ell} \frac{\psi_i(x)\psi_i^\dagger(y)}{(1 - am_q/2\rho)\,\lambda_i + m_q}\,, \tag{17}$$

where the sum extends over the eigenmodes of the n_ℓ lowest eigenvalues (including the zero modes), and the remainder. The contribution from the low-lying modes (17) is averaged over all positions of the quark sources. As the largest contribution to the correlation functions comes from the lower modes, we may expect a significant improvement in the regime of small quark masses. We have chosen $n_\ell = 40$, mainly because of memory limitations.

2 Hadron Masses

Let us now turn to the calculation of hadron masses. We consider hadrons where all quarks have degenerate masses. So far we have generated $200 - 600$ independent gauge field configurations on each of our lattices.

To compute the pseudoscalar mass, m_{PS}, we looked at correlation functions of the pseudoscalar density $P = \bar{q}\gamma_5 q$ and the time component of the axial vector current $A_4 = \bar{q}\gamma_4\gamma_5 q$. Local sinks are found to give slightly smaller error bars than smeared sinks, so that we will restrict ourselves to this case. Both correlators give consistent results. We will use the results from the axial vector current correlator here.

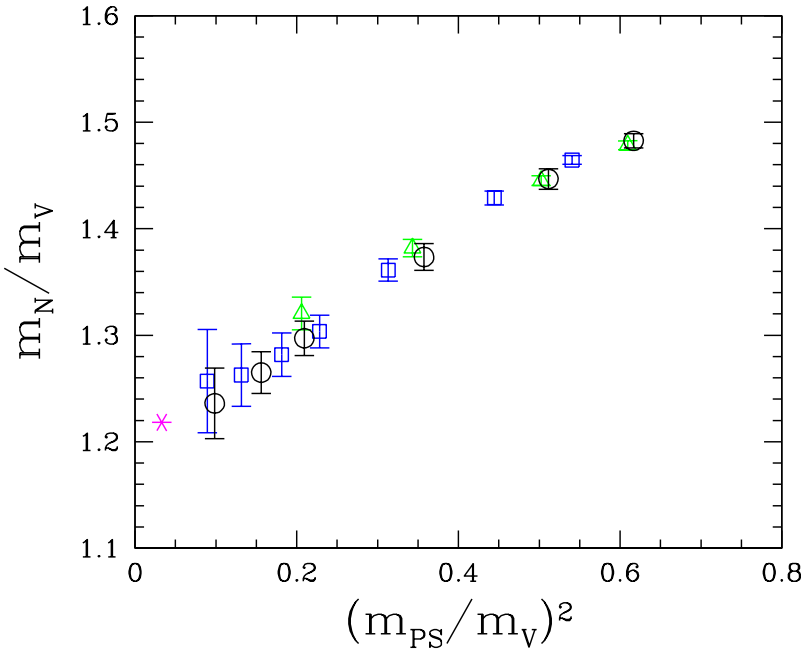

Figure 1. APE plot on the $24^3\,48$ lattice at $\beta = 8.45$ ($\bigcirc$) and on the $16^3\,32$ lattices at $\beta = 8.0$ ($\square$) and $\beta = 8.45$ ($\triangle$), together with the experimental value ($*$).

To compute the vector meson mass, m_V, we explored correlation functions of operators $V_i = \bar{q}\gamma_i q$ and $V_i^4 = \bar{q}\gamma_i\gamma_4 q$ ($i = 1, 2, 3$). We found that the operator V_i, in combination with a local sink, gives the best signal.

For the calculation of the nucleon mass, m_N, we used $B_\mu = \varepsilon_{abc} q_\mu^a (q^b C\gamma_5 q^c)$ (where $C = \gamma_4\gamma_2$) as our basic operator, where we have replaced each spinor by $q \to q^{NR} = (1/2)(1+\gamma_4)q$[17]. These so-called nonrelativistic wave functions have a better overlap with the ground state than the ordinary, relativistic ones. The nucleon mass is obtained from a fit of the data by the correlation function $A\exp(-m_N t) + B\exp(-m_{N^*}(T-t))$ (where T is the time extent of the lattice and m_{N^*} the mass of the backward moving baryon).

In Fig. 1 we show our results in form of an APE plot for our three lattices. At our smallest quark masses we have $m_{PS}/m_V \approx 0.3$, which is the lowest quark mass reached so far in any lattice simulation.

3 Nucleon Matrix Elements

Information about the internal structure of the nucleon is encoded in its structure functions. While they cannot be computed directly on the lattice, the operator product expansion (OPE) provides a connection between their moments and nucleon matrix elements of local operators. For the unpolarized structure function F_1 the OPE reads

$$2\int_0^1 dx x^{n-1} F_1(x, Q^2) = \sum_q E^q_{F_1,n} v^q_n + O(1/Q^2)\,, \tag{18}$$

where q denotes the quark flavour, $E^q_{F_1,n}$ is the (perturbative) Wilson coefficient, and the matrix element v^q_n is defined by

$$\langle N(\vec{p})| \left(O^q_{\{\mu_1 \ldots \mu_n\}} - \text{traces} \right) |N(\vec{p})\rangle = 2 v^q_n (p_{\mu_1} \ldots p_{\mu_n} - \text{traces}) \,, \tag{19}$$

where

$$O^q_{\mu_1 \ldots \mu_n} = \bar{q} \gamma_{\mu_1} \overleftrightarrow{D}_{\mu_2} \ldots \overleftrightarrow{D}_{\mu_n} q \,. \tag{20}$$

Similar relations hold for the other structure functions[17]. Both, the matrix element v^q_n and the Wilson coefficient $E^q_{F_1,n}$ depend upon the choice of a renormalization scheme and scale. Only in their product these dependencies cancel.

To compute the matrix elements (19) we consider the ratio[17]

$$R = \frac{\langle N(t_{sink}) O(\tau) \bar{N}(t_{source}) \rangle}{\langle N(t_{sink}) \bar{N}(t_{source}) \rangle} \,, \tag{21}$$

from which v^q_n can be determined in the region $t_{source} < \tau < t_{sink}$. We always set $t_{source} = 0$ and $t_{sink} = 9$ ($t_{sink} = 13$) in lattice units at $\beta = 8.0$ ($\beta = 8.45$), which corresponds to a distance between source and sink of 1.4 fm.

For lack of space we are only considering the operator

$$O^q_{44} - \tfrac{1}{3} \left(O^q_{11} + O^q_{22} + O^q_{33} \right) \tag{22}$$

and flavor nonsinglet combinations, i.e. u - d (u and d labelling u and d quark, respectively) corresponding to proton minus neutron structure function. In this case there is no contribution from disconnected diagrams.

The operator (22) needs to be renormalized. It is logarithmically divergent. We compute the renormalization factors in the $\mathrm{RI}' - \mathrm{MOM}$ scheme[18]. In this scheme the renormalization condition is formulated in terms of quark Greens functions, computed in Landau gauge, with an operator insertion at zero momentum transfer:

$$C_O(p) = \frac{1}{V} \sum_{x,y,z} e^{-ip(x-y)} \langle q(x) O(z) \bar{q}(y) \rangle \,. \tag{23}$$

From this quantity we compute the amputated vertex function Γ_O,

$$\Gamma_O(p) = S^{-1}(p) C_O(p) S^{-1}(p) \,, \tag{24}$$

where the quark propagator is given by

$$S(p) = \frac{1}{V} \sum_{x,y} e^{-ip(x-y)} \langle q(x) \bar{q}(y) \rangle \,. \tag{25}$$

The renormalization condition at scale μ is

$$Z_q(\mu) Z_O(\mu) \Pi_O \left(\Gamma_O(p) \right)|_{p^2=\mu^2} = 1 \tag{26}$$

with $\Pi_O(\Gamma_O(p)) = \frac{1}{12} \mathrm{tr} \left(\Gamma^{-1}_{O,\mathrm{Born}}(p) \Gamma_O(p) \right)$. The wave function renormalization constant Z_q is determined from the relation $Z_q Z_A \Pi_A \left(\Gamma_A \right) = 1$.

In order to convert the results to the $\overline{\mathrm{MS}}$ scheme, we first determine the renormalization group invariant renormalization constant Z^{RGI}_O,

$$Z^{\mathrm{RGI}}_O = \left(Z^{\mathrm{RI}'-\mathrm{MOM,RGI}}_O(\mu) \right)^{-1} Z^{\mathrm{RI}'-\mathrm{MOM}}_O(\mu) \,, \tag{27}$$

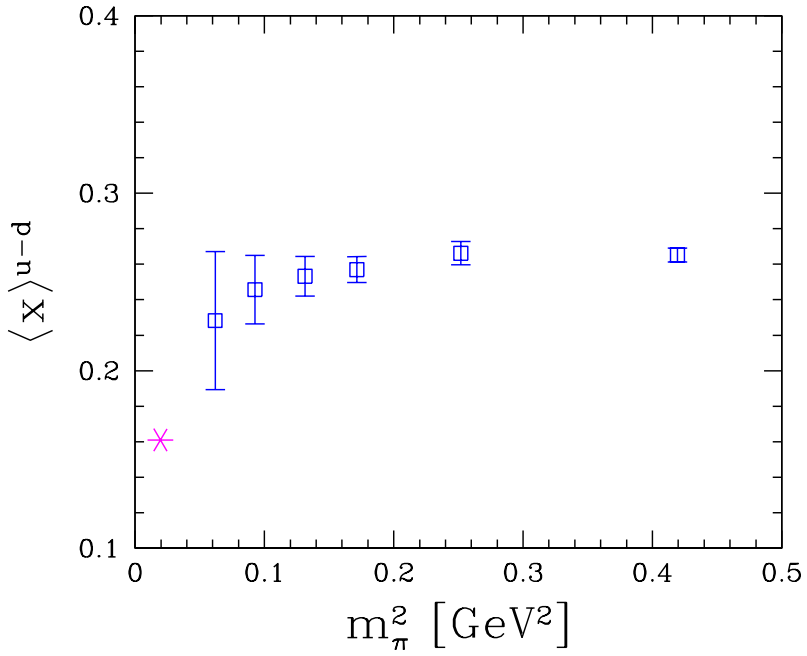

Figure 2. The first moment $\langle x^{u-d} \rangle$ of the unpolarized proton minus neutron structure function on the $16^3\,32$ lattice at $\beta = 8.0$ as a function of the pion mass in the $\overline{\rm MS}$ scheme at 2 GeV, together with the phenomenological value ($*$).

and then convert to the $\overline{\rm MS}$ scheme at scale μ' by $Z_O^{\overline{\rm MS}}(\mu') = Z_O^{\overline{\rm MS},{\rm RGI}}(\mu) Z_O^{\rm RGI}$. The conversion functions to the scheme $\mathcal{S}$ are given by

$$Z_O^{\mathcal{S},{\rm RGI}}(\mu) = \left(2 b_1 g^{\mathcal{S}}(\mu)^2\right)^{-\frac{d_{O,1}}{2b_1}} \exp\left[\int_0^{g^{\mathcal{S}}(\mu)} d\xi \left(\frac{\gamma_O^{\mathcal{S}}(\xi)}{\beta^{\mathcal{S}}(\xi)} + \frac{d_{O,1}}{b_1 \xi}\right)\right]. \qquad (28)$$

The coefficients of the β and γ functions are taken from Ref. 19.

We obtain $Z_{O_{44}}^{\rm RGI} = 2.9$ at $\beta = 8.0$ and $Z_{O_{44}}^{\rm RGI} = 2.6$ at $\beta = 8.45$, respectively. Using $Z_{O_{44}}^{\overline{\rm MS},{\rm RGI}}(2\,{\rm GeV}) = 0.737$, we finally obtain $Z_{O_{44}}^{\overline{\rm MS}} = 2.11$ at $\beta = 8.0$ and $Z_{O_{44}}^{\overline{\rm MS}} = 1.92$ at $\beta = 8.45$, respectively. A comparison with results obtained in one-loop tadpole-improved lattice perturbation theory[20] shows large discrepancies, telling us that the renormalization of lattice operators has to be done nonperturbatively.

Our results for $v_2^{u-d} \equiv \langle x \rangle^{u-d}$ are shown in Fig. 2. We see that the lattice numbers start to bend down towards the phenomenological value, but only at pion masses $\lesssim 350$ MeV. At the larger quark masses our results agree with previous results obtained from improved Wilson fermions[17].

4 Conclusions

It is important to do simulations at small quark masses, in order to reliably extrapolate the lattice results to the chiral limit. Overlap fermions allow us to do so. By the time this article goes to print we will have doubled our statistics. We hope that NIC will grant us the CPU time to perform simulations with dynamical overlap fermions in the near future.

References

1. In collaboration with M. Gürtler, R. Horsley, H. Perlt, P. E. L. Rakow, A. Schiller and T. Streuer.
2. H. Neuberger, Phys. Lett. B417 (1998) 141; *ibid.* B427 (19998) 353.
3. M. Lüscher, Phys. Lett. B428 (1998) 342.
4. S. Capitani, M. Göckeler, R. Horsley, P. E. L. Rakow and G. Schierholz, Phys. Lett. B468 (1999) 150.
5. L. Giusti, C. Hoelbling and C. Rebbi, Phys. Rev. D64 (2001) 114508 [Erratum *ibid.* D65 (2002) 079903]; N. Garron, L. Giusti, C. Hoelbling, L. Lellouch and C. Rebbi, Phys. Rev. Lett. 92 (2004) 042001; F. Berruto, N. Garron, C. Hoelbling, J. Howard, L. Lellouch, S. Necco, C. Rebbi and N. Shoresh, Nucl. Phys. Proc. Suppl. 140 (2005) 264.
6. S. J. Dong, F. X. Lee, K. F. Liu and J. B. Zhang, Phys. Rev. Lett. 85 (2000) 5051; S. J. Dong, T. Draper, I. Horvath, F. X. Lee, K. F. Liu and J. B. Zhang, Phys. Rev. D65 (2002) 054507; F. X. Lee, S. J. Dong, T. Draper, I. Horvath, K. F. Liu, N. Mathur and J. B. Zhang, Nucl. Phys. Proc. Suppl. 119 (2003) 296; N. Mathur, F. X. Lee, A. Alexandru, C. Bennhold, Y. Chen, S.J. Dong, T. Draper, I. Horvath, K.F. Liu, S. Tamhankar and J. B. Zhang, Phys. Rev. D 70 (2004) 074508.
7. D. Galletly, M. Gürtler, R. Horsley, B. Joo, A. D. Kennedy, H. Perlt, B. J. Pendleton, P. E. L. Rakow, G. Schierholz, A. Schiller and T. Streuer, Nucl. Phys. Proc. Suppl. 129 (2004) 453.
8. W. Bietenholz, T. Chiarappa, K. Jansen, K. I. Nagai and S. Shcheredin, JHEP 0402 (2004) 023.
9. P. Hernandez, K. Jansen and M. Lüscher, Nucl. Phys. B552 (1999) 363.
10. G. Colangelo, Nucl. Phys. Proc. Suppl. 140 (2005) 120.
11. T. Bakeyev, D. Galletly, M. Göckeler, M. Gürtler, R. Horsley, B. Jo, A. D. Kennedy, B. Pendleton, H. Perlt, D. Pleiter, P. E. L. Rakow, G. Schierholz, A. Schiller, T. Streuer and H. Stüben, Nucl. Phys. Proc. Suppl. 128 (2004) 82.
12. M. Gürtler, R. Horsley, V. Linke, H. Perlt, P. E. L. Rakow, G. Schierholz, A. Schiller and T. Streuer, Nucl. Phys. Proc. Suppl. 140 (2005) 707.
13. L. Giusti, C. Hoelbling, M. Lüscher and H. Wittig, Comput. Phys. Commun. 153 (2003) 31.
14. M. Lüscher and P. Weisz, Commun. Math. Phys. 97 (1985) 59.
15. C. Gattringer, R. Hoffmann and S. Schaefer, Phys. Rev. D65 (2002) 094503.
16. K. Symanzik, Nucl. Phys. B226 (1983) 187.
17. M. Göckeler, R. Horsley, E.-M. Ilgenfritz, H. Perlt, P. Rakow, G. Schierholz and A. Schiller, Phys. Rev. D53 (1996) 2317.
18. G. Martinelli, C. Pittori, C. T. Sachrajda, M. Testa and A. Vladikas, Nucl. Phys. B445 (1995) 81.
19. J. A. Gracey, Nucl. Phys. B662 (2003) 247; Nucl. Phys. B667 (2003) 242.
20. R. Horsley, H. Perlt, P. E. L. Rakow, G. Schierholz and A. Schiller, Nucl. Phys. B693 (2004) 3 [Erratum-ibid. B **713** (2005) 601]; Phys. Lett. B628 (2005) 66.

John von Neumann Institute for Computing

Non-Leptonic Kaon Decays and the Chiral Regime of the Strong Interaction

Leonardo Giusti, Pilar Hernández, Miho Koma,
Yoshiaki Koma, Mikko Laine, Silvia Necco, Carlos Pena,
Jan Wennekers, and Hartmut Wittig

published in

NIC Symposium 2006 ,
G. Münster, D. Wolf, M. Kremer (Editors),
John von Neumann Institute for Computing, Jülich,
NIC Series, Vol. **32**, ISBN 3-00-017351-X, pp. 117-124, 2006.

http://www.fz-juelich.de/nic-series/volume32

Non-Leptonic Kaon Decays and the Chiral Regime of the Strong Interaction

Leonardo Giusti[1], Pilar Hernández[2], Miho Koma[3], Yoshiaki Koma[3], Mikko Laine[4], Silvia Necco[2], Carlos Pena[1], Jan Wennekers[3], and Hartmut Wittig[5]

[1] CERN, Physics Department, TH Division, 1211 Geneva 23, Switzerland
E-mail: {Leonardo.Giusti, carlos.pena.ruano}@cern.ch

[2] Depto. de Física Teòrica and IFIC, Universitat de València, 46100 Burjassot, Spain
E-mail: Pilar.Hernandez@ific.uv.es

[3] DESY, Theory Group, Notkestr. 85, 22607 Hamburg, Germany
E-mail: {miho.koma, yoshiaki.koma, jan.wennekers}@desy.de

[4] Faculty of Physics, University of Bielefeld, 33501 Bielefeld, Germany
E-mail: laine@physik.uni-bielefeld.de

[5] Institut für Kernphysik, University of Mainz, 55099 Mainz, Germany
E-mail: wittig@kph.uni-mainz.de

We present a status report on our project to investigate the origins of the $\Delta I = 1/2$ rule in $K \to \pi\pi$ decays using lattice simulations of Quantum Chromodynamics (QCD). In particular, we seek to clarify the rôle of the charm quark, which has long been suspected to be important for the enhancement of the $\Delta I = 1/2$ transition amplitude. Among the main ingredients of our calculation is the use of fermionic discretisations which preserve chiral symmetry at non-zero lattice spacing. Furthermore, we keep an active charm quark at all stages of the calculation. Finally, we connect $K \to \pi\pi$ amplitudes to the computationally simpler $K \to \pi$ transitions by matching QCD to Chiral Perturbation Theory in the so-called ϵ-regime. This necessitates performing simulations very close to the massless limit. We report on the associated numerical difficulties and how they can be solved via an exact treatment of a number of low-lying eigenmodes of the discretised Dirac operator.

1 Introduction

K-mesons are quark-antiquark bound states in which one light quark flavour (up or down) is paired with a "strange" flavour. Since the weak interaction does not conserve strangeness, kaons exhibit many different decay modes[1], as well as mixing phenomena, such as oscillations between a neutral K-meson, K^0, and its antiparticle, $\bar{K}^0$. The decay and mixing patterns of kaons are important sources of information for our understanding of fundamental symmetries and their violations. In the Standard Model CP symmetry, which transforms particles into antiparticles, is not conserved. The strength of CP violation in weak decays is determined by the elements of the so-called Cabibbo-Kobayashi-Maskawa (CKM) matrix, and a lot of experimental and theoretical activity is currently spent to pin down their values with high accuracy.

However, many efforts of gaining quantitative insight into weak processes involving kaons are hampered by effects of the strong interaction: kaon decays cannot simply be treated at the level of weak transitions between their fundamental constituents, i.e. the quarks, as the latter are subjected to effects of the strong interaction as well. In principle,

these effects can be computed in Quantum Chromodynamics (QCD), the gauge theory of the strong interaction. However, since the strong coupling constant is not small at typical hadronic mass scales, perturbative QCD is totally inadequate for providing a quantitative description in this regime. Non-leptonic kaon decays are perhaps one of the most striking examples for this failure: if a neutral kaon, having isospin 1/2, decays into a pair of pions, the latter can either have isospin $I = 0$ or 2. The corresponding transition amplitudes are then given by the amplitudes A_0 and A_2 (up to a phase factor). The experimentally observed decay rates yield an unexpectedly large ratio of

$$A_0/A_2 \approx 22.1, \tag{1}$$

which implies that the decay in which isospin changes by 1/2 is favoured over the $\Delta I = 3/2$ transition by a large margin, and this observation is usually called the $\Delta I = 1/2$ rule. By contrast, theoretical calculations based purely on perturbative QCD can only provide a crude estimate for A_0/A_2 which turns out to be smaller by a full order of magnitude! It remains a major challenge to explain the experimentally observed enhancement in the framework of QCD.

The formulation of QCD on a discrete space-time lattice is designed specifically for a non-perturbative treatment. However, decays like $K \to \pi\pi$ are notoriously difficult to address directly in lattice QCD[2,3]. Here we follow the path of obtaining information on $K \to \pi\pi$ decays via the theoretically much simpler $K \to \pi$ transition[9]. The connection to the amplitudes A_0 and A_2 is then provided by matching results from lattice simulations of QCD to an effective low-energy description of the strong interaction, called Chiral Perturbation Theory[4].

The aim of our project is to understand the mechanism which is responsible for the $\Delta I = 1/2$ rule. In particular we seek to clarify whether the observed large enhancement in A_0 over A_2 has a single origin or if it is the result of an accumulation of several moderately large effects. To this end we specifically concentrate on the rôle of the charm quark and the fact that – owing to its large mass of around 1.3 GeV – it decouples from typical low-energy QCD scales of a few hundred MeV. Unlike all previous lattice studies we use a formulation in which the charm quark is "active" in the sense that it is not integrated out from the theory. We first determine the amplitudes A_0 and A_2 for the unphysical situation where the charm is degenerate with the light quark, $m_c = m_u = m_d = m_s$. In a second step we envisage monitoring the amplitudes for heavier charm, i.e. $m_c > m_u = m_d = m_s$. In this note we concentrate on the mass-degenerate case.

In order to keep this note accessible to a wider readership, we skip most technical details and instead refer to our previous papers [5–8].

2 Matching QCD to Chiral Perturbation Theory

Chiral Perturbation Theory (ChPT) is an effective theory of the strong interaction: its fundamental fields are not the quarks and gluons of the QCD but rather the pseudo-Goldstone bosons associated with the spontaneous breaking of chiral symmetry, i.e. the pions, kaons and η-mesons. ChPT is parameterised in terms of empirical coupling constants ("low-energy constants" – LECs) which incorporate the short-distance effects of the strong interaction, but are not calculable in ChPT. They must be computed from the underlying theory

of QCD, e.g. by matching predictions of ChPT to simulation data of lattice QCD, but are usually only determined phenomenologically using experimental data.

Since we are interested in investigating the rôle of the charm quark in $K \to \pi\pi$ we first consider the mass-degenerate case $m_c = m_u = m_d = m_s$. At leading order in ChPT the amplitudes A_0 and A_2 are then related to LECs g_1^+ and g_1^- via

$$\frac{A_0}{A_2} = \frac{1}{\sqrt{2}} \left(\frac{1}{2} + \frac{3}{2} \frac{g_1^-}{g_1^+} \right). \tag{2}$$

At lowest order the effective interaction which describes $K \to \pi\pi$ transitions in terms of Goldstone fields is given by [a]

$$\mathcal{H}_{\rm w}^{\rm ChPT} = 2\sqrt{2} G_{\rm F} (V_{us})^* V_{ud} \left\{ g_1^+ [\widehat{\mathcal{O}}_1^+] + g_1^- [\widehat{\mathcal{O}}_1^-] \right\}, \tag{3}$$

where the operators $\widehat{\mathcal{O}}_1^\pm$ mediate transitions in which strangeness changes by one unit. The expression in eq. (3) is the effective low-energy transcription of the corresponding Hamiltonian in QCD, i.e.

$$\mathcal{H}_{\rm w} = \sqrt{2} G_{\rm F} (V_{us})^* V_{ud} \left\{ k_1^+ \mathcal{Q}_1^+ + k_1^- \mathcal{Q}_1^- \right\}, \tag{4}$$

and the operators $\mathcal{Q}_1^\pm$ are expressed in terms of quark fields according to

$$\mathcal{Q}_1^\pm = \Big\{ (\overline{s}\gamma_\mu P_- u)(\overline{u}\gamma_\mu P_- d) \pm (\overline{s}\gamma_\mu P_- d)(\overline{u}\gamma_\mu P_- u) \Big\} - (u \to c). \tag{5}$$

The Wilson coefficients $k_1^\pm$ in the above expression absorb short-distance effects and can be computed reliably in perturbation theory. With these definitions, one can formulate a matching condition between ChPT and QCD, which allows to express the unknown LECs $g_1^\pm$ in terms of *correlation functions* that are evaluated in lattice simulations, as well as some additional known factors:

$$\frac{g_1^-}{g_1^+} H(x_0, y_0) = \frac{k_1^-}{k_1^+} \cdot \frac{\widehat{Z}^-}{\widehat{Z}^+} \cdot \frac{C_1^-(x_0, y_0)}{C_1^+(x_0, y_0)}. \tag{6}$$

Here, $C_1^\pm(x_0, y_0)$ denote three-point correlation functions of the operators $\mathcal{Q}_1^\pm$ and left-handed axial currents which are used as interpolating operators for the kaon and pion at Euclidean times x_0 and y_0, respectively [5]:

$$C_1^\pm(x_0, y_0) = \sum_{\vec{x},\vec{y}} \left\langle (\overline{d}\gamma_0 P_- u)(x)\, \mathcal{Q}_1^\pm(0)\, (\overline{u}\gamma_0 P_- s)(y) \right\rangle, \quad P_- = \tfrac{1}{2}(1 - \gamma_5). \tag{7}$$

The factors $\widehat{Z}^\pm$ are inserted to account for the proper renormalisation of the operators $\mathcal{Q}_1^\pm$. [10,8] Finally, the chiral correction factor $H(x_0, y_0)$ is the ChPT counterpart of the ratio of correlation functions C_1^-/C_1^+, and can be computed in ChPT [5].

In its original formulation[4] ChPT is an expansion in quark masses and momenta about the massless limit. In this case the chiral correction factor H can only be computed at leading order, since otherwise $\mathcal{H}_{\rm w}^{\rm ChPT}$ must be supplemented with additional interaction terms, whose coefficients are not known, so that predictivity is lost. From a conceptual

[a] Here $G_{\rm F}$ is the Fermi constant, and V_{us}, V_{ud} are CKM matrix elements.

point of view, an alternative kinematical region of ChPT is of particular interest: the so-called ϵ-regime[11] is defined by formulating the theory in a finite volume and for arbitrarily small quark masses:

$$m\Sigma V \lesssim 1. \tag{8}$$

Here m denotes the quark mass, Σ the chiral condensate, and V is the space-time volume. In this situation, the chiral counting rules change in such a way that at next-to-leading order no further terms in addition to those of eq. (3) must be taken into account. Therefore, if one succeeds in performing the difficult numerical task of simulating close to the massless limit, the LECs $g_1^{\pm}$ can be extracted with H determined beyond leading order. Furthermore, long chiral extrapolations, which were the main weakness of previous lattice studies, can be avoided.

3 Lattice Set-Up and Simulations

In all our simulations chiral symmetry is preserved at non-zero lattice spacing. A sufficient condition for this to be the case is the Ginsparg-Wilson relation, i.e.

$$\gamma_5 D + D\gamma_5 = aD\gamma_5 D, \tag{9}$$

where a is the lattice spacing, and D the discretised Dirac operator[12,13]. A particular solution to this relation is defined by the Neuberger-Dirac operator[14], which we have used in our simulations. Preserving chiral symmetry has two key advantages for our project: first, it allows for a clean matching between ChPT and QCD, since the underlying assumption in standard ChPT is that chiral symmetry is only softly broken by the quark masses. Second, chiral symmetry protects the operators $\mathcal{Q}_1^{\pm}$ against mixing with lower-dimensional operators[10]. Thus, the complicated non-perturbative subtraction procedures outlined in[2] can be completely avoided.

The disadvantage of using Ginsparg-Wilson fermions is their large computational cost. A particular definition of the massless Neuberger-Dirac operator is given by

$$D_{\mathrm{N}} = \frac{1}{a}\left\{1 - \frac{A}{\sqrt{A^\dagger A}}\right\}, \qquad A = 1 - aD_{\mathrm{w}}, \tag{10}$$

where D_{w} is the usual Wilson-Dirac operator. The inverse square root in eq. (10) must be approximated by a polynomial in the matrix A. The degree of this polynomial, which is typically of O(50-100), then serves as an estimate how much more expensive one single application of D_{N} is in comparison to $A = 1 - aD_{\mathrm{w}}$. Although efficient numerical techniques have been developed, especially for the ϵ-regime[15], practically all current simulations employing the Neuberger-Dirac operator are performed in the quenched approximation. Since our primary aim is not focused on a high-precision calculation but rather on explaining a large non-perturbative effect, the quenched approximation appears appropriate for this task.

During our first calculations of the correlation functions $C_1^{\pm}$ in the ϵ-regime, we observed extremely large statistical fluctuations, whose origin could be traced back to the spectrum of the Neuberger-Dirac operator. To illustrate the point it is instructive to consider the spectral representation of the quark propagator, which is just the inverse of the

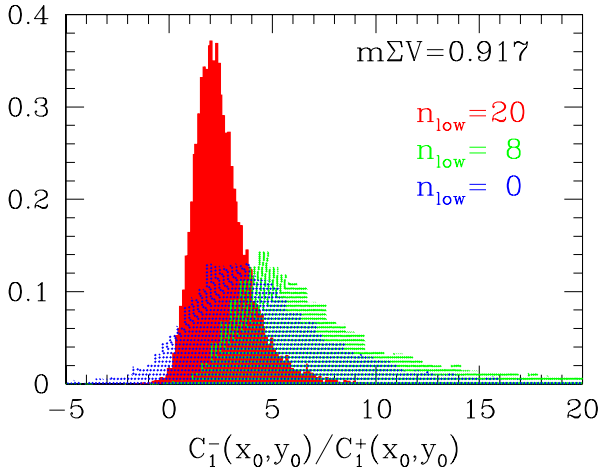

Figure 1. Bootstrap distributions of C_1^-/C_1^+ for $x_0/a = 5, y_0/a = 15$ at $\beta = 5.8$ on $8^3 \cdot 20$.

Dirac operator. It reads

$$S(x,y) = \frac{1}{V} \sum_i \frac{\eta_i(x) \otimes \eta_i(y)^\dagger}{\lambda_i + m}, \tag{11}$$

where $\eta_i(x)$ is an eigenvector of the Neuberger-Dirac operator with eigenvalue λ_i. If the quark mass is of the same size as the smallest eigenvalue or even smaller, it no longer provides an infrared cutoff on the spectrum. It is then possible that the contribution of a few low-lying modes are amplified by the denominator in eq. (11), so that they completely dominate in $S(x,y)$. Moreover, low modes $\eta_i(x)$ whose local magnitude at the point x exceeds the average magnitude by far can also make a dominant contribution to the propagator, if their weight in the spectral sum is enhanced by means of a small eigenvalue. As a result, the Monte Carlo history of correlation functions may exhibit a number of isolated "spikes", where individual gauge configurations produce values which differ by several orders of magnitude from the ensemble average. A reliable error estimate is then not possible, and the signal is virtually lost.

It turned out that the bulk of the extreme fluctuations can be cured by separating off a number of low-lying modes and treating their contributions exactly[16,17]. This technique was first tested successfully in the simpler case of two-point correlation functions[17] and subsequently extended to the three-point functions $C_1^\pm$. The effectiveness of this procedure is shown in Fig. 1. Here we plot bootstrap distributions of the ratio C_1^-/C_1^+ for a particular choice of timeslices x_0, y_0. The plot clearly shows increasingly peaked distributions as the number of low modes that are treated exactly is increased. We emphasise that without low-mode averaging it is practically impossible to obtain a meaningful signal in the ϵ-regime.

Our main results were obtained on a lattice of size $16^3 \cdot 32$ at a bare gauge coupling g_0 corresponding to $\beta \equiv 6/g_0^2 = 5.8485$. At this value the lattice spacing in physical units is $a \approx 0.12\,\mathrm{fm}$. We computed as many as 20 lowest-lying modes of the Neuberger-Dirac operator, using the techniques described in[15]. Furthermore, the gauge configurations were sorted according to their topological index $|\nu|$, which counts the number of exact zero

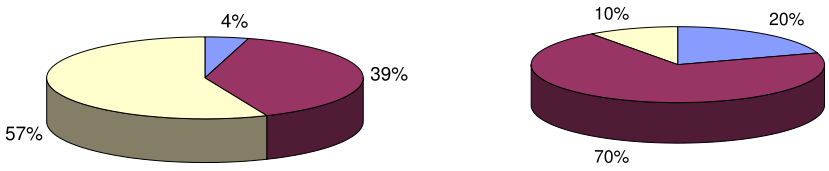

Figure 2. Left: the fraction of CPU time required for computing low modes of $D_{\rm w}$ (blue), low modes of $D_{\rm N}$ (purple) and correlation functions (white); Right: CPU time for the correlators (i.e. 57% of the total) divided up further into percentages spent on inversions (blue), low-mode averaging (purple) and propagator traces (white).

modes of $D_{\rm N}$. In addition to computing $C_1^{\pm}$ for two quark masses which lie in the ϵ-regime, we also considered four heavier masses. This allows us to investigate the systematics of our calculation, by comparing our results computed directly near the massless limit with those obtained from chiral extrapolations from those heavier masses.

Our code is written in standard C, and was originally developed and optimised for PC clusters. Thus, we made extensive use of SSE/SSE2 inline assembly statements, which on an IBM facility like JUMP had to be switched off during compilation. The code allows for communication in two of the four space-time directions, implemented via the Message Passing Interface (MPI) library. On JUMP we typically used 32 processors for our $16^3 \cdot 32$ lattice. The typical compute speed for one application of the Wilson-Dirac operator was about 1 GFlops per processor. It is interesting to compare this with the performance on a PC cluster: on the cluster at DESY Hamburg, which uses Intel Xeon 1.7 GHz CPUs along with Myrinet 2000 as the communication interconnect we achieved 950 MFlops with 32-bit arithmetics, and around 500 MFlops in 64-bit precision.

On JUMP the calculation of three-point functions for two quark masses in the ϵ-regime with 20 low-lying eigenvectors used in the low-mode averaging procedure takes on average 23 hours of CPU time for a single configuration. A detailed comparison of CPU times for the various parts of the code is shown in Fig. 2. It is interesting to note that almost 90% of the total CPU time is spent on manipulations involving the low-lying modes of the Neuberger-Dirac operator. We also wish to point out that the CPU time required to determine the index ν and the lowest non-zero eigenmodes can fluctuate quite strongly. Small values of $|\nu|$ are more frequently associated with very small eigenvalues, and in this case our algorithm needs more iterations to distinguish reliably between a mode with a small but non-zero eigenvalue and an exact zero mode. On our $16^3 \cdot 32$ lattice the maximum time required to compute the low modes could be as much as 18 hours (that is, twice the average time required for this step), which is close to the limit of the `n_long` queue. Larger lattices can therefore only be considered on JUMP if we parallelise the code in more than two space-time directions.

4 Results and Outlook

We shall now present our preliminary results for three-point correlation functions computed for a light, degenerate charm quark. In each topological sector characterised by $|\nu|$

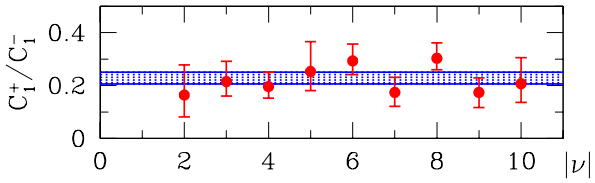

Figure 3. Results for the fitted ratio C_1^+/C_1^- in each topological sector. The weighted average is represented by the blue band.

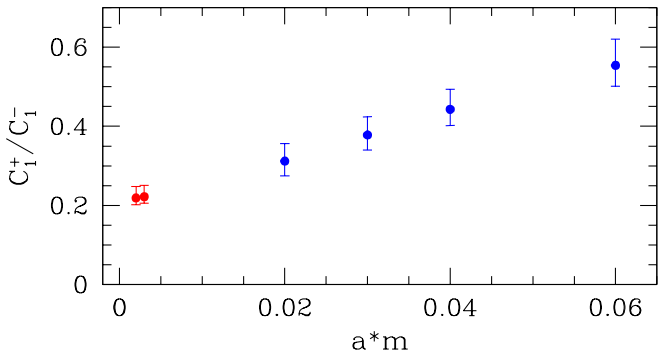

Figure 4. Quark mass dependence of the ratio C_1^+/C_1^-. The four points coloured in blue lie outside the ϵ-regime.

we fitted the correlation function $C_1^{\pm}(x_0, y_0)$ to a constant in the intervals $x_0/a \in [9, 12]$ and $y_0/a \in [20, 23]$. In Fig. 3 we plot the ratio of the fitted correlators, C_1^+/C_1^-, for each sector $|\nu|$. The formulae of ChPT in the ϵ-regime at NLO predict that this ratio should not show any dependence on $|\nu|$, and indeed our data are practically constant within errors. We therefore performed a weighted average over topological sectors, which has the added advantage that those sectors which suffer most from statistical fluctuations caused by the low-lying modes barely contribute to the final result.

The dependence of C_1^+/C_1^- on the quark mass is depicted in Fig. 4. Here we also show the four data points at heavier masses, i.e. outside the ϵ-regime. The data exhibit a smooth mass dependence, but one should be aware that over the whole mass range the data points are subjected to non-uniform chiral corrections, which must be taken into account before results for the combination of LECs g_1^-/g_1^+ can be quoted. A detailed investigation of these corrections is currently underway. Hence, we refrain from quoting an estimate for g_1^-/g_1^+ and instead refer the reader to a forthcoming paper[18].

Here we simply state that our preliminary analysis indicates that for a light, degenerate charm quark the ratio of amplitudes A_0/A_2 is significantly larger than the value derived in early order-of-magnitude theoretical estimates, but that it still falls way short of the experimental result. Our future work will focus on corroborating the current findings, but more importantly we shall consider larger charm quark masses to study their effects in relation to the $\Delta I = 1/2$ rule directly. First test runs are currently being performed.

References

1. S. Eidelman *et al.* [Particle Data Group Collaboration], *Review of particle physics*, Phys. Lett. B **592**, 1 (2004).
2. M. Bochicchio, L. Maiani, G. Martinelli, G.C. Rossi and M. Testa, *Chiral symmetry on the lattice with Wilson fermions*, Nucl. Phys. B **262**, 331 (1985); L. Maiani, G. Martinelli, G.C. Rossi and M. Testa, *The octet non-leptonic Hamiltonian and current algebra on the lattice with Wilson fermions*, Nucl. Phys. B **289**, 505 (1987).
3. L. Maiani and M. Testa, *Final state interactions from Euclidean correlation functions*, Phys. Lett. B **245**, 585 (1990).
4. J. Gasser and H. Leutwyler, *Chiral Perturbation Theory to one loop*, Annals Phys. **158**, 142 (1984); *Chiral Perturbation Theory: Expansions in the mass of the strange quark*, Nucl. Phys. B **250**, 465 (1985).
5. L. Giusti, P. Hernández, M. Laine, P. Weisz and H. Wittig, *A strategy to study the rôle of the charm quark in explaining the* $\Delta I = 1/2$ *rule*, JHEP **0411**, 016 (2004).
6. P. Hernández and M. Laine, *Charm mass dependence of the weak Hamiltonian in chiral perturbation theory*, JHEP **0409**, 018 (2004).
7. L. Giusti, P. Hernández, M. Laine, C. Pena, P. Weisz, J. Wennekers and H. Wittig, *Correlation functions at small quark masses with overlap fermions*, Nucl. Phys. Proc. Suppl. **140**, 417 (2005).
8. L. Giusti, C. Pena, P. Hernández, M. Laine, J. Wennekers and H. Wittig, *On the determination of low-energy constants for* $\Delta S = 1$ *transitions*, PoS **LAT2005**, 344 (2005), hep-lat/0510033.
9. C.W. Bernard, T. Draper, A. Soni, H.D. Politzer and M.B. Wise, *Application of Chiral Perturbation Theory to* $K \to 2\pi$ *decays*, Phys. Rev. D **32**, 2343 (1985).
10. S. Capitani and L. Giusti, *Analysis of the* $\Delta I = 1/2$ *rule and* ϵ'/ϵ *with overlap fermions*, Phys. Rev. D **64**, 014506 (2001).
11. J. Gasser and H. Leutwyler, *Thermodynamics of chiral symmetry*, Phys. Lett. B **188**, 477 (1987); *Spontaneously broken symmetries: Effective Lagrangians at finite volume*, Nucl. Phys. B **307**, 763 (1988).
12. P.H. Ginsparg and K.G. Wilson, *A remnant of chiral symmetry on the lattice*, Phys. Rev. D **25**, 2649 (1982).
13. M. Lüscher, *Exact chiral symmetry on the lattice and the Ginsparg-Wilson relation*, Phys. Lett. B **428**, 342 (1998).
14. H. Neuberger, *Exactly massless quarks on the lattice*, Phys. Lett. B **417**, 141 (1998); *More about exactly massless quarks on the lattice*, ibid. **427**, 353 (1998).
15. L. Giusti, Ch. Hoelbling, M. Lüscher and H. Wittig, *Numerical techniques for Lattice QCD in the* ϵ *regime*, Comput. Phys. Commun. **153**, 31 (2003).
16. T. DeGrand and S. Schaefer, *Improving meson two-point functions in lattice QCD*, Comput. Phys. Commun. **159**, 185 (2004).
17. L. Giusti, P. Hernández, M. Laine, P. Weisz and H. Wittig, *Low-energy couplings of QCD from current correlators near the chiral limit*, JHEP **0404**, 013 (2004).
18. L. Giusti, C. Pena, P. Hernández, M. Laine, J. Wennekers and H. Wittig, *Chiral limit of* $K \to \pi\pi$ *amplitudes with a light charm from quenched QCD*, in preparation.

John von Neumann Institute for Computing

Search for a New Kind of Particles: The $\Theta^+(1540)$ in Lattice QCD

Christian Hagen, Dieter Hierl, and Andreas Schäfer

published in

NIC Symposium 2006 ,
G. Münster, D. Wolf, M. Kremer (Editors),
John von Neumann Institute for Computing, Jülich,
NIC Series, Vol. **32**, ISBN 3-00-017351-X, pp. 125-132, 2006.

http://www.fz-juelich.de/nic-series/volume32

Search for a New Kind of Particles: The $\Theta^+(1540)$ in Lattice QCD

Christian Hagen, Dieter Hierl, and Andreas Schäfer

Institut für theoretische Physik, Universität Regensburg, 93040 Regensburg, Germany

In the last years several independent experiments have claimed the observation of a new kind of particles called pentaquarks. The most prominent of these is the $\Theta^+(1540)$. Lattice QCD should be able to decide whether such states exist or not. We report on a study of the pentaquark $\Theta^+(1540)$, using a variety of different interpolating fields. We do not find any evidence for the existence of a Θ^+ with positive parity. We do observe, however, a signal compatible with normal nucleon-kaon scattering states. For negative parity the results are inconclusive, due to the potential mixture with nucleon-kaon and N^*-kaon scattering states.

1 Introduction

The possible discovery of the pentaquark-candidate $\Theta^+(1540)$ by the LEPS Collaboration at SPring-8[1] has initiated great interest in exotic baryons. While normal hadrons consist of either three valence quarks (baryons like the proton) or a valence quark-antiquark pair (mesons like the pion) these new states are supposed to have four valence quarks and one valence-antiquark. Their possible existence has been predicted since many years, but the great question was always how stable they would be. If the experimental data were correct they would have to live about a factor 100 longer than normal hadron resonances, which would be truely spectacular. Since then, there has been a large number of experiments that have confirmed this result[2–11] but also about the same number that could not confirm it[12–19]. Presently the experimental situation is highly unsettled[20,21], but the tendency goes clearly into the direction that the experimental signals for the $\Theta^+(1540)$ were artefacts.
Lattice QCD should be able to come up with a clear prediction, implying that it should come before the experimental situation is settled, but so far no conclusive answer was reached[22–30].
The difficulties are not only lying on the theoretical side, lattice QCD calculations also require a large amount of computer resources. In our calculations we performed a qualitative study using different types of spin-$\frac{1}{2}$ operators (called sources) with the quantum numbers of the Θ^+. We compute all cross-correlators and use the variational method[31,32] to extract the lowest lying eigenvalues. The construction of the so-called cross-correlation matrix is especially complicated for a particle which is as complex as the pentaquark. Thus, high performance code and a large parallel machine with access to many CPUs are needed. This is why we could perform this project only at Jülich.

2 Theoretical Basics

Let us describe first some fundamental facts about lattice QCD and explain how the search for new hadrons is done.

All of QCD is contained in the generating functional:

$$Z[J^a_\mu, \bar{\eta}^i, \eta^i] = \int \mathcal{D}[A^{a\mu}, \bar{\psi}^i, \psi^i] \exp\left(\mathrm{i} \int d^4x \left[\mathcal{L}_{\mathrm{QCD}} - J^a_\mu A^a_\mu - \bar{\psi}^i \eta^i - \bar{\eta}^i \psi^i \right] \right) \quad (1)$$

There exists a fundamental relationship between quantum theory and statistical physics, which is exploited by lattice QCD.

$$\begin{gathered} t \leftrightarrow -\mathrm{i}\tau \\ \text{Schrödinger-Equ.} \leftrightarrow \text{Diffusion-Equ.} \\ -\mathrm{i}\frac{\partial}{\partial t}\psi(\vec{x},t) = \frac{1}{2m}\ \Delta\psi(\vec{x},t) \leftrightarrow \frac{\partial}{\partial t}P(\vec{x},t;\vec{x}_0,t_0) = D\ \Delta P(\vec{x},t;\vec{x}_0,t_0) \\ S = \int d^4x (T-V) \leftrightarrow \mathrm{i}\int d^4x_E (T+V) = \mathrm{i}S_E \\ e^{\mathrm{i}S} \leftrightarrow e^{-S_E} \end{gathered}$$

This relationship is exact in the same way as analytic continuation is an exact operation in mathematics and it implies that many classes of QCD problems can be solved by statistical means, i.e. Monte Carlo techniques, just like e.g. diffusion problems. The typical plane wave solutions of quantum mechanics translate into exponentially decaying correlations proportional to $\exp(-Ex_4)$. So, one puts combinations of quark-fields with the correct total quantum numbers onto some sites on a lattice of space-time points (typically smeared to about the physical size of the hadron under study) and evaluates their correlation as a function of separation in the Euclidean time direction. This correlation is dominated by the lowest energy state, which is the lowest mass state for the given set of quantum numbers. So for the nucleon one can use e.g. the source ($C = i\gamma^2\gamma^4 = C^{-1}$):

$$\hat{B}_\alpha(t,\vec{p}) = \sum_{\vec{x}} e^{\mathrm{i}\vec{p}\cdot\vec{x}} \epsilon_{ijk} \hat{u}^i_\alpha(x)\ \hat{u}^j_\beta(x) (C^{-1}\gamma_5)_{\beta\gamma} \hat{d}^k_\gamma(x) \quad (2)$$

and study the correlation

$$\begin{aligned} \langle 0|T\left\{\hat{B}(y_4)\hat{A}(x_4)\right\}|0\rangle \Rightarrow\ & e^{-(T-y_4+x_4)E_B} \langle B|\hat{B}(0)|0\rangle\langle 0|\hat{A}(0)|B\rangle \\ +\ & e^{-(y_4-x_4)E_A} \langle 0|\hat{B}(0)|A\rangle\langle A|\hat{A}(0)|0\rangle \end{aligned} \quad (3)$$

Where $\hat{A}$ generates a particles for which all quantum numbers are the negative of those of the nucleon but which has also negative parity, while the nucleon has positive parity (this is a consequence of the fact that the nucleon is a fermion). One can read off from equation (3) that if the correlation is plotted against $\tau = x_4$ one will find the positive parity states on the left side and the negative parity ones on the right. In the following we plot both regions seperately. As our lattice has an extent of 24 sites in the temporal direction this leaves us with a bit less than 12 sites per parity, see Fig.1.

While the ground state spectroscopy is thus very well understood, the spectroscopy of excited states is still in its infancy, especially in full QCD. Therefore, one uses very often the quenched approximation, in which the quark-antiquark fluctuations of the vaccuum are neglected. This approximation should be a reasonably good one for the pentaquark which is supposed to be stabilized by very specific properties of the gluon fluctuations, namely gluon field configurations with non-trivial topology. (The gluons are treated exactly in the

quenched approximation.) On the practical side, dynamical calculations for this problem are presently computationally simply out of reach.
For excited states, instead of calculating a single correlator, which would be sufficient to extract the ground state, one calculates a whole matrix of correlators using different operators for creating and annihilating the considered particle. Of course, these operators must have the right quantum numbers and internal structure (e.g. s- versus p-wave function) to have sufficent overlap with the physical states in question.
The operators for the pentaquark are especially complicated, for they contain five quarks, whereas mesons and baryons only contain two or three quarks, respectively. Thus, the construction of operators with the right quantum numbers is a more difficult task. Furthermore the computational effort is growing exponentialy with the number of constituent quarks of the considered particle. In our calculation we considered a large number of operators. The simplest ones which have been suggested by Csikor/Fodor[22] are the following:

$$I_{0/1} = \epsilon_{abc}[u_a^T C\gamma_5 d_b]\{u_e \bar{s}_e i\gamma_5 d_c \mp (u \leftrightarrow d)\}, \tag{4}$$

where we used vector notation for the Dirac spinors and explicitly denoted the color indices. There are also other more complicated ones which have been suggested by Sasaki[23] or L. Ya. Glozman[33]. We then use all possible combinations of these operators to compute a matrix of correlators.

Before we were able to start our calculations for the Pentaquark Θ^+, we first have performed calculations for Nucleon and Kaon on the same lattice. We needed the results from these calculations for a comparison with the results from the analysis of our Θ^+ data.

Before we discuss the analysis of the results of our calculations in Section 4 and draw a conclusion in Section 6 we would like to give some details of how these calculations have been performed on the JUMP cluster at NIC in Jülich.

3 Details of the Calculation

To get the chiral limit we use 10 different quark masses on a $12^3 \times 24$ lattice. We organize our code that every CPU is computing the correlator for quark mass and one timeslice. So, after one run we have a complete 5×5 cross correlation matrix for the whole lattice and one s-quark mass (see 4). So we need also a second s-quark mass to interpolate to the physical s-quark mass. Without a parallel computer like the JUMP cluster at NIC, we would not be able to perform this calculation. Every single parallel job takes about 3 hours of computing time. To run such a task with a serial code would last more than 800 hours because of the IO handling which is not necessary on the JUMP cluster due to the large memory on the CPUs.

4 Analysis of the Results

We use the five interpolators to calculate a cross correlation matrix $C_{ij}(t)$ on the JUMP cluster which is then inserted into the generalized eigenvalue problem

$$C_{ij}(t)\vec{v}_i^{(k)} = \lambda^{(k)}(t)C_{ij}(t_0)\vec{v}_i^{(k)}. \tag{5}$$

size $L^3 \times T$	$12^3 \times 24$
β	7.90
a [fm]	0.148
a^{-1} [MeV]	1333
L [fm]	≈ 1.8
#conf N	100
quark masses am_q	0.02, 0.03, 0.04, 0.05, 0.06, 0.08, 0.10, 0.12, 0.16, 0.20
smearing parameters:	$n = 18$, $\kappa = 0.210$
s-quark mass am_s	0.0888(17)

Table 1. Parameters of our calculations.

The solutions of this equation behave like

$$\lambda^{(k)}(t) \propto \exp\left(-m^{(k)}(t-t_0)\right). \tag{6}$$

These eigenvalues are used to compute effective masses according to

$$m_{eff}(t) = \ln\left(\frac{\lambda(t)}{\lambda(t+1)}\right). \tag{7}$$

Ordering the five eigenvalues according to their absolute value the largest eigenvalue in the positive parity channel should give the Θ^+ mass, if Θ^+ is a positive parity particle. Else the second largest eigenvalue in the negative parity channel should give the Θ^+ mass, where the largest eigenvalue corresponds to the a N-K scattering state at rest.
In our quenched calculation, we use the Chirally Improved Dirac operator[35–39]. The gauge fields are generated with the Lüscher-Weisz gauge action[40,41] at $\beta = 7.90$. The strange quark mass is fitted using the pseudoscalar K meson. The parameters of our calculation are collected in Table 1.

5 Results

The results of our calculations are shown in Fig. 1, where we plot the effective masses of the two lowest lying states of both parity channels obtained with the cross-correlation technique. These states are approaching a possible plateau very slowly as we expected, since states consisting of five quarks are very complicated and therefore should contain a large number of excited states which have to die out before the effective mass reaches a plateau. We use in addition to the cross-correlation technique Jacobi smeared Gaussian quark sources for all our quarks to improve the signal for the lowest lying states.
The lower horizontal line in the negative parity channel is the sum of the nucleon and kaon mass at rest in the ground state obtained from a separate calculation on the same lattice. Since we project the final state to zero momentum a scattering state can also be a two particle state where the two particles have the same but antiparallel momentum, i.e.

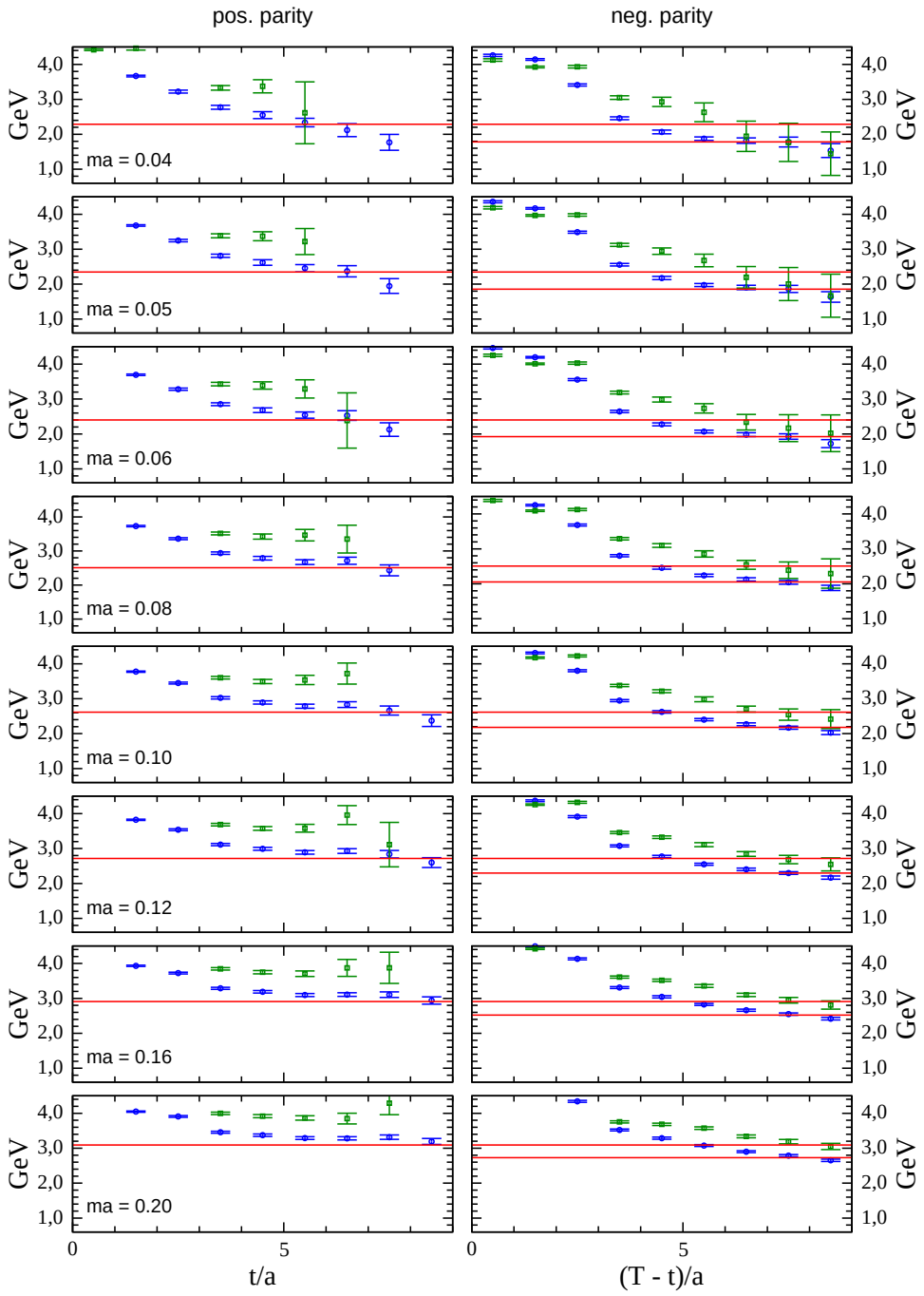

Figure 1. Results from cross-correlation of five interpolators. We use Jacobi smeared Gaussian quark sources for all our quarks. Only the effective masses of the two largest eigenvalues are plotted.

$\vec{p_N} = -\vec{p_K}$. We use the relativistic E-p-relation to calculate the energy of such states,

$$E = \sqrt{p^2 + m_N^2} + \sqrt{p^2 + m_K^2}, \tag{8}$$

where the smallest momentum is $2\pi/L \approx 700\,\mathrm{MeV}$ on our lattice. In Fig. 1 this energy is represented by the upper horizontal line.
We find effective mass plateaus which are consistent with N-K scattering states in the negative parity channel as we expect. We find that the second state is noisy but within errors consistent with the energy in (8). Therefore, it is most likely that we do not observe a Θ^+ state in the negative parity channel. However, this conclusion is not completely certain, if the Θ^+ is broad, because such a Θ^+ state would mix strongly with the continuum states. In the positive parity channel one expects to find either a bound Θ^+ or an excited N-K scattering state. For such an excited state there are several possibilities, e.g., N^*-K, or N-K with a relative angular momentum, and so on.
On the positive parity side, we also show the two lowest lying states obtained from our calculation. Both of them can be identified with continuum states in the sense of Eq. (8) Especially the second one is far too heavy to describe a Θ^+ state. It probably corresponds to an excited N-K scattering state. If there were a signal belonging to the Θ^+ it is supposed to lie below the red line assuming that the chiral extrapolation (e.g. the extrapolation to the nearly vanishing physical up- and down-quark masses) of the Θ^+ does not lead to dramatic effects below our smallest quark mass.

6 Conclusion

In this article we present the results of a pilot study of the Θ^+ using different types of operators. We find that for negative parity our results are in good agreement with a N-K scattering state in the ground state and a quite noisy signal for the first excited state.
For positive parity we find a second state typically more than $500\,\mathrm{MeV}$ heavier than the Θ^+ and which is thus not compatible with a Θ^+ mass of $1540\,\mathrm{MeV}$. This state is probably a higher scattering state.
Thus our calculation do not show any hints for a Θ^+ in the quenched approximation with chiral fermions for the positive parity channel. In the negative parity channel we would need smaller errors to be able to make a really firm statement in favour of or against the existence of a Θ^+ state, but it is clear that there is no indication for such a state in our data. One should also be aware that lattice data cannot rule out the existence of a state with near to zero overlap with the chosen sources. Therefore, it is crucial that many different attempts are made with many different sources to search for the pentaquark states. This is what happens presently.

Acknowledgements

This work was funded by DFG and BMBF. We thank Ch. Gattringer, T. Burch and L. Ya. Glozman for very helpful discussions and their support. The computations were done on the JUMP cluster at NIC in Jülich and at the Rechenzentrum in Regensburg.

References

1. **LEPS** Collaboration, T. Nakano *et al.*, *Observation of $S = +1$ baryon resonance in photo-production from neutron*, *Phys. Rev. Lett.* **91** (2003) 012002, hep-ex/0301020.
2. **CLAS** Collaboration, S. Stepanyan *et al.*, *Observation of an exotic $S = +1$ baryon in exclusive photoproduction from the deuteron*, *Phys. Rev. Lett.* **91** (2003) 252001, hep-ex/0307018.
3. **SAPHIR** Collaboration, J. Barth *et al.*, *Observation of the positive-strangeness pentaquark Θ^+ in photoproduction with the SAPHIR detector at ELSA*, hep-ex/0307083.
4. **DIANA** Collaboration, V. V. Barmin *et al.*, *Observation of a baryon resonance with positive strangeness in K^+ collisions with Xe nuclei*, *Phys. Atom. Nucl.* **66** (2003) 1715–1718,hep-ex/0304040.
5. A. E. Asratyan, A. G. Dolgolenko, and M. A. Kubantsev, *Evidence for formation of a narrow $K^0(S)p$ resonance with mass near $1533\ \mathrm{MeV}$in neutrino interactions*, *Phys. Atom. Nucl.* **67** (2004) 682–687, hep-ex/0309042.
6. **CLAS** Collaboration, V. Kubarovsky *et al.*, *Observation of an exotic baryon with $S = +1$ in photoproduction from the proton*, *Phys. Rev. Lett.* **92** (2004) 032001,hep-ex/0311046.
7. **HERMES** Collaboration, A. Airapetian *et al.*, *Evidence for a narrow $|S| = 1$ baryon state at a mass of 1528* MeV *in quasi-real photoproduction*, *Phys. Lett.* **B585** (2004) 213, hep-ex/0312044.
8. **ZEUS** Collaboration, S. Chekanov *et al.*, *Evidence for a narrow baryonic state decaying to $K_0(S)p$ and $K_0(S)\bar{p}$ in deep inelastic scattering at HERA*, *Phys. Lett.* **B591** (2004) 7–22, hep-ex/0403051.
9. **SVD** Collaboration, A. Aleev *et al.*, hep-ex/0401024.
10. **COSY-TOF** Collaboration, M. Abdel-Bary *et al.*, *Evidence for a narrow resonance at $1530\ \mathrm{MeV/c**2}$ in the K_0p system of the reaction $pp \to \Sigma^+K_0p$ from the COSY-TOF experiment*, *Phys. Lett.* **B595** (2004) 127–134, hep-ex/0403011.
11. P. Z. Aslanyan, V. N. Emelyanenko, and G. G. Rikhkvitzkaya, hep-ex/0403044.
12. **BES** Collaboration, J. Z. Bai *et al.*, *Phys. Rev.* **D70** (2004) 012004, hep-ex/0402012.
13. **HERA-B** Collaboration, K. T. Knopfle, M. Zavertyaev, and T. Zivko, *J. Phys.* **G30** (2004) S1363–S1366, hep-ex/0403020.
14. A. C. Kraan, *Eur. Phys. J.* **C37** (2004) 91–104, hep-ex/0404001.
15. **HyperCP** Collaboration, M. J. Longo *et al.*, *Phys. Rev.* **D70** (2004) 111101, hep-ex/0410027.
16. **CDF** Collaboration, D. O. Litvintsev, **142** (2005) 374–377, hep-ex/0410024.
17. **BaBar** Collaboration, T. Berger-Hryn'ova, hep-ex/0411017.
18. **Belle** Collaboration, K. Abe *et al.*, hep-ex/0411005.
19. S. R. Armstrong, *Nucl. Phys. Proc. Suppl.* **142** (2005) 364–369, hep-ex/0410080.
20. **Belle** Collaboration, hep-ex/0507014.
21. S. Ricciardi, hep-ex/0507027.
22. F. Csikor, Z. Fodor, S. D. Katz, and T. G. Kovacs, *Pentaquark hadrons from lattice*

QCD, *JHEP* **11** (2003) 070, hep-lat/0309090.
23. S. Sasaki, *Lattice study of exotic $S = +1$ baryon*, *Phys. Rev. Lett.* **93** (2004) 152001, hep-lat/0310014.
24. T.-W. Chiu and T.-H. Hsieh, *Pentaquark baryons in quenched lattice QCD with exact chiral symmetry*, hep-ph/0403020.
25. N. Ishii *et al.*, *Pentaquark in anisotropic lattice QCD*, hep-lat/0501022.
26. T. T. Takahashi, T. Umeda, T. Onogi, and T. Kunihiro, *Search for the possible $S = +1$ pentaquark states in quenched lattice QCD*, hep-lat/0503019.
27. C. Alexandrou and A. Tsapalis, *A lattice study of the pentaquark state*, hep-lat/0503013.
28. F. Csikor, Z. Fodor, S. D. Katz, T. G. Kovacs, and B. C. Toth, *A comprehensive search for the Θ^+ pentaquark on the lattice*, hep-lat/0503012.
29. B. G. Lasscock *et al.*, *Search for the pentaquark resonance signature in lattice QCD*, hep-lat/0503008.
30. **BGR (Bern-Graz-Regensburg)** Collaboration, K. Holland and K. J. Juge, *Absence of evidence for pentaquarks on the lattice*, hep-lat/0504007.
31. C. Michael, *Adjoint sources in lattice gauge theory*, *Nucl. Phys.* **B259** (1985) 58.
32. M. Lüscher and U. Wolff, *How to calculate the elastic scattering matrix in two- dimensional quantum field theories by numerical simulation*, *Nucl. Phys.* **B339** (1990) 222–252.
33. L. Y. Glozman, *Θ^+ in a chiral constituent quark model and its interpolating fields*, *Phys. Lett.* **B575** (2003) 18–24, hep-ph/0308232.
34. D. B. Leinweber, W. Melnitchouk, D. G. Richards, A. G. Williams, and J. M. Zanotti, *Baryon spectroscopy in lattice QCD*, nucl-th/0406032.
35. C. Gattringer, *A new approach to Ginsparg-Wilson fermions*, *Phys. Rev.* **D63** (2001) 114501, hep-lat/0003005.
36. C. Gattringer, I. Hip, and C. B. Lang, *Approximate Ginsparg-Wilson fermions: A first test*, *Nucl. Phys.* **B597** (2001) 451–474, hep-lat/0007042.
37. **BGR** Collaboration, C. Gattringer *et al.*, *Quenched spectroscopy with fixed-point and chirally improved fermions*, *Nucl. Phys.* **B677** (2004) 3–51, hep-lat/0307013.
38. C. Gattringer, *Recent results from systematic parameterizations of Ginsparg-Wilson fermions*, *Nucl. Phys. Proc. Suppl.* **119** (2003) 122–130, hep-lat/0208056.
39. **Bern-Graz-Regensburg** Collaboration, C. Gattringer *et al.*, *Quenched QCD with fixed-point and chirally improved fermions*, *Nucl. Phys. Proc. Suppl.* **119** (2003) 796–812, hep-lat/0209099.
40. M. Lüscher and P. Weisz, *On-shell improved lattice gauge theories*, *Commun. Math. Phys.* **97** (1985) 59.
41. G. Curci, P. Menotti, and G. Paffuti, *Symanzik's improved lagrangian for lattice gauge theory*, *Phys. Lett.* **B130** (1983) 205.

John von Neumann Institute for Computing

Materials Science

Robert O. Jones

published in

NIC Symposium 2006 ,
G. Münster, D. Wolf, M. Kremer (Editors),
John von Neumann Institute for Computing, Jülich,
NIC Series, Vol. **32**, ISBN 3-00-017351-X, pp. 133-134, 2006.

http://www.fz-juelich.de/nic-series/volume32

Materials Science

Robert O. Jones

Institut für Festkörperforschung, Forschungszentrum Jülich
52425 Jülich, Germany
E-mail: r.jones@fz-juelich.de

The science of materials has benefited immensely from the rapid improvement of computer hardware and numerical algorithms. Today it is possible to calculate structural, cohesive, and magnetic properties for complex systems with many atoms without using any information from experiment. It is also possible to perform calculations simultaneously on many smaller, but important systems in the time taken by one such calculation only a few years ago. Such calculations can provide information about the properties of materials, such as the motion of individual atoms, that is often unattainable by any other means. Radioactive, poisonous, and short-lived atoms and molecular complexes present no special problems. All this is true, in particular, for calculations using the density functional (DF) formalism, which is the basis of most calculations in condensed matter physics that have no adjustable parameters, and it has become an indispensable tool in theoretical chemistry. The following contributions provide examples of how density functional and other calculations can provide insight into important materials.

The electronic properties of interfaces present particular challenges, and three of the case studies are from this area. Silicon carbide (SiC) is a wide-bandgap semiconductor with remarkable structural and electronic properties in the bulk and at interfaces. The work by Peng et al. focuses on the structure of (001) surfaces of SiC and the nature of its reconstruction. The extension to the adsorption of acetylene (C_2H_2) on the SiC(001)-(2×1) surface has also been carried out. The hydrogen induced metallization of SiC surfaces has been studied in the case of the (001)-(3×2) surface. Surface and adsorbate structures are also the focus of Stekolnikov et al., who investigate the Si(111) surface, one of the best studied of all. This surface shows some remarkable quasi-1D structures when indium is adsorbed on it, and different structures lead to band structures that have gaps or can show metallic behaviour. Spin-polarized density functional calculations indicate that there is only a weak tendency for spin ordering on reconstruction. Spin-polarized DF calculations are, of course, essential in calculations involving magnetic properties, and these have been performed by Bihlmayer et al. for several systems with complex magnetic ground states. The systems studied include ultra-thin magnetic films and nanowires on stepped surfaces. In collaboration with experimental groups, such calculations will be invaluable in aiding the development of new devices.

The work of Entel et al. also uses spin-polarized DF calculations and focuses on other materials of technological importance, namely alloys that exhibit magnetic shape memory. These calculations provide insight into the reasons for stability (and instability) in Heusler alloys. Semiconductor quantum dots (QD) are the subject of the remaining contribution (Lorke et al.). The strong interaction between carriers and phonons in these systems requires a description in terms of polarons, and these authors have performed a quantum-kinetic calculation to study the efficiency of different scattering processes and the way they affect the optical spectra.

These contributions give but a sample of the rich variety of materials problems that are carried out on the supercomputers of the John von Neumann Institute for Computing. In spite of the range and complexity of these applications and the insight obtained from them, it should be noted that they are very demanding of computer resources. There are many phenomena that involve even larger length and time scales than are currently accessible using present computers, and much development in hardware and numerical algorithms will be needed before we can describe the details of such extended systems.

John von Neumann Institute for Computing

Structural and Electronic Properties of Clean and Adsorbate-Covered (001) Surfaces of Cubic SiC

Xiangyang Peng, Jürgen Wieferink, Peter Krüger, and Johannes Pollmann

published in

NIC Symposium 2006 ,
G. Münster, D. Wolf, M. Kremer (Editors),
John von Neumann Institute for Computing, Jülich,
NIC Series, Vol. **32**, ISBN 3-00-017351-X, pp. 135-142, 2006.

http://www.fz-juelich.de/nic-series/volume32

Structural and Electronic Properties of Clean and Adsorbate-Covered (001) Surfaces of Cubic SiC

Xiangyang Peng, Jürgen Wieferink, Peter Krüger, and Johannes Pollmann

Institut für Festkörpertheorie
Wilhelm-Klemm-Str. 10, 48149 Münster, Germany
E-mail: {pengx, wiefer, kruger, pollman}@uni-muenster.de

We report *ab initio* calculations on the atomic and electronic structure of clean and adsorbate-covered SiC(001) surfaces carried out within local density approximation of density functional theory. First we present a general structure model for clean SiC(001)-($n\times2$) surfaces that allows us to identify the origin and nature of the $n\times2$ reconstructions and to rationalize the occurrence of Si addimer nanostrings. Next, we discuss acetylene adsorption on SiC(001)-(2×1). Finally, we consider hydrogen adsorption on SiC(001)-(3×2) which has recently moved into the focus of interest because of the discovery of hydrogen-induced surface metallization.

1 Introduction

Silicon carbide (SiC) is a wide-band gap compound semiconductor with intriguing properties. It has very promising potential for applications in microelectronics and electrooptical devices[1,2]. For example, blue light emitting diodes, high-frequency devices and sensors working in harsh environments are only the first steps in the application of SiC as an advanced material. Consequently, SiC is now in the focus of detailed experimental and theoretical investigations[1–5]. From a fundamental point of view SiC is unique in that it is a fairly ionic group-IV compound semiconductor. In particular, SiC is found to occur in an extremely large number of polytypes. Among these cubic β-SiC appears to be very important for technological use.

The very basis for most of the applications is the growth of high quality crystals which turns out to be a formidable task. For a precise control of processes relevant in SiC growth a detailed understanding of structural and electronic properties of SiC surfaces is highly desirable. Ideal bulk-truncated SiC(001)-(1×1) surfaces are terminated either by a Si or a C layer. At real SiC(001) surfaces more than ten different reconstructions have been observed depending on surface stoichiometry and surface preparation conditions[2,3]. Quite a number of structural models for explaning the observed reconstructions has been suggested on the basis of experimental results[2,3]. Yet, more detailed investigations have shown that a quantitative determination of the atomic structure of clean SiC(001) surfaces remains to be a major challenge[4,5].

Adsorption of organic materials on semiconductor surfaces opens up entirely new fields of applications in microelectronics. The combination of organic chemistry and semiconductor technology has the potential to realize customized devices for special applications[6,7]. In this context SiC is an attrative substrate for the adsorption of organic molecules because of its extraordinary bulk properties, its biocompatibility making it interesting for sensor devices, and its surface reactivity which is completely different from that of Si. By using appropriately reconstructed SiC surfaces as a substrate, organic molecules that can not be bound to a Si surface may be chemisorbed on SiC.

Recently, nanochemistry of SiC surfaces has attracted considerable interest. In particular, hydrogen adsorption has led to very surprising results that are not fully understood at present. Derycke at al.[8] have shown that molecular hydrogen readily adsorbs on SiC(001)-c(4×2) while it hardly interacts with SiC(001)-(3×2) although both surfaces are characterized by similar dimers. In addition, adsorption of atomic hydrogen which usually saturates dangling bonds and eliminates surface states from the band gap making the surface semiconducting leads to an amazing metallization of the SiC(001)-(3×2) surface[9].

Our project is devoted to a thorough *ab initio* study of the structural and electronic properties of clean and adsorbate-covered SiC(001) surfaces in order to determine reliable structural models for the clean surfaces, as well as to contribute to a better understanding of the anticipated functionalization of SiC surfaces by hydrocarbon adsorption and of the observed hydrogen-induced metallization of SiC(001)-(3×2). After a brief outline of our computational method in Sec. 2 we discuss in Sec. 3 some results of our extensive calculations for clean SiC(001) surfaces. From these investigations a generalized model emerges that describes the different observed $n\times2$ reconstructions in a unified way. In Sec. 4 we address acetylene adsorption on SiC(001)-(2×1) and in Sec. 5 we discuss the hydrogen-induced metallization of the SiC(001)-(3×2) surface.

2 Calculational Method

Our calculations are carried out in the framework of density functional theory within local density approximation[10]. The electron-ion interaction is described by norm-conserving pseudopotentials[11] in separable form. The surface systems are represented by supercells containing slabs of 8 to 18 SiC layers and one layer of H atoms saturating the bottom layer of each slab to avoid artificial gap states. The top layers contain appropriate numbers of adatoms. A vacuum region larger than 10 Å is used to decouple neighboring supercells[5,12].

We expand the wave functions in a set of Gaussian orbitals with s, p, d and s^* symmetry. This very efficient basis set leads to a generalized eigenvalue problem with matrices that are about fifty times smaller than those occuring in a plane wave approach. The charge density and the local part of the potential are represented in Fourier space. Therefore, the integrals determining the matrix elements of the Hamiltonian can be evaluated analytically. The short-range nonlocal part of the pseudopotentials is treated in real space. The electrostatic potential of the supercell is calculated using Poisson's equation in a Fourier representation and by a subsequent Fast-Fourier-Transformation to real space using a grid with spacings of 0.16 Å. Structure optimizations are carried out employing Hellmann-Feynman, as well as Pulay forces[5,13]. The relative stability of surfaces with different numbers of atoms is compared by an analysis of the grand-canonical potential within the scheme suggested by Qian, Martin and Chadi[14].

Within our approach the calculation of the charge density, the evaluation of the Hamiltonian matrix elements by summation of all Fourier components and the estimation of the forces are the most time consuming parts of computation. However, these parts of our code are massively parallelized with respect to the points of the grids in real or Fourier space, respectively.

3 Generalized Reconstruction Model of SiC(001)-(n×2) Surfaces

Real Si-terminated SiC(001) surfaces, prepared by annealing SiC in a flux of Si atoms, show many different reconstructions ranging from the stoichiometric 2×1 over 3×2, 5×2, 7×2, ... up to 15×2 surfaces[2,3]. For quite some time it was believed, therefore, that SiC(001) shows only n×2 reconstructions with odd n. More recently, however, Douillard *et al.*[15] observed an 8×2 reconstruction and even more interestingly the formation of Si nanostrings on SiC(001) surfaces raising the questions whether n×2 reconstructions with even n are possible, in general, and why Si nanostrings can occur at all. Therefore, one aim of our project is to elucidate the atomic configurations in the observed n×2 superstructures and to explain their amazing order with respect to Si adatom coverage. Likewise, we want to rationalize the occurrence of Si nanostrings and identify their physical nature.

We have studied the reconstructions of the c(4×2), 3×2 and 5×2 surfaces by *ab initio* calculations, previously, and have suggested structural models following from minimum surface formation energy in each case[12,16,17]. These models are in good agreement with a host of experimental data. Employing these results we have been able to derive a general n×2 reconstruction model which is based on two structural building blocks only, which we label A and B. They are characteristic for the c(4×2) surface (A) and the 3×2 surface (B), respectively. Our optimized c(4×2) missing row asymmetric dimer model[16] has half a monolayer (ML) of Si adatoms adsorbed on the complete Si sublayer forming rows of buckeled Si adimers in the ×2 direction. Each second addimer row is missing. In our 3×2 two adlayer asymmetric dimer (TAAD) model[12] two partial layers of Si adatoms are adsorbed on the clean surface. Two Si adatoms per unit cell in the top adlayer form one buckled dimer in the 3× direction while four Si atoms in the second adlayer form two weak Si dimers in the ×2 direction. For the 5×2 reconstruction we also find a TAADM as the optimal structure[17]. Comparing the three optimized reconstructions, it occured to us that the building block of the 5×2 reconstruction is a mere superposition of the building blocks A and B of the other two reconstructions. The atomic positions in the 5×2 unit cell turn out to be virtually the same as those in the respective A and B building blocks of the c(4×2) and (3×2) surfaces. On the basis of these *ab initio* results we were led to the expectation that all higher n×2 reconstructions are just appropriate superpositions of A and B building blocks.

Therefore, we have extrapolated our TAADM to higher n values and suggest that n×2 reconstructions are simply appropriate superpositions of A- and B-type building blocks. In the general n×2 model with $n > 3$ each reconstruction contains l A-type and m B-type building blocks whereby $n = 2 \cdot l + 3 \cdot m$ with $l \geq 1$ and $m \geq 1$. To corroborate this idea we have carried out very demanding *ab initio* calculations on 7×2 and 8×2 reconstructions investigating a host of conceivable surface structures. In the latter case there are 158 atoms per supercell leading, e. g., to 3300×3300 Hamiltonian matrices. For both surfaces we find our TAADM to be the locally stable energy-minimum configuration. The optimized structures are shown in Fig 1 (a). Both reconstructions consist indeed of A- and B-type building blocks with atomic positions very similar to those in the respective c(4×2) and 3×2 reconstructions. The optimized 7×2 and 8×2 structures are obviously AAB and ABB reconstructions, respectively. The 8×2 structure exhibits one D_A and two D_B addimers per surface unit cell. The D_B dimers reside significantly higher above the surface than the D_A dimers (see the side view in Fig. 1 (a)) giving rise to pairs of Si addimer nanolines in an

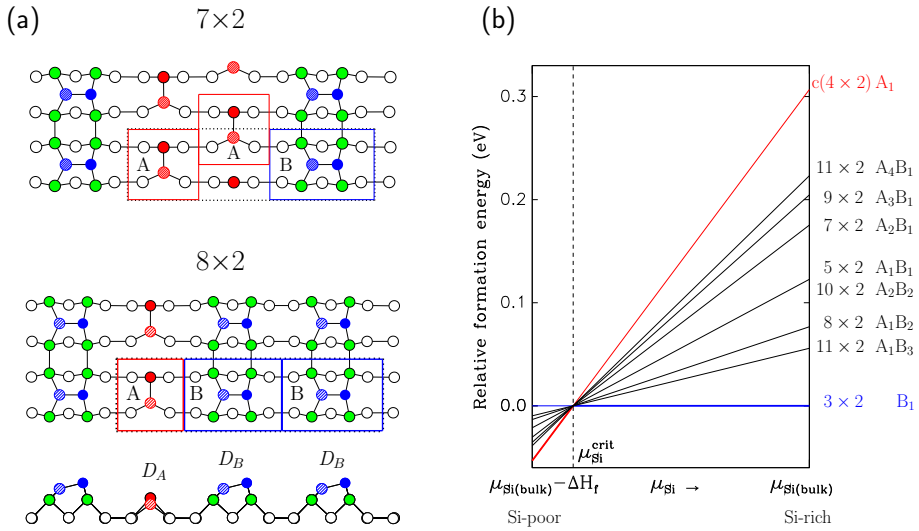

Figure 1. (a) Top views of the optimal surface structure of the 7×2 and 8×2 TAAD models of SiC(001). For the 8×2 TAADM a side view is shown, as well. The atoms of the Si sublayer are shown by open circles. Building blocks A and B are indicated by red squares and blue rectangles, respectively. (b) Relative formation energies per 1×1 unit cell of the c(4×2) and n×2 surfaces (referred to the 3×2 reconstruction) as a function of μ_{Si}.

8×2 periodic arrangement in very nice agreement with STM experiments[15].

The formation energies of some n×2 reconstructions with n up to 11 are shown in Fig. 1 (b) as functions of the chemical potential μ_{Si} of Si in the gas phase. The decompositions of these structures in A and B blocks is given in the figure, as well. Note that, e. g., the 11×2 surface has two realizations differing in adatom coverage. For Si-poor and Si-rich conditions the c(4×2) and 3×2 reconstructions are lowest in formation energy, respectively. All other n×2 reconstructions fall in between these two limits. Our general TAADM explains a wealth of observations on n×2 surfaces as discussed in detail elsewhere[18]. In particular, it shows in agreement with experiment that neither a primitive 4×2 nor a 6×2 reconstruction occurs. Other n×2 reconstructions with larger even n are possible, however. Moreover, it allows us to rationalize the occurrence of a wealth of periodic and nonperiodic Si addimer nanostrings, as observed in experiment[15].

4 Adsorption of Acetylene on SiC(001)-(2×1)

The SiC(001) surface offers a broad range of adsorption channels for organic molecules due to its rich variety of reconstructions. In this brief report we focus on acetylene (C_2H_2) adsorption on SiC(001)-(2×1). In particular, we show that acetylene experiences a completely different bonding configuration on SiC(001)-(2×1) than on the Si(001)-(2×1) surface. Fig. 2 (a) gives an overview of the investigated sites for acetylene adsorption. Acetylene has a C≡C triple bond consisting of one σ and two π bonds. The two π bonds are

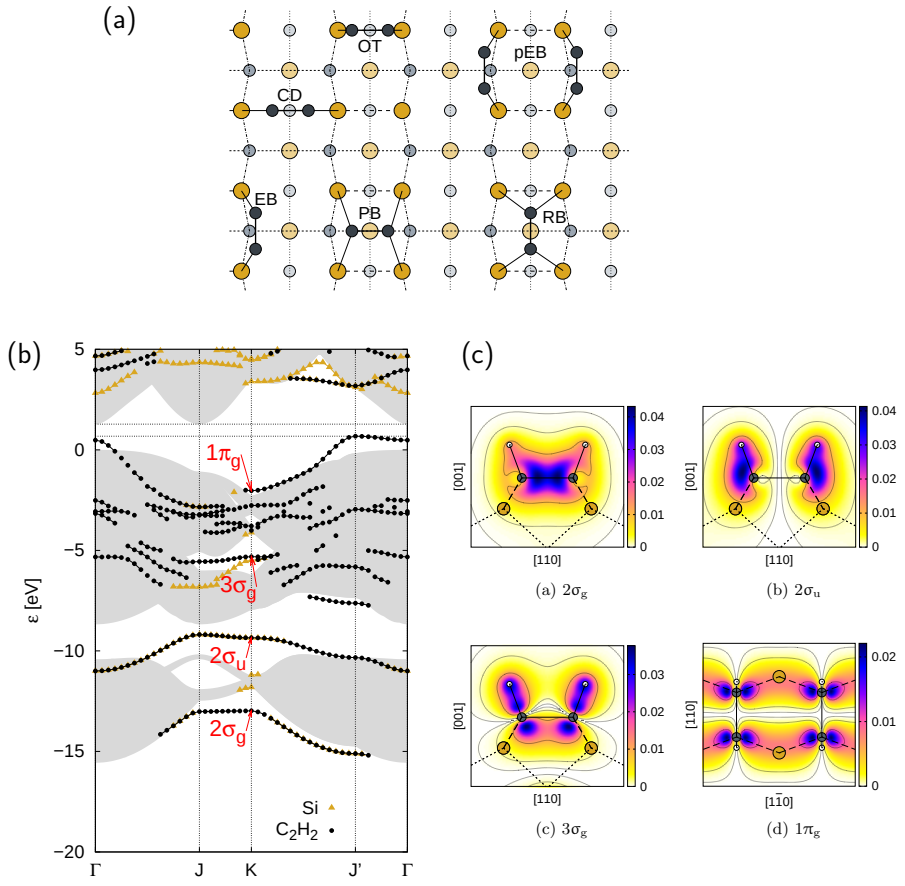

Figure 2. (a) Top view of the Si-terminated SiC(001)-(2×1) surface with various adsorption sites for acetylene. Hydrogen atoms are omitted for clarity. Carbon atoms of adsorbed molecules are shown by black dots. Large ocher and light ocher circles depict Si atoms on the first and third substrate layers while small blue and light blue circles indicate C atoms on the second and fourth substrate layers, respectively. (b) Surface band structure of an acetylene monolayer on SiC(001) in the (1×2)-RB configuration. States that are strongly localized at the adsorbed C_2H_2 molecules are indicated by black dots. (c) Charge-density distributions of the $2\sigma_g, 2\sigma_u, 3\sigma_g$, and $1\pi_g$ states at the K-point.

highly reactive and interact preferentially with surface dangling bonds, therefore. In the so called di-σ configurations acetylene is bonded to two Si atoms at the surface and a C=C double bond is retained in the molecule. These di-σ configurations lead to *cross dimer* (CD), *on top* (OT), *end bridge* (EB) and *paired end bridge* (pEB) structures. Alternatively, acetylene can be adsorbed at the surface by formation of four σ bonds between each molecule and the four Si atoms of two neighboring Si dimers leading to tetra-σ configurations. These are called *pedestal bridge* (PB) and *rotated bridge* (RB) structures.

Our investigations[19] show that acetylene adsorbs preferentially in rotated-bridge sites on SiC(001). In the optimal (1×2)-RB surface structure (not shown for shortness) each surface Si atom is bound to two C atoms of two neighboring acetylene molecules and two

C atoms on the second substrate layer. This way all atoms of the molecule and the substrate become fully coordinated. The band structure for the optimized configuration is shown in Fig. 2 (b). There are four bands of localized surface states which we label according to the corresponding orbitals of the free molecule. The bonding and antibonding states formed by the carbon σ-orbitals give rise to the bands $2\sigma_g$ and $2\sigma_u$ which show a strong dispersion along the ΓJ and KJ' direction due to the interaction between carbon σ-orbitals of neighboring molecules at the surface. Respective charge densities at the K-point are shown in the upper panels of Fig. 2 (c). The flat band $3\sigma_g$ near -5 eV mostly stems from the C-H bonds of the adsorbed acetylene molecules (see lower left panel of Fig. 2 (c)). In addition, the adsorption of acetylene leads to a hybridization of the lowest unoccupied π-orbitals of the molecule with the former Si dangling bonds of the surface. Band $1\pi_g$ results from one linear combination of these bonding orbitals (see lower right panel of Fig. 2 (c)). While acetylene perfectly fits into the center between four Si atoms at the SiC(001)-(2×1) surface, on Si(001) it adsorbes preferentially in (2×2)-pEB and (2×1)-OT configurations. Due to the correspondingly larger lattice constant of Si a strong bending of the Si-C bonds would be necessary to achieve a RB structure at the latter surface.

5 Hydrogen-Induced Metallization of the SiC(001)-(3×2) Surface

Turning a semiconducting surface into a metallic one by H adsorption is generally deemed very unlikely. Yet, recent experiments have provided clear evidence for the metallization of SiC(001)-(3×2) by hydrogenation[9]. To explain these findings, Derycke *et al.*[9] conjectured that the top adlayer Si dimers in the TAADM become saturated, at first, by formation of monohydrides. Further H adatoms were assumed to break the Si dimers in the third layer and to become bonded to one of the two Si atoms of the broken dimers, leaving a Si dangling bond at the other. Within this scenario the Si dangling bonds on the third layer are stabilized by steric hindrance and would lead to surface metallization. Very recently, this explanation has been questioned on the basis of several *ab initio* studies[20–23] which find that the lattice configuration suggested by Derycke *et al.* for the metallic surface is not stable. The calculations show that H adsorbs in the optimized structure at the topmost Si layer forming monohydrides and additional H atoms adsorb on the third layer forming angular Si-H-Si bonds. These bonds are only partially saturated leading to a surface band structure which is clearly metallic. We have found that this structure is not the only one leading to a metallic surface. In a systematic DFT study[23] we have scrutinized a number of conceivable geometries for several degrees of H exposure. We find that H atoms can also occupy bridge positions in angular Si-H-Si bonds on the second layer inducing metallization, as well. Our results show in addition that the formation of Si dihydrides instead of monohydrides at the surface leads to an even more favorable grand canonical potential at high H exposures.

As an example, Fig 3. (a) shows a top and a side view of the optimized structure for large H exposure. The Si-H bond lengths and the angles between the two Si-H bonds on the second (third) layer are 1.67 Å (1.66 Å) and 151° (127°), respectively. The corresponding surface band structure is shown in Fig. 3 (b). It clearly reveals that this adsorption configuration has a metallic surface. The adsorption of H on the second and third layer leads to the bands B_1, B_2 and B_3. The former two of these bands are located within the gap showing a large dispersion. Around the M and J' points the states B_1 and B_2 are mainly localized on the second layer. The band B_3 stems from Si-H-Si bonds on the third layer. Fig. 3 (c)

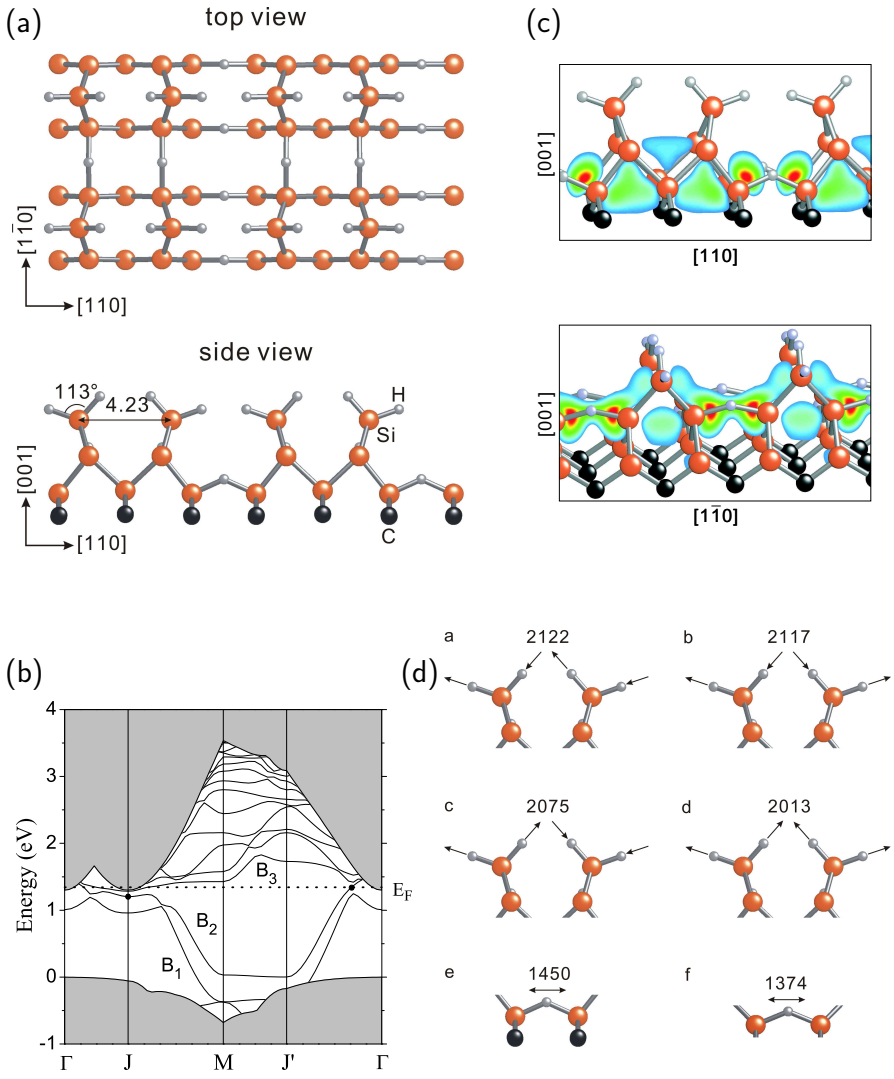

Figure 3. (a) Top and side view of the optimized H-induced metallic structure. The top dimers are broken and two canted dihydride units are formed per unit cell due to H adsorption at the top layer. The second and third layer dimers are also broken establishing angular Si-H-Si bonds with H atoms in bridge positions. (b) Corresponding surface band structure along high-symmetry lines of the surface Brillouin zone. The dots indicate states whose charge-density distributions are shown in (c). Displacement patterns of a few salient hydrogen-related vibrational modes are depicted in (d).

shows the charge density of B_2 states near the Fermi level at the J point and close to the Γ point. At J the state is strongly localized on the third layer Si-H-Si bonds (see top panel) while near Γ it is mainly localized on the second layer Si-H-Si bonds (see bottom panel). Thus the wave function character of the states in the B_2 band changes entirely from J to

the region near Γ. Band B_1 is fully occupied. The bands B_2 and B_3 are only partially occupied and cross the Fermi level giving rise to the metallic surface.

We have also calculated surface phonons at the Γ point. Fig. 3 (d) shows the displacement patterns of salient hydrogen-related vibrational modes. The four modes above 2000 cm^{-1} are antisymmetric or symmetric vibrations within or between the dihydride units. These phonon energies are close to typical energies of Si-H stretch vibrations. In contrast, the frequencies of the highest vibrational modes related to H atoms in the angular Si-H-Si bonds on the second (1374 cm^{-1}) and third layer (1450 cm^{-1}) are comparatively low. This is related to the fact that the Si-H bonds in the bridge bonds are much longer (1.67 Å) and thus much weaker than a usual short (1.50 Å) and strong Si-H bond. These fingerprints of the Si-H-Si bonds in the calculated phonon spectrum have not been observed to date[24], possibly due to a restricted experimental resolution in the low frequency range.

Acknowledgments

Grants of computer time from the John von Neumann Institute, Jülich, and financial support of this work by the Deutsche Forschungsgemeinschaft are gratefully acknowledged.

References

1. W. J. Choyke, H. Matsunami, and G. Pensl (eds.) *Silicon Carbide, Fundamental Questions and Applications to Current Device Technology* Springer, Berlin (2004).
2. P. G. Soukiassian and H.B. Enriquez, J. Phys.: Condens. Matter **16**, S1611 (2004).
3. V. Bermudez, phys. stat. sol. (b) **202**, 447 (1997).
4. A. Catellani and G. Galli, Prog. Surf. Sci. **69**, 101 (2002).
5. J. Pollmann and P. Krüger, J. Phys.: Condens. Matter **16**, S1659 (2004).
6. S.F. Bent, Surf. Sci. **500**, 879 (2002).
7. J. Yates, Science **279**, 335 (1998).
8. V. Derycke *et al.*, Phys. Rev. B **63**, R201305 (2001).
9. V. Derycke *et al.*, Nature Mat. **2**, 253 (2003).
10. W. Kohn and L.J. Sham, Phys. Rev. **140**, A1133 (1965).
11. D.R. Hamann, M. Schlüter, and C. Chiang, Phys. Rev. Lett. **43**, 1494 (1979).
12. W. Lu, P. Krüger, and J. Pollmann, Phys. Rev. B **60**, 2495 (1999).
13. P. Krüger and J. Pollmann, Phys. Rev. B **38**, 10578 (1988).
14. G.X. Qian, R. M. Martin, and D.J. Chadi, Phys. Rev. B **38**, 7649 (1988).
15. L. Douillard *et al.*, Surf. Sci. **401**, L395 (1998).
16. W. Lu, P. Krüger, and J. Pollmann, Phys. Rev. Lett. **80**, 2090 (1998).
17. W. Lu, P. Krüger, and J. Pollmann, Phys. Rev. B **61**, 2680 (2000).
18. P. Krüger and J. Pollmann, Phys. Rev. B (in print).
19. J. Wieferink, P. Krüger, and J. Pollmann, submitted to Phys. Rev. B.
20. R. Di Felice *et al.*, Phys. Rev. Lett. **94**, 116103 (2005).
21. F.B. Mota *et al.*, J. Phys.: Condens. Matter **17**, 4739 (2005).
22. H. Chang, J. Wu, B.-L. Gu, F. Liu, and W. Duan, Phys. Rev. Lett. **95**, 196803 (2005).
23. X. Peng, P. Krüger, and J. Pollmann, Phys. Rev. B (in print).
24. F. Amy and Y.J. Chabal, J. Chem. Phys. **119**, 6201 (2003).

John von Neumann Institute for Computing

Quasi-1D In/Si(111) Surface Structures

Andrey A. Stekolnikov, Xochitl López-Lozano,
Jürgen Furthmüller, and Friedhem Bechstedt

published in

NIC Symposium 2006 ,
G. Münster, D. Wolf, M. Kremer (Editors),
John von Neumann Institute for Computing, Jülich,
NIC Series, Vol. **32**, ISBN 3-00-017351-X, pp. 143-150, 2006.

http://www.fz-juelich.de/nic-series/volume32

Quasi-1D In/Si(111) Surface Structures

Andrey A. Stekolnikov[1], **Xochitl López-Lozano**[1,2], **Jürgen Furthmüller**[1], **and Friedhelm Bechstedt**[1]

[1] Institut für Festkörpertheorie und -optik, Friedrich-Schiller-Universität
Max-Wien-Platz 1, 07743 Jena, Germany
E-mail: {andrey,furth,bech}@ifto.physik.uni-jena.de

[2] Instituto de Física, Universidad Autónoma de Puebla
Apartado Postal J-48, Puebla 72570, México
E-mail: xlopez@fisica.unam.mx

The atomic geometry and electronic structure is studied by means of *ab initio* total-energy and electronic-structure calculations for quasi-one-dimensional (1D) In/Si(111) systems with different translational symmetries 4×1, 4×2, and 8×2. The chain structure and the trimer formation are related to the details of the electronic band structure. While 4×1 reconstruction shows metallic behavior, the 4×2, and 8×2 ones lead to an opening of energy gaps. We show that the phase transitions give rise to charge density waves in the electron density distribution. The electron redistributions are identified to play an important role for the transition $4\times2 \rightarrow 8\times2$. Only a weak tendency for spin ordering accompanying the surface reconstruction is found within the used spin-polarized density functional calculations.

1 Introduction

Adsorption of indium (In) on Si(111) substrates gives rise to a variety of surface reconstructions in dependence on the coverage with a tendency to be semiconducting below one monolayer or to be metallic at larger coverages. Most interesting is the borderline of these coverages for one monolayer for which a 4×1 phase occurs at room temperature (RT). Using grants of computational time by the John von Neumann Institute for Computing (NIC) we have performed highly demanding first-principle calculations in order to study atomic geometry, electronic band structure, and spin dependence of In chains on Si(111) substrates. We focus our attention to the interplay between the atomic structure of a given translational symmetry and the spatial distributions of charge, spin and electronic states. The results are discussed in terms of possibly occurring charge or spin density waves. The manifestation of charge density waves is studied in details. We try to extract driving forces for the reconstructions.

2 Motivation

True one-dimensional electronic systems have attracted great interest because of their expected exotic electronic properties, which include charge-density wave (CDW), spin-density wave (SDW), triplet superconductivity, and Luttinger-liquid (LL) behavior[1]. Properties of electrons related to charge and spin may be separated in a quasiparticle picture[2]. In a LL the electron loses its identity and separates into two quasiparticles. In a photoemission experiment the excitation should decay into a spinon that carries spin without charge and a holon that carries the positive charge of a hole without its spin. Metal chains of

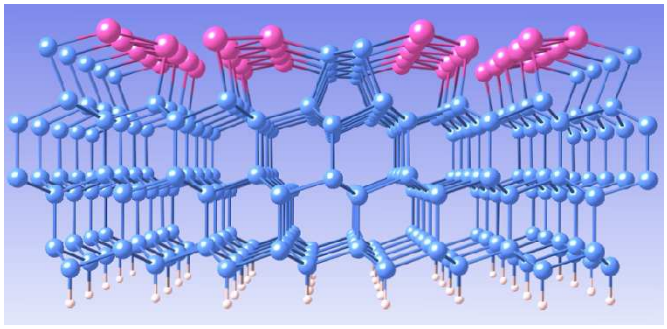

Figure 1. Side view of In/Si(111) system. The 4×1 reconstruction is based on double zig-zag chain formation of In atoms.

clear 1D character should exhibit a Peierls instability[3] which results in a phase transition accompanied by a change in the translational symmetry. In quasi-1D metallic systems, electrons and holes near the Fermi energy often couple strongly with lattice vibrations, thereby generating a periodic spatial modulation of charge, i.e., a CDW which may open a band gap, a CDW gap[1,4]. Indeed, for the quasi-1D In/Si(111) system phase transitions have been observed. The 4×1 arrangement of the In chains was found to undergo a reversible temperature-induced phase transition below 120K[4,5]. At a transition temperature of about 100K, a 4×2 phase occurs that gradually changes over into a 8×2 structure after further cooling[4–6]. The principle structure of In chains at 1 ML coverage is shown in Fig. 1. Whereas the generally accepted structural model of the RT 4×1 structure[7,8] is able to explain well the majority of experimental observations, there are limitations[6] of the structural models proposed for the 4×2 and 8×2 reconstructions[7,8]. These models are based on the assumption that mainly the outer In atoms of the paired zigzag subchains of metal atoms should be affected by the reconstruction and not the inner In atoms. A tendency for pairing of the outermost chain atoms is accompanied by the formation of trimers[5]. However, the arrangement of the trimers is under debate[9].

3 Method and Numerical Details

The total energies and the electronic structures are calculated within the density functional theory (DFT)[10] and the generalized gradient approximation (GGA)[11] for exchange and correlation. In the spin-polarized case the correlation energy for arbitrary polarization is determined by the same interpolation as for the exchange energy[12]. Explicitly we use the VASP code[13]. The electron-ion interaction is basically treated by non-norm-conserving ultrasoft pseudopotentials[14].

The Si(111) surface is simulated by repeated asymmetric slabs with six Si bilayers and a vacuum region of the same extent[15]. The bottom side of each slab with fixed atomic positions is saturated by hydrogen atoms to simulate bulk Si. The addition of a half Si adlayer and a complete In monolayer allow us to model the quasi-1D In/Si(111) systems with 4×1, 4×2, or 8×2 translational symmetry.

The **k**-space integrations for total energies and charge densities are done with a 4×8 Monkhorst-Pack (MP) type mesh[16] (32 **k**-points) in the surface Brillouin zone (BZ) of the

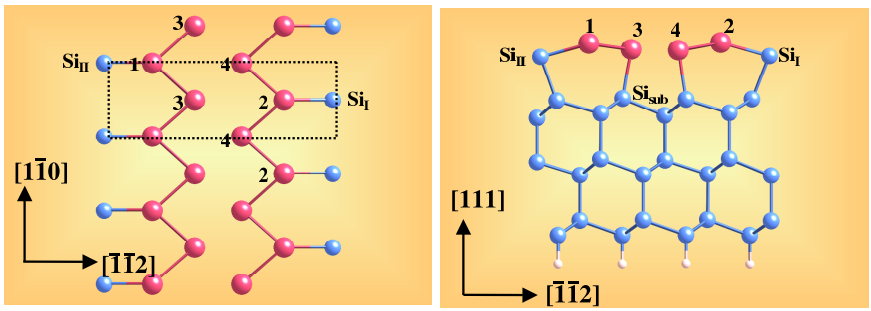

Figure 2. Top (left) and side (right) views on In/Si(111) surface with 4×1 translational symmetry.

4×1 structure. The number of **k** points is correspondingly reduced for the larger surface unit cells, 4×2 and 8×2 (4×4 and 2×4 MP type meshes). The atoms in the three lower bilayers are used to keep their bulk positions during the ionic relaxation. Using a variety of starting geometries representing a defined translational symmetry, several model structures have been tested and compared with respect to their total energy. The surface geometries are determined by relaxing the atomic positions until the Hellmann-Feynman forces are less than 10 meV/Å.

4 Results

4.1 Atomic Geometry

In the case of a monolayer In coverage on a Si(111)substrate, the lowest total energies have been obtained for the chain model[7,5] in Fig. 2 representing the 4×1 surface translational symmetry. Indium chains (wires) are composed of two zigzag rows (or subchains) parallel to the [$\bar{1}$10] direction. Below the In layer there are zigzag chains of Si atoms which separate the In nanowires in [11$\bar{2}$] direction. The arrangement of the Si atoms exhibits similarities with the reconstruction elements of the Si(111)2×1 surface assuming the π-bonded chain model[15,17]. The In atoms at the chain edges (outermost or outer In atoms) are adsorbed at almost T_4 and H_3 adsorption sites of the Si(111) surface[17]. They lie higher than the In atoms in the interior of the chains, i.e., the In atoms belonging to adjacent subchains. These inner In atoms are adsorbed at on-top sites and, in turn, lie higher than the atoms in the Si chains. Mostly the actual arrangement of the outer In atoms determines the surface translational symmetry 4×1 (Fig. 2), 4×2 or 8×2 (Fig. 3).

The overall structure of the In chains and their arrangement with respect to the Si atoms between the chains as well as the Si substrate atoms, agree well with the other first-principles calculations[8,9,18–20] as well as the data of x-ray diffraction[7] and low energy electron diffraction (LEED)[21]. The calculated In-In bond lengths in the two subchains of 2.96-2.97 Å slightly overestimate the sum 2.88 Å of two covalent radii (1.44 Å) of In atoms, while the average distance 3.12 Å of two In atoms in adjacent subchains comes closer to the nearest-neighbor value 3.25 Å in a bulk In metal. The interatomic distances of the In chain atoms to the Si atoms in the trenches as well as in the substrate are only a little bit larger than the sum 2.55 Å of the covalent radii of In (1.44 Å) and Si (1.11 Å). Our optimized structure shows excellent agreement with the LEED findings[21]. In principle, such

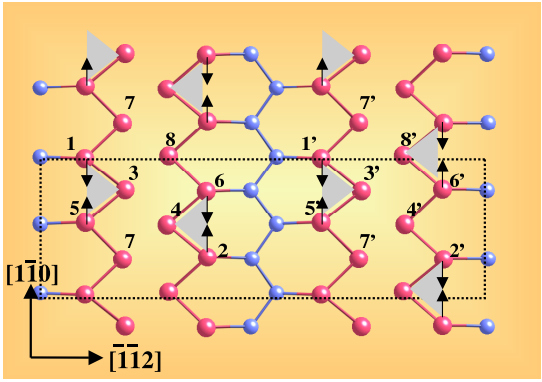

Figure 3. Top view of In/Si(111) 8×2 (4×2) translational symmetry. In the case of 4×2 reconstruction the trimers in different wires would be in phase. The pairing/trimer formation of In atoms is indicated by arrows.

a statement is also valid for the comparison with the SXRD data[7] and the other *ab-initio* calculations[8,20]. In the 4×2 case we confirm that the outer In chain atoms are displaced by about 0.3 Å towards each other to form pairs and finally trimers with one of the inner chain atom (see Fig. 3). This movement gives rise to a doubling of the periodicity along the chains. As a result, two trimers (each in one subchain) belong to a 4×2 unit cell. The remaining inner In atoms form less bonded pairs. A possible trimer arrangement (giving rise to the lowest total energy) is shown in Fig. 3. The energy gain of this reconstruction is small. We find that the 4×2 geometry is more stable than the 4×1 surface by about 3 meV per 4×1 unit cell. In the 8×2 case the trimer arrangement of Fig. 3 yields to a minimum on the total-energy surface with a rather small energy gain with respect to the 4×2 geometry. Our 8×2 structure gains 0.9 meV per 4×1 unit cell with respect to the 4×2 reconstruction.

4.2 Band Structure

The resulting electronic band structures are plotted in Fig. 3 versus high-symmetry lines in the BZs for the 4×1 and 4×2 reconstructed surfaces. The border lines of the irreducible part $\Gamma XMY\Gamma$ and $\Gamma X'M'Y'\Gamma$ of the two adopted rectangular BZs are chosen. The Fermi levels are calculated to be about 0.14 eV (4×1) or 0.13 eV (4×2) above the bulk valence band maximum for the two geometries. In the 4×1 case the band structure in Fig. 3(a) clearly represents a metallic surface. One does not observe any surface states in the projected Si band gap along the ΓY direction perpendicular to the chains. However, for the parallel direction XM at the BZ boundary four surface bands with weak dispersion are visible below the Fermi level. They show a stronger dispersion along the chains, i.e., along ΓX and MY. Three surface bands m_1, m_2, and m_3 cross the Fermi level and vary between the energetical regions of bulk valence and conduction bands. They are partially filled with 0.17 (m_1), 0.83 (m_2), and 1.00 (m_3) electrons[22]. The described band-structure picture is in agreement with calculations[8,23] and PES/IPES measurements[6].

The band structure of the In/Si(111)4×2 surface in Fig. 3(b) cannot solely be explained in terms of folding of the 4×1 bands due to the reduction of the BZ in the direction parallel to the chains. Rather, due to the discussed distortions of the geometry with respect to the

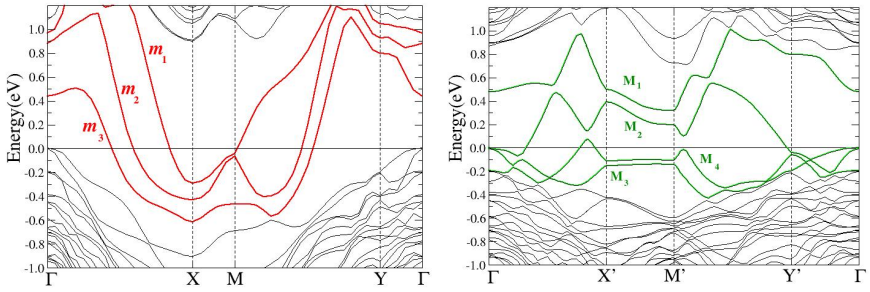

Figure 4. Electronic band band structures of In/Si(111)(4×1) (a) and 4×2 (b) surfaces versus wave vectors along high symmetry lines parallel and perpendicular to the chains in the corresponding Brillouin zones. The horizontal lines define the Fermi levels. The adsorbate-related surface bands in the projected fundamental gap of Si are denoted by m_1, m_2, and m_3 (4×1) or M_1, M_2, M_3, and M_4 (4×2).

4×1 surface, in particular the pairing mechanism, degeneracies of bands are lifted and at band-crossing points band repulsion occurs. One observes four new surface bands M_1, M_2, M_3, and M_4 in the projected bulk fundamental gap which do not cross each other. These bands consist of folded branches of the former m_1, m_2, and m_3 bands, but their dispersion is remarkably modified by the opening of band gaps[22]. However, there is no opening of a true gap separating completely occupied and empty surface bands, so that the 4×2 surface with the geometry of Fig. 3 remains metallic.

4.3 Charge Density Waves

The changes of the band structures in Fig. 3 between the 4×1 and 4×2 geometries and the small variations of the total density of states are accompanied by a redistribution of the electrons in the surface region which may result in a CDW along the chains. In order to demonstrate this effect, in Fig. 5(a) we have plotted the difference of the total electron density of the 4×2 surface and the corresponding density for the 4×1 reconstruction in the area of a 4×2 unit cell. Figure 5(b) shows a similar contour plot for the 8×2 reconstruction with respect to the 4×1 surface.

The variations of the electron density in the 4×2 case relative to the 4×1 density clearly indicate the pairing mechanism as the driving force for the phase transition 4×1→4×2. Figure 5(a) shows an increase of the electron density in the region between two paired atoms in each subchain and an electron deficit in the adjacent regions. The probability to find electrons seems to be also increased in the regions of the Si-In bonds. In-In bonds become somewhat ionic in the 4×2 case. In addition, there is also an increase of electron density in the region between two adjacent trimers belonging to two different subchains. A deficit of electrons is obvious between two trimers in one subchain. The redistribution of electrons is similar in the 8×2 case.

Considering the situations in the two subchains separately, one may immediately interpret the phase transition 4×1→4×2 as well as 4×1→8×2 as the formation of a CDW (in each subchain). It seems that in Fig. 5(a) (i.e., for 4×2 surface) two CDWs of this kind are locked in during the temperature-induced phase transition. In the 8×2 case (Fig. 5(b)), more or less one CDW is locked in for each wire.

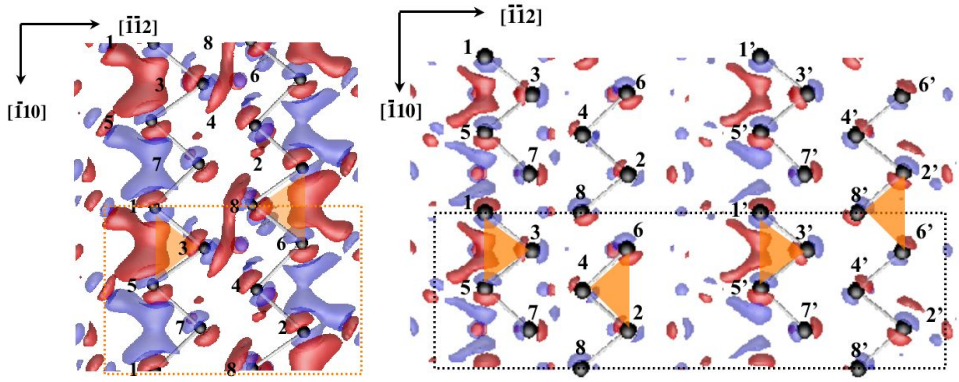

Figure 5. Difference of the total valence-electron densities of the 4×2 and 4×1 (a) or 8×2 and 4×1 (b) In/Si(111) surfaces. Red color indicates regions of electron excess, whereas blue color describes regions of electron depletion.

4.4 Spin Density Waves

The question is if such a spinol-holon separation announced for 1D systems and a Luttinger liquid can also happen in a real quasi-1D system and lead to a spatial spin distribution different from the charge distribution. One may discuss the occurrence of a periodic modulation of the distribution of the electron spins along the chain direction. Therefore, similarly to the discussion of possible CDWs accompanying the phase transitions 4×1→4×2 and 4×2→8×2, we ask the question whether a periodic spin arrangement may stabilize a certain surface reconstruction or not. For that reason we perform spin-polarized total energy calculations for a given atomic geometry but for different distributions of the electron spins over the In chain atoms in the nanowires on the 4×1-, 4×2- and 8×2-reconstructed In/Si(111) surfaces. Initial spin arrangements for 4×1, 4×2 are shown in Fig. 6. They represent antiferromagnetic orderings with a vanishing total spin of the 4×1, 4×2 and also 8×2 unit cell. We search for local minima on the total-energy surface with a finite magnetization density of the chain systems. The values of the initial local spins are varied until an energy minimum is reached. The resulting energies are compared with those obtained in the case without spin polarization.

The four initial configurations in the 4×1 case represent arrangements of subchains with ferromagnetic (configurations 3 and 4) or antiferromagnetic (configurations 1 and 2) orderings, which may be displaced against each other. The total magnetic ordering in each complete wire is antiferromagnetic in all starting configurations. However, the optimization of the total energy leads to almost vanishing magnetic effects. Consequently, the accompanying energy gains are only of the order of 1 meV and the maximum splitting of the surface bands amounts to 6 meV for m_3 near X and M. The same result is obtained for the first configuration in the 4×2 case (Fig. 8(b)). The combination of two ferromagnetic subchains is not possible. The arrangement of antiferromagnetic subchains displaced by the vector against each other (configuration 2) gives rise to a slightly larger magnetization of $0.02\mu_B$. But still all accompanying effects are negligible. We conclude that a tendency for magnetic ordering within the In chains and, hence, the tendency for formation of SDWs is extremely small for the atomic geometries under consideration. There are practically no

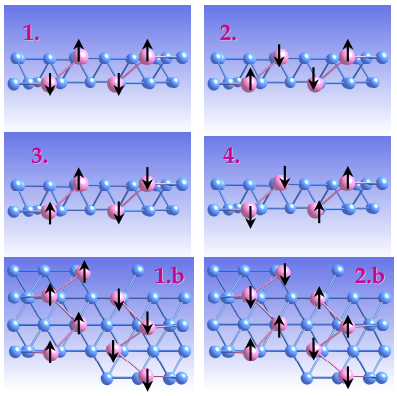

Figure 6. Initial spin configurations (top views) in the In chains of In/Si(111) with 4×1 (1-4) and 4×2 (1b, 2b) translational symmetry. Spin-up and spin-down are indicated by corresponding arrows.

additional driving forces for the studied reconstructions due to a certain antiferromagnetic ordering of the In atoms in the quantum wires.

5 Concluding Remarks

In summary, the atomic, electronic, and spin structures of arrays of quasi-1D indium chains on Si(111) substrates have been investigated by *ab initio* density-functional theory calculations. In the case of the room-temperature 4×1 surface structure, excellent agreement has been found with experimental results and results of other *ab-initio* calculations for the atomic structure and the band structure. We agree with recent x-ray diffractions measurements and total-energy optimizations that pairing of In atoms in the subchains and the accompanying formation of trimers is the basic mechanism of the observed temperature-induced surface phase transitions 4×1→4×2 and 4×2→8×2 between different surface reconstructions. The geometric distortion due to the pairing gives rise to gap openings near band crossings along chain directions. However, despite the opening of gaps in the surface band structure, there are still two bands which keep a metallic character of the surface, although with a reduced density of the free carriers. The comparison of the electron densities of the 4×1 and 4×2 surfaces clearly indicates the formation and the lock-in of phase-shifted charge density waves in each subchains. According to the simulated electron excess and deficit regions, the phase transition 4×2→8×2 should not be traced back to a CDW mechanism. Rather, the large distances of the chains of about 11 Å and the formation of a weak effective 2D ionic lattice due to the In-In pairing suggest long-range electrostatic forces as driving forces for the phase transition. The total-energy calculations with inclusion of the spin polarization clearly showed that practically there are not tendencies for magnetic orderings by antiferromagnetic spin arrangements and spin density waves. We conclude that modulations of the spin density do not contribute to a stabilization of neither the room-temperature nor the low-temperature phases of the In/Si(111) surface.

We have to mention that recently another hexagon-based 4×2 reconstruction geometry has been proposed[9]. Its band structure indicates a nonmetal but its energetical stability is under discussion[24].

Acknowledgments

We gratefully acknowledge a grant of supercomputer time provided by the NIC Jülich. We acknowledge financial support from the Deutsche Forschungsgemeinschaft (Project Nos. Be 1346/16-1), the European Community in the framework of the NoE NANOQUANTA (NMP4-CT-2004-500198).

References

1. G. Grüner, *Density Waves in Solids* (Addison-Wesley, Reading, MA 1994).
2. J.M. Luttinger, J. Math. Phys. (N.Y.) **4**, 1154 (1963).
3. R.E. Peierls, *Quantum Theory of Solids* (Clarendon, Oxford, 1964).
4. H.W. Yeom, S. Takeda, E. Rotenberg, I. Matsuda, K. Horikoshi, J. Schaefer, C.M. Lee, S.D. Kevan, T. Ohta, T. Nagao, and S. Hasegawa, Phys. Rev. Lett. **82**, 4898 (1999).
5. C. Kumpf, O. Bunk, J.H. Zeysing, Y. Su, M. Nielsen, R.L. Johnson, R. Feidenhans'l, and K. Bechgaard, Phys. Rev. Lett. **85**, 4916 (2000).
6. H.W. Yeom, K. Horikoshi, H.M. Zhang, K. Ono, and R.I.G. Uhrberg, Phys. Rev. B**65**, 241307(R) (2002).
7. O. Bunk, G. Falkenberg, J.H. Zeysing, L. Lottermoser, R.L. Johnson, M. Nielsen, F. Berg-Rasmussen, J. Baker, and R. Feidenhans'l, Phys. Rev. B**59**, 12228 (1999).
8. J.-H. Cho, J.-Y. Lee and L. Kleinman, Phys. Rev. B **71**, 081310(R) (2005).
9. C. González, J. Ortega and F. Flores, New Journal of Physics **7**, 100 (2005).
10. P. Hohenberg and W. Kohn, Phys. Rev. **136**, B864 (1964); W. Kohn and L.J. Sham, Phys. Rev. **140**, A1133 (1965).
11. J.P. Perdew, in *Electronic Structure of Solids '91*, edited by P. Ziesche and H. Eschrig (Akademie-Verlag, Berlin, 1991), p. 11.
12. U. von Barth and L. Hedin, J. Phys. C**5**, 1629 (1972).
13. G. Kresse and J. Furthmüller, Comput. Mater. Sci. **6**, 15 (1996); Phys. Rev. B**54**, 11169 (1996).
14. J. Furthmüller, P. Käckell, F. Bechstedt, and G. Kresse, Phys. Rev. B**61**, 4576 (2000).
15. A.A. Stekolnikov, J. Furthmüller, and F. Bechstedt, Phys. Rev. B**65**, 115318 (2002).
16. H.J. Monkhorst and J.D. Pack, Phys. Rev. B**13**, 5188 (1976).
17. F. Bechstedt, *Principles of Surface Physics* (Springer, Berlin 2003).
18. J. Nakamura, S. Watanabe, and M. Aono, Phys. Rev. B**63**, 193307 (2001).
19. R.H. Miwa and G.P. Srivastava, Surf. Sci. **473**, 123 (2001).
20. S.-F. Tsay, Physical Review B **71**, 035207 (2005).
21. S. Mizuno, Y.O. Mizuno, and H. Tochihara, Phys. Rev. B**67**, 195410 (2003).
22. X. López-Lozano, A.A. Stekolnikov, J. Furthmüller, and F. Bechstedt, Surf. Sci. **589**, 77 (2005).
23. F. Bechstedt, A. Krivosheeva, J. Furthmüller, and A.A. Stekolnikov, Phys. Rev. B**68**, 193406 (2003).
24. A.A. Stekolnikov *et al.*, unpublished.

John von Neumann Institute for Computing

Ultra-Thin Magnetic Films and Magnetic Nanostructures on Surfaces

Gustav Bihlmayer, Paolo Ferriani, Stephanie Baud, Marjana Ležaić, Stefan Heinze, and Stefan Blügel

published in

NIC Symposium 2006 ,
G. Münster, D. Wolf, M. Kremer (Editors),
John von Neumann Institute for Computing, Jülich,
NIC Series, Vol. **32**, ISBN 3-00-017351-X, pp. 151-158, 2006.

http://www.fz-juelich.de/nic-series/volume32

Ultra-Thin Magnetic Films and Magnetic Nanostructures on Surfaces

Gustav Bihlmayer[1], **Paolo Ferriani**[2], **Stephanie Baud**[3], **Marjana Ležaić**[1], **Stefan Heinze**[2], **and Stefan Blügel**[1]

[1] Institute for Solid State Research, IFF
Research Centre Jülich, 52425 Jülich, Germany
E-mail: {g.bihlmayer, m.lezaic, s.bluegel}@fz-juelich.de

[2] Institute for Applied Physics
University of Hamburg, 20355 Hamburg, Germany
E-mail: {pferrian, sheinze}@physnet.uni-hamburg.de

[3] Laboratoire de Physique Moléculaire, UMR
CNRS 6624, Université de Franche-Comté, F-25030 Besançon Cedex, France
E-mail: stephanie.baud@univ-fcomte.fr

We present *ab initio* calculations of low-dimensional systems with complex magnetic ground states. The computational method and its efficient implementation on massively-parallel supercomputing architectures is outlined and characteristic examples from the field of ultra-thin magnetic films and nanowires on stepped surfaces are given. These calculations allow not only the description of the ground state properties, they may be also exploited for the prediction of finite-temperature properties of this technologically important class of materials.

1 Introduction

The miniaturization of magnetic data storage devices forces modern technology to store a bit of information on increasingly smaller units of magnetic material. In the limit of a few hundred atoms that are supposed to represent this bit on a microscopic level, the stability of the magnetic structure is pushed to its limits. External fields or thermal fluctuations may destroy the magnetic order easily and thus render the storage device unuseful for many applications. The magnetic boundary between individual bits may become larger than the bits themselves. Such technological problems call for the development of new materials that are able to overcome the limitations of conventional magnetic storage materials. The Institute for Solid State Research (IFF) investigates various possible candidates for new device technology including ferroelectric materials, tunneling magnetoresistance structures, and improved magnetic material combinations. In the following examples, we will focus on the latter.

An understanding of the magnetic properties on a microscopic level can only be gained on a quantum-mechanical level. The institute Theory I in the IFF has, therefore, developed computational methods to investigate theoretically these properties based on quantum-mechanics. Such methods that require no experimental input parameters are often referred to as *ab initio* methods. The computational effort of an *ab initio* investigation of "real" materials can be tremendous and it is the combination of high-performance computing and theoretical material science that lies on the basis of success. In this respect, only the close collaboration between the Central Institute for Applied Mathematics (ZAM) and the IFF

in the Research Centre Jülich made it possible to perform leading-edge material science calculations.

2 Method & Computational Scheme

Density functional theory provides the framework of most *ab initio* methods used in solid-state physics. The quantum-mechanical equations at the basis of this theory are differential equations similar to the Schrödinger equation. They determine the wavefunctions, from which all further properties of the studied system are derived, most important of which is the electron density n entering the density functional theory. If these wavefunctions are expanded in basis-functions, the differential equation can be recast in the form of a standard problem of linear algebra, the eigenvalue problem

$$\mathcal{H}[n]\mathbf{c} = \epsilon\mathcal{S}\mathbf{c} \tag{1}$$

where the matrices $\mathcal{H}$ and $\mathcal{S}$ are of the dimension of the number of the used basis-functions. The problem is to determine the eigenvector $\mathbf{c}$, that specifies the wavefunction and the scalar ϵ that is the eigenvalue corresponding to the wavefunction. In general the ground state density n is unknown. Giving a start density, the solution of Eq. (1) determines the density entering again in Eq. (1). Obviously, this defines a selfconsistency problem in which Eq. (1) is solved during each self-consistency step.

In an infinite periodic system the number of basis-functions, that have to be used, is of course infinite. But the translational symmetry of the periodic crystal allows to block-diagonalize the matrices $\mathcal{H}$ and $\mathcal{S}$ into an infinite number of finite matrices that are labeled by a vector, the $\mathbf{k}$-point. The size of one such matrix is determined by the chemical and structural complexity of the system at study, i.e. the larger the unit-cell of the crystal, the larger the size of the matrix. Of this infinite number of matrices, only a subset is actually calculated and then an interpolation is done, to account for the remainder. Here, a small unit-cell (or periodicity) requires a larger set of samples that have to be taken for the interpolation.

In summary, the (main) computational problem consists of either the solution of a few large eigenvalue problems or the solution of many small ones. Both tasks can be parallelized, the latter one very simple and efficiently by distributing the small eigenvalue problems over individual nodes of a parallel-computer. Distribution of a single, large eigenvalue problem over many nodes can be handled by optimized libraries like ScaLAPACK. This kind of parallelization requires more communication than the previous one, but reduces the memory requirements on a singe node, thus enabling calculations of systems with very large unit cells. Our parallelization scheme, employed in the FLEUR-code[1] relies on a combination of both strategies to optimize the performance for all types of problems (cf. Fig. 1)

Compared to non-magnetic problems, the accurate treatment of magnetic systems in density functional theory is a computationally much more demanding task: non-collinearity (i.e. if the magnetic order is not simply ferro-, ferri- or antiferromagnetic) and/or spin-orbit coupling effects increase the dimension of the eigenvalue problem by a factor of two. The magnetic unit cell is usually larger than the chemical one, and its size is generally not known in advance. The symmetry, that can be exploited in these calculations is normally reduced (e.g. changing a real symmetric eigenvalueproblem into a

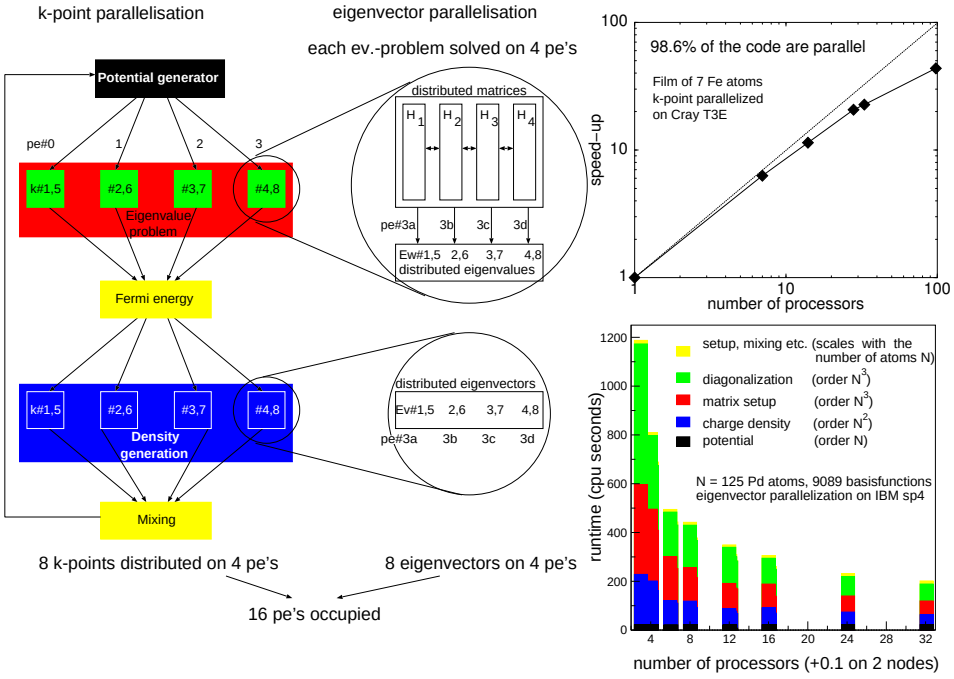

Figure 1. Combined parallelization used in the Fleur-code: depending on the problem, either a large number of small matrices or a small number of large matrices have to be diagonalized. In the former case, the "k-point parallelization" is most efficient, the latter case calls for "eigenvector parallelization". Both schemes can be combined as indicated on the left. Performance tests (right) allow to find optimized ways, how both parallelizations should be combined for specific problems.

complex hermitian one) and the involved energy scales are very small. Not many *ab initio* methods worldwide are suited for such complex calculations. The full-potential linearized plane wave method, as implemented in the FLEUR-code, provides a powerful tool for the computational investigation of general, non-collinear magnetic structures[2].

3 Applications

Low-dimensional magnetic systems differ in many respects from what is known from bulk structures: the magnetic order, the ordering temperature, the magnetization direction, the magnetic domains and their separating walls are not only different in a thin film or a wire, they can also depend on different physical parameters than in a three-dimensional solid. While in bcc Fe, hcp Co, or fcc Ni the magnetic properties are mainly determined by the elements interaction with its 8 or 12 nearest neighbor atoms, in low dimensions the coordination is reduced (2 – 6 nearest neighbors) and a more "atomic like" behavior can be observed: the magnetic moment is higher, orbital magnetism becomes important, the ordering temperatures (in the ferromagnetic case the Curie temperature) is lowered. Since the thin film or wire has usually to be stabilized on a supporting surface, interactions with this substrate can further influence the magnetic properties.

3.1 Thin Magnetic Films

Thin films of iron or manganese on a transition-metal substrate illustrate the peculiarities met in low-dimensional systems: the spin moment of Fe, which is $2.2\mu_{\mathrm{B}}$ in bcc Fe, increases to $2.7\mu_{\mathrm{B}}$ for a Fe monolayer on Cu(111) and even $3.2\mu_{\mathrm{B}}$ on Ag(111). On the weakly interacting close-packed surfaces of the coinage metals Cu and Ag, that only provide a template on which the Fe atoms are grown, the magnetic (spin) moment increases to almost atomic-like values ($4\mu_{\mathrm{B}}$). Also on the (001) surface of Cu, Fe has a large magnetic moment, and in all these examples Fe forms a ferromagnetic film. Unfortunately, this ferromagnetic order, which is technologically desirable, is not very stable against temperature fluctuations. The weak interaction with the substrate, which on the one hand increases the magnetic moment, on the other hand does nothing to increase the Curie temperature, which is – in these systems – determined both by the (exchange) interactions to the neighboring atoms and by the magnetic anisotropy, a relativistic effect. The latter effect is strong for heavy atoms, but the atoms at the bottom of the periodic table do not easily form magnetic moments in the condensed state. Therefore, combinations of light magnetic species and heavy substrate atoms become technologically more and more important.

If one tries to increase the interaction with the substrate and the magnetic anisotropy by e.g. replacing copper by the heavier element tungsten, surprisingly also the magnetic order is changed: a monolayer of Fe on W(001) is no longer ferromagnetic, but shows instead a checkerboard like magnetic structure (cf. Fig. 2). This unexpected change of magnetic order was not only predicted by our calculations, it was also confirmed experimentally[3]. But further calculations revealed more surprises: many magnetic elements change their magnetic ground state on the W(001) substrate, Co becomes antiferromagnetic, but Cr and Mn, normally antiferromagnetic, turn into ferromagnets with large spin moments[4]. Using different substrates, it is possible to tune the magnetic interactions to form a variety of magnetic structures in a way unknown in bulk systems.

Beautiful examples of complex magnetic structures are formed, when the magnetic interactions are on the border between antiferromagnetic and ferromagnetic and for certain topologies of the crystal lattice: e.g. we have predicted a complex, three-dimensional magnetic structure for Mn on Cu(111), which is formed from four chemical unit cells[5]. Recently, a magnetic structure consisting of at least 15 chemical unit cells was found experimentally for Fe/Ir(111)[6]. Theoretical considerations have shown, that such a magnetic structure can arise from an even more complex non-collinear state, which is currently under investigation. The unit cells required for such a study contain 150 atoms and the matrices, that have to be diagonalized numerically require not only more than 10 GB of memory, but also computing time that is only available on massively parallel supercomputers.

While these magnetic superstructures are probably only stable at low temperatures, other complex magnetic patterns are formed when the temperature is above zero. A snapshot of an (e.g. ferro-) magnetic material at finite temperatures will show a superposition of various elementary magnetic excitations, or magnons, which form a non-collinear magnetic state. *Ab initio* calculations of these snapshots allow – in conjunction with statistical methods – to access important material properties like the Curie temperature[7]. As we pointed already out, the ordering temperature of two-dimensional systems depends not only on the interactions between the neighboring spins in the lattice, but also on the interaction of the spin with the field of the crystal lattice itself. This arises from spin-orbit interaction and our method allows us to investigate this tiny relativistic effect (which be-

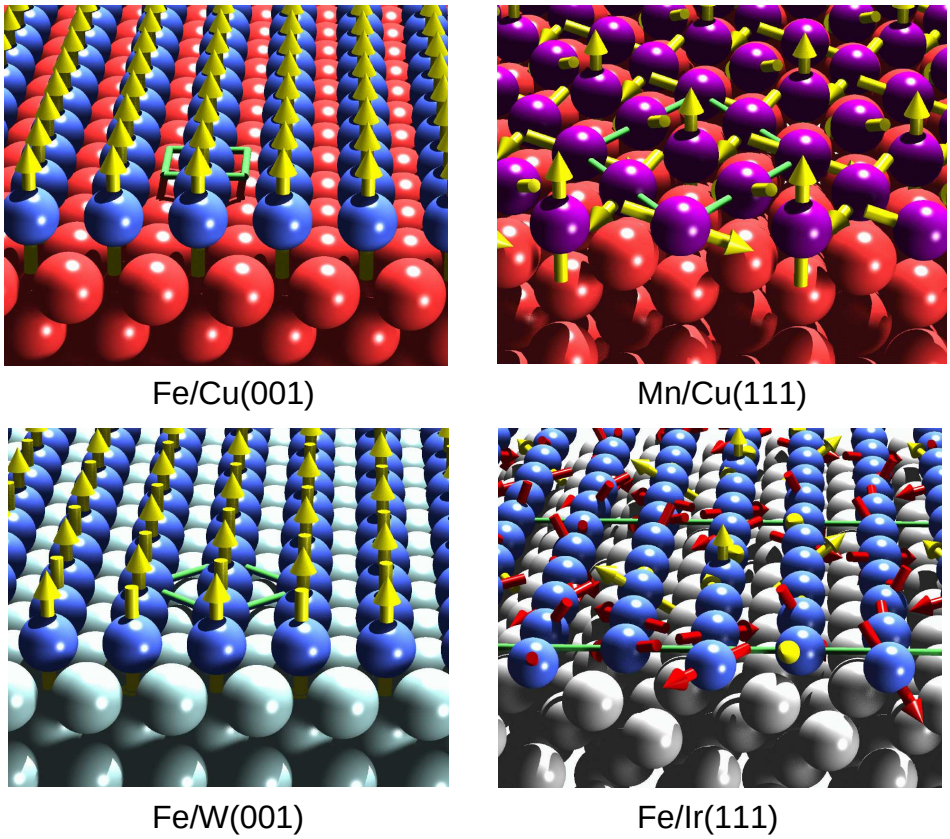

Figure 2. Magnetic structures of thin Fe and Mn films on different substrates: on a square lattice, like Cu(001), collinear magnetic order is common, on triangular lattices, like Cu(111), more complex, non-collinear magnetic ground states can be obtained. The magnetic ground-state of Fe on Ir(111) (lower right) is currently under investigation.

comes important on a large scale) from first principles. To determine this effect accurately, a large number of **k**-points has to be sampled, requiring that many eigenvalue-problems have to be solved.

3.2 Magnetic Nanostructures

Even more exotic properties can be encountered in magnetic materials, when the dimensionality is lowered further to one or zero dimensions. Of course, in practice these wires or clusters have to be supported on some substrate again, so that strictly speaking only quasi-lowdimensional structures are obtained. But experimental techniques have been refined in the last years, to produce well-defined magnetic nanostructures and to characterize their magnetic properties in some detail.

One way to stabilize a one-dimensional magnetic structure is to grow magnetic atoms along the step-edges that occur on surfaces. E.g. a Pt(997) surface has rather smooth

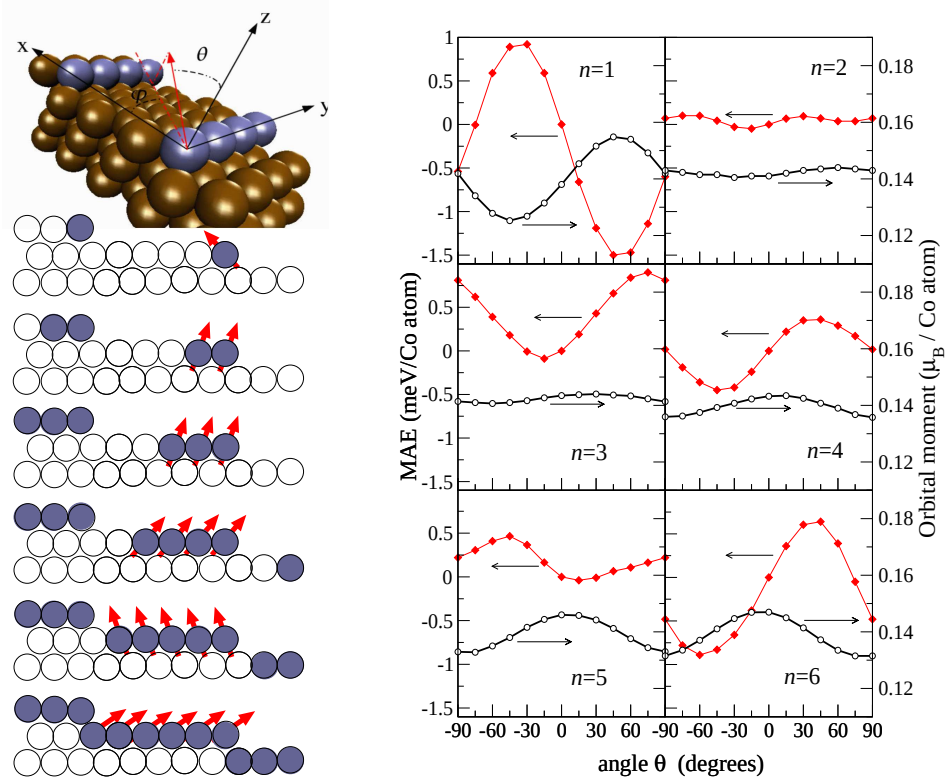

Figure 3. Left: Schematic picture of a single Co chain on a stepped Pt substrate (top) and chains of different width ($n = 1-6$) on a step-edge. The magnetization direction (indicated by red arrows) oscillates as the wires increase in width. Right: Magnetocrystalline anisotropy energy (MAE, full diamonds) and average orbital moment on Co (empty circles) for Co chains of different width (denoted by n) on Pt(664). Note the different scales for MAE (left) and orbital moments (right).

step-edges that are separated by about 2nm and close-packed Pt(111) terraces in between. Experimentally, it was possible to grow not only a singe Co-wire along these edges, but also thicker wires consisting of n strands ($n = 2, 3, 4, ...$). The magnetic measurements of these wires revealed a peculiar behavior[8]: While the magnetization of the single wire is perpendicular to the wire-axis and points towards the upper terrace, for thicker wires the direction of the magnetization changes towards the lower terrace and finally – for a closed Co overlayer – stands perpendicular to the vicinal surface. The magnetic anisotropy also oscillates from large ($n = 1$), to very small ($n = 2$) then rises again for $n = 4$, and finally settles down to the value known for Co layers on Pt(111).

To explain this surprising magnetic behavior, we performed *ab initio* calculations of Co wires on a Pt(664) surface[9,10]. On this surface, the step-edges are a little bit denser packed than on Pt(997), nevertheless the unit-cells required to calculate this surface has to include already 45 atoms. In such a calculation the surface is modeled by a film of finite thickness, so that the innermost layer of this film has already bulk-like properties. In

the present case this thickness corresponds to about 7 Pt(111)-type layers. We studied the effects of relaxation for the case of a single Co wire on this surface[9]. To compensate for the loss of coordination, these relaxations tend to decrease the distance of the step-edge atoms to their nearest neighbors, restoring partially a bulk-like magnetic behavior (e.g. smaller orbital moments and a smaller magnetic anisotropy). But this effect seems to be counteracted by the increasing importance of correlations in low-dimensional materials, so that experimentally the signatures of low-dimensional magnetism are clearly seen.

Our calculations of thicker Co wires not only revealed the same oscillatory behavior of the magnetization direction and magnetic anisotropy as was found experimentally (cf. Fig. 3), with the help of our calculations we can also propose a simple physical model that accounts for the experimental observations[10]: If we decompose the overall magnetic properties into contributions of the individual strands of the multi-wires, we can identify four different types of strands, which show a characteristic behavior of the magnetic properties on the magnetization direction (which we can choose freely in the calculation). Since exchange-coupling requires all the magnetic moments of the wires to point in a common direction, this can lead to frustration effects: Properties, like the magnetic anisotropy of the multi-wire can get very small as compared to a single wire, due to a compensation of contributions of different strands. This explains e.g. the tiny anisotropy of the double-wire, but also the increase of the anisotropy in thicker wires.

4 Conclusion

We presented examples of calculations of magnetic monolayers of Fe and Mn on different substrates, as well as Co wires on stepped surfaces. Due to their complexity, these calculations quickly go beyond the limits of conventional computational resources and call for supercomputers as provided by the John von Neumann Institute for Computing (NIC) and the Central Institute for Applied Mathematics (ZAM) in the Research Centre Jülich. The close connection to experimental institutes within and outside the Research Centre in combination with a critical amount of CPU time on supercomputers gives us a cutting edge in responding to the challenging questions in the physics of modern magnetism and on magnetic materials with technological relevance where the investigation by *ab initio* calculations can lead to deeper understanding and the prediction of new promising materials.

Acknowledgments

We are indebted to Dr. Inge Gutheil for her help with the handling of the ScaLAPACK libraries and for the coding of the interface. All calculations were performed with a grant of computer time provided by the VSR of the Research Centre Jülich.

References

1. `http://www.flapw.de`.
2. Ph. Kurz, F. Förster, L. Nordström, G. Bihlmayer, and S. Blügel, *Ab initio treatment of noncollinear magnets with the full-potential linearized augmented plane wave method*, Phys. Rev. B **69**, 024415 (2004).
3. A. Kubetzka, P. Ferriani, M. Bode, S. Heinze, G. Bihlmayer, K. von Bergmann, O. Pietzsch, S. Blügel, and R. Wiesendanger, *Revealing Antiferromagnetic Order of the Fe Monolayer on W(001): Spin-Polarized Scanning Tunneling Microscopy and First-Principles Calculations*, Phys. Rev. Lett. **94**, 087204 (2005).
4. P. Ferriani, S. Heinze, G. Bihlmayer, and S. Blügel, *Unexpected trend of magnetic order of $3d$ transition-metal monolayers on W(001)*, Phys. Rev. B **71**, 024452 (2005).
5. Ph. Kurz, G. Bihlmayer, K. Hirai, and S. Blügel, *Three-Dimensional Spin-Structure on a Two-Dimensional Lattice: Mn/Cu(111)*, Phys. Rev. Lett. **86**, 1106 (2001).
6. K. von Bergmann, S. Heinze, M. Bode, E.Y. Vedmedenko, G. Bihlmayer, S. Blügel, and R. Wiesendanger, *Observation of a complex nanoscale magnetic structure in a hexagonal Fe monolayer*, Phys. Rev. Lett. , submitted (2005).
7. M. Ležaić, Ph. Mavropoulos, J. Enkovaara, G. Bihlmayer, S. Blügel, *Influence of thermal spin fluctuations on the half-metallic band gap*, Phys. Rev. Lett. , submitted (2005).
8. P. Gambardella, A. Dallmeyer, K. Maiti, M. C. Malagoli, S. Rusponi, P. Ohresser, W. Eberhardt, C. Carbone and K. Kern, *Oscillatory Magnetic Anisotropy in One-Dimensional Atomic Wires*, Phys. Rev. Lett. **93**, 077203 (2004).
9. S. Baud, Ch. Ramseyer, G. Bihlmayer, and S. Blügel, *Relaxation effects on the magnetism of decorated step edges: Co/Pt(664)* Phys. Rev. B , submitted (2005).
10. S. Baud, G. Bihlmayer, S. Blügel, and Ch. Ramseyer, *Magnetic anisotropy of Co n-wires ($n = 1 - 6$) on Pt(664)* Surf. Sci. , submitted (2005).

John von Neumann Institute for Computing

Supercomputer Based *ab initio* Investigations of Martensitically Transforming Alloys

Peter Entel, Waheed A. Adeagbo, Alexey T. Zayak,
and Markus E. Gruner

published in

NIC Symposium 2006 ,
G. Münster, D. Wolf, M. Kremer (Editors),
John von Neumann Institute for Computing, Jülich,
NIC Series, Vol. **32**, ISBN 3-00-017351-X, pp. 159-166, 2006.

http://www.fz-juelich.de/nic-series/volume32

Supercomputer Based *ab initio* Investigations of Martensitically Transforming Alloys

Peter Entel[1], **Waheed A. Adeagbo**[1,2], **Alexey T. Zayak**[3], **and Markus E. Gruner**[1]

[1] Theoretische Physik, Universität Duisburg-Essen
Campus 47048 Duisburg, Germany
E-mail: {entel,adeagbo}@thp.uni-duisburg.de

[2] Lehrstuhl für Theoretische Chemie, Ruhr-Universität Bochum
Universitätsstraße 150, 44780 Bochum, Germany
E-mail: waheed.adeagbo@theochem.ruhr-uni-bochum.de

[3] Department of Physics and Astronomy, Rutgers University
Piscataway, NJ 08854-8019, U.S.A.
E-mail: zayak@physics.rutgers.edu

We give a short review of first-principles computational investigations carried out on the high-performance supercomputer facility JUMP at the Forschungszentrum Jülich. Within the framework of Density Functional Theory (DFT) and Density Functional Perturbation Theory (DFPT) we calculate force constants and phonon spectra of various Heusler alloys and Fe based Invar materials using the Vienna *Ab Initio* Simulation Package (VASP) and the Plane Wave Self-Consistent Field (PWSCF) method.

1 Introduction

Recent technological developments concerning "smart materials" show that a microscopic understanding on an *ab initio* basis is needed, for example, for a breakthrough in the field of magnetic shape memory (MSM) alloys recently discovered[1]. Magnetic Heusler alloys exhibit the MSM effect with magnetic-field-induced strains up to 10%, which opens a field of tremendous technological applications. In order to understand this effect, a detailed knowledge of the difference between structurally stable and unstable Heusler alloys on a microscopic scale is needed. In this investigation we concentrate on two kinds of systems, ternary Heusler alloys and binary alloys like Fe_3Ni and Fe_3Pt, which in turn will be shown to behave in similar manner to the Heusler systems.

2 Method

2.1 First-Principles Calculations

The Vienna ab inito Simulation Package[2,3] (VASP) has been used to perform the electronic structure calculations. The projector-augmented wave formalism (PAW) implemented in this package[3] leads to very accurate results comparable to other all-electron methods. The electronic exchange and correlation are treated within density functional theory by using the generalized gradient approximation. The expansion of the electronic wave-functions in terms of plane waves was done using the "High Precision" option, which corresponds to the kinetic energy cutoff as high as 337.3 eV or more, depending on the system. Integrations

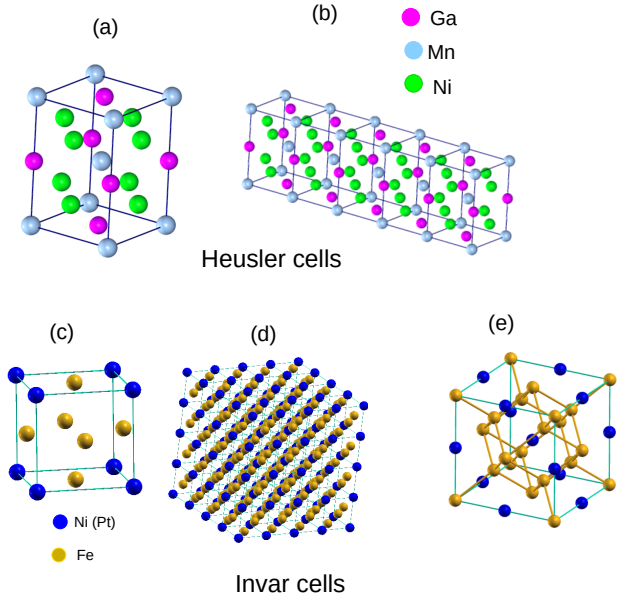

Figure 1. On top: (a) A conventional tetragonal cell used in the electronic structure calculation of Heusler alloys and (b) corresponding supercell used in the phonon calculation. All Hesuler compounds considered in this work have the same structure and formula unit X_2YZ. Below: (c) The $L1_2$(Cu_3Au) structure with unit cell of space group $Pm\bar{3}m$ number 221, (O_h^1 cubic) of Fe_3Ni (Fe_3Pt) used in the electronic structure calculations. (d) The $4 \times 4 \times 4$ supercell containing 256 atoms (192 Fe- and 64 Ni-atoms) used in the direct force constants method for the calculation of phonon dispersions using the packages PHONON[4]+VASP[2] and (e) the $D0_3$ structure (bcc) with unit cell space group $Fm\bar{3}m$ (O_h^5) of $AlFe_3$[5].

over the whole Brillouin zone were performed using special k-points. For Heusler alloys, the electronic structure calculations were done using the conventional tetragonal cell (see Fig. 1(a)) with a high density of k-point mesh of $12\times12\times10$ points. For the phonon calculations in a $1\times5\times1$ supercell (see Fig. 1(b)) the k-points mesh was $10\times2\times8$. While the dimensions of the supercell are given with respect to the conventional tetragonal cell.

For binary alloys of Fe_3Ni and Fe_3Pt (fcc cell of $L1_2$ and bcc-like $D0_3$ structures, see Fig. 1(a and c)) we used a Monkhorst-Pack grid of $12\times12\times12$ k-points while a $2\times2\times2$ mesh was used for the phonon calculations of fcc Fe_3Ni shown in Fig. 1(d).

2.2 Phonon Calculations

2.2.1 Direct Method

In order to calculate the phonon dispersions we have used the direct force constant method[4] with forces determined from total energy calculations by using the Hellmann-Feynman theorem. The reference lattice parameters ($a = b = c$) refer to the conventional cubic (CC) $L2_1$ structure of the Heusler alloys, all crystallographic directions in this work are specified with respect to the CC cell. While the calculations were done using smaller conventional tetragonal (CT) cell with lattice parameters $a_t = b_t = a/\sqrt{2}$, $c_t = c$ (see Fig. 1(a)).

System	a_{L1_2} (Å) (fcc)	a_{D0_3} (Å) (bcc-like)
Fe_3Ni	3.58785644	5.71118938
Fe_3Pt	3.60052116	5.93777408

Table 1. Lattice parameters obtained from VASP calculations for the $L1_2$ (fcc) and the $D0_3$ (bcc-like) structure for Fe_3Ni and Fe_3Pt in the ferromagnetic state.

The phonon calculations for Heusler alloys were done with an elongated $1\times5\times1$ supercell based on the CT cell, see Fig. 1(b). The supercell is subject to periodic boundary conditions and has orthorhombic symmetry. Five CT cells were joined together along [110] giving ten subsequent (110) atomic planes along the [110] direction. Displacements of each single atom induce forces acting on all other atoms within the supercell, which yields the force-constant matrix and, consequently, the phonon frequencies and corresponding eigenvectors. In this work, $1\times5\times1$ geometry yields five points in the Brillouin zone along the [110] direction where phonon parameters are exact. These five vectors satisfy $\exp(2\pi\imath\mathbf{k}_L\cdot\mathbf{L})=1$, where L denotes indices of the lattice constants in the supercell (in our case from 0 to 4, giving points $\zeta=0.0, 0.25, 0.5, 0.75, 1.0$, for the normalized wave vector $[\zeta,\zeta,0]$, which spans our Brillouin zone from its center to the boundary). For the $1\times5\times1$ supercell, within the half supercell length (five atomic planes), the force constants decrease by several orders of magnitude, thus being sufficient for accurate calculations of the phonons. The atomic displacements were of the order of 0.03 Å. The force constants have been calculated for the relaxed and completely force-free equilibrium structures, the lattice parameters of which are given in Table 1.

The method is also applied to fcc Fe_3Ni to calculate phonons along high symmetry directions for the $L1_2$ structure (see Fig. 1(c)) at lattice constant 3.58795644 Å obtained from VASP calculations. The supercell used in the phonon calculation was a $4\times4\times4$ periodic supercell (see Fig. 1 (d)).

2.2.2 Linear Response

In the linear response method the dynamical matrix is obtained from the modification of the electron density, via the inverse of the dielectric matrix describing the response of the valence electron density to a periodic lattice perturbation. The dielectric matrix is then calculated from the eigenfunctions and energy levels of the unperturbed system[14]. Phonon dispersions can be determined at any wave vector in the Brillouin zone. The method has been applied with success to Ni_2MnGa[6] and to alloys related to our present study[6,7].

We have applied this method to calculate the phonon density of states of Ni_2MnGa (reproducing the anomalous inversion of optical modes found previously by using the direct method[8]) and the phonon dispersions along high symmetry for bcc-like $D0_3$ Fe_3Ni, $L1_2$ Fe_3Pt and $D0_3$ Fe_3Pt (crystal structures are shown in Fig. 1(c) (for fcc) and Fig 1(e)). The phonon calculations were carried out again at the theoretical lattice constants shown in Table 1.

For Fe and Ni in Fe_3Ni we used ultrasoft pseudo-potentials generated using the exchange correlation of Perdew-Burke-Ernzerhof (PBE); for Fe and Pt in Fe_3Pt we used pseudo-potentials generated using exchange correlation of Perdew-Zunger (see Ref. 14 for the source).

System	a_{L2_1} (Å)	$\mu_{total}(\mu_B)$	$L2_1$	Magn. order	e/a
Co_2MnGa	5.7100	4.14	stable	FM	7.000
Co_2MnGe	5.7285	4.99	stable	FM	7.250
Ni_2MnGa-e	5.4647	4.20	unstable	FM	7.250
Co_2MnGe+e	6.1957	6.02	-	FM	7.500
Ni_2MnGa	5.8067	4.35	unstable	FM	7.500
Ni_2MnAl	5.7000	4.20	unstable	FM	7.500
Ni_2MnIn	6.0624	4.22	unstable	FM	7.500
Ni_2MnGa+(e/2)	5.8668	3.96	unstable	FM	7.625
Ni_2MnGe	5.8039	4.10	unstable	FM	7.750
Ni_2MnSi	5.6041	3.78	unstable	FM	7.750
Ni_2CoAl	5.6041	1.78	unstable	FM	8.000
Ni_2CoGa	5.6865	1.54	unstable	FM	8.000
Ni_2CoGe	5.7067	1.45	unstable	FM	8.250
Ni_2CoSb	5.9411	1.34	unstable	FM	8.500
Cu_2MnAl	5.9153	3.51	unstable	FM	7.75
Cu_2MnGa	5.9701	3.61	stable	FM	7.75
Cu_2MnSn	6.1674	3.89	unstable	FM	8.00
Ni_2FeGa	5.7554	3.29	unstable	FM	7.75
Ni_2MnSn	6.0576	4.05	unstable	FM	7.75
Co_2FeGa	5.7177	5.02	stable	FM	7.50
Co_2MnSn	5.9837	5.03	stable	FM	7.50
Ni_2TiGa	5.8895	0.00	unstable	NM	6.75
Fe_2MnGa	5.6882	2.15	stable	Ferri	6.50

Table 2. Computed lattice parameters, magnetic moments per unit cell, types of magnetic order and valence-electron-to-atom ratios, e/a, for a series of Heusler compounds with the $L2_1$ structure (Ref. 8). 'Instability' of the cubic structure means here that a soft mode appears in the calculated phonon dispersion.

In both alloys we used a kinetic energy cutoff of 50 Ry for the plane wave basis set. The augmentation charges requiring the use of ultrasoft pseudo-potentials were expanded with energy cutoff of 600 Ry which is high enough to yield accurate results. Structural properties and most of the phonon frequencies are well converged using a first-order smearing parameter $\sigma = 0.02$ Ry for the BZ integration. For self-consistent and non-self-consistent calculations, a Monkhorst-Pack grid of $12\times12\times12$ k-points was used. A set of special $\mathbf{q}$-points in the BZ with finite weight generated from Monkhorst-Pack was used for both the fcc and the simple cubic cell. For the fcc structure we used a $4\times4\times4$ $\mathbf{q}$-point mesh yielding 8 sets of $\mathbf{q}$-vectors with finite weight while for the simple cubic, a $2\times2\times2$ $\mathbf{q}$-point mesh was used yielding 4 sets of special $\mathbf{q}$-vectors.

3 Results and Discussions

3.1 Heusler Alloys

With the help of the supercomputer facilities of the Forschungszentrum Jülich we succeeded to obtain phonon dispersions and the electronic structure of 27 different Heusler

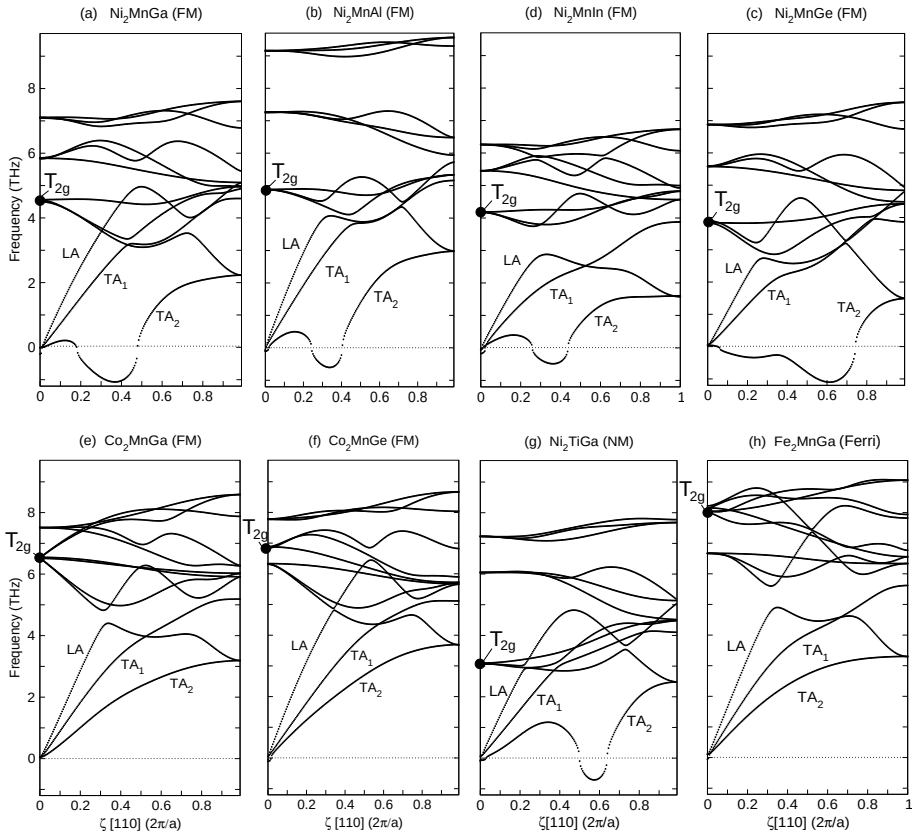

Figure 2. Phonon dispersion curves of (a) FM Ni_2MnGa, (b) FM Ni_2MnAl, (c) FM Ni_2MnGe, (d) FM Ni_2MnIn (e) FM Co_2MnGa, (f) FM Co_2MnGe, (g) NM Ni_2TiGa and (h) FerriM Fe_2MnGa in the $L2_1$ structure. Here, the reduced wave vector coordinate ζ spans the fcc Brillouin zone from Γ to X. Imaginary frequencies of the unstable modes are shown in the real negative frequency range. The frequency of the optical modes T_{2g} at Γ is marked by a black dot; note that it appears at lower values as compared to the stable systems.

structures listed in Table 2. Fig. 2 shows the dispersion curves of 8 of them. Comparison of the phonon dispersions of Ni_2MnGa with existing experimental data and calculations by other groups employing the linear response method show that the direct method used here yields fairly accurate results[6,9].

For the five compounds Ni_2Mn(Ga, Al, In, Ge) and Ni_2TiGa, the TA_2 branch is unstable for some range of ζ. In addition, in Ni_2MnGe the TA_2 mode has a negative slope at Γ, indicating a pure elastic instability. The instability of the $L2_1$ structure in NM Ni_2TiGa shows that magnetic order is not a necessary condition for the phonon softening to occur.

Figure 3 shows the force constants vs. e/a ratio for various Heusler alloys listed in Table 2. Note that negative force Ni-Ni constants in Ni-based compounds are responsible for the structural instability of the compounds. This leads also to inverted optical modes, i.e., Ni vibrates with lower frequency compared to the heavier Ga in the optical frequancy range. Ni vibrations are also Raman active. The Co-based systems have postive force constants and do not undergo a martensitic transformation.

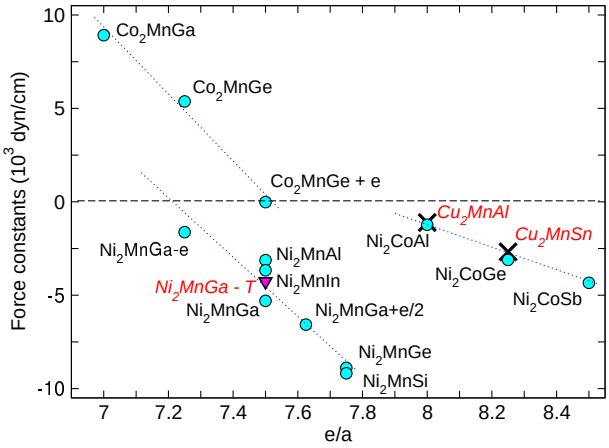

Figure 3. The plot of Ni-Ni and Co-Co force constants vs. e/a ratio for various Heusler alloys. The structurally unstable alloys have negative Ni-Ni force constants.

4 Fe Based Binary Alloys

The second part of this paper is concerned with Fe based binary alloys, in particular the bcc phase of Fe_3Ni.

The most prominent feature in fcc phonon dispersions, which is similar to some of the unstable Heusler alloys, is the instability of the TA acoustic mode which begins at about one third of the length of the wave vector from Γ and extends to the zone boundary M where the softening is highly pronounced. The region Γ-M corresponds to the [110] direction in which the elastic softening has been observed from most experiments[11–13].

It is known from experiment that the bcc phase of Fe_3Ni is the stable phase. The bcc phonon dispersion relations obtained from linear response calculations for Fe_3Ni show different features. As expected, the structure is perfectly stable as none of the phonon branches in the three windows corresponding to [100], [110] and [111] directions show softening unlike in the case of fcc dispersions. In this case the partial contributions of the atoms in the optical range of vibrations obey the expected order, whereby the heavier Ni atoms vibrate at relatively low frequency as compared to Fe.

This behaviour has been a subject of systematic experimental investigations for Fe_3Ni[10]. Inelastic neutron scattering data clearly showed excess states of Ni at relatively lower energies of the optical range in agreement with what we obtained from the calculations.

4.1 Comparison of the Methods

Our comparative study includes analysis of the methods we are using. The two techniques of calculating phonons lead to very similar results, but certain differences appear (not to be discussed here). Taking advantage of working on a supercomputer, we calculated for a large supercell of Ni_2MnGa (216 atoms) in order to obtain accurate vibrational densities of

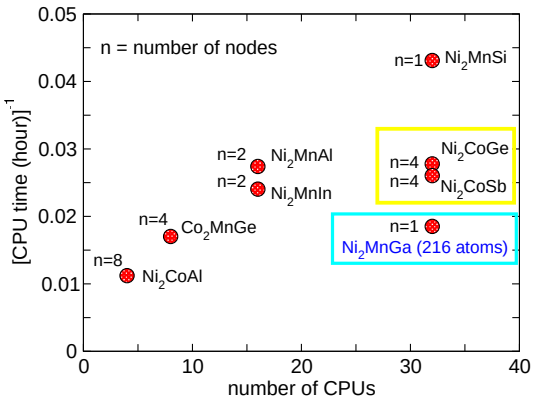

Figure 4. The inverse of CPU time versus the number of tasks per node for the phonon calculation of Heusler alloys with 40 atoms using VASP.

states and compare them with what we get from the linear response calculations. We find that both techniques show good agreement.

4.2 Performance Issues

The calculations presented in this work were carried out on the JUMP (IBM p690) supercomputer at the Forschungszentrum Jülich. From our test calculations we know that 32 processors taken on a single node is the optimal choice for our plane-wave calculations with a 40 atoms cell. However, there are some specific demands on the hardware, which are common to plane-wave codes. Especially for our calculations, we need a large amount of main memory and there is a lot of data transfer between processors. Keeping this in mind, we have done some additional calculations, showing that the data exchange between different nodes of JUMP decreases the efficiency of the calculations considerably. Figure 4 presents data of several test we did by taking our standard 40 atoms supercell with different Heusler systems. We took 32 processors for each of these calculations, but distributed processors among several nodes.

The situation changes, if we want to do calculations with larger cells. Our tests with a 216 atoms supercell have shown that 32 processors are not sufficient to achieve results in reasonable time. On the other hand the distribution over the nodes becomes more efficient. Again, the best choice is if we take complete nodes.

One has to be aware of some difficulties related to input parameters, which VASP code provides in order to control the parallization of the code. A bad choice of the parameters may lead to a significant reduction of the performance. Figure 4 shows such a breakdown, which we experienced in the case of Heusler systems Ni_2CoGe and Ni_2CoSb, when we used 128 processors. Using $NPAR = 128$, which tells vasp to distribute all bands during over the processors, the calculations were even slower than on 32 processors.

5 Concluding Remarks

From this study we have found general properties responsible for structural instabilities in Heusler compounds and Fe-based binary alloys.

Our rough estimate of the supercomputer performance allows to suggest that further investigations in this project may include calculations with very large supercells allowing the treatment of imperfections in the martensitic structure like twin variants.

Acknowledgments

We thank the NIC for providing the supercomputer facilities to perform *ab initio* supercell calculations of magnetic shape memory alloys.

References

1. I. Takeuchi, O .O. Famodu, J. C. Read, M. A. Aronova, K. S. Chang, C. Craciunescu, S. E. Lofland, M. Wuttig, F. C. Wellstood, L. Knauss and A. Orozco, *Identification of novel compositions of ferromagnetic shape-memory alloys using compositional spreads*, Nature Mater. **2**, 180 (2003).
2. G. Kresse and J. Furthmüller, *Efficient iterative schemes for ab initio total energy calculations using a plane-wave set*, Phys. Rev. B **54**, 11169 (1996).
3. G. Kresse and D. Joubert, *From ultrasoft pseudopotentials to the projector augmented-wave method*, Phys. Rev. B **59**, 1758 (1999).
4. K. Parlinski, *PHONON* , (Cracow, Poland, 2002).
5. P. J. Webster, K. R. A. Ziebeck, S. L. Town and M. S.Peak, *Magnetic order and phase transformation in Ni_2MnGa*, Phil. Mag. **49**, 295 (1984).
6. C. Bungaro, K. M. Rabe and A. Dal Corso, *First-principles study of lattice instabilities in ferromagnetic Ni_2MnGa*, Phys. Rev. B **68**, 134104 (2003).
7. A. Dal Corso and S. de Gironcoli, *Ab initio phonon dispersion of Fe and Ni*, Phys. Rev. B **62**, 273 (2000).
8. A. T. Zayak, P. Entel, K. M. Rabe, W. A. Adeagbo and M. Acet, *Anomalous vibrational effects in non-magnetic and magnetic Heusler alloys*, Phys. Rev. B **72**, 054113 (2005).
9. A. Zheludev, S. M. Shapiro, P. Wochner and L. E. Tanner *Precursor effects and premartensitic transformation in Ni_2MnGa*, Phys. Rev. B **54**, 15045 (1996).
10. O. Delaire, M. Kresch and B. Fultz *Vibrational entropy of the γ-α martensitic transformation in $Fe_{71}Ni_{29}$* , Phil. Mag. **85**, 3567 (2005).
11. E. Maliszewski and S. Bednarski, *Lattice dynamics of $Fe_{0.65}Ni_{0.35}$ classical Invar*, phys. stat. sol. (b) **211**, 621 (1999).
12. E. Maliszewski and S. Bednarski, *The lattice dynamics of $Ni_{0.88}Fe_{0.12}$, $Ni_{0.76}Fe_{0.24}$ and Ni single crystals*, phys. stat. sol. (b) **200**, 435 (1997).
13. E. D. Hallman and B. N. Brockhouse, *Crystal dynamics of nickel-iron and copper-zinc alloys*, Can. J. Phys. **47**, 1117 (1969).
14. S. Baroni, S. de Gironcoli, A. Dal Corso and P. Giannozzi, *Plane-Wave Self-Consistent Field Method*, `http://www.pwscf.org`.

John von Neumann Institute for Computing

Many-Body Effects in Semiconductor Quantum Dots

Michael Lorke, Jan Seebeck, Torben R. Nielsen,
Paul Gartner, and Frank Jahnke

published in

NIC Symposium 2006 ,
G. Münster, D. Wolf, M. Kremer (Editors),
John von Neumann Institute for Computing, Jülich,
NIC Series, Vol. **32**, ISBN 3-00-017351-X, pp. 167-172, 2006.

http://www.fz-juelich.de/nic-series/volume32

Many-Body Effects in Semiconductor Quantum Dots

Michael Lorke, Jan Seebeck, Torben R. Nielsen, Paul Gartner, and Frank Jahnke

Institute for Theoretical Physics
University of Bremen
28334 Bremen, Germany
E-mail: {mlorke, jseebeck, tnielsen, frank.jahnke}@itp.uni-bremen.de,
gartner@physik.uni-bremen.de

1 Introduction

In recent years, semiconductor quantum dots (QDs) have been studied extensively due to possible applications in optoelectronic devices like LEDs, lasers, or amplifiers[1,2]. In the rapidly emerging field of quantum information technology, QDs have been successfully used to demonstrate the generation of single photons or correlated photon pairs[3–5]. Furthermore, the strong coupling regime for QD emitters in optical microcavities has been demonstrated[6,7]. A common aspect in fundamental studies and practical applications of QDs is the critical role of correlation and scattering processes of carriers which are studied within this project.

Optical studies of QDs have been recently focused on self-assembled systems which are typically grown in the Stranski-Krastanoff mode. The resulting QDs are randomly distributed on a two-dimensional wetting layer (WL). The energy spectrum of this system consists of discrete states which correspond to a three-dimensional carrier localization in the QDs and a quasi-continuum of states at higher energies in connection with the two-dimensional motion of carriers within the WL. Scattering processes of carriers between the localized QD states as well as between localized and delocalized states are possible due to the Coulomb interaction in addition to carrier-phonon interaction.

2 Quantum Kinetics of Carrier-Phonon Interaction

At low carrier densities and elevated temperatures the interaction of carriers with LO-phonons provides the dominant contribution to scattering channels for redistributing carriers in QDs as well as to the dephasing of optical excitations. Due to the discrete nature of the QD energy spectra, a phonon bottleneck has been predicted by energy conservation arguments based on Fermi's golden rule: if the energy spacing between QD states does not exactly match the LO-phonon energy $\hbar\omega_{\mathrm{LO}}$, carrier scattering would not be possible in this picture. The phonon-bottleneck problem is still a debated topic because there is experimental evidence for[8,9] as well as against it[10,11]. Recently it has been discussed, that a perturbational treatment of the carrier-phonon interaction based on Fermi's golden rule is not applicable to discrete QD systems.

Because of the strong interaction between carriers and phonons in QDs, a theoretical description has to be based on polarons[12,13]. The physical picture of a polaron as a carrier in a crystal interacting with a surrounding cloud of lattice distortions is shown in Fig. 1a. The energy spectrum of polarons differs significantly from that of free carriers as shown in

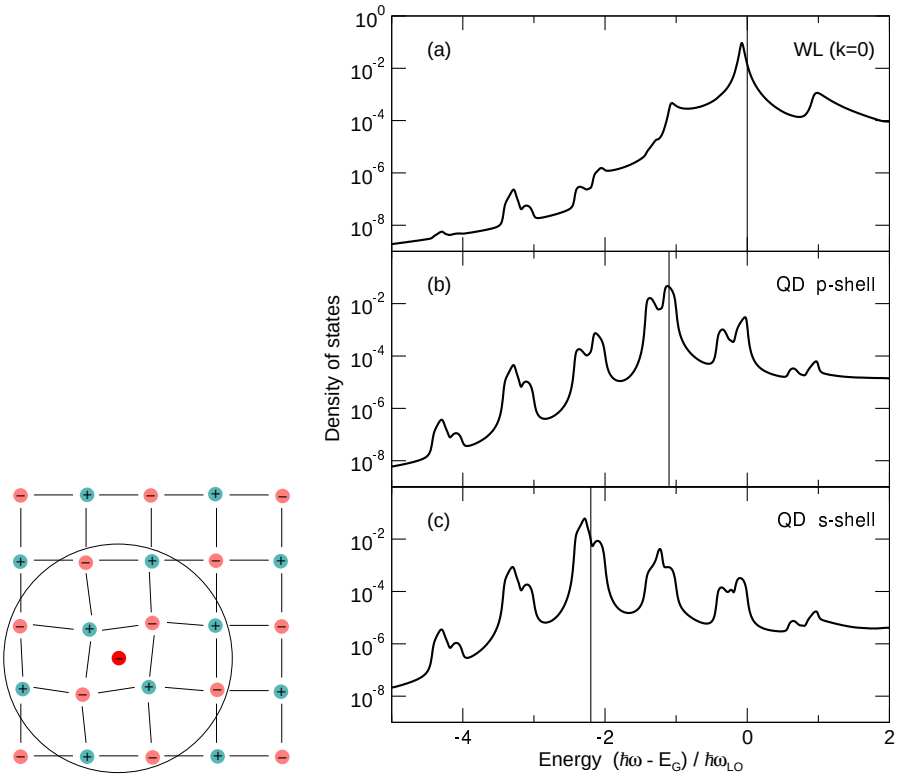

Figure 1. Electron interacting with surrounding cloud of lattice distortions (left) and density of states (DOS) for a polaron at the bandedge a), in the p-shell b) and in the s-shell c) (right). Vertical lines indicate the δ-like DOS of free electrons.

Fig. 1. There and in the following examples we consider QDs with two confined shells for electrons and holes. For the assumed cylindrical symmetry they are called s- and p-shell where the latter is two-fold degenerate in addition to the spin degeneracy[14]. In the polaron picture, energy renormalizations that incorporate shifts and broadening of the electronic states as well as phonon satellites and hybridization effects immediately invalidate the simple arguments for the phonon bottleneck.

To study the experimentally observed fast carrier relaxation in QDs on the level of a microscopic theory, we solve numerically the coupled quantum-kinetic equations for the carrier and polarization dynamics. These equations incorporate high-dimensional scattering integrals for the carrier-phonon interaction as well as memory integrals over the history of the system[14,15].

The scattering rate between polaron states is proportional to the overlap of the density-of-states (DOS) of the involved states, shifted by one phonon energy against each other. From Fig. 1 one immediately finds that in the free particle picture scattering between QD states only is possible if the level-spacing exactly matches the LO-phonon energy due to the δ-like DOS. This corresponds to the prediction of the phonon bottleneck. In the polaron picture even for large detunings between the level spacing and the LO-phonon energy, sufficient overlap is present which gives rise to fast carrier scattering.

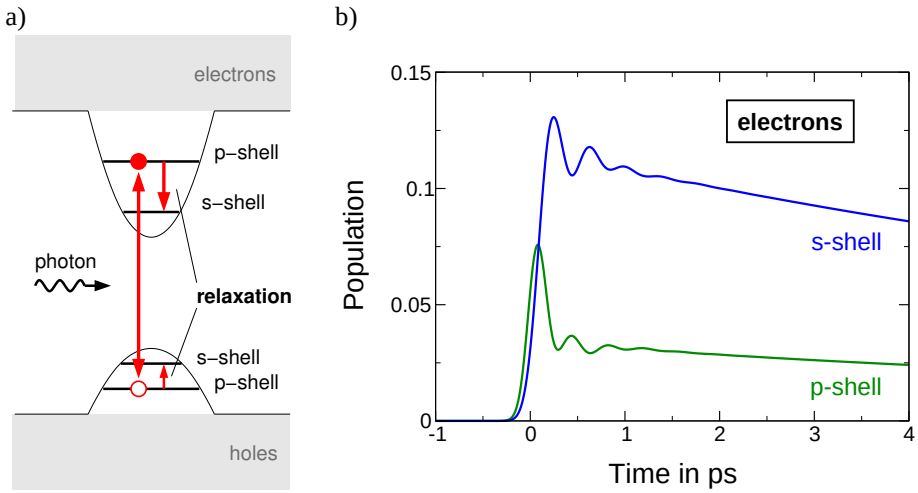

Figure 2. Resonant optical excitation condition for the semiconductor QD system a) and corresponding temporal evolution of the population probability for the QD states. Calculations are done for InGaAs/GaAs QDs at 300K and a detuning of 10% between level spacing and phonon energy.

In the following example we consider the situation where a resonantly tuned laser pulse excites carriers only in the p-shell and the subsequent relaxation of carriers into the s-shell is studied, see Fig. 2a. The corresponding evolution of the carrier population is shown in Fig. 2b. First the p-shell is populated due to pulse excitation which is followed by a fast relaxation into the s-shell. Rabi-oscillations due to memory effects indicate the strong coupling regime for the carrier-phonon interaction. At later times a decrease of the QD population is observed due to escape of carriers into the WL, which is also included in the calculation.

Our results show that even for materials with weak polar coupling, like InGaAs, QD polarons lead to fast carrier scattering on a sub-picosecond timescale which is influenced only weakly by the level spacing[14].

3 Quantum Kinetics of Carrier-Carrier Interaction

For optoelectronic applications of semiconductor nano-structures the optical gain spectra of the active material are of central importance. Under the assumption that the carrier system is in a thermodynamic quasi-equilibrium, we evaluate the temperature and carrier-density dependence of the optical gain spectra theoretically. To achieve this, the knowledge of the many-body effects is of central importance, because the line-broadening as well as the lineshape of the optical spectra is governed by dephasing and correlation processes[16]. At room temperatures and elevated carrier densities the important dephasing mechanisms are the carrier-carrier Coulomb interaction as well as the interaction of carriers with LO phonons.

For the case of a high excitation density, the screening of the Coulomb interaction in the coupled QD-WL system justifies a treatment of the carrier-carrier scattering in the second-order Born approximation while the carrier-phonon interaction is included in the random phase approximation (RPA). It turns out that in the coupled QD-WL system the Markov

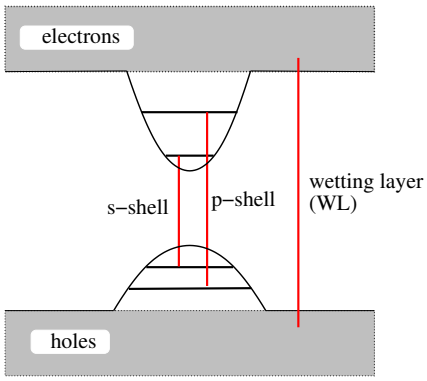

Figure 3. Shell structure of the combined QD-WL system showing localized QD states for electrons (holes) which are energetically below a quasi-continuum of delocalized WL states corresponding to the free motion in the WL. The red lines show the allowed optical transitions.

approximation cannot be applied and renormalized quasi-particle properties (which in the case of low carrier densities are the polarons) need to be included for a proper description of the optical spectra[17]. In Fig. 3 the electronic structure of the discussed system is schematically shown. We consider two confined shells for electrons as well as for holes so that from the allowed transitions (red lines in Fig. 3) we expect three resonances in the optical spectra, namely the ground state resonance, the excited state resonance and the excitonic resonance of the WL.

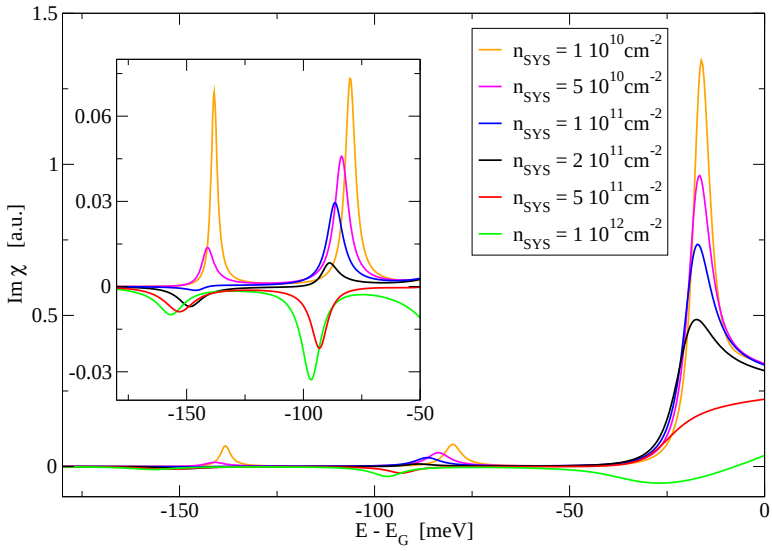

Figure 4. Optical absorption spectra for the combined QD-WL system including interaction-induced dephasing and line shifts due to Coulomb interaction and carrier-phonon interaction for various total carrier densities. The inset shows a scale up of the QD resonances.
Calculations are done for InGaAs/GaAs QDs at 300K.

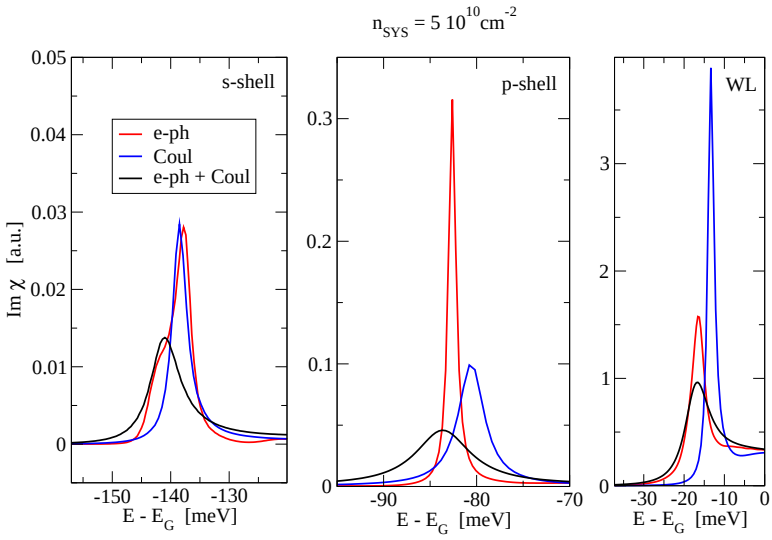

Figure 5. Influence of carrier-carrier and carrier-phonon interaction on the optical absorption spectra. Given are the energetic region of the ground state resonance, excited state resonance, and excitonic resonance of the WL. The red (blue) line is a calculation with carrier-phonon (carrier-carrier) interaction only, while the black line shows the full calculation.
Calculations are done for InGaAs/GaAs QDs at 300K.

In Fig. 4 the results of the calculations are presented. Given is the absorption vs. energy (relative to the band-gap energy E_G). We obtain the mentioned three resonances at around -130meV,-85meV, and -15meV, respectively. With increasing carrier density the resonances are bleached out, reach transparency, and switch to negative absorption (optical gain). Additionally observed is a distinct, correlation-induced red-shift of the QD resonances with increasing carrier-density, which has also been found in recent photoluminescence experiments[18].

In Fig. 5 we compare the role of carrier-carrier and carrier-phonon interaction for a fixed carrier density. We find that both mechanisms are equally important to properly describe the broadening of all three resonances even at intermediate to high excitation conditions.

4 Summary

A quantum-kinetic treatment for carrier-phonon and carrier-carrier interaction in semiconductor quantum dots has been used to analyze the efficiency of scattering processes and their influence on the carrier-density dependent optical spectra. The absence of a phonon bottleneck is explained in terms of polaron renormalizations. The combined influence of the scattering processes is responsible for the observed dephasing and line-shift effects in the optical gain spectra.

Acknowledgments

This work was supported by the Deutsche Forschungsgemeinschaft. We acknowledge a grant for CPU time at the NIC, Forschungszentrum Jülich.

References

1. Y. Masumoto and T. Takagahara, eds., *Semiconductor Quantum Dots* (Springer-Verlag, Berlin, 2002), 1st ed.
2. P. Michler, ed., *Single Quantum Dots* (Springer-Verlag, Berlin, 2003), 1st ed.
3. P. Michler, A. Imamoglu, M. D. Mason, P. J. Carson, G. F. Strouse, and S. K. Buratto, Nature **406**, 968 (2000).
4. E. Moreau, I. Robert, L. Manin, V. Thierry-Mieg, J. M. Gerad, and I. Abram, Phys. Rev. Lett. **87**, 183601 (2001).
5. M. Pelton, C. Santori, J. Vuckovic, B. Zhang, G. S. Solomon, J. Plant, and Y. Yamamoto, Phys. Rev. Lett. **89**, 233602 (2002).
6. J. P. Reithmaier, G. Sek, A. Löffler, C. Hofmann, S. Kuhn, S. Reitzenstein, L. V. Keldysh, V. D. Kulakovskii, T. L. Reinecke, and A. Forchel, Nature **432**, 197 (2004).
7. T. Yoshie, A. Scherer, J. Hendrickson, G. Khitrova, H. M. Gibbs, G. Rupper, C. Ell, O. B. Shchekin, and D. G. Deppe, Nature **432**, 200 (2004).
8. J. Urayama, T.B. Norris, J. Singh, and P. Bhattacharya. Observation of phonon bottleneck in quantum dot electronic relaxation. *Phys. Rev. Lett.*, **86**:4930, 2001.
9. W.W.E. Minnaert, A.Yu. Silov, W. van der Vleuten, J.E.M. Haverkort, and J.H. Wolter. Fröhlich interaction in InAs/GaAs self-assembled quantum dots. *Phys. Rev. B*, **63**:75303, 2001.
10. E. Tsitsishvili, R.v. Baltz, and H. Kalt. Temperature dependence of polarization relaxation in semiconductor quantum dots. *Phys. Rev. B*, **66**:R161405, 2002.
11. E. Péronne, F. Fossard, F.H. Julien, J. Brault, M. Gendry, B. Salem, G. Bremond, and A. Alexandrou. Dynamic saturation of an intersublevel transition in self-organized InAs/$In_xAl_{1-x}As$ quantum dots. *Phys. Rev. B*, **67**:205329, 2003.
12. T. Inoshita and H. Sakaki. Density of states and phonon-induced relaxation of electrons in semiconductor quantum dots. *Phys. Rev. B*, **56**:R4355, 1997.
13. O. Verzelen, R. Ferreira, G. Bastard, T. Inoshita, and H. Sakaki. Polaron effects in quantum dots. *phys. stat. sol. (a)*, **190**:213, 2002.
14. J. Seebeck, T.R. Nielsen, P. Gartner, and F. Jahnke. Polarons in semiconductor quantum dots and their role in the quantum kinetics of carrier relaxation. *Phys. Rev. B*, **71**:125327, 2005.
15. J. Seebeck, T.R. Nielsen, P. Gartner, and F. Jahnke. Quantum kinetic theory of phonon-assisted carrier transitions in nitride-based quantum-dot systems. *arXiv:cond-mat/cond-mat/0509692*, 2005.
16. H. Haug and S.W. Koch. *Quantum Theory of the Optical and Electronic Properties of Semiconductors*, World Scientifiv Publ., Singapore, 4. edition, 2004.
17. M. Lorke, T. R. Nielsen, J. Seebeck, P. Gartner, and F. Jahnke , Influence of carrier-carrier and electron-phonon correlations on optical absorption and gain in quantum-dot systems, *arXiv.org:cond-mat/0509543*, 2005.
18. K. Matsuda, K. Ikeda, T. Saiki, H. Saito, K. Nishi Carrier-carrier interaction in single $In_{0.5}Ga_{0.5}As$ quantum dots at room temperature investigated by near-field scanning optical microscope, Appl. Phys. Lett., **83**, 2250 (2003).

John von Neumann Institute for Computing

Condensed Matter

Kurt Binder and Alejandro Muramatsu

published in

NIC Symposium 2006 ,
G. Münster, D. Wolf, M. Kremer (Editors),
John von Neumann Institute for Computing, Jülich,
NIC Series, Vol. **32**, ISBN 3-00-017351-X, pp. 173-174, 2006.

http://www.fz-juelich.de/nic-series/volume32

Condensed Matter

Kurt Binder[1] **and Alejandro Muramatsu**[2]

[1] Institut für Physik, Johannes Gutenberg-Universität
55099 Mainz, Germany
E-mail: kurt.binder@uni-mainz.de

[2] Institut für Theoretische Physik III, Universität Stuttgart
70550 Stuttgart, Germany
E-mail: mu@theo3.physik.uni-stuttgart.de

The physics of condensed matter deals with various physical phenomena (mechanical response, electrical conductivity, magnetism, optical properties, etc.) of solids and liquids, trying to provide a link between macroscopic properties of matter and the basic characteristics of the nuclei and electrons which constitute it. A crucial aspect for many of these phenomena is the fact that this many-body problem cannot be simply reduced to a one-body problem (with an effective field resulting from the other degrees of freedom), since nontrivial correlations, central for a correct description of the system, develop. Since there is no general analytic method which could deal with such correlations, large-scale computer simulation is the most promising tool to tackle such problems.

This crucial role of correlations and the corresponding importance of state-of-the art computer simulation methods to deal with them is very much apparent in the articles which will follow in this section. Note that only a small number of NIC projects dealing with applications in condensed matter physics could be selected for the present section of this volume, due to restricted space. Furthermore, closely related applications can be found in the sections on chemistry, materials science and polymers (soft matter) as well: nontrivial correlations resulting either from the quantum many-body problem or from entropic effects (or both) are present there in a similar way.

Strongly correlated electron systems are a common theme in the papers of Assaad and Hanke, Anders et al. and Keller et al. Assaad and Hanke first describe a methodic advance to deal with the famous "minus sign problem" of Quantum Monte Carlo (QMC) methods, based on a representation of the density matrix in terms of Gaussian operators. This so-called "Gaussian Monte Carlo method" then is applied to gain insight into the phase diagram of the SU(N) Hubbard-Heisenberg model.

A completely different approach in order to deal with strongly correlated electrons is based on a combination of the local density approximation (LDA) of density functional theory with the dynamical mean field theory (DMFT). The resulting equations then also need to be solved by QMC methods. Keller et al. demonstrate that with this approach one can compute properties of real materials, such as photoemission spectra of V_2O_3, and thus explain pertinent experiments.

The third approach we discuss here, applied by Anders et al. in order to understand the conductance in coupled quantum dots, is based on a numerical renormalization group method to solve the effective quantum Hamiltonian near the quantum phase transition that the model exhibits.

An alternative method (namely the density matrix renormalization group) also proves useful for the calculation of spectral properties of strongly correlated electron phonon properties by Schubert et al.

Still another, and very promising, approach on how to deal with strongly correlated quantum systems is based on Stochastic Series Expansion Quantum Monte Carlo (SSE-QMC). Wessel applies this methods to ultracold atom gases in optical lattices to describe the transition from the suprafluid state to the Mott insulator.

Also on a more mesoscopic scale, quantum-mechanical correlations may be very important. Meier et al. give an example for this statement by their treatment of semiconductor nanostructures and their optoelectronic properties. Such nanostructures are discussed in the context of photonic crystals and hence, a hot topic of materials science. The dynamics of electrons and hole excitations, which interact with Coulomb forces, are obtained by numerical solutions of a high-dimensional set of coupled nonlinear differential equations, the so-called semiconductor Bloch equations.

Nontrivial correlations are certainly the key problem when one deals with the statistical mechanics of magnetic systems. While the equilibrium behavior of the two-dimensional Ising model is well understood, Pleimling shows that the dynamical scaling associated with far from equilibrium behavior (domain growth, ageing) exhibits the so-called "local scale invariance" which was recently proposed.

Finally, nontrivial correlations also arise in classical model systems for colloids, as demonstrated by Vink et al. The Asakura-Oosawa (AO) model of colloid-polymer mixtures coarse grains both colloids and polymers as spheres with excluded volume interactions (but polymers may overlap each other with no interaction). The resulting (purely entropically driven) phase separation falls in the universality class of the Ising model. Similarly, hard spherocylinders exhibit phase separation between a nematic and an isotropic phase. Computer simulation techniques were developed allowing to estimate the interfacial tensions for such systems. The relation of this work to simulations of polymeric and other soft matter systems is evident.

At the end of this introduction, we note that successful simulations in condensed matter require several ingredients which are all crucial for obtaining relevant results: clever "model building" needs to be combined with a carefully chosen and optimized algorithm, and only then the computational power of the supercomputer fully pays off. The following papers will illustrate this importance of algorithmic improvements in more detail.

John von Neumann Institute for Computing

Numerical Simulations of Strongly Correlated Electron Systems

Fakher F. Assaad and Werner Hanke

published in

NIC Symposium 2006 ,
G. Münster, D. Wolf, M. Kremer (Editors),
John von Neumann Institute for Computing, Jülich,
NIC Series, Vol. **32**, ISBN 3-00-017351-X, pp. 175-182, 2006.

http://www.fz-juelich.de/nic-series/volume32

Numerical Simulations of Strongly Correlated Electron Systems

Fakher F. Assaad and Werner Hanke

Institut für Theoretische Physik und Astrophysik, Universität Würzburg
Am Hubland, 97074 Würzburg, Germany
E-mail: {*assaad, hanke*}*@physik.uni-wuerzburg.de*

After an introduction aimed at motivating the numerical study of correlated electron systems, we concentrate on two aspects of our work. The fisrt concerns algorithmic developments, namely the so called Gaussian Monte Carlo method which has the potential of circumventing the minus sign problem occurring in simulations of correlated electron systems. We then describe an application, the phase diagram of the $SU(N)$ Hubbard Heisenberg model, which exhibits exotic and novel phases of matter.

1 Introduction

The goal of solid state physics is to explain the physical properties of numerous materials in a unified framework. For simple metals, semiconductors and a class of insulators it is fair to say that this goal has been to a large extent achieved. There is however a class of materials where $d-$ and/or $f-$ shells are partially filled whose properties are harder to explain. Here, and since the electrons are confined to narrow orbitals, the Coulomb repulsion between them turns out to play a dominant role. Such strongly interacting or correlated electrons cannot be described as embedded in a static mean-field generated by the other electrons. The effect of an electron on the others is too pronounced for each to be treated independently.

The effect of correlations on material properties is often profound, and lead to a whole zoo of exotic ordering phenomena. The competition between many different order phases make those systems very sensitive to small changes in external parameters such as temperature, pressure or band-filling. For instance correlations are at the origin of the exceptionally high transition temperature (above liquid-nitrogen temperatures) of superconductors with copper-oxygen planes. In materials called heavy fermion systems the mobile electrons at low temperature behave as if their masses were a thousand time the mass of a free electron in a simple metal. Some strongly correlated electron systems exhibit big changes in resistivity as a function of applied magnetic field; colossal magneto-resistance. Such properties render the prospect of developing applications for correlated electron systems very exciting. However the very richness in phenomena and the extreme sensitivity to microscopic details, renders the theoretical study of those materials very challenging. The difficultly lies in complexity and the understanding of the emergent collective phenomena.

Our research project is centered around numerical simulations of models of correlated electron systems. The first question which one will have to address is the very choice of the model. The effect of correlations shows up at low temperatures and low energy scale. Hence, one first needs to derive effective models which describe the low temperature physical properties of the material under consideration. To this aim, one can use methods

such as the contractor-renormalization-group (CORE) method. Starting from a high energy model, the CORE essentially successively integrates out high energy degrees of freedom and produces a hierarchy of model Hamiltonians. At each iteration the model Hamiltonian is restricted to lower and lower energy or longer length scales. Hence the method acts like a magnifying glass. For example a CORE iteration will map the Hubbard model on the so-called $t - J$ model.

The second step is to solve numerically the effective low energy model. Given the complexity of the models at hand, the numerical approach is attractive since it is unbiased. At the onset the numerical problem scales exponentially with the size (i.e. the number of unit cells) of the the system. This scaling reflects the very dimension of the Hilbert space. Given this complexity it is adequate to use stochastic methods based on importance sampling; the Monte Carlo approach. In many non-trivial cases, the quantum Monte Carlo method can reduce the exponential scaling to a powerlaw. When this is achievable, it is fair to say that many properties of the system can be investigated in details on large enough system sizes so as to carry out size scaling and hence obtain results relevant for the thermodynamic limit.

In this article we will review briefly two research topics in which we are involved and which are centered around high performance computing.
i) In too many cases, simulations of systems of correlated electrons are plagued with the so called sign problem which inhibits the reduction from an exponential to algebraic scaling. There has recently been tremendous progress in this domain, in terms of algorithmic developments. In section 2 we will briefly review our activities in this domain.
ii) As mentioned above, a characteristic of correlated electron systems are competing phases leading to exotic ground states. Here we will review our work on the $SU(N)$ Hubbard-Heisenberg model, in which broken symmetry states (spin-dimerized, and d-density wave states) appear. Furthermore, the phase diagram shows an intriguing spin liquid state whose understanding is up to now not complete.

2 Gaussian Monte Carlo Methods: A Way to Circumvent the Minus Sign Problem?

As mentioned in the introduction, the stochastic approach to simulations of correlated electron systems is too often plagued by the so-called minus sign problem. Configurations, which we sample stochastically, occur with positive and negative signs thus canceling each other. This cancellation becomes nearly perfect in the limit of large lattices and low temperatures thus leading to exponential increase of the noise to signal ratio. Hence accurate low temperature results on large lattices are limited to a class of problems where one can show that the sign problem is absent. This includes non-frustrated one-dimensional systems[1], impurity models[2], electron-phonon models in arbitrary dimensions as described by the Holstein Hamiltonian, models with particle-hole symmetry[3] , multi-flavored models[4], etc. However, the physics of Hubbard type models away from the particle-hole symmetric point remains elusive.

It has long been known that the sign problem is representation dependent. In particular world line methods are unable to simulate the Hubbard model at the particle-hole symmetric point but auxiliary field methods can. The recent advance is based on a novel representation of the density matrix in terms of Gaussian operators[5]. In fact, the key point is the

observation that the density matrix of an arbitrary physical Hamiltonian can be expanded in a positive sum of Gaussian operators. This allows for sign free stochastic simulations for a wide class of models[6], including the Hubbard model.

Let us very briefly summarize the major ideas lying behind the Gaussian QMC (GQMC) approach. The interested reader may find details of the calculations in[6]. The expansion of the density matrix is done in a basis of Gaussian operators:

$$\hat{\Lambda}(\mathbf{n}) = \det(\mathbf{1}-\mathbf{n}) : e^{-\hat{\mathbf{c}}^\dagger \left(\mathbf{2}+\left(\mathbf{n}^T-\mathbf{1}\right)^{-1}\right)\hat{\mathbf{c}}} : \tag{1}$$

with $\mathbf{n}$ an $N_s \times N_s$ real matrix where N_s corresponds to the number of single particle states. $\hat{\mathbf{c}}^\dagger = \left(\hat{c}_1^\dagger, \cdots, \hat{c}_{N_s}^\dagger\right)$ where $\hat{c}_x^\dagger$ is the creation operator of a fermion in the single particle state x. Finally, $: \hat{A} :$ denotes the normal ordering of the operator $\hat{A}$. It is very convenient to work with Gaussian operators since they satisfy $\mathrm{Tr}\left[\hat{\Lambda}(\boldsymbol{n})\right] = 1$ and obey Wick's theorem such that

$$\mathrm{Tr}\left[\hat{\Lambda}(\mathbf{n})\hat{c}_x^\dagger \hat{c}_y\right] = \boldsymbol{n}_{x,y}, \quad \mathrm{Tr}\left[\hat{\Lambda}(\mathbf{n})\hat{c}_x^\dagger \hat{c}_y \hat{c}_w^\dagger \hat{c}_z\right] = \boldsymbol{n}_{x,y}\boldsymbol{n}_{w,z} + \boldsymbol{n}_{x,z}\left(\mathbf{1}-\boldsymbol{n}\right)_{w,z}. \tag{2}$$

Hence we can very easily compute the expectation value of an arbitrary observable. Since the Gaussian operators are a vastly overcomplete basis of the Fock space, it is possible to prove that an arbitrary physical density matrix can be expanded as a positive sum of Gaussian operators:

$$\hat{\rho}(\tau) = \sum_i P_i(\tau)\hat{\Lambda}(\mathbf{n}_i), \quad P_i \geq 0. \tag{3}$$

Clearly $\mathrm{Tr}\left[\hat{\rho}(\tau)\right] \equiv \sum_i P_i(\tau)$ grows exponentially with τ. One can account for this exponential growth by attaching a weight factor to the Gaussian operators thereby obtaining:

$$\hat{\rho}(\tau) = \int \mathrm{d}\underline{\boldsymbol{\lambda}} P(\underline{\boldsymbol{\lambda}}, \tau)\hat{\Lambda}(\underline{\boldsymbol{\lambda}}) \ \text{ with} \tag{4}$$

$$\underline{\boldsymbol{\lambda}} = (\Omega, \boldsymbol{n}), \ \ \hat{\Lambda}(\underline{\boldsymbol{\lambda}}) = \Omega\hat{\Lambda}(\boldsymbol{n}) \ \text{ and } \ \int \mathrm{d}\underline{\boldsymbol{\lambda}} P(\underline{\boldsymbol{\lambda}}, \tau) = 1.$$

The aim is now to formulate a stochastic process which samples the probability distribution, $P(\underline{\boldsymbol{\lambda}}, \tau)$ in the space of Gaussian operators. To achieve this goal, one can recast the imaginary time evolution of the density operator to a Fokker-Planck equation for the time evolution of the probability distribution. For a vast set of Hamiltonians $\hat{H}$, the Fokker-Planck equation can be shown to take the form:

$$\frac{\partial}{\partial\tau}P(\underline{\boldsymbol{\lambda}}, \tau) \ = \left[\frac{\partial}{\partial\Omega}\Omega h(\boldsymbol{n}) + \sum_{x,y}\frac{\partial}{\partial \boldsymbol{n}_{x,y}}\boldsymbol{A}_{x,y} + \frac{1}{2}\sum_{m,x,y,w,z}\frac{\partial^2}{\partial \boldsymbol{n}_{x,y}\partial \boldsymbol{n}_{w,z}}\boldsymbol{B}_{x,y}^{(m)}\boldsymbol{B}_{w,z}^{(m)}\right]P(\underline{\boldsymbol{\lambda}}, \tau)$$

where $\boldsymbol{B}^m$ and $\boldsymbol{A}$ are real $N_s \times N_s$ with functional dependence on $\boldsymbol{n}$ and $h(\boldsymbol{n}) = \mathrm{Tr}\left[\hat{\Lambda}(\boldsymbol{n})\hat{H}\right]$. Since the density matrix at $\tau = 0$ takes the value $\hat{\rho}(\tau = 0) = \hat{1}$ the initial condition for the Fokker-Planck equation reads: $P(\underline{\boldsymbol{\lambda}}, 0) = \delta\left(\underline{\boldsymbol{\lambda}} - (1, \mathbf{1/2})\right)$.

To solve the Fokker-Planck equation numerically, it is convenient to consider the associated stochastic differential equation. In the Ito formulation, it takes the form:

$$\mathrm{d}\Omega = -\Omega h(\boldsymbol{n})\mathrm{d}\tau \tag{5}$$

$$\mathrm{d}\boldsymbol{n} = -\boldsymbol{A}\mathrm{d}\tau + \sum_m \boldsymbol{B}^m \mathrm{d}W_m \tag{6}$$

with Wiener increments $\langle \mathrm{d}W_m \rangle = 0$, and $\langle \mathrm{d}W_m \mathrm{d}W_{m'} \rangle = \mathrm{d}\tau \delta_{m,m'}$. Eq. (5) describes the time evolution of walkers, $\underline{\boldsymbol{\lambda}}$, in the space of Gaussian operators. At $\tau = 0$, $\rho(\tau = 0) = 1$ such that all the Walkers are parameterized by $\underline{\boldsymbol{\lambda}} = (1, \mathbf{1/2})$. At imaginary time τ they are distributed according to $P(\underline{\boldsymbol{\lambda}}, \tau)$ so that we have access to the density matrix. In particular, any equal time observable is given by:

$$\langle \hat{O} \rangle \simeq \frac{\sum_i \mathrm{Tr}\left[\hat{\Lambda}(\underline{\boldsymbol{\lambda}}_i)\hat{O}\right]}{\sum_i \mathrm{Tr}\left[\hat{\Lambda}(\underline{\boldsymbol{\lambda}}_i)\right]} \tag{7}$$

where the sum runs over the set of walkers generated by the SDE. Since Wick's theorem applies for a single Gaussian operator the numerator of the above equation may easily be calculated.

As apparent from Eq. (5) the weight of a Walker at imaginary time τ reads :

$$\Omega(\tau) = e^{-\int_0^\tau \mathrm{d}\tau' h(\boldsymbol{n}(\tau'))}. \tag{8}$$

Since $\boldsymbol{n}$ is a real matrix, $h(\boldsymbol{n})$ is real and the weights remains positive! Hence the algorithm shows no explicit manifestation of the sign problem. However, the weights grow exponentially with imaginary time thus yielding an exponential increase in the variance. To circumvent this problem, one can adopt population control schemes used in Green function Monte-Carlo methods[7].

We have tested extensively the method for the Hubbard model. At high temperatures we find good agreement with benchmark results. However in the low temperature limit the sampling fails to produce a density matrix with the correct symmetries of the model. Understanding the origin of this problem is a central challenge since it opens the door to accurate, sign free, simulations of the doped Hubbard model. On the other hand, we can a posteriori impose the correct symmetries on the density matrix by projecting it on the symmetry sector of the ground state[6]. Using this procedure we find very good agreement with exact results for parameter ranges where known Monte Carlo methods such as the auxiliary field approach[8] fail due to the minus sign problem (See Fig. 1).

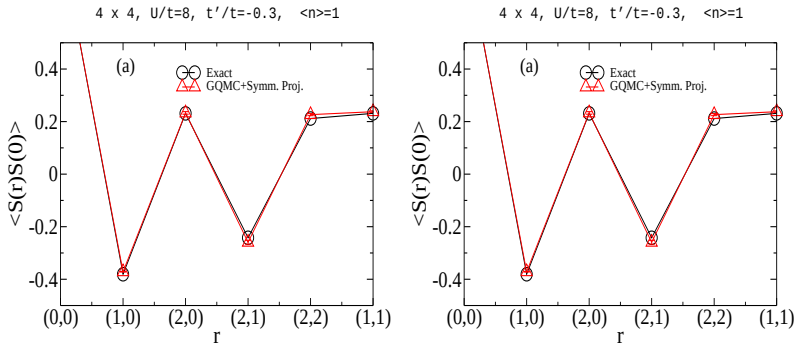

Figure 1. Real space spin-spin correlations as obtained from the GQMC and comparison with exact-diagonalization results.

3 Phase Diagram of the $SU(N)$ Hubbard-Heisenberg Model

As mentioned in the introduction, competing phases are a characteristic of systems of correlated electron systems. Here we will summarize recent numerical work on the $SU(N)$ Hubbard-Heisenberg model. Those models are relevant for the understanding of Mott insulators with orbital degeneracy as described by the Kugel-Khomskii Hamiltonian[9]. For two-fold orbital degeneracy and at a point where orbital and spin degrees of freedom play a very symmetric role, this model maps onto an $SU(4)$ symmetric Hubbard, or Heisenberg model with fundamental representation on each site[10]. On the other hand it has been argued that realizations of $SU(N)$ symmetric Hubbard models are at reach in the context of optical lattices[11].

The model we consider reads:

$$\begin{aligned} H &= H_t + H_U + H_J \quad \text{with} \\ H_t &= -t \sum_{\langle \vec{i},\vec{j} \rangle} \vec{c}^{\dagger}_{\vec{i}} \vec{c}_{\vec{j}} + \text{H.c.} \\ H_U &= \frac{U}{N} \sum_{\vec{i}} \left(\vec{c}^{\dagger}_{\vec{i}} \vec{c}_{\vec{i}} - \rho \frac{N}{2} \right) \\ H_J &= -\frac{J}{2N} \sum_{\langle \vec{i},\vec{j} \rangle} \left(D^{\dagger}_{\vec{i},\vec{j}} D_{\vec{i},\vec{j}} + D_{\vec{i},\vec{j}} D^{\dagger}_{\vec{i},\vec{j}} \right). \end{aligned} \tag{9}$$

Here, $\vec{c}^{\dagger}_{\vec{i}} = (c^{\dagger}_{\vec{i},1}, c^{\dagger}_{\vec{i},2}, \cdots, c^{\dagger}_{\vec{i},N})$ is an N-flavored spinor, $D_{\vec{i},\vec{j}} = \vec{c}^{\dagger}_{\vec{i}} \vec{c}_{\vec{j}}$ and ρ corresponds to the band-filling. In the $SU(2)$ case, the operator identity

$$\begin{aligned} \frac{-1}{4} & \left(D^{\dagger}_{\vec{i},\vec{j}} D_{\vec{i},\vec{j}} + D_{\vec{i},\vec{j}} D^{\dagger}_{\vec{i},\vec{j}} \right) = \\ & \vec{S}_{\vec{i}} \cdot \vec{S}_{\vec{j}} + \frac{1}{4} \left[(n_{\vec{i}} - 1)(n_{\vec{j}} - 1) - 1 \right] \end{aligned} \tag{10}$$

holds. Here, the fermionic representation of the spin $1/2$ operator reads $\vec{S} = \frac{1}{2} \sum_{s,s'} c^{\dagger}_{s} \vec{\sigma}_{s,s'} c_{s'}$ where $\vec{\sigma}$ are the Pauli spin matrices. Hence, at $N = 2$ the model reduces to the standard Hubbard-Heisenberg model.

In the strong coupling limit, $U/t \to \infty$, and at integer values of $\rho N/2$, charge fluctuations are suppressed. The model maps onto the $SU(N)$ Heisenberg Hamiltonian

$$H = \frac{J}{N} \sum_{\langle \vec{i},\vec{j} \rangle} \sum_{\alpha,\beta} S_{\alpha,\beta,\vec{i}} S_{\beta,\alpha,\vec{j}} \tag{11}$$

with

$$S_{\alpha,\beta,\vec{i}} = c^{\dagger}_{\alpha,\vec{i}} c_{\beta,\vec{i}} - \frac{1}{N} \delta_{\alpha,\beta} \sum_{\gamma} c^{\dagger}_{\gamma,\vec{i}} c_{\gamma,\vec{i}} \tag{12}$$

the generators of $SU(N)$ satisfying the commutation relation:

$$\left[S_{\alpha,\beta,\vec{i}}, S_{\gamma,\delta,\vec{j}} \right] = \delta_{\vec{i},\vec{j}} \left(S_{\alpha,\delta,\vec{i}} \delta_{\gamma,\beta} - S_{\gamma,\beta,\vec{i}} \delta_{\alpha,\delta} \right). \tag{13}$$

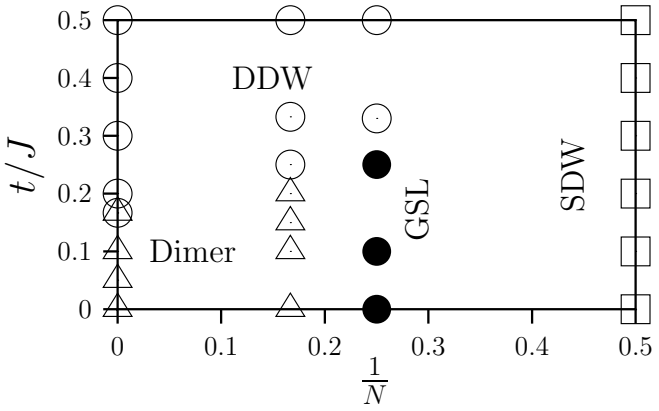

Figure 2. Phase diagram of the half-filled Hubbard-Heisenberg model as a function of t/J. Here we have set $U = 0$. The $t = 0$ line corresponds to the Heisenberg model where charge fluctuations are completely suppressed. The symbols denote the parameters where we have carried out simulations and denote the following phases: $\triangle$: Spin-dimerized phase, $\bigcirc$: DDW phase, $\square$: Spin-density wave phase, and $\bullet$: insulating phase with no broken lattice and spin symmetries and no gap spin excitations (gapless spin-liquid phase).

The representation of the $SU(N)$ group is determined by the local constraint

$$\vec{c}_{\vec{i}}^{\dagger}\vec{c}_{\vec{i}} = \rho\frac{N}{2}. \tag{14}$$

In the terminology of Young tableaux the above leads to a tableau with $\rho N/2$ rows and a single column[12]. In particular, at $N = 4$, and $\rho = 1/2$ (quarter band-filling) the model maps onto the $SU(4)$ symmetric Kugel-Khomskii Hamiltonian with fundamental representation of $SU(4)$ on each lattice site.

Our results are summarized in phase diagram of Fig. 2, and have been published in[4]. This phase diagram has attracted considerable interest, since it provides first realizations of exotic states such as the d-density wave state and the gapless spin liquid state. Let us start with the ordered phases, which are schematically shown in Fig. 3. In the spin dimerized phase, bonds joined by solid lines have a stronger exchange. This leads to an insulating spin gaped phase with broken translation symmetry. In the spin density wave phase, the spins order antiferromagnetically. Hence, translation as well as spin symmetry is broken. The DDW phase is characterized by alternating currents around elementary plaquettes. This leads to broken time and lattice symmetries. The DDW phase is a semi-metal; the single particle density of sates vanishes at the Fermi energy, but is finite at any excitation energy.

The gapless spin liquid phase (GPL) is an insulating state with algebraic staggered spin-spin correlations. It hence may be seen as a genuine Mott insulator. It's theoretical understanding is at present uncertain. A possible route one can follow to obtain a theoretical understanding is to assume that it is well described by a π-flux phase. In this case, Hermele et. al.[13] have recently argued that the SU(4) π-flux phase has a higher, $SU(8)$, emergent symmetry at low energies. The consequence of such a higher symmetry is that the asymptotic behavior of a priori very different correlation functions are locked together. For instance for our model, this higher symmetry predicts that the the $(0, \pi)$ spin-dimer

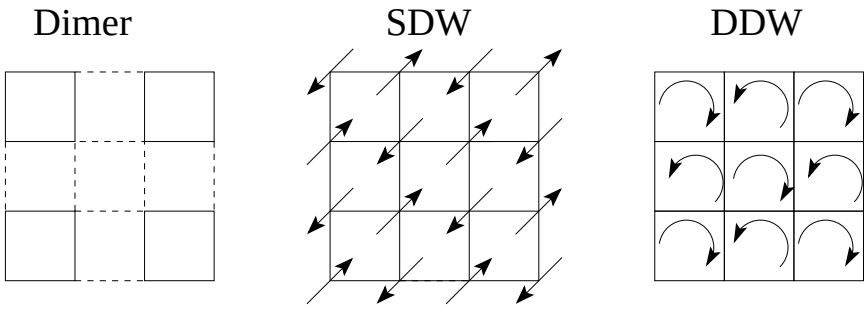

Figure 3. Schematic description of ordered phases.

correlations should have the same asymptotic behavior as the (π, π) spin-spin correlations. High accuracy large scale calculations to confirm this point of view are highly desirable.

4 Conclusions

In this article we have highlighted the complexity and interest in studies of correlated electron systems. One major challenge is on the algorithmic front. Here we are actively involved in the understanding and development of novel methods which have the potential of circumventing the so called minus sign problem for a large range of models of correlated electron systems. On the other hand, we have presented one typical application of numerical simulations of correlated electron system which leads to fascinating phase diagrams containing novel phases of matter.

Acknowledgments

The calculations presented here were carried out on the IBM p690 cluster of the NIC in Jülich. We would like to thank this institution for allocation of CPU time.

References

1. R. Preuss, A. Muramatsu, W. von der Linden, P. Dieterich, F.F. Assaad, and W. Hanke. Spectral properties of the one-dimensional hubbard model. *Phys. Rev. Lett.*, 73:732, 1994.
2. M. Feldbacher, F. F. Assaad, and K. Held. Projective quantum monte carlo method for the anderson impurity model and its application to dynamical mean field theory. *Phys. Rev. Lett.*, 93:136405, 2004.
3. F. F. Assaad. Quantum monte carlo simulations of the half-filled two-dimensional kondo lattice model. *Phys. Rev. Lett.*, 83:796, 1999.
4. F. F. Assaad. Phase diagram of the half-filled two-dimensional su(n) hubbard-heisenberg model: a quantum monte carlo study. *Phys. Rev. B*, 71:075103, 2005.
5. J. F. Corney and P. D. Drummond. Gaussian quantum monte carlo methods for fermions and bosons. *Phys. Rev. Lett.*, 93:260401, 2004.

6. F. F. Assaad, P. Werner, P. Corboz, E. Gull, and M. Troyer. Symmetry projection schemes for gaussian monte carlo methods. *Preprint cond-mat/0509149, to appear in PRB*.
7. M. Calandra Buonaura and S. Sorella. Numerical study of the two-dimensional heisenberg model using a green function monte carlo technique with a fixed number of walkers. *Phys. Rev. B*, 57:11446–11456, 1998.
8. F. F. Assaad. Quantum monte carlo methods on lattices: The determinantal method. In J. Grotendorst, D. Marx, and A. Muramatsu., editors, *Lecture notes of the Winter School on Quantum Simulations of Complex Many-Body Systems :From Theory to Algorithms.*, volume NIC series Vol. 10., pages 99–155. Publication Series of the John von Neumann Institute for Computing., 2002.
9. K. I. Kugel' and D. I. Khomskii. *Sov. Phys. Usp.*, 25:232, 1982.
10. Y. Q. Li, Michael Ma, D. N. Shi, and F. C. Zhang. Su(4) theory for spin systems with orbital degeneracy. *Phys. Rev. Lett.*, 81:3527, 1988.
11. C. Honerkamp and W. Hofstetter. Ultracold fermions and the su(n) hubbard model. *Phys. Rev. Lett.*, 92:170403, 2004.
12. N. Read and S. Sachdev. Some features of the phase diagram of the square lattice su(n) antiferromagnet. *Nucl. Phys. B*, 316:609, 1989.
13. Michael Hermele, T. Senthil, and Matthew P. A. Fisher. Algebraic spin liquid as the mother of many competing orders. `http://xxx.lanl.gov/cond-mat/0502215`.

John von Neumann Institute for Computing

Realistic Modeling of Materials with Strongly Correlated Electrons

Georg Keller, Karsten Held, Volker Eyert,
Vladimir I. Anisimov, Krysztof Byczuk, Markus Kollar,
Ivan Leonov, Xinguo Ren, and Dieter Vollhardt

published in

NIC Symposium 2006 ,
G. Münster, D. Wolf, M. Kremer (Editors),
John von Neumann Institute for Computing, Jülich,
NIC Series, Vol. **32**, ISBN 3-00-017351-X, pp. 183-190, 2006.

http://www.fz-juelich.de/nic-series/volume32

Realistic Modeling of Materials with Strongly Correlated Electrons

Georg Keller[1], Karsten Held[2], Volker Eyert[1], Vladimir I. Anisimov[3], Krzysztof Byczuk[1], Markus Kollar[1], Ivan Leonov[1], Xinguo Ren[1], and Dieter Vollhardt[1]

[1] Theoretical Physics III, Center for Electronic Correlations and Magnetism
Institute for Physics, University of Augsburg, 86135 Augsburg, Germany
E-mail: {Georg.Keller, Dieter.Vollhardt}@physik.uni-augsburg.de

[2] Max-Planck-Institut für Festkörperforschung, 70569 Stuttgart, Germany
[3] Institute of Metal Physics, S. Kovalevskoj Str. 18, Ekaterinburg GSP-170, 620219 Russia

1 Introduction

Modern solid state physics explains the physical properties of numerous materials such as simple metals, and some semiconductors and insulators. But materials with open d and f shells, where electrons occupy narrow orbitals, have properties that are harder to explain. In transition metals such as vanadium, iron and their oxides, for example, electrons experience strong Coulombic repulsion because of their spatial confinement in those orbitals. Such strongly interacting or "correlated" electrons cannot be described as embedded in a static mean field generated by the other electrons[1,2]. The d and f electrons have internal degrees of freedom (spin, charge, orbital moment) whose interplay leads to a whole "zoo" of exotic ordering phenomena at low temperatures. As a consequence, strongly correlated electron systems are extremely sensitive to small changes in their control parameters (temperature, pressure, doping, etc.), resulting in strongly nonlinear responses, and tendencies to phase separate or form complex patterns in chemically inhomogeneous situations. For this reason strongly correlated materials display dramatic effects which range from large changes of the resistivity across the metal-insulator transitions in V_2O_3, and considerable volume changes across phase transitions (volume collapse effect) in actinides and lanthanides, to exceptionally high transition temperatures (above liquid nitrogen temperatures) in superconductors with copper oxygen planes, and remarkable mass renormalizations in materials called heavy fermion systems which at low temperatures behave as free electrons with masses as large as a thousand times the mass of a free electron. Furthermore, some strongly correlated materials have a very large thermoelectric response. A great sensitivity of the resistivity to applied magnetic fields, dubbed colossal magnetoresistance was discovered recently and a gigantic nonlinear optical susceptibility with an ultrafast recovery time was discovered in Mott insulating chains. These properties make the prospects for applications of correlated materials exciting, and their theoretical and experimental study very challenging.

One especially striking correlation phenomenon is the phase transition between a paramagnetic metal and a paramagnetic insulator caused by the Coulomb interaction between the electrons which is referred to as Mott-Hubbard metal-insulator transition[1–3]. Reliable

microscopic investigations of this many-body phenomenon are known to be exceedingly difficult. Indeed, the question concerning the nature of this transition poses one of the fundamental theoretical problems in condensed matter physics. Correlation-induced metal-insulator transitions (MIT) of this type are found, for example, in transition metal oxides with partially filled bands near the Fermi level. In these systems band theory typically predicts metallic behavior. The most famous example is V_2O_3 doped with Cr[4]. While at low temperatures V_2O_3 is an antiferromagnetic insulator (AFI) with monoclinic crystal symmetry, the high-temperature paramagnetic phase has a corundum structure. The MIT in the paramagnetic phase is iso-structural; only the ratio of the c/a axes changes discontinuously. This may be taken as an indication for a predominantly electronic origin of this transition.

The investigation of electronic many-particle systems is made especially complicated by quantum statistics, and by the fact that the phenomena of interest (e.g., metal-insulator transitions and magnetism) usually require the application of nonperturbative theoretical techniques. In the last decade, a new approach for treating electronic lattice models, the dynamical mean-field theory (DMFT), has led to new analytical and numerical opportunities to study correlated electronic systems[1,5]. This theory – initiated by Metzner and Vollhardt in 1989 – is exact in the limit of infinite dimensions ($d = \infty$)[6]. In this limit, the problem is reduced to a single-impurity Anderson model with self consistency condition[7,8], allowing for quantum Monte-Carlo (QMC) simulations without a sign problem for one-band models (for multi-band models, see Ref. 9), i.e., down to temperatures $T \sim 10^{-2}W$ where W is the bandwidth.

Recently, the LDA+DMFT, a new computation scheme that merges electronic band structure calculations and the dynamical mean field theory, was developed[1,10,11]. Starting from conventional band structure calculations in the local density approximation (LDA) the correlations are taken into account by a Hubbard interaction term and a Hund's rule coupling term. The resulting DMFT equations are solved numerically with a parallelized auxiliary-field quantum Monte-Carlo algorithm (QMC). In contrast to LDA or LDA+U the many-body scheme LDA+DMFT provides the correct physics for all Coulomb interactions and dopings. Namely, LDA yields an uncorrelated metal even if the material at hand is a strongly-correlated metal or a Mott insulator. Similarly, LDA+U yields an insulator for the *ab-initio*-calculated U-values of 3d transition metal oxides, even for materials which should be metallic.

So far the LDA+DMFT method is the most successful tool available to investigate correlation effects in transition metal oxides. Recent developments will allow us to apply the method to a wider range of systems. In most previous studies the LDA band structure served only as input information for the DMFT, but there was no feedback from DMFT to LDA. Since the DMFT result can in principle change the charge distribution on which the LDA band structure depends one should feed back the changes introduced by the DMFT into LDA and repeat the calculation until convergence is reached in both parts. This procedure is currently being investigated. Furthermore, calculations should not only include the orbitals of the correlated electrons, but *all* hybridizing orbitals. Such an extended computational scheme has recently been developed and applied in Wannier basis[12]. For crystal structures with strong hybridization and/or low symmetry it is also necessary to obtain the off-diagonal matrix elements of the local Green function from the QMC calculation. This extension is currently being tested and will be applied in our future computational

investigations of correlated materials.

In this paper we limit our discussion to the LDA+DMFT investigation of only one material, namely V_2O_3 in the paramagnetic insulating and metallic phase.

2 The LDA+DMFT Method

In a first step, the LDA band structure and the densities of states for the crystal structures of metallic V_2O_3 and insulating $(V_{0.962}Cr_{0.038})_2O_3$ are calculated. The LDA DOS for both materials are found to be metallic in contrast to experimental results. The reason for this failure is the fact that LDA deals with electronic correlations only very rudimentarily, namely, the dependence of the LDA exchange-correlation energy on the electron density is given by perturbative or quantum Monte-Carlo calculations for jellium[13], which is a weakly correlated system. To overcome this shortcoming, we supplement the LDA band structure by the the most important Coulomb interaction terms, i.e., the local Coulomb repulsion U and the local Hund's rule exchange J. The local Coulomb repulsion U gives rise to a genuine effect of electronic correlations, the Mott-Hubbard metal-insulator transition[1,5,14]. If the LDA bandwidth is considerably larger than the local Coulomb interaction, the LDA results are slightly modified but the system remains a metal. If the LDA bandwidth is much smaller than the local Coulomb interaction one essentially has the atomic problem where it costs an energy of about U to add an electron and the system is an insulator. In between the Mott-Hubbard metal-insulator transition occurs, with V_2O_3 being on the metallic side whereas $(V_{0.962}Cr_{0.038})_2O_3$, which has a 0.1-0.2 eV smaller bandwidth, is on the insulating side.

Interpreting the LDA band structure as resulting from a one-particle Hamiltonian $\hat{H}^0_{\mathrm{LDA}}$ and supplementing the latter with the local Coulomb interactions gives rise to the multi-band many-body Hamiltonian[10,15]

$$\hat{H} = \hat{H}^0_{\mathrm{LDA}} + U \sum_{i\ m} \hat{n}_{im\uparrow}\hat{n}_{im\downarrow} + \sum_{i\ m\neq\tilde{m}\ \sigma\tilde{\sigma}} (V - \delta_{\sigma\tilde{\sigma}} J)\ \hat{n}_{im\sigma}\hat{n}_{i\tilde{m}\tilde{\sigma}}. \quad (1)$$

Here, i denotes the lattice site and $\hat{n}_{im\sigma}$ is the operator for the occupation of the t_{2g} orbital m with spin $\sigma \in \{\uparrow, \downarrow\}$. The interaction parameters are related by $V = U - 2J$ which is a consequence of orbital rotational symmetry. This holds exactly for degenerate orbitals and is a good approximation for V_2O_3 where the t_{2g} bands have similar centers of gravity and bandwidths. As in the local spin density approximation (LSDA), the spin-flip term of the exchange interaction is not taken into account in Eq. (1). Furthermore, a pair hopping term proportional to J is neglected since it requires that one orbital is entirely empty while another is entirely full which is a rare situation and corresponds to highly excited states. For the Hund's rule coupling J we take the value $J = 0.93$ eV obtained from constrained LDA. By contrast, a reliable calculation of the Coulomb repulsion U is made difficult by the fact that U depends sensitively on screening, leading to uncertainties of about 0.5 eV[11]. For our present purposes this uncertainty is too large since V_2O_3 is on the verge of a Mott-Hubbard metal-insulator transition, and, thus, small changes of U have drastic effects. Therefore we will choose U in such a way as to ensure that the LDA+DMFT solution for V_2O_3 is metallic while that for $(V_{0.962}Cr_{0.038})_2O_3$ is insulating. *A posteriori*, we will

compare the adjusted value with those calculated by constrained LDA calculations and those extracted from the experiment.

So far, we did not specify $\hat{H}^0_{\rm LDA}$. In principle, it should contain the valence orbitals, i.e., the oxygen $2p$ orbitals and the five vanadium $3d$ orbitals per atom and, perhaps, even some additional s orbitals. In V_2O_3 the three t_{2g} bands at the Fermi energy are well separated from the other orbitals. Therefore, as a first step we restrict ourselves to the three t_{2g} bands at the Fermi energy which are made up of the corresponding atomic vanadium $3d$ orbitals with some admixtures of oxygen p orbitals. In the case of three degenerate t_{2g} orbitals, which is a good approximation in the case of V_2O_3 since the bandwidths and centers of gravity of the a_{1g} and the doubly-degenerate e^π_g band are very similar, the $\boldsymbol{k}$-integrated Dyson equation simplifies to become an integral over the DOS[15]

$$G_m(\omega) = \int \mathrm{d}\epsilon \frac{N^0_m(\epsilon)}{\omega + \mu - \Sigma_m(\omega) - \epsilon}. \tag{2}$$

Here $G_m(\omega)$, $\Sigma_m(\omega)$, and $N^0_m(\epsilon)$ are the Green function, self energy, and LDA density of states, respectively, for the t_{2g} orbital m. In principle, $N^0_m(\epsilon)$ should contain a double counting correction, which takes into account the fact that parts of the local Coulomb interaction are already included in the LDA. However, this correction results in the same effect for all three orbitals and, hence, only translates into a simple shift of the chemical potential μ. This makes the issue of how to calculate the double counting correction irrelevant for the present purposes. The (shifted) μ has to be controlled according to the vanadium valency, i.e., in such a way that there are two electrons in the three bands at the Fermi energy.

Within DMFT the $\boldsymbol{k}$-integrated Dyson equation (2) has to be solved self-consistently together with a one-site (mean field) problem which is equivalent to an Anderson impurity model with hybridization $\Delta_m(\omega')$ fulfilling[5]

$$[G_m(\omega)]^{-1} + \Sigma_m(\omega) = \omega + \mu - \int_{-\infty}^{\infty} \mathrm{d}\omega' \, \frac{\Delta_m(\omega')}{\omega - \omega'}. \tag{3}$$

The self-consistent solution of the Anderson impurity model given by (3) together with the Dyson equation (2) allows for a realistic investigation of materials with strongly correlated electrons. At small values of U this procedure typically yields a spectrum with a central quasiparticle resonance at the Fermi energy and incoherent Hubbard side bands, while at larger values of U the quasiparticle resonance disappears and a metal-insulator transition occurs. This approach has been successfully applied to a number of transition metal oxides, transition metals, and elemental Pu and Ce[15].

In the present paper, we solve the multi-band Anderson impurity model by QMC[16,5], where by means of the Trotter discretization and Hubbard-Stratonovich transformations the interacting Anderson impurity model is mapped into a sum of non-interacting problems, the sum being performed by the Monte-Carlo technique. We employ a Trotter discretization of $\Delta\tau = 0.25\,\mathrm{eV}^{-1}$ unless noted otherwise and follow Ref. 17 for the Fourier transformation between Matsubara frequencies and imaginary time τ.

To obtain the physically relevant spectral function $A_m(\omega) = -\frac{1}{\pi}\mathrm{Im}G_m(\omega)$ we employ the maximum entropy method[18]. This statistical approach allows one to solve

$$G_m(\tau) = \int_{-\infty}^{\infty} \mathrm{d}\omega \, \frac{e^{\tau(\mu-\omega)}}{1 + e^{\beta(\mu-\omega)}} A_m(\omega) \tag{4}$$

for $A_m(\omega)$, i.e., to analytically continue from imaginary time to real frequencies. The QMC has the advantage of being numerically exact, the main disadvantage being the inability to reach very low temperatures. Indeed, the room temperature calculations of this paper were computationally very expensive, using up to 40 iterations with up to 2×10^5 sweeps and requiring about 2×10^5 hours CPU time. For the implementation of QMC in the context of LDA+DMFT, including flow diagrams, see Ref. 15.

3 Results for V_2O_3

Using the crystal structure of paramagnetic metallic (PM) V_2O_3 and paramagnetic insulating (PI) $(V_{0.962}Cr_{0.038})_2O_3$, respectively, as input we performed LDA+DMFT(QMC) calculations with one a_{1g} and two degenerate e_g^π bands. At $U = 4.5\,\mathrm{eV}$ both crystal structures lead to spectra showing metallic behavior, with a lower Hubbard band between $-2\,\mathrm{eV}$ and $-0.5\,\mathrm{eV}$ (peaked at about $-1\,\mathrm{eV}$), an upper Hubbard band between $1\,\mathrm{eV}$ and $6\,\mathrm{eV}$ and a quasiparticle peak at the Fermi edge. The peak at about $1\,\mathrm{eV}$ is split from the upper t_{2g} Hubbard band due to Hund's rule exchange.

By contrast, at $U = 5.5\,\mathrm{eV}$, both crystal structures lead to spectra showing nearly insulating behavior. The lower Hubbard band is strongly enhanced whereas at the Fermi edge a pseudo-gap is formed. Above the Fermi energy, the two-peak structure is changed only slightly.

Apparently, qualitatively different spectra for the two crystal structures require an intermediate value of U. This is indeed observed at $U = 5.0\,\mathrm{eV}$. Whereas pure V_2O_3 now shows a small peak at the Fermi edge (a residue of the quasiparticle peak obtained at $U = 4.5\,\mathrm{eV}$) and is therefore metallic, the Cr-doped system exhibits a pronounced minimum in the spectrum implying that it is nearly insulating. Due to the rather high temperature at which the QMC simulations were performed ($T = 0.1\,\mathrm{eV} \approx 1160\,\mathrm{K}$) one observes only a smooth *crossover* between the two phases with a metal-like and insulator-like behavior of the respective curves instead of a sharp metal-insulator transition as would be expected for temperatures below the critical point (i.e., for $T < 400\,\mathrm{K}$ in the experiment).

To study V_2O_3 near the metal-insulator transition at experimentally relevant temperatures we performed calculations at $T = 700\,\mathrm{K}$ and $T = 300\,\mathrm{K}$. Since the computational effort is proportional to T^{-3}, those low temperature calculations were computationally very expensive. Fig. 1 shows the results of our calculations at $T = 1160\,\mathrm{K}$, $T = 700\,\mathrm{K}$, and $T = 300\,\mathrm{K}$ for metallic V_2O_3 and at $T = 1160\,\mathrm{K}$ and $T = 700\,\mathrm{K}$ for insulating $(V_{0.962}Cr_{0.038})_2O_3$[19]. In the metallic phase the incoherent features are hardly affected when the temperature is changed, whereas the quasiparticle peak becomes sharper and more pronounced at lower temperatures.

In Fig. 2, the LDA+DMFT results at $300\,\mathrm{K}$ are compared with early photoemission spectra by Schramme[20] and recent high-resolution bulk-sensitive photoemission spectra by Mo *et al.*[21]. The strong difference between the experimental results is now known to be due to the distinct surface sensitivity of the earlier data. In fact, the photoemission data by Mo *et al.*[21] obtained at $h\nu = 700\,\mathrm{eV}$ and $T = 175\,\mathrm{K}$ exhibit, for the first time, a pronounced quasiparticle peak. This is in good qualitative agreement with our low temperature calculations. However, the experimental quasiparticle peak has more spectral weight. We note that while in the theory the peak considerably sharpens with decreasing temperatures, its weight only increases by 11% from 1160K to 300K. The origin for this discrepancy for a system as close to a Mott transition as V_2O_3 is presently not clear.

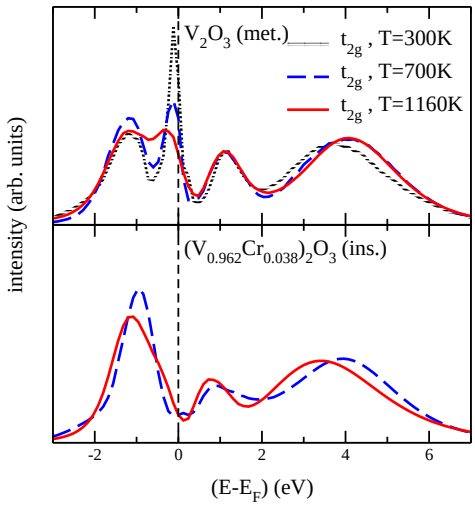

Figure 1. LDA+DMFT(QMC) spectra for paramagnetic insulating $(V_{0.962}Cr_{0.038})_2O_3$ and metallic V_2O_3 at $U = 5$ eV.

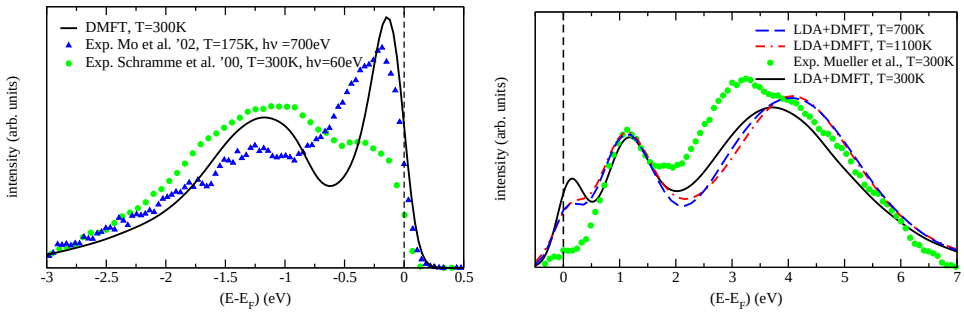

Figure 2. Right: Comparison of LDA+DMFT(QMC) results at $T = 300\,\mathrm{K}$ and $U = 5$ eV with photoemission data by Schramme *et al.*[20] and Mo *et al.*[21] for metallic V_2O_3; Left: Comparison of LDA+DMFT(QMC) results at $U = 5$ eV with X-ray absorption data by Müller *et al.*[22] for metallic V_2O_3

While the comparison with PES data provides important insight into the physics of V_2O_3, more than half of the theoretical spectrum lies above E_F. For this region we compare our results at $1160\,\mathrm{K}$, $700\,\mathrm{K}$, and $300\,\mathrm{K}$ with O $1s$ X-ray absorption spectra (XAS) for V_2O_3 at $300\,\mathrm{K}$ by Müller *et al.*[22] (see Fig. 2). Since in the XAS-data the Fermi energy is not precisely determined, the data were shifted so that the peaks at $1.1\,\mathrm{eV}$ coincide; all curves were normalized to the same area.

The theoretical spectra above E_F are found to be almost independent of temperature. Just above the Fermi energy they all show some structure (i.e., a shoulder at higher temperatures developing into a small peak at low temperatures ($300\,\mathrm{K}$)) which is the residue of the quasiparticle peak. Furthermore, at $1.1\,\mathrm{eV}$ there is a rather narrow peak, and at about

4.2 eV a broad peak. The latter two structures are parts of the upper Hubbard band which is split due to the Hund's rule coupling J. Hence, the relative position of those two peaks can be expected to depend sensitively on the value of J. A slightly smaller value of J will therefore yield an even better agreement with experiment.

The absence of any quasiparticle weight near E_F in the XAS data is puzzling. This quasiparticle weight is not only present in the theoretical spectra above *and* below E_F, but is also seen in the high resolution PES measurements by Mo *et al.*[21] below E_F.

4 Concluding Remarks

At present, LDA+DMFT is the only available *ab initio* computational technique which is able to treat heavy fermions, f-electron materials and correlated electron systems close to a Mott-Hubbard metal-insulator transition. Using LDA-calculated densities of states for paramagnetic metallic V_2O_3 as well as paramagnetic insulating $(V_{0.962}Cr_{0.038})_2O_3$ as input, we performed DMFT(QMC) calculations at 300 K, 700 K, and 1160 K for various U values. For $U \approx 5$ eV, the calculated spectra show a Mott-Hubbard MIT (or, rather, a sharp crossover).

The 300 K spectrum calculated for metallic V_2O_3 is in good overall agreement with new bulk-sensitive PES measurements[21]. On the other hand, the difference in the quasiparticle weight remains to be explained. The comparison with X-ray absorption measurements shows that our LDA+DMFT(QMC) calculations also give a good description of the spectrum above the Fermi energy.

All calculations described above were performed using the integral over the LDA density of states (Eq. (2)) to obtain the lattice Green function. For a non-cubic system, this procedure is an approximation to the exact LDA+DMFT scheme. In the future we plan to make use of the full Hamiltonian H^0 (Eq. (1)). In this way it will be possible to study the influence of correlation effects on all orbitals including the e_g^σ orbitals and the oxygen states.

The multi-orbital quantum Monte-Carlo simulations used in our LDA+DMFT calculations are computationally very expensive and require powerful computing resources, especially for calculations at experimentally relevant temperatures.

Acknowledgments

We thank J. W. Allen, I. S. Elfimov, M. Feldbacher, S. Horn, A. I. Lichtenstein, A. I. Poteryaev, Th. Pruschke, G. A. Sawatzky and L.H. Tjeng for valuable discussions. This work was supported in part by the Deutsche Forschungsgemeinschaft (DFG) through Sonderforschungsbereich 484, the Emmy Noether program of the DFG (K. H.), the Russian Foundation for Basic Research Grant No. RFFI-01-02-17063 (V. I. A.), the Leibniz-Rechenzentrum, München, and the John von Neumann - Institut für Computing, Jülich. We thank A. Sandvik for making his maximum entropy code available to us.

References

1. For an introductory discussion see G. Kotliar and D. Vollhardt, Physics Today **57**, No. 3 (March), 53 (2004).

2. For a recent review of the electronic correlation problem, see M. Imada, A. Fujimori, and Y. Tokura, Rev. Mod. Phys. **70**, 1039 (1998).
3. N. F. Mott, Rev. Mod. Phys. **40**, 677 (1968); *Metal-Insulator Transitions* (Taylor & Francis, London, 1990).
4. D. B. McWhan, A. Menth, J. P. Remeika, W. F. Brinkman, and T. M. Rice, Phys. Rev. B **7**, 1920 (1973).
5. A. Georges, G. Kotliar, W. Krauth and M. Rozenberg, Rev. Mod. Phys. **68**, 13 (1996).
6. W. Metzner and D. Vollhardt, Phys. Rev. Lett. **62**, 324 (1989).
7. A. Georges and G. Kotliar, Phys. Rev. B **45**, 6479 (1992).
8. M. Jarrell, Phys. Rev. Lett. **69**, 168 (1992).
9. One limitation of QMC is that it is very difficult to deal with the spin-flip term of the Hund's rule coupling because of a "minus-sign problem" which arises in a Hubbard-Stratonovich decoupling of this spin-flip term, see K. Held, Ph.D. thesis, Universität Augsburg 1999 (Shaker Verlag, Aachen, 1999).
10. V. I. Anisimov, A. I. Poteryaev, M. A. Korotin, A. O. Anokhin, and G. Kotliar, J. Phys.: Cond. Matt. **9**, 7359 (1997); A. I. Lichtenstein and M. I. Katsnelson, Phys. Rev. B **57**, 6884 (1998).
11. I. A. Nekrasov, K. Held, N. Blümer, V. I. Anisimov, and D. Vollhardt, Euro. Phys. J. B **18**, 55 (2000).
12. V. I. Anisimov, D. E. Kondakov, A. V. Kozhevnikov, I. A. Nekrasov, Z. V. Pchelkina, J. W. Allen, S.-K. Mo, H.-D. Kim, P. Metcalf, S. Suga, A. Sekiyama, G. Keller, I. Leonov, X. Ren, and D. Vollhardt, Phys. Rev. B **71**, 125119 (2005).
13. L. Hedin and B. Lundqvist, J. Phys. C: Solid State Phys. **4**, 2064 (1971); U. von Barth and L. Hedin, J. Phys. C: Solid State Phys. **5**, 1629 (1972); D. M. Ceperley and B. J. Alder, Phys. Rev. Lett. 45, 566 (1980).
14. R. Bulla, T. A. Costi, D. Vollhardt, Phys. Rev. B **64**, 045103 (2001).
15. For reviews see K. Held, I. A. Nekrasov, G. Keller, V. Eyert, N. Blümer, A.K. McMahan, R.T. Scalettar, Th. Pruschke, V.I. Anisimov und D. Vollhardt, "Realistic investigations of correlated electron systems with LDA+DMFT", Psi-k Newsletter #56, 65 (2003) `http://psi-k.dl.ac.uk/newsletters/News_56/Highlight_56.pdf`; A. I. Lichtenstein, M. I. Katsnelson, G. Kotliar, *Electron Correlations and Materials Properties 2*, 2nd ed., A. Gonis, N. Kioussis, M. Ciftan, ed. Kluwer Academic/Plenum, New York (2003), available at `http://arXiv.org/abs/cond-mat/0211076`.
16. J. E. Hirsch and R. M. Fye, Phys. Rev. Lett. **56**, 2521 (1986).
17. M. Ulmke, V. Janiš, and D. Vollhardt, Phys. Rev. B **51**, 10411 (1995).
18. M. Jarrell and J. E. Gubernatis, Physics Reports **269**, 133 (1996).
19. In spite of extensive computations the calculations at 300 K in the insulating phase did not yield sufficiently converged results and are therefore not shown in Fig. 1.
20. M. Schramme, Ph.D. thesis, Universität Augsburg, 2000; M. Schramme *et al.* (unpublished).
21. S.-K. Mo, J. D. Denlinger, H.-D. Kim, J.-H. Park, J. W. Allen, A. Sekiyama, A. Yamasaki, K. Kadono, S. Suga, Y. Saitoh, T. Muro, P. Metcalf, G. Keller, K. Held, V. Eyert, V. I. Anisimov, D. Vollhardt, Phys. Rev. Lett. **90**, 186403 (2003).
22. O. Müller, J.-P. Urbach, E. Goering, T. Weber, R. Barth, H. Schuler, M. Klemm, S. Horn, and M. L. denBoer Phys. Rev. B **56**, 15056 (1997).

John von Neumann Institute for Computing

Conductance in Coupled Quantum Dots: Indicator for a Local Quantum Phase Transition

Frithjof B. Anders, Eran Lebanon, and Avraham Schiller

published in

NIC Symposium 2006 ,
G. Münster, D. Wolf, M. Kremer (Editors),
John von Neumann Institute for Computing, Jülich,
NIC Series, Vol. **32**, ISBN 3-00-017351-X, pp. 191-200, 2006.

http://www.fz-juelich.de/nic-series/volume32

Conductance in Coupled Quantum Dots: Indicator for a Local Quantum Phase Transition

Frithjof B. Anders[1,2], **Eran Lebanon**[3], **and Avraham Schiller**[4]

[1] Theoretische Physik, Universität des Saarlands
66041 Saarbrücken, Germany
[2] Institut für Theoretische Physik, Universtät Bremen
P.O. Box 330 440, 28334 Bremen, Germany *E-mail: anders@itp.uni-bremen.de*
[3] Department of Physics and Astronomy, Rutgers University
136 Frelinghuysen Road, Piscataway, NJ 08854-8019, USA
[4] Racah Institute of Physics, The Hebrew University
Jerusalem 91904, Israel

We report on transport properties of a nanostructed device consisting of an ultra-small quantum dot coupled to two leads and a larger quantum dot. The finite capacitance of both quantum dots leads to new and unusual transport properties when the temperature is lower than the charging energy E_c of the larger dot. The zero-bias transport is governed by the filling of the large dot as well as the ratio of the tunnel matrix elements between the small dot and leads, t_L, and between small and the large dot, t_B. For given external gate voltages of small and large dot, we find a critical ratio $t_c = t_B/t_L$ at which the zero-bias jumps from a high to a low conductance value. The quantum critical point is described by an unstable fixed point with non-Fermi liquid properties and governs the transition from one Fermi-liquid to another.

1 Introduction

Since the discovery of the Kondo effect in ultra-small quantum dots[1,2], nano-devices have become an increasingly important tool to test our fundamental understanding of elementary excitations in solid state physics. Measurements on the metallic heavy fermion (HF) compounds and high temperature superconductors[3,4] have challenged the paradigm of Landau's Fermi-liquid concept. For those deviations, the phenomenological term non-Fermi liquid (nFL) was attributed to such regimes appearing in a large variety of different materials[3,4]. The understanding of the observed nFL behavior is one of the most challenging and unsolved theoretical puzzles. In many materials, it is ascribed to a quantum critical point (QCP) at which a transition temperature is suppressed to $T = 0$ by an external control parameter such as pressure or doping[5,6].

Quantum dots behave in many respects as an artificial atom. One has experimental control over the "atomic" level position as well as coupling to the environment by external gate electrodes. Therefore, they are expected to be an ideal test system for concepts of *local quantum phase transitions*. In this work, we present numerical calculations on a system of coupled quantum dots as depicted in figure 1. Such a coupled quantum dot device consisting of a large quantum dot or quantum box and a small quantum dot or single electron transistor[7] (SET) undergoes a quantum phase transition at $T = 0$ for odd filling of the small dot which can be seen by the following arguments. When the small dot is tuned to odd occupation the $T \to 0$ physics is described by a strong coupling fixed point. If t_B is set to zero the dot is strongly coupled to the leads, and the conductance approaches its optimal (unitary) value. If, on the other hand, t_B finite and $t_l = t_r = 0$, the dot is coupled

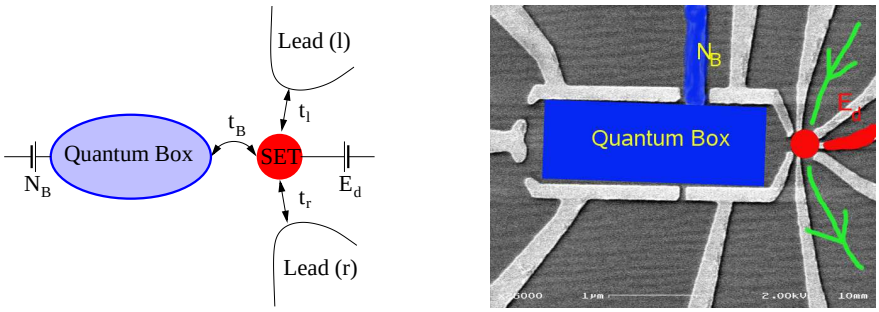

(a) (b)

Figure 1. A sketch (a) of an ultra-small quantum dot coupled to two leads and a large quantum dot and its experimental realization by the group of D. Goldhaber-Gordon, who provided us with a picture of their realization.

strongly to the box (the renormalization group flow stops when T is reduced below the mean level spacing of the large dot), and the conductance is obviously zero. Switching on a very small coupling between the leads and the small dot does not change the physics since (i) the fixed point is stable, and (ii) the charging energy of the large dot will suppress charge fluctuations between leads and the small dot. Since these two limits are described by *two* complementary stable Fermi-liquid fixed points, there will be a quantum phase transition (QPT) at some critical coupling ratio $t_c = t_B/t_L$. This quantum critical point is associated with an unstable two-channel Kondo fixed point which has non-Fermi liquid properties[8]. Oreg and Goldhaber-Gordon conjectured the existence of such a non-Fermi liquid fixed point[9] for the local moment regime of the SET. We, however, have shown that the QPT is generic and associated with a dynamical generation of the channel symmetry and spin-conserving tunneling[10].

2 Modelling the Coulomb Blockade on Quantum Dots

Due to the confinement of the electrons in such an ultra-small quantum dot to a diameter of a few $100nm$, it has a mean one-particle level spacing of $\Delta E \approx 300 - 400\mu eV$ and a charging energy of $E_c \approx 1meV$. The energy on the dot is given by the Hamiltonian $\hat{H}_{qdot}$

$$\hat{H}_{qdot} = \sum_{i\sigma} E_i d^\dagger_{i\sigma} d_{i\sigma} + E_c \left(\hat{N} - N_B\right)^2 \tag{1}$$

where the charging energy $E_c = e^2/2C_0$ is related to the classical capacitance C_0 of the dot[7], and $\hat{N}$ measures its total number of electrons. Here, $d^\dagger_{i\sigma}$ creates an electron on the dot in level i with energy E_i and N_B denotes the external dimensionless potential governing the filling of the dot. Since spin-orbit scattering is proportional to the velocity it is strongly suppressed in quantum dots due to the confinement, and the pseudo spin σ is a good quantum number. The Hamiltonian (1) describes a classical capacitor for temperatures $k_B T \gg E_c$ with a linear dependence of the charge $Q = e\langle\hat{N}\rangle$ on the external voltage V. At temperatures much smaller that E_c, the quantization of the charge leads to

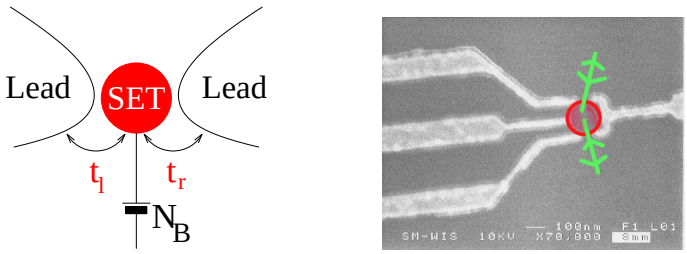

Figure 2. Single electron transistor[7] coupled to two leads (a) and its experimental realization, Figure taken from Ref.[1]

the discrete fillings. When $N_B = n + 1/2$, the energy is degenerate for the filling with n and $n + 1$ electrons. At $T = 0$, the charging will occur in steps as a function of N_B, and the charge Q is constant for $n - 1/2 < N_B < n + 1/2$.

2.1 Coupling to Leads

When coupling such a device weakly to two leads, as depicted in Fig. 2, a current can only flow at those charge degeneracy points for very small bias difference $|V_{sd}| \ll E_c$ and $k_B T \ll E_c$. Due to the finite charging energy, one electron can hop onto the dot only after the previous one has left the device, and the current flow is controllable by the potential N_B. The device operates as *single-electron transistor*[7] (SET) at temperatures $k_B T \ll E_c$. Characteristic for such a device are the nearly equally spaced conductance peaks as function of N_B from which E_c is obtained[7]. The width of these conductance peaks are fully determined by the temperature broadening which is used in commercially available low temperature thermometers[11].

If operated in a strong coupling mode, the line width is determined by the charge fluctuation scale $\Gamma_0 = \pi t^2 \rho_F$ rather than the temperature, where ρ_F denotes the density of states of the lead electrons at the chemical potential. At odd fillings, a new exponentially small low energy scale $T_K \propto \exp(-\alpha E_c/\Gamma_0)$ occurs due to the Kondo effect[12] (α measures the particle-hole asymmetry.) At temperatures below this crossover scale T_K an additional conduction channel opens up, and the Coulomb blockade is lifted[1]. Therefore, an increasing conductance is experimentally observed for decreasing T[1,2] saturating at the unitary limit of $2e^2/h$. In order to observe the Kondo effect experimentally, the devices are operated in a strong coupling regime of $k_B T \ll \Gamma \approx E_c/10$.

For ultra-small quantum dots, ΔE is larger than the charge fluctuation scale, $\Delta E > \Gamma_0$. At sufficiently low temperatures ($\beta \Delta E > 1$,) $\hat{H}_{qdot}$ can be replaced by an single effective spin degenerate level with the external controllable energy $E_d \propto N_B$ and the Coulomb repulsion U. In this case, Eqn. (2) is identical to the single impurity Anderson model[13].

2.2 Description of the Coulomb Blockade of a Large Quantum Dot

The coupled quantum dot–lead system is conventionally modelled by the Hamiltonian

$$\mathcal{H} = \hat{H}_{qdot} + \sum_{\gamma=l,r} \sum_{k\sigma} \epsilon_{\gamma k} c^\dagger_{\gamma k\sigma} c_{\gamma k\sigma} + \sum_\gamma t_\gamma \sum_{k,i\sigma} \left(c^\dagger_{\gamma k\sigma} c_{i\sigma} + \text{H.c.} \right), \tag{2}$$

where $c^\dagger_{\gamma k\sigma}$ creates a lead electron with momentum k and spin σ in the lead $\gamma = l, r$. t_γ is the tunneling matrix element, taken for simplicity to be momentum and level independent. The single-particle levels in the leads $\epsilon_{\gamma k}$ are assumed to be continuous (dense energy levels). It is obvious, that in equilibrium only the binding linear combination of lead states $c_{k\sigma} = (t_l c_{Lk\sigma} + t_r c_{Rk\sigma})/\sqrt{t_l^2 + t_r^2}$ couples to the quantum dot with the effective tunnel matrix element $t_L = \sqrt{t_l^2 + t_r^2}$. We drop the anti-binding combination and treat the leads as as single fermionic bath.

Since the charging term $E_c(\hat{N} - N_B)^2$ in $\hat{H}_{qdot}$ is long ranged for a large dot with many one-particle levels, perturbation theory as well as RG methods fail to describe the crossover from the classical to the quantum regime of Hamiltonian (2). The problem becomes accessible to Wilson's numerical renormalization group (NRG) by introducing an effective charge degree of freedom $\hat{N} = \sum_n n|n\rangle\langle n|$ and the corresponding ladder operators $N^\pm = \sum_n |n \pm 1\rangle\langle n|$ independent of the number of Fermions. The price is a modification of the tunneling term[14] to

$$H_T = t \sum_{ik\sigma} \left(c^\dagger_{k\sigma} c_{i\sigma} N^- + c^\dagger_{i\sigma} c_{k\sigma} N^+ \right) \tag{3}$$

in order to keep track of the change of charge on the dot. The charging term $E_c(\hat{N} - N_B)^2$ becomes part of an effective impurity, and H_T can easily be treated within the NRG. We have shown that our theory describes accurately the crossover from the classical to the quantum regime[14] for all parameter regimes. Moreover, the effective capacitance diverges logarithmically with temperature at the charge step, indicating a quantum phase transition between two Fermi-liquids with different dot charges. The QCP is characterized by a charge two channel Kondo fixed point[14,15].

3 Modelling of Coupled Quantum Dots

Interesting new physics[9,10,16] arises when we combine these two limits for quantum-dots into one single nano-device. An ultra-small quantum dot with a large level spacing is coupled to two leads and also to a quantum box. This device and its experimental realization is shown in Fig. 1. For $k_B T \gg E_c$, the device behaves as simple SET. For $\beta E_c \gg E_c$, however, a second conduction channel is dynamically generated: charge fluctuations from the leads to the quantum box through the SET, possible at high temperatures, are now suppressed. We expect a quantum phase transition as function of the ratio t_B/t_L where the quantum critical point is described by a non-Fermi liquid fixed point.

The Hamiltonian for such a device is given by extension[10] of (2)

$$\begin{aligned} \mathcal{H} = &\sum_\sigma (E_d + \frac{U}{2} n_{-\sigma}) n_\sigma + E_c(\hat{N} - N_B)^2 + \sum_{\alpha=L,B,k\sigma} \epsilon_{\alpha k} c^\dagger_{\alpha k\sigma} c_{\alpha k\sigma} \\ &+ t_L \sum_{k\sigma} \left(c^\dagger_{Lk\sigma} d_\sigma + d^\dagger_\sigma c_{Lk\sigma} \right) + t_B \sum_{k\sigma} \left(c^\dagger_{Bk\sigma} d_\sigma N^+ + d^\dagger_\sigma c_{Bk\sigma} N^- \right), \end{aligned} \tag{4}$$

where we restrict ourselves to a single level with energy E_d on the SET and to the binding combination of lead states. The charging energy of the SET is given by U. While electrons tunnel between the binding combination of leads and SET with the amplitude t_L, the tunneling term to the quantum box is modified by the ladder operators $N^{\pm}$ in order to take into account the change of charge.

4 Theory

We accurately solve Hamiltonian (4) using Wilson's numerical renormalization group[12,17] best suited for this quantum impurity problem. The key ingredient in the NRG is a logarithmic discretization of the continuous bath, controlled by the parameter $\Lambda > 1$[12]. The Hamiltonian is mapped onto a semi-infinite chain, where the Nth link represents an exponentially decreasing energy scale $D_N \sim \Lambda^{-N/2}$. Using this hierarchy of scales the sequence of finite-size Hamiltonians $\mathcal{H}_N$ for the N-site chain is solved iteratively, truncating the high-energy states at the conclusion of each step so as to maintain a manageable number of states. The reduced basis set of $\mathcal{H}_N$ so obtained faithfully describes the spectrum of the full Hamiltonian on a scale of D_N, corresponding to the temperature $T_N \sim {D_N}$[12] from which all thermodynamic expectation values are calculated.

In addition to the total spin component S_z^{tot}, we also use the particle number and the conserved flavor $\tau_z^{tot} = \hat{N} + (\hat{N}_L - \hat{N}_B)/2$ to classify the symmetries of subspaces of the Hamiltonians H_N. Since all subspaces can be diagonalized independently, we have fully parallelized our NRG code on the IBM Regatta using POSIX threads. The setup of the Hamiltonian matrices is mainly performed using ESSL and BLAS routines so that our C^{++} code runs highly efficiently on SMP platforms such as the Regatta.

5 Results

5.1 Thermodynamics

By investigating the effective capacitance of the quantum box, $C_{eff} = e\partial\langle N\rangle/\partial N_B$ near the charge step[16], we have shown that $C_{eff}(T)$ diverges logarithmically for a particular gate voltage at fixed coupling ratio: the slope of the charge becomes infinitely steep. The associated non-Fermi liquid quantum critical point consists of a charge two-channel Kondo fixed point[15,8] plus a marginal operator describing the particle-hole asymmetry[18]. The charge on the quantum box is screened through charge fluctuations[16] with the SET which resembles an anisotropic Kondo interaction in the flavor space[15].

In this work, we focus on the local spin screening. For a given set of parameters, we tune the ratio t_B/t_L to its critical value t_c such that the Pauli-like local spin susceptibility of the SET $\chi_{spin} = \partial\langle\hat{S}_z^{SET}\rangle/\partial_H$, for $|t_B/t_L - t_c| > 0$ becomes logarithmically divergent at t_c. The results of such computational expensive scans are depicted in Fig. 3 for different values of gate voltage E_d of the SET and experimentally typical ratios of parameters $U/E_c \approx 10$, $E_c/\Gamma_L = 1$. By fitting of χ to $\chi(T) = -(1/20T_K^{QPT})\ln\left(T/T_K^{QPT}\right) + b$, we have extracted the characteristic energy scale T_K^{QPT} of the non-Fermi liquid fixed point. The crossover from a Curie law to a logarithmically divergent $\chi(T)$ approaching the QCP is governed by $T_{min} = \min\{T_K, E_c\}$. We observed that the charge[16] and spin[9,10] QCP

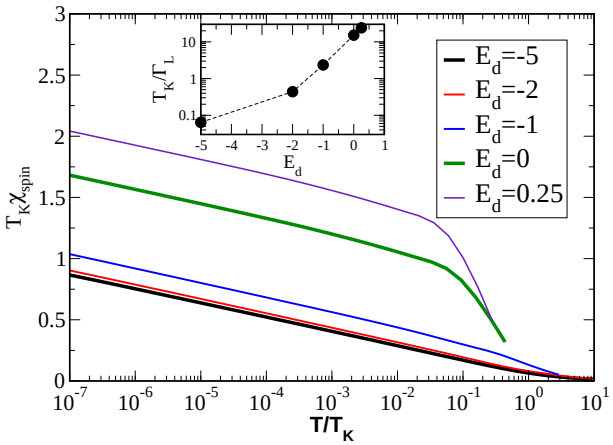

Figure 3. The spin susceptibility χ of the dot versus T, for $\Gamma_L = E_c = 0.1D$, $N_B = 0$, $U/E_c = 10$ and different gate voltages E_d. Here t_B is tuned for each value of U to quantum phase transition. Inset: T_K versus E_d. NRG parameters: $\Lambda = 2.8$, $N_s = 2000$.

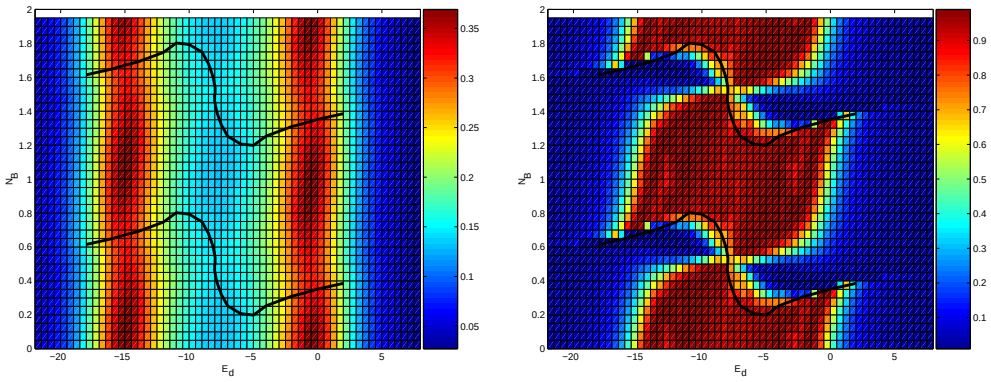

Figure 4. Color coded zero Bias conductance as function of the two gate voltages E_d and N_B for a fixed coupling ratio $t_B^2/t_L^2 = 1.2$ and $E_c/\Gamma_L = 2, U/\Gamma = 16$ at (a) $T/\Gamma_L = 0.65$. and (b) $T/\Gamma_L = 3.1 * 10^{-4}$. The black line indicates the quantum critical line. NRG parameters: $\Lambda = 4$, $N_s = 800$. Each point consumed about 15h CPU time on the IBM Regatta.

points are connected, in fact, can be identical. That implies that this distinction is somewhat misleading and arises since physical operators such as charge, spin or flavor (not investigated yet) couple with different matrix elements to the leading irrelevant operator of the non-Fermi liquid fixed point.

5.2 Zero-Bias Conductance

For calculating the zero bias conductance $G(T)$ through the SET,

$$G(T)/G_0 = \Gamma_L \sum_\sigma \int d\omega \, \left(-\frac{\partial f(\omega)}{\partial \omega}\right) \rho_\sigma^d(\omega, T) \tag{5}$$

we need the finite temperature spectral function $\rho_\sigma^d(\omega)$ of the Green function $\ll d_\sigma | d_\sigma^\dagger \gg$, where $\Gamma_L = \pi t_L^2 \rho_F$, and $G_0 = (2e^2/h) 4 t_l^2 t_r^2/(t_r^2 + t_r^2)^2$ measures the optimal conductance for generic couplings t_l and t_r between the two leads where $t_L^2 = t_l^2 + t_r^2$. The spectral function obtained directly with the NRG, however, is not accurate enough to calculate the conductance reliably. We use an equation of motion[19,20] technique in combination with an new algorithm to calculate finite temperature spectral functions for multi-band models as described in detail in the appendix of reference[21]. Since our algorithm allows to evaluate $\rho(\omega, T)$ independently for each ω, we use a massively parallelized algorithm to generate $\rho(\omega, T)$ for frequencies on a logarithmic mesh for a whole set of frequencies and temperatures independently in one NRG run.

Experimentally, however, the ratio of t_B/t_L is kept fixed since t_α does not depend linearly on the external potentials. The zero bias conductance for large set of parameters (E_d, N_B) at fixed $t_B^2/t_L^2 = 1.2$ is plotted for two different temperatures in Fig. 4. Since each color point stems from one NRG run, we needed to reduce the number of state N_s kept at each iteration and increase Λ. At high temperatures, $k_B T \approx E_c/4$, the conductance is almost independent of the filling of the large dot. The conductance peaks at the charge steps of the small dot at $E_d/\Gamma_L \approx -15$ and $E_d \approx 0$. The picture changes completely at low temperatures. For $N_B \approx 0$, we find a regime of high conductance at filling $\langle n_d \rangle \approx 1$ due to the Kondo effect where the conductance is close to the optimal conductance G_0. At an E_d dependent value of N_B, however, we observe sharp drop in the conductance. This correlates with the quantum critical line (QCL) added as a black line in the plots. On the other hand, the conductance changes gradually at half integer filling of the coupled dot which occurs at $-15 < E_d < -12$ in the depicted conductance plots of Fig. 5.

The conductance for four different values of N_B, horizontal lines in Fig. 4b, is depicted in 5a. For $N_B = 0.2$, the QCL is not crossed and the usual lifting of the Coulomb blockade due to the Kondo effect is seen at odd SET filling between $-16 < E_d < 0$. For $N_B = 0.25, 0.3, 0.35$, the parameter E_d intersects twice the QCL as can be seen in Fig.4. Consequently, the three curves for $N_B = 0.25, 0.3, 0.35$ show a pronounced supression of the conductance between these intersection points. At $T = 0$, the conductance will exhibit a jump at these two intersection values of E_d defining the QCP. For particle-hole symmetry, the conductance curves collapse onto two master curves when scaled as $x = T/(t_B/t_L - t_c)^2$ shown in Fig. 5b.

6 Concluding Remarks

We calculate the thermodynamical and transport properties of a novel coupled quantum dot device using our extension to the NRG. Since the subspaces of the Hamiltonians can be diagonalized independently, we can use a highly efficient parallelized code on the IBM Regatta to solve this complex many-body problem accurately. We find a line of quantum critical points which governs the crossover from a high to a low conducting Fermi liquid.

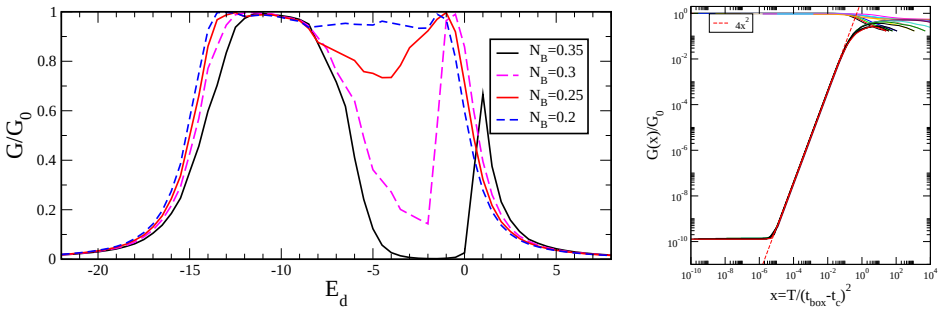

(a) (b)

Figure 5. Conductance (a) vs E_d for four different values of N_B at $T/\Gamma_L = 3.1 * 10^{-4}$. For $N_B = 0.2$, the Coulomb blockade is lifted, and $G/G_0 \approx 1$ for $\langle n_d \rangle \approx 1$. For $N_B > 0.2$ the QCL is crossed twice leading to sudden decrease of G. Data taken from Fig. 4. (b) Conductance vs $x = T/(t_B/t_L - t_c)^2$ (b) for $E_d/\Gamma_0 = -5$, $U/\Gamma_0 = 10$, $N_B = 0$, $\Lambda = 2.8$ and $N_s = 2500$ and 21 different values of t_B/t_L.

We showed that the zero-bias conductance can be used to indicate the phase line since a drop of the conductance is observed which becomes increasingly sharp. Since our theory is valid for arbitrary parameters, we can make contact to the experimentally relevant parameter regime where spin and charge fluctuation scales are not well separated.

Acknowledgments

We have benefited from discussions with D. Goldhaber-Gordon and R. Potok and are thankful for letting us use the image of their device. F.B.A. acknowledges funding of the NIC, Forschungszentrum Jülich, under project no. HHB000. EL was supported by DOE grant DEFE02-00ER45790.

References

1. D. Goldhaber-Gordon *et al.*, Nature **391**, 156 (1998).
2. W.G. van der Wiel *et al.*, Science **289**, 2105 (2000).
3. M. B. Maple *et al.*, J. Low Temp. Phys. **99**, 223 (1995).
4. G. R. Stewart, Rev. Mod. Phys **73**, 797 (2001).
5. H. von Löhneyen, J. Phys., Condens. Matter **8**, 9689 (1996).
6. F. Steglich *et al.*, J. Phys., Condens. Matter **8**, 9909 (1996).
7. M A Kastner, Rev. Mod. Phys. **64**, 849 (1992).
8. D. L. Cox and A. Zawadowski, Advances in Physics **47**, 599 (1998).
9. Y. Oreg and D. Goldhaber-Gordon, Phys. Rev. Lett. **90**, 136602 (2003).
10. F. B. Anders, E. Lebanon, and A. Schiller, Phys. Rev. B **70**, 201306 (2004).
11. J. P. Pekola *et al.*, Phys. Rev. Lett. **73**, 2903 (1994).
12. K. G. Wilson, Rev. Mod. Phys. **47**, 773 (175).
13. P. W. Anderson, Phys. Rev. **124**, 41 (1961).
14. E Lebanon, A Schiller, and F B Anders, Phys. Rev. B **68**, 041311 (2003).

15. K A Matveev, Zh. Eksp. Teor. Fiz. **99**, 1598 (1991).
16. E. Lebanon, A. Schiller, and F. B. Anders, Phys. Rev. B **68**, 155301 (2003).
17. H. R. Krishna-murthy, J. W. Wilkins, and K. G. Wilson, Phys. Rev. B **21**, 1003 (1980).
18. H. R. Krishna-murthy, J. W. Wilkins, and K. G. Wilson, Phys. Rev. B **21**, 1044 (1980).
19. R. Bulla, A. C. Hewson, and Th. Pruschke, J. Phys., Condens. Matter **10**, 8365 (1998).
20. F. B. Anders, Phys. Rev. B **71**, 121101 (2005).
21. F. B. Anders and G. Czycholl, Phys. Rev. B **71**, 125101 (2005).

John von Neumann Institute for Computing

Spectral Properties of Strongly Correlated Electron Phonon Systems

Gerald Schubert, Andreas Alvermann, Alexander Weiße,
Georg Hager, Gerhard Wellein, and Holger Fehske

published in

NIC Symposium 2006 ,
G. Münster, D. Wolf, M. Kremer (Editors),
John von Neumann Institute for Computing, Jülich,
NIC Series, Vol. **32**, ISBN 3-00-017351-X, pp. 201-210, 2006.

http://www.fz-juelich.de/nic-series/volume32

Spectral Properties of Strongly Correlated Electron Phonon Systems

Gerald Schubert[1], **Andreas Alvermann**[1], **Alexander Weiße**[1], **Georg Hager**[2], **Gerhard Wellein**[2], **and Holger Fehske**[1]

[1] Institut für Physik, Universität Greifswald
17487 Greifswald, Germany
E-mail: {*schubert, alvermann, weisse, fehske*}*@physik.uni-greifswald.de*

[2] Regionales Rechenzentrum Erlangen, Universität Erlangen
91058 Erlangen, Germany
E-mail: {*georg.hager, gerhard.wellein*}*@rrze.uni-erlangen.de*

1 Introduction

In the last few years solid state physics has increasingly benefited from scientific computing, and the importance of numerical techniques is likely to keep on growing quickly in this field. Because of the high complexity of solids, which are made up of a huge number of interacting electrons and nuclei, a full understanding of their properties cannot be developed using analytical methods only. Numerical simulations do not only provide quantitative results for the properties of specific materials but are also widely used to test the validity of theories and analytical approaches.

Unbiased numerical approaches, like exact diagonalisation (ED)[1], or the density matrix renormalisation group (DMRG)[2] are of particular importance for the investigation of low-energy and low-temperature electronic, optical, or magnetic properties of various novel materials, which cannot be understood within traditional many-particle theory. In such strongly correlated systems, the interactions between the constituents of the solid are so strong that they can no longer be considered separately and collective effects emerge. As a result, these systems may exhibit new and fascinating macroscopic properties. Quasi-one-dimensional (1d) electron-phonon (EP) systems like MX-chain compounds are prominent examples of electronic systems very different from traditional ones[3]. Their study is particularly rewarding for a number of reasons. First they exhibit a remarkably wide range of competing forces, which gives rise to a rich variety of different phases, characterised by symmetry-broken ground states and long-range orders. Second, 1d models allow us to investigate this complex interplay, which is important but poorly understood also in 2d and 3d highly-correlated electron systems, in a context more favourable to numerical simulations. Because the complexity of the systems leads to huge requirements of memory and CPU time, access to large computational resources is necessary.

2 Models

Experiments on a variety of novel materials, ranging from quasi-1d MX solids[3], organics[4] and quasi-2d high T_c cuprates[5] to 3d colossal-magnetoresistive manganites[6], provide clear evidence for the existence of polaronic carriers, i.e., quasi particles consisting of an electron

and a surrounding lattice distortion. This has motivated considerable theoretical efforts to archive a better understanding of strongly coupled EP systems in the framework of microscopic models.

To describe the interplay between electrons and the dynamics of the lattice, which is known to play a key role for instance in quasi-1d metals and charge-density-wave (CDW) systems, one of the simplest model is the Holstein-Hubbard model (HHM):

$$H = -t \sum_{\langle i,j\rangle\sigma} c^\dagger_{i\sigma} c_{j\sigma} - g\omega_0 \sum_{i\sigma} (b^\dagger_i + b_i) n_{i\sigma} + \omega_0 \sum_i b^\dagger_i b_i + U \sum_i n_{i\uparrow} n_{i\downarrow} \,. \qquad (1)$$

Here $c^\dagger_{i\sigma}$ ($c_{i\sigma}$) denote fermionic creation (annihilation) operators of electrons with spin $\sigma =\uparrow, \downarrow$ on site i of a 1d lattice with N sites, $n_{i\sigma} = c^\dagger_{i\sigma} c_{i\sigma}$, and $b^\dagger_i$ (b_i) are the corresponding bosonic operators for dispersionless optical phonons. The physics of the HHM is governed by three competing effects: The itinerancy of the electrons ($\propto t$), their on-site Coulomb repulsion ($\propto U$), and the local EP coupling ($\propto g$). Since the EP interaction is retarded, the phonon frequency (ω_0) defines a further relevant energy scale. Hence, besides the adiabaticity ratio (ω_0/t) we need two dimensionless coupling constants ($u = U/4t$ and $\lambda = 2\varepsilon_{\rm p}/2t$ or $g^2 = \varepsilon_{\rm p}/\omega_0$). In the single-electron case, where the spin degree of freedom and the Coulomb interaction are irrelevant, the Holstein model[7],

$$H = -t \sum_{\langle i,j\rangle} c^\dagger_i c_j - \sqrt{\varepsilon_p \omega_0} \sum_i (b^\dagger_i + b_i) n_i + \omega_0 \sum_i b^\dagger_i b_i \,, \qquad (2)$$

has been studied extensively as a paradigmatic model for polaron formation[8]. Here $\varepsilon_{\rm p}$ gives the polaron binding energy.

As yet, none of the various analytical treatments, based on weak- and strong-coupling adiabatic and anti-adiabatic perturbation expansions[9], are suited to investigate the physically most interesting polaron transition region. Here, the characteristic electronic and phononic energy scales are not well separated and non-adiabatic effects become increasingly important. This implies a breakdown of the standard Migdal approximation. Quasi-approximation-free numerical methods like quantum Monte Carlo (QMC)[10,11] or ED and DMRG can, in principle, bridge the gap between the weak- and strong-EP-coupling limits, and currently represent the most reliable tools to study polarons close to the cross-over regime[12].

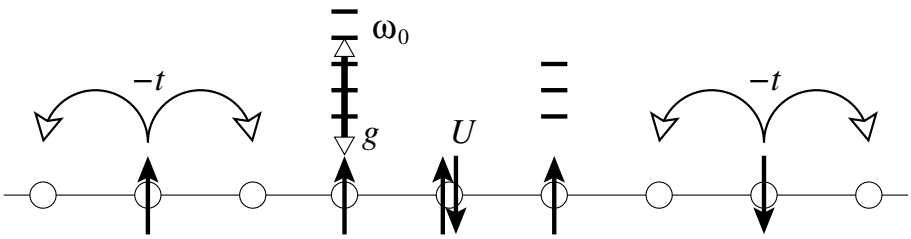

Figure 1. Schematic representation of the 1d Holstein-Hubbard model.

3 Implementation of Matrix Vector Multiplication (MVM)

The core operation of most ED and DMRG algorithms is a MVM. It is quite obvious, that our matrices are extremely sparse because the number of non-zero entries per row of our Hamilton matrix scales linearly with the number of electrons. Therefore a standard implementation of the MVM step uses a sparse storage format for the matrix, holding the non-zero elements only. Two data schemes are in wide use, the compressed row storage (CRS) and the jagged diagonal storage (JDS) format, where the latter one is the method of choice for vector computers. The typical storage requirement per non-zero entry is 12-16 Byte for both methods, i.e. for a matrix dimension of $\tilde{D} = 10^9$ about one TByte main memory is required to store only the matrix elements of the EP Hamiltonian. Both variants can be applied to any sparse matrix structure and the MVM step can be be done in parallel by using a parallel library such as PETSc (see `http://www-unix.mcs.anl.gov/petsc/petsc-as/`).

To extend our EP studies to even larger matrix sizes we store no longer the non-zero matrix elements but generate them in each MVM step. Of course, at that point standard libraries are no longer useful and a parallel code tailored to each specific class of Hamiltonians must be developed. For the Holstein-Hubbard EP model we have established a massively parallel program using the Message Passing Interface (MPI) standard. The minimal total memory requirement of this implementation is three vectors with Hilbert space dimension.

The parallelisation approach follows the inherent natural parallelism of the Hilbert space, which can be constructed as the tensorial product space of electrons and phonons $\{|\tilde{b}\rangle = |\tilde{e}\rangle \otimes |p\rangle\}$. Assuming, that the electronic dimension ($\tilde{D}_e$) is a multiple of the number of processors used (N_{cpu}) we can easily distribute the electronic basis states among these processors, i.e. processor $i (0 \leq i \leq N_{\mathrm{cpu}} - 1)$ is holding the basis states ($\tilde{e}_i = i\tilde{D}_e/N_{\mathrm{cpu}} + 1, \ldots, (i+1)D_e/N_{\mathrm{cpu}}$). As a consequence of this choice only the electronic hopping term generates inter-processor communication in the MVM while all other (diagonal electronic) contributions can be computed locally on each processor.

Furthermore, the communication pattern remains constant within a single run for all MVM steps and the message sizes (at least D_p words) are large enough to ignore the latency problems of modern interconnects. Using supercomputers with hundreds of processors and one TBytes of main memory, such as IBM p690 clusters or SGI Altix systems, we are able to run simulations up to a matrix dimension of 30×10^9.

4 Spectral Properties

4.1 Photoemission Spectra

Examining the dynamical properties of polarons, it is of particular interest whether a quasi-particle-like excitation exists in the spectrum. This is probed by direct (inverse) photoemission, where a bare electron is removed (added) from (to) the many-particle system containing N_e electrons. The intensities (transition amplitudes) of these processes are determined by the imaginary part of the retarded one-particle Green's functions,

$$G^{\pm}(k,\omega) = \langle\langle c_k^{\mp}; c_k^{\pm}\rangle\rangle_{\omega} = \lim_{\eta \to 0^+} \langle\psi_0| c_k^{\mp} \left[\omega + \mathrm{i}\eta - H\right]^{-1} c_k^{\pm} |\psi_0\rangle \,, \tag{3}$$

i.e., by the momentum resolved spectral functions

$$A^{\pm}(k,\omega) = -\frac{1}{\pi}\mathrm{Im}\, G^{\pm}(k,\omega) = \sum_m |\langle\psi_m^{\pm}|c_k^{\pm}|\psi_0\rangle|^2\, \delta[\omega \mp (E_m^{\pm} - E_0)] \qquad (4)$$

and $A(k,\omega) = A^+(k,\omega) + A^-(k,\omega)$, with $c_k^+ = c_k^\dagger$ and $c_k^- = c_k$. These functions test both the excitation energies $E_m^{\pm} - E_0$ and the overlap of the ground state $|\psi_0\rangle$ with the exact eigenstates $|\psi_m^{\pm}\rangle$ of a $(N_\mathrm{e} \pm 1)$-particle system. Hence, $G^+(k,\omega)$ $[G^-(k,\omega)]$ describes the propagation of an additional electron [a hole] with momentum k $[-k]$ and energy ω. The electron spectral function of the single-particle Holstein model corresponds to $N_\mathrm{e} = 0$, i.e., $A^-(k,\omega) \equiv 0$. $A(k,\omega)$ can be determined, e.g., by cluster perturbation theory (CPT)[13,12]: We first calculate the Green's function $G_{ij}^c(\omega)$ of a N_c-site cluster with open boundary conditions for $i,j = 1,\ldots,N_c$, and then recover the infinite lattice by pasting identical copies of this cluster along the edges, treating the inter-cluster hopping in first-order perturbation theory.

Figure 2 shows that at *weak coupling* (left panel), the electronic spectrum is nearly unaffected for energies below the phonon emission threshold. Hence, for the case considered here with ω_0 lying inside the bare electron bandwidth $4t$, the renormalised dispersion $E(k)$ follows the tight-binding cosine dispersion (lowered $\propto \varepsilon_p$) up to some k_X, where the dispersionless phonon intersects the bare electron band. For $k > k_X$, electron and phonon states "hybridise", and repel each other, leading to the well-known band-flattening phenomenon[14]. The high-energy incoherent part of the spectrum is broadened $\propto \varepsilon_p$, with the k-dependent maximum again following the bare cosine dispersion.

The inverse photoemission spectrum in the *strong-coupling case* is shown in the right panel of Fig. 2. First, we observe all signatures of the famous polaronic band-collapse, where a well-separated, narrow (i.e., strongly renormalised), coherent QP band is formed at $\omega \simeq -\varepsilon_p$. If we had calculated the polaronic instead of the electronic spectral function (4), nearly all spectral weight would reside in the coherent part, i.e., in the small-polaron band[15]. In contrast, the wave-vector renormalisation factor $Z(k)$ is extremely small and approaches the strong-coupling result $Z = \exp(-g^2)$ for $\lambda, g^2 \gg 1$. Note

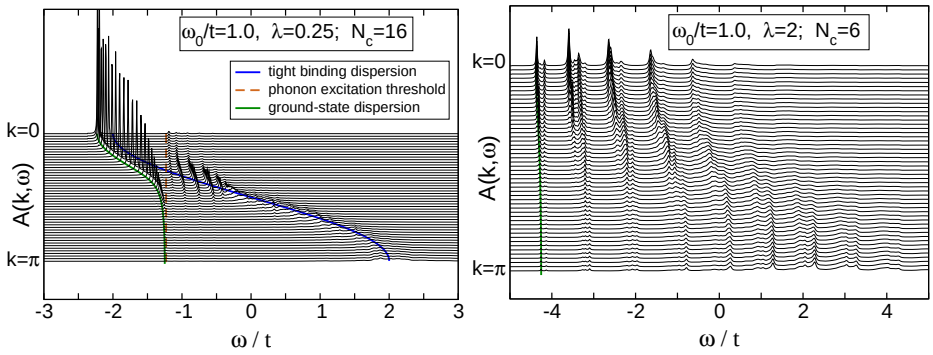

Figure 2. Spectral function of the 1d Holstein polaron calculated within CPT in the weak (left) and strong (right) non-adiabatic EP coupling regime. CPT is based on ED of a finite cluster with N_c sites and $M = 7$ ($\lambda = 0.25$) and $M = 25$ ($\lambda = 2$) phonon quanta.

that the inverse effective mass m^*/m_0 and $Z(k)$ differ if the self-energy is strongly k-dependent. This discrepancy has its maximum in the intermediate-coupling regime for 1D systems, but vanishes in the limit $\lambda \to \infty$ and, in any case, for $D = \infty$[16]. The incoherent part of the spectrum is split into several sub-bands separated in energy by ω_0, corresponding to excitations of an electron and one or more phonons (Fig. 2).

4.2 Optical Response

We apply the ED-KPM scheme outlined in[12,17,18] to calculate the optical absorption of the single-electron Holstein model. The results for the (regular) real part of the conductivity,

$$\mathrm{Re}\,\sigma(\omega) = \frac{\pi}{\omega N} \sum_{E_m > E_0} |\langle \psi_m | \hat{\jmath} | \psi_0 \rangle|^2 \, \delta[\omega - (E_m - E_0)] \tag{5}$$

(here $\hat{\jmath} = -\mathrm{i}et \sum_i (c_i^\dagger c_{i+1} - c_{i+1}^\dagger c_i)$ is the current operator), and possible deviations from established polaron theory are important for relating theory to experiment. For $T = 0$ the standard description of small polaron transport[19] yields (in leading order) the ac conductivity $\mathrm{Re}\,\sigma(\omega) = (\sigma_0/\omega\sqrt{\varepsilon_p \omega_0}) \exp\left[-(\omega - 2\varepsilon_p)^2/4\varepsilon_p\omega_0\right]$, which for sufficiently strong coupling predicts a weakly asymmetric Gaussian absorption peak centred at twice the polaron binding energy.

Figure 3 shows $\mathrm{Re}\,\sigma(\omega)$ when polaron formation sets in (left panel), and above the transition point (right panel). For $\lambda = 2$ and $\omega_0/t = 0.4$, i.e., at rather large EP coupling but not in the extreme small-polaron limit, we find a pronounced maximum in the low-temperature optical response, which, however, is located below $2\varepsilon_p$, the value for small polarons at $T = 0$. At the same time, the line-shape is more asymmetric than in small-polaron theory, with a weaker decay at the high-energy side, fitting even better to experiments on standard polaronic materials such as TiO_2[20]. At smaller couplings, significant deviations from a Gaussian-like absorption are found, i.e., polaron motion is not adequately described as hopping of a self-trapped carrier almost localised on a single site.

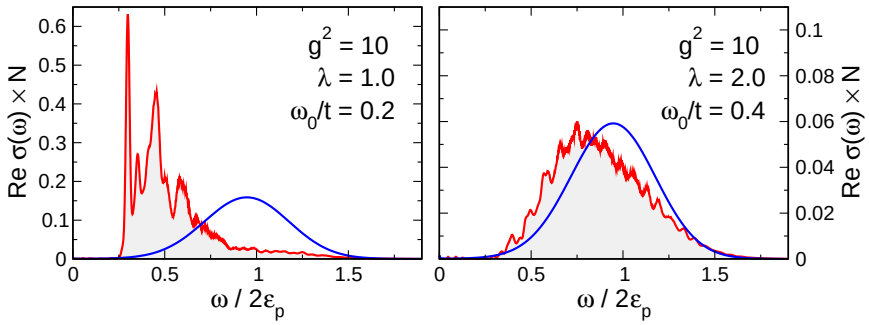

Figure 3. Optical conductivity (red, in units of $\pi e^2 t^2$) of the 1d Holstein model at $T = 0$ compared to the analytical small-polaron result (blue). ED data are for a system with six sites and 45 phonons; σ_0 is determined to give the same integrated spectral weight as $\mathrm{Re}\,\sigma(\omega > 0)$.

5 Quantum Phase Transitions in 1d Electron-Phonon Systems

Most notably quasi-1d materials are very susceptible to structural distortions driven by EP interaction. Probably the most famous one is the Peierls instability[21] of 1d metals: As the temperature is lowered the system creates a periodic variation in the carrier density by shifting the ions from their symmetric positions. For the half-filled band case this CDW is commensurate with the lattice, the unit cell doubles, and the system possesses a spontaneous broken-symmetry ground state. Since a static dimerisation of the lattice opens a gap at the Fermi surface the metal gives way to a Peierls insulator (PI) [see Fig. 4].

The on-site Coulomb interaction, on the other hand, tends to immobilise the charge carriers and establish a Mott insulating ground state. The Mott insulator (MI) exhibits strong spin density wave (SDW) correlations but has continuous symmetry and therefore shows no long-range order in 1d. Then, of course, the question arises, whether the PI and MI phases are separated by one (or more than one) quantum critical point(s) at $T = 0$, and if so, how the cross-over is modified by quantum phonon effects.

The challenge of understanding such quantum phase transitions has stimulated intense work on the Holstein Hubbard model. As yet there exist almost no exact (analytical) results for this model. At least at half-filling, however, it has become generally accepted that the interplay of charge, spin and lattice degrees of freedom gives rise to the phase diagram sketched in Fig. 5. This scenario is supported by dynamical mean field investigations of

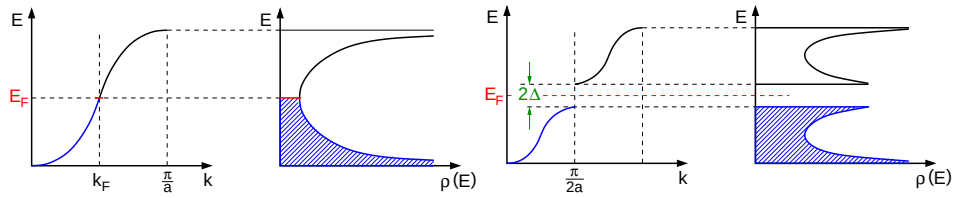

Figure 4. Peierls scenario: A gap 2Δ opens in the electronic band structure $E(k)$ [density of states $\rho(E)$] of an 1d metal if, as a result of the EP coupling, a static lattice distortion occurs, implicating a new lattice period $2a$ in real space.

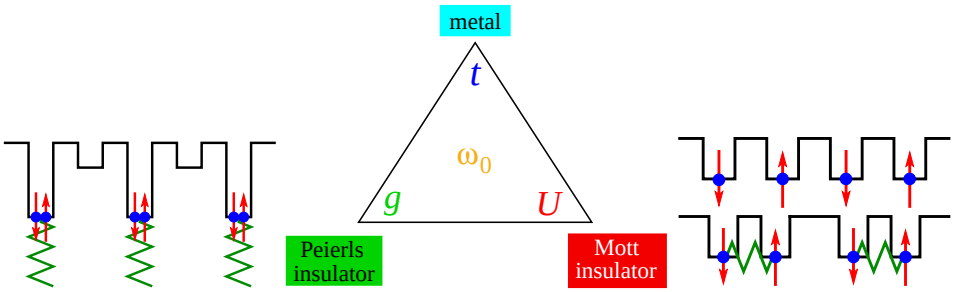

Figure 5. Schematic phase diagram of the 1d Holstein Hubbard model. At half-filling, Peierls (left) or Mott (right) insulating phases may be favoured over the metallic state. In the case of localised electrons interacting via antiferromagnetic exchange and magneto-elastic couplings even a spin-Peierls distorted state can emerge (right, lower panel).

the HHM, which become reliable at least in infinite spatial dimension[22].

Besides the properties of the ground state, the nature of the physical excitations is puzzling as well, especially in 1d. While one expects "normal" electron-hole pair excitations in the PI phase ($U = 0$), charge (spin) excitations are known to be massive (gapless) in the MI state of the Hubbard model ($\lambda = 0$). Thus, varying the control parameter u/λ, a cross-over from standard quasi-particle behaviour to spin-charge separation can be observed in the 1d HHM.

Since many-body gaps to excited states form the basis for making contact with experimentally measurable excitation gaps and can also be used to characterise different phases

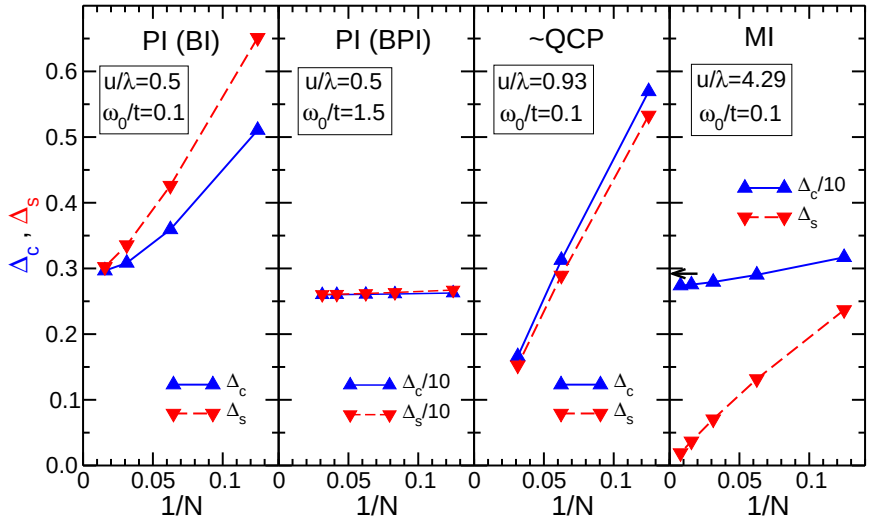

Figure 6. DMRG finite-size scaling of spin- and charge excitation gaps in the HHM at $\lambda = 0.35$ and $\omega_0/t = 0.1$). Open and filled symbols denote DMRG results for PBC and OPC boundary conditions, respectively. The accessible system sizes are smaller at larger λ/u, where an increasing number of (phononic) pseudo-sites is required to reach convergence with respect to the phonons. Stars represent the ED results for the eight-site system. The arrow marks the value of the optical gap $\Delta_{\rm opt}$ for the Bethe ansatz solvable 1d Hubbard model, which is given by $\Delta_{\rm opt}/4t = u - 1 + \ln(2)/2u$ in the limit of large $u > 1$[23].

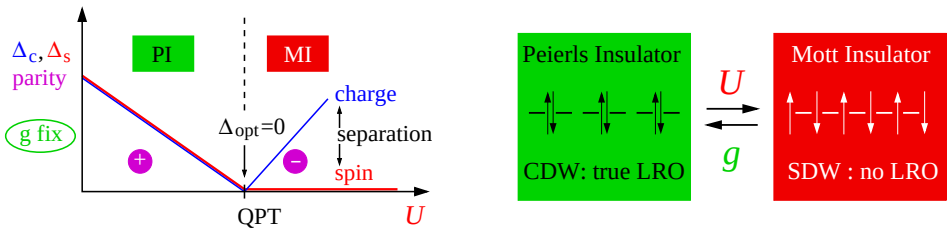

Figure 7. Sketch of the PI-MI quantum phase transition in the Holstein Hubbard model.

of the HHM, we have determine the charge and spin gaps,

$$\Delta_{\rm c} = E_0^+(1/2) + E_0^-(-1/2) - 2E_0(0) \tag{6}$$

$$\Delta_{\rm s} = E_0(1) - E_0(0)\,, \tag{7}$$

using DMRG, supplemented by a finite-size scaling. Here $E_0^{(\pm)}(S^z)$ is the ground-state energy of the HHM at half-filling (with $N_{\rm e} = N \pm 1$) particles in the sector with total spin-z component S^z.

Obviously, $\Delta_{\rm c}$ and $\Delta_{\rm s}$ are finite in the PI and converge to the same value for $N \to \infty$. Both gaps seem to vanish at the QCP of the HHM with finite-frequency phonons, but the finite-size scaling is extremely delicate in the critical region. In the MI we found a finite charge excitation gap, which in the limit $u/\lambda \gg 1$ scales to the optical gap of the Hubbard model, whereas the extrapolated spin gap remains zero. This can be taken as a clear indication for spin charge separation.

From our conductivity data for the half-filled band case (not shown) we found evidence for only one critical point separating Peierls and Mott insulating phases in the Holstein Hubbard model with dynamical phonons (by contrast in the adiabatic limit ($\omega_0 = 0$) two successive transitions have been detected for weak couplings u, $\lambda \ll 1$[24]). We have explicitly verified that the parity is $P = +1$ ($P = -1$) in the PI (MI) phase. The emerging physical picture can be summarised by the phase diagram shown in Fig. 7.

6 Summary

In this contribution, we have analysed the spectral properties of Holstein polarons as well as the transition from a Peierls- to Mott-insulator by means of quasi-exact numerical methods, such as Jacobi-Davidson based exact diagonalisation, kernel polynomial expansion techniques, density matrix renormalisation group and cluster perturbation theory, implemented on the NIC supercomputers. Our numerical approaches yield unbiased results in all parameter regimes, and are of particular value in the non-adiabatic intermediate-coupling regime, where perturbation theories and other analytical techniques fail.

Acknowledgements

We are grateful to A. R. Bishop, M. Hohenadler, D. Ihle, E. Jeckelmann and J. Loos for helpful discussions. Special thanks go to NIC Jülich for granting access to their supercomputer facilities.

References

1. J. Ranninger and U. Thibblin. *Phys. Rev. B*, 45:7730, 1992.
2. E. Jeckelmann and S. R. White. *Phys. Rev. Lett.*, 80:2661, 1998.
3. A. R. Bishop and B. I. Swanson. *Los Alamos Science*, 21:133, 1993.
4. I. H. Campbell and D. L. Smith. *Solid State Physics*, 55:1, 2001.
5. A. S. Alexandrov and N. F. Mott. *Polarons and Bipolarons*. World Scientific, Singapore, 1995.
6. G. Zhao, K. Conder, H. Keller, and K. A Müller. *Nature*, 381:676, 1996.
7. T. Holstein. *Ann. Phys. (N.Y.)*, 8:325, 1959.
8. H. Fehske, A. Alvermann, M. Hohenadler, and G. Wellein. *Proceedings of the "Enrico Fermi" Summer School, Course CLXI -"Polarons in Bulk Materials and Systems with Reduced Dimensionality"*, Varenna, 2005.
9. A. B. Migdal. *Sov. Phys. JETP*, 7:999, 1958.
10. H. De Raedt and A. Lagendijk. *Phys. Rev. B*, 27:6097, 1983.
11. M. Hohenadler, D. Neuber, W. von der Linden, G. Wellein, J. Loos, and H. Fehske. *Phys. Rev. B*, 71:245111, 2005.
12. E. Jeckelmann and H. Fehske. *Proceedings of the "Enrico Fermi" Summer School, Course CLXI -"Polarons in Bulk Materials and Systems with Reduced Dimensionality"*, Varenna, 2005.
13. D. Sénéchal, D. Perez, and M. Pioro-Ladrière. *Phys. Rev. Lett.*, 84:522–525, 2000.
14. G. Wellein and H. Fehske. *Phys. Rev. B*, 56:4513, 1997.
15. H. Fehske, J. Loos, and G. Wellein. *Z. Phys. B*, 104:619, 1997.
16. L.-C. Ku, S. A. Trugman, and J. Bonča. *Phys. Rev. B*, 65:174306, 2002.
17. A. Weiße, G. Wellein, A. Alvermann, and H. Fehske. preprint, 2005, `http://arXiv.org/abs/cond-mat/0504627`.
18. G. Schubert, G. Wellein, A. Weiße, A. Alvermann, and H. Fehske. *Phys. Rev. B*, 72:104304, 2005.
19. D. Emin. *Phys. Rev. B*, 48:13691, 1993.
20. E. K. Kudinov, D. N. Mirlin, and Y. A. Firsov. *Fiz. Tverd. Tela*, 11:2789, 1969.
21. R. Peierls. *Quantum theory of solids*. Oxford University Press, Oxford, 1955.
22. M. Capone and S. Ciuchi. *Phys. Rev. Lett.*, 91:186405, 1990.
23. A. A. Ovchinnikov. *Sov. Phys. JETP*, 30:1160, 1970.
24. H. Fehske, A. P. Kampf, M. Sekania, and G. Wellein. *Eur. Phys. J. B*, 31:11, 2003.

John von Neumann Institute for Computing

Quantum Monte Carlo Simulations of Strong Correlations

Stefan Wessel and Alejandro Muramatsu

published in

NIC Symposium 2006 ,
G. Münster, D. Wolf, M. Kremer (Editors),
John von Neumann Institute for Computing, Jülich,
NIC Series, Vol. **32**, ISBN 3-00-017351-X, pp. 211-218, 2006.

http://www.fz-juelich.de/nic-series/volume32

Quantum Monte Carlo Simulations of Strong Correlations

Stefan Wessel and Alejandro Muramatsu

Institut für Theoretische Physik III
Universität Stuttgart, Pfaffenwaldring 57, 70550 Stuttgart, Germany
E-mail: wessel@theo3.physik.uni-stuttgart.de

We employ large-scale quantum Monte Carlo simulations to study the properties of ultra-cold bosonic atom gases in optical lattices. Based on the stochastic series expansion technique, we analyze the ground state phase diagram of the effective Bose-Hubbard model describing the strongly correlated atom gas. After examining the superfluid to Mott-insulator transition of ultra-cold gases on cubic lattices, we analyze the novel phases induced by extending the setup to include a frustrated lattice geometry or randomness in the interatomic interaction strength. We find that on the triangular lattice the presence of frustration in the underlying lattice leads to the emergence of a supersolid state of matter, due to a novel order-by-disorder effect from a macroscopic degeneracy of the model in the classical limit. Furthermore, we show that the presence of randomness in the interaction strength leads to the formation of a Bose-glass phase of the atoms, and the presence of a tri-critical point in the zero-temperature phase diagram. We discuss possible experimental realization of these scenarios.

1 Strongly Correlated Systems

Strong electronic correlations have become an active research area of solid state physics in the last decades, due to their relevance for e.g. heavy fermion compounds[1], high-temperature superconductors[2], and quantum magnetism[3]. Furthermore, ultra-cold atomic gases in optical lattices provide a new exciting bridge between the physics of these quantum condensed matter systems and the field of quantum optics[4,5]. In the project "Numerical studies of correlated quantum systems" novel numerical schemes are developed and employed to effectively simulate such systems. In addition to the work detailed below, research at the Institut für Theoretische Physik III focuses on the following topics: Efficient quantum Monte Carlo algorithms were constructed, which allow a detailed analysis of the spectral properties of the one-dimensional $t-J$ model[6]. Using large scale numerical simulations, evidence for the presence of spinon, holon and antiholon excitation was provided[6]. Ultra-cold atoms in optical lattices were examined using novel exact numerical methods, which allow for the study of both equilibrium and non-equilibrium properties [7–16]. E.g., a quasi-condensate was found to emerge during free expansion of the atomic cloud out of a Fock state, where the coherent matter wave forms an atom laser[11,15]. Novel numerical techniques were developed and tested at NIC Jülich for the study of time-dependent and non-equilibrium properties of strongly correlated systems, based on the density matrix renormalization group[17]. After successful testing, this method is now applied to a detailed study of coherent matter wave formations of ultra-cold atoms under non-equilibrium conditions. Furthermore, we analyze quantum magnetic systems. In particular, we studied the ground state properties and dynamics of quasiperiodic quantum antiferromagnets[18–20]. Using large scale numerical simulations we also studied thermal and quantum phase transitions in systems of weakly-coupled spin-dimers in the presence of high magnetic fields[22]. We established universal critical properties for the Bose-Einstein condensation (BEC) of

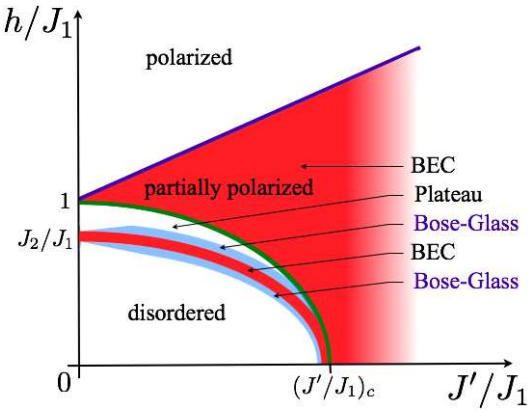

Figure 1. Schematic phase diagram of weakly coupled dimers with a bimodal random distribution of intra-dimer exchange interactions ($J_1 > J_2$) and a weak inter-dimer exchange J' in the presence of an external magnetic field h. Red regions indicate BECs of the magnet excitations, and blue regions the novel Bose-glass phases, emerging from the bond-randomness. $(J'/J_1)_c$ denotes the quantum critical point at $h = 0$ in the absence of randomness.

magnetic excitations in such systems[21], and recently proved the formation of a Bose-glass phase of these magnetic excitations in the presence of randomness[23]. A schematic phase diagram of such a system is shown in Fig 1, exhibiting two Bose-glass phases next to a BEC of magnetic excitations.

2 Ultra-Cold Atom Gases in Optical Lattices

Since the first realizations of BEC in magnetically trapped dilute alkali vapors[24–26], the study of ultra-cold atomic gases (of temperatures down to fractions of microkelvins) has become an active research area of physics. After these first experiments with weakly interacting bosons, among many other achievements the creation of spinor[27] and dipolar[28] condensates has extended the range of observed phenomena. Furthermore, quantum degeneracy was observed in the fermionic case[29], and first steps towards strongly correlated systems have been made[4,5]. Confining the atomic cloud to an optical lattice formed by interfering laser beams leads to physical situations similar to the one encountered in solid state physics[30]. A gas of bosonic atoms under such conditions is described by the Hamiltonian of the Bose-Hubbard model[31],

$$H = -t \sum_{\langle i,j \rangle} \left(b_i^\dagger b_j + h.c. \right) + \frac{U}{2} \sum_i n_i(n_i - 1) + \sum_i V_i n_i. \qquad (1)$$

Here, t denotes the nearest neighbor hopping amplitude, and U an on site repulsion between the bosons. Furthermore, b_i ($b_i^\dagger$) denote annilation (creation) operators for bosons on lattice site i, and $n_i = b_i^\dagger b_i$ the local density. The ratio t/U is tuneable by varying the depth of the optical lattice potential[30], which in allows particular to access the regime $U \gg t$ of strongly correlated bosons. V_i denotes a local potential due to the presence of a (usually harmonic) external trapping potential, which confines the atomic gas. In the

uniform case ($V_i = 0$), this model has a superfluid phase for low values of U/t and Mott-insulator regions of commensurate densities for stronger interactions[31]. The transition from a superfluid BEC to a Mott-insulator has been achieved for atoms in both one- and three-dimensional optical lattices upon increasing the optical lattice depth[5,32]. Quantum Monte Carlo simulations allow for a qualitative analysis of these experiments.

3 Stochastic Series Expansion Quantum Monte Carlo

We use the stochastic series expansion (SSE) quantum Monte Carlo technique[33,34], which is based on a high temperature series expansion of the partition function Z of the quantum lattice model in Eq. (1) in the inverse temperature $\beta = 1/k_B T$:

$$Z = \mathrm{Tr} \exp(-\beta H) = \sum_{n=0}^{\infty} \frac{\beta^n}{n!} \sum_{\{i_1,\ldots,i_n\}} \sum_{\{b_1,\ldots,b_n\}} \langle i_1| - H_{b_1}|i_2\rangle \cdots \langle i_n| - H_{b_n}|i_1\rangle. \quad (2)$$

The Hamiltonian H is decomposed into a sum of single-bond terms $H = \sum_b H_b$, and we inserted complete sets of basis states. For a bosonic system with a positive hopping amplitude $t > 0$ all terms contributing to Eq. (2) have a positive weight, and thus a Monte Carlo importance sampling of Z can be performed efficiently. Each Monte Carlo step consists of two consecutively applied update schemes: First, in a local, diagonal update, the expansion order n changes by adding/removing diagonal single-bond terms, while keeping the intermediate states and offdiagonal terms fixed. Then in a second, nonlocal update scheme, the offdiagonal terms and intermediate states are modified using a directed loop update scheme[35,36], which allows efficient simulations at low temperatures and quantum phase transitions. The results presented below were obtained using an highly optimized C++ implementation of the algorithm based on the ALPS library[37] with native checkpointing and MPI inter-node communication.

4 The Superfluid to Mott-Insulator Transition

The presence of a magnetic confinement potential in the experiments on bosonic atoms in optical lattices[5,32] leads to spatial confinement and an inhomogeneous density distribution of the atoms inside the trap[30]. The local density of the atoms can however not be measured in current experiments. Instead, absorption images are taken during free expansion of the atomic cloud, which reveal the initial momentum distribution $n(\mathbf{k})$ of the atoms. The gradual loss of interference patterns in such images upon increasing the optical lattice depth gave first indications for the passage from a coherent superfluid BEC to the coexistence of large incoherent Mott-insulator and small superfluid regions[5]. Using quantum Monte Carlo simulations, the corresponding changes in the density distribution of the confined Bose gas inside the optical lattice can be analyzed[38–40]. As an example, in Fig. 2 density distributions are shown for the case of bosons confined to a two-dimensional lattice in (a) the superfluid and (b) the coexistence regime. In the latter case, the strong interactions lead to the formation of a Mott-insulating region with integer density (here $n_i = 1$) at the trap center, surrounded by a superfluid shell. We confirmed the coexistence of superfluid and Mott-insulating regions by analyzing the local compressibility κ in these inhomogeneous

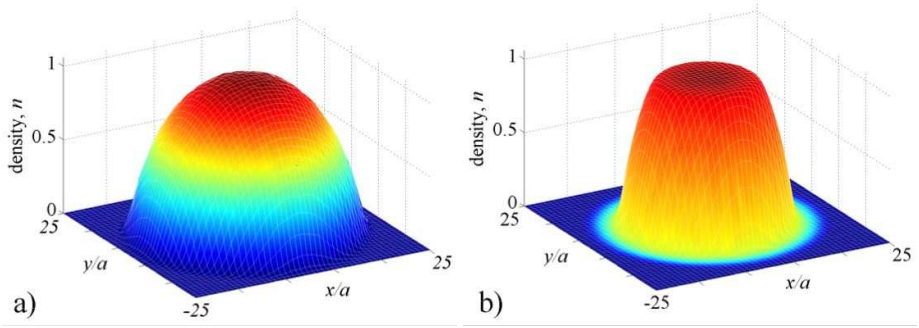

Figure 2. Local density distribution of two-dimensional confined bosonic atoms, (a) in the superfluid phase for $U/t = 6.7$, and (b) in the coexistence regime for $U/t = 25$.

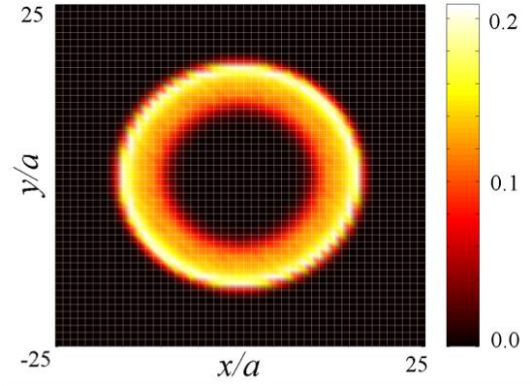

Figure 3. Spatial dependence of the local compressibility κ of bosons confined to a two-dimensional lattice for $U/t = 25$. A superfluid shell surrounds the central Mott-insulator.

systems[38,39]. As an example, the spatial dependence of κ for the case of Fig. 2 b) is shown in Fig. 3, clearly resolving a compressible superfluid ring surrounding the cental incompressible Mott-insulator. In the following, we consider possible extensions of the experimental setup, by including novel lattice geometries and the effects of disorder in our numerical simulations.

5 Supersolid Lattice Bosons

Recently, evidence was reported for a possible supersolid phase of ^{4}He, derived from non-classical momenta of inertia in torsional oscillator experiments[41]. Such a state of matter is characterized by the simultaneous presence of both diagonal and off-diagonal long range order in form of a superfluid with periodic density modulations, breaking both U(1) and

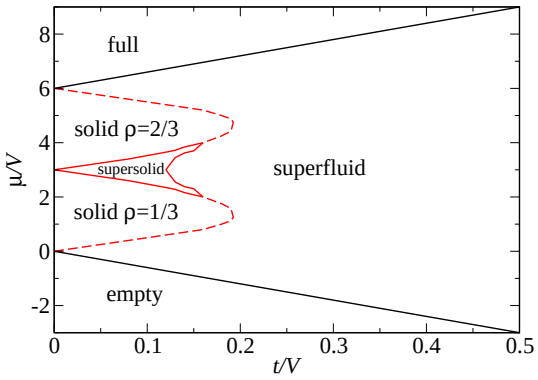

Figure 4. Ground state phase diagram of hard-core bosons on the triangular lattice, obtained from quantum Monte Carlo simulations. Solid lines denote continuous quantum phase transition lines, whereas dashed lines denote first-order transitions. The system is half-filled for $\mu/V = 3$.

translational symmetry[42,43]. Whether the recent observations on ^{4}He are indeed due to the presence of a supersolid state, is still under debate[44–46], and thus the possibility of supersolid phases in translational invariant systems remains unsettled.

Turning to the case of an underlying regular lattice, various proposals have been presented, how to realize a supersolid by loading ultra-cold atoms in optical lattices: such schemes are based on the generation of longer ranged interparticle interactions using dipolar gases[47], Bose-Fermi mixtures[48] or excited states in higher bands[49]. The crystalline order relevant for diagonal long range order in such a supersolid is not the trivial density modulation enforced by the optical lattice but implies an additional superstructure in the bosonic density distribution. Analytical studies using mean-field theory and renormalization group methods indeed found stable supersolid phases in many models, such as the extended Bose-Hubbard model on the square lattice,

$$H = -t \sum_{\langle i,j \rangle} \left(b_i^\dagger b_j + h.c. \right) + V \sum_{\langle i,j \rangle} n_i n_j + \frac{U}{2} \sum_i n_i (n_i - 1) - \mu \sum_i n_i, \qquad (3)$$

in particular in the hard-core limit, $U/V \to \infty$ close to half-filling. Here, V denotes a nearest-neighbor repulsion and μ the chemical potential of the bosons. However, subsequent numerical calculations showed, that the supersolid state is unstable towards phase separation for $U > 4V$, i.e. for dominant on-site interactions[50,51].

Since it is possible to generate optical lattices which depart from the square lattice geometry[52], the question arises, if stable supersolid phases exist in realistic parameter regimes using different lattice structures. We performed quantum Monte Carlo simulations for the extended Bose-Hubbard model, Eq. (3), on the triangular lattice to study the interplay of supersolidity and geometric frustration[53]. In Fig. 4 we show the phase diagram obtained from our simulations in the hard-core limit.

In addition to the superfluid phase at large values of t/V, the system shows two solid phases for low values of $t/V < 0.2$, with densities $\rho = 1/3$ and $\rho = 2/3$, respectively. We found that upon doping these solid phases towards half-filling, $\rho = 1/2$, two supersolid phases emerge, with a first order transition line at $\rho = 1/2$, separating the low- and high-

density supersolids[53]. Supersolidity in this model emerges by an order-by-disorder effect[54] out of a hugely degenerate state of the frustrated classical model at $t = 0$[55], driven by quantum fluctuations[53]. Doping the $\rho = 2/3$ solid with additional bosons (or the $\rho = 1/3$ solid with holes), a possible super-solid is unstable towards phase separation due to the proliferation of domain-walls, giving rise to a first-order transition to the superfluid[53,51]. Our results are in qualitative agreement with analytical findings[56], which however overestimated the extents of the solid and supersolid phases. While an earlier numerical study[57] did not find a supersolid phase at half-filling, recent studies confirm our calculations[58,59].

Our preliminary results for the case of hard-core bosons on the Kagomé-lattice, for which a supersolid phase was obtained in spin-wave approximation[56], indicate that the increased quantum fluctuations destroy supersolidity. Compared to the case of the square lattice, the triangular lattice thus offers the experimentally easiest possibility for realizing order-by-disorder phenomena and supersolid phases of ultra-cold atoms on optical lattices.

6 Bosons with Random Interaction Strength

Another means of realizing novel quantum phases of bosons in optical lattices is randomness produced by e.g. additional incommensurable lattices[60], or by laser speckles[61]. They can lead to Anderson localization[62] and Bose-glass phases[31].

We proposed a novel means of realizing randomness for bosons in optical lattices, by employing the extreme sensitivity of the bosonic scattering potential at the verge of a Feshbach resonance[63,64], leading to a random interaction strength U in the Bose-Hubbard model[65]. In our scenario bosons on an atom chip[66] are considered close to an electric wire, producing a spatially random magnetic field[66]. This will induce random variations in the local interaction strength, if the bosons are set near the Feshbach resonance by the overall off-set field[65]. We studied the phase diagram of the one-dimensional random-U Bose-Hubbard model using both a strong coupling expansion (SCE)[67] and SSE quantum Monte Carlo simulations[65], and contrasted our model to the case of randomness in the chemical potential[31]. The resulting zero-temperature phase diagram for a uniformly distributed interaction strength, $U(1-\epsilon) \leq U_i \leq U(1+\epsilon)$, is shown in Fig. 5 for $\epsilon = 0.25$. Similar to the case of a random chemical potential[31], the disordered system exhibits a Bose-glass regime, identified as an insulating, but compressible phase. However, in the random-U case, the disorder selectively destroys all Mott-insulating regions above an ϵ-dependent filling factor ($n \geq 3$ for $\epsilon = 0.25$). Furthermore, we find that the Bose-glass phase does not extend into the low-density region of the phase diagram, $\mu < 0$, giving rise to a tricritical point along the lower boundary of the $n = 1$ Mott-lobe. Estimates of the relevant length scales indicate that our scenario can indeed be realized using currently available experimental techniques[65].

Acknowledgments

We wish to thank HLRS-Stuttgart (Project CorrSys) and NIC Jülich for the allocation of computer time.

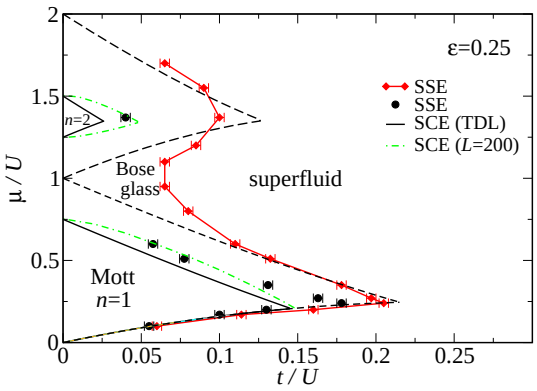

Figure 5. Zero-temperature phase diagram of bosons on a one-dimensional optical lattice with random interaction strength of $\epsilon = 0.25$, obtained from SSE simulations of 200 sites and a third-order SCE for the thermodynamic limit (TDL). The extent of the Mott-lobes in the pure case ($\epsilon = 0$) from SCE is indicated by the dashed line, whereas the dot-dashed line shows the SCE results for a finite system of $L = 200$ sites.

References

1. P. Fulde, J. Keller and G. Zwicknagl, Solid State Physics - Advances in Research and Applications **41**, 1 (1988).
2. J. G. Bednorz and K. A. Müller, Z. Phys. B **64**, 189 (1986).
3. U. Schollwöck, J. Richter, D. J. J. Farnell and R. F. Bishop (Eds.), *Quantum Magnetism*, Lecture Notes in Physics 645, Springer, Berlin (2004).
4. B. Paredes *et al.*, Nature **429**, 277 (2004).
5. M. Greiner *et al.*, Nature **415**, 39 (2002).
6. C. Lavalle *et al.*, Phys. Rev. Lett. **90**, 216401 (2003).
7. M. Rigol *et al.*, Phys. Rev. Lett. **91**, 130403 (2003).
8. M. Rigol, A. Muramatsu, Phys. Rev. A **69**, 053612 (2004).
9. M. Rigol and A. Muramatsu, Phys. Rev. A **70**, 031603(R) (2004).
10. M. Rigol and A. Muramatsu, Phys. Rev. A **70**, 043627 (2004).
11. M. Rigol and A. Muramatsu, Phys. Rev. Lett. **93**, 230404 (2004).
12. M. Rigol and A. Muramatsu, Opt. Commun. **243**, 33 (2004).
13. M. Rigol and A. Muramatsu, Phys. Rev. Lett. **94**, 240403 (2005).
14. M. Rigol and A. Muramatsu, Phys. Rev. A **72**, 013604 (2005).
15. M. Rigol and A. Muramatsu, Mod. Phys. Lett. B bf 19, 861 (2005).
16. M. Rigol *et al.*, Phys. Rev. Lett. **95**, 218901 (2005).
17. S. R. Manmana, A. Muramatsu, and R. M. Noack, AIP Conf. Proc. **789**, 269 (2005).
18. S. Wessel, A. Jagannathan, and S. Haas, Phys. Rev. Lett. **90**, 177205 (2003).
19. S. Wessel, and I. Milat, Phys. Rev. B **71**, 104427 (2005).
20. S. Wessel, Phys. Rev. Lett. **94**, 029701 (2005).
21. O. Nohadani *et al.*, Phys. Rev. B **69**, 220402(R) (2004).
22. O. Nohadani, S. Wessel, and S. Haas, Phys. Rev. B **72**, 024440 (2005).
23. O. Nohadani, S. Wessel, and S. Haas, Phys. Rev. Lett. **95**, 227201 (2005).
24. M. H. Anderson *et al.*, Science **269**, 198 (1995).

25. C. C. Bardley *et al.*, Phys. Rev. Lett. **75**, 1687 (1995).
26. K. B. Davis *et al.*, Phys. Rev. Lett. **75**, 3969 (1995).
27. J. Stenger *et al.*, Nature **396**, 345 (1999).
28. A. Griesmaier *et al.*, Phys. Rev. Lett. **94**, 160401 (2005).
29. B. DeMarco and D. S. Jin, Science **285**, 1703 (1999).
30. J. Jaksch *et al.*, Phys. Rev. Lett. **81**, 3108 (1998).
31. M. P. A. Fisher *et al.*, Phys. Rev. B **40**, 546 (1989).
32. T. Stöferle *et al.*, Phys. Rev. Lett. **91** 130403 (2004).
33. A. W. Sandvik and J. Kurkijärvi, Phys. Rev. B **43**, 5950 (1991).
34. A. W. Sandvik, Phys. Rev. B **59**, R14157 (1999).
35. O. F. Syljuåsen and A. W. Sandvik, Phys. Rev. E **66**, 046701 (2002).
36. F. Alet, S. Wessel, and M. Troyer, Phys. Rev. E **71**, 036706 (2005).
37. F. Alet *et al.*, J. Phys. Soc. Jpn. Suppl. **74**, 30 (2005); source codes available at `http://alps.comp-phys.org/`.
38. S. Wessel, *et al.*, Adv. Solid State Phys. **44**, 265 (2004).
39. S. Wessel, *et al.*, Phys. Rev. A **70**, 053615 (2004).
40. S. Wessel, *et al.*, J. Phys. Soc. Jpn. Suppl. **74**, 10 (2005).
41. E. Kim and M. H. W. Chan, Nature **427**, 225 (2004); Science **305**, 1941 (2004).
42. O. Penrose and L. Onsager, Phys. Rev. **104**, 576 (1956).
43. A. J. Leggett, Phys. Rev. Lett. **25**, 1543 (1970).
44. A. Leggett, Science **305**, 1921 (2004).
45. N. Prokof'ev and B. Svistunov, Phys. Rev. Lett. **94**, 155302 (2005).
46. E. Burovski *et al.*, Phys. Rev. Lett. **94**, 165301 (2005).
47. K. Góral, L. Santos and M. Lewenstein, Phys. Rev. Lett. **88**, 170406 (2002).
48. H. P. Büchler and G. Blatter, Phys. Rev. Lett. **91**, 130404 (2003).
49. V. W. Scarola and S. Das Sarma, Phys. Rev. Lett. **95**, 03303 (2005).
50. G. G. Batrouni and R. T. Scalettar, Phys. Rev. Lett. **84**, 1599 (2000).
51. P. Sengupta *et al.*, Phys. Rev. Lett. **94**, 207202 (2005).
52. L. Santos *et al.*, Phys. Rev. Lett. **93** 030601 (2004).
53. S. Wessel and M. Troyer, Phys. Rev. Lett. **95**, 127205 (2005).
54. J. Villain *et al.*, J. Phys. **41**, 1263 (1980).
55. G. H. Wannier, Phys. Rev. **79**, 357 (1950).
56. G. Murthy, D. Arovas and A. Auerbach, Phys. Rev. B **55**, 3104 (1997).
57. M. Boninsegni, J. Low Temp. Phys. **132**, 39 (2003).
58. D. Heidarian and K. Damle, Phys. Rev. Lett. **95**, 127206 (2005).
59. R. Melko *et al.*, Phys. Rev. Lett. **95**, 127207 (2005).
60. R. B. Dimer *et al.*, Phys. Rev. A **64**, 033416 (2001).
61. P. Horak, J.-Y. Courtois and G. Grynberg, Phys. Rev. A **58**, 3953 (2000).
62. P. W. Anderson, Phys. Rev. B **109**, 5 (1958).
63. E. Tiesinga *et al.*, Phys. Rev. A **47**, 4114 (1993).
64. S. Inouye *et al.*, Nature **392**, 151 (1998).
65. H. Gimperlein, S. Wessel, J. Schmiedmayer, and L. Santos, Phys. Rev. Lett. **95**, 170401 (2005).
66. S. Wildermuth *et al.*, Nature **435**, 440 (2005).
67. J. K. Freericks and H. Monien, Phys. Rev. B **53**, 2691 (1996).

John von Neumann Institute for Computing

Computational Optoelectronics of Semiconductor Nanostructures Including Many-Body Effects

Torsten Meier, Huynh Thanh Duc, Matthias Reichelt,
Bernhard Pasenow, Tineke Stroucken,
and Stephan W. Koch

published in

NIC Symposium 2006 ,
G. Münster, D. Wolf, M. Kremer (Editors),
John von Neumann Institute for Computing, Jülich,
NIC Series, Vol. **32**, ISBN 3-00-017351-X, pp. 219-226, 2006.

http://www.fz-juelich.de/nic-series/volume32

Computational Optoelectronics of Semiconductor Nanostructures Including Many-Body Effects

Torsten Meier[1], **Huynh Thanh Duc**[1,2], **Matthias Reichelt**[1,3], **Bernhard Pasenow**[1], **Tineke Stroucken**[1], **and Stephan W. Koch**[1]

[1] Department of Physics and Material Sciences Center, Philipps University
Renthof 5, 35032 Marburg, Germany
E-mail: {Torsten.Meier, Bernhard.Pasenow, Tineke.Stroucken, Stephan.W.Koch}@physik.uni-marburg.de

[2] Institute of Physics, Mac Dinh Chi 1, Ho Chi Minh City, Vietnam
E-mail: htduc@vast-hcm.ac.vn

[3] Arizona Center for Mathematical Sciences, University of Arizona
Tucson, AZ 85721, USA
E-mail: reichelt@acms.arizona.edu

The linear and nonlinear optical properties of semiconductors are strongly influenced by the Coulomb interaction among the photoexcited carriers. Within the framework of the semiconductor Bloch equations such many-body effects can be described on the basis of a microscopic theory. In this article, we briefly review our recent contributions to two specific topics. First, the coherent optical generation of charge and spin currents and their subsequent decay via scattering processes is discussed. As a second example, the spatially-inhomogeneous optical properties of hybrid structures which consist of photonic crystals and semiconductor nanostructures are described. Many of the numerical results have been obtained using massively parallel computer programs which were run on the IBM p690-Cluster Jump in Jülich.

1 Introduction

The analysis of the optical and electronic properties of semiconductors and, in particular, semiconductor nanostructures is of great current interest. On the one hand, one can study in these systems questions which are of relevance in the area of fundamental physics, i.e., many-body and non-equilibrium effects, ultrafast dynamics, coherent phenomena, influence of disorder, etc. On the other hand, semiconductors and semiconductor nanostructures are useful for a great variety of applications including optoelectronic devices.

A microscopic theoretical description of the optical properties of semiconductors has to properly describe the light field, the material excitations, and their interaction. When the electronic system is excited by the light field, electrons are raised energetically to the previously unoccupied conduction band and so-called holes are generated in the valence band. Since these quasi-particles are charged, their mutual Coulomb interaction gives rise to a many-body problem. Within the framework of the semiconductor Bloch equations a number of important many-body effects can be computed on a microscopic theoretical basis[1,2]. These equations describe the dynamical evolution of electronic distributions and coherences during and after the photoexcitation. By numerically solving this high-dimensional set of coupled nonlinear differential equations one obtains the macroscopic optical polarization which appears as a source term in Maxwell's equations and thus determines the light-matter interaction.

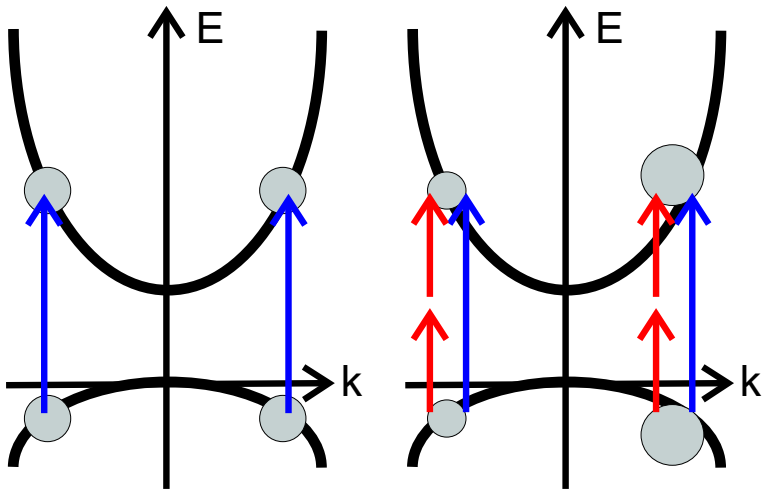

Figure 1. Schematical drawings of optical interband excitations in a two-band model. Left: A single field with frequency 2ω resonantly generates electrons and holes above the band gap of a semiconductor $E_{\rm gap}$. In this case, the excitation is symmetric in k-space. Right: The incident field consists of two frequencies ω and 2ω satisfying $\hbar\omega < E_{\rm gap} < 2\hbar\omega$. In this case, it is possible to create excitations which are not symmetric in k-space, i.e., correspond to a finite current, since the initial and final states are connected by two pathways. The direction and the magnitude of the photoinduced current can be controlled coherently by adjusting the phase difference between the two field components.

In this brief review, we describe our recent contributions to two specific topics. For further details of the theoretical approach and additional information we have to refer the reader to the cited articles and the literature cited therein. In the first example, see Sect. 2.1, the coherent optical generation of charge and spin currents and their subsequent decay via scattering processes is analyzed. As a second example, the spatially-inhomogeneous optical properties of hybrid structures consisting of photonic crystals and semiconductor nanostructures are described in Sect. 2.2.

2 Examples

2.1 Coherent Optical Generation and Decay of Charge and Spin Currents

Recently, the coherent control of electronic excitations in semiconductors by sequences of optical laser pulses has received great attention. For example, it has been predicted[3] that it should be possible to generate photocurrents in semiconductors on ultrashort time scales via the excitation with two light beams with frequencies ω and 2ω satisfying $\hbar\omega < E_{\rm gap} < 2\hbar\omega$, where $E_{\rm gap}$ is the band gap energy. This effect has been observed[4] and is illustrated schematically in Fig. 1.

A few years later, it has been predicted that basically the same type of interference scheme can also be employed to create pure spin currents which are not accompanied by any charge current[5], see Fig. 2. The existence of such spin currents generated on ultrafast time scales has been confirmed experimentally[6,7]. They could, in particular, be useful for possible future applications in the area of spintronics.

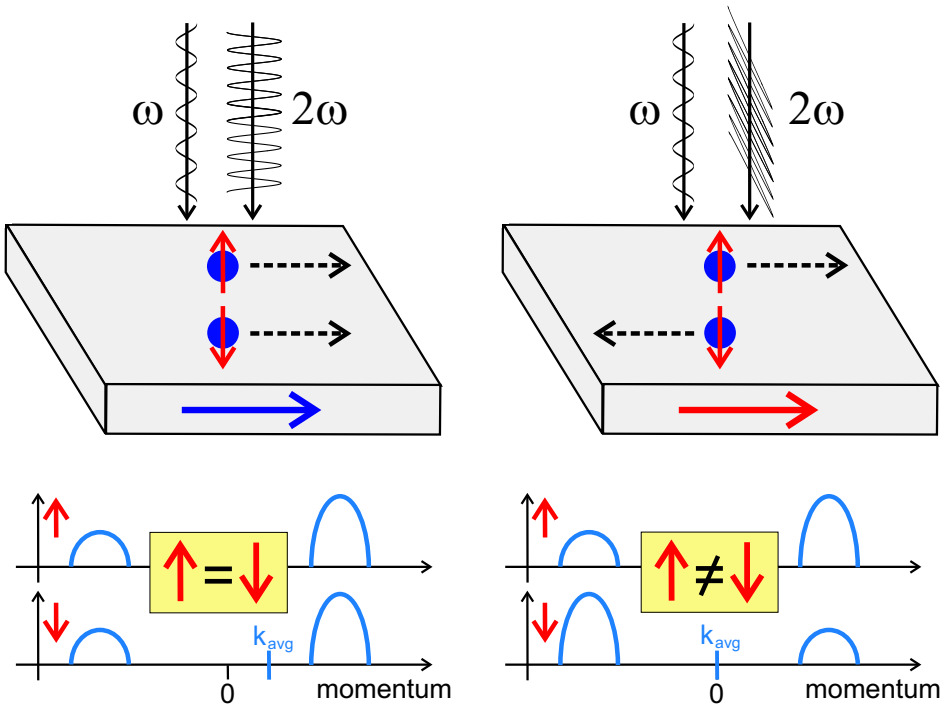

Figure 2. Schematical illustration of the coherent optical generation of currents. Left: (Right:) By using linear parallel (perpendicular) polarization directions of the ω and the 2ω beams a charge (spin) current is injected. When a charge current is generated, both spins are excited identically, i.e., $n^e_{\uparrow,k} = n^e_{\downarrow,k}$, and the excitations carry a nonvanishing average momentum $k_{\rm avg}$. For the case of a spin current, the distributions of the two spins satisfy $n^e_{\uparrow,k} = n^e_{\downarrow,-k}$ and thus the momentum averaged over both spins vanishes.

In Ref. 8, we have presented and analyzed a microscopic many-body theory at the quantum-kinetic second Born-Markov level which is capable of describing the dynamical generation, the coherent evolution, and the decay of charge and spin currents. Our approach is based on the semiconductor Bloch equations[1,2] and includes light-field-induced intraband and interband excitations nonperturbatively and beyond the rotating wave approximation, excitonic effects, as well as correlation contributions arising from the carrier LO-phonon coupling and the Coulomb interaction which describe scattering processes.

Figure 3 shows the time-dependence of the electron and hole distributions of a quantum well in k-space. The short laser pulses generate carriers with a combined excess energy of 150 meV above the band gap. Due to their smaller mass most of this kinetic energy is given to the electrons. Immediately after the photoexcitation, the electron and hole distributions are very similar, since the optical transitions are diagonal in k-space. Due to the quantum interference between the ω and 2ω components of the field, the distributions are larger for positive k_x than for negative k_x. Therefore, this situation corresponds to a current in x-direction. In the course of time, the distributions relax towards quasi equilibrium, i.e., towards the band edges. In the limit of long times, due to their larger mass the distribution of the holes is wider than that of the electrons.

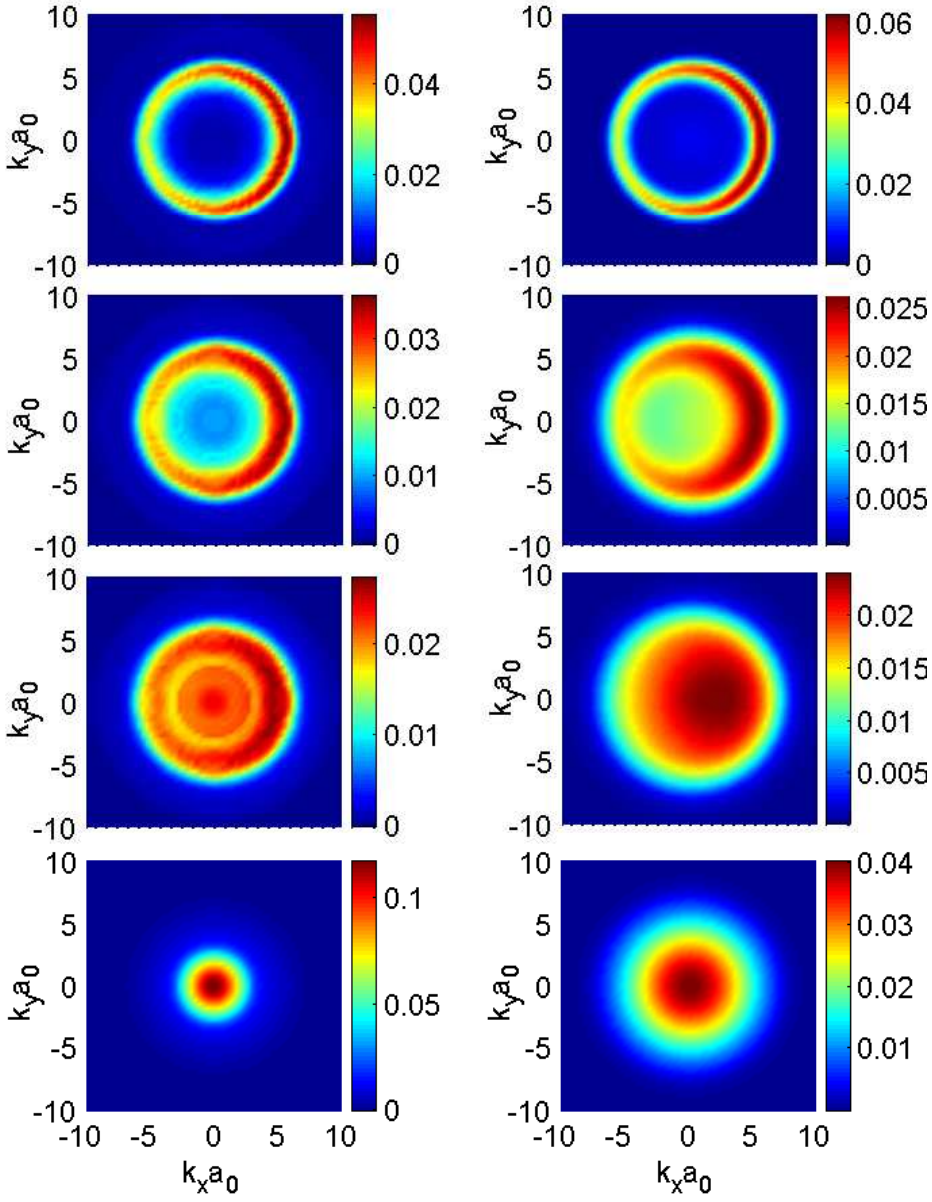

Figure 3. Left (right) column: Contour plots of the electron (hole) distributions in a quantum well in **k**-space at t =50, 100, 150, and 400 fs, respectively. The incident pulses have a duration of 20 fs and the amplitudes of the two fields are $A_\omega = 2A_{2\omega} = 108A_0$, with $A_0 = E_0/ea_0 \approx 4$ kV/cm, where E_0 is the exciton Rydberg and a_0 the exciton Bohr radius. The excitation frequency is chosen such that $2\hbar\omega$ is 150 meV above the band gap, the density of photoinjected carriers is $N = 10^{11}$ cm^{-2}, and the temperature is $T = 50$ K. Taken from Ref. 8.

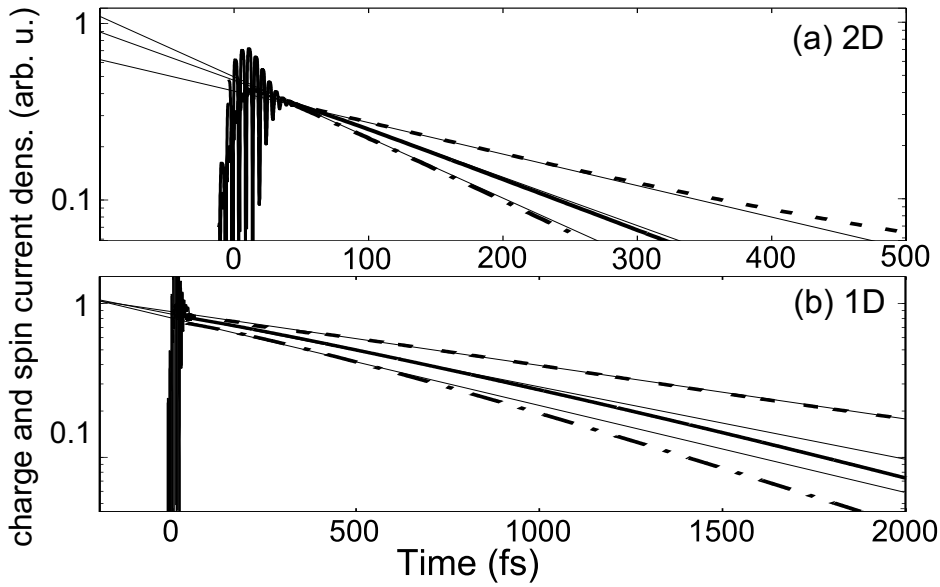

Figure 4. (a) Time-dependent charge (solid) and spin (dash-dot) currents of a quantum well for the same parameters as in Fig. 3. Also shown is the identical decay of both currents if only carrier LO-phonon scattering is considered (dashed). The thin solid lines represent exponential decays with time constants of 240, 155, and 125 fs, respectively. (b) Same as (a) for a quantum wire. The density of the photoinjected carriers is $N = 5 \times 10^5$ cm^{-1} and the other parameters are the same as in (a). The thin solid lines represent exponential decays with time constants of 1250, 900, and 740 fs, respectively. Taken from Ref. 8.

Figure 4(a) demonstrates that for the considered excitation conditions the dynamical evolution of the currents is influenced by both carrier LO-phonon and carrier-carrier scattering. If only carrier LO-phonon scattering is considered, the charge and spin currents decay similarly. This decay is not exponential, however, its onset can be approximated by an exponential decay with a time constant 240 fs. Including also carrier-carrier scattering in the analysis, speeds up the decay of both currents. Additionally, we find that *the spin current decays more rapidly than the charge current*. This effect can be understood by considering that the excitation of a charge current corresponds to identical electron distributions for the different spins, see Fig. 2. Therefore, the average momentum of the electron system is finite. Since carrier-carrer scattering only exchanges momentum among the carriers, the finite average momentum cannot be reduced by this process. The situation is, however, different when a spin current is excited. In this case, the opposite electron distributions for the two spins correspond to a vanishing total electronic momentum, see Fig. 2. Consequently, Coulomb scattering can exchange and thus relax the photoexcited momenta of the spin-up and spin-down electrons.

Figure 4(b) shows that qualitatively similar results are obtained for quantum wires. However, since the phase space is smaller in one dimension, the scattering is reduced and the decay times are longer than in two dimensions. Additional investigations of the dependence of the currents on the intensities of the incident laser pulses can be found in Ref. 8.

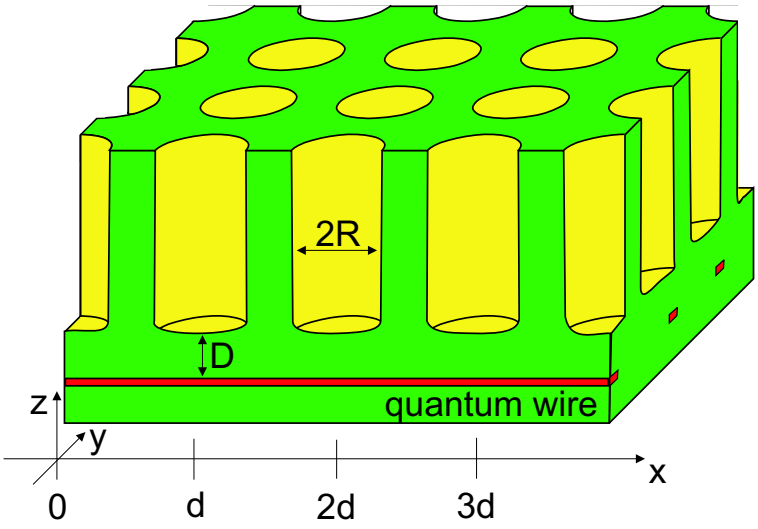

Figure 5. Schematical drawing of the considered structure which consists of an array of semiconductor quantum wires in the vicinity of a two-dimensional photonic crystal. The photonic crystal has a finite thickness and is made of periodically arranged air cylinders which are surrounded by a dielectric medium. Taken from Ref. 15.

2.2 Optical Properties of Semiconductor Photonic-Crystal Structures

A periodic wavelength scale dielectric structuring strongly influences the transverse part of the electromagnetic field. Dielectric photonic crystals can be used to design the dispersion of the electromagnetic field modes, i.e., so-called photonic band structures[9–12]. Important aspects of the light-matter interaction can be modified with these structures and, furthermore, a suitable tailoring of the field modes may improve the properties of various optoelectronic devices.

The dielectric structuring influences, however, also the longitudinal part of the electromagnetic field, i.e., the Coulomb interaction. This results in a space dependence of the band gap and the exciton energies in a nearby semiconductor nanostructure which follows the periodicity of the photonic crystal[13,14].

In Ref. 15, we have analyzed the optical gain properties of such spatially-inhomogeneous semiconductor photonic-crystal structures. The developed theoretical approach provides a self-consistent solution of the dynamics of the electromagnetic field and the material excitations in the framework of coupled Maxwell semiconductor Bloch equations which include many-body interactions on the Hartree-Fock level.

The considered structure consists of an array of quantum wires in the vicinity of a two-dimensional photonic crystal of finite thickness, see Fig. 5. Shown in Fig. 6. are density-dependent optical absorption and gain spectra. For small densities, two excitonic absorption peaks are visible. The lower one is associated with positions underneath the dielectric part of the photonic crystal whereas the higher one originates from positions underneath the air cylinders. With increasing density, the height of both peaks decreases due to bleaching. However, the rate of change for the energetically lower peak is larger. This

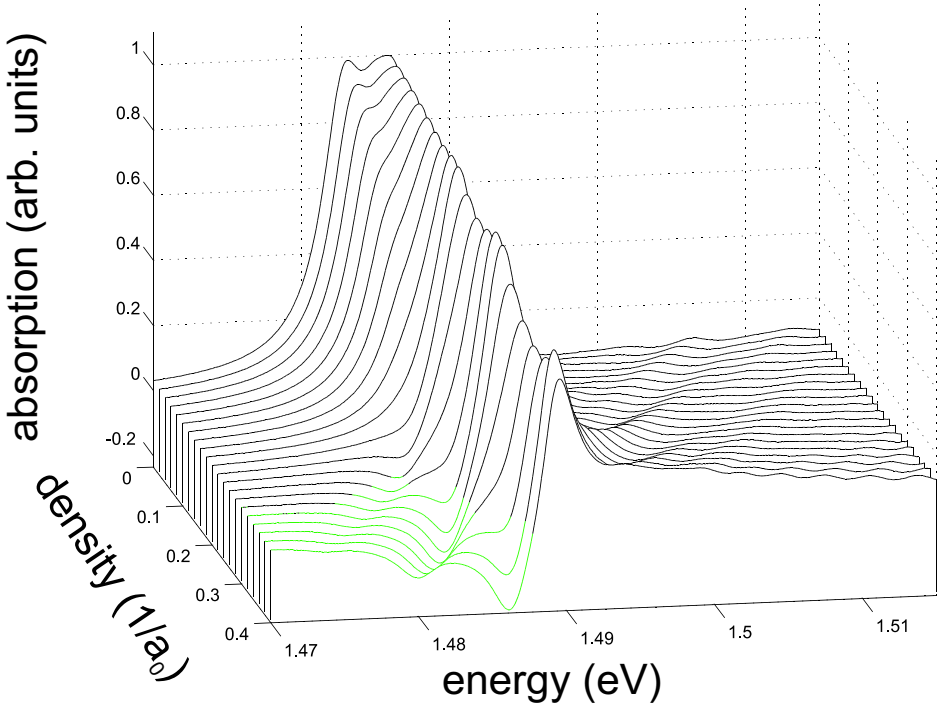

Figure 6. Density-dependent absorption/gain spectra for an array of wires that is separated by $D = 0.2a_0$ from the photonic crystal with air cylinder radius $R = 2.65a_0$. The presence of negative absorption, i.e., optical gain, is highlighted by changing the lines from black to green. Taken from Ref. 15.

is due to the fact that because of the spatially-varying band gap the carriers accumulate at positions underneath the dielectric and avoid the regions underneath the air cylinders. As a result the sign of the absorption at the lower peak becomes negative, i.e., optical gain is present, in a range of densities where the higher peak is still absorbing. A detailed analysis shows that in this spatially-inhomogeneous structure the transition from absorption to gain occurs at an approximately 20% smaller density than in a structure which is in a homogeneous dielectric environment[15].

Besides the gain, we have also studied nonlinear optical properties and electronic wave-packet dynamics of spatially-inhomogeneous semiconductor photonic-crystal structures[16]. Furthermore, a strong enhancement of the optical gain has been found in structures consisting of one-dimensional photonic crystals and semiconductor quantum wells[17].

3 Summary

The two examples presented here demonstrate that many-body effects strongly influence the optoelectronic properties of semiconductors. Many of our numerical results on the examples discussed here and also on other topics were obtained using massively parallel computer programs which were run on the IBM p690-Cluster Jump in Jülich.

Acknowledgments

This work is supported by the Deutsche Forschungsgemeinschaft (DFG), by the Ministry of Education and Research (BMBF), and by the Interdisciplinary Research Center Optodynamics, Philipps-University Marburg. T.M. thanks the DFG for support via a Heisenberg fellowship (ME 1916/1). We thank the John von Neumann-Institut für Computing (NIC), Forschungszentrum Jülich, Germany, for continued grants of computer time on their supercomputer systems.

References

1. H. Haug and S.W. Koch, *Quantum Theory of the Optical and Electronic Properties of Semiconductors*, 4th ed., (World Scientific, Singapore, 2004).
2. W. Schäfer and M. Wegener, *Semiconductor Optics and Transport Phenomena*, (Springer, Berlin, 2002).
3. R. Atanasov, A. Haché, J.L.P. Hughes, J.E. Sipe, and H.M. van Driel, Phys. Rev. Lett. **76**, 1703 (1996).
4. A. Haché, Y. Kostoulas, R. Atanasov, J.L.P. Hughes, J.E. Sipe, and H.M. van Driel, Phys. Rev. Lett. **78**, 306 (1997).
5. R.D.R. Bhat and J.E. Sipe, Phys. Rev. Lett. **85**, 5432 (2000).
6. M.J. Stevens, A.L. Smirl, R.D.R. Bhat, A. Najmaie, J.E. Sipe, and H.M. van Driel, Phys. Rev. Lett. **90**, 136603 (2003).
7. J. Hübner, W.W. Rühle, M. Klude, D. Hommel, R.D.R. Bhat, J.E. Sipe, and H.M. van Driel, Phys. Rev. Lett. **90**, 216601 (2003).
8. H.T. Duc, T. Meier, and S.W. Koch, Phys. Rev. Lett. **95**, 086606 (2005).
9. E. Yablonovitch, Phys. Rev. Lett. **58**, 2059 (1987).
10. S. John, Phys. Rev. Lett. **58**, 2486 (1987).
11. J.D. Joannopoulos, R.D. Meade, and J.N. Winn, *Photonic crystals: Molding the flow of light*, (Princeton University Press, Princeton, 1995).
12. *Photonic Crystals - Advances in Design, Fabrication and Characterization*, Eds. K. Busch, S. Lölkes, R.B. Wehrspohn, and H. Föll, (Wiley-VCH, Berlin, 2004).
13. T. Stroucken, R. Eichmann, L. Banyai, and S.W. Koch, J. Opt. Soc. Am. B **19**, 2292 (2002).
14. R. Eichmann, B. Pasenow, T. Meier, T. Stroucken, P. Thomas, and S.W. Koch, Appl. Phys. Lett. **82**, 355 (2003).
15. M. Reichelt, B. Pasenow, T. Meier, T. Stroucken, and S.W. Koch, Phys. Rev. B **71**, 035346 (2005).
16. B. Pasenow, M. Reichelt, T. Stroucken, T. Meier, and S.W. Koch, Phys. Rev. B **71**, 195321 (2005).
17. B. Pasenow, M. Reichelt, T. Stroucken, T. Meier, S.W. Koch, A.R. Zakharian, and J.V. Moloney, J. Opt. Soc. Am. B **22**, 2039 (2005).

John von Neumann Institute for Computing

Dynamical Scaling Behaviour Far from Equilibrium

Michel Pleimling

published in

NIC Symposium 2006 ,
G. Münster, D. Wolf, M. Kremer (Editors),
John von Neumann Institute for Computing, Jülich,
NIC Series, Vol. **32**, ISBN 3-00-017351-X, pp. 227-234, 2006.

http://www.fz-juelich.de/nic-series/volume32

Dynamical Scaling Behaviour Far from Equilibrium

Michel Pleimling

Institut für Theoretische Physik, Universität Erlangen-Nürnberg
Staudtstr. 7B3, 91058 Erlangen, Germany
E-mail: michel.pleimling@physik.uni-erlangen.de

Ageing phenomena and dynamical scaling behaviour are studied both in ferromagnets and in critical spin glasses. For the ferromagnetic systems we find that dynamical scaling functions measured after a quench into the ordered low temperature phase are in complete agreement with predictions coming from the recently proposed theory of local scale invariance. For a quench to the critical point corrections to these predictions are shown to exist. Critical spin glasses are found to display the same ageing phenomenology as critical ferromagnets. Numerical evidence indicates that the concept of universality is weaker in critical spin glasses than in critical ferromagnets.

1 Introduction

Ageing phenomena are encountered in a large variety of out-of-equilibrium systems (see[1] for a recent review). Well-known examples are found in glasses, spin glasses, polymers and colloids, but also simple ferromagnets, quenched to or below their critical point, display this intriguing behaviour. In praxis ageing behaviour is used in order to change the properties of materials undergoing a quench from high to low temperatures.

Many of the investigations in this field study the dynamical scaling behaviour often encountered in systems being far from equilibrium. Dynamical scaling follows directly from the existence of a unique typical dynamical length scale which increases in time with a power law. The power law behaviour is thereby due to the presence of slow degrees of freedom.

The description of ageing phenomena starts from the observation that dynamical correlation and response functions transform covariantly under the dynamical scale transformation $t \longrightarrow (1+\varepsilon)^z t$, $\vec{r} \longrightarrow (1+\varepsilon)\vec{r}$. Here t is time, $\vec{r}$ denotes the space point, and z is the dynamical exponent. It has been shown recently[2,3] that the dynamical symmetry with ε constant can be generalized to a local symmetry with $\varepsilon = \varepsilon(t, \vec{r})$. Starting from this generalized space-time symmetry exact expressions for dynamical response and correlation functions have been derived for the first time[2,4,5].

In the last years I studied the dynamical scaling behaviour of nonequilibrium systems through extensive numerical simulations. The purpose of this study was two-fold. On the one hand the predictions coming from the theory of local scale invariance were confronted with numerical data obtained for ferromagnets quenched to temperatures equal or less than the critical temperature. This yielded interesting results on the applicability of the concept of generalized space-time symmetries to nonequilibrium systems. On the other hand the investigation of the phenomenology of ageing was extended to other, more complex, systems as for example spin glasses quenched to their critical point.

As discussed in the following, these numerical studies have yielded new insights into the universal features of the dynamical behaviour of systems brought out of equilibrium by a sudden change of external conditions.

2 Ageing Phenomena in Ferromagnets

In order to better understand ageing, consider a ferromagnet prepared at very high temperatures in a completely disordered state and then quenched to low temperatures. In case the final temperature is below the critical temperature, phase ordering sets in, and, due to the competition of different ordered equilibrium states, formation of domains take place. This is shown in Figure 1 for the case of an uniaxial ferromagnet with two competing ordered states. The typical size $L(t)$ of the domains increases as a power law of time t: $L(t) \sim t^{1/z}$. The exponent z, which is called dynamical exponent, takes on the value 2 when no quantities are conserved. The slow degrees of freedom, responsible for the ageing phenomena, are thereby provided by the movement of the walls separating the different domains.

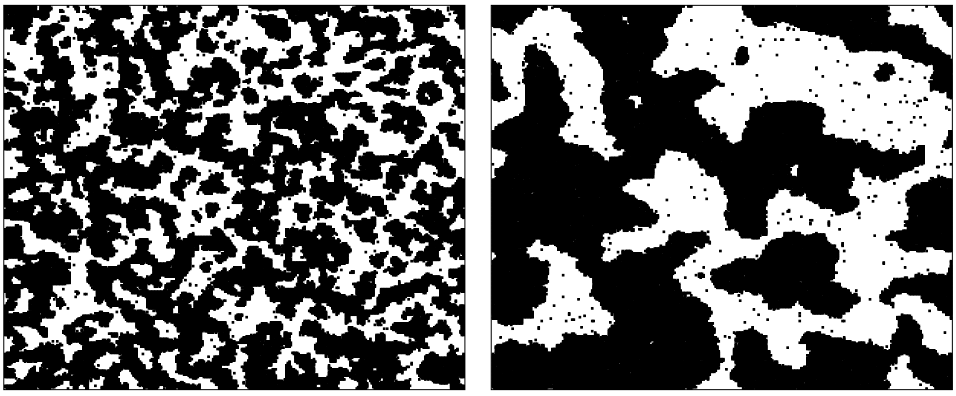

Figure 1. Formation of domains in an uniaxial ferromagnet with two competing ordered states (black and white patches) quenched to temperatures below the critical temperature. The typical size of the domains increases as a function of time (from left to right).

Ageing manifests itself most readily through the behaviour of two-time quantities as dynamical correlation and response functions. Indeed, in the ageing regime these quantities depend in a complicated way on both times and not only on the time difference, as this is the case at equilibrium. To be specific, consider the autocorrelation function $C(t, s)$ which measures to what extent configurations at two times s and $t > s$ are correlated. As shown in Figure 2a for the case of a quench of the two-dimensional Ising model (a very simple model which nevertheless captures most of the physics of uniaxial ferromagnets) to low temperatures the autocorrelation is not a simple function of the time difference $t - s$. In fact, the decay of C is the slowest for the largest value of s. It is this behaviour which we call ageing.

A characteristic behaviour of $C(t, s)$ is encountered in the dynamical scaling regime $t - s \gg s \gg 1$ where one has the simple scaling form

$$C(t, s) = s^{-b} f_c(t/s). \tag{1}$$

Here f_c is a dynamical scaling function, whereas b is a nonequilibrium exponent. Plotting C as a function of t/s indeed yields an excellent data collapse for $b = 0$, see Figure 2b.

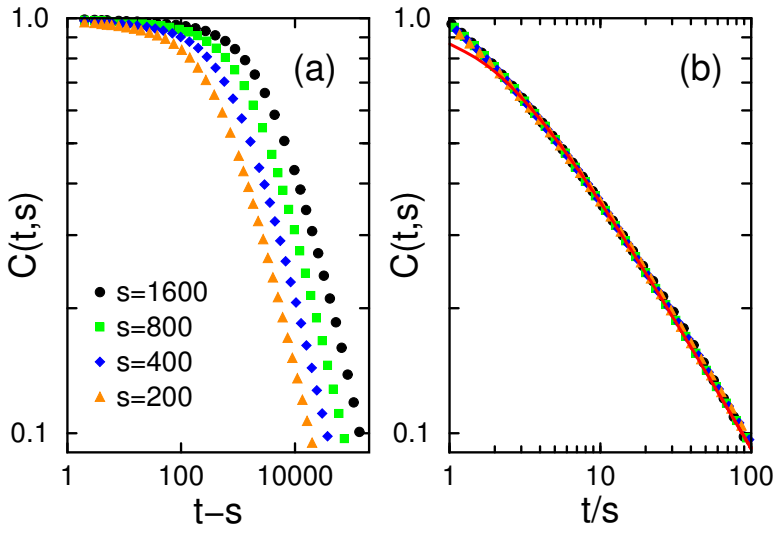

Figure 2. Computed autocorrelation function $C(t,s)$ of the two-dimensional Ising model after a quench to $T=0$ for different values of s as a function of (a) $t-s$ and (b) t/s. The red line in (b) is the theoretical prediction coming from the theory of local scale invariance.

The red line shown in that Figure is the theoretical prediction derived under the assumption of local scale invariance[5]. Clearly, the theoretical curve nicely describes the numerical data for values of $t/s \geq 2$. The observed deviations for smaller values of t/s are expected as here one is not yet in the dynamical scaling regime $t-s \gg s \gg 1$.

The same conclusions are reached when looking at response functions instead of correlation functions. As an example one may consider the space-time response which gives the reaction of the system at time t at a position $\vec{r}$ to a perturbation which was applied at an earlier time s at a different position $\vec{r}\,'$. Figure 3 displays the spatially and temporally integrated response which is easily accessible in numerical simulations. Predictions coming from the theory of local scale invariance (full lines) again describe the numerical data in a perfect way[2,4].

It has to be stressed that a similar good agreement between theory and numerics is also found for other systems quenched below their critical point[6]. This leads us to the important conclusion that the generalized space-time symmetries, underlying the theory, are indeed realized in systems that undergo phase ordering.

However, there do exist situations for which local scale invariance does not yield the exact scaling functions. This is for example the case when one quenches a ferromagnet to its critical point. Whereas early simulations showed a very good agreement between theory and numerics also for this case[2], field theoretical calculations[7] pointed to the existence of corrections to the scaling functions derived under the assumption of local scale invariance. We recently succeeded in proving numerically the existence of these correction terms in critical systems by studying the response of the total magnetization to a homogeneous external field[8]. As shown in Figure 4 for the critical Ising model in two and three

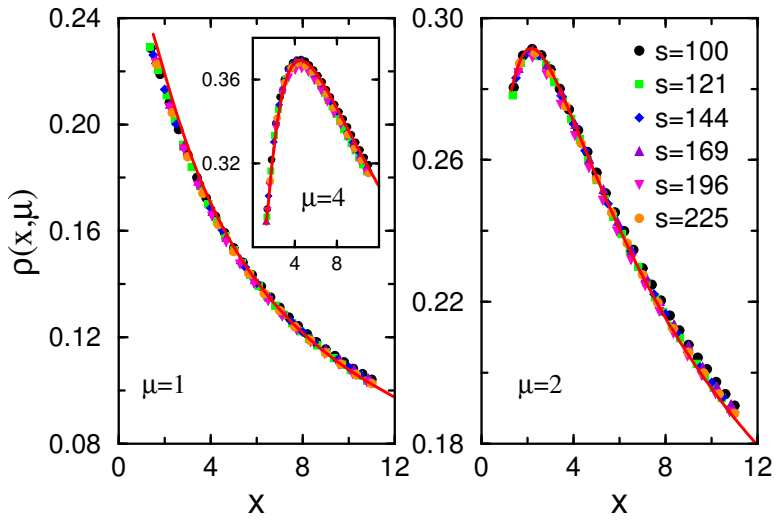

Figure 3. Computed scaling function $\rho(x, \mu)$ of the spatially and temporally integrated response of the two-dimensional Ising model after a quench to $T = 1.5$ for different values of s. Here x is the scaling variable t/s and μ is a measure of the distance over which one has integrated spatially. The red lines are the theoretical predictions coming from the theory of local scale invariance.

dimensions the local scale invariance prediction systematically deviates from the numerical data, whereas the inclusion of the corrections brings the theoretical curve closer to the data. In fact, this is the first time that the existence of corrections to the predictions of the theory of local scale invariance has been proven unambiguously.

Why are quenches to the critical point so different from quenches into the low temperature phase? In fact at a critical point one has no well-defined domains, but instead correlated regions are formed. One can define a dynamical correlation length which increases again with a power law of time, but now the dynamical exponent is different from 2. As a further consequence of the critical fluctuations the time evolution of the magnetization is non-markovian, a feature not captured by the theory of local scale invariance in its present form.

3 Ageing in Critical Spin Glasses

Recently, we have extended our studies to disordered systems. As a first example we looked at the ageing phenomenology of spin glasses at their critical point. Spin glasses are highly frustrated systems which are characterized by very slow dynamics. The nature of their low temperature phase is still intensively debated. In fact, due to the very slow dynamics it is extremely difficult to equilibrate in numerical simulations even systems of very moderate size, making equilibrium simulations of spin glasses very tedious. In our approach we concentrated on the out-of-equilibrium behaviour which can be studied for large systems.

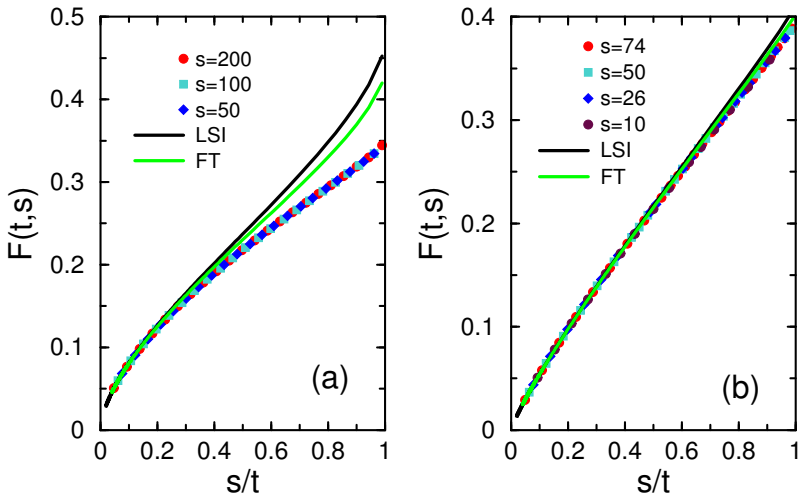

Figure 4. Scaling function of the reponse of the total magnetization to an homogeneous external field for (a) the two-dimensional and (b) the three-dimensional Ising model quenched to its critical point. LSI denotes the theoretical prediction coming from the theory of local scale invariance. In the FT curve the corrections coming from field theoretical calculations have been included.

We focused on the spin glass transition, as earlier investigations had shown that at this point one again has the situation that the dynamical correlation length increases with a power law of time, similar to what is observed in critical ferromagnets[9]. In fact, the similarities with the out-of-equilibrium behaviour of critical ferromagnets go much farther. Figure 5 shows the behaviour of the autocorrelation function after a quench to the critical point for a typical spin glass, the so-called Edwards-Anderson Ising spin glass with a bimodal distribution of the random couplings. Plotted against the time difference $t - s$, ageing is again obvious, see Figure 5a. Assuming the validity of the scaling ansatz (1) also for critical spin glasses, one obtains a perfect scaling behaviour as a function of t/s when choosing the appropriate value of the nonequilibrium exponent b, as shown on Figure 5b. The same observation holds when considering other dynamical two-time quantities. Thus the phenomenology of ageing at the critical point of spin glasses is the same as for critical ferromagnets, and this despite the fact that the free energy surface of spin glasses is very rugged due to frustration effects[10].

Looking a little bit more closely into the out-of-equilibrium behaviour of critical spin glasses, one nevertheless can identify unexpected features which greatly differ from the behaviour of the corresponding ferromagnetic systems. At a critical point it is expected that quantities like critical exponents or critical amplitude ratios are universal and do not depend on details of the considered system (as long as there are no global features involved, like the dimensionality of the system or the symmetry of the order parameter, which lead to a change of the universality class). The origin of this universal behaviour is well understood and has been verified in numerous cases. However, looking at nonequilibrium quantities in critical spin glasses one has the surprise that these quantities, which have been shown to be universal in critical ferromagnets, depend on the choice of the distribution of the

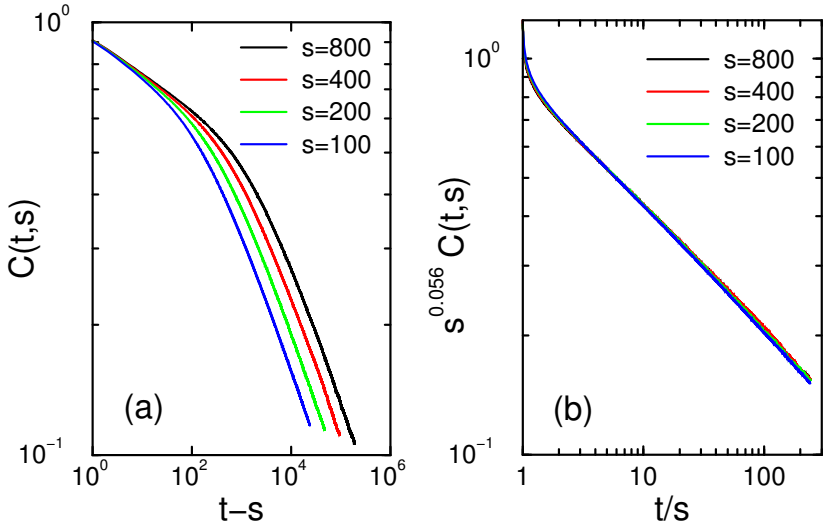

Figure 5. Autocorrelation function $C(t,s)$ as a function of (a) $t-s$ and (b) t/s for the three-dimensional Edwards-Anderson Ising spin glass with a bimodal distribution of the couplings after a quench to the critical point. As shown in (b) the scaling ansatz (1) yields an excellent data collapse.

	bimodal	gaussian	laplacian
b	0.056(3)	0.043(1)	0.032(2)
λ/z	0.362(5)	0.320(5)	0.259(2)
X_∞	0.12(1)	0.09(1)	0.055(2)

Table 1. Various nonequilibrium quantities determined numerically in the critical three-dimensional Edwards-Anderson Ising spin glass for different distributions of the random couplings.

couplings[11]. One example is given by the already mentioned exponent b whose value depends on the distribution function. This can be seen in Table 1 where the values of b are displayed for Edwards-Anderson spin glasses in three space dimensions with three different distributions of the couplings: bimodal, gaussian and laplacian. Also given are two other quantities, again supposed to be universal: the exponent λ/z which governs the decay of the autocorrelation function for large times, $C(t, s=0) \sim t^{-\lambda/z}$, and the limit value X_∞ of the so-called fluctuation-dissipation ratio X which can be used to assign an effective temperature to our nonequilibrium system[1]. It is obvious from the table that these quantities also depend on the choice of the distribution function. This fact is illustrated in Figure 6 where I show $C(t, s=0)$ and $X(s/t)$ for the three studied distributions.

Our nonequilibrium simulations yield therefore evidence that universality in critical spin glasses is much weaker than in critical ferromagnets. The dependence of critical quantities on the choice of the distribution of the couplings is unexpected and right now not well understood. It must be noticed, however, that equilibrium simulations of small systems also indicate a dependence of static quantities on the distribution function[12], even though the situation is not as clear-cut as it is for our nonequilibrium simulations.

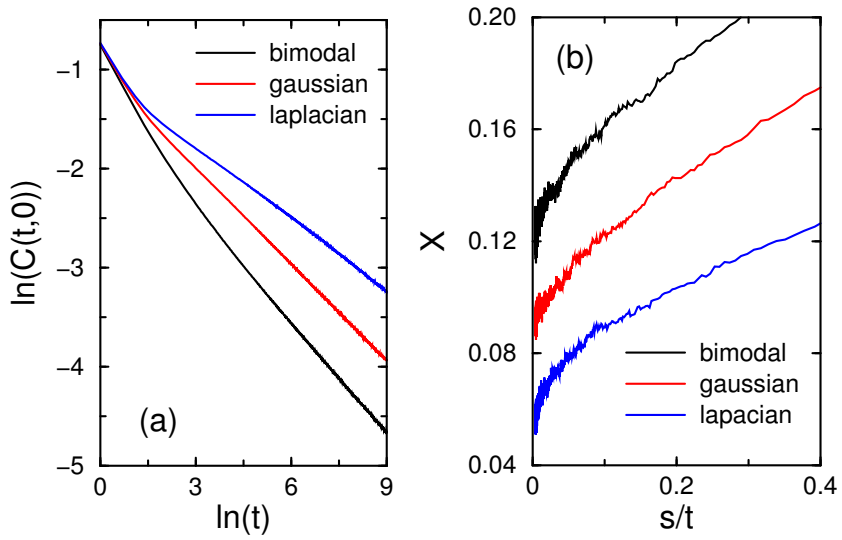

Figure 6. (a) $C(t, s = 0)$ as a function of time t and (b) fluctuation-dissipation ratio X as a function of s/t (yielding the limit value X_∞ when $s/t \longrightarrow 0$) for the three-dimensional Edwards-Anderson Ising spin glass with different distributions of the couplings.

4 Conclusion

In this contribution I have discussed ageing phenomena and dynamical scaling in systems which are brought out of equilibrium by a sudden change of temperature. For systems undergoing phase ordering one finds complete agreement between numerical simulations and the predictions coming from the recently developed theory of local scale invariance. At criticality, the existence of correction terms to the theoretical predictions has been proven numerically. Interestingly, critical spin glasses have the same phenomenology of ageing as critical ferromagnets. Surprisingly, for critical spin glasses the values of the studied nonequilibrium quantities depend on the choice of the distribution function of the random couplings. This points to the possibility that universality in critical spin glasses is weaker than in critical ferromagnets.

Acknowledgments

The numerical studies discussed here were made possible with a grant of computer time provided by the John von Neumann - Institut für Computing of the Research Centre Jülich.

References

1. L. F. Cugliandolo, in *Slow relaxation and non equilibrium dynamics in condensed matter*, J-L Barrat, J Dalibard, J Kurchan, M V Feigel'man eds (Springer, Berlin, 2003).
2. M. Henkel, M. Pleimling, C. Godrèche, and J.-M. Luck, *Aging, phase ordering, and conformal invariance*, Phys. Rev. Lett. **87**, 265701 (2001).
3. M. Henkel, *Phenomenology of local scale invariance: from conformal invariance to dynamical scaling*, Nucl. Phys. B **641**, 405 (2002).
4. M. Henkel and M. Pleimling, *Local scale invariance as dynamical space-time symmetry in phase-ordering kinetics*, Phys. Rev. E **68**, 065101(R) (2003).
5. M. Henkel, A. Picone, and M. Pleimling, *Two-time autocorrelation function in phase-ordering kinetics from local scale-invariance*, Europhys. Lett. **68**, 191 (2004).
6. E. Lorenz and W. Janke, in preparation.
7. P. Calabrese and A. Gambassi, *Ageing properties of critical systems*, J. Phys. A: Math. Gen. **38**, R133 (2005).
8. M. Pleimling and A. Gambassi, *Corrections to local scale invariance in the non-equilibrium dynamics of critical systems: Numerical evidences*, Phys. Rev. B **71**, 180401(R) (2005).
9. N. Kawashima and H. Rieger, in *Frustrated magnetic systems*, H. Diep (ed.) (World Scientific, Singapure, 2004).
10. M. Henkel and M. Pleimling, *Ageing and dynamical scaling in the critical Ising spin glass*, Europhys. Lett. **69**, 524 (2005).
11. M. Pleimling and I. A. Campbell, *Dynamic critical behaviour in Ising spin glasses*, Phys. Rev. B **72**, 184429 (2005).
12. L. W. Bernardi and I. A. Campbell, *Critical exponents in Ising spin glasses*, Phys. Rev. B **56**, 5271 (1997).

John von Neumann Institute for Computing

Interfacial Properties of Colloidal Model Systems

Richard Vink, Andres de Virgiliis, Stefan Wolfsheimer,
Tanja Schilling, Jürgen Horbach, and Kurt Binder

published in

NIC Symposium 2006 ,
G. Münster, D. Wolf, M. Kremer (Editors),
John von Neumann Institute for Computing, Jülich,
NIC Series, Vol. **32**, ISBN 3-00-017351-X, pp. 235-242, 2006.

http://www.fz-juelich.de/nic-series/volume32

Interfacial Properties of Colloidal Model Systems

Richard Vink, Andres de Virgiliis, Stefan Wolfsheimer, Tanja Schilling, Jürgen Horbach, and Kurt Binder

Institut für Physik, Johannes Gutenberg–Universität Mainz
Staudinger Weg 7, 55099 Mainz, Germany
E-mail: {schillit, horbach, kurt.binder}@uni-mainz.de

Monte Carlo (MC) simulations are presented in which the phase behavior of colloid-polymer mixtures and of colloidal liquid crystals is investigated. The simulations demonstrate that colloidal systems are good model systems to study the critical behavior of confined systems and the phase behavior of liquid crystals.

1 Introduction

Colloidal systems consist of big molecules (colloids) with a typical size ranging from about 1 nm to several μm, that are suspended in an atomistic solvent. With respect to the phase behavior, colloids are often similar to atomistic systems. However, in the case of colloids, one can often extract much more detailed information than in comparable atomistic systems. For instance, confocal microscopy can be used to make colloids visible and to measure their trajectories as in a computer simulation. Moreover, in experiment, the effective interactions between the colloids can be tuned to some extent by changing the properties of the solvent. Thus, colloids can be used as model systems for the more complicated atomistic world.

Information that is complementary to that extracted from experiments can be obtained in computer simulations of colloidal systems. From a simulation, thermodynamic quantities such as the free energy of the system can be determined, that are not accessible in an experiment. In addition the simple effective interactions between colloidal particles that can be realized in an experiment are well suited for computer simulations. In this work, we demonstrate this for two examples where "hard core" interactions between colloidal particles are considered. The first part of what follows is devoted to the phase behavior of colloid-polymer mixtures in confinement and the second part is on the phase behavior of colloidal liquid crystals (modeled by hard rods or platelets).

2 Phase Behavior of the Asakura-Oosawa (AO) Model in Confinement

Mixtures of colloids with non-adsorbing polymers are of particular interest because they may exhibit a fluid-fluid phase separation which is of purely entropic origin. This transition is driven by a depletion effect[1]: Each colloidal particle is surrounded by a depletion zone from which polymers are excluded. When two colloids are close together, their depletion zones overlap, thereby increasing their free volume, and hence the entropy of the system. If the gain in entropy is sufficient, the system demixes into a colloid-rich phase, the liquid phase, and a colloid-poor phase, the vapor phase. It is of particular interest to consider

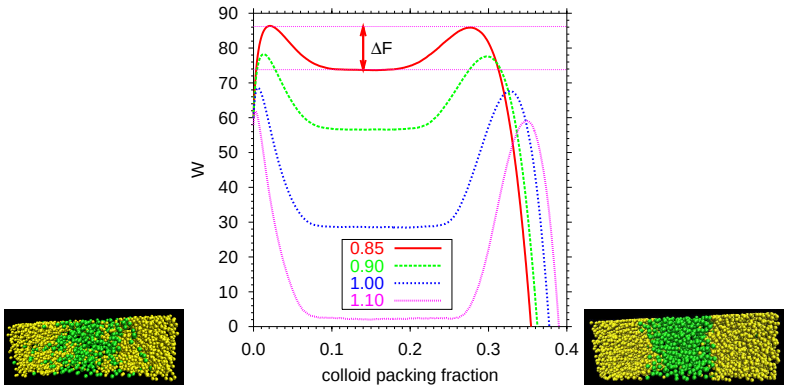

Figure 1. Logarithm of the probability $P(\eta_c)$ of observing a colloidal packing fraction η_c for an AO mixture with $q = 0.8$ at coexistence for several values of η_p^r as indicated. The simulations were performed in a box with $L_x = L_y = 16.7$ and $L_z = 33.4$ using periodic boundary conditions. The snapshots show the system in the phase separated region at $\eta_c = 0.13$ for $\eta_p^r = 0.85$ (left snapshot) and $\eta_p^r = 1.1$ (right snapshot). Polymers and colloids are shown as yellow and green spheres, respectively. From Ref.[6].

colloid-polymer mixtures confined between walls. In confined geometry, new phenomena are found such as capillary condensation, wetting transitions etc. and near the critical point a crossover scaling from 3D Ising to 2D critical Ising behavior is expected.

As a very simple model for a colloid-polymer mixture we use the so-called Asakura-Oosawa (AO) mixture[1]. Here, colloids and polymers are considered as spheres with respective radii R_c and R_p. Hard sphere interactions are assumed between colloid-colloid and colloid-polymer pairs, whereas polymer-polymer pairs can interpenetrate freely. Apart from a bulk system, we also consider a thin film geometry where the system is confined between two parallel hard walls.

In order to study the phase behavior of the AO model, we used Monte Carlo (MC) simulations in the grand canonical ensemble, in which the volume V, the respective fugacities $\{z_c, z_p\}$ of colloids and polymers, and the temperature T are fixed[2]. Note that the number of particles inside V is a fluctuating quantity in the grand canonical ensemble: in a grand canonical move, particles are inserted into the system or removed from it. Since in the AO model all allowed configurations have zero potential energy, temperature plays a trivial role and the phase behavior is controlled by the colloid-to-polymer size ratio q and the fugacities $\{z_c, z_p\}$. We consider here a size ratio $q = 0.8$ and put $R_c \equiv 1$ to set the length scale. One defines the quantity $\eta_p^r \equiv z_p(4\pi/3)R_p^3$, the so-called polymer reservoir packing fraction, which plays a role similar to the inverse temperature in simple fluids. In the bulk case, the simulations are performed in a box with edges $L_x \times L_y \times L_z$ using periodic boundary conditions. In the thin film case, periodic boundary conditions are only applied in the x and y directions, while in the z direction two parallel walls are placed, one at $z = 0$ and the other one at $z = L_z = D$ (with D being the film thickness).

The use of the grand canonical ensemble allows to fully characterize the fluid-fluid demixing transition of the AO model. As we shall see below, finite-size scaling can be applied to determine critical properties, the interfacial tension and other properties of the interface separating the colloid vapor from the colloid liquid phase. However, a common

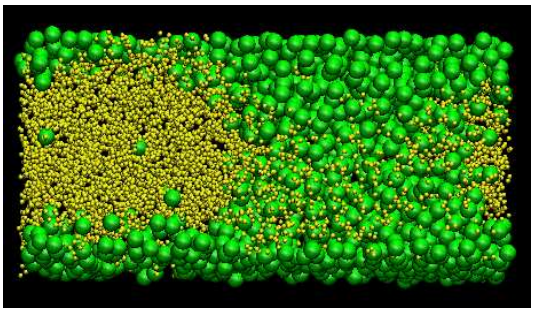

Figure 2. Snapshot of the AO model confined between hard walls ($L_x = L_y = 20$ and $D = 10$) in the phase separated region for $\eta_{\rm p}^{\rm r} = 1.1$ and $\eta_{\rm c} = 0.15$. Polymers and colloids are shown as yellow and green spheres, respectively. Note that the size of the polymers is not at scale to allow for a better visibility of the colloids.

problem of grand canonical MC is a low probability for particle insertions at high densities. In our case, high densities have to be considered due to the presence of the polymers. We have solved this problem by using a cluster move: instead of inserting or removing particles one at a time, clusters of polymers are removed for each colloid that is inserted. The details of this move can be found elsewhere[3]. Moreover, a reweighting scheme enables the simulation to cross the free energy barrier separating the colloid vapor phase from the colloid liquid phase, and sample the phase-separated regime. Here, we use successive umbrella sampling the details of which can be found in the original reference[4].

The grand canonical MC yields the probability $P(\eta_{\rm c})$ that a certain colloid packing fraction $\eta_{\rm c} = (4\pi/3)R_{\rm c}^3 N_{\rm c}/V$ is observed, i.e. one obtains a histogram counting how often a certain colloid packing fraction has occurred. If phase separation emerges, the distribution $P(\eta_{\rm c})$ is bimodal. Fig. 1 shows the logarithm of distributions for different values of $\eta_{\rm p}^{\rm r}$. Note that $-\ln(P)$ is proportional to the free energy of the system. The peaks at low $\eta_{\rm c}$ correspond to the colloidal vapor and those at high $\eta_{\rm c}$ to the colloidal liquid phase. The region in between is the phase-separated regime. The distributions in Fig. 1 are for the bulk case and were obtained at coexistence, which means that the fugacity $z_{\rm c}$ was tuned such that the area under both peaks is equal. The height of the barrier marked ΔF in Fig. 1 corresponds to the free energy barrier separating the coexisting phases[5]. This barrier is related to the interfacial tension γ via $\gamma = \Delta F/(2A)$ (with $A = L_x \times L_y$ the area of the interface) provided that the size of the system is large enough. The factor $1/2$ in the latter equation for γ stems from the use of periodic boundary conditions that yield the formation of two interfaces in the system (see snapshots in Fig. 1). It is crucial to use an elongated box for an accurate determination of γ since this enforces the flat region seen in the distribution $P(\eta_{\rm c})$ which indicates that the two interfaces in the phase-separated regime are well-separated from each other and thus interactions between the interfaces are suppressed. A detailed analysis of the interfacial tension and other interfacial properties such as capillary waves can be found in recent publications[3,6–8].

Fig. 2 shows a snapshot of a confined AO mixture for the film thickness $D = 10$ in the phase-separated regime. As one can infer from the figure, the wall effectively attracts the colloids and thus colloid-rich layers are formed at the walls. We have studied how the presence of walls affects the critical behavior of the AO model by determining the phase

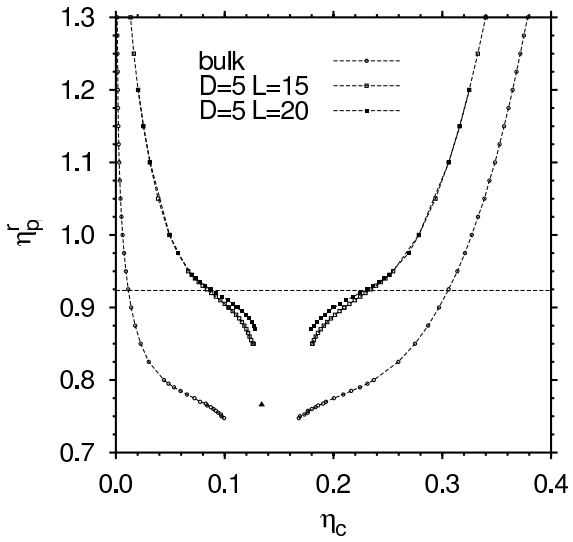

Figure 3. Phase diagram of the AO model with $q = 0.8$ in bulk (open circles) and confinement (open and closed squares for film thickness $D = 5$ for different lateral dimensions L). The black triangle marks the bulk critical point. The dashed horizontal line marks the critical polymer packing fraction of the confined systems in the limit $L \to \infty$ which is estimated from the cumulant intersection method (see text). From Ref.[9].

diagrams (binodals) from the probability distributions $P(\eta_c)$ as obtained from the grand canonical MC simulations. To this end, the packing fractions for the colloid vapor and colloid liquid phase, denoted respectively by η_c^v and η_c^l, have been calculated from the probability distributions at coexistence via

$$\eta_c^v = 2 \int_0^{<\eta_c>} P(\eta_c) d\eta_c \tag{1}$$

$$\eta_c^l = 2 \int_{<\eta_c>}^{\infty} P(\eta_c) d\eta_c \tag{2}$$

where $< \eta_c >$ is the first moment of $P(\eta_c)$, $< \eta_c >= \int_0^\infty \eta_c P(\eta_c)$.

Fig. 3 shows the binodals for the bulk and for a thin film of thickness $D = 5$ for two different values of L. Since η_p^r plays the role of inverse temperature, the phase diagram appears inverted compared to temperature-density phase diagrams of simple fluids. As the figure demonstrates, confinement shifts the critical point towards higher η_p^r and slightly higher values of η_c. In the vicinity of the critical point pronounced finite size effects are present which can be infered from a comparison of the curves for $L = 15$ and $L = 20$ in the case of the confined geometry. The critical points that are indicated in the figure were estimated from a finite size scaling analysis using the cumulant intersection method[2]. From the latter method, we have also infered that properties near the critical point seen in the simulation of the confined AO model can neither be attributed to the 2D nor to the 3D Ising model universality class. This can be intuitively understood in terms of the correlation length ξ that diverges near the critical point: when ξ exceeds the film thickness D, the system becomes effectively two-dimensional, such that a crossover from 2D to 3D

Ising critical behavior is expected. A detailed discussion of this issue can be found in a forthcoming publication[9].

In summary, we have performed extensive MC simulations to investigate the phase behavior of an AO model in the bulk and in confined geometry. We have demonstrated that the simulation allows an accurate description of interfacial properties and critical phenomena.

3 Interfacial Properties of Colloidal Liquid Crystals

Suspensions of anisotropic particles form liquid crystals at sufficiently high pressure or low temperature. In particular, suspensions of rod-like as well as plate-like particles undergo a phase transition from a phase in which the particle orientations are disordered ("isotropic" phase) to a phase in which there is a direction of preferred alignment ("nematic" phase). In many materials the direction of preferred alignment of the particles can be easily manipulated with electric or magnetic fields, which means that the optical properties of these materials can be tuned. This has made liquid crystals the basis for a large range of technological devices[10].

Liquid crystals also pose fundamental questions about the role which particle anisotropy plays in phase transitions and interfacial properties. In the 1940s Onsager showed that the transition between the isotropic phase (I) and the nematic phase (N) is of entropic nature and that it can be explained by a simple geometrical argument[15]. However, the calculation of interfacial properties in the Onsager model proved to be far more difficult than the prediction of the phase transition.

Also, there is a crucial difference between the nematic ordering of rod-like and of plate-like particles: The former may be quantitatively understood at the level of second virial theory (at least for infinite aspect ratios) whereas this is not the case for the latter. Local order differs strongly between platelets and rods. One feature that is affected by this is the isotropic nematic interface ("IN-interface"). We have used the super computing resources in Jülich to investigate the interfacial tension γ_{IN} in suspensions of rods and of platelets. (For an introduction to interfacial tensions in colloidal systems see reference[14].)

As a model for rods we used spherocylinders of length l and diameter d; as a model for platelets we used cut spheres of thickness l and diameter d. We studied IN-coexistence by means of grand canonical MC simulations, where the volume V, the temperature T, and the chemical potential μ are fixed, while the number of particles in the simulation box fluctuates.

Fig. 4 shows a configuration snapshot taken during a simulation of a suspension of soft spherocylinders. Different orientations are labeled by colour. On the left the system is isotropic, on the right it is nematic. Because of the periodic boundary conditions, there are two interfaces. The interfaces are marked by dashed lines.

Fig. 5 shows the probability distribution $P(\rho)$ of the density of particles in the system. (The quantity plotted on the x-axis, ρ^* is the number density N/V divided by the density at closest packing).

The interfacial tension γ_{IN} turns out to be very small. For rods we find[11,12] $\gamma_{\mathrm{IN}}^{\mathrm{rods}} = (0.09 \pm 0.01)\, k_{\mathrm{B}}T/ld$. For platelets the biphasic gap becomes so narrow, that we could only determine[13] an upper bound for the interfacial tension $\gamma_{\mathrm{IN}}^{\mathrm{platelets}} < (0.013 \pm 0.004)\, k_{\mathrm{B}}T/d^2$. These numbers are several orders of magnitude smaller than interfacial

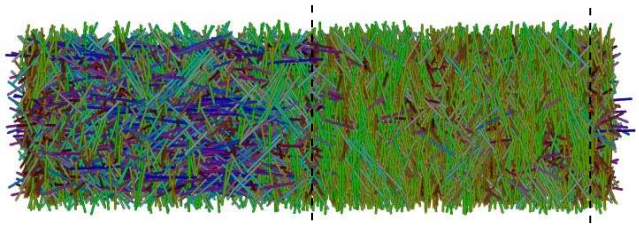

Figure 4. Configuration snapshot of spherocylinders with l/d=15. Orientations are labeled by colour. On the left the system is isotropic, on the right it is nematic. The interfaces are marked by dashed lines. (There are two interfaces because of the periodic boundary conditions.)

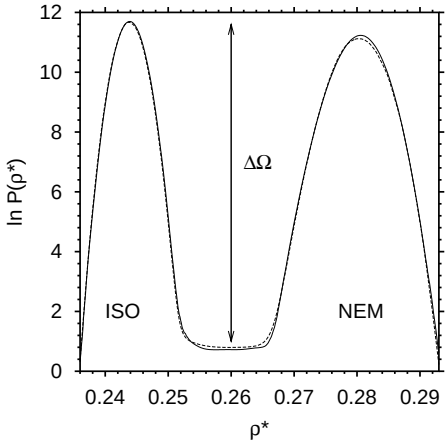

Figure 5. Density distribution at coexistence for soft spherocylinders, l/d=15. The tension of the isotropic nematic interface can be determined from the height of the peaks $\Delta\Omega$.

tensions in typical atomistic or molecular sustems. This is due to the fact that the IN-interface is of purely entropic origin. Such small interfacial tensions are very difficult to compute in simulations, and we had to develop new sampling techniques to be able to reach these values. Details can be found in[11].

In particular, the extremely low value of $\gamma_{\mathrm{IN}}^{\mathrm{plates}}$ was surprising. Therefore our collaborators in Utrecht performed an experiment to check the simulation results. In experiments, one standard and popular way to measure an interfacial tension is the "capillary rise method", where the interfacial tension is determined from the rise of the miniscus between two phases at a hard wall. In general however, this method can not be applied to liquid crystals. The walls and the interface orient the liquid crystal ("interfacial anchoring"), causing deformations of the director field. Platelets anchor homeotropically (i.e. they lie flat) on hard walls and on the IN-interface. The capillary rise is thus determined by a compromise between interfacial anchoring and Frank elasticity.

Before we could interpret our experimental results on the capillary rise, we therefore needed to analyze the elastic contributions. A colloidal suspension of sterically stabilized

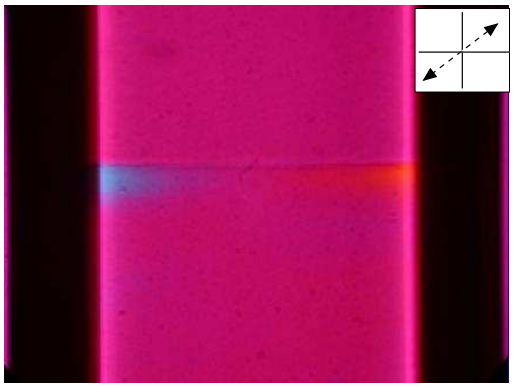

Figure 6. Polarised light micrographs of the IN interface taken between crossed polarisers. Polariser orientation is indicated by the cross. A retardation plate was used to show the orientation of the director field; its slow axis is indicated by the dashed arrow.

gibbsite [$Al(OH)_3$] platelets in toluene was synthesized according to van der Kooij and Lekkerkerker[16]. To investigate the IN-interface, we prepared a sample of the suspension in the IN-biphasic gap in a 500 μm$\times$500 μm glass capillary[13]. Phase separation occurred over a time scale of a few days; annealing of the domains in the nematic phase took several weeks.

A polarised light microscope was then used to study the IN-interface near the wall and the orientation of the director field in the capillary "foot", i.e. in the region of risen nematic phase at the wall. Fig. 6 shows a micrograph of the interface taken between crossed polarizers with a retardation plate of $\Delta n\, D = 530$ nm, where Δn is the birefringence and D is the thickness of the sample. A retardation plate permits to obtain the direction of the so-called fast and slow axes in a birefringent sample. Depending on the mutual orientation of slow and fast axes in the retardation plate and in the sample, the retardation due to the plate is either added to or subtracted from the samples' birefringence. In regions where the slow axis of the sample is parallel to the slow axis of the retardator "addition" occurs and the pink colour shifts to higher orders, i.e. blue. Whereever they are perpendicular, subtraction occurs and the colour becomes orange. In a separate experiment, we found that the slow axis of a well-oriented suspension of our colloidal gibbsite platelets is parallel to the nematic director. In Fig. 6 the slow axis of the retardation plate is indicated by the arrows. The "corners" of the nematic phase are shifted in colour as compared to the bulk, which is pink. Hence we can conclude that the defect of the director field, which would be expected to lie at the contact line, has a large uniform core. Therefore the capillary "foot" is not affected by a bend director field and we can extract $\gamma_{\rm IN}$ without knowledge of the elastic constants of the sample. (For details of the analysis see[13].) From the height of the capillary rise we conclude $\gamma_{\rm IN} < (0.04 \pm 0.02)\, k_B T/d^2$.

In summary, we have performed computer simulations of the isotropic-nematic interface in colloidal liquid crystals. We have found that the interfacial tension in suspensions of rod-like particles is one order of magnitude larger than in plate-like particles. Our results could be compared to experiments on the capillary rise of the IN-interface without the need to know the elastic constants of the system.

4 Acknowledgmens

T.S. and J.H. were supported by MWFZ Forschungsfonds and the Emmy Noether Programm of the Deutsche Forschungsgemeinschaft (DFG). Furthermore, we acknowledge support from SFB TR6, projects A5 and D5. We thank Ronald Blaak for helpful comments. Allocation of computer time on the JUMP at the Forschungszentrum Jülich is gratefully acknowledged. A Part of this work was financially supported by the "Nederlandse Organisatie voor Wetenschappelijk Onderzoek" (NWO).

References

1. S. Asakura and F. Oosawa, Surface Tension of High-Polymer Solutions, J. Chem. Phys. **22**, 1255 (1954).
2. D. P. Landau and K. Binder, *A Guide to Monte Carlo Simulations in Statistical Physics* (Cambridge University Press, Cambridge, 2000).
3. R. L. C. Vink and J. Horbach, Grand canonical Monte Carlo simulation of a model colloid-polymer mixture: Coexistence line, critical behavior, and interfacial tension, J. Chem. Phys. **121**, 3253 (2004).
4. P. Virnau and M. Müller, Calculation of free energy through successive umbrella sampling, J. Chem. Phys. **120**, 10925 (2004).
5. K. Binder, Monte Carlo calculation of the surface tension for two- and three-dimensional lattice-gas models, Phys. Rev. A **25**, 1699 (1982).
6. R. L. C. Vink and J. Horbach, Critical behaviour and interfacial fluctuations in a phase-separating model colloid-polymer mixture: grand canonical Monte Carlo simulations, J. Phys.: Condens. Matter **16**, S3807 (2004).
7. R. L. C. Vink, J. Horbach, and K. Binder, Critical phenomena in colloid-polymer mixtures: Interfacial tension, order parameter, susceptibility, and coexistence diameter, Phys. Rev. E **71**, 011401 (2005).
8. R. L. C. Vink, J. Horbach, and K. Binder, Capillary waves in a colloid-polymer interface, J. Chem. Phys. **122**, 134905 (2005).
9. R. L. C. Vink, J. Horbach, and K. Binder, Critical behavior of a colloid-polymer mixture confined between walls, in preparation.
10. P. G. de Gennes and J. Prost, *The Physics of Liquid Crystals* (Clarendon Press, Oxford, 1993).
11. R. L. C. Vink, S. Wolfsheimer, and T. Schilling, Isotropic-nematic interfacial tension of hard and soft rods: application of advanced grand canonical biased sampling techniques, in press (2005).
12. R. L. C. Vink and T. Schilling, Interfacial tension of the isotropic-nematic interface in suspensions of soft spherocylinders, Phys. Rev. E **71**, 051716 (2005).
13. T. Schilling, P. van der Schoot, D. van der Beek, R. L. C. Vink, R. van Roij, M .Dijkstra, and H. Lekkerkerker, Ultra-low interfacial tension in suspensions of colloidal platelets, in preparation (2005).
14. P. van der Schoot, Remarks on the interfacial tension in colloidal systems, J. Phys. Chem. B **103**, 8804 (1999).
15. L. Onsager, Ann. N. Y. Acad. Sci. **51**, 627 (1949).
16. F. M. van der Kooij and H. N. W. Lekkerkerker, J. Phys. Chem. B **102**, 7829 (1998).

John von Neumann Institute for Computing

Polymers - Soft Matter

Kurt Kremer

published in

NIC Symposium 2006 ,
G. Münster, D. Wolf, M. Kremer (Editors),
John von Neumann Institute for Computing, Jülich,
NIC Series, Vol. **32**, ISBN 3-00-017351-X, pp. 243-244, 2006.

http://www.fz-juelich.de/nic-series/volume32

Polymers - Soft Matter

Kurt Kremer

Max Planck Institute for Polymer Research
55021 Mainz, Germany
E-mail: {*kremer@mpip-mainz.mpg.de*}

Synthetic polymeric materials, most biological, colloidal and many other systems are nowadays termed soft matter. They are soft because they are dominated by a typically nanometer (and larger) length scale and the corresponding energy density for the non-bonded interactions is many orders of magnitude smaller than for conventional solids. This energy density to a very first approximation is a good guess of the elastic constants, thus they are "very soft". In particular for the above mentioned materials the thermal energy k_BT is the characteristic energy scale and consequently entropy plays an important role. Soft matter means strongly fluctuating matter. When the fluctuations are mostly frozen one usually is left with a disordered, glassy system. Only in exceptional cases one can obtain (then very important) crystalline structures. For simulation studies and a quantitative understanding in general, this means that it is not sufficient to study just local interactions but one must link this to larger scales. Depending on the problem this can reach from the Å-level up into the μm scale and some times beyond. Each length scale under consideration has its own characteristic methods of investigation. Sometimes they are treated individually in order to study specific effects; in other cases they are combined in order to derive a more quantitative overall understanding. In this respect the four contributions on macromolecules in this report to some extent represent the width and the typical questions of the field. They range from basic studies towards a better design of specific fuel cell components to highly idealized protein models where generic aspects of how a large molecule can fold/unfold in the presence of a (selective) surface are studied. Similarly they range from aspects close to application to fundamental first principle tests.

First Bachmann and Janke study a lattice model of HP proteins. This is a most basic model, where the protein is reduced to hydrophilic (polar) and hydrophobic units and is frequently employed to study fundamental aspects of protein folding. Each unit models a residue. By the use of an improved growth algorithm for the condensed phase they were able to study different heteropolymers (statistical proteins) of up to 103 units. Their emphasis was not so much on the folded configuration itself but rather on the behavior close to an adsorbing surface, where this surface attracts the P, the H or both units. With the help of their improved algorithm and massive CPU time support from NIC they were able to map out a characteristic structure diagram as function of the surface coupling. Questions like this occur in fields like protein crystallization as well as many technical applications where protein coatings are wanted or are encountered as contamination. Surfaces and interfaces in general play an important role in polymer physics, chemistry and technology. Seidel and Kumar study polyelectrolyte chains bound by one end to the surface, so called polyelectrolyte brushes. Most synthetic polymers are strongly hydrophobic, thus they are not at all water soluble. One way to change that is to add side groups, which dissociate ions in water. Then the chains are charged and become water soluble due to the high

osmotic pressure of the released ions. Attached to the surface of e.g. a colloid, the colloid can not coagulate any more; they are electrostatically and sterically stabilized. Seidel and Kumar now treat such a polyelectrolyte brush as a function of salt added to the solution. The addition of salt reduces the osmotic pressure of the counter ions and consequently the brushes shrink. It is this shrinking which they study in comparison to analytic theory and also in relation to experiment.

So far simple chains or rather dilute systems have been discussed. Dense polymeric melts and solutions, however, represent a continuing challenge to scientists. For simulations the extremely long relaxation times often limit the studies. Thus there is a continued effort to overcome this by new methods. Müller, Paul and Binder shortly review extensive work on phase transitions employing so called single chain mean field (SCMF) simulations. The trick is to couple a Monte Carlo simulation of a single polymer with a density field of the surrounding polymers and then in a self consistent way evolve the surrounding field due to the simulation of the chain. The power of this approach is demonstrated for several examples and compared to more conventional Monte Carlo simulations. For the cases applicable it reduces the computational effort dramatically. They start out with the benchmark problem of spinodal decomposition in binary polymer blends, a very well studied problem which allows best to test the power of the method. Then this is applied to two cases, which are important to nanotechnology, namely the drying of thin polymer films and the microphase separation of block copolymers on patterned substrates, which selectively bind one of the two components with a pattern which is commensurable or incommensurable with the ordered block copolymer melt.

Finally Kulikovsky and Spohr look at low temperature fuel cells as a whole as well as at specific components. They follow an integrated ansatz in order to support the technology developed at the FZ Jülich. These calculations are very involved and link quantum chemical studies, all atoms force field simulations as well as systems engineering methods. In each case specific problems which are crucial for a better technical design are investigated. On the quantum chemical side they study the oxidation of methanol on noble metal catalysis as it occurs in DMFCs (Direct Methanol Fuel Cell). Currently the technological setup requires a high, thus costly load of noble metals, which also turns out to participate in performance limitations. Therefore the authors study such processes under realistic conditions. In a second part the mobility of protons in typical fuel cell membrane such Nafion is studied by careful all atom force field molecular dynamics simulation of type, which allows the formation of strong hydrogen bonds and proton transfer. Finally the whole system is studied with a continuum approach on an engineering level in order to better understand fluxes of charges, heat but also gases and water in the PEFLs (Polymer Electrolyte Fuel Cell) which use hydrogen instead of methanol as fuel. These are just three problems of recent fuel cell research, which require significant support from computer simulations.

These examples give a short overview of the soft matter activities at NIC. Current scientific and technological developments which more and more incorporate knowledge and capabilities from very different areas, such as physics, chemistry, biology and materials engineering to name just the most important ones, demand a comprehensive understanding of complicated systems. Such an understanding is not possible without the use of well focussed massive computer simulations.

John von Neumann Institute for Computing

Chain-Growth Simulations of Lattice-Peptide Adsorption to Attractive Substrates

Michael Bachmann and Wolfhard Janke

published in

NIC Symposium 2006 ,
G. Münster, D. Wolf, M. Kremer (Editors),
John von Neumann Institute for Computing, Jülich,
NIC Series, Vol. **32**, ISBN 3-00-017351-X, pp. 245-252, 2006.

http://www.fz-juelich.de/nic-series/volume32

Chain-Growth Simulations of Lattice-Peptide Adsorption to Attractive Substrates

Michael Bachmann and Wolfhard Janke

Institut für Theoretische Physik
Universität Leipzig, 04109 Leipzig, Germany
E-mail: {bachmann, janke}@itp.uni-leipzig.de

Based on a newly developed contact-density chain-growth algorithm, we have simulated a non-grafted peptide in the vicinity of different attractive substrates. We analyzed the specificity of the peptide adsorption by focussing on the conformational transitions the peptide experiences in the binding/unbinding processes. In a single simulation run, we obtained the contact density, i.e., the distribution of intrinsic monomer-monomer contacts and monomer-substrate nearest-neighbor contacts. This allows a systematic reweighting to all values of external control parameters such as temperature and solvent quality after the simulation. The main result is the complete solubility-temperature pseudo-phase diagram which is based on the corresponding specific-heat profile. We find a surprisingly rich structure of pseudo-phases that can roughly be classified into compact and expanded conformations in both regimes, adsorption and desorption. Furthermore, underlying subphases were identified, which, in particular, appear noticeably in the compact pseudo-phases.

1 Introduction

In recent experiments it could be shown that the affinity of peptides to self-assemble at metal[1] and semiconductor substrates[2–4] is highly influenced by the amino acid content of the peptide, the order of the residues within the sequence, the specific substrate, and its crystal orientation at the surface.

In this study, we investigate the binding specificity with a minimalistic lattice model for the hybrid system of a peptide in the vicinity of an attractive substrate. Due to the specific properties of the peptide, this problem is distinguishingly different from the hybrid system of a (homo)polymer near an adsorbing substrate, which has already been extensively studied[5–10]. The peptide sequence consists of hydrophobic and polar residues, i.e., the 20 protein-building amino acids are classified into only two groups. The idea behind this hydrophobic-polar (HP) model[11] is that proteins usually possess a compact hydrophobic core surrounded by a shell of polar residues which screen the core from the aqueous environment. For this reason and for simplicity, only an effective, short-range attractive force between the hydrophobic monomers is employed. Furthermore, the peptide is restricted to live on a simple-cubic lattice. The volume exclusion of the side chains is simply taken into account by considering only self-avoiding linear chains. The energy of such a lattice peptide is related to the number of hydrophobic nearest-neighbor contacts, n_{HH}.

The power of this highly abstract model lies in its simplicity. Peptides with more than 100 residues can be studied – this is in striking contrast to refined all-atom protein models, where a systematic analysis of thermodynamic properties is only reliably possible for peptides with hardly more than 20 amino acids. It is expected that for longer peptides atomic details become less relevant and, therefore, simplified (“coarse-grained”) heteropolymer

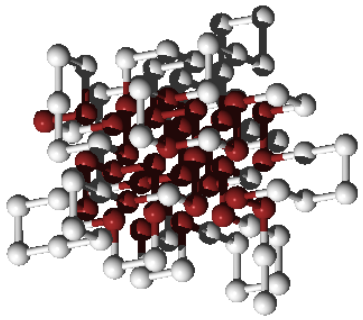

Figure 1. Putative ground-state conformation of the model peptide in the bulk (or in the desorbed pseudo-phase).

models can give satisfying qualitative answers to specific questions, e.g., regarding tertiary conformational transitions[15,16], and systematic sequence analyses[17].

2 Lattice Peptide and Hybrid System Model

As a model peptide, we use the HP transcription of the 103-residue protein *cytochrome c*, which was extensively studied in the past[12–14,18]. We have first performed a detailed analysis of this model peptide in the bulk[18] by applying the newly developed multicanonical chain-growth algorithm[15]. This method allowed the precise determination of the density of states for this system covering more than 50 orders of magnitude. The lowest-energy conformation we identified[18] possesses 56 hydrophobic contacts (see Fig. 1) and exhibits a degeneracy of the order of 10^{16}. It is therefore likely that there still exist lower-lying energetic states.

Here, this lattice peptide resides in a cavity with an attractive substrate. In order to study the specificity of residue binding, we distinguish three substrates with different affinities to attract the peptide monomers: (a) the type-independent attractive, (b) the hydrophobic, and (c) the polar substrate. The number of corresponding nearest-neighbor contacts between monomers and substrate shall be denoted as n_s^{H+P}, n_s^H, and n_s^P, respectively. The energy (in arbitrary units) of the hybrid system is then given by

$$E_s(n_s, n_{\rm HH}) = -n_s - s n_{\rm HH}, \tag{1}$$

where $n_s = n_s^{H+P}$, n_s^P, or n_s^H, depending on the substrate. Besides the temperature T, the solubility (or reciprocal solvent parameter) s is an external control parameter which governs the quality of the solvent (the larger the value of s, the worse the solvent). The simulation of this model is based on a recently developed contact-density chain-growth algorithm[10] which allows a direct estimation of the degeneracy (or contact density) $g(n_s, n_{\rm HH})$ of macro-states of the system with given contact numbers n_s and $n_{\rm HH}$.

3 Contact-Density Chain-Growth Algorithm

The contact-density chain-growth algorithm is a suitably enhanced version of the multicanonical chain-growth algorithm[15], which is based on the pruned-enriched variant[19] of

the Rosenbluth chain-growth method[20]. In contrast to move-set based Metropolis Monte Carlo or conventional chain-growth methods which would require many separate simulations to obtain results for different parameter pairs (T, s) and which frequently suffer from slowing down in the low-temperature sector, our method allows the computation of the *complete* contact density for each system within a *single* simulation run. Since the contact density is independent of temperature and solubility, energetic quantities such as the specific heat can easily be calculated for all values of T and s (nonenergetic quantities require accumulated densities to be measured within the simulation, but this is also no problem). For all systems, 10 independent runs were initialized, each generating 10^8 conformations.

In order to regularize the influence of the unbound conformations and for computational efficiency, the heteropolymer is restricted to reside in a cage, i.e., in addition to the physically interesting attractive surface there is a steric, neutral wall parallel to it in a distance z_w. The value of z_w is chosen sufficiently large to keep the influence on the unbound heteropolymer small (in this work we used $z_w = 200$).

4 Pseudo-Phase Diagram of Conformational Transitions

Our main interest is devoted to the conformational transitions the peptide experiences in the binding or adsorption process to the substrates. For a first overview, it is convenient to study the specific heat C_V as a function of the external parameters temperature T and solubility s. Respective ridges and peaks of the specific heat can be considered as signals of conformational activity. Due to the fixed length of the peptide sequence, a conventional discussion of thermodynamic phase transitions (e.g., in terms of finite-size scaling) is not possible. It should also noted that the behavior of *finite* polymer and peptide systems in future nanotechnological applications will be of essential interest as a consequence of the need for maximally possible space reduction, e.g., for nanoelectronic circuits. In such cases, subphase crossover transitions, which are of marginal or no importance in large systems, strongly influence the self-assembling structure of the polymer or peptide at the substrate.

In Figs. 2(a)-(c) the color-coded profiles of the specific heats for the different substrates are shown (the brighter the colour, the larger the value of C_V). We interpret the ridges (for accentuation marked by white and gray lines) as the boundaries of the pseudo-phases. It should be noted, however, that in such a finite system the exact positions of active regions exhibited by fluctuations of other quantities usually deviate, but the qualitative behavior is similar.[15] Despite the surprisingly rich and complex phase behavior there are main "phases" that can be distinguished in all three systems. These are separated in Figs. 2(a)-(c) by gray lines. Comparing the three systems we find that they all possess pseudo-phases, where adsorbed compact (AC), adsorbed expanded (AE), desorbed compact (DC), and desorbed expanded (DE) conformations dominate, similar to the generic phase diagram of a homopolymer[10]. "Compact" here means that the heteropolymer has formed a dense hydrophobic core, while expanded conformations form dissolved, random-coil-like structures. The sequence and substrate specificity of heteropolymers generates, of course, new interesting and selective phenomena not available for homopolymers. One example is the pseudo-phase of adsorbed globules (AG), which is noticeably present only in those systems, where all monomers are equally attractive to the substrate (Fig. 2(a)) and where polar monomers favour contact with the surface (Fig. 2(b)). In this phase, the con-

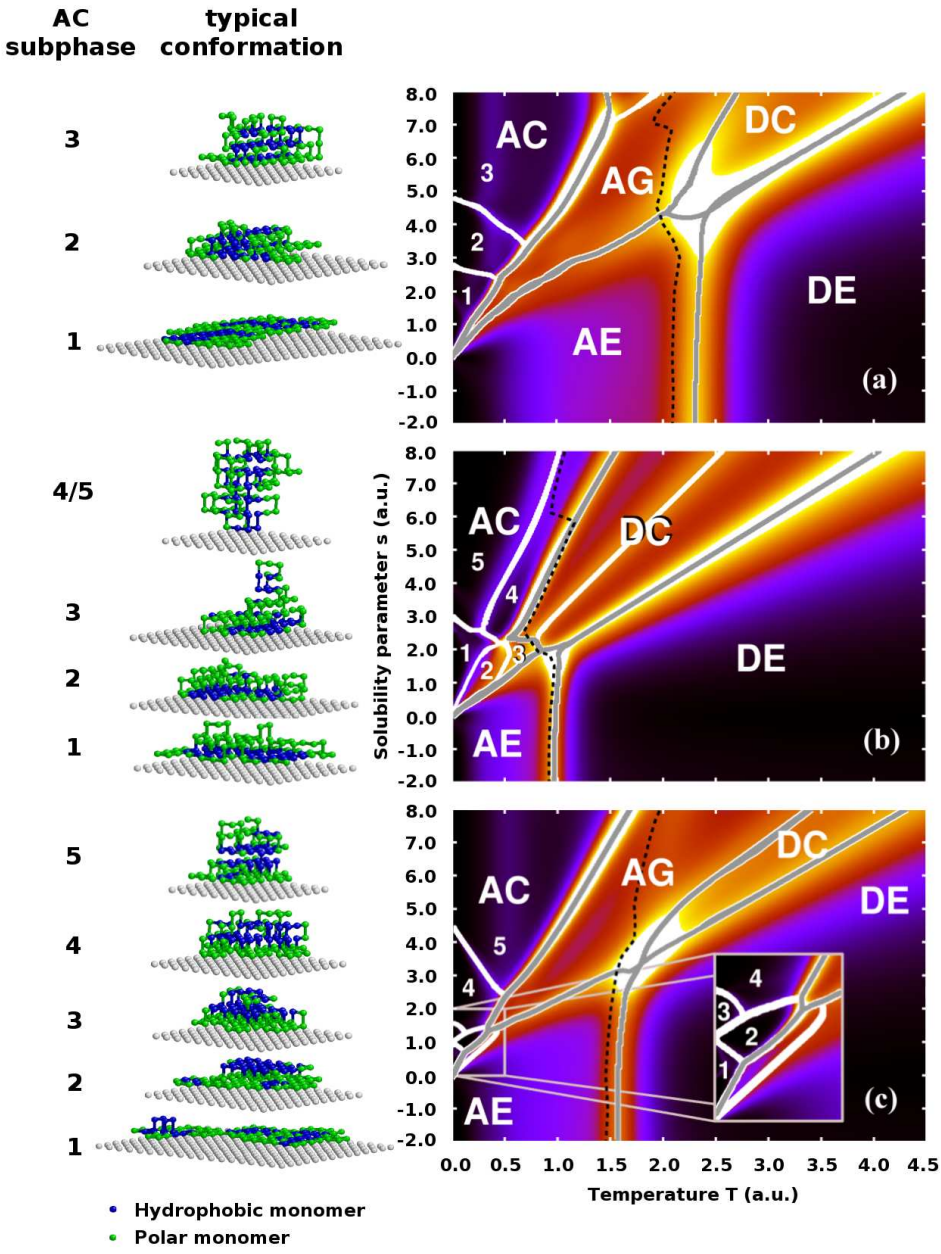

Figure 2. Specific-heat profiles as a function of temperature T and solubility parameter s of the 103-mer near three different substrates that are attractive for (a) all, (b) only hydrophobic, and (c) only polar monomers. White lines indicate the ridges of the profile. Gray lines mark the main "phase boundaries". The dashed black line represents the first-order-like binding/unbinding transition state, where the contact free energy possesses two minima (the adsorbed and the desorbed state). In the left panel typical conformations dominating the associated AC phases of the different systems are shown.

formations are intermediates in the binding/unbinding region. This means that monomers currently desorbed from the substrate have not yet found their position within a compact conformation.

The strongest difference between the three systems is their behavior in pseudo-phase AC, which is roughly parameterized by $s > 5T$. Representative conformations for all AC subphases are shown in the left panel of Fig. 2. If hydrophobic and polar monomers are equally attracted by the substrate (Fig. 2(a)), we find three AC subphases in the parameter space plotted. In AC1 film-like conformations dominate, i.e., all 103 monomers are in contact with the substrate. The formation of a single, compact hydrophobic core proceeds by layering transitions from AC1 to AC3 via AC2. The reason for the existence of phase AC2 is the reduced cooperativity of the polar monomers due to their surface attraction. In AC3, the heteropolymer has maximized the number of hydrophobic contacts and only local arrangements of monomers on the surface of the very compact structure lead to the still possible maximum number of substrate contacts.

The AC heteropolymer conformations adsorbed at a surface that is only attractive to hydrophobic monomers (Fig. 2(b)) depend on two concurring hydrophobic forces: substrate attraction and formation of intrinsic contacts. The *single* film-like hydrophobic domain in AC1 is maximally compact, at the expense of displacing polar monomers into upper layers. In subphase AC2 intrinsic hydrophobic contacts are entropically broken, while AC3 exhibits hydrophobic layers at the expense of hydrophobic substrate contacts. A dramatic, highly cooperative, hydrophobic collapse accompanies the transitions from AC1 to AC4/5, where in a one-step process the compact two-dimensional domain transforms to the compact three-dimensional hydrophobic core.

Not less exciting is the subphase structure of the heteropolymer interacting with a polar substrate (Fig. 2(c)). For small values of s and T, the behavior of the heteropolymer is dominated by the concurrence between polar monomers contacting the substrate and hydrophobic monomers favouring the formation of a hydrophobic core, which, however, also requires cooperativity of the polar monomers. In AC1, film-like conformations with disconnected hydrophobic clusters dominate. Entering AC2, a second hydrophobic layer forms at the expense of a reduction of polar substrate contacts. In contrast to the case of a hydrophobic substrate (Fig. 2(b)), the strong surface attraction of polar monomers hinders here the formation of a compact hydrophobic core (AC2/3 to AC5) which results in the intermediate subphase AC4.

5 Free-Energy Landscape from a Different Perspective

The contact numbers n_s and n_{HH} are kind of order parameters adequately describing the macro-state of the system. With its degeneracy $g(n_s, n_{\mathrm{HH}})$, we define the contact free energy as $F_{T,s}(n_s, n_{\mathrm{HH}}) \sim -T \ln g(n_s, n_{\mathrm{HH}}) \exp(-E_s/T)$ and the probability for a macro-state with n_s substrate and n_{HH} hydrophobic contacts as $p_{T,s}(n_s, n_{\mathrm{HH}}) \sim g(n_s, n_{\mathrm{HH}}) \exp(-E_s/T)$. Assuming that the minimum of the free-energy landscape $F_{T,s}(n_s^{(0)}, n_{\mathrm{HH}}^{(0)}) \to \min$ for given external parameters s and T is related to the class of macro-states with $n_s^{(0)}$ surface and $n_{\mathrm{HH}}^{(0)}$ hydrophobic contacts, this class dominates the phase the system resides in. For this reason, it is instructive to calculate all minima of the contact free energy and to determine the associated contact numbers in

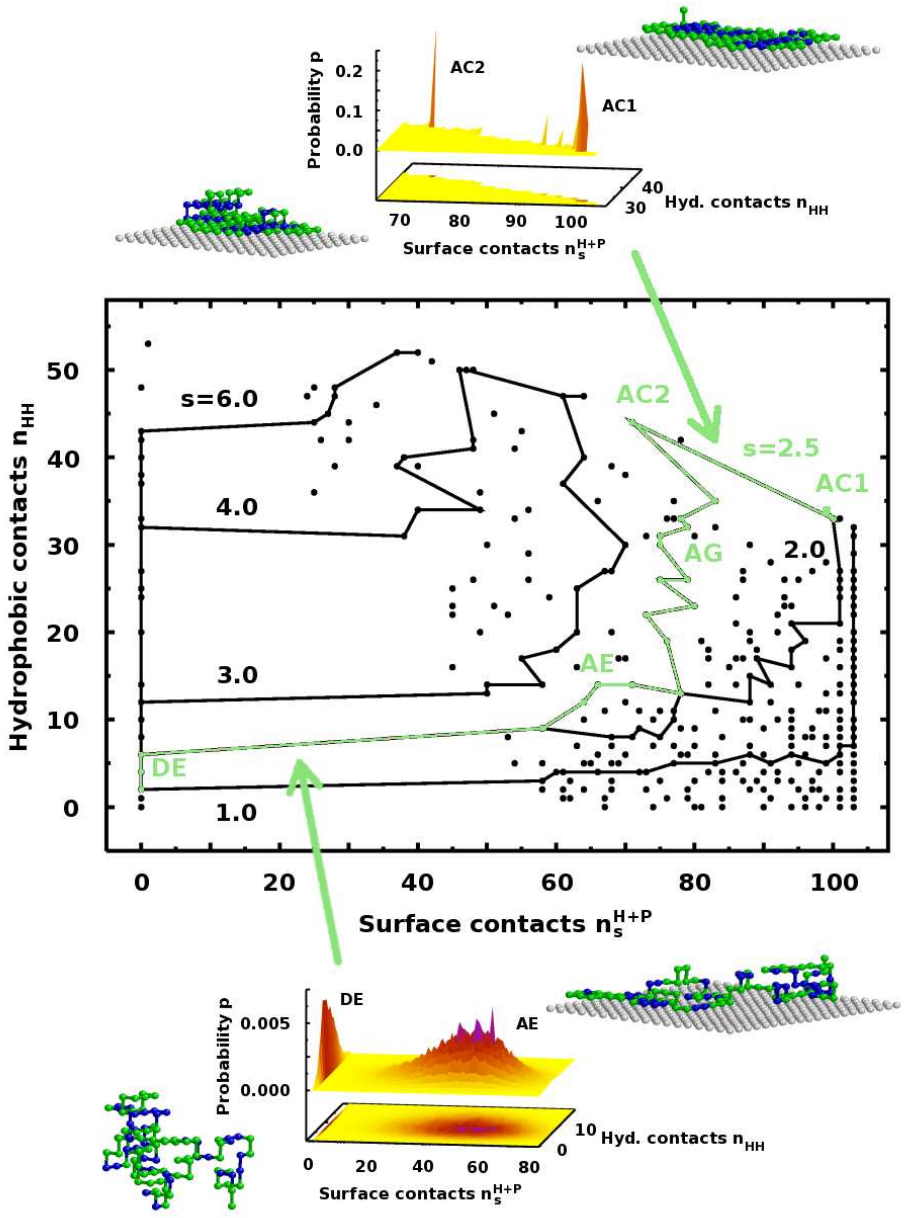

Figure 3. Contact-number map of all free-energy minima for the 103-mer and substrate equally attractive to all monomers. Full circles correspond to minima of the contact free energy $F_{T,s}(n_s^{\mathrm{H+P}}, n_{\mathrm{HH}})$ in the parameter space $T \in [0, 10]$, $s \in [-2, 10]$. Lines illustrate how the contact free energy changes with the temperature at constant solvent parameter s. For the exemplified solvent with $s = 2.5$, the peptide experiences near $T = 0.35$ a sharp first-order-like layering transition between single- to double-layer conformations (AC1,2). Passing the regimes of adsorbed globules (AG) and expanded conformations (AE), the discontinuous binding/unbinding transition from AE to DE happens near $T = 2.14$. In the DE phase the ensemble is dominated by desorbed, expanded conformations. Representative conformations of the phases are shown next to the respective peaks of the probability distributions.

a wide range of values for the external parameters. The map of all possible free-energy minima in the range of external parameters $T \in [0, 10]$ and $s \in [-2, 10]$ is shown in Fig. 3 for the peptide in the vicinity of a substrate that is equally attractive for both hydrophobic and polar monomers. Solid lines visualize "paths" through the free energy landscape when changing temperature under constant solvent ($s = \mathrm{const}$) conditions. Let us follow the exemplified trajectory for $s = 2.5$. Starting at very low temperatures, we know from the pseudo-phase diagram in Fig. 2(a) that the system resides in pseudo-phase AC1. This means that the macro-state of the peptide is dominated by the class of compact, film-like single-layer conformations. The system obviously prefers surface contacts at the expense of hydrophobic contacts. Nonetheless, the formation of compact hydrophobic domains in the two-dimensional topology is energetically favored but maximal compactness is hindered by the steric influence of the substrate-binding polar residues. Increasing the temperature, the system experiences close to $T \approx 0.35$ a sharp first-order-like conformational transition, and a second layer forms (AC2). This is a mainly entropy-driven transition as the extension into the third dimension perpendicular to the substrate surface increases the number of possible peptide conformations. Furthermore, the loss of energetically favored substrate contacts of polar monomers is partly compensated by the energetic gain due to the more compact hydrophobic domains. Increasing the temperature further, the density of the hydrophobic domains reduces and overall compact conformations dominate in the globular pseudo-phase AG. Reaching AE, the number of hydrophobic contacts decreases further, and also the total number of substrate contacts. Extended, dissolved conformations dominate. The transitions from AC2 to AE via AG are comparatively "smooth", i.e., no immediate changes in the contact numbers passing the transition lines are noticed. Therefore, these conformational transitions could be classified as second-order-like. The situation is different when approaching the unbinding transition line from AE close to $T \approx 2.14$. This transition is accompanied by a dramatic loss of substrate contacts – the peptide desorbs from the substrate and behaves in pseudo-phase DE like a free peptide, i.e., only the substrate and the opposite neutral wall regularize the translational degree of freedom perpendicular to the walls, but rotational symmetries are unbroken (at least for conformations not touching one of the walls). As the probability distribution in Fig. 3 shows, the unbinding transition is also first-order-like, i.e., close to the transition line, there is a coexistence of adsorbing and desorbing classes of conformations.

6 Concluding Remarks

Summarizing, we have performed a detailed analysis of the pseudo-phase diagrams in the T-s plane for a selected heteropolymer with 103 monomers in cavities with an adsorbing substrate being either attractive independently of the monomer type, or selective to hydrophobic or polar monomers, respectively. Although our model is very simple and the focus is on hydrophobic and polar effects only, we find, beyond the expected adsorbed and desorbed phases, a rich subphase structure in the adsorbed phases. In these regions, the substrate-specificity depends in detail on the quality of the solvent.

Since current experimental equipment is capable to reveal molecular structures at the nanometer scale, it should be possible to investigate the grafted structures dependent on the solvent quality. This is essential for answering the question under what circumstances binding forces are strong enough to refold peptides or proteins. The vision of future biotech-

nological and medical applications is fascinating as it ranges from protein-specific sensory devices to molecular electronic devices at the nanoscale.

Acknowledgments

This work is partially supported by a DFG (German Science Foundation) grant under contract No. JA 483/24-1. We thank the the John von Neumann Institute for Computing (NIC), Forschungszentrum Jülich, for providing access to their supercomputer JUMP under grant No. hlz11.

References

1. S. Brown, Nature Biotechnol. **15**, 269 (1997).
2. S. R. Whaley, D. S. English, E. L. Hu, P. F. Barbara, A. M. Belcher, Nature **405**, 665 (2000); B. R. Pelle, E. M. Krauland, K. D. Wittrup, and A. M. Belcher, Langmuir **21**, 6929 (2005).
3. K. Goede, P. Busch, and M. Grundmann, Nano Lett. **4**, 2115 (2004).
4. R. L. Willett, K. W. Baldwin, K. W. West, and L. N. Pfeiffer, Proc. Natl. Acad. Sci. (USA) **102**, 7817 (2005).
5. T. Vrbová and S. G. Whittington, J. Phys. A **29**, 6253 (1996); J. Phys. A **31**, 3989 (1998); T. Vrbová and K. Procházka, J. Phys. A **32**, 5469 (1999).
6. Y. Singh, D. Giri, and S. Kumar, J. Phys. A **34**, L67 (2001); R. Rajesh, D. Dhar, D. Giri, S. Kumar, and Y. Singh, Phys. Rev. E **65**, 056124 (2002).
7. M. S. Causo, J. Chem. Phys. **117**, 6789 (2002).
8. J. Krawczyk, T. Prellberg, A. L. Owczarek, and A. Rechnitzer, Europhys. Lett. **70**, 726 (2005).
9. J.-H. Huang and S.-J. Han, J. Zhejiang Univ. SCI. **5**, 699 (2004).
10. M. Bachmann and W. Janke, Phys. Rev. Lett. **95**, 058102 (2005).
11. K. F. Lau and K. A. Dill, Macromolecules **22**, 3986 (1989).
12. E. E. Lattman, K. M. Fiebig, and K. A. Dill, Biochemistry **33**, 6158 (1994).
13. L. Toma and S. Toma, Prot. Sci. **5**, 147 (1996).
14. H.-P. Hsu, V. Mehra, W. Nadler, and P. Grassberger, J. Chem. Phys. **118**, 444 (2003); Phys. Rev. E **68**, 21113 (2003).
15. M. Bachmann and W. Janke, Phys. Rev. Lett. **91**, 208105 (2003).
16. M. Bachmann and W. Janke, Comp. Phys. Comm. **169**, 111 (2005).
17. R. Schiemann, M. Bachmann, and W. Janke, J. Chem. Phys. **122**, 114705 (2005); Comp. Phys. Comm. **166**, 8 (2005).
18. M. Bachmann and W. Janke, J. Chem. Phys. **120**, 6779 (2004).
19. P. Grassberger, Phys. Rev. E **56**, 3682 (1997).
20. M. N. Rosenbluth and A. W. Rosenbluth, J. Chem. Phys. **23**, 356 (1955).

John von Neumann Institute for Computing

Molecular Dynamics Simulations of Polyelectrolyte Brushes

Christian Seidel and N. Arun Kumar

published in

NIC Symposium 2006 ,
G. Münster, D. Wolf, M. Kremer (Editors),
John von Neumann Institute for Computing, Jülich,
NIC Series, Vol. **32**, ISBN 3-00-017351-X, pp. 253-260, 2006.

http://www.fz-juelich.de/nic-series/volume32

Molecular Dynamics Simulations of Polyelectrolyte Brushes

Christian Seidel and N. Arun Kumar

Max Planck Institute of Colloids and Interfaces, Theory Department
Science Park Golm, 14424 Potsdam, Germany
E-mail: {*seidel, kumar*}*@mpikg.mpg.de*

We give a short overview about molecular dynamics simulations of polyelectrolytes end-grafted to a surface. The simulation model includes counterions as well as additional salt ions explicitly and treats the full Coulomb interaction. Here we address two problems. The first one is the effect of the grafting density on the chain stretching. The second one is the effect of additional salt ions on the structure of the brush.

1 Introduction

Polyelectrolytes (PELs) are macromolecules that contain subunits having the ability to dissociate charges in polar solvents such as, e.g., water. Due to their importance in materials science, soft matter research, and molecular biology, PELs have received a lot of attention in recent years.

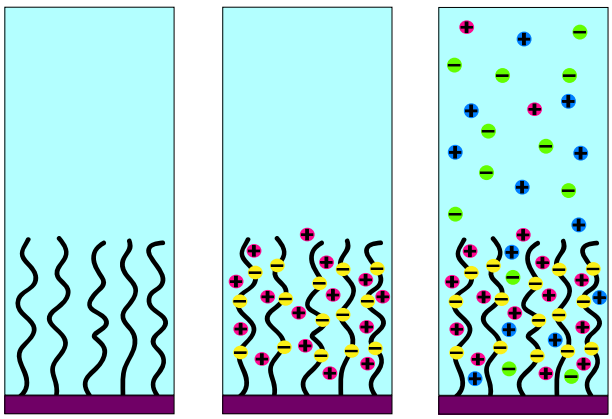

Figure 1. Schematic picture of polymer brushes. Left-hand side: made of uncharged polymers, middle: polyelectrolyte brush in the osmotic regime, right-hand side: polyelectrolyte brush with additional salt ions.

Polymer brushes consist of chains densely end-grafted to a surface. Due to various forces, tethered chains are enforced to take an elongated conformation. A schematic representation of an uncharged polymer brush is shown in Fig. 1 (left-hand part). PEL brushes form the subject of increasing interest in theory, simulation and experiment. From the application point of view, they are an effective means for, e.g., preventing colloids from flocculation.

Brushes made of charged chains have the advantage that stabilization occurs due to both steric and electrostatic effects. In addition, a surface coated with PELs is less sensitive to the salinity of the surrounding medium than a bare charged surface because a strongly charged brush is able to trap its own counterion generating a layer of high effective ion strength (Fig. 1, middle part). Nevertheless varying salt concentration is an important parameter to tune the polyelectrolyte effect and to change the structure of PELs in experiments (see Fig. 1, right-hand part). PEL brushes are also used in small devices for pH-controlled gating and are thought to be a model for the protecting envelope of cells (glycocalix).
Both in experiment and in theoretical studies, PELs are a subject with specific and unsolved problems. In such a situation, simulations are a promising tool to validate theoretical models and to probe data which are not easily accessible in experiment. However, despite strong effort in recent years, due to the long-ranged Coulomb interaction simulations of PELs remain still challenging.

2 Simulation Model and Method

The brush is represented by M freely jointed bead-spring chains of length $N+1$ which are anchored by one end to an uncharged planar surface at $z=0$. The uncharged anchor segments are fixed and form a square lattice. For completely charged chains, due to electroneutrality there are $M \times N$ monovalent counterions. Additional salt ions of monovalent 1:1 type are modeled exactly in the same way as counterions.
The chains are assumed to be in a good solvent modeled by a purely repulsive short-range interaction that is described by a shifted Lennard-Jones potential U_{LJ}. Along the chains, beads are connected by a FENE bond potential U_{bond}. With our choice of parameters we obtain an average bond length $b \approx \sigma$ where σ is the Lennard-Jones parameter. All particles except the anchor segments are exposed to a short-ranged repulsive interaction U_{wall} with the grafting surface at $z=0$. An identical wall is placed at the top boundary of the simulation box $z=L_z$. In particular the second wall is necessary to reach a finite salt concentration.
Counterions and salt ions are treated as individual, non-bonded particles and all charged entities interact with the bare Coulomb potential

$$u_{\mathrm{Coul}}(r) = k_{\mathrm{B}}T\, q_i q_j\, \frac{l_{\mathrm{B}}}{r}, \tag{1}$$

with q_i and q_j being the corresponding charges in units of elementary charge e and l_{B} is the Bjerrum length that sets the strength of the interaction. It is well known that the handling of long-range forces in simulations requires special methods[1]. To treat them in the particular $2\mathrm{D}+1$ slab geometry (the simulation box is periodic only in x and y directions while perpendicular to the grafting surface the system is restricted to one layer), now we use the so-called MMM technique introduced by Strebel and Sperb[2] and modified for laterally periodic systems $(\mathrm{MMM2D})$ by Arnold and Holm[3]. Although, due to symmetry breaking, the MMM scaling $\mathcal{O}(N_{\mathrm{tot}}\log(N_{\mathrm{tot}}))$ is not maintained in the $2\mathrm{D}+1$ case, the remaining $\mathcal{O}(N_{\mathrm{tot}}^{5/3}\log(N_{\mathrm{tot}})^2)$ behavior enables to increase significantly the total number of charged particles.
To study the system in equilibrium at constant temperature, we use stochastic molecular

dynamics where all particles are coupled to a heat bath. For using the IBM Regatta supercomputer the molecular dynamics code was parallelized by means of a self-scheduling (master-slave) algorithm[4]. We typically consider between 2 000 and 8 000 charges. Typical runtime ranges from about two to 10 days for a single data point. That is why we are forced to use supercomputers in order to be able to effectively study polyelectrolyte brushes by simulation techniques.

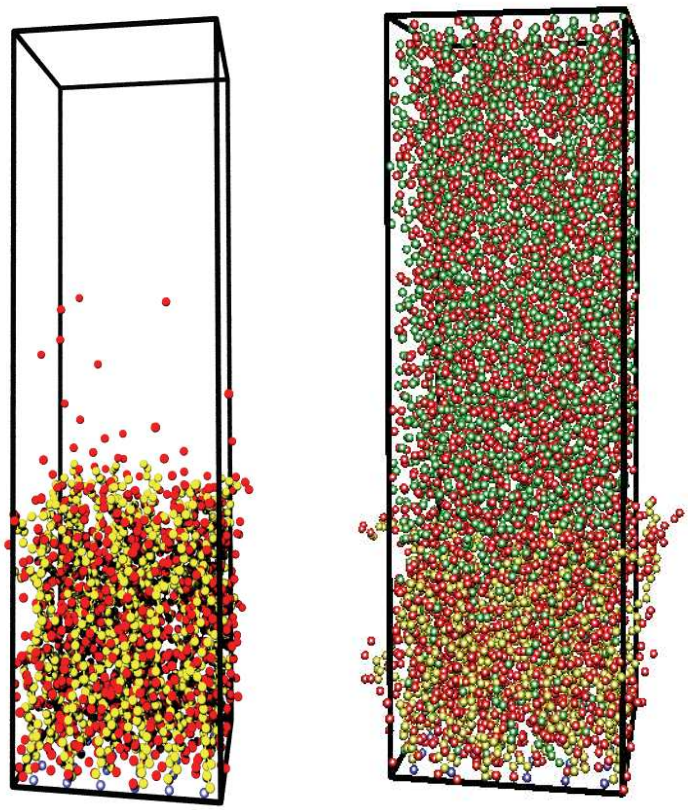

Figure 2. Snapshots of polyelectrolyte brushes with 36 chains of 30 monomers each (yellow) from MD simulations. The chains are fully charged; Bjerrum length is set $l_B = \sigma$. Left-hand side: saltless, counterions are colored red; right-hand side: with additional salt, coions are colored green, counterions red. The snapshots out of equilibrium trajectories have been represented by using the visualization program VMD[5] and the rendering program POV-Rays[6].

3 Nonlinear Osmotic Brush Regime

Figure 2 (left-hand side) shows a snapshot from the simulation at electrostatically intermediate coupling strength ($l_B = \sigma$). Note that there are only about 1% of counterions

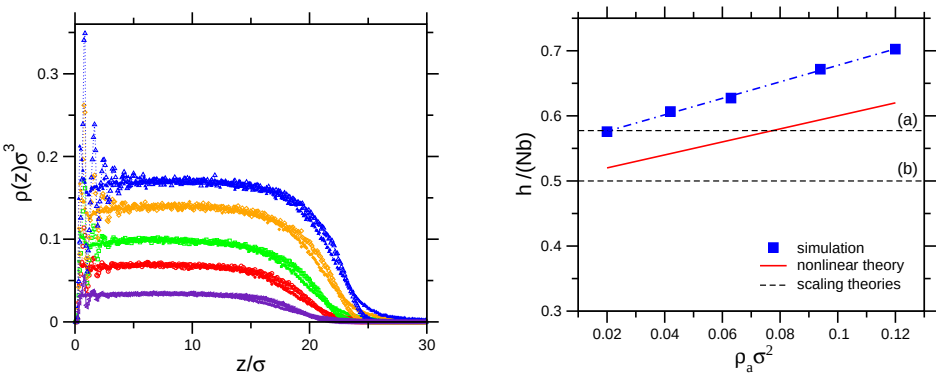

Figure 3. Simulation results of fully charged brushes ($N = 30, l_B = \sigma$). Left-hand side: density profiles of monomers and counterions (see the text) at grafting densities between $0.02\sigma^{-2}$ (bottom) and $0.12\sigma^{-2}$ (top); right-hand side: brush height as a function of grafting density, simulation data and theoretical predictions.

outside the brush, i.e., in a quite reasonable approximation the brush can be considered to be locally electro-neutral. Simulated density profiles of monomers and counterions are plotted for several grafting densities ρ_a) in Fig. 3 (left-hand side). In agreement with the snapshot, both monomers and counterions follow very similar nearly steplike profiles with uniform amplitude inside the brush, which increases with grafting density. Only at the rim of the brush there appear some differences: a depletion of counterions occurs inside and a corresponding tail of the density profile outside the brush. At that point the conclusion is that the brush is in the strong-charging limit where the stretching of the chains is caused by the osmotic pressure of counterions[7]. The average height of end-points of the chains is shown in Fig. 3 (right-hand side). The simulated brush height varies slowly with the grafting density, contrary to the predictions of standard scaling theories[8,9], but in agreement with recent experimental results and in agreement with a scaling theory that incorporates nonlinear elastic and nonlinear osmotic effects[7].

The brush height h in the osmotic regime is given by the balance of the osmotic pressure of counterions and the elastic response due to the stretching of chains. From Fig. 3 (right-hand side) one can see that the chains are stretched up to about 60% of their contour length. Thus their behavior is far beyond the linear regime. But, non-linear elasticity alone does not change the dependence on grafting density. However, the counterion free energy contains entropic contributions that depend on the volume being available for the counterions. Using a free volume approximation very much in the spirit of the van der Waals equation for the liquid-gas transition, the available volume (per chain) $V_0 = h/\rho_a$ is reduced by the self-volume of the chain $\upsilon = Nb\sigma_{\rm eff}^2$. Note that the effective polymer radius $\sigma_{\rm eff}$ takes into account both the monomer and counterion size. Thus the free volume is given by $V = V_0(1-\eta)$ with $\eta = \rho_a\sigma_{\rm eff}^2 Nb/h$ being the degree of close packing in the brush. Balancing the resulting nonlinear entropy of counterions with the high stretching chain elasticity, the equilibrium brush height in the nonlinear osmotic regime becomes[7]

$$h_{\rm NlOsB} = Nb\,\frac{f+\sigma_{\rm eff}^2\rho_a}{1+f}, \qquad (2)$$

where f is the degree of charging. The theoretical line (nonlinear theory) shown in Fig. 3 (right-hand side) is calculated with $\sigma_{\rm eff}^2 = 2\sigma^2$. This choice corresponds to a two-dimensional square-lattice packing of monomers and counterions on two interpenetrating sublattices. The nonlinear prediction given in Eq. 2 qualitatively captures the slow increase of the brush height with grafting density. The deviations from the simulation data may be explained by considering additional effects which go beyond the simple extension of the scaling analysis.

4 Effect of Additional Salt

According to Pincus[8] the brush shrinks with increasing salt concentration, but only as a relatively weak power law $c_s^{-1/3}$. There is some experimental and theoretical work that confirms this prediction, but there are other results that are in contradiction. The aim of our simulation study is to clarify that question.

Figure 2 (left-hand side) shows a snapshot from the simulation at electrostatically intermediate coupling strength ($l_B = \sigma$) and rather high salt concentration ($c_s = 0.11\sigma^{-3}$). In contrast to the saltless case, now the particle distribution looks rather homogeneous over the total height of the simulation box. Because polyelectrolyte counterions and salt counterions are considered to be identical they are subject to an unrestricted exchange. As one can see from the snapshot, salt coions are diffusing into the brush layer. Although it can not be seen directly in snapshots, due to local electroneutrality these coions are escorted by a corresponding number of counterions. The different aspects of the ion distribution inside and outside the brush layer will be discussed below in detail.

The average thickness of the brush is measured by taking the first moment of the monomer density profile. To obtain an universal scaling curve in Fig. 4 (left-hand side) we plot $h(c_{\rm s})/h_0$ vs $bc_{\rm s}/(\rho_{\rm a} f^{1/2})$. However, to rescale the brush height with the theoretical salt-free value h_0 instead of the osmotic brush height we use that of the non-linear osmotic

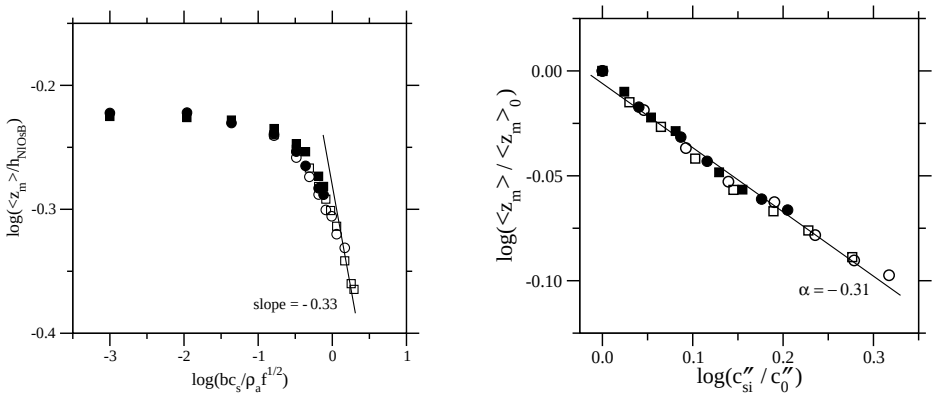

Figure 4. Simulation results of fully charged brushes ($N = 30, l_B = \sigma$) with additional salt. Left-hand side: brush height versus salt concentration; right-hand side: brush height versus ion concentration inside the brush.

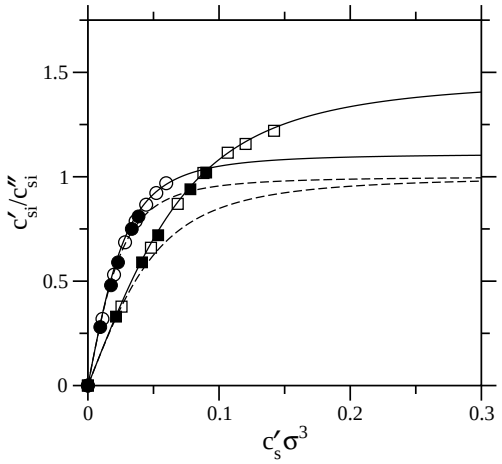

Figure 5. Relation between the ion concentration inside the brush $c''_{\rm si}$ and buffer concentration $c'_{\rm si}$ versus salt concentration $c'_{\rm s}$ for two different grafting densities. Simulation results (symbols) and predictions of original (dashed lines) and modified (solid lines) Donnan approach.

brush given in Eq. (2), where the effective polymer thickness is set again $\sigma^2_{\rm eff} = 2\sigma^2$[10]. Thus, all the data points fall indeed onto a universal curve in a log-log plot, which tends to a slope of zero in the low salt regime indicating the validity of the non-linear osmotic brush relation.

On the other hand, obviously the limit of a salted brush $c_{\rm s} \gg c_{\rm ci}$ where the influence of counterions can be neglected, is hard to reach. Although at the largest salt concentration we consider one observes indeed a slope that is in agreement with the Pincus prediction one has to pay attention to the very few data points in that region. However, a further increase of the total number of charges would enlarge the CPU time beyond a reasonable limit and a reduced size of the simulation box would cause serious finite size effects. Therefore, to account properly for the screening within the brush, the counterion concentration $c_{\rm ci}$ cannot be neglected.

The concentration of small ions inside the brush $c''_{\rm si}$ is obtained by counting the mobile ions within the layer $0 < z < z_{\rm i}$ where $z_{\rm i}$ is the inflection point in the monomer density profile that is used as a measure of the rim of the brush. On a log-log scale, in Fig. 4 (right-hand side), we plot the average brush height $\langle z_{\rm m} \rangle$ versus the ion concentration inside the brush $c''^{10}_{\rm si}$. Both $\langle z_{\rm m} \rangle$ and $c''_{\rm si}$ are rescaled with the corresponding salt-free values $\langle z_{\rm m} \rangle_0$ and c''_0 respectively. The brush height scales with $c''_{\rm si}$ showing an exponent $\alpha \approx -0.31$. This result is in good agreement with the scaling law $h \sim c_{\rm s}^{-1/3}$ predicted by Pincus for the salt dependence of the brush height in the osmotic regime[8]. Note that different symbols in Fig. 4 refer to different grafting densities while open and filled symbols indicate different system sizes. Thus, from Fig. 4 it becomes clear that finite-size effects due to the setting of the box height do not affect the scaling behavior.

To get the relationship between the ion concentration inside the brush $c''_{\rm si}$ and the buffer concentration $c'_{\rm si}$, in Fig. 5 we plot the ratio $c'_{\rm si}/c''_{\rm si}$ versus the salt concentration $c'_{\rm s}$. From

the point of view of the ion distribution perpendicular to the grafting plane a polyelectrolyte brush is very similar to the membrane equilibria problem where the membrane is impermeable to macro-ions but permeable to small ions. Hence one can divide the simulation box into two compartments with the membrane "boundary" located at the rim of the brush that is defined in our model by z_i. Due to the presence of the macro-ions in one compartment similarly charged ions are expelled from this compartment, giving rise to a somewhat non-homogeneous distribution of the small ions as already pointed out by Donnan in 1911[11]. Applying the Donnan approach to the brush system the ratio of the small ions in both compartments becomes

$$\frac{c'_\mathrm{si}}{c''_\mathrm{si}} = \left[1 + \left(\frac{fN\rho_\mathrm{a}}{2z_\mathrm{i}c'_\mathrm{s}}\right)^2\right]^{-1/2}. \tag{3}$$

In Fig. 5, the predictions following from Eq. (3) are given by dashed lines. Obviously the behavior disagrees with the simulation data that do not give a uniform ion concentration in the high-salt limit. We find a surplus of small ions on the polymer-free side that is growing with increasing grafting density, i.e., with enhanced polymer concentration.
Note that the Donnan effect has been evaluated for a system of point-like constituents. While such an approximation is appropriate for dilute solutions it fails for rather dense phases like polymer brushes. Including the polymer self-volume in a free-volume approximation as introduced above the Donnan equilibrium reads[10]

$$\frac{c'_\mathrm{si}}{c''_\mathrm{si}} = \frac{1}{1-\eta}\left[1 + \frac{1}{(1-\eta)^2}\left(\frac{fN\rho_\mathrm{a}}{2z_\mathrm{i}c'_\mathrm{s}}\right)^2\right]^{-1/2}. \tag{4}$$

Using the same σ_eff as above, finally we obtain an almost perfect agreement with the simulation data.

5 Conclusion

Performing extensive molecular dynamics simulations which require the use of massively parallel supercomputers new insight into the behavior of polyelectrolyte brushes could be obtained. These new findings stimulated both the development of theory and the realization of new or improved experiments. Thus numerical simulations gave rise to an increased knowledge about a polymer system that is of high interest from the point of view of both fundamental and applied research.

Acknowledgments

We gratefully acknowledge a grant for the IBM Regatta supercomputer at NIC Jülich, Germany. We thank Axel Arnold for helpful comments on his MMM2D code and Roland Netz for useful discussions.

References

1. M. P. Allen and D. J. Tildesley, *Computer Simulation of Liquids*, Oxford University Press (1987).
2. R. Strebel and R. Sperb, Mol. Simul. **27**, 61–74 (2001).
3. A. Arnold and C. Holm, Comput. Phys. Commun. **148**, 327–348 (2002).
4. W. Gropp, E. Lusk, and A. Skjellum, *Using MPI*, The MIT Press (1994).
5. `http://www.ks.uiuc.edu/Research/vmd/`
6. `http://www.povray.org/`
7. H. Ahrens, S. Förster, C. A. Helm, N. A. Kumar, A. Naji, R. R. Netz, and C. Seidel, *Nonlinear Osmotic Brush Regime: Experiments, Simulations and Scaling Theory*, J. Phys. Chem. B **108**, 16870–16876 (2004).
8. P. Pincus, Macromolecules **24**, , (2912–2919) 1991.
9. O. V. Borisov, T. M. Birshtein, and E. B. Zhulina, J. Phys. II (Paris) **1**, 521–526 (1991).
10. N. A. Kumar and C. Seidel, *Polyelectrolyte Brushes with Added Salt*, Macromolecules **38**, 9341–9350 (2005).
11. F. G. Donnan, Z. Elektrochem. **17**, 572 (1911).

John von Neumann Institute for Computing

Phase Transitions in Macromolecular Systems

Marcus Müller, Wolfgang Paul, and Kurt Binder

published in

NIC Symposium 2006 ,
G. Münster, D. Wolf, M. Kremer (Editors),
John von Neumann Institute for Computing, Jülich,
NIC Series, Vol. **32**, ISBN 3-00-017351-X, pp. 261-268, 2006.

http://www.fz-juelich.de/nic-series/volume32

Phase Transitions in Macromolecular Systems

Marcus Müller[1], Wolfgang Paul[2], and Kurt Binder[2]

[1] Institut für Theoretische Physik
Georg August-Universität, 37077 Göttingen, Germany
E-mail: mmueller@theorie.physik.uni-goettingen.de

[2] Institut für Physik, WA331
Johannes Gutenberg-Universität, 55099 Mainz, Germany

A new simulation method to study equilibrium properties and diffusive ordering kinetics in multicomponent polymer systems is discussed. Selected results for spinodal decomposition in symmetric binary polymer blends, solvent evaporation from thin polymer films and the order of diblock copolymer materials on nanopatterned surfaces are presented.

1 Introduction

Multi-component polymeric "alloys" are industrially and technologically omnipresent. In general, blending of different polymer species can reduce cost, improve processibility, provide synergy between components, allow for recycling, and improve overall properties. If one takes a binary blend of immiscible or partially miscible homopolymers, the blend may appear homogeneous on the length scale of centimeters, but it will consists of domains of μmeter size. The morphology of the phase separated material depends on the kinetics of phase separation. In this fine dispersion interfaces between the coexisting phases dictate many of the materials properties. In systems where the different components are chemically bonded together, i.e., a diblock copolymer, formation of macroscopic domains is impossible and the system forms domains on the size of the molecular extension, i.e., several tens of nanometers. If one could achieve defect-free ordering over macroscopic areas these materials would find applications in semiconductor industry or as filtration devices.

Properties on the length scales of molecular extension are universal, i.e. they depend on the chemical structure only via a small number of coarse-grained parameters: The molecular extension, R_e, sets the length scale. The incompatibility, χN, between different molecules sets the energy scale where χ is the Flory-Huggins parameter and N the molecular weight. The invariant degree of polymerization, $\bar{\mathcal{N}} \equiv (\rho R_e^3/N)^2$ where ρ denotes the monomer density, determines the strength of fluctuation effects[1].

In the SCF theory a system of interacting molecules is replaced by that of a single molecule in an external field which, in turn, depends on the local densities. This external external field mimic the interactions of the molecule with its neighbors. In the limit of large $\bar{\mathcal{N}}$ one molecule has interactions with $\mathcal{O}(\sqrt{\bar{\mathcal{N}}})$ neighboring molecules and replacing these fluctuating fields by their thermal averages (i.e., the mean field approximation) becomes accurate. While the SCF theory has found ample successful applications it is numerically difficult to study complex three-dimensional geometries, to incorporate details of the molecular architecture beyond the Gaussian chain model and to extend the theory to the description of the kinetics of phase separation and ordering[1,2].

Our report is arranged as follows: In the next section, we describe a computational method – single chain in mean field simulations – that is able to partially overcome the difficulties mentioned above. Then, we present selected applications to the kinetics of phase

separation and ordering as well as the self-assembly of diblock-copolymers on patterned substrates. The paper closes with a brief outlook.

2 Single Chain in Mean Field (SCMF) Simulations

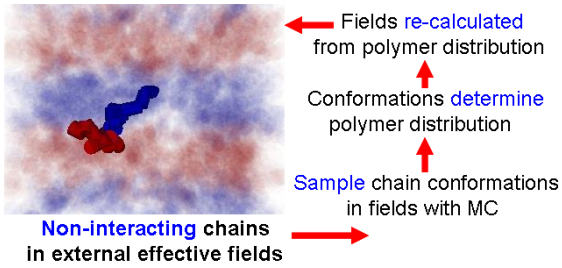

Figure 1. Sketch of Single Chain in Mean Field (SCMF) simulations.

We consider a large ensemble of independent chains in an external field. The chains are described by a coarse-grained polymer model. In our applications we have utilized a simple bead-spring model comprising N beads. The single chain probability distribution takes the form of a discretized Edwards-Hamiltonian augmented by a bending potential[3]:

$$\mathcal{P}_{A,\alpha}[\{\mathbf{r}_\alpha\}] \sim \Pi_{i=1}^{N-1} e^{-\frac{3(\mathbf{r}_{\alpha,i}-\mathbf{r}_{\alpha,i+1})^2}{2b^2}} \Pi_{i=1}^{N-2} e^{f_{\text{stiff}}(\mathbf{r}_{\alpha,i}-\mathbf{r}_{\alpha,i+1})(\mathbf{r}_{\alpha,i+1}-\mathbf{r}_{\alpha,i+2})} \quad (1)$$

The simulation method is sketched in Fig. 1[3]: Chain conformations are updated in the external fields via a standard Monte Carlo scheme utilizing local random displacements of the beads. After a short, predetermined number of Monte Carlo steps, the spatial density distribution created by the large ensemble of independent molecules is determined and the relation of the SCF theory between density and field is employed to calculate the new, external fields. Then, the process is iterated.

- This particle-based simulation method utilizes coarse-grained polymer models (e.g., bead-spring model with bond angle potential) and is not limited to the Gaussian chain model of the SCF theory. The use of explicit molecular conformations allows details of the chain architecture to be incorporated (e.g., stiffness along the backbone or branching).

- The density (and external fields) accurately mimic the instantaneous chain conformations. SCMF simulations converge to a solution of the equilibrium SCF theory in the limit of an infinitely large ensemble, $\bar{\mathcal{N}} \to \infty$. Numerical calculations for binary blends and diblock copolymers demonstrate that this simulation scheme can describe composition fluctuations (cf. Fig. 2) if the fields are updated frequently. This finding has been corroborated by approximate but analytical techniques.

- The explicit propagation of the chain conformations avoids the need of an Onsager coefficient and intramolecular correlations (that give rise to a non-local Onsager coefficient in field-theoretic schemes) are taken into due account.

- Propagating the explicit chain conformations in time we are able to investigate blends with strong dynamic asymmetries (e.g., where one component vitrifies during the phase separation process).

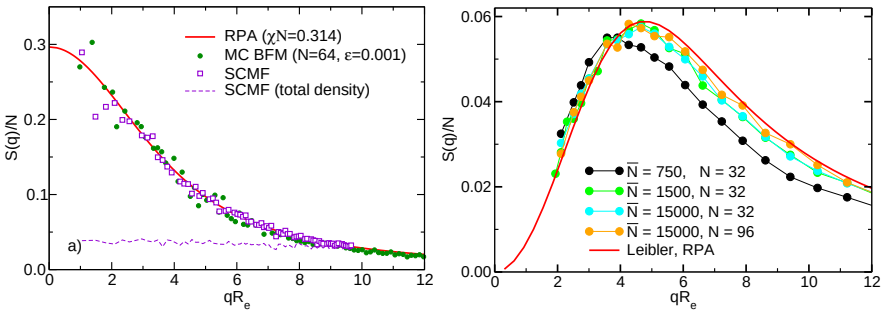

Figure 2. (a) Equilibrium composition fluctuations of a symmetric binary polymer blend at $\chi N = 0.314$ as obtained from Random Phase Approximation, MC simulations of the bond fluctuation model, and SCMF simulations. The horizontal dashed line also depicts the structure factor of the total density in the SCMF simulations which utilize a small but finite compressibility. From Ref. 3. (b) Equilibrium composition fluctuations of a symmetric diblock copolymer at $\chi N = 2$ as obtained from SCMF simulations and Random Phase Approximation for a system of linear dimension, $L = 3R_e$. To achieve an invariant degree of polymerization of $\bar{\mathcal{N}} = 15000$ (which corresponds to an intermediate molecular weight) in a typical bead spring model ($\rho = 0.83$) requires a large system of very long chains, i.e., 3400 chains each comprising $N = 3000$ beads. In the SCMF simulations we can reproduce these experimental values of $\bar{\mathcal{N}}$ simply by increasing the density rather than the chain discretization, N.

Additionally the scheme is computationally efficient, permits us to study large system sizes and it is suitable for parallel computers. To this end, we distribute the independent chain conformations evenly across the processors independent of their location in space. Each processors performs the Monte Carlo simulations for "its" molecules which are mutually independent but only interact with the external field. Each processors calculates the density of its molecules after the Monte Carlo simulation and the results are summed across the processors to construct the new external field for the next simulation. Typically we utilize between 8 and 64 processors on the IBM Regatta at the NIC, Jülich.

3 Applications

3.1 Spinodal Decomposition in Binary Polymer Blends

First we discuss the growth of composition fluctuations in a binary symmetric polymer blend in response to a temperature quench from the one-phase region, $\chi N = 0.314$ into the miscibility gap, $\chi N = 5$. Early stages of spinodal decomposition are characterized by an exponential growth of collective concentration fluctuations. The growth rate, $R(q)$, depends on the wavevector, q, the equilibrium thermodynamics of the mixture, and the dynamics of the molecules. The latter enter the field theoretical description via an Onsager coefficient which describes the relation between a gradient of the chemical (exchange) potential and the concomitant concentration current. Due to the extended shape of the

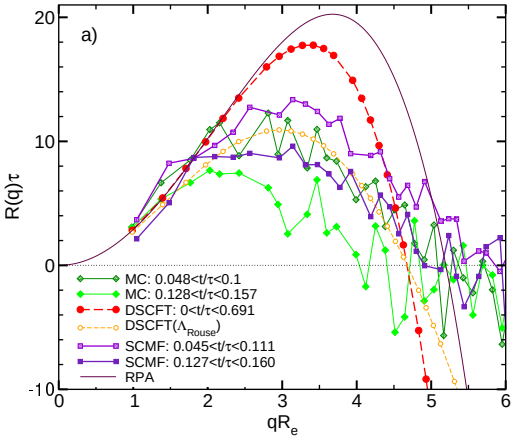

Figure 3. Growth rate, $R(q)\tau$, of the collective structure factor, $S(q) \sim \exp[R(q)t]$, as a function of the wavevector, q. Data from MC simulations of the bond fluctuation model at an early and intermediate time regime and the results from the dynamic SCF theory using a local and a Rouse-like Onsager coefficient are adapted from Ref. 2. The results of the SCMF simulations slightly overestimate the initial growth rate at large wavevectors, but capture the fastest growing mode, the decrease of the rate with time and do not predict negative rates (damping) at high wavevectors in agreement with the MC simulations. The prediction of the Random Phase Approximations is also included as thin solid line.

macromolecules the Onsager coefficient is non-local and explicit expressions exists for the homogeneous system[4]. The results from Monte Carlo simulations of the bond fluctuation model, dynamic SCF calculations calculations with a local Onsager coefficient and an Onsager coefficient for Rouse-dynamics, and the results of SCMF simulations are compared in Fig. 3. Clearly, a local Onsager coefficient fails to describe the simulation results, but dynamic SCF calculations using a non-local Onsager coefficient and SCMF simulations that do not utilize an Onsager coefficient but rather propagate the explicit chain conformations in time yield an improved description.

It is also instructive to compare the computational effort between the different schemes: For the MC simulations of 64 independent systems over the time interval 0.33τ a computational effort of 40 days on 64 processors of a CRAY T3E was needed. Using $7\times7\times7 = 343$ grid points in Fourier space the corresponding dynamic SCF calculations required about 25 days on a CRAY J90. The single chain mean field calculations of 64 independent systems, each with twice as many polymers than in the MC simulations and a spatial resolution of 4096 grid points, took 19 hours on a 32×2 node Beowulf cluster of Opteron (1.8GHz) processors.

While explicit analytical expression for the non-local Onsager coefficient exist for spatially homogeneous systems (appropriate, e.g., for the early stages of spinodal decomposition), no such expression exist at spatial inhomogeneities (e.g., interfaces or surfaces). Under those circumstances the chain conformations are distorted and the calculation of the Onsager coefficient amount to calculate intramolecular correlations which is computationally infeasible.

3.2 Solvent Evaporation from Thin Polymer Films

The kinetics of phase separation in the presence of strong spatial and dynamic inhomogeneities is explored in Fig. 4 where we compare SCMF simulations with Molecular Dynamics simulations of the evaporation of a volatile solvent from a thin polymer film. To match the SCMF simulations with the Molecular Dynamics simulations we utilized the single chain structure factor to adjust the bond length, b, and the chain stiffness, $f_{\rm stiff}$ in Eq. (1). The interactions were modelled via a virial expansion[5] and the coefficients were

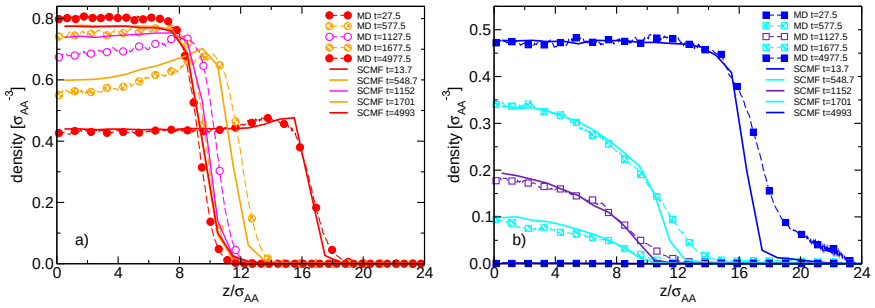

Figure 4. Polymer (a) and solvent (b) density, $\phi_A(\mathbf{r},t)$ and $\phi_B(\mathbf{r},t)$, as a function of time during the evaporation process as observed by MD simulations of a bead-necklace model and by SCMF simulations using a parameterization for the coexistence densities and segmental mobilities. All times are measured in units of Lennard-Jones time units. From Ref. 3.

adjusted to reproduce the phase equilibrium. The time scales were matched by comparing the self-diffusion constants in the bulk.

The time evolution as well as the details of the density profiles of polymer and solvent are quantitatively well predicted by SCMF simulations (cf. Fig. 3) even if interfaces are present. Upon evaporation of the solvent a dense polymer layer ("skin") builds up at the polymer-vapor interface at intermediate times. One advantage of the SCMF simulations is that we can control the mobility of the species without changing the equilibrium thermodynamics. Altering the mobilities, we obtain rather direct insight into the importance of the density dependence of the segmental dynamics, which is less straightforward to extract from simulations of the interacting multi-particle system. For instance, if we neglect the concentration dependence of the solvent mobility we do not find the formation of a skin.

3.3 Microphase Separation of Block Copolymers on Nanopatterned Substrates

We have used SCMF simulations to explore the self-assembly of copolymers and their mixtures with the corresponding homopolymers in nanopatterned substrates[6–8]. The self-assembly is dictated by an intricate interplay between interfacial interactions, breaking of translational symmetry, and structural frustration due to the incompatibility between the natural periodicity of the bulk structure and film thickness and the substrate pattern. Confinement and surface effects can result in morphologies that are absent in the bulk, e.g., surface reconstructions.

Fig. 5 shows the ordering of a lamellar-forming diblock on top of a stripe pattern. There is a slight mismatch between the bulk lamellar period, $L_0 = 1.786R_e$ at $\chi N =$ and the pattern period, $L_S = 1.7$. In the initial stage perfectly registered lamellae are formed at the substrate (substrate-directed ordering). The top (bulk) of the film segregates into microdomains later and they are not registered with the substrate pattern. Defects in the structure anneal not by lateral diffusion but the order of the registered lamellae propagates from the substrate to the top surface[6].

It is of interest to explore what geometrical patterns can be reproduced by diblock copolymer materials. Generally, only a small mismatch between the natural morphology of the diblock and the substrate pattern is permissible if defect-free registration and order

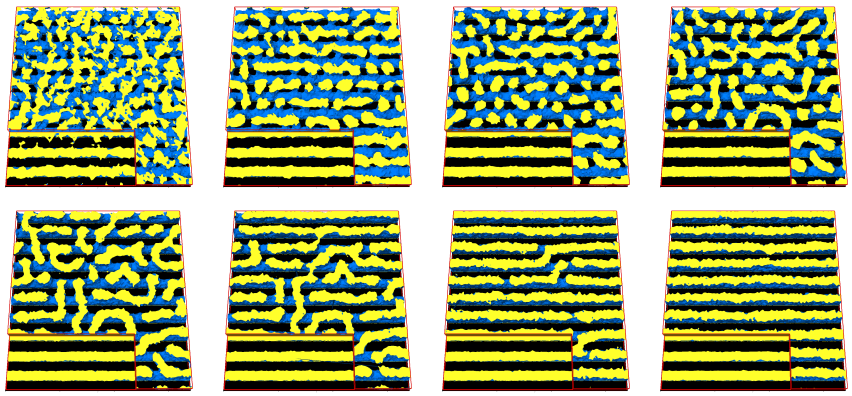

Figure 5. Snapshot images of the three dimensional behavior of diblock copolymers on chemically nanopatterned substrates. The lateral system size is $17R_e \approx 0.5\mu$m. The time increases from left to right and from top to bottom. One component has been removed from the image and blue surfaces represent the interface between the different components. In the lower left corner 75% of the film has been removed to reveal the near-substrate morphology. From Ref. 6.

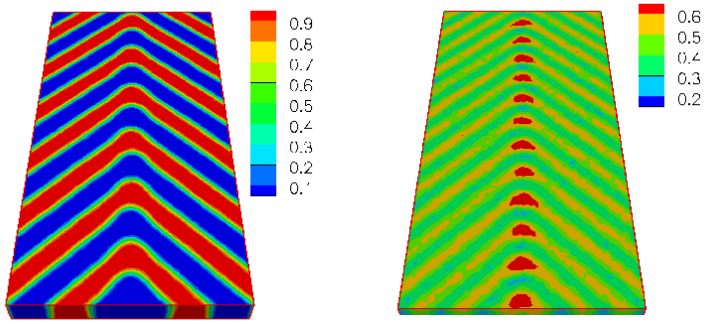

Figure 6. Three-dimensional contour plots of the composition (left) and the total homopolymer concentration (right) obtained from SCMF simulations. In the left panel the red and blue areas represent A- and B-rich domains, respectively. In the right panel, the periodic red areas are enriched alternatively in A and B homopolymers, whereas the blue stripes represent the domain interfaces that are depleted of homopolymers. From Ref. 7.

is required. Using blends of AB-diblock copolymers with the corresponding A- and B-homopolymers is an experimentally convenient way to adjust (enlarge) the periodicity and it also is crucial for replicating more complex patterns. This is illustrated in Fig. 6 where the ordering of a ternary blend on a nested array of bends is shown. The periodicity of the stripes matches the bulk lamellar spacing but the distance between the AB interfaces at the corners is larger. The homopolymers redistribute as to selectively swell the morphology at the corners resulting in defect free ordering. Note also the Ω-shape of the AB-interface at the corners which resembles domain shapes observed at grain boundaries in the bulk[7].

If one increases the mismatch between the length scale or the symmetry of the substrate pattern and the bulk morphology of the diblock the copolymers do no longer register with

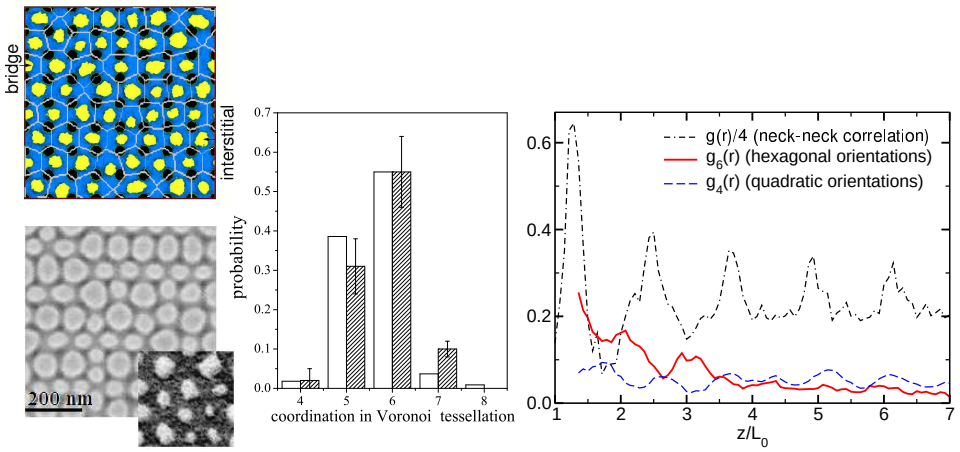

Figure 7. Morphology of a copolymer/homopolymer blend film of thickness $D_0 = 0.63L_0$ and lateral dimensions of $9.77L_0$ on a square array of spots. (top left) SCMF simulation showing only the top view of the PS-rich domains (white/yellow) and the interface between PS and PMMA (dark grey/blue). Regions on top of the spots are PMMA-rich (transparent) and one looks through to the substrate (black). The position between two PMMA-attracting spots of the substrate is denoted as "bridge", while the position at the center of a plaquette of four spots is denoted "interstitial". The Voronoi tessellation of the necks is indicated by thin white lines. (bottom left) SEM image of the composition at the film surface. The PS-domains are shown in light grey while PMMA-rich surface areas correspond to dark grey regions. Note that the PS-domains appear artificially larger in the SEM images so a more accurate view of the domain sizes is provided by an AFM phase image shown as an inset at the lower right corner. (middle) Probability distribution of the coordination (number of edges) of Voronoi cells (c.f. top left panel). The "errorbars" of experimental data (shown in grey) characterize the variance of results obtained by analyzing different SEM images of size $9.77L_0$. SCMF simulation results are shown as open bars. (right) Pair correlation of the necks and orientational correlation functions for hexagonal and square orientations extracted from large SEM images. From Ref. 8

the bulk pattern. This is illustrated in Fig. 7 which shows the disordered bicontinuous morphology of a lamellar-forming ternary blend on top of a surface pattern that consists of a square array of spots with center-to-center distance, $\lambda = 1.21L_0$, and radii, $R = 0.30L_0$.

Near the substrate the morphology replicates the substrate pattern and forms a quadratically perforated lamellar (QPL) sheet[8]. Necks of polystyrene (PS) connect to this QPL. The near-substrate morphology favors a square geometry of the necks while the packing of dense necks rather results in a hexagonal structure. This competition prevents the formation of long-range order and one observed in the SCMF simulations as well as in the experiments a disordered bicontinuous structure. The local geometry can be characterized by a Voronoi tessellation which reveals a substantial amount of 6-fold coordinated necks. The local hexagonal structure is also revealed by the orientational correlation function, g_6[9]

$$g_n(r) = \left\langle \left| \frac{1}{n} \sum_{\alpha \in \langle \mathrm{nn} \rangle_i} e^{in\phi_{\alpha i}} \frac{1}{n} \sum_{\beta \in \langle \mathrm{nn} \rangle_j} e^{-in\phi_{\beta j}} \right| \right\rangle \tag{2}$$

where α and β run over all nearest neighbors (nn) (as identified via the neck-neck-pair

correlation function) of the two necks i and j a distance r apart and $\phi_{\alpha i}$ is the angle of the vector between the center of the neck i and its neighbor α. Hexagonal correlations are strong but short-ranged while orientational correlations with $n = 4$ are weaker but longer-ranged and are mediated over long distances by the substrate pattern.

4 Concluding Remarks

Single chain in mean field simulations are a computationally efficient method to study the morphology of multi-component polymer systems on parallel computers. Nevertheless a careful investigation of the potential and limitations of the method is still required to clarify under which conditions fluctuations are correctly described and how to optimally choose the spatial discretization and updating frequency of the fields. Other interesting aspects consist in extending the dynamics to entangled systems by using the slithering snake algorithm (in addition to local random displacements) or to introduce a fine network of strings which do not influence the equilibrium behavior but are uncrossable and, thus, will lead to reptation-like motion.

Acknowledgments

It is a great pleasure to thank the John von Neumann Institute for Computing for a generous allocation of CPU time on the IBM Regatta and to acknowledge K. Daoulas, E.W. Edwards, P.F. Nealy, J.J. de Pablo, Y.J. Papakonstantopoulos, S.-M. Park, E. Reister, G.D. Smith, F. Schmid, and M. Stoykovich for fruitful and enjoyable collaboration. Financial support was provided by the Volkswagen foundation and the DFG und grant Mu 1674/3.

References

1. M. Müller and F. Schmid, Adv. Polym. Sci. **185**, 1 (2005).
2. E. Reister, M. Müller and K. Binder, Phys. Rev. **E 64**, 041804 (2001).
3. M. Müller and G.D. Grant, J. Polym. Sci. **B 43**, 934 (2005).
4. K. Binder, J. Chem. Phys. **79**, 6387 (1983).
5. K. Binder, M. Müller, P. Virnau, and L.G. Mac Dowell, Adv. Polym. Sci. **173**, 1 (2005).
6. E.W. Edwards, M.P. Stoykovich, M. Müller, H.H. Solak, J.J. de Pablo and P.F. Nealey, J. Polym. Sci. **B 43**, 3444 (2005).
7. M.P. Stoykovich, M. Müller, S.O. Kim, H.H. Solak, E.W. Edwards, J.J. de Pablo, and P.F. Nealey, Science **308**, 1442 (2005).
8. K.Ch. Daoulas, M. Müller, M.P. Stoykovich, S.-M. Park, Y.J. Papakonstantopoulos, J.J. de Pablo, and P.F. Nealey (submitted).
9. D.R. Nelson and B.I. Halperin, Phys. Rev. **B 19**, 2457 (1979).

John von Neumann Institute for Computing

Computer Simulation of Low Temperature Fuel Cells and their Components

Andrei A. Kulikovsky and Eckhard Spohr

published in

NIC Symposium 2006 ,
G. Münster, D. Wolf, M. Kremer (Editors),
John von Neumann Institute for Computing, Jülich,
NIC Series, Vol. **32**, ISBN 3-00-017351-X, pp. 269-278, 2006.

http://www.fz-juelich.de/nic-series/volume32

Computer Simulation of Low Temperature Fuel Cells and their Components

Andrei A. Kulikovsky and Eckhard Spohr

Institut für Werkstoffe und Verfahren der Energietechnik (IWV-3)
Forschungszentrum Jülich, 52425 Jülich, Germany
E-mail: {a.kulikovsky, e.spohr}@fz-juelich.de

Modeling of Low Temperature Fuel Cells is a multi–disciplinary and multi–scale problem utilizing methods and techniques from mathematics, physics, chemistry and engineering. Some recent studies performed in our group at IWV-3 are summarized.

1 Introduction

Low temperature fuel cells such as the hydrogen-fed polymer electrolyte membrane fuel cell (PEFC) and the direct methanol fuel cell (DMFC) are regarded as promising technologies to replace combustion engines and batteries in mobile and stationary applications. Fuel cells convert chemical energy of combustion directly into electricity by spatial separation of anodic oxidation of fuel and cathodic reduction of oxygen. Protons generated at the anode migrate to the cathode, where they recombine with oxygen anions to form water. The reactions lead to the non-toxic products $\mathrm{H_2O}$ and $\mathrm{CO_2}$. The anodically generated electrons perform useful work on their external path to the cathode.

Forschungszentrum Jülich maintains a leading position in Europe in PEFC and DMFC research. As part of the Helmholtz community program on rational energy conversion our institute (IWV–3) performs a wide spectrum of research aimed at improving PEFC efficiency and at creating prototypes of commercial DMFC stacks in the 1 to 5 kW class. Modeling of components, single cells and stacks is an integral part of this effort. The technological goals are also supported by fundamental studies of the molecular mechanisms of species transport in polymer electrolyte membranes (PEMs) and of the kinetics of electrochemical reactions.

Prior to a broad introduction of fuel cell technology into the energy market substantial barriers still need to be overcome. These are, in the case of the PEFC

- low cell efficiency when using dry gases, which mandates elaborate humidification;
- cell flooding at high current densities due to a large amount of water produced at the cathode;
- the problem of catalyst poisoning by CO. This problem is critical for PEFCs with on–board reforming of liquid hydrocarbon fuels to hydrogen.

In the case of the liquid–fed DMFC the major problems are

- the slow kinetics of the methanol oxidation, leading to high voltage losses, high noble metal catalyst loadings and concomitant high costs;

- the high rate of methanol crossover through currently available membrane materials, which reduces cell power;
- flooding of the cathode catalyst layer due to the high electroosmotic flux of water through the membrane;
- large amount of gaseous CO_2 on the anode side, which reduces cell performance.

Last but not least, lowering the aging rate is crucial for commercialization of the cells of both types.

Fuel cell research and development thus has two aspects: The first one is the design of new components (catalyst layers, membranes and backing layers) with improved performance and lower cost. The second one is the proper assembly of these components into cells and stacks with high performance and low rate of aging.

Clarifying the transport mechanisms in the membrane and the mechanisms of the electrocatalysed chemical reactions in a fuel cell are subject of extensive experimental and theoretical work. Molecular dynamics simulations and quantum chemical calculations are indispensable tools in understanding these mechanisms. Transport parameters in the fuel cell components can be obtained by comparing the experimental data with the predictions of continuum models. This led us to studies of the following topics:

- Numerical modelling of DMFCs and PEFCs within the scope of continuum models.
- Classical molecular dynamics (MD) simulation of proton, water and methanol transport through polymer electrolyte membranes.
- *ab initio* MD simulation of methanol oxidation in the anodic catalyst layer.

In the first topic the fuel cell is considered as a whole, as a macroscopic "electrical machine". Here we aim at understanding the mechanisms of voltage loss in real cells and optimization of cell design. Modeling structure and dynamics on the atomic scale is performed in order to derive relationships between the macroscopic properties of materials, such as conductance, and the molecular motions.

2 Cell Simulations

A typical cross section of a polymer electrolyte fuel cell (PEFC) is sketched in the left part of Figure 1. The membrane electrode assembly (MEA) is clamped between two metal or graphite plates with the channels for feed gases supply, called the "flow field". The MEA usually consists of two gas–diffusion layers (GDLs) and two catalyst layers, separated by a proton conducting membrane.

Current production in a cell induces fluxes of gases, liquid water, heat and charged particles. The distribution of the respective parameters (concentrations, fields etc.) is usually very non–uniform. Furthermore, the characteristic scale of the parameter variation ranges from several micrometers (the thickness of the catalyst layer) to several meters (the length of the channel). In general, the problem of fuel cell modeling is multi–scale and multi–dimensional.

Several approaches to model such a system exist. The number and complexity of the processes in the MEA together with sophisticated geometries of the flow fields almost inevitably lead to 3D CFD models. Differently, our quasi–3D (Q3D) model of a PEFC[1] is based on the following idea. In many cases one may neglect the in–plane fluxes in the MEA. The full 3D problem (Figure 1) can then be split into a problem of flow in the channel and a 2D problem in the MEA cross–section, as shown in Figure 1. The channel problem provides concentrations of reactants for the problem in the MEA. The latter returns local current density required to calculate the profiles of reactants concentration along the channels. Both problems are, therefore, coupled and the solution has to be determined iteratively[1].

Furthermore, the cell cross-section consists of a number of geometrically identical elements (Figure 1). This allows an efficient code parallelization. The physical model is formulated for a single element (2D element in Figure 1). The code is then replicated, so that each element "is solved" on a separate processor. Upon completion of an iteration step the elements exchange with the "boundary conditions", as shown on the right side of Figure 1. The cross-section of a typical cell contains several tens of such elements; the time of simulation of such a system is only 2–3 times larger than the time of simulation of a single element. This algorithm efficiently exploits the capability of a massively parallel computer system.

The typical solution is shown in Figure 2. Note that to represent the details the scale of this figure is strongly distorted: the size of the computational domain along x–axis is about 1 mm, whereas along y–axis its size is about 21 cm (Figure 2). The two elements at the inlet are "zoomed" in Figure 3.

Figures 2 and 3 show that there are three types of non–uniformities in a cell. The first is a small–scale non–uniformity (maps of Q_c and σ_m) in the through–plane direction. Proton conductivity of the catalyst layers is rather poor and the electrochemical reaction is largely confined to the region close to the membrane interface, where protons are "cheaper" (i. e., found with higher probability). Analysis of the governing equations shows, that this regime of the catalyst layer operation leads to high polarization losses[2].

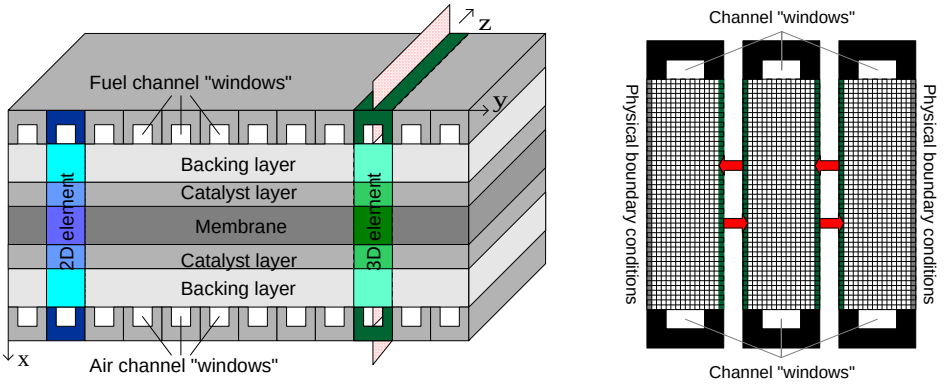

Figure 1. Left: Sketch of the fuel cell. Right: The idea of parallelization. Adjacent cell elements exchange with the "boundary conditions" upon completion of an iteration step.

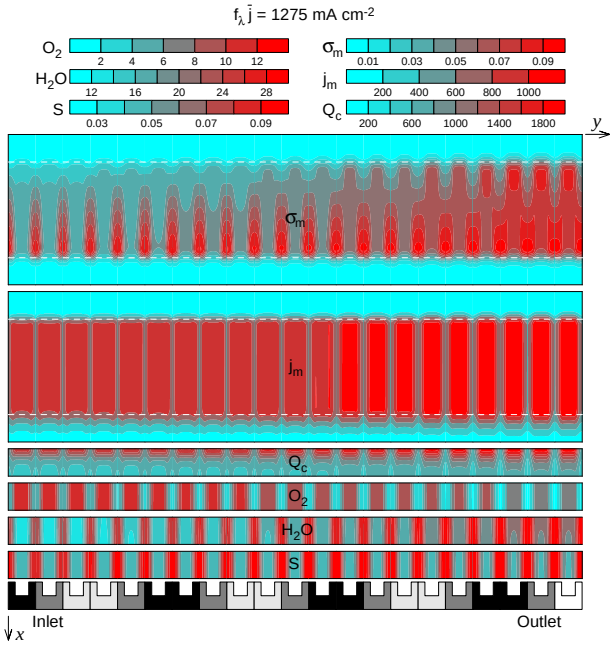

Figure 2. 3D maps of the PEM fuel cell[1]. Shown are (top to bottom): proton conductivity σ_m (Ω^{-1} cm^{-1}) and proton current density j_m (mA cm^{-2}) in membrane and catalyst layers, the rate of the electrochemical reaction Q_c (A cm^{-3}), oxygen and water molar concentrations (10^{-6} mole cm^{-3}) and liquid saturation in the cathode catalyst layer. White dashed lines indicate the membrane/catalyst layers interfaces.

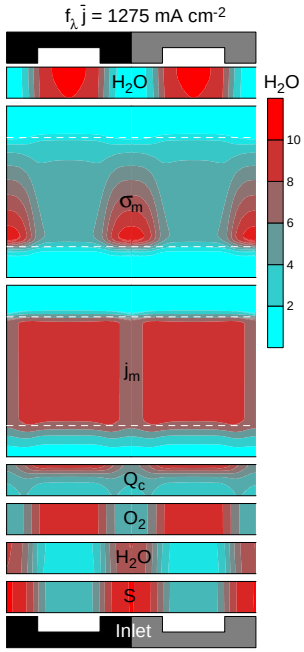

Figure 3. The same as in Figure 2 plus liquid saturation in the anode catalyst layer (on top) in two elements at the inlet. For the notations and scales please see Figure 2.

Proton conductivity of the bulk membrane is higher at the cathode side and lower at the anode side (Figures 2,3) due to proton–driven electroosmotic flux of water (from the anode to the cathode side). Back diffusion of water does not fully compensate the electroosmotic flux and the anode side of the membrane is dried. In this particular regime of cell operation the membrane drying limits the current, due to the poorer membrane conductivity at low water content (see below).

The second is a medium–scale non–uniformity due to the alternation of channel "windows" and current collector ribs along the y–axis (Figures 2,3). Oxygen transport to and water transport from the regions above the ribs is poor; thus water tends to accumulate there and lack of oxygen reduces the rate of the reaction in these domains (Figures 2,3).

The third is a large–scale non–uniformity due to oxygen exhaustion and accumulation of water along the channel. Close to the outlet the membrane is well humidified, though the last elements experience "oxygen starvation" (Figure 2).

The problem of this particular cell design is to mitigate the negative effect of non–uniformities of all three types. The non–uniformity of the reaction rate across the catalyst layer can be diminished by increasing the proton conductivity of the layer. Medium–scale non–uniformity (channel / rib) can be reduced by increasing oxygen and water diffusivity in the backing layer, i.e., by enlarging its porosity. Large–scale non–uniformity can be diminished by increasing the oxygen stoichiometry of the cathode flow.

The results thus give hints how to improve cell design and help to optimize operating conditions. Besides, Q3D simulations provide invaluable information for construction of simplified analytical and semi–analytical models of a cell[3]. These *fast* models can be used for rough characterization of cells. Comparison of analytical, numerical and experimental data gives a much more reliable information, than any single model. We believe that in the near future the approach based on such a hierarchy of models will play a substantial role in fuel cell studies.

3 Proton Transport in Membranes

PEMs like Nafion are phase-separated on the nanometer scale into a polymer phase consisting of a polytetrafluoroethylene backbone with pendant end-group sulfonated side chains and an aqeuous phase. The (continuous) polymer phase provides the structural stability for separating anodic and cathodic compartments. It is experimentally well established that above a percolation threshold, when the aqueous phase is thought to become continuous, proton conductance in Nafion or related materials increases significantly with water content λ (λ is the ratio of water molecules to sulfonate groups). The sulfonic acid groups are strongly acidic so that protons become solvated and conducting in the aqueous phase. From the magnitude and the temperature dependence of the experimental proton conductance in fully humidified Nafion membranes (where $\lambda \approx 14$) it has been concluded that the proton transport mechanism follows the well-established proton-hopping or structural diffusion mechanism characteristic for the high proton mobility in bulk acids. At low water content ($\lambda \approx 3 - 5$) the proton transport mechanism is best described by an interplay between a surface mechanism (transfer along the sulfonate groups) and the bulk mechanism[4].

Describing (i) the structural complexity of the biphasic polymer / water material and (ii) the bond-forming and -breaking nature of the elementary act of proton transfer can best be reconciled by modeling the materials using so-called empirical valence bond (EVB)

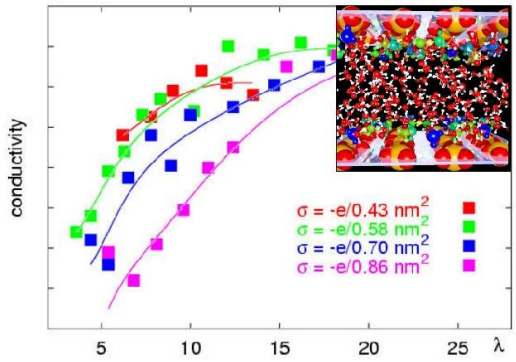

Figure 4. Dependence of proton conductivity (scaled units) on water content λ for several slab pores with different surface charge densities (spacings) of sulfonate groups. Note that the variance of instantaneous proton states (blue: H_3O^+-like, yellow-green: $H_5O_2^+$-like) in the snapshot is characteristic for the aqueous pores, and their easy interconversion is essential for proton mobility, thus warranting the use of complex molecular models.

interaction potentials. In such a model, the proton can be regarded as being in a superposition state between different valence bond states, in which an excess proton belongs to one of a subset of water molecules. In the most simple form, only two resonance states $\phi_1 : H_3O^+ \cdots H_2O$ and $\phi_2 : H_2O \cdots H_3O^+$ are considered. In one state the proton is localized on the first oxygen, in the other one on the second hydrogen. Using a configuration-dependent coupling between these two states, one can describe proton transfer as a continuous sequence of $H_5O_2^+ \rightarrow H_3O^+ \rightarrow H_5O_2^+ \rightarrow H_3O^+$transitions. Besides being conceptually simple, such an empirical valence bond force field allows the simultaneous simulation of many protons over time periods of nanoseconds, i.e., the minimum requirements for studying a concentrated proton solution in a disordered polymer framework[5].

Taking the most extreme viewpoint, one can treat the polymer as an immobile framework with simple pores of slab or cylinder shape, in which proton transport can be studied as function of a variety of *generic* structural and dynamical features of the polymer (such as acid strength, head group and side chain mobility, equivalent weight) and *operational* parameters of the working fuel cell (such as temperature and water content). Here, the power of a massively parallel computer can be harnessed for parallelization on the level of the single simulation, each one of which typical lasts 2-3$\cdot 10^7$ relatively short time steps (Per step parallelization based on domain decomposition or interaction decomposition is not very effective due to communication overheads.) Figure 4 shows, as an example, the calculated dependence of proton conductance on water content for different equivalent weights of the polymer (which is modeled by the spacing of sulfonate groups on the slab wall)[5]. It demonstrates how the single pore mobility leads to the water-content dependent proton conductance in PEMs that was mentioned above.

On the basis of the temperature dependence of proton mobility in single pores it was concluded that the experimentally observed behavior is most likely associated with the dynamics of the polymer at low water content. In a next generation of models, local pore structure and dynamics was investigated using a fully atomistic model of the Nafion polymer, employing for the aqueous phase a simple classical force field which treats hydronium and water like rigid molecular ions or molecules interacting through standard force fields[6]. Such simulations can be conveniently parallelized by decomposing the system into several equivalent interacting subsystems of identical composition. Since meaningful results can be collected only from a series of runs at different temperatures and for different water

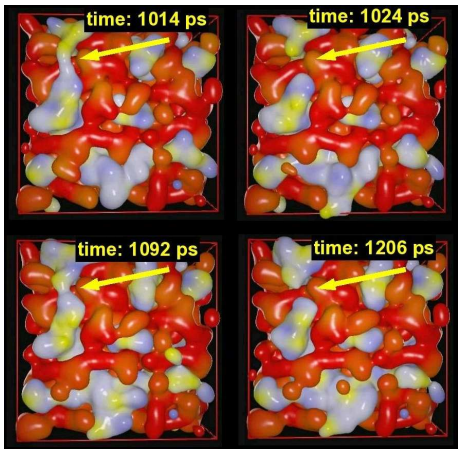

Figure 5. Snapshots at different times of a jelly-bean representation of a simulated mixture of water and Nafion in protonated form (at water content $\lambda = 5$). Red regions denote polymer, grey, blue and yellow regions denote water, hydronium and sulfonate groups, respectively, in the aqueous phase. The indicated box corresponds to a length of 4.5 nm. Note that the jelly-bean surfaces hide a large number of molecules [E. Spohr, work in progress].

contents, distribution of the jobs over 2–4 processors made optimal use of the allocated resources at NIC. As a representative result of these studies, Fig. 5 shows time dependent snapshots of aqueous domains at $\lambda = 5$, which are consistent with the view of activated fluctuative bridging of the aqeous pores, reducing the overall proton conductance as well as increasing the activation energy. With atomistic simulations on the united-atom level, where only the essential topological features of the Nafion base unit are retained, morphological transitions between inverse micellar aqueous pores at low water content to channel like structures at high water content are currently studied.

4 Methanol Oxidation on Noble Metal Catalysts

The protons in the membrane originate from electrocatalytic processes in the anodic catalyst layer. In the DMFC these processes are, to some extent, performance limiting. At least, they mandate high noble metal catalyst loadings and concomitant high device costs. We have thus investigated the catalytic oxidation of methanol in realistic, i.e. fuel cell-relevant environments, using quantum mechanical density functional theory to describe

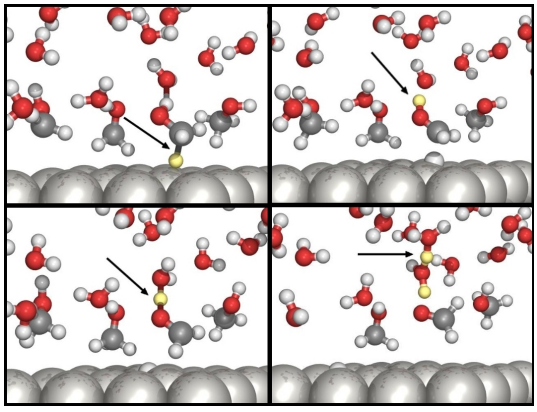

Figure 6. Chemical reaction dynamics of methanol oxidation to formaldehyde: One of the C–H bonds of the methyl group becomes elongated (top left) and eventually breaks (top right). The adsorbed hydrox-methyl group stabilized by forming a hydrogen bonded complex to a water molecule (bottom left) and dissociates rapidly into adsorbed formaldehyde and a hydronium ion (bottom right) which further stabilized by undergoing structural diffusion steps to form Zundel ions $H_5O_2^+$.

the coupling between electronic structure and nuclear dynamics. As a starting point, we considered the oxidation of adsorbed methanol at a water / platinum interface. For our calculations we have employed the VASP package[7] which showed for our purposes good scaling characteristics up to 8 processors per job, and allowed us to perform *ab initio* molecular dynamics calculations of uncharged and charged interfaces. Water did not only influence the reaction pathway as compared to the corresponding gas phase reaction, it actively changed the sequence of reactive events by directly, i. e., without intermediate adsorption, incorporating hydrogen ions into its hydrogen bond network, as illustrated in Fig. 6 (see Ref.[8]). These calculations are currently extended to investigate the influence of fuel cell environment on the later oxidation steps.

5 Concluding Remarks and Outlook

Modeling of transport processes in low temperature fuel cells is a true multidisciplinary and multi–scale effort, which requires joint efforts by physicists, chemists, applied mathematicians and engineers. In our group at IWV-3 we tightly integrate analytical theory[3] together with our computational studies into FZJ's research and development of viable fuel cell technology. In spite of dramatic progress in computer technology some key problems in PEFC and DMFC fuel cell technology remain unsolved, largely due to the extremely complicated media and materials used in fuel cells, in which the physics of species transport is still not completely understood. Bringing these "electrical machines" to market is a challenge not only for experimental research but also for "silicon machines" such as NIC's Regatta system.

Acknowledgements

Many of our simulations were performed with a grant of computer time provided by the VSR of the Research Centre Jülich.

References

1. A. A. Kulikovsky, T. Wüster, T. Egmen, and D. Stolten. Analytical and numerical analysis of PEM fuel cell performance curves. *J. Electrochem. Soc.*, **152** (2005) A1290.
2. M. Eikerling, A. A. Kornyshev, and A. A. Kulikovsky. Physical modeling of fuel cells and their components. In E. Bard and J. Stratmann, editors, *Encyclopedia of Electrochemistry*, volume 5. Wiley, New–York, 2006 (in press).
3. A. A. Kulikovsky. Analytical models of direct methanol fuel cells. In T. S. Zhao, editor, *Advances in Fuel Cells*. Elsevier, 2006 (in press).
4. K. D. Kreuer, S. J. Paddison, E. Spohr and M. Schuster, Transport in Proton Conductors for Fuel Cell Applications: Simulations, Elementary Reactions and Phenomenology, *Chem. Rev.*, **104**, (2004) 4637.
5. P. Commer, A. G. Cherstvy, E. Spohr and A. A. Kornyshev, The nature of water content effect on the proton transport in polymer electrolyte membrane, *Fuel Cells*, **2**, (2002) 127.

6. D. Seeliger, C. Hartnig and E. Spohr, Aqueous Pore Structure and Proton Dynamics in Solvated Nafion Membranes, *Electrochim. Acta*, **50**, (2005) 4234.
7. G. Kresse and J. Hafner, *Ab initio* molecular dynamics for liquid metals, *Phys. Rev. B*, **47**, (1993) RC558.
8. C. Hartnig and E. Spohr, The role of water in the initial steps of methanol oxidation on Pt(111), *Chem. Phys.*, **319**, (2005) 185.

John von Neumann Institute for Computing

Environment

Ulrich Hansen

published in

NIC Symposium 2006 ,
G. Münster, D. Wolf, M. Kremer (Editors),
John von Neumann Institute for Computing, Jülich,
NIC Series, Vol. **32**, ISBN 3-00-017351-X, pp. 279-280, 2006.

http://www.fz-juelich.de/nic-series/volume32

Environment

Ulrich Hansen

Institute for Geophysics
Westfälische-Wilhelms Universität Münster
Corrensstr. 24, 48149 Münster, Germany
E-mail: hansen@earth.uni-muenster.de

Especially the last year has reminded us how vulnerable the human habitat is to natural hazards. The large Sumatra earthquake from Dec. 27th 2005 and the subsequently triggered tsunami have caused one of the biggest catastrophic events in recent history. At the same time these phenomena give us an idea about the tremendous power sleeping in the interior of our planet. These forces move continents and ocean floor. Over geological time scales they let mountains grow and new ocean basins develop. On short time scales the same forces lead to earthquakes and volcanic eruptions. There is little hope that man will ever be able to gain control over these forces. Nevertheless it seems wise to understand the processes operating in the interior, in order to wisely estimate and possibly predict potential hazards. Much more accessible to -and also much more influenced by- human activity is the atmosphere of the Earth. As compared to the interior we have much more information about this part of the 'System Earth' and consequently, our expectations with respect to the predictive power of numerical models are higher. The distribution of pollutants is of significant importance and especially the distribution of fine and ultra-fine dust particles currently receives growing attention. Two projects, conducted on NIC resources have been selected to exemplify the diversity and likewise the topicality of projects carried out in the Environmental section of research at NIC.

One, by Wolke et al, aims at a better understanding of the transport of chemical species in the atmosphere, being an example of applied research, guided by practical questions. The authors have developed a multiscale approach, in which a model, simulating the transport of chemical constituents is embedded into another model, providing the various aspects of atmospheric dynamics. The coupled model is employed to study the distribution of (a) fine dust in an industrial region in Saxonia and (b) of Saharan Dust Aerosols. While the first application is of direct regional meaning the latter is of importance on even larger scale. Dust influences the amount of sunlight received by Earth. Dust scatters and absorbs sunlight and such also affects the temperature. In their contribution Wolke et al. present further steps towards a model that can be routinely employed for process analysis, as well as to interpret field data.

The study of Hansen et al. addresses fundamental aspects of planetary evolution. Plate tectonics and its relation to the internal dynamics of planets is the central topic of their efforts. At present, the phenomenon of plate tectonics seems to be a unique feature on Earth. Other planets, like Mars, may have shown plate tectonics earlier in their history. Can plate tectonics suddenly appear on a previously inactive planet, or, alternatively, can it vanish, thus leaving a stagnant lid covering the planet and keep it from further cooling? Numerical experiments are virtually the only tool, allowing to go into such matters. Exploiting the conservation laws for mass, energy and momentum leads to a set of nonlinear

partial differential equations, describing the transport properties under such extreme conditions. In their studies the authors demonstrate the important role played by the rheology of the material. Especially the dependence of the viscosity on (a) temperature, (b) pressure and (c) stress governs the style of surface tectonics. An important conclusion says that is dynamically feasible that a planet may undergo a change in its surface behaviour, i.e from an active planet to one without surface tectonics, and vice versa. The question if a planet exhibits plate tectonics has thus been extended by the dimension time.

John von Neumann Institute for Computing

Modelling of Atmospheric Chemistry Transport Processes

Ralf Wolke, Bernd Heinold, Jürgen Helmert,
Detlef Hinneburg, Matthias Lieber, Eberhard Renner,
Wolfram Schröder, and Ina Tegen

published in

NIC Symposium 2006 ,
G. Münster, D. Wolf, M. Kremer (Editors),
John von Neumann Institute for Computing, Jülich,
NIC Series, Vol. **32**, ISBN 3-00-017351-X, pp. 281-288, 2006.

http://www.fz-juelich.de/nic-series/volume32

Modelling of Atmospheric Chemistry Transport Processes

Ralf Wolke, Bernd Heinold, Jürgen Helmert, Detlef Hinneburg, Matthias Lieber, Eberhard Renner, Wolfram Schröder, and Ina Tegen

Leibniz Institute for Tropospheric Research
Permoserstr. 15, 04318 Leipzig, Germany
E-mail: wolke@tropos.de

Regional modelling of atmospheric trace gases and particulate matter is of major importance for air pollution studies as well as climate considerations. In this context, the chemistry transport model system LM-MUSCAT is applied for several air quality studies and the investigation of local climate effects. Two selected applications from different objects of research are presented in the paper. The first study enables a detailed quantification of the contributions of cooling tower emissions to particle concentration levels in specific Saxonian urban areas. In the second project, the influence of Saharan dust emissions on radiative forcing and, hence, on the meteorology is quantified. These regional effects are also relevant for climate change studies. Regional scale models are well suited for simulation of individual dust storm events, or for comparisons with *in-situ* observations made during field experiments. Improvements in the parameterisation of dust processes which are obtained by such regional model investigations can help to improve parameterisations in global scale models. Both applications require a detailed process description as well as a high spatial resolution. Such simulations are very expensive in terms of computing time and demand the use of powerful parallel computers.

1 Introduction

The physical and chemical processes in the atmosphere are very complex. The systems of differential equations resulting from atmospheric chemistry transport models are nonlinear, highly coupled and extremely stiff. Therefore, CPU costs are very high for advanced air pollution models containing a large number of species. Furthermore, the physical and chemical processes that determine the distribution of air pollutants occur simultaneously, coupled and in a wide range of scales. Here, the lack of adequate resolution limits the ability to accurately model individual processes and their interactions. For example, when plumes are injected into coarse grid cells in regional models with a uniform grid, the emitted material is diluted immediately within the cell and the details of the near field chemistry are lost. Multiscale models can provide finer resolution in certain key regions.

The modelling department of the IfT has developed the state-of-the-art multiscale model system LM-MUSCAT[19,20]. It is qualified for process studies as well as the operational forecast of pollutants in local and regional areas. The model system consists of two online coupled codes. The operational forecast model LM[4] (Local Model) of the German Weather Service is a non-hydrostatic and compressible meteorological model and solves the governing equations on the basis of a terrain-following grid. The model includes the dynamic kernel for the atmosphere as well as the necessary parameterisation schemes for various meteorological processes, boundary conditions and surface exchange relations. It describes the atmospheric flow and phenomena between the meso-β and micro-α scale (i.e. grid resolutions from 50 km to 50 m), in particular near-surface properties, convection, clouds, precipitation, orographical and thermal wind systems. The model is capable of self-nesting and four-dimensional data-assimilation.

Driven by the meteorological model, the chemistry transport model MUSCAT[18,7] (Multi-Scale Atmospheric Transport Model) treats the atmospheric transport as well as chemical transformations for several gas phase species and particle populations. The transport processes include advection, turbulent diffusion, sedimentation, dry and wet deposition. Due to the online coupling between LM and MUSCAT, the calculations exploit the actual properties of the atmosphere. The implicit-explicit time integration scheme of MUSCAT operates independently from the meteorological model, thus allowing for autonomous time steps and different horizontal grid resolutions in selected regions of the model domain. For this purpose, the required LM fields (e. g., wind, temperature, humidity, exchange coefficients) are interpolated temporarily and spatially. The chemical part of MUSCAT contains the gas phase mechanism of RACM[15] considering 76 reactive gas species with 239 reactions. Secondary particle formation and appropriate interactions with the gas phase are also included. The radiation activity and biogenic emissions are calculated autonomously, whereas information on the cloud cover, temperature, and other meteorological parameters is taken from LM. The anthropogenic emissions in Saxony are accounted for by several spatial registers of point, line, and area sources (including plume rise). Annual averages of emissions are disaggregated in time (monthly, weekly, daily). EMEP emission data were used in the outer region.

Both models work widely independent and have their own separate time step control. Coupling between meteorology and chemistry transport takes place at each horizontal advection time step only. Inter-processor communication is realised by means of MPI. The parallelisation is performed by domain decomposition techniques, but LM and MUSCAT use different horizontal grid structures. In MUSCAT, finer and coarser resolutions can be used for individual sub-domains in the multiblock approach[7]. This structure originates from dividing the meteorological grid into rectangular blocks of different sizes. The code is parallelised by distributing these blocks on the available processors. In the first version, both parallel codes work on their own predefined fraction of the available processors. This fixed *a priori* partitioning of the processors leads to imbalances between LM and MUSCAT. Therefore an alternative coupling scheme is implemented which guarantees the load balance between the both codes[9].

2 Formation and Dispersion of Secondary Aerosols by Single Cooling Towers Modelled for an East-German Region

Motivation. Fine and ultra-fine particles are suspected to cause damages in human health and natural environment. Several methods to reduce emissions by traffic, industry, agriculture and other sources have been successfully realised. Nowadays, the focus of environmental sciences and politics is directed towards understanding the physico-chemical formation and growth processes of secondary particles rather than the primary production[2]. Modifying factors in this context are the meteorological conditions, and the variable effective heights of the dominant emission sources. Therefore, long-term real weather simulations were performed in a mesoscale industrial region of Saxony. To investigate, to which extent the plume exhaust of the natural draft cooling towers in Boxberg and Lippendorf contributes to the formation of secondary aerosols. In spite of the relatively low emissions of primary particulate matter (PPM), interferences of the air quality are expected from the formation of sulfate and nitrate aerosols by the SO2 and NOx gas emissions and reactions with ammonia.

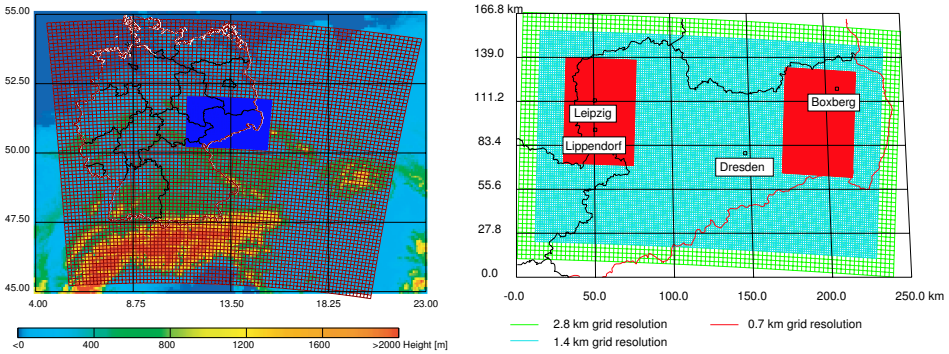

Figure 1. Model regions of Central Europe (left side) and Saxony (right side) with structure of nesting and grid refinement, respectively.

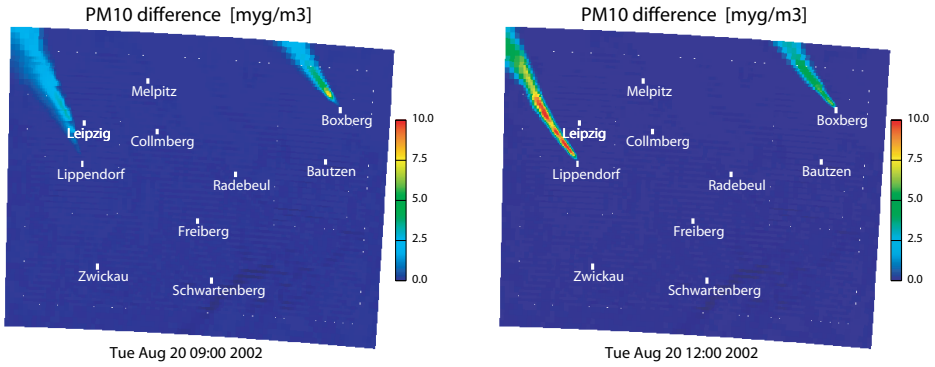

Figure 2. PM_10 concentration in Saxony caused by the emissions in Boxberg and Lippendorf at August 20-th 2002, 9:00 LT (left side) and 12:00 LT (right side).

Model setup. The study mainly aims at problems of the secondary formation and growth of anorganic particles with sizes below 10 μm (PM10). The dominant contribution to mass accretion is provided by the heterogeneous condensation of gaseous compounds on preexisting aerosols[1], involving pollutants such as ammonia and sulfuric or nitric acid (generated by complex pathways from the precursor species SO2 and NO2). The model system LM-MUSCAT was applied in a nested hierarchy with the superior control by the global reanalysis data of GME (Fig. 1). The innermost region of interest covers an area of 240 km x 156 km (Saxony) with variable resolution between 2.8 km and 0.7 km, where the finest grid was arranged around the dominant emission sites Boxberg and Lippendorf. The outer region extends over about 1200 km x 1000 km (Central Europe) with a constant resolution of 8 km in the main part. The model simulation in this domain generates the initial and boundary concentrations for the inner region.

Two typical summer/winter periods in 2002 each of 36 days were chosen for the simulations. The plume rise of the cooling towers in dependence on the meteorological conditions was accounted for by utilizing the adequate model of Schatzmann and Policastro[12]. One virtual neutral tracer per cooling tower was additionally emitted for identification purposes. Considering the meteorological and emission/immission conditions within the reference periods, two 8-day intervals were selected, for which the simulations on Saxony were repeated with the cooling tower emissions switched off. Thus, the difference between the switch-on/off simulations allows extracting the direct and indirect influence of the corresponding emissions on the immission situation[3]. The outstanding SO2 production rates by the sites Boxberg (1.2 t/h) and Lippendorf (2.1 t/h) as compared to the extremely small dust emissions (0.04 t/h, 0.06 t/h, resp.) actually require the examination of the secondary formation of particulate matter. In this respect, the assumed partitioning of the cooling tower SO2 emission data (88% SO2, 12% SO4 ions) is of great significance for the results.

Simulation results. The results are summarised as follows (an example is shown in Fig. 2):

1. Significant direct or indirect influences of the cooling tower gas emissions on the particle immission situation can be noticed only within limited zones of very narrow (highly concentrated) plumes and mainly for several hours about noon in summer.
2. The intrinsic particle formation caused by the considered emission sites frequently reaches peak values of about 10 μg/m^3 PM10 (maximal 20 μg/m^3), consisting predominantly of ammonium sulfate. Primary particles and ammonium nitrate formation contribute to only 10%.
3. The small probability for maximum plume intensities at a fixed location on the surface lowers the temporal averaged particle exposition down to 0.1 μg/m3 PM10.

3 Regional Modelling of Saharan Dust Aerosol

Motivation. Soil derived mineral dust contributes significantly to the global aerosol load and is suspected to impact the climate system by changing the energy balance of solar and thermal radiation[6]. The worldwide largest sources of dust are located in North Africa; about 50-70 percent of global dust emissions are estimated to originate from the Saharan desert. Radiative forcing by soil dust aerosol is complex, since dust not only scatters but also partly absorbs incoming solar radiation, and also absorbs and emits outgoing longwave radiation ('greenhouse effect'). Any changes in atmospheric dust loads result in changes of the radiation balance and surface temperatures. The magnitude and even the sign of the dust forcing depends on the optical properties of the dust, on the vertical distribution of the dust, on the presence of clouds, and on the albedo of the underlying surface[8]. Dust can also influence the climate indirectly by altering cloud optical properties[10]. The research project SAMUM[13] (2005-2007)) has the goal of quantification of radiative properties and effects of Saharan dust aerosols by means a field experiment in Morocco.

Model setup. The model computes dust emissions in non-vegetated areas depending on surface wind friction velocities, surface roughness, soil particle size distribution, soil moisture, and snow cover[16]. Soil particle size distributions are derived from global soil texture data. Enclosed topographic depressions are treated as preferential 'hot-spot' source regions, and the soils in these areas are assumed to consist of uniformly textured particles

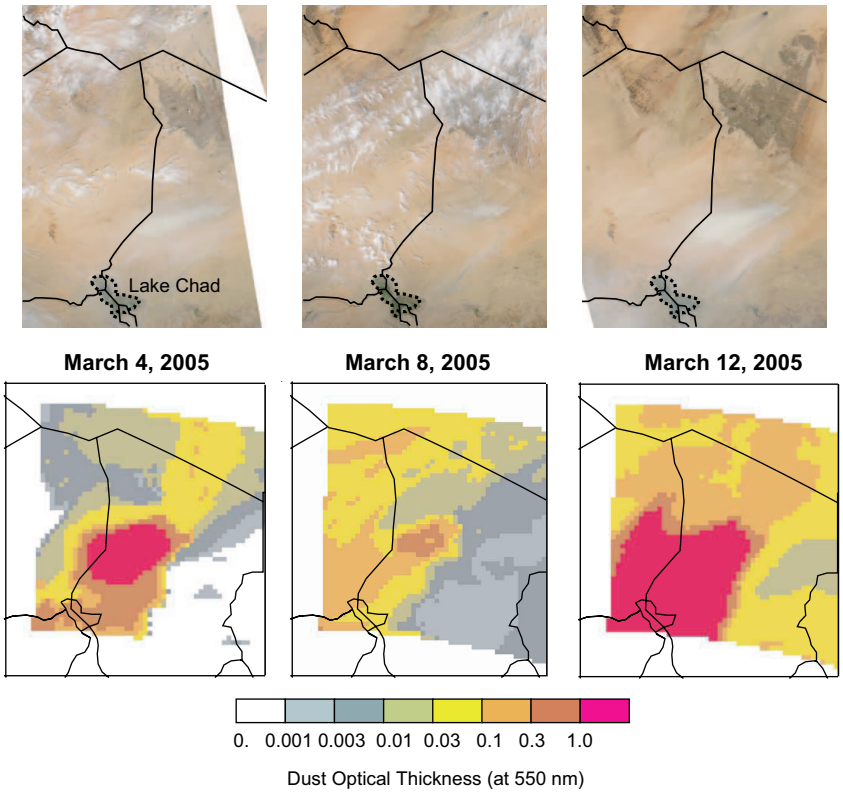

Figure 3. Dust episodes during the BODEX field study: True-colour retrievals by the NASA MODIS instrument on the Aqua satellite for the days March 4, March 8 and March 12, 2005 for the Lake Chad region (Chad) (top panels, source: NASA) and dust optical thickness for the same days simulated with the regional dust model at 7 km horizontal resolution (bottom panels).

which disaggregate into micrometer-sized particles during saltation events. The threshold friction velocities which must be reached for initiation of dust emission are computed depending on soil particle size distribution following the approach by Marticorena and Bergametti (1995), but assuming constant surface roughness within each model gridcell. Size distributions of the mobilised dust depends on surface properties as well as the surface wind speed. This dust emission scheme is coupled online into LM-MUSCAT. Emission fluxes are computed with surface winds and soil moisture fields from the meteorological model LM, dust is transported as passive tracer in 5 independent size bins covering the size range from 0.1 to 25 microns with the MUSCAT tracer scheme, and the aerosol deposition parameterisation in LM-MUSCAT is adapted for dust aerosol properties. The development of the regional Saharan dust model started late 2004, and tests of the model are carried out for previously observed Saharan dust episodes.

Simulation results. So far, the performance of this regional dust model has been tested for two well documented events of Saharan dust transport to Europe in August and October 2001, and a dust storm that occurred in the Bodele depression (Chad) in March 2005 during

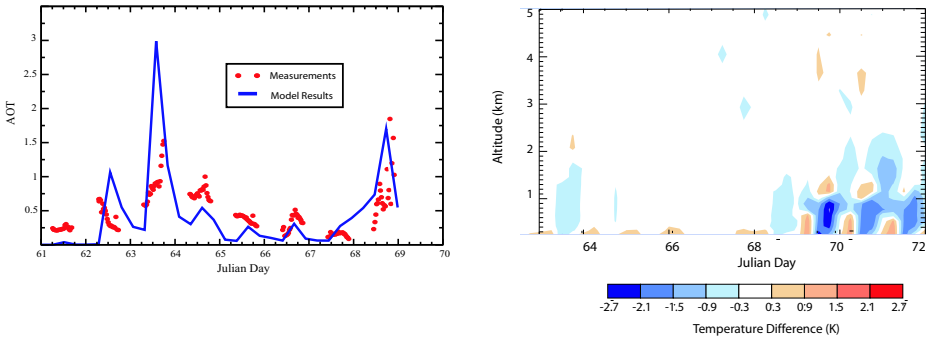

Figure 4. Modelled dust optical thickness at BODEX field site (at 16.5N, 18.3E) compared to sunphotometer measurements (left) and vertical distribution of simulated differences in air temperature compared to a simulation without dust forcing (right) for March 1 to March 12, 2005.

the British BOdele Dust EXperiment (BODEX). We present first results for this latest dust event, for which *in-situ* measurements of meteorological parameters like wind speed and surface temperatures as well as measurements of dust optical properties are available. The Bodele depression, which lies between the Tibesti Mountains, Lake Chad, and the Djouf region in Mali is the most active dust source in the Sahara desert, where the presence of dust is detected throughout the year. For simulation of this dust episode, dust production and transport was computed for an area of ca. 200000 km^2 using a horizontal model resolution of 7 km. Deposition of the large dust particles is mostly by dry deposition, the stronger gravitational settling of larger particles leads to changes in the size distribution of atmospheric dust. Dust optical thicknesses are computed from the size-resolved dust concentrations. Within LM-MUSCAT, changes in radiative fluxes caused by dust are computed online, using dust aerosol optical properties derived from sunphotometer measurements (Todd et al., submitted). The radiative forcing by dust aerosol is allowed to impact on the meteorology and feeds back on dust emissions and atmospheric distributions.

With an updated parameterisation for the dust emission model, the BODEX dust case was simulated twice, once including the dust feedback on climate, and once with dust as passive tracer. Size-resolved dust emission fluxes for the BODEX location and time period of the field study are computed with the regional dust model. Although satellite retrievals of the regional extent of the dust plumes are difficult to obtain over highly reflective desert surfaces, a comparison of true-color retrievals by the MODIS instrument onboard the NASA Aqua satellite with model results for the days March 4, 8, and 12, 2005 shows good agreement in the occurrence of modeled dust plumes with the remote sensing images (Fig. 3). The variation of modeled dust aerosol optical thickness during the dust episode compared to measurements from the sunphotometer instrument (Fig. 4, left) also shows good agreement. Only on March 4 (Julian day 63), the modeled optical thicknesses briefly exceed the measurements by about a factor of two. The difference in modeled air temperatures for the field site between the LM-MUSCAT model run in which dust was included as radiatively interactive tracer and temperatures computed with the LM without including dust aerosol for the same period shows the effects of the presence of dust aerosol on the atmospheric temperatures (Fig. 4, right). Atmospheric cooling occurs during daytime when

the atmospheric dust scatters or absorbs a part of the incoming sunlight, which results in a reduction in solar radiation fluxes below ca. 1 km height. This cooling is only evident for days when the dust optical thickness exceeds the value of 1, with a maximum cooling reaching about 3 degrees. During night the presence of dust caused a slight warming by about 0.5 K compared to the simulation without dust, because the large dust particles absorb a small part of the outgoing terrestrial radiation. Surface temperature measurements show a drop in maximum day temperatures by about 10K from March 10 to March 11, which is well matched by the modeled surface temperatures.

4 Concluding Remarks

The availability of a full coupled meteorology chemistry aerosol model with well defined interfaces to external emission inventories and regional scale forcing data for chemistry and aerosols, e.g., *EMEP*, is an important step forward in regular model applications on behalf of the European Community or other entities. The model system LM-MUSCAT is also a powerful instrument for process studies[14] and the interpretation of field experiments[5]. In this context, the nested mesoscale model LM-MUSCAT could fill the gap between local measurements and the rather coarse resolution of large scale models. The model performance and parallel efficiency is encouraging[20].

Acknowledgments

The work was supported by the LfUG of Saxony, the DFG (project 07ATF40) and the NIC Jülich. Furthermore, we thank the DWD Offenbach for good cooperation.

References

1. I. Ackermann, *MADE: Entwicklung und Anwendung eines Aerosol-Dynamikmodells für dreidimensionale Chemie-Transport-Simulationen in der Troposphäre*, Mitteilungen aus dem Institut f. Geophys. u. Meteorol. Univ. Köln **115**, 1–153 (1997).
2. S. Andreani-Aksoyoglu, S. H. Prévot, U. Baltensperger, J. Keller, J. Dommen, J., *Modeling of formation and distribution of secondary aerosols in the Milan area (Italy)*, J. Geophys. Res. **109**, D05306 (2004).
3. C. L. Blanchard and G. M. Hidy, *Effects of SO2 and NOx emission reductions on PM2.5 mass concentrations in the southeastern United States*, Journal of Air& Waste Management Association **55**, 265–272 (2005).
4. G. Doms and U. Schättler, *The Nonhydrostatic Limited-Area Model LM (Lokal-Modell) of DWD: Part I: Scientific Documentation (Version LM-F90 1.35)*, (Deutscher Wetterdienst, Offenbach, 1999).
5. B. Heinold, A. Tilgner,W. Jaeschke, W. Haunold, O. Knoth, R. Wolke, and H. Herrmann, *Meteorological characterisation of the FEBUKO hill cap cloud experiments, Part II: Tracer experiments and flow characterisation with nested non-hydrostatic atmospheric models*, Atmos. Env. **39**, 4195-4207 (2005).

6. IPCC (Intergovernmental Panel on Climate Change), *Climate Change 2001* (New York: Cambridge Univ. Press, 2001).
7. O. Knoth and R. Wolke, *An explicit-implicit numerical approach for atmospheric chemistry-transport modelling*, Atmos. Env. **32**, 1785-1797 (1998).
8. H. Liao and J. H. Seinfeld, 1998, *Radiative forcing by mineral dust aerosols: Sensitivity to key variables*, J. Geophys. Res. **103**, 31,637–31,645 (1998).
9. M. Lieber, *Die Optimierung der Kopplung von Simulationsmodellen mit unterschiedlichen Gitterstrukturen auf Parallelrechnern*, (Diplomarbeit, Hochschule für Technik und Wirtschaft, Dresden, 2005).
10. Z. Levin, E. Ganor, and V. Gladstein, *The effects of desert particles coated with sulfate on rain formation in the eastern Mediterranean*, J. Appl. Meteor. **35**, 1511–1523 (1996).
11. B. Marticorena and G. Bergametti, *Modeling the atmospheric dust cycle, 1995, 1. Design of a soil-derived dust emission scheme*, J. Geophys. Res. **100**, 16,415–16,430 (1995).
12. M. Schatzmann and A. J. Policastro, *An advanced integral model for cooling tower plume dispersion*, Atmos. Env. **18**, 663-674 (1984).
13. `http://www.tropos.de/samum`
14. A. M. Sehili, R. Wolke, J. Helmert, M. Simmel, W. Schröder, E. Renner, *Cloud chemistry modeling: Parcel and 3D simulations*, in: C. Borrego, A. L. Norman, Eds., (*Air Pollution Modeling and Its Application XVII, Kluwer Academic Publishers, New York), in press.*
15. *R. W. Stockwell, F. Kirchner, M. Kuhn, and S. Seefeld,* A new mechanism for regional atmospheric chemistry modeling, *J. Geophys. Res.* **102**, *25,847–25,879 (1997).*
16. *I. Tegen, S. P. Harrison, K. E. Kohfeld, I. C. Prentice, M. C. Coe, and M. Heimann,* The impact of vegetation and preferential source areas on global dust aerosol: Results from a model study, *J. Geophys. Res.* **107 (D21)**, *4576, doi:10.1029/2001JD000963 (2002).*
17. *M. C. Todd, V. Martins, R. Washington, G. Lizcano, S. M'Bainayel, S. Engelstaedter,* Optical properties of mineral dust from the Bodl depression, Northern Chad during BodEx, *submitted , (2005).*
18. *R. Wolke and O. Knoth,* Implicit-explicit Runge-Kutta methods applied to atmospheric chemistry-transport modelling, *Env. Mod. & Software* **15**, *711–719 (2000).*
19. *R. Wolke, O. Knoth, E. Renner, W. Schröder, and J. Weickert,* Modelling of atmospheric chemistry-transport processes, *in: H. Rollnik and D. Wolf, Eds., NIC-Symposium 2001, (John von Neumann Institute for Computing, Jülich, 2002), 453-462.*
20. *R. Wolke, O. Knoth, O. Hellmuth, W. Schröder, E. Renner,* The parallel model system LM-MUSCAT for chemistry-transport simulations: Coupling scheme, parallelization and application, *in: G.R. Joubert, W.E. Nagel, F.J. Peters, and W.V. Walter, Eds., Parallel Computing: Software Technology, Algorithms, Architectures, and Applications, (Elsevier, Amsterdam, The Netherlands, 2004), 363-370.*

John von Neumann Institute for Computing

Numerical Modelling of the Internal Dynamics and Surface Tectonics of the Terrestrial Planets

Ulrich Hansen, Helmut Harder, Claudia Stein,
and Alexander Loddoch

published in

NIC Symposium 2006 ,
G. Münster, D. Wolf, M. Kremer (Editors),
John von Neumann Institute for Computing, Jülich,
NIC Series, Vol. **32**, ISBN 3-00-017351-X, pp. 289-296, 2006.

http://www.fz-juelich.de/nic-series/volume32

Numerical Modelling of the Internal Dynamics and Surface Tectonics of the Terrestrial Planets

Ulrich Hansen, Helmut Harder, Claudia Stein, and Alexander Loddoch

Institute for Geophysics
Westfälische-Wilhelms Universität Münster
Corrensstr. 24, 48149 Münster, Germany
E-mail: {*hansen,harder,stein,loddoch*}*@earth.uni-muenster.de*

1 Introduction

The terrestrial planets can be separated roughly into two classes with respect to their interior dynamics. Mercury and the silicate-moons (e.g. of Jupiter) are in a so-called single plate regime, which is characterised by an immobile and rigid lithosphere. The lithosphere on Earth, however, is divided into several mobile but individually rigid plates. Oceanic crust is created and destroyed at mid-ocean ridges and subduction zones, respectively. The Earth's surface is therefore characterised by a process of constant renewal, at least partially.

Venus and Mars have a special position in this classification, as both planets do not show any evidence for recently active plate tectonics as observed on Earth. However, statistics on impact crater counts for Venus indicate a global resurfacing event approximately 100 million years ago[1]. This suggests an episodic behaviour of surface tectonics with alternating periods of surface mobility and stagnation. Mars also appears as a one-plate planet. However recent findings by the MAG/ER magnetometer experiment on board of the Mars Global Surveyor spacecraft have revealed the existence of magnetic anomalies within the Martian crust that resemble the magnetic line patterns found at the mid-ocean ridges on Earth[2,3]. This suggests the presence of an episode of active plate tectonics on Mars, limited to the first 500 million years after the formation of the planet[4,5].

Within the scope of the DFG priority program "Mars and the terrestrial planets" we investigate these different convective styles and focus especially on a self-consistent description of a temporal transition between two regimes and its consequences on the subsequent thermal evolution of the planet.

The thermal evolution of terrestrial planets is widely investigated[6–11]. This is commonly done by applying a scaling relationship which comprises a parameterisation of the heat flux in terms of the Rayleigh number. Seperate parameterisations have been discussed for different convective regimes by[12]. A transition from one convective style to another is thus achieved by prescribing scaling laws appropriate for each regime[13]. Our fluid dynamical approach allows us to investigate the interior dynamics and the surface tectonics as a coupled system. We are therefore able to address the question whether the proposed transition from a tectonically active plate to a nowadays stagnant surface is indeed plausible.

2 The Model

In order to study the convective processes that govern the dynamics of the Earth's mantle and that of other terrestrial planets we follow a fluid dynamical approach. This allows us

to investigate mantle convection and the dynamics of the planetary surface as a coupled system.

2.1 The Mathematical Model

We consider thermally driven convection of an incompressible Boussinesq medium with infinite Prandtl number. The governing equations describing the conservation of mass, momentum and energy, respectively, are as follows:

$$\boldsymbol{\nabla} \cdot \mathbf{u} = 0 \tag{1}$$

$$-\boldsymbol{\nabla} p + \boldsymbol{\nabla} \boldsymbol{\sigma} + Ra\, T \hat{z} = 0 \tag{2}$$

$$\frac{\partial T}{\partial t} + \boldsymbol{\nabla} \left(\mathbf{u} T \right) - \boldsymbol{\nabla}^2 T = Q \tag{3}$$

Here, $\mathbf{u}$ is the velocity vector, p the dynamic pressure (i.e. the pressure without the hydrostatic component) and $\boldsymbol{\sigma}$ the stress tensor with $\boldsymbol{\sigma} = \eta \left[(\nabla \mathbf{u}) + (\nabla \mathbf{u})^t \right]$. T is the temperature and $\hat{z}$ the vertical unit vector. The rate of internal heat production Q is assumed to be constant in space and time. All variables have been non-dimensionalised by using a common scaling based on thermal diffusion time and vertical temperature difference. The Rayleigh number resulting from this scaling reads:

$$Ra = \frac{\alpha \rho g \Delta T d^3}{\kappa \eta_0} \tag{4}$$

where α denotes the (constant) thermal expansivity, ρ the density, g the gravitational acceleration, ΔT the vertical temperature difference, d the height of the model volume and κ the (constant) coefficient of thermal conductivity. η_0 is the reference viscosity defined at the surface of the domain.

The experiments were carried out in a Cartesian box with stress-free, impermeable boundaries. The box was heated from below and cooled from above with constant temperatures of $T_{top} = 0$ and $T_{bot} = 1$. Reflecting conditions were employed at the sides.

2.2 The Rheological Model

The key parameter for the investigation of the convective processes taking place within planetary mantles is the viscosity η, which directly controls the ability of the material to flow and thus influences the dynamics of the system. Laboratory experiments with mantle material analogs have shown that the viscosity within the mantle is not constant but varies with pressure, strain-rate and, most important, with temperature. In fact, the viscosity variations induced by temperature alone may span more than six orders of magnitude making the numerical solution of the governing equations extremely delicate.

We employ the following rheology, which has proven to be suitable to describe the dynamics of planetary mantles[14–16]

$$\eta(T, z, E) = 2 \cdot \left[\frac{1}{\eta_{Tz}} + \frac{1}{\eta_E} \right]^{-1} \tag{5}$$

with

$$\eta_{Tz} = \exp\left(-r \cdot T + r_d \cdot (1-z)/d\right) \quad \text{and} \quad \eta_E = \eta^* + \frac{\sigma_0}{E} \tag{6}$$

being the temperature/depth- and strain-rate-dependent part of the viscosity, respectively. r determines the strength of the temperature dependency, with $R = \exp(r)$ being the viscosity contrast between the material with maximum (i.e. $T = 1$) and minimum temperature ($T = 0$). r_d describes the dependency of viscosity on depth (pressure), which is neglected in the investigations presented here. All calculations shown in this work have been carried out with $R = 10^5$. $\eta^* = 10^{-5}$ is the plastic viscosity, σ_0 the yield stress and E the second invariant of the strain-rate tensor.

2.3 Numerical Technique

The set of non-linear equations 1-3 is solved numerically using a technique presented by Trompert and Hansen[17]: A finite volume approach is applied for spatial discretisation and an implicit Crank-Nicholson scheme for discretisation in the time domain. The algebraic equations are solved iteratively employing a multigrid technique with SIMPLER as smoother.

Due to the large viscosity variations that have to be accounted for, the calculations are extremely demanding in terms of computation power and time. A single model run easily takes several months on a Pentium IV–class workstation, limiting the possibilities to carry out investigations at high resolution and extensive parameter studies. We therefore developed a modified version of the original program code that can benefit from parallel computer architectures. We applied a domain decomposition technique and used MPI for explicit message passing. This allows us to use the Intel-based cluster system located in our university's computer center and, even more important, high performance computer systems like the JUMP-system of the John-von-Neumann Institute for Computing, Jülich, Germany.

3 Results

3.1 Styles of Mantle Convection

Investigations of mantle convection considering a temperature- and strain-rate dependent viscosity have revealed the existence of three different styles of convection[12,14].

- Stagnant Lid regime: A rigid and immobile layer develops at the surface of the mantle. Vigorous convection takes place underneath this stagnant lid. This mode of convection is associated with the present state of Mars, which currently shows a plate-tectonically inactive surface.

- Mobile Lid regime: The surface layer is mobile and is constantly subducted by the convective cycle. The system behaviour in this regime resembles that observed for constant viscosity convection. By further assuming a depth-dependency of the yield stress σ_0, a plate-like surface behaviour is obtained, similar to what is observed on Earth.

- Episodic regime: An initially stagnant lid develops at the surface. The thickening lid gets mobilised by increasing strain rates and is subducted into the interior. The now hot surface cools and a new lid develops which is again mobilised. This mode of convection is often proposed to be relevant for Venus.

Figure 1 gives a visual impression of the episodic and the stagnant lid regime by showing snapshots of the colour-coded temperature field. In the episodic case (left picture) the surface is repeatedly mobilised at least partially, as indicated by the velocity vectors (white arrows). In the stagnant lid regime, a relatively thick cold surface layer develops, which does not take part in the convection process that dominates the interior of the system.

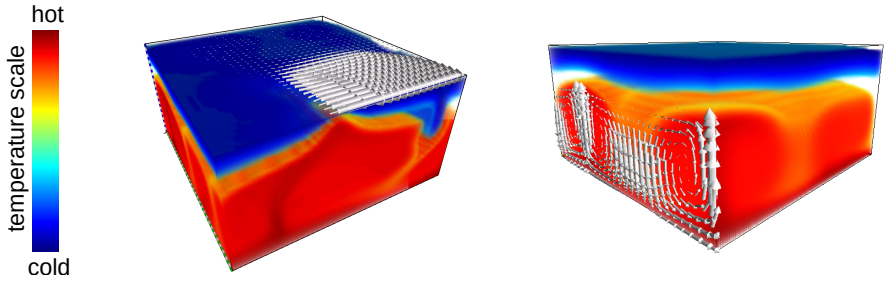

Figure 1. Two snapshots of model calculations showing the episodic regime (left picture) and the stagnant lid regime (right picture). In both cases the temperature field is visualised according to the colour scale shown. White arrows indicate the velocity field at the surface and at the left side of the box, respectively. For the episodic regime an event of surface mobilisation is shown with about a quarter of the surface being mobilised.

The actual choice of thermal and rheological parameters determines the state of convection finally emerging. A variation of the yield stress for example changes the system behaviour from the mobile lid regime, which is found for small values of σ_0 to the episodic regime for intermediate yield stresses. Finally, for large values of the yield stress the system exhibits the stagnant lid mode of convection. We carried out a systematic investigation of the dependency of the convective style on the various system parameters[14] and mapped the location of the different regimes in the parameter space, as shown in figure 2

3.2 Temporal Variations Between Convective Styles

Our investigations indicate that a change in the convective style is not only possible by means of a variation of parameters but can also appear temporally, for fixed parameters. For a critical set of parameters, that mark the border between the episodic and the stagnant lid regime (cf. figure 2) we observed the system behaviour illustrated in figure 3 by means of the non-dimensional surface heat flux. The system initially shows stagnant lid convection for more than one thermal diffusion time but eventually changes to an episodic behaviour.

Apart from this prominent example for a transitional behaviour, we also observed systems that show stagnant lid convection being interrupted by isolated events of surface mobilisation, as also shown in figure 3, again, by means of the surface Nusselt number, i.e.

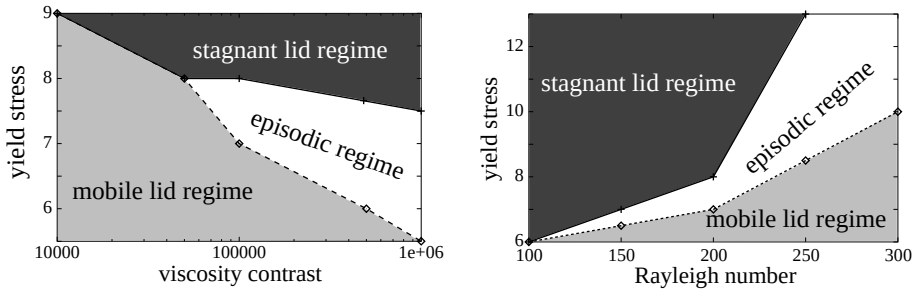

Figure 2. Two snapshots of the parameter space spanned by the Rayleigh number, the viscosity contrast and the yield stress indicating the location of the three different convective regimes. Taken from ref.[14].

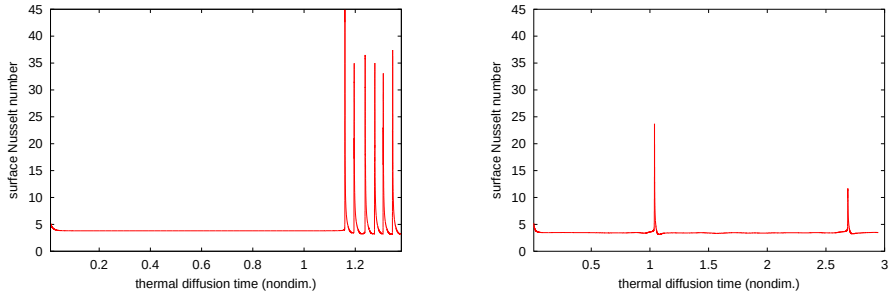

Figure 3. The surface Nusselt number as a function of time for two different model runs showing a temporal variation in the surface behaviour: A transition from stagnant lid convection to an episodic behaviour (left figure) and stagnant lid convection being interrupted by two sporadic events of sporadic surface mobilisation (right figure)

the non-dimensional surface heat flux. In both cases shown, the transition occurs out of an quasi-steady state with a thermally equilibrated heat budget.

Such a transition in the convective style is not only a fluid dynamical curiosity but is of major interest for planetological considerations. A transition of from a plate tectonically active, i.e. mobile surface to a nowadays stagnant surface has often been postulated for Mars in order to explain the remanent magnetisations of the Martian crust found by the MGS MAG/ER experiment and the presence of the crustal dichotomy[5,4,3].

Based on the rheological law (eq. 6), we were able to deduce a mobilisation criterion, that quantifies the stability of the stagnant surface layer:

$$\epsilon_M > 1 \qquad \text{with} \qquad \epsilon_M = \left.\frac{E}{\sigma_0}\right|_{surface} \tag{7}$$

Where E denotes the effective strain-rate as calculated from the velocity field and σ_0 is the yield stress parameter. The criterion serves as a necessary condition for a sporadic event of surface mobilisation. It is therefore possible to predict the occurrence of these events using our criterion as shown in figure 4.

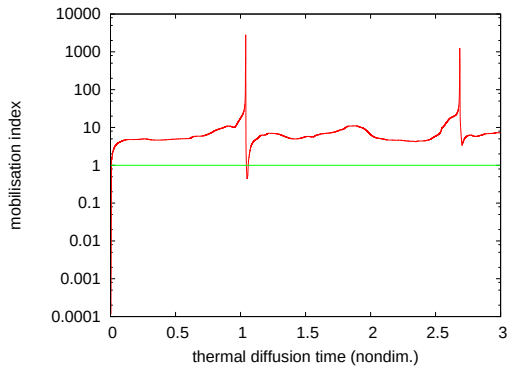

Figure 4. Value of our mobilisation index as a function of time for the model run shown in figure 3(right). Mobilisation of the otherwise stagnant surface occurs at $t = 1.0$ and $t = 2.7$. As clearly seen, the mobilisation criterion is fulfilled even during the periods of vanishing surface mobility, thus allowing a prediction of the occurrence of further mobilisation events

Acknowledgments

This work is funded by the DFG priority program “Mars and the Terrestrial Planets” (SPP 1115) under grant number Ha1765/10-2.
We are grateful for the computing resources provided by the John von Neuman Center for Computing (project number hms10)

.

References

1. R. A. Phillips and 6 authors. Impact craters and venus resurfacing history. *J. Geophys. Res.*, 97:15923–15948, 1992.
2. M. H. Acuña and 12 authors. Global distribution of crustal magnetisation discovered by the mars global surveyor mag/er experiment. *Science*, 284:790–793, 1999.
3. J. E. P. Connerney, M. H. Acuña, N. F. Ness, G. Kletetschka, D. L. Mitchell, R. P. Lin, and H. Reme. From the cover: Tectonic implications of mars crustal magnetism. *Proc. Nat. Acad. Sci. USA*, 102(42):14970–14975, 2005.
4. N.H. Sleep. Martian plate tectonics. *J. Geophys. Res.*, 99:5639–5655, 1994.
5. F. Nimmo and D.J. Stevenson. Influence of early plate tectonics on the thermal evolution and magnetic field of mars. *J. Geophys. Res.*, 105:11969–11979, 2000.
6. G. Schubert. Subsolidus convection in the mantles of terrestrial planets. *Ann. Rev. Earth Planet. Sci.*, 7:289–342, 1979.
7. G. Schubert and T. Spohn. Thermal history and the sulfur content of its core. *J. Geophys. Res.*, 95:14095–14104, 1990.
8. T. Spohn. Mantle differentiation and thermal evolution of mars, mercury, and venus. *Icarus*, 90(2):222–36, 1991.
9. J. Arkani-Hamed. On the thermal evolution of mars. *J. Geophys. Res.*, 99:2019–2033, 1994.

10. O. Grasset and E. M. Parmentier. Thermal convection in a volumetrically heated, infinite prandtl number fluid with strongly temperature-dependent viscosity: implications for planetary thermal evolution. *J. Geophys. Res.*, 103(B8):18171–81, 1998.
11. C.C. Reese, V.S. Solomatov, and L.-N Moresi. Non-newtonian stagnant lid convection and magmatic resurfacing of venus. *Icarus*, 139:67–80, 1999.
12. V. S. Solomatov. Scaling of temperature- and stress-dependent viscosity convection. *Phys. Fluids*, 7:266–274, 1995.
13. D. Breuer and T. Spohn. Early plate tectonics versus single-plate tectonics on mars: Evidence from magnetic field history and crust evolution. *J. Geophys. Res.*, 108:5072, 2003.
14. C. Stein, J. Schmalzl, and U. Hansen. The effect of rheological parameters on plate behaviour in a self-consistent model of mantle convection. *Phys. Earth Planet. Int.*, 142:225–255, 2004.
15. P.J. Tackley. Self-consistent generation of tectonic plates in time-dependent, three-dimensional mantle convection simulations, part 1: Pseudoplastic yielding. *Geochem. Geophys. Geosyst.*, 1, 2000.
16. L. Moresi and V. Solomatov. Mantle convection with a brittle lithosphere: thoughts on the global tectonic styles of the earth and venus. *Geophys. J. Int.*, 133(3):669–82, 1998.
17. R.A. Trompert and U. Hansen. The application of a finite volume multigrid method to three-dimensional flow problems in a highly viscous fluid with a variable viscosity. *Geophys. Astrophys. Fluid Dyn.*, 83:261–291, 1996.

John von Neumann Institute for Computing

Computer Science and Numerical Mathematics

Michael Griebel

published in

NIC Symposium 2006 ,
G. Münster, D. Wolf, M. Kremer (Editors),
John von Neumann Institute for Computing, Jülich,
NIC Series, Vol. **32**, ISBN 3-00-017351-X, pp. 297-298, 2006.

http://www.fz-juelich.de/nic-series/volume32

Computer Science and Numerical Mathematics

Michael Griebel

Institut für Numerische Simulation
Wegelerstr. 6, 53115 Bonn, Germany
E-mail: griebel@ins.uni-bonn.de

Computer science aspects and numerical simulation on modern parallel hardware platforms such as the JUMP are discussed in the following section. Here, we put the emphasis on numerical software aspects and their interplay with modern hardware, on the question on how to obtain a cheap crossbar switch with full bisectional bandwidth and on tools which help the programmer of parallel codes on multiprocessor systems.
In their contribution *FEAST: Development of HPC technologies for FEM applications*, Ch. Becker, S. Buijssen, H. Wobker and S. Turek discuss current trends in software developments for PDEs for hierarchical adaptive finite elemente methods. Here, the usually employed data structures and algorithms are not tuned to the specific performance facilities of modern hardware platforms and thus the obtained computational efficiency is far away from the peak rate of the respective processors. To this end hardware-oriented numerics is necessary, i.e. cache-oriented techniques must be employed and locally structured data must be exploited. The authors present such techniques for the FEM package FEAST ("Finite Element Analysis & Solution Tools") which numerically solves fluid dynamics and structure mechanic problems. They present recent results on the JUMP for their hardware oriented multigrid/domain decomposition solvers and discuss scalability, clustering and recursion for their approach. Altogether such developments are important to obtain a good portion of the peak performance on modern parallel hardware platforms for advanced numerical techniques which involve multiscale methods, adaptivity and domain decomposition.

In their contribution *A Scalable Ethernet Clos-Switch*, Norbert Eicker and Thomas Lippert discuss techniques to realize large crossbar-switches which are built from standard Gigabit-Ethernet switches as components. They follow an idea of Charles Clos from 1953 who proposed a similar technique in the context of telephone switching networks. Here, a special topology of cascaded crossbar-switches results in full bisectional bandwidth. The authors show how to build such a large crossbar-switch with up to 1152 ports which achieves full bandwidth at a cost of about 125 Euro per port and has a point-to-point throughput of 220 MB/s where the latency is less than 10 μsec. This approach turns out to be superior to any existing monolithic switch on the market.

In their contribution *The IBM eServer pSeries 690 as a Research Instrument for Computer Scientists*, G. Juckeland, M. Kluge, R. Müller-Pfefferkorn, W.E. Nagel and B. Trenkler discuss some features of the IBM p690 system at the Forschungszentrum Jülich which they tested and analysed with the PARbench, BenchIT and EPcache environment. Their results might help users and administrators to optimize performance and system behavior in their specific applications. Furthermore, they allow in an automatic way to detect MPI overhead which assists a programmer to create efficient parallel code on the IBM p690.

John von Neumann Institute for Computing

FEAST: Development of HPC Technologies for FEM Applications

Christian Becker, Sven Buijssen, Hilmar Wobker,
and Stefan Turek

published in

NIC Symposium 2006 ,
G. Münster, D. Wolf, M. Kremer (Editors),
John von Neumann Institute for Computing, Jülich,
NIC Series, Vol. **32**, ISBN 3-00-017351-X, pp. 299-306, 2006.

http://www.fz-juelich.de/nic-series/volume32

FEAST: Development of HPC Technologies for FEM Applications

Christian Becker, Sven Buijssen, Hilmar Wobker, and Stefan Turek

Institute for Applied Mathematics and Numerics
University of Dortmund, 44227 Dortmund, Germany
E-mail: feast@math.uni-dortmund.de

One current trend in software development for PDEs, and here especially for FE approaches, clearly goes towards very sophisticated hierarchical techniques and adaptive methods in any sense. In contrast, the employed data and solver structures are mostly chosen as 'globally defined' types which neglect the very specific performance facilities of modern hardware platforms. As a result, the observed computational efficiency is often far from the expected peak rates of (potentially available) several GFLOP/s per processor. These discrepancies, between numerics and software concepts and the available hardware, often lead to unreasonable calculation times for 'real world' problems as can be easily seen from recent benchmark comparisons for commercial as well as research codes. Hence, strategies for massive efficiency enhancement are necessary, not only from the mathematical (algorithms, discretisations) but also from the software side of view. To realise some of these aims our FEM package FEAST ('Finite Element Analysis & Solution Tools') is under development. Recent results on JUMP, including applications from CFD and CSM, are given.

1 Introduction

1.1 Hardware Oriented Numerics

Processor technology is still dramatically advancing and promises further enormous improvements in processing data for the next decade. On the other hand, much lower advances in moving data are expected such that the efficiency of many numerical software tools for PDEs is restricted by the cost of memory access. So, one can state:

- Not data processing, but data moving is costly.
- Employing cache-oriented techniques is a must.
- Exploiting locally structured data is a must.

Examples[1, 2] indicate that many of today's numerical simulation tools – based on the standard sparse MV techniques (see Fig. 1) – are not able to achieve a significant percentage of the high performance on recent processors which is in the range of more than 1 GFLOP/s (Table 1). In the case of fully adaptive FEM codes our measurements show that we better talk about performance rates of 1–10 MFLOP/s for matrix-vector multiplications which are already the fastest components in numerical codes. Complete multigrid solvers often perform even more slowly.

Sparse techniques are basis for most of the recent software packages (Fig. 1). With respect to Table 1 it can be seen that different numberings can lead to identical numerical results and work (w.r.t. arithmetic operations and data accesses) but to huge differences in CPU time. But how to gain more performance? One possibility is to rearrange the data

```
      DO 10 IROW=1,N
      DO 10 ICOL=KLD(IROW),KLD(IROW+1)-1
10    Y(IROW)=DA(ICOL)*X(KCOL(ICOL))+Y(IROW)
```

Figure 1. Standard sparse matrix vector multiplication with indirect adressing in Fortran77 notation

Computer	#unknowns	**CM**	**TL**	**STO**
	33,280	125	105	**100**
Alpha ES40	133,120	81	71	**58**
(667 Mhz)	532,480	60	51	**21**
(1.1 GFLOP/s Peak Linpack)	2,129,920	58	47	**13**
	8,519,680	58	45	**10**

Table 1. Performance rates (MFlop/s) of the FEATFLOW code with different numbering schemes (Cuthill–McKee, TwoLevel, Stochastic) for matrix vector multiplication

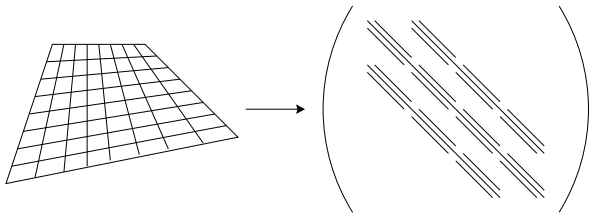

Figure 2. Line- or rowwise numbering of unknowns and resulting matrix structure

structures such that data accesses are more structured and indirect adressing is avoided. Another important topic to consider is cache locality. Modern processor architectures realise most of the possible performance via a sophisticated cache mechanism. To get regular cache-friendly data structures, unknowns should be numerated in a line- or rowwise manner (Fig. 2).

Most finite element discretisations on tensorproduct meshes lead to band structured matrices. The matrix entries are stored in bands of equal size. The matrix vector multiplication is applied bandwise with certain 'windows' to fit cache locality. In case of equidistant meshes band entries are even constant for certain operators, so a complete FEM matrix can be described by a few double values only. Table 2 shows recent results for different architectures (AMD Opteron, NEC vector, JUMP) for some basic operations.

1.2 Solver Schemes: Generalised MG/DD Solvers of SCARC Type

In view of their typically excellent convergence rates, multigrid methods seem to be most suited for the solution of many PDEs. However, as examples[1] have shown, multigrid on general domains has often poor computational efficiency, at least if the implementation is based on standard sparse techniques. Our performance measurements[1] show that realistic MFLOP/s rates for complete multigrid codes are often in the range of 1–10 MFLOP/s only, even on very modern high performance workstations. Moreover, the linear relationship be-

2D case	#unknowns	DAXPY(I)	MV-V	MV-C	MG-TGS-V	MG-TGS-C
Sun V20z	65^2	2172 (633)	1806	3334	1541	2086
(2600 MHz)	257^2	574 (150)	627	2353	751	1423
'**Opteron**'	1025^2	**300 (64)**	**570**	**1774**	**538**	**943**
NEC SX-8	65^2	5070 (1521)	3611	3768	1112	1061
(2000 MHz)	257^2	5283 (1321)	6278	8363	1535	1543
'**Vector**'	1025^2	**5603 (1293)**	**7977**	**15970**	**1918**	**2053**
IBM POWER4	65^2	1521 (845)	2064	3612	906	1071
(1700 MHz)	257^2	943 (244)	896	2896	7111	962
'**JUMP**'	1025^2	**343 (51)**	**456**	**1916**	**438**	**718**

Table 2. Performance rates (MFlop/s) of some basic linear algebra operations: DAXPY: vector vector addition, DAXPY(I) : vector vector addition with indexed factor (sparse matrix multiplication), MV-V/C: matrix vector multication with variable/constant matrix entries, MG-TGS-V/C: complete multi grid cycle with Tri-Gauss-Seidel preconditioner and variable/constant matrix entries

tween problem size and CPU time may sometimes get hardly realisable, due to problem size dependent performance rates of the sparse components. Additionally, the robust treatment of complex mesh structures with locally varying details is often hard to satisfy by typical 'Black Box' components, even for ILU smoothing, and particularly on parallel systems. Motivated by these facts, a more general strategy for solving discretised PDEs is developed (particularly in a parallel framework), which satisfies several conditions:

- The parallel efficiency shall be high due to a non-overlapping decomposition and a low communication overhead.
- The convergence rates ρ are supposed to be independent of the mesh size h, the complexity of the domain and the number of subdomains N, and they shall be in the range of typical multigrid rates (as $\rho \sim 0.1$).
- The method shall be easily implementable and use only existing standard methods.
- The approach shall guarantee treatment of complicated geometries with local anisotropies (huge aspect ratios) without impairment of overall (parallel) convergence rates.

The underlying idea is to 'hide recursively all anisotropies in single subdomains' combined with an outer 'block Jacobi/Gauss-Seidel smoothing' within standard multigrid. This approach is based on the numerical experience[3] that these 'simple' block-oriented schemes perform well as soon as all occurring anisotropies are locally hidden, that means if the local problems on each block are solved (more or less) exactly. These ideas are combined with corresponding hierarchical data and matrix structures, which exploit the described tensorproduct-like meshes on each element of the coarse grid (so-called macro) to achieve the high performance rates for the necessary numerical linear algebra components in the local (multigrid) solvers. Consequently, all solution processes are recursively performed via sequences of more 'local' steps until the lowest level, for instance a single macro with the described generalised tensorproduct mesh, is reached.

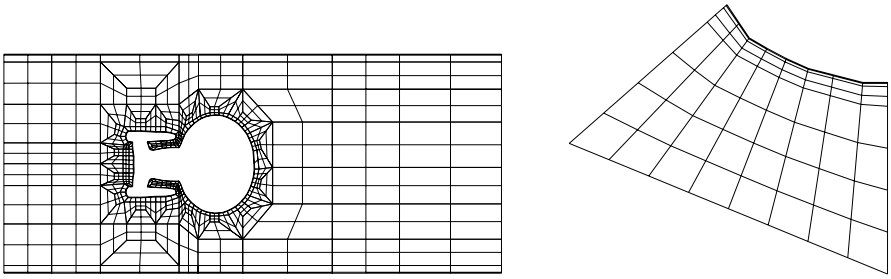

Figure 3. 2D decomposition and zoomed (macro) element (level 3) with locally anisotropic refinement towards the wall

#unknowns	Dirichlet 'Velocity'		Neumann 'Pressure'	
	$AR \approx 10$	$AR \approx 10^6$	$AR \approx 10$	$AR \approx 10^6$
$210,944$	0.17 (**8**)	0.18 (**8**)	0.21 (**9**)	0.15 (**8**)
$843,776$	0.17 (**8**)	0.17 (**8**)	0.20 (**9**)	0.17 (**8**)
$3,375,104$	0.18 (**9**)	0.19 (**9**)	0.22 (**10**)	0.22 (**10**)
$13,500,416$	0.19 (**9**)	0.18 (**9**)	0.23 (**10**)	0.23 (**10**)

Table 3. Global parallel convergence rates and number of SCARC iterations: SCARC-CG solver (smoothing steps: 1 global SCARC; 1 local 'MG-TriGS') for locally (an)isotropic refinement

Consequently, the complete SCARC approach[3] can be characterised as:

- Scalable (with respect to 'quality and number of local solution steps' at each stage)
- Recursive ('independently' for each stage in the hierarchy of partitioning)
- Clustering (for building blocks via 'fixed or adaptive blocking strategies')

Table 3 shows some typical numerical results for a prototypical Poisson problem. The grid for this computation is shown in Fig. 3.

2 Current Research Areas

2.1 FEAST Kernel Development

In this area main work is employed for the optimisation of the basic linear algebra components and generally the optimisation to the JUMP architecture (compiler settings), further the optimisation of the message passing infrastructure for massive parallel computations. Recent results are shown in Table 4.

2.2 Computational Structural Mechanics/ Computational Fluid Dynamics

Aim of this section is to illustrate how problems from CSM and CFD can be tackled in the FEAST framework. Since this basic library only provides facilities to solve scalar problems, the question is how to treat multi-field simulations. The main focus of this

#unknowns	#CPUs	runtime [sec]	(overall) MFLOP/s
3,381,504	8	8.46	927
13,513,216	12	15.28	2031
54,027,264	12	46.61	2281
216,057,856	24	114.24	3709
864,129,024	255	159.42	24276

Table 4. Large scale computations for a prototypical Poisson problem for the NCC configuration (Fig. 3) on JUMP.

section is concentrated on the design of appropriate preconditioners for the resulting saddle point problems which have a major impact on the numerical efficiency of the underlying iterative algorithms.

2.2.1 Generalised Stokes Equation

The incompressible nonstationary Navier–Stokes equations describe the behaviour of a Newtonian fluid at constant temperature with constant kinematic viscosity enclosed in a given volume with Dirichlet and/or Neumann boundary conditions. Neglecting the nonlinear convection term and applying a simple time-discretisation method with timestep k leads to the generalised Stokes equation:

$$\mathbf{u} - \nu k \Delta \mathbf{u} + \nabla p = \mathbf{f}, \qquad \nabla \cdot \mathbf{u} = 0 \tag{1}$$

A similar equation arises in CSM: One possibility to address the problem of *nearly incompressible* elastic material is to introduce, beside the displacements $\mathbf{u}$, a second variable $p := -\lambda \nabla \cdot \mathbf{u}$, which results in a mixed formulation. When a Newmark time discretisation scheme is applied, it comes to the following generalised equation

$$\mathbf{u} - 2\mu\, \tilde{k}\, \nabla \cdot \varepsilon(\mathbf{u}) + \nabla p = \mathbf{f}, \qquad \nabla \cdot \mathbf{u} + \frac{1}{\lambda} p = 0, \tag{2}$$

with $\tilde{k} := \beta k^2$ and β coming from the Newmark scheme. Due to the similarity between equation (1) and (2) we will concentrate only on the Stokes equation from now on. Most of the following applies to the elasticity case, as well, while differences will be emphasised.

At present, FEAST and its underlying SPARSEBANDEDBLAS library only feature discretisation with bilinear elements. Since a straight-forward discretisation with bilinear elements for both velocity and pressure (Q_1/Q_1) would violate the so-called Babuška-Brezzi condition appropriate stabilisation is needed.[4,5] In order not to lose the ability of dealing with irregular grids we extend the standard stabilisation technique by considering directional derivatives

$$c(p,\psi) = \sum_K (h_K^\xi)^2 \left(\xi \nabla p, \xi \nabla \psi\right)_K + (h_K^\eta)^2 \left(\eta \nabla p, \eta \nabla \psi\right)_K$$

where h_K^ξ, h_K^η measure the extensions of each element K for the local coordinate system (ξ, η). After discretisation the problem is brought down to repeatedly solving linear systems of the following type:

$$\begin{pmatrix} A & B \\ B^{\mathsf{T}} & C \end{pmatrix} \begin{pmatrix} u \\ p \end{pmatrix} = \begin{pmatrix} f \\ g \end{pmatrix} \tag{3}$$

2.2.2 Solving Strategies for Saddle Point Problems

Disregarding the matrix C consisting of stabilisation terms (and the compressibility constraint in the elasticity case) equation (3) is a classic saddle point problem. For nonsingular matrices A the velocity u can be eliminated formally, yielding the scalar equation

$$\left(B^{\mathsf{T}} A^{-1} B - C\right) p = B^{\mathsf{T}} A^{-1} f - g \tag{4}$$

with the so called *pressure Schur complement* $S := B^{\mathsf{T}} A^{-1} B - C$. This equation is solved with a preconditioned Krylov-space method.

Within such a method matrix-vector-multiplications with S have to be performed. As S is only given implicitly this means three matrix-vector-multiplications and "inverting" the matrix A. The latter has to be done exactly — at least in the first iterations — to maintain S-orthogonality of the iterates. The inversion of A can be overcome if the algorithm is embedded in an outer defect correction method acting on the whole system (3). The corresponding basic iteration looks like:

$$\begin{pmatrix} u^{n+1} \\ p^{n+1} \end{pmatrix} = \begin{pmatrix} u^n \\ p^n \end{pmatrix} + \mathcal{N}_S^{-1} \left[\begin{pmatrix} f \\ g \end{pmatrix} - \begin{pmatrix} A & B \\ B^{\mathsf{T}} & C \end{pmatrix} \begin{pmatrix} u^n \\ p^n \end{pmatrix} \right] \tag{5}$$

Thus the Schur complement method merely acts as a preconditioner (formally written as $\mathcal{N}_S^{-1}$), which allows the approximate treatment of A^{-1}. The basic iteration (5) is realised as Krylov-space method.

A second approach is to choose in the basic iteration (5) the block triangular matrix

$$\mathcal{N} := \begin{pmatrix} A & 0 \\ B^{\mathsf{T}} & -S \end{pmatrix}. \tag{6}$$

as *block-preconditioner* for the whole system (3). For the preconditioned system matrix it can easily be shown that the corresponding Krylov subspace has dimension 2, i. e. the solution of the preconditioned system would require only two iterations of a Krylov-space method.

The application of $\mathcal{N}^{-1}$, which involves the exact computation of A^{-1} and S^{-1}, is much too expensive, such that (6) is actually replaced by

$$\tilde{\mathcal{N}} := \begin{pmatrix} \tilde{A} & 0 \\ B^{\mathsf{T}} & -\tilde{S} \end{pmatrix}, \tag{7}$$

where $\tilde{A}$ and $\tilde{S}$ denote preconditioners for A and S, respectively. While the design of $\tilde{S}$ requires a closer look at the underlying equations, which will be done in the next section, the realisation of $\tilde{A}$ is straightforward: In the Stokes case, A consists of two non-zero block matrices L_1, L_2 on the diagonal (discretisations of scalar Laplace operators for the x- and the y-component) and zero off-diagonal block matrices. So, the preconditioner $\tilde{A}$ is simply realised, e. g. by independently doing one SCARC iteration for each component. In the elasticity case, however, x- and y-direction are coupled, resulting in non-zero off-diagonal blocks in A. Consequently, we cannot simply do two independent SCARC iterations as in Stokes case, but we have to resolve the coupling by embedding the SCARC solves as preconditioner into another outer Krylow-space method applied to A.

Anyway, in both cases the treatment of a multi-dimensional system is brought down to the solution of scalar equations, which enables us to exploit the SCARC solvers' strengths.

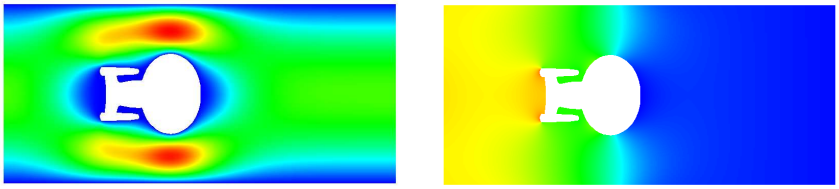

Figure 4. Example calculation for Stokes problem, velocity and pressure, NCC grid (see Fig. 3)

#CPUs	#unknowns	#vertices	runtime [sec]	(overall) MFLOP/s
51	2,540,928	846,976	560.47	291
103	2,540,928	846,976	556.07	293
103	10,144,512	3,381,504	1280.34	804
206	162,081,792	54,027,264	1095.13	7639

Table 5. Results for Stokes simulation on JUMP

2.2.3 Preconditioning of the Schur Complement

In both approaches to solve the system (3) we face the problem that a preconditioner $\tilde{S}$ for the Schur complement $S = B^{\mathsf{T}}A^{-1}B - C$ is needed. Examining the generalised Stokes equation (1) we can deduce the structure of the system matrix $A = M + \nu kL$, where M is the (lumped) mass matrix and L the Laplacian, both block-structured with zero off-diagonals. The "nature" of A clearly depends on the size of the timestep k: For very small timesteps the mass matrix dominates, while it has, in fact, no influence for very large timesteps and even vanishes for the stationary Stokes case. To construct a preconditioner that efficiently covers the whole range of relevant timesteps we exploit the additive decomposition of A. We design the preconditioner for the distinct parts of the Schur complement S. The *reactive part*, $B^{\mathsf{T}}M_l^{-1}B$, can be interpreted as a discretisation matrix steeming from a mixed formulation of the (continuous) Poisson problem. So, the preconditioning operator is chosen as L_p, the Laplacian matrix corresponding to the discrete pressure space. The continous operator associated with the *diffusive part*, $B^{\mathsf{T}}L^{-1}B$, is spectrally equivalent to the identity[6], so $M_{l,p}$, the lumped pressure mass matrix, is an optimal preconditioner. This also holds for the elasticity case, where we have, instead of νkL, the matrix $2\mu\tilde{k}K$ with K being the discretisation of $\nabla \cdot \varepsilon(\mathbf{u})$. A linear combination of the two parts gives the desired Schur complement preconditioner:

$$\tilde{S}^{-1} = L_p^{-1} + \nu k M_{l,p}^{-1} \tag{8}$$

This preconditioner seems not to cover the matrix C from (4). Its entries are of magnitude $O(h^2)$. Only if the time step k is about the size of h^2 or smaller it has to be incorporated. In the elasticity case, the part of C coming from the compressibility constraint is simply a pressure mass matrix and thus can be covered by the diffusive part of the preconditioner (8).

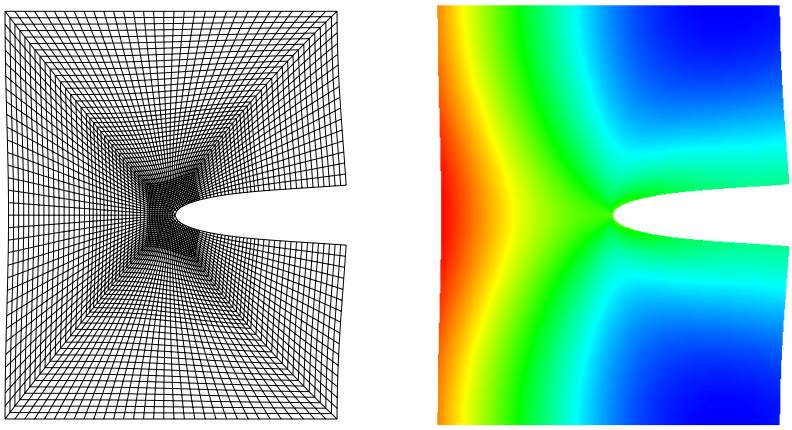

Figure 5. Computational domain and displacement (x direction) field for example elasticity problem

#elements	runtime [sec]	(overall) MFLOP/s
327,680	3.66	1382
1,310,720	9.77	2046
5,242,880	29.60	2683
20,971,520	129.13	2455

Table 6. Results for example elasticity problem on JUMP with 20 CPUs

References

1. S. Turek, A. Runge, and Ch. Becker. The feast indices – realistic evaluation of modern software components and processor technologies. *Computers and Mathematics with Applications*, 41:1431–1464, 2001.
2. Ch. Becker, S. Kilian, and S. Turek. Hardware–oriented numerics and concepts for PDE software. In *FUTURE 1095*, pages 1–23. Elsevier, 2003. International Conference on Computational Science ICCS2002, Amsterdam.
3. S. Kilian. *ScaRC als verallgemeinerter Mehrgitter– und Gebietszerlegungsansatz für parallele Rechnerplattformen*. Logos Verlag, Berlin, 2002. ISBN 3-8325-0092-8.
4. L. P. Franca and Th. J. R. Hughes. A new finite element formulation for computational fluid dynamics: VII. The Stokes–problem with various well–posed boundary conditions: Symmetric formulations that converge for all velocity/pressure spaces. *Computer Methods in Applied Mechanics and Engineering*, 65:85–96, 1987.
5. R. Becker. *An Adaptive Finite Element Method for the Incompressible Navier—Stokes Equations on Time–Dependent Domains*. PhD thesis, Universität Heidelberg, 1995.
6. S. Turek. *Efficient Solvers for Incompressible Flow Problems: An Algorithmic and Computational Approach*. Springer, Berlin, 1999.

John von Neumann Institute for Computing

A Scalable Ethernet Clos-Switch

Norbert Eicker and Thomas Lippert

published in

NIC Symposium 2006 ,
G. Münster, D. Wolf, M. Kremer (Editors),
John von Neumann Institute for Computing, Jülich,
NIC Series, Vol. **32**, ISBN 3-00-017351-X, pp. 307-314, 2006.

http://www.fz-juelich.de/nic-series/volume32

A Scalable Ethernet Clos-Switch

Norbert Eicker[1] **and Thomas Lippert**[1,2]

[1] Central Institute for Applied Mathematics, John von Neumann Institute for Computing (NIC)
Research Center Jülich, 52425 Jülich, Germany
E-mail: {n.eicker, th.lippert}@fz-juelich.de

[2] Department C, Bergische Universität Wuppertal, 42097 Wuppertal, Germany

The Scalability of Cluster Computers with Gigabit-Ethernet interconnect is limited by the unavailability of scalable Gigabit-Ethernet switches that can achieve full bisectional bandwidth. Clos' idea of connecting small crossbar-switches to a large, non-blocking crossbar is not applicable in a straight-forward manner on Ethernet fabrics. This paper presents techniques to realize large crossbar-switches built up on standard Gigabit-Ethernet switches as components. We show how to build Gigabit-Ethernet crossbar switches with up to 1152 ports, achieving full bisectional bandwidth at a cost of about € 125 per port. The latency of our Clos-switch is less than 10 μsec. These numbers are superior to any monolithic switch on the market. Using the ParaStation cluster middle-ware[2], a full bisectional bandwidth is achieved and a bi-directional point-to-point throughput of 220 MB/s is found.

1 Introduction

Sophisticated software accelerators render Gigabit-Ethernet[1] a true alternative as an interconnect for Cluster Computers. Since small- and medium-sized switches are available at attractive prices, this technology is able to serve as an inexpensive network for clusters with up to 64 nodes—as long as the applications do not require high-end communication technologies like *e.g.* Infiniband[6]. However, Gigabit Ethernet networking technology suffers from the unavailability of larger, reasonably priced switches. In order to build larger clusters one either has to purchase an expensive monolithic switch or one is forced to use a tree of cascaded switches with decreasing accumulated bandwidth from stage to stage.

A way out of this dilemma was proposed by Clos in the early 50's[3] in the field of telephony-networks by setting up a special topology of cascaded crossbar-switches providing full bisectional bandwidth; this scheme is used for instance by Myrinet[4] or Infiniband[6].

In principle it is also possible to build a similar setup with Gigabit Ethernet switches. Unfortunately, some specific features of the Ethernet protocol to a large extent inhibit the exploitation of the bandwidth offered by this topology.

This paper shows how to solve the problem. The capabilities of the building-blocks play an essential role for the construction of efficient Ethernet Clos-switches. On the one hand, they have to be able to support virtual LANs (VLAN)[9]. On the other hand, it must be possible to perform a modification of the routing tables on the MAC level. Switches that fulfill these conditions often are characterized as "level 2 manageable".

The paper is organized as follows: In the next section, the concept of Clos-networks is briefly reviewed. Sections 3 and 4 discuss spanning trees, virtual LANs and multiple spanning trees, followed by a sketch of the the setup of cascaded Ethernet crossbar switches. In section 6, we present the testbed used for prove of concept and give results in section 8. We conclude and give a short outlook on further work to be done in the context of the ALiCEnext project at Wuppertal University.

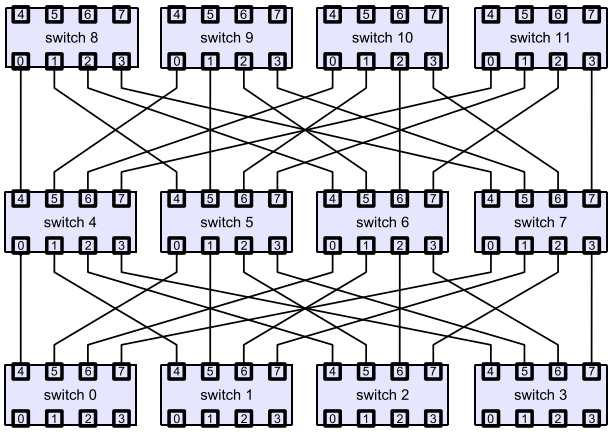

Figure 1. Example of a full 3-stage Clos-network based on 8-port switches. The full hierarchical switch provides 8×4 ports with full bisectional bandwidth.

2 Clos-Switches

In 1953 Clos[3] introduced the idea of multiple cascaded switches interconnected in a mesh-like topology originally addressing telephone networks. The main idea behind this topology was twofold: On the one hand, it should render the network more fault tolerant, *i.e.* more robust in case of failure of one or more switches. On the other hand, scalability of the accumulated bandwidth of such systems is by far superior than that of centralized systems.

Eventually, Clos' topology paved the way to set up multi-stage crossbar networks with full bisectional bandwidth. The maximum size of a fully connected network is no longer limited by the numbers of ports offered by the biggest switch available. With increasing numbers of ports more switch levels are necessary, each adding to the latency.

Today, all available switched high performance networks (*e.g.* Myrinet[4], Quadrics[5] or InfiniBand[6]) make use of Clos' idea in order to provide a full connectivity for large networks. This is necessary since the switch boxes available with these technologies typically offer not more than $\mathcal{O}(32)$ ports.

The basic topology of a 3-stage Clos-network is sketched in figure 1. It is easy to show that at any level the same number of connections is provided and that full bisectional bandwidth is guaranteed in this manner. In order to make maximal usage of the connectivity, an appropriate routing strategy has to be introduced. The main result of the present work is a technique devising such routing on a hierarchy of Gigabit-Ethernet switches. Furthermore, figure 1 can serve us to introduce the nomenclature used in the following:

- Switches connected to nodes are called *level-1 switches*. In figure 1, these are the switches 0, 1, 2, 3, 8, 9, 10 and 11.

- Switches connecting level-1 switches only are called *level-2 switches*. Hence, switches 4, 5, 6 and 7 are the example's level-2 switches.

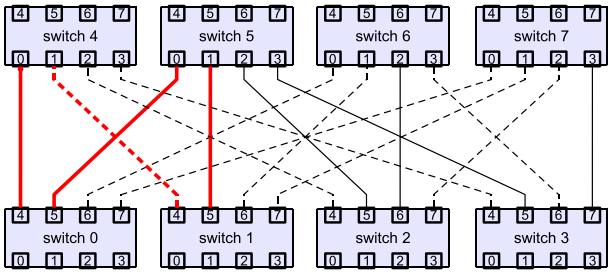

Figure 2. Basic loop appearing in Clos-switch topologies marked red. In order to suppress such loops, STAs will switch off the dashed links.

3 Spanning Trees

The major problem setting up a Clos-switch topology via Ethernet technology lies in the fact that Ethernet switches build spanning trees in order to avoid closed loops within the network. While this feature is mandatory for an Ethernet fabric to function at all, it prevents the parallel exploitation of more than one path between two switches. Therefore, the accumulated bandwidth of the network is the same as the bandwidth of cascaded switches.

The very importance of spanning trees to avoid loops within an Ethernet fabric is due to the fact that, on the Ethernet level, packets don't have a restricted life time. On the one hand, this will enable packets to live forever, if the routing-information within the switches creates loops due to misconfiguration. On the other hand—even if the routing is set up correctly—the existence of broadcast packets within the Ethernet protocol provokes packet storms inside the fabric: whenever a switch receives a broadcast packet on a given port, it will forward this packet to all other ports irrespective of any available routing information. *E.g.*, if there are two connections between two switches, a broadcast package sent from one switch to another via one of the connections will be sent back to its originating switch via the second connection. Once the originating switch is reached again, the packet will be sent along its former way once more, and a loop is created.

Unfortunately, Ethernet broadcast packets play a very important role within the Internet protocol family, since ARP messages on Ethernet hardware are implemented using this type of communication[7]. Every time the MAC-address corresponding to a destination's IP address is unknown, broadcast messages are sent on Ethernet level.

In order to avoid this extreme vulnerability of the Ethernet concept, spanning trees were introduced[8]. The main idea behind this concept is the detection of loops within a given network fabric and the selective deactivation of such connections which would close possible loops. Unfortunately, the deactivation happens on a quite fundamental level of the switch's functioning and thus it does not allow the link to carry any data at all.

For a Clos-switch topology one can find closed loops even for the simplest possible example. Figure 2 sketches a loop in a setup of 2×4 switches[a]. Many loops are found preventing the fabric from working correctly.

[a] In fact, closed loops already appear in 2×2 setups. Since figure 2 also illustrates the effects of STAs, the 2×4 setup was chosen.

4 Virtual LANs and Multiple Spanning Trees

In the context of Ethernet fabrics the concept of virtual local area networks (VLAN)[9] is particularly important for our purposes. The main idea is to implement multiple, virtually disjunct local area networks (LAN) on top of a common hardware layer. This is realized through an additional level of indirection marking every native Ethernet packet with a tag identifying the VLAN it belongs to. The benefit is twofold: it is possible to rearrange the topology of the network's fabric just by reconfiguration of the switches without touching any hardware physically. Furthermore, with the support of the operating system, it is possible to assign a computer to different virtual networks via a single network interface card. As this technology is very useful for mapping a company's organization virtually onto a single physical network fabric it is available in many so-called department switches.

For VLANs, the idea of spanning trees has to be adapted. Every VLAN requires its own spanning tree for three reasons:

- For the sake of security, broadcast messages shall only be visible within the VLAN they where created. Otherwise, as far as the the high-level protocol is concerned[b], it would be possible to spoof data transmitted within one VLAN from another.
- Within each VLAN there might be loops. The loops would compromise the functionality of the fabric as a whole if they are not eliminated.
- Even if the various VLANs as a whole might build loops, the connectivity within each separate VLAN has to be guaranteed as long as a physical connection is available. It is possible to encounter situations where a connection has to be shut down for a given VLAN but is mandatory for the correct functioning of another VLAN. This dichotomy can only be cured by spanning trees separately assigned to each VLAN.

In order to meet these needs of the VLAN technology, the spanning tree algorithm discussed above has been extended to the concept of multiple spanning trees (MST). Like the STA, the MST is standardized[10].

In practice, this mechanism does not seem to help, however. For the experimental setup described below, we found that the implementation of the MST algorithm we have tested is not robust enough to detect the—admittedly very special—setup of our Ethernet Clos-switch correctly. In fact, the switches locked up and the network was no longer usable.

We came to the conclusion, that one has to be very careful when setting up a Clos-network based on Ethernet technology. One has to avoid any loop within the various VLANs, because the automatic loop detection and elimination provided by the MST mechanism has to be be switched off explicitely. In particular, the default VLAN which usually includes all the ports of the different switches and thus contains many loops has to be eliminated from the fabric.

5 Ethernet Clos-Network Configuration

Putting together the technologies described in the last sections it is possible to avoid the problem of packet-flooding by loops in Ethernet fabrics. We proceed as follows:

[b] Here everything above Ethernet protocol level is seen as high-level.

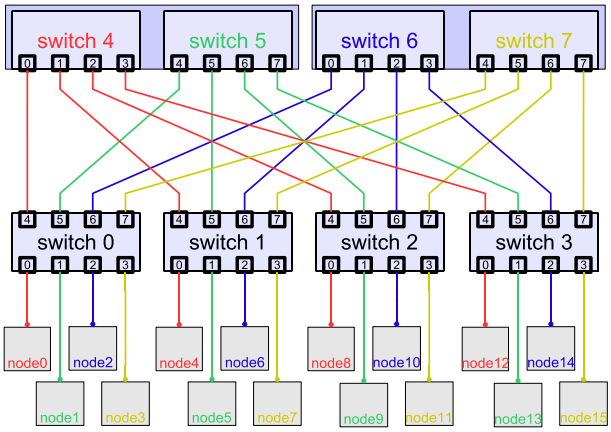

Figure 3. Crossbar configuration with virtual switches. Each VLAN is depicted with a different color. The lines between nodes and level-1 switches are only in node → switch direction used exclusively by one VLAN; in switch → node direction each link is used by all VLANs.

- Various VLANs are configured, each forming a spanning tree.
- In total, as many VLANs are needed as nodes are attached to a single level-1 switch.
- The node-ports (*i.e.* ports with nodes attached) are configured to use a specific VLAN (depending on the port) whenever they receive inbound traffic. This implements the required traffic shaping.
- All the node-ports are configured to send outbound traffic from every VLAN. *I.e.* data from every VLAN (and thus from every node) can be sent to any other node, independent of the VLAN the sending node is mapped to.

It is essential that traffic sent from any switch directly to a node is not spoiled by VLAN information. Hence from the nodes' point of view the network is completely transparent and no modification of the configuration of the nodes has to be carried out.

Figure 3 sketches the setup of the crossbar configuration. Here VLANs are depicted by the same colors, *i.e.*, colored switches only carry traffic sent by nodes of the same color into the corresponding VLAN. On the other hand, nodes receive data irrespectively of the sending node's color. The traffic shaping is implemented as follows:

- Traffic sent from a node to another one connected to the same level-1 switch does not touch any other switch. Thus `node6` will talk directly to `node4`.
- With respect to the color of a node the level-2 switch of the same color will be used in order to talk to nodes connected to other level-1 switches. This ensures the efficient usage of the complete network fabric.

Lets assume the machines `node0` to `node3` try to concurrently send data to the nodes on `switch2`. The traffic from `node0` will be sent via `switch4`, `node1` will use `switch5`, *etc.* Hence there are 4 independent routes between any two level-1 switches in this example. Thus, the full bisectional bandwidth of the setup is guaranteed.

Furthermore, figure 3 shows another important detail. In this setup, `switch4` and `switch5` are only virtual switches, *i.e.* they are assumed to use the same hardware. As only 4 ports of a virtual level-2 switch are occupied, one virtual switch can use the first 4 ports of a physical switch while another virtual switch can use the remaining 4 ports. Again the configuration is realized via the VLAN mechanism. It guarantees that there is no exchange of data between ports of a level-2 switch dedicated to different VLANs.

Note that no further effort is introduced since both—virtual and physical level-2 switches—have to handle the corresponding VLAN anyhow. The same arguments hold for `switch6` and `switch7`.

6 Testbed ALiCEnext

Our testbed consists of 144 nodes of the ALiCEnext[11] cluster located at Wuppertal University, Germany. The dual-Opteron nodes are connected via 10 SMC 8648T Gigabit-Ethernet switches[12]. They are attached to 6 of the 48-port switches, and each level-1 switch serves 24 nodes. The other 24 ports are connected to the 4 remaining switches. Every level-1 switch is connected via 6 lines to each of the 4 level-2 switches. Therefore, each physical level-2 switch hosts 6 virtual ones with VLANs in total corresponding to the number of nodes connected to a level-1 switch[c]. This setup delivers the full bisectional bandwidth.

In a first experiment the fabric was configured in such a way that only 24 VLANs were created for all the switches. Unfortunately, this approach introduced major problems which resulted in a total inaccessibility of both the nodes and the switches. The main reason is that the switches were unable to find a stable MST setup with all the loops introduced by our cabling. The only solution we found was to explicitely switch off the MST algorithm.

After switching off MST a first proof of concept was obtained by confirmation of complete connectivity between the nodes; therefore every node was pinged from any other node. Nevertheless, a detailed investigation of the fabric unveiled a deeper problem lurking in this setup. In fact, communication between nodes attached to the same VLAN, *i.e.* connected to the same port number of different switches, worked as expected. But while communication from one VLAN to another worked in principle, we observed a significantly reduced performance.

7 Routing Tables

A detailed investigation of the dynamic routing tables unveiled the underlying problem: they are created on the fly while the switch is listening to the network traffic between the nodes. Since all inbound traffic is sent via specific VLANs, most switches will never see traffic sent by a given node. For the example of figure 3, `switch5` will never see any traffic from `node0`. As soon as a switch receives a packet addressed to a node not yet in the routing tables, it will start to broadcast this packet to all ports. The broadcast introduces a plethora of useless traffic within the fabric, leading to packet loss and a significantly reduced performance.

[c] In principle, 3 level-2 switches are sufficient to build a 144 port crossbar fabric. The extra ports in our setup were used to implement a connection to the outside world.

In order to prevent the switches from creating unnecessary traffic one has to harness them with static routing tables. These tables explicitly shape the traffic addressed to a distinct node in a given VLAN to a specific port. One has to keep in mind that the size of such routing tables is proportional to both, the number of VLANs and the number of nodes connected to the fabric. Thus the tables needed for the testbed will have $24 \times 144 = 3456$ entries. Correspondingly, the routing tables of the entire ALiCEnext machine (with 512 nodes) will contain 12288 entries. Fortunately, switches providing this number of static entries are available, *e.g.* the SMC 8648T switch allows up to 16k entries.

8 Results

First we determined the basic parameters of the building-blocks. These measurements where carried out using two nodes of the ALiCEnext cluster with their Gigabit-Ethernet ports connected by a twisted pair cable and no switch in between. We used the very efficient ParaStation protocol for low level communication in order to reduce the latencies as far as possible[d]. As a high-level benchmark the Pallas MPI Benchmark suite[13] (PMB) was employed. Two tests have been applied, `pingpong` to determine the latency and `sendrecv` for bandwidth measurements.

	Back-to-back	single switch	3-stage crossbar
Throughput / node [MB/s]	214.3	210.2	210.4
Latency [μs]	18.6	21.5	28.0

Table 1. PMB. Throughput: `sendrecv` for 512 kByte. Latency: `pingpong` for 0 byte messages.

The performance numbers of the directly connected ports can be found in the left column of table 1. The latency presented there is the half-round-trip time for 0 byte length messages as determined via the `pingpong` test. The low latency found in our setup is due to the ParaStation protocol[e]. On the same hardware a fine-tuned TCP-setup will reach a latency of about $28\,\mu$s on MPI-level; out of the box the MPI latency over TCP is often in the range of $60 - 100\,\mu$s. The throughput numbers are for 512 kByte messages. Larger messages give slightly less throughput of about 200 MB/s. This is due to cache effects when the main memory has to be accessed. The message size for half-throughput was found to be 4096 Byte for all setups.

In order to determine the influence of a single switch stage on the network performance the same benchmark was carried out communicating via a switch, *i.e.* using two nodes connected to the same level-1 switch. The corresponding results marked as "single switch" can also be found in table 1. It can be seen that there is almost no influence of the switch on the throughput. Since the latency rises from $18.6\,\mu$s to $21.5\,\mu$s each switch stage is expected to introduce a penalty of only $2.9\,\mu$s. The total latency when sending messages through all three stages of our testbed is anticipated to be about $27.5\,\mu$s which would correspond to a latency of about $9\,\mu$s from the switch alone. The throughput is not affected.

The above tests where done with a single pair of processes. Of course in order to show the full bisectional bandwidth of the crossbar switch configuration one has to use as many

[d] ParaStation uses a fine-tuned high-performance protocol reducing the overhead of protocols like TCP.
[e] In fact on other hardware latencies as small as $10\,\mu$s were found.

pairs as possible concurrently. Furthermore, the processes have to be distributed in such a way that a pair's ones are connected to different level-1 switches.

We have run our benchmarks on 140 processors accessible to us, with 70 pairs of processes. The first 24 pairs where distributed over the first two level-1 switches, *etc.* For each pair the two processes were placed on different level-1 switches. Therefore, all the traffic had to be sent via the level-2 switches. Of course this is a worst case communication pattern since real applications normally have traffic running also within a level-1 switch.

The numbers for the test case presented in table 1 are worst case numbers. *I.e.* the result for the pair giving the least throughput is displayed there. If one would take the average value of all pairs, the throughput is about 5% larger, the best performing pair even gives a result of about 218 MB/s. The total throughput is larger than 15 GB/s.

Based on the observed latency of $28.0\ \mu$s the actual latency introduced by the crossbar-switch was found to be $9.4\ \mu$sec. This result is far below the values of big Gigabit-Ethernet switches with full bisectional bandwidth—at a much lower price! We expect this number to be constant for up to 1152 ports.

9 Conclusion and Outlook

We have constructed a scalable crossbar switch using off-the-shelf Gigabit-Ethernet components. We ran our performance benchmarks on the Wuppertal ALiCEnext cluster system. Full bisectional bandwidth could be achieved at a price of less than € 125 per port[f]. So far we demonstrated our concept to work for 144 ports. As a next step we will scale up the ALiCEnext cabling to 528 processors and include additional mesh topologies. An international patent for our approach was submitted and is pending[14].

Acknowledgments

We thank the ALiCEnext team in Wuppertal for patience and help.

References

1. IEEE standard 802.3z, IEEE standard 802.3ab.
2. ParaStation (`http://www.par-tec.com`).
3. Charles Clos, "A Study of Non-blocking Switching Networks", The Bell System Technical Journal, 1953, vol. 32, no. 2, pp. 406-424.
4. `http://www.myri.com`.
5. `http://www.quadrics.com`.
6. `http://www.infinibandta.org`.
7. David C. Plumme, "An Ethernet Address Resolution Protocol" RFC 826, Nov. 1982.
8. IEEE standard 802.1D.
9. IEEE standard 802.1Q, IEEE standard 802.3ac.
10. IEEE standard 802.1s.
11. `http://www.alicenext.uni-wuppertal.de`.
12. `http://www.smc.com`.
13. Pallas MPI Benchmark now available from Intel as Intel MPI Benchmark (IMB) `http://www.intel.com/software/products/cluster/mpi/mpi_benchmarks_lic.htm`.
14. Patent: "Data Communication System and Method", EP 05 012 567.3.

[f] `http://www.pricewatch.com`.

John von Neumann Institute for Computing

The IBM eServer pSeries 690 as a Research Instrument for Computer Scientists

Guido Juckeland, Michael Kluge,
Ralph Müller-Pfefferkorn, Wolfgang E. Nagel,
and Bernd Trenkler

published in

NIC Symposium 2006 ,
G. Münster, D. Wolf, M. Kremer (Editors),
John von Neumann Institute for Computing, Jülich,
NIC Series, Vol. **32**, ISBN 3-00-017351-X, pp. 315-322, 2006.

http://www.fz-juelich.de/nic-series/volume32

The IBM eServer pSeries 690 as a Research Instrument for Computer Scientists

Guido Juckeland, Michael Kluge, Ralph Müller-Pfefferkorn, Wolfgang E. Nagel, and Bernd Trenkler

Technische Universität Dresden
Center for Information Services and High Performance Computing
01062 Dresden, Germany
E-mail: {Guido.Juckeland, Michael.Kluge, Ralph.Mueller-Pfefferkorn, Wolfgang.Nagel, Bernd.Trenkler}@tu-dresden.de

1 Introduction

Currently, there is quite a number of different system architectures of HPC systems available on the market. Often, details of the complex system - from the hardware to the operating system - determine the performance of an application on a specific architecture. Examples for such small but important details are the cache hierarchy or the operating system's scheduling algorithms.

We tested and analyzed some features of the IBM p690 system at the Forschungszentrum Jülich to help users and administrators in the analysis of their applications and machine behavior, thus to optimize performance and system behavior (sections 2, 3 and 4).

Furthermore, the programming paradigms applied in parallel applications introduce an overhead and can be a potential source of performance loss. MPI, as a widely used standard, needs strict rules to be adopted by the developer, for example in the communication between the parallel processes. Assisting the programmer in the process of MPI problem detection can thus be of invaluable help (section 5).

2 Examination of the Scheduling Properties on the IBM p690 with the PARbench Environment

Benchmarking in the field of HPC is mostly realized with special programs which run separately on the system. However, utilization of expensive hardware quite often requires running multiple programs on the machine simultaneously in the multiprogramming mode. Competition for resources, runtime conflicts and sometimes even scheduling problems are the consequences. The goal of our study has been to measure the behavior of the machine when workloads compete.

2.1 PARbench

The PARbench Benchmark System was developed at Forschungszentrum Jülich in the early 90's. Over the last years, it was enhanced and ported to many parallel machines by our research group at Technische Universität Dresden. PARbench enables the simulation of virtually every workload the user might have in mind and specifies. It is able to

execute many benchmark programs in parallel and record their behavior with regards to time flow and several other parameters. OpenMP is used as the concept for parallelization to support parallel jobs within a chosen benchmark workload.

2.2 A Selection of Tests

The IBM p690 system used for these tests was running AIX 5L Version 5.2 as the operating system. The system consists of SMP nodes with 32 processors as the building block for the whole cluster. It uses a thread based scheduling system with priority queues (256 stages). The scheduling algorithm is a fair round robin algorithm with dynamic priorities where each processor has its own queue. There also exists one global queue for all processors. However, this queue must be explicitly activated as it overwrites the system of local queues.

As part of our activities, we have run many different workloads to investigate several aspects of the machine. Here, we will concentrate on one test where we have looked at the situation of parallel jobs running in a multiprogramming environment. Further results can be found in[10,12].

2.3 Results

The test scenario mentioned above is a situation where 32 sequential jobs (CPU time: each job is running for 100 seconds) are concurrently generated completely filling one node with 32 CPUs for 100 seconds. This is an ideal situation where the utilization is about 100%. This workload is kept constant now but every second group of four jobs is executed as a parallel job using OpenMP as the parallelization paradigm (each job uses 4 threads). The result is indicated in figure 1.

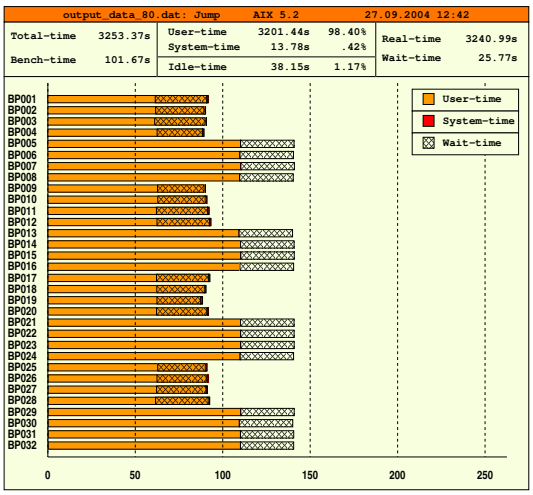

Figure 1. PARbench experiment with 16 jobs with 4 threads each and 16 serial jobs running on 32 processors using the global queue.

It clearly shows that the parallel jobs finished earlier (after about 60 seconds, left end of the overlapped pattern) – which means that in the average they have got more than one CPU allocated over time. The sequential jobs ended after about 140 seconds (right end of the bar). So far, these results are not completely surprising and are acceptable. The work done by each job, however, has been kept constant. On the other hand, it clearly can be seen that the parallel jobs were accounted for only about 85 seconds (right end of the bar for the parallel jobs) – which suggests that they have not used the full CPU time they have used before. At the same time, the sequential jobs were accounted for more than 115 CPU seconds. In sum, the total accounted CPU time stays constant at 3200 CPU seconds (32 times 100 seconds). These different user times for sequential and parallel jobs indicate shortcomings in the accounting system where CPU time used by the parallel jobs is accounted for the sequential ones. This discovery has been reported to IBM and is still under examination.

3 BenchIT

Performance analysis of computer systems is an interesting but quite challenging task. A first approach is given by standard benchmarks and their results available on-line for a wide variety of computer systems (e.g. LINPACK[14] or SPEC[15]). Own measurements normally require some detailed knowledge of the system architecture and most of the other machine components. Nevertheless, there are plenty of options for getting measured performance results which are inconsistent, unreliable, and sometimes even incorrect. However, such results are sometimes used to choose the system architecture in the next procurement.

With BenchIT we want to improve the measurement and the comparison of archived performance data. BenchIT offers a uniform and flexible architecture for the measurement and presentation of such data[13,16]. BenchIT consists of two parts for the measurement and the presentation of performance data.

The BenchIT main kernel driver initiates and controls the performance measurement. It repeatedly calls the measurement kernel which implements a measurement algorithm with varying problem sizes (e.g. vector sizes or matrix dimensions). When the processing of the kernel is done with all problem sizes (or a time limit is reached) the data is analyzed, outliers are corrected, and all information is written into a result file.

The results of a BenchIT measurement run are written into a plain ASCII file. It is clear that the result file has also to contain information about the measurement environment as well as the system architecture, since only the result file is uploaded to the BenchIT web server. Only with this additional information the measurement becomes comparable.

The BenchIT web server (`http://www.benchit.org`) is the key element in the data analysis process. It offers sharing files with different user groups, therefore, it enables the user to compare his results with the ones of colleagues or any other BenchIT user.

The assembly of plots occurs in steps where all available data is filtered in order to contain just the results the user wishes to see. The data is presented using gnuplot – parts of the website are therefore a mere front end to make all gnuplot options available. Plots are shown online or are exported in png, eps or emf format for including them in presentations as well as in articles. Furthermore, plots can be stored, easily accessed, and postprocessed.

One of the main design goals in the development of BenchIT is portability between different platforms. Real portability problems arise in considering the main kernel driver

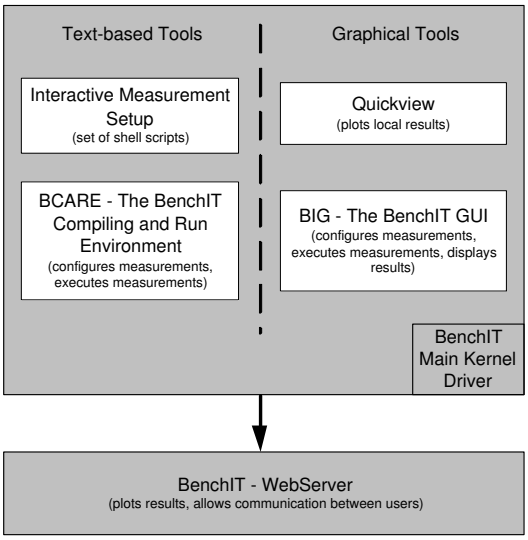

Figure 2. BenchIT components

since the measurements are to run on a large variety of platforms and operating systems. The greatest common denominator among all those systems seems to be a shell, a compiler, and some degree of POSIX-compatibility. Therefore, the whole main kernel driver is steered by a set of shell scripts invoking the system compiler(s) for each measurement run and kernel. Some of the results obtained on the IBM p690 can be found on our website `http://www.benchit.org`.

4 EP-Cache: Optimizing Cache Access – Compiler Tests and Source-To-Source Transformations

Usually, a developer focuses on implementing a correct program which solves a problem by using an algorithm. Frequently, applications which do not take the cache hierarchy of modern microprocessors into account achieve only a small fraction of the theoretical peak speed. Fine-tuning a program for better cache utilization has become an expensive and time consuming part of the development cycle. One way to optimize the cache usage of applications are source-to-source transformations of loops. There are a number of known transformations that improve data locality by reusing the data in the cache, such as loop interchange, blocking and unrolling.

Modern compilers claim to use loop transformations in code optimization. In the EP-Cache project (funded by the BMBF contract number 01IRB04) we have tested three FORTRAN90 compilers (IBM xlf for AIX V8.1.1[1], Intel ifc 7.1[2] and SGI MIPSpro 7.3[3]) for loop transformations. In addition, the same source code was optimized manually.

Our measurements (see figure 3 for two compilers) demonstrate that the capabilities of the tested FORTRAN compilers to optimize cache behavior vary. Only MIPSpro7 is able to automatically optimize sequential code in such a way that the resulting speedup is

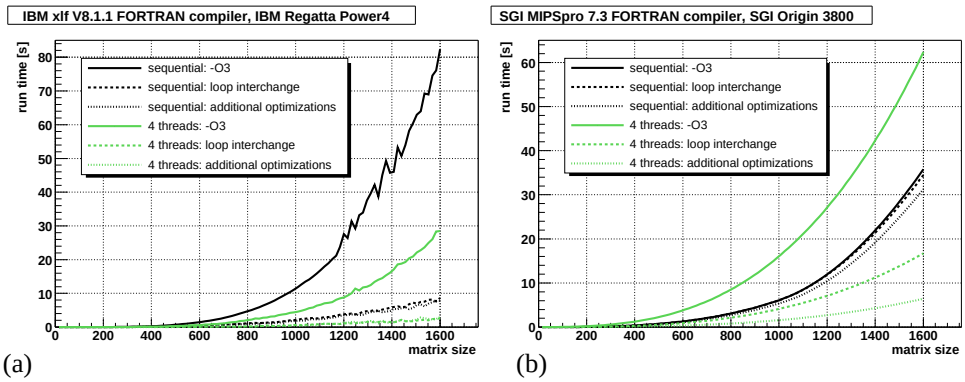

Figure 3. Runtime as function of the matrix dimension (a) on a IBM Regatta p690 system with IBM's xlf for AIX FORTRAN V8.1.1 compiler; the measurement curves of the two manually optimized parallel codes are on top of each other and (b) the SGI Origin 3800 with the MIPSpro 7.3 FORTRAN compiler

comparable with a manual optimization. In the case of parallel OpenMP processing none of the compilers can improve the original source code.

Currently, the only way to deal with cache access problems in FORTRAN programs seems to be manual optimizations, like loop transformations[5]. However, there are three drawbacks in a manual optimization: it is time consuming, error-prone, and can become quite complicated.

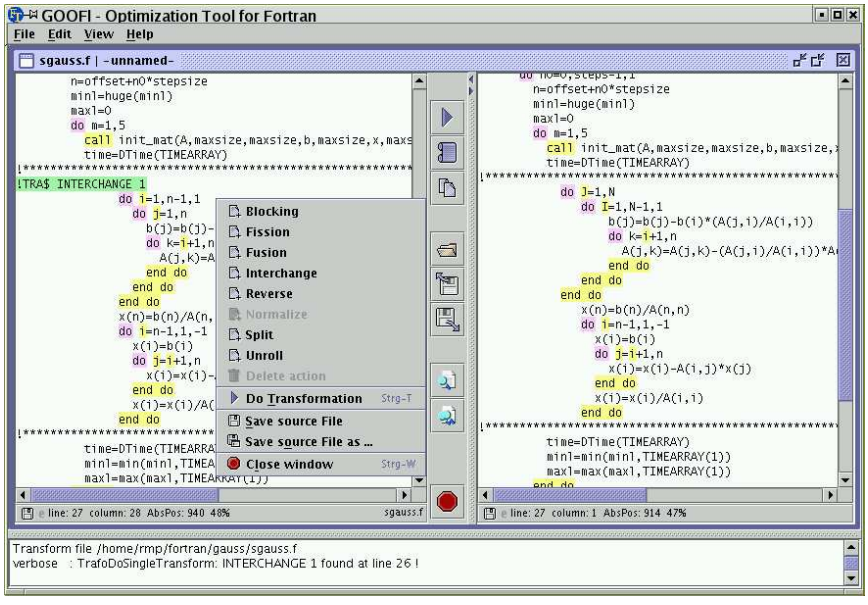

Figure 4. Screenshot of GOOFI with original and transformed source files and the transformation selection window

Therefore, we have developed a tool to assist developers in optimizing their FORTRAN applications: loop transformations are performed automatically on user request. GOOFI (Graphical Optimization Of Fortran Implementations) provides a graphical user interface (figure 4) where the user loads his/her source code (left side of the window) and requests transformations for a loop (by a mouse click). By another mouse click, he/she receives the transformed code, which appears up in the right window of the split screen, making direct visual comparison easily possible. The entire results of these studies and developments were published at EuroPar 2004[4].

5 Automatic Scalability Analysis for MPI Programs

Identifying performance problems can be a time consuming and difficult task especially for parallel applications.

5.1 Automatic MPI Overhead Detection

Within the MPI Standard, most of the communication between the processes running in parallel is performed by simply exchanging messages between these processes. To understand what is going on during an execution of an MPI program, many tools have been developed. Typically, these tools keep track of the messages within a system and are able to show a timeline of the program activities as well as message statistics and other useful data after the program has terminated. There are many current research activities trying to analyze the behavior of an application automatically.

One of the activities at the Technische Universität Dresden within this research area during 2004 was to automatically find the lines within the source code of an MPI program causing unnecessary waiting time as well as scalability problems[6–8]. For achieving this goal, it was necessary to define a 'normal behavior' for a call to an MPI function. If a communication function is called multiple times under the same conditions it is most likely that the execution time for this MPI function call varies, even under ideal conditions on a dedicated system (see figure 5). To be able to distinguish between the normal variations that will happen everytime from those variations that are caused by a bad parallelization scheme within the users application, those normal variations have to be defined. Once this is accomplished, each call to an MPI function can be inspected, and thereupon the execution time can be named within or beyond the normal variations.

Our approach is based on the assumption that the variations observed by calling the same function multiple times under ideal conditions are statistically distributed. By taking a quantile above 0.9, the value for a maximum time for a call to an MPI function is found.

At this point we are able to detect unnecessary waiting time within an MPI application. By mapping those waiting times back to the source code level, the user is given helpful information about his program.

5.2 MPI Scalability Analysis

The second part of this project was dedicated to the automatic detection of scalability problems. An application that has the same input data but runs on two processors instead on one processor is expected to finish within about half the runtime. However, the amount

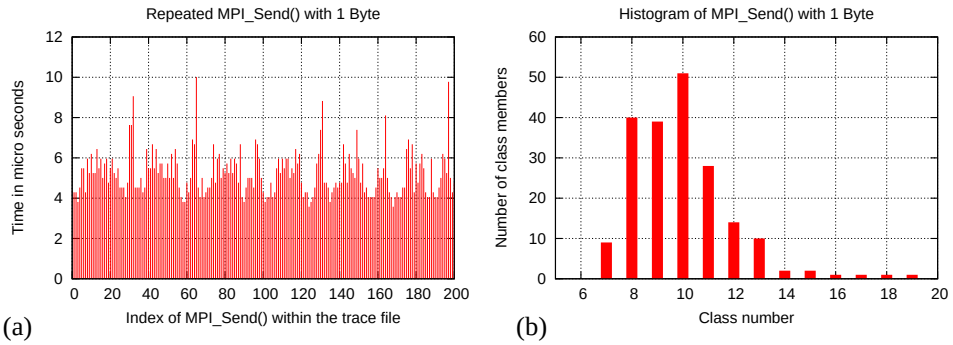

Figure 5. Example of normal variations of a repeated MPI_Send() with a small message size (a) and the histogram by using a class width of $500ns$. Depending on the (user selectable) quantile the method will automatically select a value around 9 Milliseconds as the acceptable maximum for a call to this MPI function call with this attributes.

of work within an application that actually can be parallelized limits the scalability of an application. How an application performs during a parallel program run is also determined by the amount of communication and synchronization between the processes. How the amount of communication changes with increasing number of processors depends on the algorithm used. If the communication increases faster than linear it will result in a scalability problem. This working thesis is used to map the amount of communication back to the line number within the source code of a program where the appropriate MPI function has been called. By fitting a quadratic polynomial to these numbers (one number for each program run) at the source code level it can be expected that the factor for the quadratic term in the polynomial is close to zero. By identifying the MPI calls in the source code where this is not true, a possible scalability issue has been detected.

An architecture for a tool implementing the ideas mentioned above has been proposed and implemented in a prototype. By applying the tool to some ASCI-Benchmarks it was possible to find possible scalability problems and unnecessary waiting time automatically.

Acknowledgments

We want to thank the German Federal Ministry of Education and Research (BMBF) for the funding of the project EP-Cache (contract 01IRB04).

We thank the Forschungszentrum Jülich (John von Neumann Institute for Computing) for giving us the possibility to use their computing facilities (e.g. IBM Regatta p690 ”Jump”) for our research and development. The fact that the systems is built from 32 CPU SMP Clusters makes it easy to get reproducible results when doing performance analysis. By allocation of one of the clusters in the system one user gets 32 processors exclusively. So the noise usually generated from a multi user mode is practically inexistent. This makes the machine a valuable and easy-to-use research instrument for a computer scientist.

References

1. XL Fortran for AIX V8.1.1, IBM (2003).
2. Intel Fortran Compiler for Linux Systems, Intel Corporation (2003).
3. MIPSpro Fortran 90, Silicon Graphics Inc. (2003).
4. R. Müller-Pfefferkorn, W.E. Nagel and B. Trenkler; *Optimizing Cache Access: A Tool for Source-To-Source Transformations and Real-Life Compiler Tests*, Euro-Par 2004 - Parallel Processing , Springer, LNCS 3149, 72–81 (2004).
5. J. Blum; Transit: Ein interaktives Werkzeug zur Programmoptimierung mittels Code-Transformationen, FZ Jülich, Technical report No. Jül-3302, November 1996.
6. Michael Kluge; Statistische Analyse von Programmspuren für MPI-Programme. Diploma thesis, December 2004.
7. Michael Kluge, Andreas Knüpfer and Wolfgang E. Nagel; Statistical Methods for Automatic Performance Bottleneck Detection in MPI Based Programs In *Computational Science - ICCS 2005, Volume I*, pages 3307–337, 2005.
8. Michael Kluge, Andreas Knüpfer and Wolfgang E. Nagel; Knowledge Based Automatic Scalability Analysis and Extrapolation for MPI Programs In *11th International Euro-Par Conference 2005*, 176–184, 2005.
9. Sebastian Boesler; Performance-Analyse von Hochleistungsrechnern im Multiprogramming-Betrieb: Untersuchungen auf der SGI Origin. Diploma thesis, Technische Universität Dresden, December 2001.
10. Heiko Dietze; Das PARbench-System: Untersuchungen zum Scheduling von parallelen Programmen auf der IBM p690. Diploma-Thesis, Technische Universität Dresden, November 2004.
11. Wolfgang E. Nagel and Markus A. Linn; Benchmarking parallel programs in a multiprogramming environment: The PARbench system, 1991.
12. H. Dietze, W.E. Nagel and B. Trenkler; Scheduling issues on IBM p690: Performance Analysis with the PARbench Environment. accepted for publication in *Proceedings of Parallel Computing ParCo 2005*, Malaga, Spain.
13. G. Juckeland, S. Börner, M. Kluge, S. Kölling, W. E. Nagel, S. Pflüger, H. Röding, S. Seidl, T. William, and R. Wloch; BenchIT – Performance Measurement and Comparison for Scientific Applications. In *Proceedings of the ParCo 2003*, Dresden, Germany, ISBN 0-444-51689-1.
14. LINPACK. `http://www.netlib.org/benchmark/`.
15. The SPEC Benchmarks. `http://www.spec.org`.
16. G. Juckeland, M. Kluge, W.E. Nagel and S. Pflüger; *Performance Analysis with BenchIT: Portable, Flexible, Easy to Use*, In Proc. of QEST 2004, September 27 - 30, 2004, Enschede, The Netherlands, IEEE Computer Society Order Number P2185, ISBN 0-7695-2185-1.

John von Neumann Institute for Computing

Others

Peter Grassberger

published in

NIC Symposium 2006 ,
G. Münster, D. Wolf, M. Kremer (Editors),
John von Neumann Institute for Computing, Jülich,
NIC Series, Vol. **32**, ISBN 3-00-017351-X, pp. 323-324, 2006.

http://www.fz-juelich.de/nic-series/volume32

Others

Peter Grassberger

Complex Systems Research Group
John von Neumann Institute for Computing
Research Centre Jülich, 52425 Jülich, Germany
E-mail: p.grassberger@fz-juelich.de

The contributions to this section are, as its title suggests, rather heterogeneous. Most are related to physics, at least by the fact that they were written by physicists who ventured out of the more narrowly defined discipline.

This is particularly true for the contribution of D. Stauffer, which is extreme in dealing on just eight pages with a number of problems taken from genetics, linguistics, social dynamics, and economics. Of course he cannot go into great depths, and of course the models are grossly simplified, so that they might look strange to "classical" researchers in these disciplines. But there is an increasing awareness that such simple and provocative models, usually agent-based and studied by simulations, can yield basic insights which cannot be obtained either from more realistic models or from mathematical models amenable to analytic treatment.

On the other extreme of particle based simulations is the contribution by P. Gibbon. Here the problem, the formation of plasmas by the impact of high intensity laser beams, is much less speculative and of direct technological relevance. The simulation uses state of the art methods, which find also applications in other fields such as astrophysics (stellar clusters), molecular biology (simulation of large macromolecules), and hydrodynamics. In all these fields one wants to simulate systems with millions of particles, often with long range interactions. Two main tricks help in reducing the formidable complexity of such problems: The introduction of 'mesoscopic' quasi-particles, and the approximation of potentials by the lowest terms of their multipole expansions. The contribution by Dr. Gibbon illustrates the difficulties in implementing them (together with other details), and the astonishing results obtainable thereby.

The contribution by E. Zienicke *et al.* is related to this in dealing also with plasma physics, but otherwise it is as far from it as it can be. The problem there is the transition to turbulence in magnetohydrodynamics, studied numerically by solving the relevant partial differential equations with a pseudospectral code. The chosen geometry, channel flow, is linearly stable in the regime where the transition to turbulence is found experimentally. This is similar to channel and pipe flow in ordinary hydrodynamics, where the last years have seen a break-through in understanding the mechanism for instability against *finite* perturbations from the laminar flow. Although the problem is much more difficult in the present case and requires the use of highest performance computers, it seems from the results obtained by Zienicke *et al.* that similar mechanisms are at work.

A rather different subject is dealt with in the contribution by G. Arnold *et al.*. As first pointed out by Feynman long ago, quantum mechanics has the potential of giving rise to extremely efficient computers. A general (pure) quantum mechanical state is a superposition of arbitrarily many eigenstates of any given operator, so that evolution of this state

is equivalent to the parallel evolution of arbitrarily many individual components. At this level, a computer based on this idea might seem just like a classical analog computer, but this is misleading because of the role played by the very structure of quantum mechanics. By now, not only algorithms for quantum computers exist which explicitly demonstrate their efficiency, but there are already first hardware prototypes – although using only very few qbits. The main difficulty in going to more qbits and thereby to real applications is decoherence. In order to understand its details, one has to make simulations (on classical computers!), which is what G. Arnold *et al.* do. Just because quantum computers are so efficient, simulating them on classical computers can be extremely time consuming and requires considerable resources, as illustrated well in their contribution.

Finally, with the last contribution by Bui Quang Minh *et al.*, we close the cycle by going from computer science back to genetics. The problem addressed there is the central one in molecular genetics, namely to find phylogenetic trees from DNA. With the complete genomes available for more and more species, one might think that it should become easier to reconstruct the tree of life. But all known methods are either inaccurate, or they require prohibitively much computational power (are NP-hard). Bui Quang Minh *et al.* first give a brief overview over these methods and present their own version. Then, they discuss in detail the implementation of their algorithm on the Jülich supercomputers, which makes up the main part of their paper. Although I personally would have preferred a more thorough discussion of the general problem, their treatment illustrates in an impressive way the achievements possible – and the efforts needed – when implementing state of the art algorithms on state of the art computers. Since this volume is edited by a supercomputer center and will be read mainly by its potential users, this might be exactly the information most useful for its readers.

John von Neumann Institute for Computing

Interdisciplinary Monte Carlo Simulations

Dietrich Stauffer

published in

NIC Symposium 2006 ,
G. Münster, D. Wolf, M. Kremer (Editors),
John von Neumann Institute for Computing, Jülich,
NIC Series, Vol. **32**, ISBN 3-00-017351-X, pp. 325-332, 2006.

http://www.fz-juelich.de/nic-series/volume32

Interdisciplinary Monte Carlo Simulations

Dietrich Stauffer

Institute for Theoretical Physics, Cologne University
50923 Cologne, Germany
E-mail: stauffer@thp.uni-koeln.de

Biological, linguistic, sociological and economical applications of statistical physics are reviewed here. They have been made on a variety of computers over a dozen years, not only at the NIC computers. A longer description can be found in[1], an emphasis on teaching in[2].

1 Introduction

The Monte Carlo methods invented for physics problems half a century ago were later also applied to fields outside of physics, like economy[3], biology[4], or sociology[5]. Instead of atoms one simulates animals, including people. These physics methods are often called "independent agents" when applied outside physics, to distinguish them from "representative agent" approximations and other mean field theories. "Emergence" in these fields is what physicists call self-organization, that means systems of many simple particles showing complex behaviour (like freezing or evaporating) which is not evident from the single-particle properties.

The three people cited in Refs.3-5 were not physicists; two got the economics Nobel prize. But also physicists have entered these fields intensively in the last years (and much earlier for biology; see Erwin Schrödinger's question: What is life?). The German Physical Society has since several years a working group on socio-economic problems, started by Frank Schweitzer. And our university just got approved a new Special Research Grant (SFB) where geneticists and theoretical physicists are supposed to work together. The NIC Research Group in Jülich is an earlier physics-biology example.

An important difference between physics and applications outside physics is the thermodynamic limit. A glass of Cologne beer has about 10^{25} water molecules, which is close enough to infinity for physicists. Economists, in contrast, are less interested in stock markets with 10^{25} traders. Thus finite-size effects, which often are a nuisance in Statistical Physics simulations, may be just what we need outside of physics.

Of this large area of computer simulations by physicists for fields outside physics I now select: population genetics, language competition, opinion dynamics, and market fluctuations, mostly following Ref. 1, 2.

2 Population Genetics

Darwinian Evolution is similar to thermal physics in that two effects compete: Mother Nature wants to select the fittest and to minimize energy; but more or less random accidents (mutations in biology, thermal noise or entropy in statistical physics) lead to deviations from ideality, like biological ageing or minimization of the free energy. The following example is ongoing work together with Cebrat, Pękalski, Moss de Oliveira and de Oliveira and can be regarded as an improved Eigen quasispecies model.

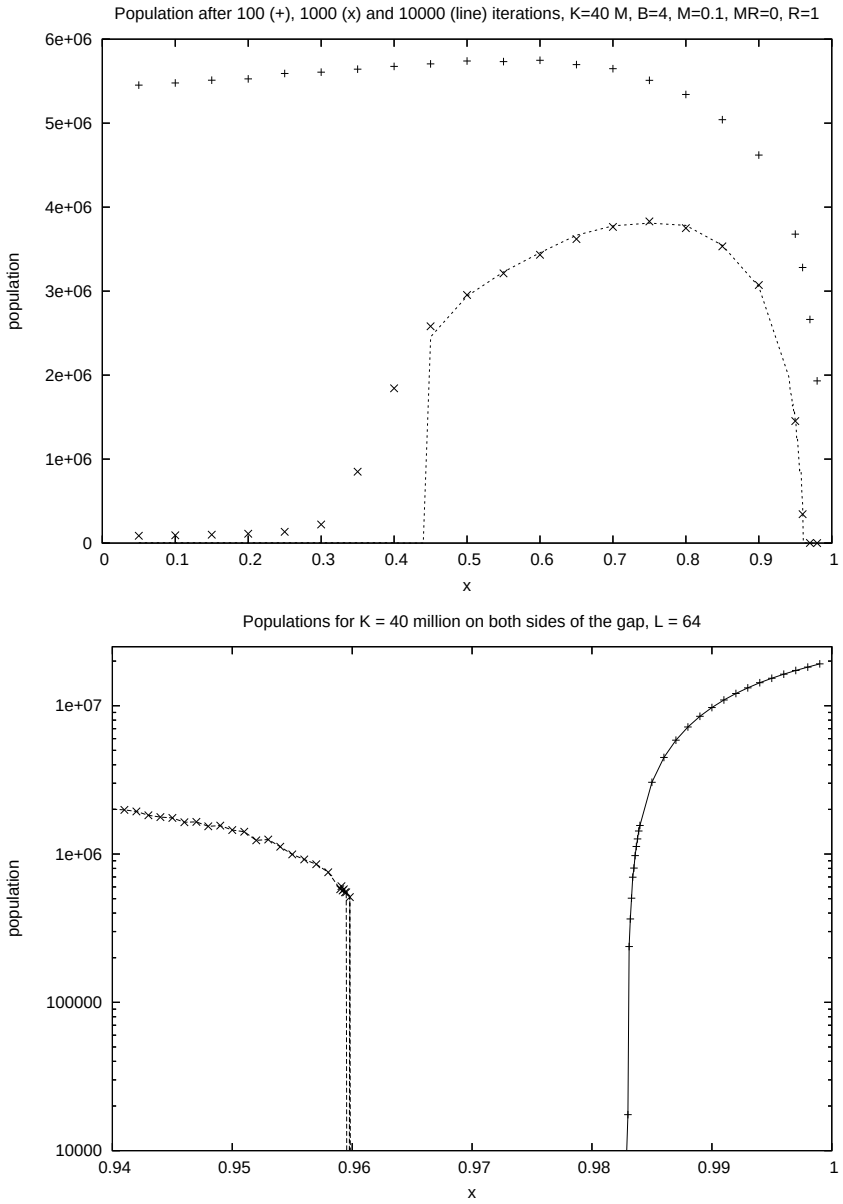

Figure 1. $M = 0.1,\ M_R = 0,\ R = 1,\ B = 4,\ L = 64$. Top part: First and second phase transition, for various observation times; the third one at $x = 0.983$ is not shown for clarity. Bottom part: Expanded semilogarithmic view of second and third phase transition.

Each individual in the population has a genome, which consists of two bit-strings inherited from the mother and the father, respectively. Each bit-string has L bits with $L = 8, 16, 32, 64$, as is convenient for Fortran words (byte to integer*8). A bit set to one means

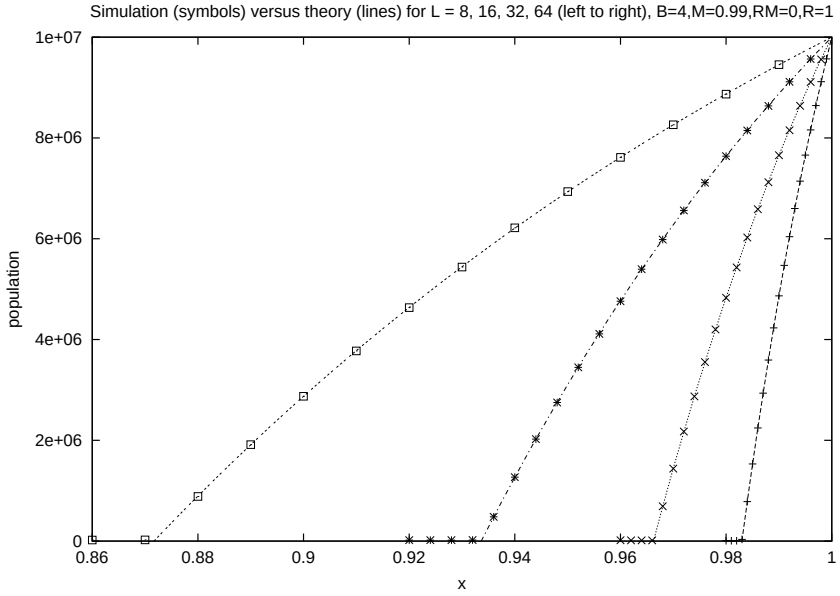

Figure 2. Simulation (symbols) versus theory (lines) for the large-x region at $L = 8$, 16, 32 and 64 (from left to right).

a bad mutation in the DNA, while a zero bit is a healthy gene. All mutations are assumed to be recessive, that means they diminish the survival probability by a factor $x < 1$ if and only if both the paternal and the maternal bit-string have their corresponding bits mutated. At reproduction, the bit-strings in both the father and the mother are mutated with probability M at a randomly selected position; then with probability R they undergo a crossover (recombination) at some randomly selected position (like in genetic algorithms); then the bits neighbouring the crossover point are mutated with probability M_R; and finally one bit-string of the mother and one of the father give one child genome, with B such births per iteration and per female. (The mother selects the father at random.) Mutation attempts for an already mutated bit leave this bit unchanged.

At each iteration the genetic survival probability is x^n where n is the number of active mutations (bit-pairs set to 1) and x an input parameter. To account for limitations in space and food, as well as for infections from other individuals, additional Verhulst death probabilities proportional to the current number of individuals are applied to both the newborns and at each iteration to the adults.

For very small x, only mutation-free individuals survive: $n = 0$. With growing x the survival chances grow, but so does the mutation load $< n >$ which in turn reduces the survival chances. As a result, for $L = 64$ three different phase transitions can be found in Fig.1: For $0 < x < 0.45$ the population dies out; for $0.45 < x < 0.96$ it survives; for $0.96 < x < 0.98$ it dies out again, and for $0.98 < x < 1$ it survives again. The transitions at 0.45 and 0.96 seem to be first-order (jump in population and load) while the one at 0.98 is second-order (continuous). For $x > 0.98$ all bits of both bit-strings are mutated to one, which allows a simple scaling prediction of the population for general L in agreement with

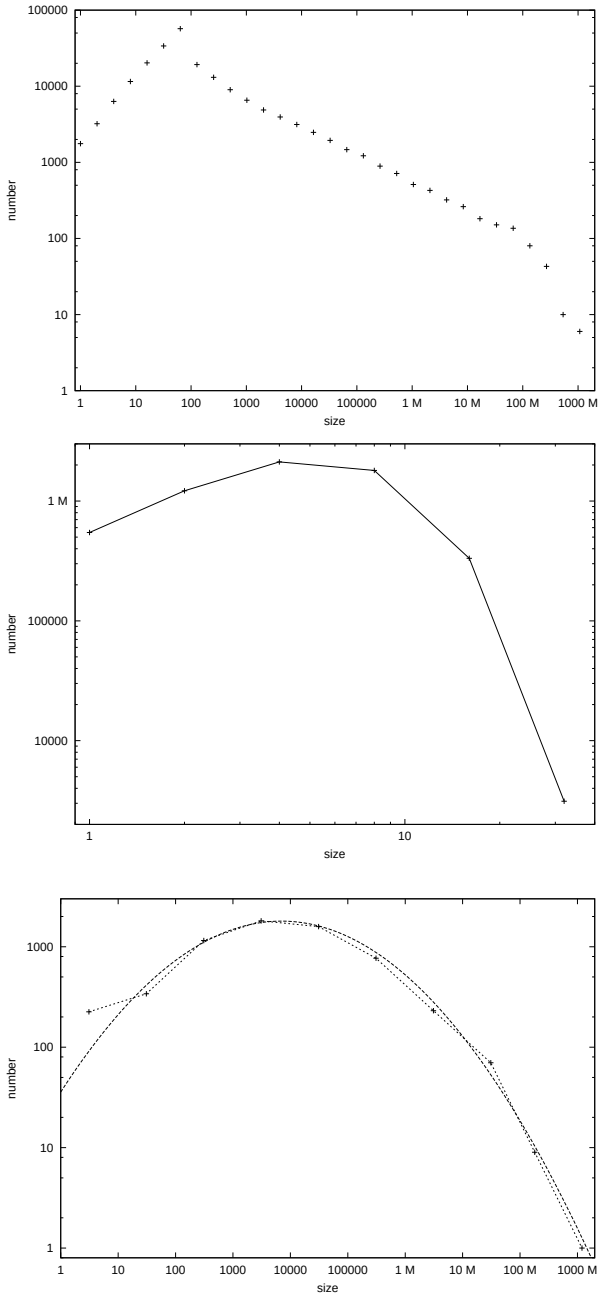

Figure 3. Distribution of language sizes in Viviane model[8] (top), in Schulze model[7] (middle) and reality[9] (bottom). The curve in the bottom part is a log-normal fit.

the simulations: Results depend on x^L as seen in Fig.2. For example, the critical point at birth rate B is at $x = (1 + B/2)^{-1/L}$.

Real animals get old with increasing age, and that can be simulated with similar techniques. The more complicated Penna bit-string model[6] simulates the ageing of individuals and agrees well with the empirical Gompertz law of 1825, that the mortality of adult humans increases exponentially with age[1].

3 Language Competition

Every ten days on average one human language dies out. Simulations of the bit-string Schulze model are very similar to the above population genetics, with random mutations, transfer of language bits from one language to another, and flight from small to large languages[7]. The alternative Viviane model[8] simplifies mutation and flight from small to large languages into one process, and ignores transfer. It gives in Fig.3 a wide range of language sizes, i.e. of the number of people speaking one language, from dying languages with only one speaker, to Chinese with 10^9 speakers. The Schulze model gives a more realistic nearly log-normal shape for this distributions, but not the wide range of language sizes. Both the proper shape and the large size range of reality (bottom part of Fig.3) might come from non-equilibrium statistics.

In the last version of the Schulze model, each language (better interpretation: its grammar) is characterized by F features each of which can adopt one of Q different integer values $1, 2, ...Q$. Each site of a large square lattice is occupied by a person speaking one language. At each iteration, each feature of each person is mutated with probability p. This mutation is random with probability $1 - q$ while with probability q the corresponding feature from one of the four lattice neighbours is adopted. Also, at each iteration, each person independently, with a probability proportional to $1 - x^2$ abandons the whole language and adopts the language of one randomly selected person in the population.

In the last version of the Viviane model, each lattice site is either empty of carries a population with a size randomly fixed between 1 and, say, like 127. Initially one lattice site is occupied and all others are empty. Then at each time step one empty neighbour of an occupied site is occupied with a probability proportional to the number of people which can live there. Then this new site adopts the language of one of its four lattice neighbours, with a probability proportional to the size of the language spoken at that neighbour site. However, this adopted language is mutated to a new language with probability inversely proportional to the new size of the adopted language. (This denominator is not allowed to exceed a maximum, set randomly between 1 and, say, 2048.) The whole process ends once the last lattice site has become occupied.

4 Opinion Dynamics

Can a single person make a difference in public life? In chaos theory we ask whether a single butterfly in Brazil can influence a hurrican in the Caribbean. Kauffman[4] asked the analogous question whether a single biological mutation has a minor effect or disturbs the whole genetic network[4]. Physicists call this damage spreading and ask, for example, how the evolution of an Ising model is changed if one single spin is flipped and otherwise the

system, including the random numbers to simulate it, remains unperturbed. This question was discussed[10,1] for three models: The opportunists of Krause and Hegselmann[11], the negotiators of Deffuant et al[12], and the missionaries of Sznajd[13].

The opportunists take as their new opinion the average opinion of the large population to which they belong, except that they ignore those who differ too much from their own opinion. Also the negotiators ignore opinions which differ too much from their own; otherwise a randomly selected pair gets closer in their two opinions without necessarily agreeing fully. A randomly selected pair of missionaries, neighbouring on a lattice or network, convinces its neighbours if and only if the two people in the pair have the same opinion. Simulations show that the opinion change of a single person may influence the whole population for suitable parameters[10,1].

For the missionaries on a scale-free network, simulations agreed nicely with election results in Brazil, apart from fitted scale factors, Fig.4.

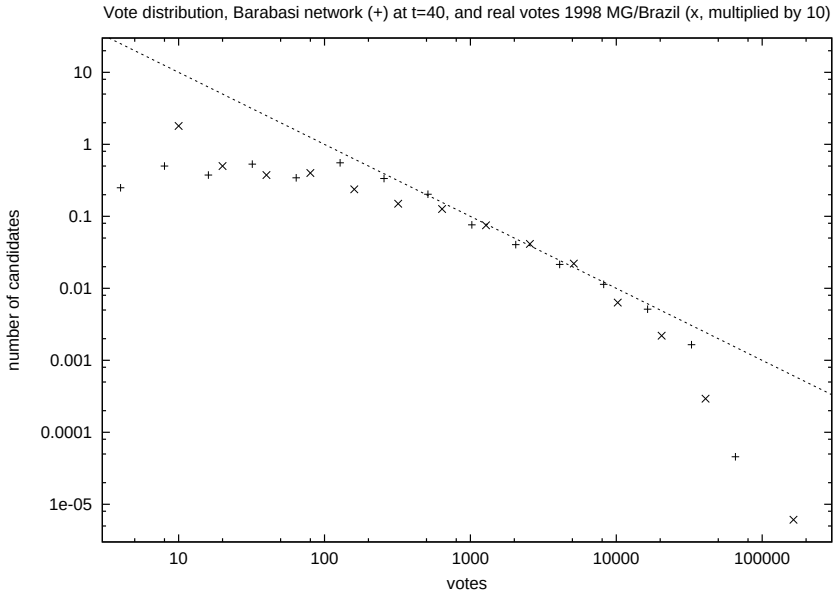

Figure 4. Distribution of the number of candidates getting a certain number of votes in simulations[14] and in elections in Minas Gerais, Brazil.

5 Market Fluctuations

How can we get rich fast by speculating on the stock market? This writer earned about one Heugel (a local currency unit of about 10^4 Euro) by believing some theory for the Tokyo stock market[15]. Details, of course, are given out only for more JUMP time. Instead this section summarizes the Cont-Bouchaud model of stock market fluctuations[16], because it is closest to the pre-existing physics model of percolation.

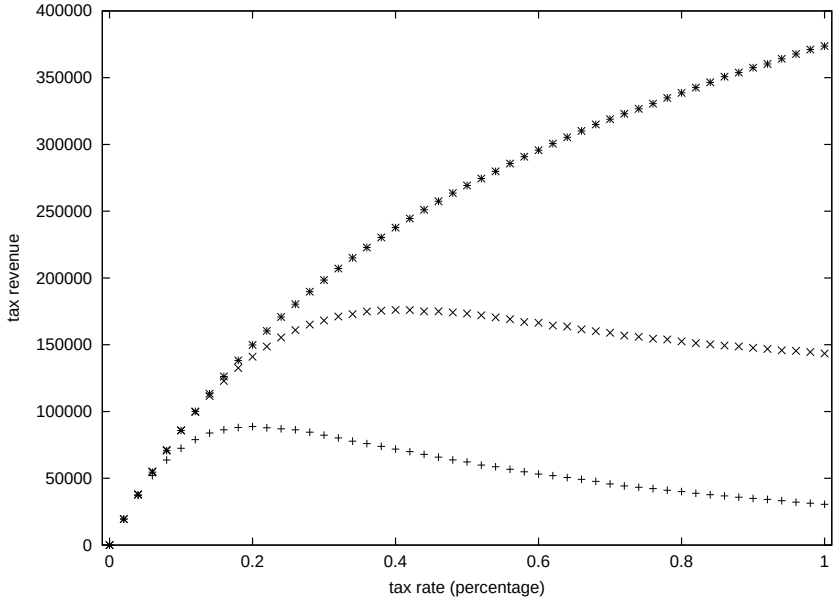

Figure 5. Tax revenue for the government versus percentage of Tobin tax to be paid for each transaction, in various versions of the Cont-Bouchaud model[17].

Each site of a large square lattice is either occupied by an investor (with probability p), or empty with probability $1 - p$. Sets of occupied neighbours are called clusters and are identified with groups of investors which act (buy or sell) together. At each iteration a cluster either buys (with probability a), sells (also with probability a) or sleeps (with probability $1 - 2a$). The traded amount is proportional to the number of investors in the trading cluster. The difference between supply and demand drives the market values up and down. This basic model gives on average: i) as many ups as downs on the market; ii) a power-law decay ("fat tail") for the probability to have a large price change, and with modifications also: iii) volatility clustering (markets have turbulent and calm times), iv) effective multi-fractality, v) sharp peaks and flat valleys for the prices, but no prediction on how the market will move tomorrow.

Apart from these nice basic properties also practical applications were made[17]: Does a small "Tobin" tax of a few tenths of a percent on all transactions reduce fluctuations and earn tax revenue without killing the whole market? It does, but apart from more government control over individuals there is another danger which can be simulated: If the tax revenue increases with increasing tax rate, then governments will be tempted to increase this tax again and again (as Germans just saw in fall 2005 and German students may observe in future tuition hikes.) Much better is a maximum of tax revenue at some moderate tax rate; then the government should settle on this moderate tax rate, provided it regards the simulations as reliable. Fig.5 shows that in this model such a desirable maximum exists for some parameters but not for all. Another application is the confirmation that halting the trade when excessive price changes are observed indeed helps to calm the market.

6 Discussion

Interdisciplinary applications of physics methods are no longer as exotic as they were years ago; biologists and economists have started to publish papers together with computational physicists on these non-physics fields.

Thanks to S. Cebrat, P.M.C. de Oliveira and S. Moss de Oliveira for comments on the manuscript.

References

1. D. Stauffer, S. Moss de Oliveira, P.M.C. de Oliveira and J.S. Sá Martins, *Biology, Sociology, Geology by Computational Physicist*. Elsevier, Amsterdam 2006 in press. ISBN-13: 978-0-444-52146-0 and ISBN-10: 0-444-52146-1. S. Moss de Oliveira, P.M.C. de Oliveira and D. Stauffer, *Evolution, Money, War and Computers*, Teubner, Leipzig and Stuttgart 1999.
2. D. Stauffer, Eur. J. Phys. 26, S 79 (2005) and AIP Conf. Proc. 779, 49, 56, 69 and 75 (2005).
3. G.J. Stigler, Journal of Business 37, 117 (1964).
4. S.A. Kauffman, J. Theoretical Biology 22, 437 (1969).
5. T.C. Schelling, J. Mathematical Sociology 1 143 (1971).
6. T.J.P. Penna, J. Stat. Phys. 78, 1629 (1995).
7. C. Schulze and D. Stauffer, Int. J. Mod. Phys. C 16, issue 5 (2005) and Physics of Life Reviews 2, 89 (2005); T. Teşileanu and H. Meyer-Ortmanns, 2006, Int. J. Mod. Phys. C17, issue 3 = physics/0508229. For other models of language competition see D.M.Abrams and S.H. Strogatz, Nature 424, 900 (2003); M. Patriarca and T. Leppänen, Physica A 338, 296. (2004); J. Mira and A. Paredes, Europhys. Lett. 69, 1031 (2005); K. Kosmidis, J.M. Halley and P. Argyrakis, Physica A 353, 595 (2005) and in press; V. Schwämmle, Int. J. Mod. Phys. C 16, 1519 (2005) and 17, issue 3; W.S.Y. Wang, J.W. Minett, Trans. Philological Soc. 103, 121 (2005), A. Baronchelli et al., physics/059075, 0511201 and 0512045.
8. V.M. de Oliveira, M.A.F. Gomes and I.R. Tsang, Physica A, in press = physics/0505197 and 0510249 (2006).
9. W.J. Sutherland, Nature 423, 276 (2003).
10. S. Fortunato and D. Stauffer, page 231 in: *Extreme Events in Nature and Society*, edited by S. Albeverio, V. Jentsch and H. Kantz. Springer, Berlin - Heidelberg 2005.
11. R. Hegselmann and U. Krause, Journal of Artificial Societies and Social Simulation 5, issue 3, paper 2 (jasss.soc.surrey.ac.uk) (2002).
12. G. Deffuant, F. Amblard, G. Weisbuch and T. Faure, Journal of Artificial Societies and Social Simulation 5, issue 4, paper 1 (jasss.soc.surrey.ac.uk) (2002).
13. K. Sznajd-Weron and J. Sznajd, Int. J. Mod. Phys. C 11, 1157 (2000).
14. A. T. Bernardes, D. Stauffer and J. Kertész: Eur. Phys. J. B 25, 123 (2002).
15. A. Johansen and D. Sornette, Int. J. Mod. Phys. C 10, 563 (1999).
16. R. Cont and J.P. Bouchaud, eprint cond-mat/9712318 = Macroeconomic Dynamics 4, 170 (2000); D. Stauffer, Adv. Complex Syst. 4, 19 (2001).
17. G. Ehrenstein, F. Westerhoff and D. Stauffer, Quantitative Finance 5, 213 (2005); G. Ehrenstein and F. Westerhoff, Int. J. Mod. Phys. C 17, issue 5 (2006).

John von Neumann Institute for Computing

Mash-Free Simulation of High Intensity Laser Interactions with Collisional Plasmas

Paul Gibbon

published in

NIC Symposium 2006 ,
G. Münster, D. Wolf, M. Kremer (Editors),
John von Neumann Institute for Computing, Jülich,
NIC Series, Vol. **32**, ISBN 3-00-017351-X, pp. 333-340, 2006.

http://www.fz-juelich.de/nic-series/volume32

Mesh-Free Simulation of High Intensity Laser Interactions with Collisional Plasmas

Paul Gibbon

Central Institute for Applied Mathematics
Research Centre Jülich, 52425 Jülich, Germany
E-mail: p.gibbon@fz-juelich.de

The acceleration and transport of energetic particles produced by high intensity laser interaction with solid targets is studied using a recently developed plasma simulation technique. Based on a parallel tree algorithm, this method provides a powerful, mesh-free approach to numerical plasma modelling, permitting 'whole target' investigations without the need for artificial particle and field boundaries. Moreover, it also offers a natural means of treating three-dimensional, collisional transport effects hitherto neglected or suppressed in conventional explicit particle-in-cell simulation. Multi-million particle simulations of this challenging interaction regime using the code PEPC (Pretty Efficient Parallel Coulomb-solver: `http://www.fz-juelich.de/zam/pepc`) have been performed on the JUMP and BlueGene/L computers for various open-boundary geometries. These simulations highlight the importance of target resisitivity and surface effects on the fast electron current flow.

1 Introduction

Numerical simulation of hot, ionized matter poses a constant challenge to the plasma theorist because of the effectively unlimited degrees of freedom, extreme nonlinear behaviour and vast range of length- and timescales characteristic of both natural and laboratory plasmas. Usually, the intractability of first-principles simulation is overcome by first simplifying the problem in phase space; replacing individual particle trajectories by a smooth velocity distribution and then solving a Vlasov-Boltzmann-type equation. By formal application of kinetic theory, many problems can be further reduced to the magnetohydrodynamics picture – the plasma equivalent of the Navier-Stokes equations. Whether particle or fluid, virtually all plasma modelling over the past four decades has relied on a spatial mesh to mediate the interplay between plasma particles and their self-consistent electric and magnetic fields. While these models have proved highly successful, the presence of a grid ultimately places restrictions on the spatial resolution or geometry which can be considered – especially in three dimensions.

In the Computer Simulations Division at ZAM, a new mesh-free plasma simulation paradigm has been developed which overcomes some of these limitations. Inspired by the N-body tree algorithms designed to speed up gravitational problems in astrophysics[1], this approach reverts to first principles by computing forces on individual particles directly, following their trajectories in a Lagrangian, 'molecular dynamics' fashion[2]. We have now combined this technique with a finite-sized-particle (FSP) model to study particle transport in high-intensity laser-plasma interactions, a field of fundamental importance to future compact laser-based particle and radiation sources[3].

2 Lagrangian Finite-Sized-Particle Kinetics

We first give a brief description of the electrostatic FSP model as currently implemented in PEPC: a generalisation of this scheme to include self-generated magnetic fields and a set of radiation-free Maxwell equations will be presented elsewhere. The choice of units is somewhat subtle for macroscopic mesh-free plasma simulation, and contrasts with the microscopic 'Debye' system used, for example in previous work[2]. The quantities time, space, velocity, charge and mass are normalized to $\omega_p^{-1}, c\omega_p^{-1}, c, N_p e, N_p m_e$ respectively, so that the equation of motion for a particle i with charge q_i and mass m_i becomes:

$$m_i \frac{d\boldsymbol{u}_i}{dt} = \frac{1}{3} q_i \sum_{i \neq j} \frac{q_j \boldsymbol{r}_{ij}}{(r_{ij}^2 + \varepsilon^2)^{3/2}} + q_i \boldsymbol{E}^p(\boldsymbol{r}_i), \tag{1}$$

where $\boldsymbol{r}_{ij} = \boldsymbol{r}_i - \boldsymbol{r}_j$ is the separation between particles i and j, and $\boldsymbol{u}_i = \gamma \boldsymbol{v}_i$ is its proper velocity; $\gamma = (1 + \mid \boldsymbol{u} \mid^2 / c^2)^{1/2}$ the relativistic factor. We have also added an external field $\boldsymbol{E}^p$, and made use of the plasma frequency definition, $\omega_p^2 = 4\pi e^2 n_e / m_e$ for electron density n_e. The constant N_p is thus eliminated by setting:

$$N_p = \frac{4\pi}{3} n_e \left(\frac{c}{\omega_p} \right)^3 .$$

In a tree code, the $O(N)$ sum over all other particles is replaced by a sum over *multipole* expansions (expanded here up to quadrupole) of groups of particles, whose size increases with distance from particle i. The number of terms in this sum is $O(\log N)$, which even after the additional overhead in computing the multipoles, results in a substantial saving in effort for large N[4].

As in classical MD simulation, we cannot use the pure Coulomb law for point charges because of the finite timestep, which will cause some particles to experience large, stochastic jumps in their acceleration, eventually destroying the energy conservation. We therefore include a softening parameter ε in Eq. (1) to ensure that $\boldsymbol{E}(\boldsymbol{r}) \to 0$ as $r \to 0$. Physically, we no longer have point charges, but rather charge clouds with a smooth charge density. It is instructive to compute the latter by applying Gauss' law to (1) with $\boldsymbol{E}^p = 0$, giving (density normalized to en_e):

$$\rho(r) = \frac{q\varepsilon^2}{(r^2 + \varepsilon^2)^{5/2}} \tag{2}$$

Charge assignment is then straightforward: the total charge contained within a cuboid volume $V = x_L \times y_L \times z_L$ (in normalized units) is

$$Q = \sum_i q_i = \rho_0 V = N_e Q_s,$$

where N_e is the total number of simulation electrons and Q_s is the macro-charge carried by them. Since the initial density $\rho_0 = -1$, we simply have $Q_s = -\frac{V}{N_e}$. Assigning charges Q_s and $-Q_s Z$ to the electrons and ions respectively, and masses $M_s^e = |Q_s|, M_s^i = A|Q_s|$, where Z and A are the atomic number and mass, sets up a macroscopic plasma system whose internal dynamics is governed solely by Equation 1.

One can show that the effective collision frequency for this system of finite-sized cloud charges is given by:[5,6]

$$\frac{\nu_c}{\omega_p} \simeq \frac{Z}{30N_D}\left(\frac{\lambda_D}{\varepsilon}\right)^2 = \frac{Z}{30N_c}\left(\frac{\varepsilon}{\lambda_D}\right), \tag{3}$$

where $N_c = \frac{4\pi}{3} n_e \varepsilon^3$ (the number of particles within the cloud radius) and λ_D is the Debye length.

Since electromagnetic wave propagation cannot be included in the present (electrostatic) model, a ponderomotive standing wave ansatz for the laser field E_L is applied at the vacuum-plasma boundary on the front-side of the target. Essentially the laser field is represented by a relativistic potential

$$\gamma_p = (1 + \Psi)^{1/2},$$

where

$$\Psi = 4a_0^2 X^2(x) R(r) T(t), \tag{4}$$

where a_0 is the normalized laser pump strength and $X(x), R(r)$ and $T(t)$ are the longitudinal, radial and temporal components determined by (analytically) solving the Helmholtz equations for a density step-profile[7].

The radius $r = (y^2 + z^2)^{1/2}$ is taken relative to the center of the focal spot. This form is used in order to create a sharp radial cutoff at $r = 2\sigma_L$ (σ_L is the *half*-width, half-maximum of the laser spot). The time-dependent component $T(t)$ provides both the $j \times B$ heating and DC push on the electron density. Finally, the longitudinal and radial ponderomotive field components (applied as external forces in the momentum equation for the electrons) are found from $E_x^p = d\gamma_p/dx$ and $E_r^p = d\gamma_p/dr$ respectively. Despite its obvious simplicity, this model exhibits surprisingly good agreement with one-dimensional, electromagnetic PIC simulations in terms of the field structure, fast electron heating and ion shock dynamics, provided the electron density scale-length L remains small compared to the laser wavelength λ .

3 Proton Acceleration in Resistive Targets

In contrast to standard particle-in-cell simulations[8], the finite electrical conductivity of the target can be included quite easily within FSP model. Previous theoretical[9] and experimental[10] work has demonstrated that resistive effects already inhibit hot electron penetration for intensities as low as 10^{17} Wcm^{-2} . The Spitzer resistivity can be related to the effective collision frequency $\tilde{\nu}_{ei} \equiv \nu_c/\omega_p$ used in the model (Eq. 3) simply via:

$$\begin{aligned} \eta_e &= \frac{m_e \nu_{ei}}{n_e e^2} = \frac{1}{\omega_p \varepsilon_0}\tilde{\nu}_{ei} \qquad \text{(SI)} \\ &= 6.3 \times 10^{-6} n_{23}^{-1/2} \tilde{\nu}_{ei} \quad \Omega\,\text{m}, \end{aligned} \tag{5}$$

where n_{23} is the electron density in units of 10^{23} cm^{-3}.

To illustrate how the inhibition of electron transport affects ion acceleration, we compare two simulations with different target conductivities but otherwise identical parameters: $I\lambda^2 = 2.5 \times 10^{19}$ Wcm$^{-2}\mu$m^2 ($a_0 = 4$), $\sigma_L = 15\ c/\omega_p$, (square) pulse duration

$\tau_L = 100$ fs and initial plasma density $n_0/n_c = 4$. The initial electron temperatures in the two cases are 5 keV and 500 eV; the particle diameters $\varepsilon = 3$ and 0.7, giving effective normalized resistivities $\tilde{\eta}_e \equiv \tilde{\nu}_{ei} = 7 \times 10^{-3}$ and 0.45 respectively.

In the high-temperature case, the effective hot electron range determined by electrostatic stopping is[9] $R_h \approx 80$ μm, so we expect the simulation to behave much like a collisionless PIC code would. This is just what we observe in Fig. 1, which shows three-dimensional snapshots of the ion density and hot electron temperature. This first plot encapsulates many of the salient features of high-intensity interactions familiar from 2- and 3D PIC simulations to date: bursts of $j \times B$-accelerated electrons generated at 2ω freely traversing the target; formation of a ponderomotively driven ion shock on the front side; and a hot electron Debye sheath being formed on the rear side, pulling ions away from the surface. We also find that the whole foil has been heated to over 50 keV in under 100 fs, in agreement with PIC simulations.

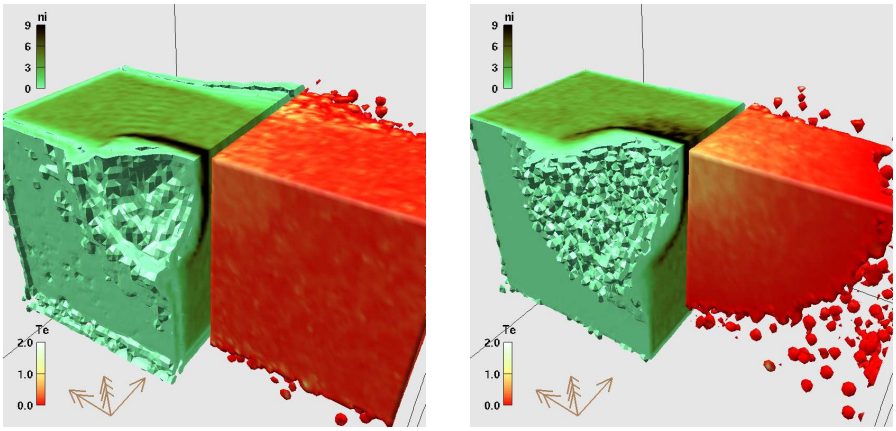

Figure 1. Isovolume sequences of ion density (left; threshold $n_c/20$) and mean electron energy (right; threshold $U_h \geq 10$ keV) sliced half-way through the target in the xz-plane for targets with initial normalized resistivities of a) $\overline{\eta}_e = 7 \times 10^{-3}$ and b) $\overline{\eta}_e = 0.45$ at a time $\omega_p t = 650$ (170 fs).

Comparing this now with Fig. 1b), a similar sequence for the 500 eV 'resistive' simulation for which the effective hot electron range is now reduced to $R_h \approx 1.2$ μm by electrostatic inhibition. This time we see a completely different picture: despite having energies in the MeV range, the hot electrons are confined to a hemispherical heat-front, 1–2 μm ahead of the shock and are virtually absent from the rear-side vacuum region at this time. This is consistent with analytical models[9] and 2D Fokker-Planck simulations[11], which predict a *diffusive* rather than free-streaming behaviour at intensities high enough to induce electrostatic transport inhibition.

The consequences of hot electron transport inhibition for the proton acceleration are dramatic: the absence (or significantly delayed presence) of the hot Debye sheath on the rear side clearly suppresses ion acceleration there[6]. On the other hand, the resistively induced electric field in front of the shock will act to enhance the front-side acceleration. These observations are summarized in Fig. 2, which shows how the relative maximum

energy of protons originating from the front and rear of the foil respectively *reverses* as the target resistivity is increased.

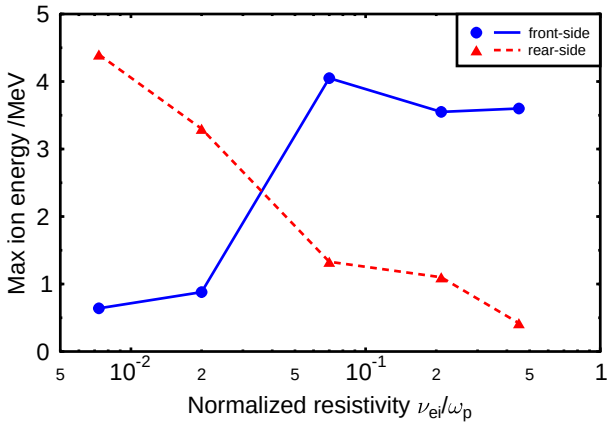

Figure 2. Maximum energy in MeV of protons originating from the front (solid line) and rear (dashed line) of the foil at 150 fs as a function of target resistivity.

4 Mass-Limited Targets

One of the problems in modelling laser-solid interactions at ever higher intensities is that the particle fluxes become so large that the periodic or reflective boundary conditions which are usually applied start to acquire dubious validity. By contrast, the present model sidesteps this issue completely: particles are permitted to fly freely away from and around the target surface. This feature is essential when modelling 'mass-limited' or mesoscopic targets, such as atomic clusters or thin wires.

An example of a laser interaction with a 1 μm -radius wire target is depicted in Fig. 3, which shows a sequence of ion density iso-volumes, but this time consisting of a 1/2-wire vertical slice. Superimposed on these plots are slices of the instantaneous electron temperature, showing that while the laser is incident, the hottest electrons are actually confined to the shock region (a,b). At the same time, there is also a strong circulation of hot electrons *around* the wire.

A striking feature of this simulation is that the entire mid-section of the wire is pushed out by the laser: the beamlet visible in Fig. 3d) has detached itself completely from the wire and continues to propagate away, spreading as it does so. This is reminiscent of three-dimensional PIC simulations of double-layer targets in which a proton beam was created from the low-Z coating on the *rear*-side[12]. By contrast, the main push in this case comes unmistakably from the target front side, even though the beamlet comprises ions which originate from across the whole wire. A further outcome of simulations in this geometry is a disc-like component in the ion emission appearing at later times – also observed in recent experiments[13,14].

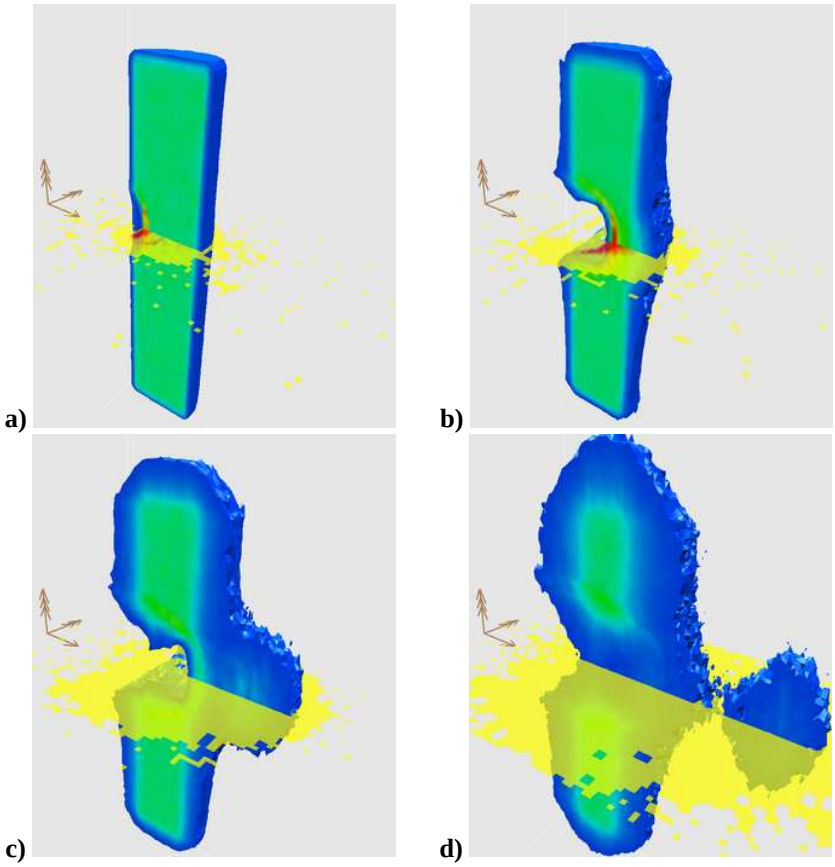

Figure 3. Time-sequence of ion density iso-volume $n_i/n_c \geq 0.25$ and electron temperature T_e slice in plane of laser incidence for a 1/2 wire-section sliced along the wire z-axis. Times shown are a) 200/ω_p , b) 400/ω_p , c) 600/ω_p and d) 800/ω_p .

5 Performance

The examples shown here were set up with between 2 and 6 million electrons and ions uniformly distributed in targets with dimensions $12 \times 12 \times 5$ μm^3. A typical simulation for a 100fs laser pulse would consume 5000 hours on a single Power4 CPU, but this reduces to around 50 wall-clock hours when run on 192 processors of the JUMP machine. By far the most algorithmically demanding part of this code is the tree walk, which in PEPC combines a previous list-based vectorised algorithm[15] with the asynchronous scheme of Warren & Salmon[16] for requesting multipole information on-the-fly from non-local processor domains. In the present scheme, rather than performing complete traversals for one particle at a time, as many 'simultaneous' traversals are made as possible, thus maximising the communication bandwidth by bundling multipole-swaps via collective operations[17]. Benchmark tests indicate that the code currently scales up to at least 256 CPUS on JUMP and 1024 CPUs on the new BlueGene/L architecture – Fig.4.

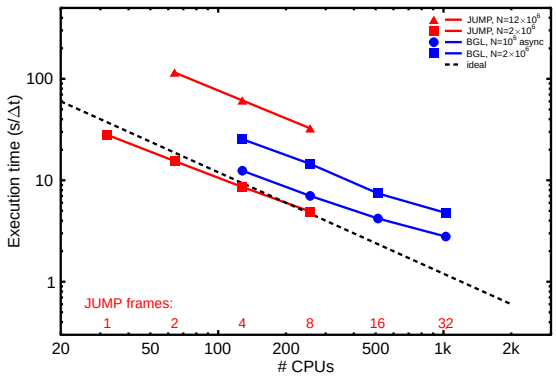

Figure 4. Timings on IBM-p690 cluster and BlueGene/L for multi-million charge spheres.

6 Concluding Remarks

Although slower than their mesh-based particle-in-cell equivalents, parallel tree codes offer exciting new possibilities in plasma simulation, particularly where collisions are important; for modelling complex geometries; or for mass-limited systems in which artificial boundaries would severely compromise the simulation's validity. The generic nature of this algorithm, combined with excellent parallel scalability, means that it can be easily adapted to other systems dominated by long-range interactions.

Acknowledgments

The author gratefully acknowledges support in performance issues from Bernd Mohr, Wolfgang Frings (ZAM) and Christoph Pospiech (of ACTC, IBM); and Sonja Dominiczak (ZAM) for assistance with visualisation. Simulations were performed with computing resources granted by the VSR of the Research Centre Jülich under project JZAM04.

References

1. J. Barnes and P. Hut, *A hierarchical $O(N \log N)$ force-calculation algorithm*, Nature **324**, 446–449 (1986).
2. S. Pfalzner and P. Gibbon, *Direct calculation of inverse-bremsstrahlung absorption in strongly coupled, nonlinearly driven laser plasmas.*, Phys. Rev. E **57**, 4698–4705 (1998).
3. P. Gibbon, *Short Pulse Laser Interactions with Matter: An Introduction*, Imperial College Press/World Scientific London/Singapore (September 2005), ISBN 1-86094-135-4 (hardback).
4. S. Pfalzner and P. Gibbon, *Many Body Tree Methods in Physics*, Cambridge University Press New York (1996).

5. H. Okuda and C. K. Birdsall, *Collisions in a plasma of finite-size particles*, Phys. Fluids **13**, 2123–2134 (1970).
6. P. Gibbon, *Resistively enhanced proton acceleration via high-intensity laser interactions with cold foil targets*, Phys. Rev. E **72**(026411), 1–8 (2005).
7. P. Gibbon, F. N. Beg, R. G. Evans, E. L. Clark, , and M. Zepf, *Tree code simulations of proton acceleration from laser-irradiated wire targets*, Phys. Plasmas **11**, 4032–4040 (2004).
8. A. Pukhov, *Three-dimensional simulations of ion acceleration from a foil irradiated by a short-pulse laser*, Phys. Rev. Lett. **86**, 3562–3565 (2001).
9. A. R. Bell, J. R. Davies, S. Guérin, and H. Ruhl, *Fast-electron transport in high-intensity short-pulse laser-solid experiments*, Plasma Phys. Control. Fusion **39**, 653–659 (1997).
10. D. Batani, A. Antonicci, F. Pisani, T. A. Hall, D. Scott, F. Amiranoff, M. Koenig, L. Gremillet, S. Baton, E. Martinolli, C. Rousseaux, and W. Nazarov, *Inihibition in the propagation of fast electrons in plasma foams by resistive electric fields*, Phys. Rev. E **65** (2002).
11. J. R. Davies, A. R. Bell, M. G. Haines, and S. M. Guérin, *Short-pulse hight-intensity laser-generated fast electron transport into thick solid targets*, Phys. Rev. E **56**, 7193–7203 (1997).
12. T. Z. Esirkepov, S. V. Bulanov, K. Nishihara, T. Tajima, F. Pegoraro, V. S. Khoroshkov, K. Mima, H. Daido, Y. Kato, Y. Kitagawa, K. Nagai, and S. Sakabe, *Proposed double-layer target for the generation of high-quality laser-accelerated ion beams*, Phys. Rev. Lett. **89**, 175003 (2002).
13. F. N. Beg, M.-S. Wei, A. E. Dangor, A. Gopal, M. Tatarakis, K. Krushelnick, P. Gibbon, E. L. Clark, R. G. Evans, K. L. Lancaster, P. A. Norreys, K. W. D. Ledingham, P. McKenna, and M. Zepf, *Target charging effects on proton acceleration during high intensity short pulse laser-solid interactions*, Appl. Phys. Lett. **84**, 2766–2768 (2003).
14. F. N. Beg, E. L. Clark, M.-S. Wei, A. E. Dangor, R. G. Evans, P. Gibbon, A. Gopal, K. L. Lancaster, P. A. Norreys, M. Tatarakis, M. Zepf, and K. Krushelnick, *Return current and proton emission from short pulse laser interactions with wire targets*, Phys. Plasmas **11**, 2806–2813 (2004).
15. S. Pfalzner and P. Gibbon, *A hierarchical tree code for dense plasma simulation*, Comp. Phys. Commun. **79**, 24–38 (1994).
16. M. S. Warren and J. K. Salmon, *A portable parallel particle program*, Comp. Phys. Commun. **87**(266–290) (1995).
17. P. Gibbon, W. Frings, S. Dominiczak, and B. Mohr, *Performance analysis and visualization of the N-body tree code PEPC on massively parallel computers*, Proc. Parallel Computing 2005, Malaga (2005).

John von Neumann Institute for Computing

Transition to Turbulence in Magnetohydrodynamic Channel Flow of Liquid Metals

Egbert Zienicke, Thomas Boeck, and Dmitry Krasnov

published in

NIC Symposium 2006 ,
G. Münster, D. Wolf, M. Kremer (Editors),
John von Neumann Institute for Computing, Jülich,
NIC Series, Vol. **32**, ISBN 3-00-017351-X, pp. 341-348, 2006.

http://www.fz-juelich.de/nic-series/volume32

Transition to Turbulence in Magnetohydrodynamic Channel Flow of Liquid Metals

Egbert Zienicke[1], **Thomas Boeck**[2], **and Dmitry Krasnov**[2]

[1] Institut für Physik
Technische Universität Ilmenau, 98684 Ilmenau, Germany
E-mail: egbert.zienicke@tu-ilmenau.de

[2] Fakultät für Maschinenbau
Technische Universität Ilmenau, 98684 Ilmenau, Germany
E-mail: {thomas.boeck, dmitry.krasnov}@tu-ilmenau.de

A pseudospectral flow solver is implemented for the solution of the magnetohydrodynamic (MHD) equations in the quasistatic approximation which is valid for liquid metal flows in experimental and industrial setups. The code is based on a poloidal-toroidal decomposition of the velocity field and well suited for parallelization. Only the transposition of coefficient matrices needed in the Fast Fourier Transformation requires a higher amount of communication between processors. The MHD solver is applied to the problem of transition to turbulence in MHD channel flow. The streak breakdown scenario is investigated numerically for different Reynolds and Hartmann numbers to clear up the details of the transition process and to compare the numerically found critical Reynolds numbers with experimental values. A very good agreement is found.

1 Introduction

The goal of our project is to study wall bounded flow of an electrically conducting fluid under the influence of an external magnetic field. The motivation for these studies are industrial processes where electromagnetic processing of materials (EPM) is applied. This is very useful for casting of liquid metals as well as for growing of semiconductor crystals. The hot melt can be influenced by externally applied magnetic fields. An example is the electromagnetic brake, consisting of a strong, inhomogeneous, external magnetic DC field, that is used to brake the flow of a liquid metal melt. It is widely used in the process of continuous casting of steel. The braking prevents an inclusion of slag from the free surface and also limits the transport of the hot molten steel downward the already cooled slab. For an optimization of the product of the casting process the influence of the magnetic field on the melt flow has to be well understood. Therefore, we have first concentrated on the investigation of the transition to MHD turbulence and of MHD turbulence itself in wall bounded flows. The simplest geometry, for which this is possible, is an infinite slab bounded by a lower and an upper wall. A vertical, homogenous magnetic field is applied normal to the walls. The laminar pressure driven flow in this configuration is known as *Hartmann flow*[1]. The braking effect of the Lorentz force is created by induced currents in the fluid interacting with the external magnetic field. As a result one observes a flat profile in the middle of the channel and two Hartmann layers at the walls, in which current loops are closed and the main velocity gradient is located. The thickness δ of the Hartmann

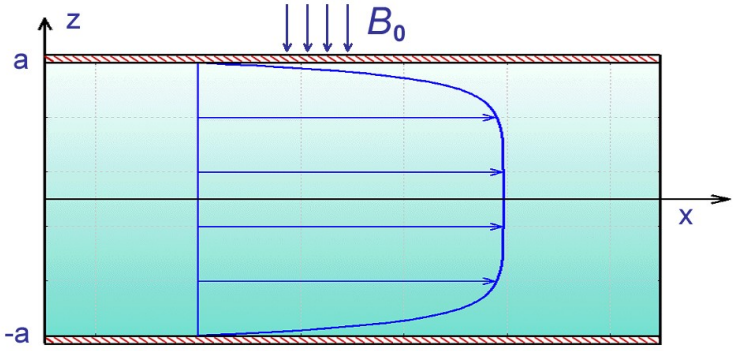

Figure 1. Schematic picture of channel geometry.

layers is determined by the dimensionless Hartmann number Ha:

$$\delta = \frac{a}{Ha} \qquad \text{with} \qquad Ha = B_0 a \sqrt{\frac{\sigma}{\rho\nu}}, \tag{1}$$

where a is the channel half-width, B_0 the imposed magnetic field, σ the electric conductivity, ρ the density and ν the kinematic viscosity. The Hartmann number gives a dimensionless measure of the ratio between the Lorentz force and viscous forces in the flow. For the discussion of the transition to turbulence in section 3 we also introduce the Reynolds number $R = U\delta/\nu$ based on the Hartmann layer thickness and the centerline velocity U.

2 Governing Equations and Code Description

The basic equations are the incompressible Navier-Stokes equations

$$\rho\left(\frac{\partial \boldsymbol{v}}{\partial t} + (\boldsymbol{v}\cdot\nabla)\boldsymbol{v}\right) = -\nabla p + \rho\nu\nabla^2\boldsymbol{v} + \boldsymbol{j}\times\boldsymbol{B}_0, \tag{2}$$

$$\nabla\cdot\boldsymbol{v} = 0, \tag{3}$$

for the velocity field $\boldsymbol{v}$ including the Lorentz force term $\boldsymbol{j}\times\boldsymbol{B}_0$, where $\boldsymbol{B}_0$ denotes the external magnetic field. The induced current $\boldsymbol{j}$ giving rise to the Lorentz force is computed in the quasistatic approximation[2] for low magnetic Reynolds numbers, which is appropriate for the flows found in the laboratory and industrial facilities. It is given by Ohm's law

$$\boldsymbol{j} = \sigma\left(-\nabla\phi + \boldsymbol{v}\times\boldsymbol{B}_0\right), \tag{4}$$

where we have introduced the electric potential ϕ and the conductivity σ. The electric potential is found from the condition

$$\nabla\cdot\boldsymbol{j} = 0 \Rightarrow \nabla^2\phi = \nabla\cdot\left(\boldsymbol{v}\times\boldsymbol{B}_0\right). \tag{5}$$

The boundary condition for the velocity on the channel walls is the no-slip condition $\boldsymbol{v} = 0$. For electrically insulating channel walls the normal component j_n of the electric current

vanishes. This provides the boundary conditions for the Poisson equation of the electric potential.

Our pseudospectral code is based on the so-called poloidal-toroidal representation of the velocity field as

$$\boldsymbol{v}(x,y,z,t) = \boldsymbol{\nabla} \times (\boldsymbol{\nabla} \times \boldsymbol{e}_z \varphi(x,y,z,t)) + \boldsymbol{\nabla} \times \boldsymbol{e}_z \psi(x,y,z,t). \tag{6}$$

This decomposition satisfies the incompressibility condition $\nabla \cdot \boldsymbol{v} = 0$ automatically, and we can therefore eliminate the pressure when we substitute (6) into the Navier-Stokes equations. The evolution equations for the velocity potentials φ and ψ and the electric potential ϕ are of the form

$$\mathcal{M}\partial_t f = \mathcal{L}f + \mathcal{N}(\phi, \psi, \varphi), \tag{7}$$

where $\mathcal{L}$ and $\mathcal{M}$ are linear (spatial) operators, $\mathcal{N}$ is the nonlinearity, and the variable f denotes one of the three variables φ, ψ, ϕ.

Our computational domain is periodic in the horizontal directions x and y with periodicity intervals L_x and L_y. We expand every quantity in a double Fourier series with respect to those coordinates and the basic wave numbers $k_x = 2\pi/L_x$ and $k_y = 2\pi/L_y$. With respect to the vertical direction, Chebyshev polynomials T_p are used (p denotes the order of the polynomial and $2a$ the channel width), i.e.

$$f(x,y,z,t) = \sum_{r=-N_x/2}^{N_x/2-1} \sum_{s=-N_y/2}^{N_y/2-1} \sum_{p=0}^{N_z} \mathrm{e}^{irk_x x + isk_y y}\, T_p(z/a)\, \hat{f}^{(r,s,p)}(t). \tag{8}$$

The numbers N_x and N_y denote the number of Fourier modes with respect to the x and y direction, N_z stands for the number of Chebyshev polynomials and $\hat{f}^{(r,s,p)}(t)$ for the time-dependent expansion coefficients. Upon substitution of the expansions (8) into the partial differential equations (7) we obtain a system of coupled ordinary differential equations for the coefficients $\hat{f}^{(r,s,p)}(t)$. The linear operators $\mathcal{L}$ and $\mathcal{M}$ couple only the expansion coefficients for the same wave numbers rk_x and sk_y. For this reason, we can treat the different wave numbers separately in what follows. The expansion coefficients $\hat{f}^{(r,s,p)}(t)$ with the same r and s are written as a column vector $\hat{\boldsymbol{f}}_{r,s}$ with dimension $N_z + 1$. The systems of differential equations for each set of (r, s) are therefore

$$\boldsymbol{\mathcal{M}}_{r,s}\partial_t \hat{\boldsymbol{f}}_{r,s} = \boldsymbol{\mathcal{L}}_{r,s}\hat{\boldsymbol{f}}_{r,s} + \boldsymbol{\mathcal{N}}_{\boldsymbol{r,s}}(\phi, \psi, \varphi), \tag{9}$$

where we have introduced the indices (r, s) on the linear and nonlinear operators. The nonlinear term $\mathcal{N}$ couples expansion coefficients for different wave numbers and acts therefore not only on $\hat{\boldsymbol{f}}_{r,s}$. To solve the time-evolution problem we apply a finite-difference method with time step Δt. It can be denoted as

$$\begin{aligned} \boldsymbol{\mathcal{M}}_{r,s}\frac{3\hat{\boldsymbol{f}}^{n+1}_{r,s} - 4\hat{\boldsymbol{f}}^{n}_{r,s} + \hat{\boldsymbol{f}}^{n-1}_{r,s}}{2\Delta t} &= \boldsymbol{\mathcal{L}}_{r,s}\hat{\boldsymbol{f}}^{n+1}_{r,s} \\ +2\boldsymbol{\mathcal{N}}_{r,s}(\phi^n, \psi^n, \varphi^n) - \boldsymbol{\mathcal{N}}_{r,s}(\phi^{n-1}, \psi^{n-1}, \varphi^{n-1}). & \end{aligned} \tag{10}$$

The left hand side approximates the time derivative at the time level $n+1$ using the previous two time levels. The nonlinear term is treated using the second-order Adams-Bashforth method, where the prefactors correspond to a linear extrapolation to the time level $n + 1$.

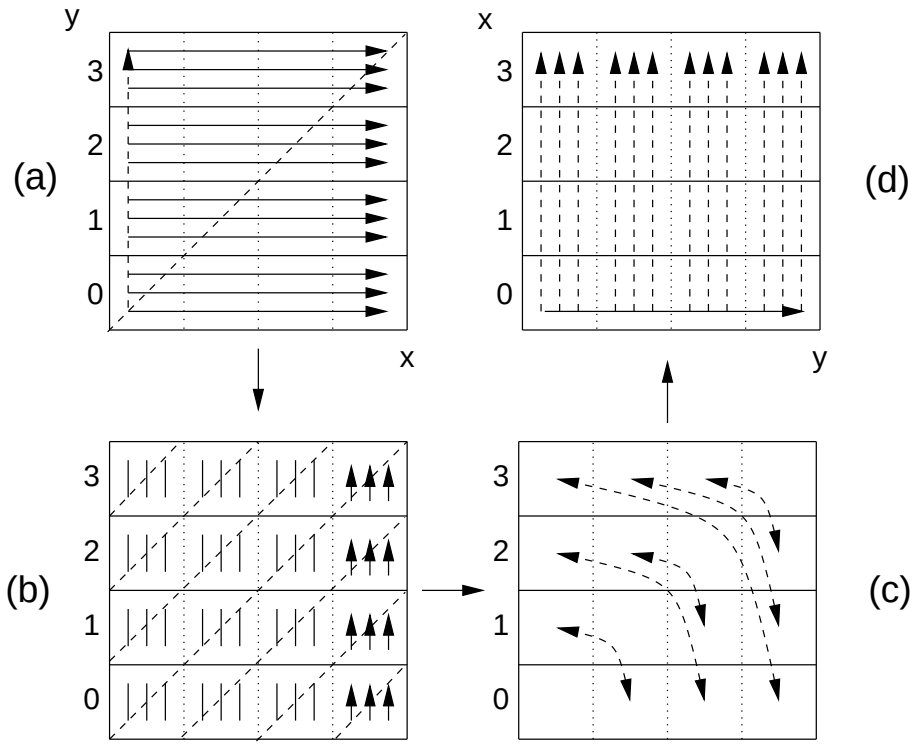

Figure 2. Data array transposition across processes for parallelized FFT. Initial distribution of data is indicated by the full arrows in (a), where the frame boxes correspond to the individual processes numbered from 0 to 3. The dashed arrow indicates that one-dimensional transforms in y direction cannot be computed this way. To remedy this problem, a transposition about the diagonal (shown as dashed line) is necessary. It proceeds by local sub-array transposition (b) and swapping sub-arrays between processes (c) in order to arrive at the desired distribution (d).

This method is second-order accurate in the time step Δt. To find $\hat{\boldsymbol{f}}_{r,s}^{n+1}$ we only have to solve a system of linear equations of dimension $N_z + 1$ with a banded structure.

Most of the computational time is spent on the nonlinear terms $\mathcal{N}$. A direct evaluation of these terms in the spectral representation is neither simple nor computationally efficient. They are therefore calculated in physical space using inverse Fourier transforms, which provide us the values of the variable ϕ, ψ and φ at certain collocation points from the expansion coefficients. Direct Fourier transforms are then used to calculate the expansion coefficients of $\mathcal{N}$ from its values at these collocation points[3].

The parallelization of the numerical algorithm can be accomplished by domain decomposition with respect to the x or y direction. Only the Fourier transforms will then require inter-process communication. In our implementation, the transform proceeds as a successive application of one-dimensional transforms with respect to x, y and z. The transform for the divided direction is avoided by a transposition of the data array containing the expansion coefficients, which is explained in Fig. 2. The transposition requires fast inter-process communication and therefore benefits greatly from using the high-end parallel computers at the NIC.

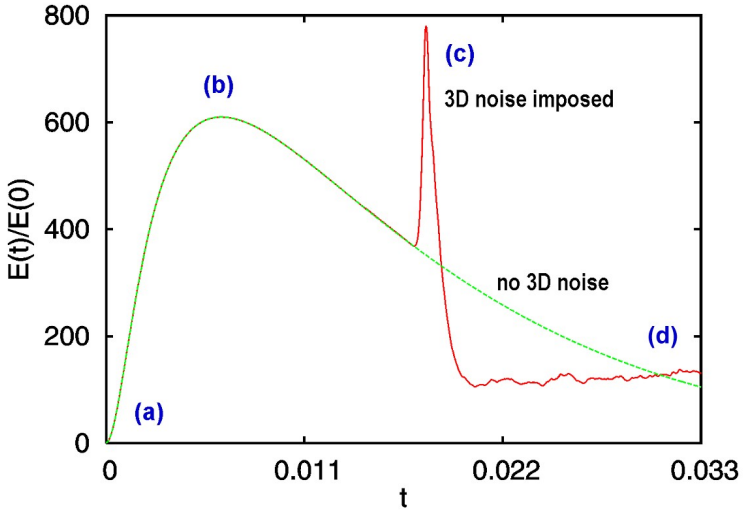

Figure 3. Evolution of the energy of the perturbation from the basic flow profile. The green curve shows the 2D evolution in which the nonlinearity of the Navier-Stokes equation is suppressed. After reaching the maximum the perturbation decays exponentially corresponding to stability of the linear system. A small random 3D perturbation applied at the maximum of the perturbation (marked by (b)) grows exponentially for full 3D evolution of the system and at a certain point the transition to turbulence begins marked by a sharp spike of the perturbation (red curve).

3 Transition by the Streak Breakdown Mechanism

With the pseudospectral code the transition to turbulence in the Hartmann flow was investigated[4,5]. From several experiments it was clear that the linear instability threshold of the Hartmann profile, located at a Reynolds number of $R_c = 48250$ cannot be responsible for the transition to turbulence[6]. The transition was found to be in the range $150 \leq R_c \leq 250$ in the older experiments[7,8] and localized more precisely in a recent experiment[9] at $R_c \approx 380$. Our hypothesis was that the transition to turbulence in this system takes place by the streak breakdown scenario which is one of the possible bypass scenarios proposed for several shear flows in the last decade[10]. The common feature of these scenarios is that they all involve two steps, where the first depends on finite-sized perturbations explaining the fact that one cannot identify a unique critical Reynolds number. Instead, the transition takes place in a whole range of Reynolds numbers.

The streak breakdown scenario, which we tested numerically on the Hartmann flow, takes place in the following way: In a first step we have applied so called optimal disturbances[10] to the basic flow. Optimal disturbances are stable for the linearized Navier-Stokes equation, but they can have a very strong initial growth after which they decay exponentially. The maximum amplification depends on the Reynolds number and can easily attain a value of 2000 measured in units of the initial perturbation energy. For our system the optimal disturbances are streamwise vortices which are located in the Hartmann layer and whose wavelength is of the order of the thickness of the Hartmann layers. To suppress the nonlinearity of the Navier-Stokes equation we forced the flow to stay on a two-dimensional

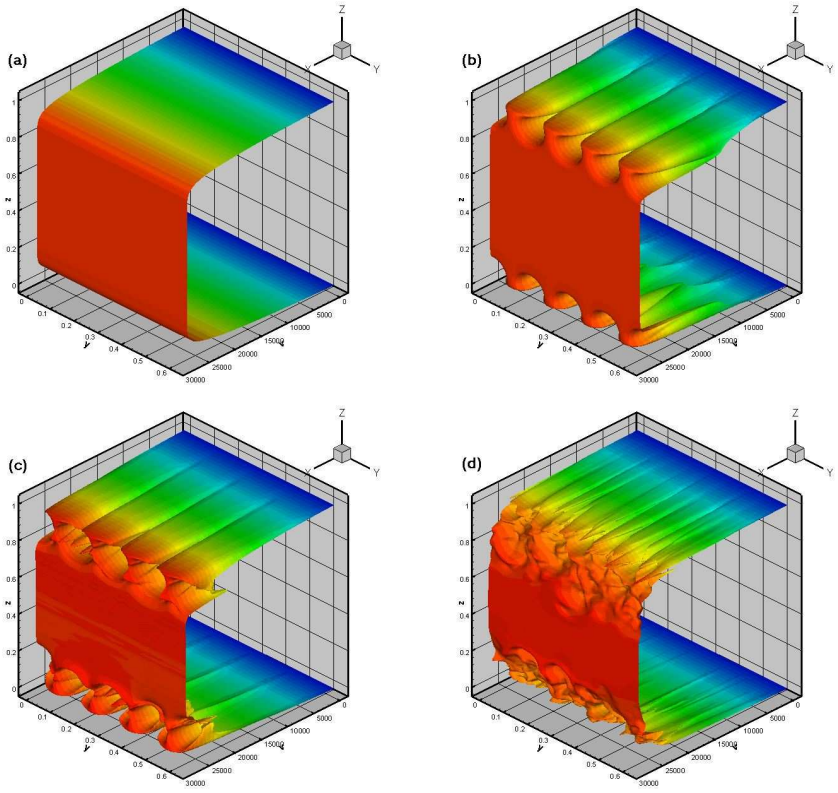

Figure 4. Flow profiles in a plane $x = const$ for four chosen time moments of the streak breakdown scenario at Reynolds number $R = 500$ and Hartmann number $Ha = 40$. (a) Initial condition consisting of laminar Hartmann flow plus 2D-optimal disturbance. The latter is so small that the perturbation is not visible in the profile. (b) After time evolution in two dimensions the 2D-disturbance has reached its maximum energy. The streaks at both boundaries can be clearly seen. (c) After the application of the 3D-perturbation the computation of the time evolution is fully three-dimensional. Here the streak breakdown begins starting the transition to turbulence. (d) The turbulent state has been reached.

evolution by suppressing all Fourier modes belonging to a spacial dependence in streamwise direction. This growth phase can be seen in figure 3 showing the energy evolution of the perturbation. With (a) the initial condition is marked, whose velocity profile can be seen in plot (a) of figure 4. The perturbation of the Hartmann profile in the initial state is too small to be visible. With the growth of the optimal perturbations streamwise streaks in the flow evolve which are characterized by alternating stripes of low and high velocity in spanwise direction (see flow profile (b) of figure 4). If the 2D evolution, suppressing the nonlinearity of the Navier-Stokes equation, is pursued further the energy of the perturbation decays exponentially. This corresponds to the fact that the Hartmann flow is linearly stable.

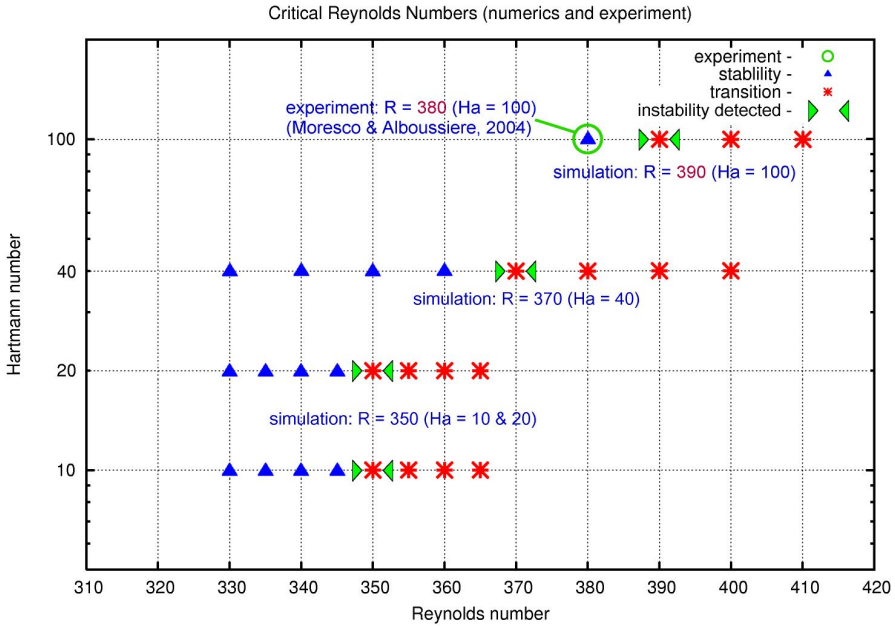

Figure 5. Critical Reynolds number R vs Hartmann number. Filled triangles mark points (R, Ha) in the parameter space, where no transition could be detected independent on the size of 2D- and 3D-perturbations. Empty triangles mark parameter pairs, where a transition by the streak breakdown scenario could be observed. The numerical value of the critical Reynolds number approaches the experimental value for $Ha = 40$ and 100 giving a better agreement with reference[9].

At the time of the maximum ampification of the optimal perturbation a random 3D perturbation is added and the full 3D evolution of the system is switched on in the flow solver. This constitutes the second step of the streak breakdown scenario and allows the nonlinearity of the Navier-Stokes equation to act on the flow which is unstable against small 3D perturbations. Plot (c) of figure 3 shows the profile directly after the application of the 3D random perturbation, and plot (d) is a snapshot of the turbulent state which is reached after the transition phase.

So far, it has been shown that the streak breakdown mechanism is able to trigger transition to turbulence for the Hartmann flow. We find critical Reynolds numbers for the transition that are very close to the experiment of Moresco & Alboussière[9]. We interpret this as a strong indication that the streak breakdown scenario really describes the physics of the transition to turbulence in our system. However, the experiments were carried out in a Hartmann number range between 130 and 1690, which extends to much higher values than our numerical calculations. To close the gap between the Hartmann numbers of our numerical simulations and the experiment we performed a systematic check of stability and instability dependent on Reynolds number R and Hartmann number Ha. This is shown in Figure 5. The black filled triangles denote that for the corresponding R and Ha no transition to turbulence was observed with the two-step scenario, irrespective of how large the 2D-optimal disturbances and 3D-random perturbations were chosen. Blank

triangles mark the runs, where a transition to turbulence could be found with the two-step mechanism with a certain choice of 2D- and 3D-perturbations. The runs for $Ha = 10$ and 20, which were first presented in[4], all yield a critical Reynolds number in the interval $345 < R_c < 350$, which is already very close to the experimental value of $R_c = 380$ found by Moresco & Alboussière. In our recent paper 5 computations for the higher Hartmann numbers $Ha = 40$ and 100 are presented leading to slightly higher values $360 < R_c < 370$ and $380 < R_c < 390$, respectively, for the critical Reynolds number. This is closer to the result of the experiment and closes the gap between numerics and experiment well. As the critical Reynolds number still varies with the Hartmann number the numerical calculations show that the limit of an isolated Hartmann layer is not yet reached for $Ha = 40$ and $Ha = 100$. Because one needs several runs to bracket the critical Reynolds number for a given Hartmann number, it was not possible to treat the case of higher Hartmann numbers (the next would have been $Ha = 200$) with our computational resources.

Acknowledgements

The authors are grateful for financial support of the Deutsche Forschungsgemeinschaft in the framework of the Research Group Magnetofluiddynamics and through an Emmy Noether fellowship (Bo 1668/2-2). Most of the numerical simulations were performed on the computers at the John von Neumann - Institut für Computing.

References

1. J. Hartmann. Hg-dynamics i: Theory of the laminar flow of an electrically conductive liquid in a homogeneous magnetic field. *K. Dan. Vidensk. Selsk. Mat. Fys. Medd.*, 15(6):1–28, 1937.
2. P. A. Davidson. *An Introduction to Magnetohydrodynamics*. Cambridge University Press, 2001.
3. C. Canuto, M. Y. Hussaini, A. Quateroni, T. A. Zang. *Spectral Methods in Fluid Dynamics*. Springer Verlag, 1988.
4. D. S. Krasnov, E. Zienicke, O. Zikanov, T. Boeck, and A. Thess. Numerical study of instability and transition to turbulence in the Hartmann flow. *J. Fluid Mech*, 504:183–211, 2004.
5. E. A. Zienicke, D. S. Krasnov. Parametric study of streak breakdown mechanism in Hartmann flow *Phys. Fluids*, 17:114101, 2005.
6. R. J. Lingwood and T. Alboussiere. On the stability of the Hartmann layer. *Phys. Fluids*, 11:2058–2068, 1999.
7. W. Murgatroyd. Experiments on magnetohydrodynamic channel flow. *Philos. Mag.*, 44:1348–1354, 1953.
8. G. Branover and A. Tsinober. *Magnetohydrodynamics of incompressible fluids*. Nauka, Fys.Mat.Lit., 1970.
9. P. Moresco and T. Alboussiere. Experimental study of the instability of the Hartmann layer. *J. Fluid Mech*, 504:167–181, 2004.
10. P. J. Schmid and D. S Henningson. *Stability and Transition in Shear Flows*. Springer Verlag, 2001.

John von Neumann Institute for Computing

High Performance Simulation of Ideal Quantum Computers

Guido Arnold, Marcus Richter, and Thomas Lippert

published in

NIC Symposium 2006 ,
G. Münster, D. Wolf, M. Kremer (Editors),
John von Neumann Institute for Computing, Jülich,
NIC Series, Vol. **32**, ISBN 3-00-017351-X, pp. 349-356, 2006.

http://www.fz-juelich.de/nic-series/volume32

High Performance Simulation of Ideal Quantum Computers

Guido Arnold[1], **Marcus Richter**[1], **and Thomas Lippert**[1,2]

[1] Central Institute for Applied Mathematics, John von Neumann Institute for Computing
Research Centre Jülich, 52425 Jülich, Germany
E-mail: {g.arnold, m.richter, th.lippert}@fz-juelich.de

[2] Department C, Bergische Universität Wuppertal, 52425 Wuppertal, Germany

1 Relevance of Quantum Computing

Quantum processing of information has become a rapidly evolving field of research in physics, mathematics, computer science, and engineering[1] and has led to substantial progress in quantum computation, quantum communication and control of quantum systems. Quantum computers have become of great interest primarily due to their potential of solving certain computationally hard problems such as factoring integers[2] and searching databases faster than a conventional computer[3]. Candidate technologies for realizing quantum computers include trapped ions, atoms in QED cavities, Josephson junctions, nuclear or electronic spins, quantum dots, and molecular magnets. Grover's quantum search[3] and Shor's quantum prime factorization algorithm[2] have been successfully implemented on systems of up to 7 qubits using liquid NMR techniques[4], experimentally demonstrating the viability of the concept of quantum computation. Recently the first quantum byte has been realized using linear ion traps[5].

In spite of this impressive development, a demonstration that quantum computation can solve a non-trivial problem is still lacking. To be of practical use, quantum computers will need error correction, which requires at least several tens of qubits and the ability to perform hundreds of gate operations. This imposes a number of strict requirements[6], and narrows down the list of candidate physical systems. Simulating numbers of qubits in this range is important to numerically test the scalability of error correction codes and fault tolerant quantum computing schemes and their robustness to errors typically encountered in realistic quantum computer architectures.

2 The Need for Simulation

A physically realizable quantum computer is a complex many-body quantum system. In order to exercise control over many qubits and to suppress the rate at which errors are introduced during a quantum computation, it is in principle necessary to understand the full time evolution of the whole quantum system. Sources of errors are the loss of coherence (decoherence) due to unwanted interaction with the environment[7] and systematic errors due to imperfections of the operational pulse sequences.

In *first principle* simulations the time dependent behavior can be derived from the Hamiltonian of the physical model chosen to describe a specific hardware realization. Pulses are modeled as time-dependent external fields acting on the relevant degrees of

freedom. The coupling of the environment is taken into account by including interactions with other degrees of freedom, also represented by pseudo-spins.

This kind of simulations is needed to analyze decoherence resulting from interactions with the environment. Depending on the assumptions that where made in deriving the microscopic Hamiltonian and/or the manner in which the effect of the coupling to the environment is taken into account, the calculation of the real-time quantum dynamics of the quantum computer readily requires the simulation of systems of many (20-40) qubits over extended periods of time. To perform such very demanding computations, highly optimized simulation code that runs on different high-end computer systems has to be developed.

3 Simulation of Ideal Quantum Computers

In a first step towards realistic quantum computer simulations we implement so called *ideal simulations*, where each gate is modeled by a quantum operation that acts instantaneously on the internal state of the quantum computer, neglecting both implementation imperfections and interactions with the environment. The drawback is that the state of the quantum computer is known only after the application of each gate, but this is sufficient for most algorithmic purposes.

In contrast to a classical bit the state of an elementary storage unit of a quantum computer, the quantum bit or qubit, is described by a two-dimensional vector of Euclidean length one. Denoting two orthogonal basis vectors of the two-dimensional vector space by $|0\rangle$ and $|1\rangle$, the state $|\psi\rangle$ of a **single qubit** can be written as a linear superposition of the basis states $|0\rangle$ and $|1\rangle$:

$$|\psi\rangle_1 = a_0|0\rangle + a_1|1\rangle \; = \begin{pmatrix} a_0 \\ a_1 \end{pmatrix}, \tag{1}$$

where a_0 and a_1 are complex numbers such that $|a_0|^2+|a_1|^2 = 1$. Useful computations require more than one qubit. The state of a quantum computer with N qubits can be represented in the 2^N- dimensional Hilbert space as

$$\begin{aligned} |\psi\rangle_N &= a_{0\ldots00}|0\ldots00\rangle + a_{0\ldots01}|0\ldots01\rangle + \ldots + a_{1\ldots10}|1\ldots10\rangle + a_{1\ldots11}|1\ldots11\rangle, \\ &= a_0|0\rangle + a_1|1\rangle + \ldots + a_{2^N-1}|2^N-1\rangle \\ &= (a_0, a_1, \ \ldots \ , a_{2^N-1})^T . \end{aligned} \tag{2}$$

According to the rules of quantum mechanics any evolution in time means changing the system state unitarily. Each operation on a quantum computer can be described by a 2^Nx 2^N dimensional unitary transformation $U = e^{-iHt}$ acting on the state vector $|\psi'\rangle = U|\psi\rangle$, with the hermitian matrix H being the Hamiltonian of the quantum computer model. In this paper we will not describe any details of quantum computer hardware modeled by appropriate Hamiltonians. It is sufficient to know that an ideal quantum computer can be modeled by simple spin models such as the Ising model associating the two single-spin states *up*$= |\uparrow\rangle$ and *down*$=|\downarrow\rangle$ with the single-qubit basis states $|0\rangle$ and $|1\rangle$[8].

As the unitary transformation U may change all amplitudes simultaneously, a quantum computer is a massively parallel machine. In order to simulate an arbitrary unitary operation on a conventional computer the resulting matrix-vector multiplication requires in the worst case $\mathcal{O}(2^{2N})$ complex valued arithmetic operations.

As in the case of programming a conventional computer, it is extremely difficult to write down explicitly that single one-step operation that transforms the input state into a desired output state. Usually a quantum algorithm consists of a sequence of many elementary gates. These elementary gates are represented by very sparse unitary matrices. The resultant matrix-vector multiplication can be implemented very efficiently and requires typically $\mathcal{O}(2^N)$ arithmetic operations per elementary gate. A small set of elementary **one-qubit gates** (such as the Hadamard gate and the Phase shift gate) and a nontrivial **two-qubit gate** (such as the controlled NOT gate) are sufficient (but not unique) to construct a *universal* quantum computer[9]. In the framework of ideal quantum operations any one-(two-) qubit operation can be decomposed into a sequence of 2x2 (4x4) matrix operations each acting on an orthogonal subspace of the 2^N dimensional Hilbert space.

In the following we describe an efficient parallel simulation of ideal quantum computers on a high-end computer system that allows simulating up to 37 qubits requiring 3 TB of memory and a considerable compute power.

4 Quantum Operations

We will discuss in detail the implementation of a typical one-qubit operation, the Hadamard gate. This gate is often used to prepare the state of uniform superposition. The Hadamard operation on a single-qubit state is defined by

$$|0\rangle \rightarrow \frac{1}{\sqrt{2}}(|0\rangle + |1\rangle)$$
$$|1\rangle \rightarrow \frac{1}{\sqrt{2}}(|0\rangle - |1\rangle).$$

$$H = \frac{1}{\sqrt{2}} \begin{pmatrix} 1 & 1 \\ 1 & -1 \end{pmatrix}.$$

Let us consider a quantum computer consisting of three qubits and its state vector $|\psi\rangle = (a_{000}, a_{001}, a_{010}, a_{011}, a_{100}, a_{101}, a_{110}, a_{111})^T$. Instead of computing the 8x8 matrix appropriate to a Hadamard operation H_q acting on qubit q we can compute $H_q|\psi\rangle$ as given by the scheme in Fig. 1.

From this simple example we can learn some characteristics of any one-qubit operation on a N-qubit quantum computer influencing qubit $q = 0, \ldots, N-1$ by acting on the 2^N-dimensional state vector $|\psi\rangle$:

i) H_q can be decomposed into 2^{N-1} applications of H involving a pair of state vector components (k, l) with relative stride $|l - k| = 2^q$ each.

ii) the (2x2) matrices H operate on orthogonal subspaces of the 2^N- dim Hilbert space. Hence they commute and computations can be done in parallel.

From i) we can derive that with the exception of H_0 all Hadamard gates operate purely on even *or* odd state vector elements. This claim also holds for any other quantum operation that does not involve qubit 0. Thus we will split the state vector $|\psi\rangle$ given by Eq.(2)

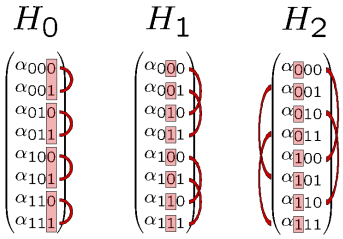

Figure 1. Decomposing a Hadamard transformation acting on qubit q on a three qubit computer $H_q|\psi\rangle$ into four parallel applications of the single-qubit Hadamard gate H. H_0 for example splits into $\binom{a_{ij0}}{a_{ij1}} \mapsto H\binom{a_{ij0}}{a_{ij1}}$ with $i, j \in \{0, 1\}$.

into an even part $|\psi_e\rangle$ and its odd counterpart $|\psi_o\rangle$. For $0 \leq k \leq 2^{N-1} - 1$ we define:

$$|\psi_e(k)\rangle = |\psi(2k)\rangle \quad \text{and} \quad |\psi_o(k)\rangle = |\psi(2k+1)\rangle. \tag{3}$$

This state vector splitting saves half the effort to determine all pairs of indices (k, l) involved in the corresponding one-qubit operation. For H_q with $q > 0$ consecutive pairs (k, l) are mapped to identical pairs $(k', l')_e = (k', l')_o$ with stride $|l' - k'| = 2^{q-1}$. Only H_0 shows an even and odd mixing but trivial pattern that is implemented differently.

5 Parallelization and Computational Resources

More important than gaining half of the integer arithmetics, needed for state vector referencing, the splitting decreases communication overhead in the parallelized simulation code due to sending and receiving *non-stridden* sections of the state vectors $|\psi_e\rangle$ and $|\psi_o\rangle$. This leads to a gain of up to 30% of the wall clock time for one-qubit operations (depending on the system size N and the qubit number q the gate operates on).

The problem of simulating quantum computers is clearly memory bounded. Due to the exponentially increasing amount of memory needed we developed and implemented a large scale simulation on the Juelich SMP supercomputer IBM p690 providing enough memory to handle a 37 qubit system. Simple storage of the state vector in case of a 37 qubit system requires a memory of 2 TB. An efficient implementation of quantum operations on that state vector even requires 3 TB of memory.

The Juelich IBM p690 is a *cluster of 32 compute nodes each containing 32 Power4+ processors* (64bit) and 112 GB memory per node leading to 3.5 TB overall memory available to user access. A quantum computer with up to $N = 32$ qubits reserving at max. $2^{36} = 64$ GB memory to store the complex valued state vector in double precision can be simulated on one node using 32 processors. In the following table we describe the typical simulation requirements depending on the system size N. The last row indicates the overall memory requirements to efficiently simulate quantum operations.

#qubits N	32	33	34	35	36	*37*
#procs	32	64	128	256	512	*1024*
#nodes	1	2	4	8	16	*32*
memory (state vector)	64 GB	128 GB	256 GB	512 GB	1 TB	*2 TB*
memory (operation)	96 GB	192 GB	384 GB	768 GB	1.5 TB	*3 TB*

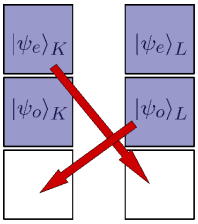

Figure 2. Communication pattern for a one-qubit operation on qubit $q > N - p$. The N qubit state vector is partitioned into 2^p tasks. The computational effort is equally distributed to 2^{p-1} disjoint pairs of tasks (K, L). Task K (L) operates on all odd (even) state vector elements $|\psi_o\rangle_{K+L}$ ($|\psi_e\rangle_{K+L}$).

Partitioning the 2^N- dimensional state vector into $P = 2^p$ *tasks* allows to store the state vector of an N-qubit quantum computer on 2^{N-32} compute nodes equivalent to 2^{N-27} processors with the obvious limitation

$$N - 32 \leq p \leq N - 27. \tag{4}$$

MPI-based exchange of the local $|\psi_e\rangle$ and $|\psi_o\rangle$ allows computation of one-qubit operations on "nonlocal" qubits $q \geq N - p$. In that case the relevant state vector components (k, l), the single-qubit gate operates on, are separated as wide as (or wider than) the number of states per task: $|l-k| = 2^q \geq 2^{N-p}$. As shown in Fig.2 task K (containing all components k) sends its local $|\psi_e\rangle_K$ to task L and receives the local part $|\psi_o\rangle_L$ from task L.

After task K has computed locally the operation $H|\psi_o\rangle_{K+L}$ on all $(k, l)_o$ and task L has computed the even part $H|\psi_e\rangle_{K+L}$ on all $(k, l)_e$ respectively, both send back their results: K sends $H|\psi_o\rangle_L$ to L and receives $H|\psi_e\rangle_K$ from L. After that K contains the updated vectors $|\psi'_{e/o}\rangle_K = H|\psi_{e/o}\rangle_K$. L respectively stores $|\psi'_{e/o}\rangle_L = H|\psi_{e/o}\rangle_L$ in place. Thus the operation requires an intermediate buffer of 2^{N-p-1} elements (half the size of the local state vector). Remember that any one-qubit operation on qubit 0 is local.

- Setting p to the maximum given by Eq.(4) *(finest graining)* means distributing the state vector on all processors of the nodes involved. This is equivalent to a pure MPI parallelization ansatz. For data exchange within a node the MPI-library is mapped to fast shared memory access.

- Choosing the minimal number of tasks given by Eq.(4) *(coarsest graining)* leads to one task per node which means that 32 processors are available to that task in parallel. To do this the core routine (a double loop) is done in parallel by $T = 2^t = 32$ OpenMP threads using shared memory access to the whole node memory of 64 GB reserved for the "local" state vector.

- Any other choice of $p + t = N - 27$ with $t \geq 0$ leads to an *a priori* reasonable *hybrid* parallelization strategy in the sense that all processors of the involved nodes are used for computation.

Our detailed investigation on systems of sizes $N = 32, 33, 34, 35, 36$ shows that different OpenMP parallelization strategies using more than 4 threads per MPI-task fail to reach the efficiency of the pure MPI-parallelization. Since we cannot provide a large enough additional buffer, task K for example is forced to operate "in place" on the state vector parts

$H|\psi_o\rangle_{K+L}$ having write access to a *global=shared* vector. In that case synchronization of different OpenMP threads becomes necessary (within a task) and slows down computation.

Finest graining in the pure MPI-ansatz benefits from simple coding of one qubit operations on nonlocal qubits $q \geq N - p$ with maximal p according to Eq.(4). Since the stride $|l - k|$ is as large as (or larger than) the size of the local state vector stored by each task these gates operate *consecutively on all* components. The compiler can build two streams prefetching the entire local state vector.

Since the memory access dominates the time needed to perform a quantum operation, it is crucial a) to minimize consecutive access to widely separated memory entries and b) to use a simple access pattern allowing for efficient (compiler driven) prefetching. We investigate different ways to code the core routine, that determines the state vector components k, l and performs the computation on local qubits $q < N - p$.

version 1

```
do i=imin,imax,i1
   do k=i,i+i1n-1
      l=k+i1n
      ...
   enddo k
enddo i
```

version 2

```
do i=imin,imax,2
     i2=iand(i,i1n)
     k=i-i2+i2/i1n
     l=k+i1n
     ...
enddo i
```

Recoding of the core routine shifting from version 1 (nested loop) to version 2 (single loop) makes OpenMP loop parallelization simpler but hampers streaming because of additional "jumps" in the sequence of index k. To comprehend this we respectively present a part of a typical sequence of consecutive pairs of state vector elements (k, l) to be read from memory.

version 1	k	**0**	1	2	3	4	5	6	7	**16**	17	18	19	20	21	22	23	**32**
	l	**8**	9	10	11	12	13	14	15	**24**	25	26	27	28	29	30	31	**40**
version 2	k	**0**	2	4	6	**1**	3	5	7	**16**	18	20	22	**17**	19	21	23	**32**
	l	**8**	10	12	14	**9**	11	13	15	**24**	26	28	30	**25**	27	29	31	**40**

To halve the number of co-resident streams to be prefetched from memory we additionally split the computation of $|\psi_e\rangle$ and $|\psi_o\rangle$ into two sequential loops of version 1. This speeds up computation considerably. We measure that our fastest nested OpenMP parallelization of version 1 is about 25% faster than the dense coded version 2. This gain applies to the usage of 1,2,4 and 8 OpenMP threads.

Analyzing the time needed to compute H_q depending on the qubit q the operation acts on (see Fig.3), we can identify three regions according to different speeds of memory access. In case of $T = 1$ we obtain fast computation for $q < N - p = 27$, because all state vector components involved are located within processor memory. Higher timings for $N - p \leq q < N - p + 5 = 32$ arise from intra-node communication. The communication between processors is mapped to shared memory access, which is slower than access to the memory associated to a single processor, but faster than MPI based inter-node communication for $q \geq 32$. Timings for parallelizations using 16 (32) threads per MPI process are not given in Fig.3, since computation gets slower by a factor of about 3 (6) compared to pure MPI. This is due to the machine architecture: each node is built up by 4 multichip modules each containing 8 processors. The memory access within a multichip module is

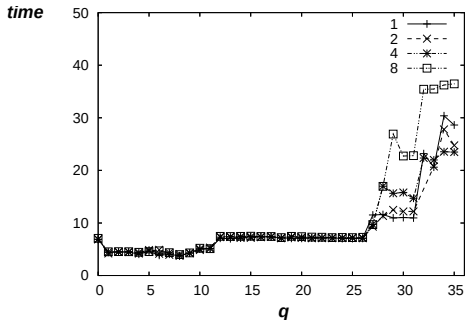

Figure 3. Timings for a Hadamard operation on qubit q at system size N=36 depending on the number of threads $T = 1, 2, 4, 8$ per MPI-task using $T * 2^p = 512$ processors.

faster than getting data from memory associated to another module.

Keeping the local size of the state vector fixed at 2 GB per processor we compare the time needed to compute Hadamard operations on all qubits for different choices for the number of tasks and threads. Fig.4 shows the average timings $t_{av}(N)$ for a complete Hadamard transformation $N^{-1}\prod_{q=0}^{N-1} H_q$ on different system sizes N depending on the number of MPI tasks $P = 2^p$ and different numbers of OpenMP threads $T = 2^t$ respecting $t + p = N - 27$. Multiple measurements indicate a statistical timing error of max 5%. On this error level we identify the usage of one or two OpenMP-threads per MPI-task as optimal. Using 4 threads gives a slightly worse timing.

Taking the best average timing results normalized to $\min(t_{av}(32))$ from the l.h.s of Fig.4 for each system size N we observe the weak (=local size fixed) scaling behavior plotted on the r.h.s of Fig.4. Compared to the optimal (weak) scaling of a constant $\min(t_{av}(N))/\min(t_{av}(32)) = 1$ we still have an efficiency of 70% simulating a 37 qubit-system. The efficiency loss at larger systems is due to the linearly increasing fraction of operations on nonlocal qubits $q \geq 32$ using internode MPI-communication.

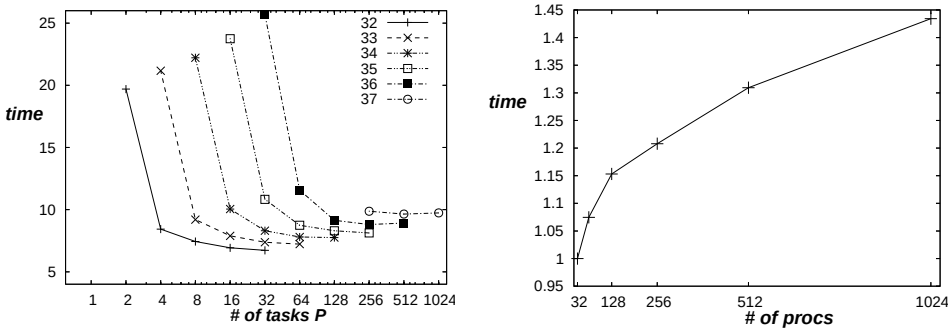

Figure 4. Left: average timings $t_{av}(N)$ for a Hadamard operation on different system sizes N depending on the number of MPI tasks $P = 2^p$ using $T = 2^t$ OpenMP threads with $t + p = N - 27$. Right: scaling of the minimal average timings for the system sizes $N = 32, 33, 34, 35, 36, 37$ using 32,64,128,256,512,1024 processors respectively.

A universal quantum computer also needs two-qubit operations such as the CNOT gate to incorporate qubit interaction. We illustrate the action of the $CNOT_{CT}$ gate on a two qubit state that flips the target qubit T if the control qubit C is set to $|1\rangle$

$$CNOT_{10} \begin{pmatrix} a_{00} \\ a_{01} \\ a_{10} \\ a_{11} \end{pmatrix} = \begin{pmatrix} 1\,0\,0\,0 \\ 0\,1\,0\,0 \\ 0\,0\,0\,1 \\ 0\,0\,1\,0 \end{pmatrix} \begin{pmatrix} a_{00} \\ a_{01} \\ a_{10} \\ a_{11} \end{pmatrix}. \tag{5}$$

Even though the CNOT-gate depending additionally on a control qubit its enfolded compute pattern is very similar to the one given in Fig.1. The stride of the state vector components involved in the operation is given by the target qubit $|l - k| = 2^T$. Without presenting further details our simulator includes load balanced implementations of the controlled NOT and the controlled phase shift operations as fundamental two-qubit gates.

6 Results

An efficient parallelization technique was applied to the memory bounded problem of simulating ideal quantum computers, based on hybrid usage of MPI and inner node OpenMP communication using 1,2 and 4 threads. A compact state vector referencing reduces significantly cache misses produced by irregular access to widely separated parts of the memory. An algorithm built up from elementary one- and two-qubit gates scales very well on the IBM p690 up to the max. available memory of 3 TB using 1024 processors (keeping the local state vector size fixed at 2 GB memory per processor).

7 Acknowledgments

Our presented investigations of simulating ideal quantum computers on high-end classical computer systems are part of an ongoing collaboration with H. De Raedt, K. Michielsen and K. De Raedt from the University of Groningen. We thank them for the initial incentive and a series of very instructive discussions.

References

1. ”Quantum Computation and Quantum Information”, M.A. Nielsen and I.L. Chuang, Cambridge University Press, Cambridge, 2004.
2. P. W. Shor, SIAM J. Computing 26, 1484 (1997).
3. L. K. Grover, Phys. Rev. Lett. 79, 4709 (1997).
4. L.M.K. Vandersypen, M. Steffen, G. Breyta, C.S. Yannoni, M.H. Sherwood, and I.L. Chuang, Nature 414, 883 (2001).
5. H. Haeffner et al., Nature 438, 643-646 (01 Dec 2005).
6. D. P. Di Vincenzo, http://arxiv.org/abs/quant-ph/0002077.
7. W. H. Zurek, Phys. Rev. D 24, 1516 (1981), Phys. Rev. D 26, 1862 (1982); E. Joos and H. D. Zeh, Z. Phys. B 59, 223 (1985).
8. S. Lloyd, Science **261**, 1569 (1993).
9. A. Barenco et al., Phys. Rev. A 52, 3457 (1995).

John von Neumann Institute for Computing

Large Maximum Likelihood Trees

Bui Quang Minh, Le Sy Vinh, Heiko A. Schmidt,
and Arndt von Haeseler

published in

NIC Symposium 2006 ,
G. Münster, D. Wolf, M. Kremer (Editors),
John von Neumann Institute for Computing, Jülich,
NIC Series, Vol. **32**, ISBN 3-00-017351-X, pp. 357-366, 2006.

http://www.fz-juelich.de/nic-series/volume32

Large Maximum Likelihood Trees

Bui Quang Minh[1], **Le Sy Vinh**[2],
Heiko A. Schmidt[1], **and Arndt von Haeseler**[1]

[1] Center for Integrative Bioinformatics Vienna
Max F. Perutz Laboratories, Austria
E-mail: {*arndt.von.haeseler, heiko.schmidt*}*@univie.ac.at*

[2] Central Institute for Applied Mathematics
Research Center Jülich, 52425 Jülich, Germany
E-mail: vinh@cs.uni-duesseldorf.de

We introduce the underlying principles of phylogenetic reconstruction, avoiding all technicalities. Since phylogenetic reconstruction based on DNA-sequence data is a computational expensive undertaking, efficient algorithms are required to suggest reasonable solutions with respect to an objective function. However, even efficient programs like IQPNNI cannot cope in reasonable time with extremely large data sets. Thus, we summarize our results on implementing a hybird parallelization scheme for IQPNNI.

1 Introduction

1.1 Motivation

Charles Darwin (1859) said in his famous *evolutionary theory*[4] that all species have evolved from a common ancestor under the pressure of *natural selection*. The phylogenetic relationship of contemporary organisms is therefore best represented in a *phylogenetic tree*. It is one of the main objectives in biology to reconstruct this tree.

With the advent of molecular biology and the incredible pace at which new sequences from all sorts of life forms are generated, phylogenetic trees are nowadays inferred from DNA-sequence data. DNA-sequences are easy to read. A DNA is simply a long word over a finite alphabet of four letters: $A, C, G,$ and T. This word is subject to subtle changes (mutations) in the course of time. Among mutations, the simple replacement of a letter by another letter is called substitution. These substitution accumulate during time. Thus, a DNA sequence transmitted from a grand-grand-(grand)^k-mother to its contemporary will accumulate mutations. Thus, when comparing the two sequences they will be different. These differences reflect the amount of time (in an apropriate scaling) that went by. As DNA is ubiquitously occurring in all organisms and because DNA cannot be generated de-novo, the history of species can be inferred by simply comparing their DNA sequence. As simple as this sounds, as difficult is the actual implementation of such approaches. We cannot possibly spell out all the details here, and thus refer to the pertinent literature[6].

One of the reasons, why phylogenetic reconstruction is difficult, is the sheer amount of trees as the number of species increases. If we consider only trivalent, unrooted trees, i.e. those trees -from a graph theoretic point of view - with node degree 3 (interior nodes) and 1 (exterior nodes), where the exterior nodes are labelled with a species name, then the number $t(n)$ of trees with $n \geq 3$ exterior nodes is given by

$$t(n) = 1 \cdot 3 \cdot \ldots \cdot (2n-5). \tag{1}$$

Unfortunately, most currently used tree reconstruction algorithms that aim to optimize an objective function belong to the class of NP-hard problems[7, 5, 2], therefore it seems hopeless to actually find the truely optimal tree if the data at hand comprise more than 10 species or so. To overcome the problem of finding the best tree(s), several heuristics have been suggested such as Neighbor Joining[12, 8], Quartet Puzzling[18, 20], Nearest Neighbor Interchange (NNI)[9].

In a series of studies based on computer generated data, it has been shown that these heuristics perform reasonably in terms of speed (computational efficiency) and in terms of accuracy, i.e. the potential to rediscover the tree from the data at the exterior nodes (the sequences). However, for data sets of thousands of species the heuristics turn out to be too slow, to really evaluate the data based on different models of evolution and on different tree reconstruction methods.

Thus, in recent years, people have invoked parallel computing[19] to reduce the computational burden such as fastDNAml[11], TREE-PUZZLE[13], RAxML[16], MrBayes[1], pIQPNNI[10]. These programms make use of several parallel architectures.

The most popular parallel architecture nowadays is a cluster of Symmetric Multi Processors (SMPs). An SMP is a *shared memory* computer in which several processors have access to the same physical memory space. Such SMPs are clustered by a high bandwidth network to create a hybrid system. Processes on different SMP nodes can communicate with each other using the *Message Passing Interface* (MPI)[15], an industry standard for programming on *distributed memory* systems. Inside an SMP, a process can be furthermore divided into several concurrent threads applying OpenMP, a standard for shared memory programming[3]. The SMP cluster motivates the application of hybrid programming models with both MPI and OpenMP in order to take full advantage of the hybrid parallel architecture. Care should be taken as such an approach does not always guarantee an improvement over the pure MPI parallelization[14]. In the following we will summarize our experience to parallelize the IQPNNI program[20].

1.2 The Data

To understand the rest of the paper it is necessary to have a closer look at the data. Consider a dataset of molecular sequences from n species. To account for the different mutation processes acting on the sequences in the course of time, one has to compute first a multiple sequence alignment[21]. We will not explain how a multiple sequence alignment (MSA) is computed. It suffices to say, that a MSA is a two-dimensional table, where each row represents the sequence from an organism and each column represent a position in the sequence

	1	2	3	4	5	6	7	8	9	10	…
Human	A	T	G	C	G	C	A	T	C	A	…
Chimpanzee	A	T	G	C	G	G	G	T	G	T	…
Gorilla	G	C	G	A	G	A	C	T	T	A	…
Rhesus	T	C	C	A	A	G	G	T	C	T	…
⋮	⋮	⋮	⋮	⋮	⋮	⋮	⋮	⋮	⋮	⋮	⋱

Figure 1. An example multiple sequence alignment.

that traces back to a common ancestral position (see Fig. 1). In other words sequences are aligned in a matrix of n rows (i.e. presenting species) and m columns, where m denotes the alignment length. In MSA, columns are also called *sites*. All phylogenetic reconstruction approaches start with this type of data and try to reconstruct a tree that explains the variability observed in the MSA. We are interested in a probabilistic framework, that models the evolutionary process. To this end, we introduce a model of sequence evolution that acts on the tree.

Based on such a model it is straightforward to compute the likelihood of a tree relating these sequences[6] . We obtain the likelihood of the tree as the conditional probability of the data given the tree:

$$L(tree) = P(data|tree). \tag{2}$$

Thus, the likelihood acts as an objective function and we want to find the tree(s) that maximize(s) L given the data, i.e. the MSA. The function $P(\cdot)$ represents the evolutionary model, that is the way we think how sequences change.

The computation of the likelihood can be very expensive. Hence, to keep computation tractable, several assumptions are made. One of them is to assume that every site evolves independently of each other. We also assume that the model P is the same for all parts of the tree and for each position in the sequence. According to this, the likelihood can now be rewritten as the product of the likelihood at each site:

$$P(data|tree) = \prod_{i=1}^{m} P(site_i|tree). \tag{3}$$

Normally, $P(site_i|tree)$ is very close to zero, and to eliminate numerical inaccuracies, one typically takes the logarithm of the likelihood function:

$$\log L(tree) = \sum_{i=1}^{m} \log P(site_i|tree). \tag{4}$$

This so-called likelihood function needs to be maximized by finding the best tree. This is a combinatorial optimization problem.

1.3 IQPNNI Algorithm

The IQPNNI algorithm[20] was recently proposed to reconstruct phylogenetic trees. Compared to other approaches IQPNNI performs well with respect to accuracy. Unfortunately, the extra accuracy is paid for by an increased computing time.

The IQPNNI algorithm comprises two major steps (Fig. 2a). In the *initial step*, an initial tree is obtained based on BIONJ tree[8] combined with fast NNI[9].

In the subsequent *optimization step*, the tree topology is reorganized by Important Quartet Puzzling (IQP)[20] and NNI to improve its likelihood. If the likelihood of the resulting tree exceeds that of the current best tree, then the current best tree is replaced by the new tree. The optimization step is repeated many times to thoroughly search the tree space. Typically the iteration stops after a user-defined number of repetitions.

Because we early noticed that the sequential IQPNNI implementation (sIQPNNI) runs relatively slowly, a pure MPI parallelization (pIQPNNI) was developed[10]. pIQPNNI substantially reduced the running time. We could show that its speedup is nearly optimal for up to 30 processors.

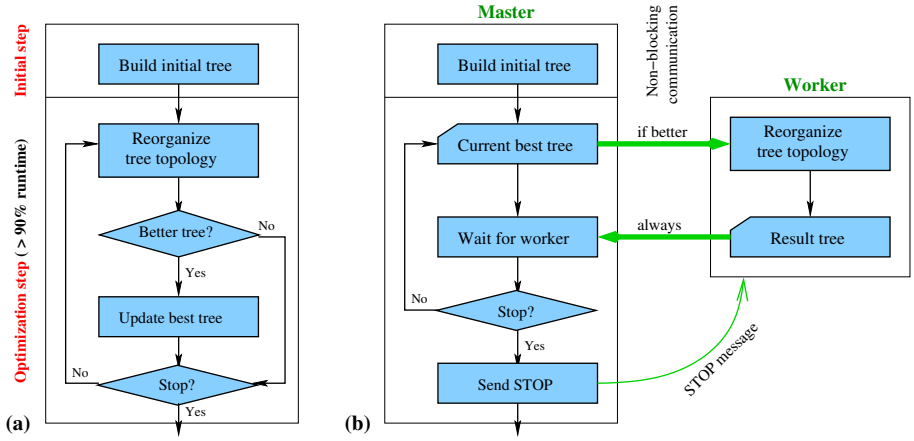

Figure 2. (a) Sequential and (b) MPI parallel scheme of IQPNNI algorithm.

2 Parallelization

2.1 MPI Parallelization

pIQPNNI was described in details in Minh et al.[10] and here we outline the main idea. A preliminary analysis revealed that the optimization step consumes 90% to 99% of the total running time. Hence, the initial step is mainly carried out sequentially and the parallelization of the optimization step was done using a master/worker scheme (Fig. 2b). Starting from the current best tree, every worker runs its own optimization step as explained before. After finishing one iteration, the worker always sends back its resulting tree to the master. The master receives and updates the current best tree if the received tree shows a higher likelihood. In such case, the master will broadcast the better tree to all other workers by non-blocking communication.

The worker now synchronizes with the master and starts the next iteration with its current best tree. In addition, the master checks whether the stop condition applies and, if so, sends a stop message to all workers.

2.2 Hybrid MPI/OpenMP Parallelization

In a hybrid scheme, the program runs with p MPI processes, each process contains t OpenMP threads. That means, a total number of $p \cdot t$ processors are consumed. For p processes, we preserve the master/worker scheme as described in the previous section. For each process, the OpenMP parallelization is done in the following way.

A flow-chart analysis shows, that IQPNNI spends most of its running time (at least 90%) to calculate the likelihood of specific trees. As can be seen from the Equation 4, this involves for-loops, whose iterations are independent of each other. Therefore, we parallelized these loops. Loop-level OpenMP parallelization can be easily employed by adding a pragma directive immediately before any “for” loop involving the computation of the likelihood. A similar approach was also discussed in Stamatakis[17].

By this way, the MPI and the OpenMP codes are independent of each other and one can have a pure MPI or a pure OpenMP version simply by setting $t = 1$ or $p = 1$, respectively. In the subsequent analysis, we tested the program on the JUMP (Juelich Multi Processor) system, a cluster of 41 IBM Regatta p690+ SMP nodes. Each node has 32 Power4+ processors of 1.7 GHz. We used up to 128 CPUs on this supercomputer for the experiments.

3 Performance Analysis

3.1 Datasets

The experiments were conducted on two biological datasets (Table 1). The first data, abbreviated 218dna, comprise a selection of 218 smal subunit ribosomal RNA sequences (*ssu rRNA*) from the Ribosomal Database Project II `http://rdp.cme.msu.edu/`. The second dataset, 74aa, was kindly compiled by colleagues H.A. Schmidt and D. Liebers. This data set consist of amino acid sequences .

Type	Name	#Seqs	#Sites	#Iterations	Initial step	Opt. step	Total
DNA	218dna[a]	218	4182	150	70s	47m:55s	49m:05s
AA	74aa[b]	74	4013	50	77s	32m:41s	33m:58s

[a] prokaryotic sequences from the small ribosomal subunit.

[b] vertebrate amino acid sequences.

Table 1. The datasets used for analysis and sequential runtime of sIQPNNI.

Table 1 also displays the sequential running time of sIQPNNI. The initial step took only about 3% of the whole time on both datasets (about 70 seconds out of 50 and 34 minutes, respectively). Compared to sIQPNNI, the parallel version pIQPNNI needed a batch of about 3 minutes for both datasets using 30 CPUs.

3.2 OpenMP-IQPNNI

Firstly, we measured the performance of the pure OpenMP parallelization on a JUMP node using up to 32 processors as depicted in Fig. 3 using the 218dna and 7aa data. Interestingly, the speedup on both datasets is nearly optimal up to $t = 8$ threads and suddenly drops sharply with more than 8 threads. The runtimes with 16 threads on dataset 218dna and with 32 threads on both datasets are even greater than the sequential time, and thus not shown.

This break-down in overall performance seems to be connected to compiler issues on the JUMP system. Due to the limited time and an expected imbalance with too many threads in the hybrid version, this phenomenon was not further investigated. For that reason, we restricted further analysis to a maximum of 8 threads per process.

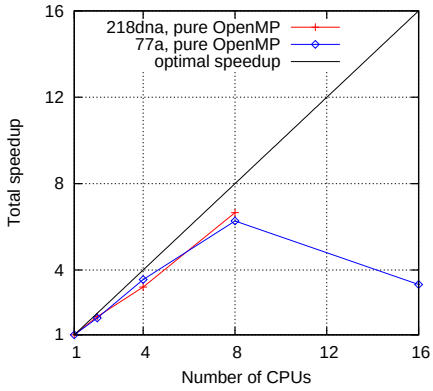

Figure 3. Pure OpenMP speedup for the whole program.

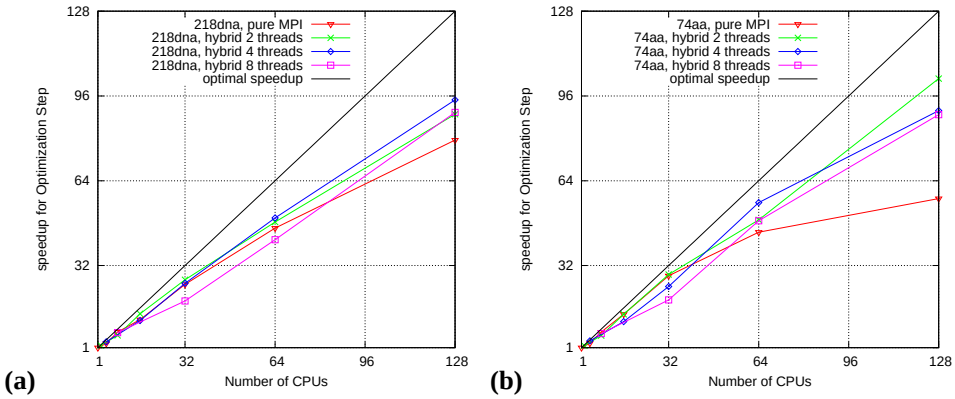

Figure 4. Speedup of optimization step for dataset (a) 218dna and (b) 74aa.

3.3 pIQPNNI vs. Hybrid IQPNNI

We tested the performance of the pIQPNNI against our newly implemented hybrid version with 2, 4 and 8 OpenMP threads per process.

Fig. 4 shows the speedup for the optimization step for 218dna (Fig. 4a) and 74aa (Fig. 4b). For both datasets, the scaling of the pIQPNNI (red line) and the hybrid versions are comparable with a near linear speedup, except that the 8-threads parallelization (pink line) shows a slightly poorer speedup for less than 4 processes, i.e. 32 CPUs. However, this effect disappears with 8 processes or more. This can be explained by the fact that the master process consumes actually only one processor and the other $t-1$ processors are unused. So a fraction of $\frac{t-1}{pt}$ CPUs are idle during the optimization step. The effect will be large if p is small and otherwise becomes more apparent if p increases.

In addition, we observe that the speedup of the pIQPNNI version on the dataset 74aa is quite poor when running on 128 CPUs. This is, however, due to the fact that we only

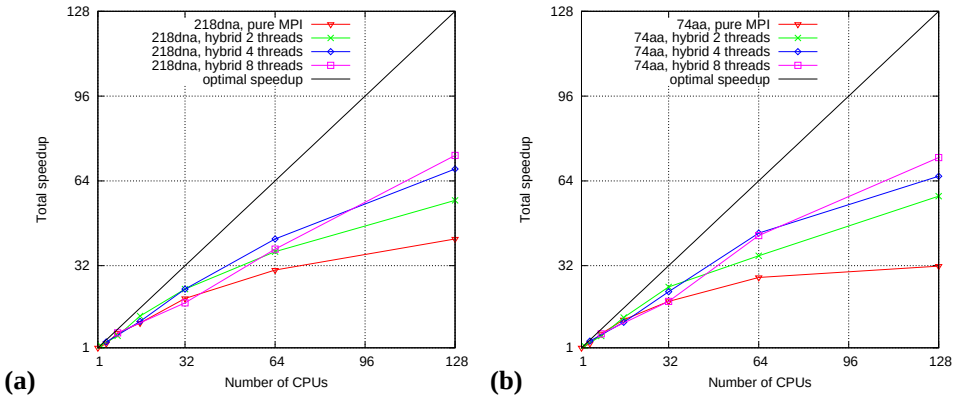

Figure 5. Total speedup for dataset (a) 218dna and (b) 74aa.

#Processes	#Threads	Initial step	Opt. step	Total	Speedup
128	pure MPI	34s	36s	70s	42.1
64	2	20s	32s	52s	56.6
32	4	13s	30s	43s	68.5
16	8	08s	32s	40s	73.6

Table 2. Runtime on dataset 218dna with 128 CPUs.

set the number of iterations to 50 on this dataset. Since each iteration on each worker process consumed roughly the same amount of time, then we would need only 50 workers to finish the whole optimization step. This effect will not occur if we increase the number of iterations to at least the number of MPI processes. Unfortunately, this could not be experimentally tested, due to limitations in computing time.

The total speedup of the pIQPNNI and hybrid-IQPNNI is depicted in Fig. 5. The hybrids with 4- and 8-threads (blue and pink line) scaled best. Whereas the 2-threads hybrid performed a bit worse. The pIQPNNI shows a saturation effect. This shows a tendency that raising the number of threads per process will improve the performance with the growing number of CPUs.

Moreover, the speedup curves are not similar to those for the optimization step since the main part of the initial step is carried out sequentially in the MPI parallelism. As a result, its runtime proportion will be more significant with the increasing number of CPUs. Table 2 displays the running time with 128 CPUs on the dataset 218dna. The initial step of the pIQPNNI consumed 50% of the total time and the time reduction for the hybrid parallelization is mainly due to the shorter time used in the initial step.

4 Conclusions

In this study we gave an overview of different methods to improve the performance of phylogenetic applications. The first is to incorporate efficent heuristics and the second is

to parallelize the curent algorithms. To this end, we illustrate an efficent way to parallelize the IQPNNI algorithm.

Furthermore, we studied how to port a pure MPI parallelization of the IQPNNI algorithm into a hybrid MPI/OpenMP parallelism. The loop-level parallelism is applied to the time-consuming for-loops calculating the likelihood of the phylogenies. These loops appeared at a low level and all MPI functions are called outside the parallel OpenMP regions. Hence, this ensures portability even when the MPI libraries are not thread safe.

Analyses on two real datasets showed improved performance of the hybrid parallelization over the pure MPI on a cluster of SMPs. We tested up to 128 CPUs and 8 threads per process. With large numbers of processors, the pure MPI implementation indicated a saturation effect. In contrast, the hybrid version scaled better, especially when increasing the number of threads. This is due to the fact that we make full use of the capabilities of the hybrid architecture.

Acknowledgements

Support from the guest student programme 2005 at FZJ for B.Q.M is greatly appreciated. A.v.H and H.A.S were formerly members of NIC. The use of computing facilities at ZAM/NIC is gratefully acknowledged.

References

1. G. Altekar, S. Dwarkadas, J. P. Huelsenbeck, and F. Ronquist. Parallel metropolis coupled markov chain monte carlo for bayesian phylogenetic inference. *Bioinformatics*, 20:407–415, 2004.
2. B. Chor and T. Tuller. Maximum likelihood of evolutionary trees is hard. In *Proceedings of the 9th Annual International Conference on Research in Computational Molecular Biology (RECOMB 2005)*, volume 3500 of *Lecture Notes in Computer Science*, pages 296–310, New York, USA, May 2005. ACM Press.
3. L. Dagum and R. Menon. OpenMP: An industry-standard API for shared-memory programming. *IEEE Comput. Sci. Eng.*, 5:46–55, 1998.
4. C. Darwin. *On the Origin of Species by Means of Natural Selection*. John Murray, London, 1859.
5. W. H. E. Day and D. Sankoff. Computational complexity of inferring phylogenies by compatibility. *Syst. Zool.*, 35:224–229, 1986.
6. J. Felsenstein. *Infering Phylogenies*. Sinauer Associates, Sunderland, Massachusetts, 2004.
7. L. R. Foulds and R. L. Graham. The Steiner problem in phylogeny is NP-complete. *Adv. Appl. Math.*, 3:43–49, 1982.
8. O. Gascuel. BIONJ: An improved version of the NJ algorithm based on a simple model of sequence data. *Mol. Biol. Evol.*, 14:685–695, 1997.
9. S. Guindon and O. Gascuel. A simple, fast, and accurate algorithm to estimate large phylogenies by maximum likelihood. *Syst. Biol.*, 52:696–704, 2003.
10. B. Q. Minh, L. S. Vinh, A. von Haeseler, and H. A. Schmidt. pIQPNNI-parallel reconstruction of large maximum likelihood phylogenies. *Bioinformatics*, 21(19):3794–3796, 2005.

11. G. J. Olsen, H. Matsuda, R. Hagstrom, and R. Overbeek. fastDNAml: A tool for construction of phylogenetic trees of DNA sequences using maximum likelihood. *Comput. Appl. Biosci.*, 10:41–48, 1994.
12. N. Saitou and M. Nei. The neighbor–joining method: A new method for reconstructing phylogenetic trees. *Mol. Biol. Evol.*, 4:406–425, 1987.
13. H. A. Schmidt, K. Strimmer, M. Vingron, and A. von Haeseler. TREE-PUZZLE: Maximum likelihood phylogenetic analysis using quartets and parallel computing. *Bioinformatics*, 18:502–504, 2002.
14. L. Smith and M. Bull. Development of mixed mode MPI/OpenMP applications. *Scientific Programming*, 9:83–98, 2001.
15. M. Snir, S. W. Otto, S. Huss-Lederman, D. W. Walker, and J. Dongarra. *MPI: The Complete Reference - The MPI Core*, volume 1. The MIT Press, Cambridge, Massachusetts, 2 edition, 1998.
16. A. P. Stamatakis, T. Ludwig, and H. Meier. RAxML-III: a fast program for maximum likelihood-based inference of large phylogenetic trees. *Bioinformatics*, 21:456–463, 2005.
17. A. P. Stamatakis. An efficient program for phylogenetic inference using simulated annealing. In *Online Proceedings of the 4th IEEE International Workshop on High Performance Computational Biology (HICOMB 2005)*, page 8, Denver, April 2005.
18. K. Strimmer and A. von Haeseler. Quartet puzzling: A quartet maximum–likelihood method for reconstructing tree topologies. *Mol. Biol. Evol.*, 13:964–969, 1996.
19. O. Trelles. On the parallelisation of bioinformatics applications. *Brief. Bioinform.*, 2:181–194, 2001.
20. L. S. Vinh and A. von Haeseler. IQPNNI: Moving fast through tree space and stopping in time. *Mol. Biol. Evol.*, 21:1565–1571, 2004.
21. M. S. Waterman. *Introduction to Computational Biology*. Chapman and Hall, London, 1995.